ADVISORY BOARD

I. Bertini
Università Degli Studi di Firenze
Florence, Italy

A. H. Cowley, FRS
University of Texas
Austin, Texas

H. B. Gray
California Institute of Technology
Pasadena, California

M. L. H. Green, FRS
University of Oxford
Oxford, United Kinddom

O. Kahn
Institut de Chimie de la Matière Condensée de Bordeaux (I.C.M.B.)
Pessac, France

A. Ludi
Universität Bern
Bern, Switzerland

D. M. P. Mingos, FRS
Imperial College of Science, Technology, and Medicine
London, United Kingdom

J. Reedijk
Leiden University
Leiden, The Netherlands

A. M. Sargeson, FRS
The Australian National University
Canberra, Australia

Y. Sasaki
Hokkaido University
Sapporo, Japan

D. F. Shriver
Northwestern University
Evanston, Illinois

K. Wieghardt
Ruhr-Universität Bochum
Bochum, Germany

Advances in
INORGANIC CHEMISTRY

EDITED BY

A. G. Sykes

Department of Chemistry
The University of Newcastle
Newcastle upon Tyne
United Kingdom

VOLUME 43

ACADEMIC PRESS
San Diego New York Boston
London Sydney Tokyo Toronto

This book is printed on acid-free paper. ♾

Copyright © 1995 by ACADEMIC PRESS, INC.

All Rights Reserved.
No part of this publication may be reproduced or transmitted in any form or by any means, electronic or mechanical, including photocopy, recording, or any information storage and retrieval system, without permission in writing from the publisher.

Academic Press, Inc.
A Division of Harcourt Brace & Company
525 B Street, Suite 1900, San Diego, California 92101-4495

United Kingdom Edition published by
Academic Press Limited
24-28 Oval Road, London NW1 7DX

International Standard Serial Number: 0898-8838

International Standard Book Number: 0-12-023643-5

PRINTED IN THE UNITED STATES OF AMERICA
95 96 97 98 99 00 EB 9 8 7 6 5 4 3 2 1

ADVANCES IN INORGANIC CHEMISTRY, VOL. 43

ADVANCES IN THALLIUM AQUEOUS SOLUTION CHEMISTRY

JULIUS GLASER

Department of Chemistry, Inorganic Chemistry, The Royal Institute of Technology (KTH), S-100 44 Stockholm, Sweden

I. Introduction

Thallium, especially Tl(III), has much interesting solution chemistry as this review aims to demonstrate. The element has, however, been much less studied than its neighbors in the periodic table. There are several reasons for this. The chemistry of thallium(I) (s^2) is relatively limited, and it is reminiscent of the alkali metal ions. Thallium in the oxidation state II (s^1) is very unstable and difficult to study. Thallium-(III) is the most interesting oxidation state, but it is a strong oxidant with reduction potential e° for the Tl_{al}^{3+}/Tl_{aq}^{+} couple of +1.25 V vs nhe (*1*). A large part of its rich chemistry is dominated by redox reactions. Moreover, the aqua Tl^{3+} ion is a very strong Brønsted acid, $pK_a = 1.14$ in 3 M $NaClO_4$ (*2, 3*), and is the most acidic three-valent metal ion (*4–6*). Thus, in the absence of complexing ligands, thallium(III) is partially

Copyright © 1995 by Academic Press, Inc.
All rights of reproduction in any form reserved.

hydrolyzed even in 1 M $HClO_4$ and may already precipitate as Tl_2O_3 at pH 1. These circumstances help to explain why thallium is more difficult to study in aqueous solution than other metal ions.

A further point which may have impeded studies of the chemistry of thallium is its reputation as a poison. The most significant contribution to this fame is probably Agatha Christie's novel *The Pale Horse* (*7*), which describes an almost commercial enterprise concerned with poisoning people upon order, preferably rich uncles and aunts. The realistic description of the thallium-caused death of victims in this novel may have prompted others to use thallium compounds in an equally unhealthy way (*8–10*). This reputation, combined with the low natural abundance of thallium, has resulted in relatively few applications; except for some uses in medicine, thallium compounds have been used mainly as rodenticide and depilatory materials. It is now clear, however, that thallium compounds are not more toxic than those of many other common elements. For example, a person has to *consume* between 0.8 g (*11–14*) and 1.7 g (*15, 16*) of thallium(I) sulfate before this proves fatal. There are many quite widely used substances with about the same toxicity, e.g., nickel sulfate, silver nitrate, vanadium pentoxide, hydroxylamine or dinitro-*p*-cresol (*17*), and many widely used organic substances which are very much more toxic (*17*).

In earlier work three areas have attracted attention:

1. During the 1950s and 1960s, a large number of reactions involving electron transfer between thallium and other metal ions in aqueous solution were investigated by the groups of, e.g., Dodson, Halpern, Higginson, Nord-Waind, Sutin, and others. Such studies were largely concerned with the question of the formation of thallium(II) as an intermediate in redox interconversions, and the nature of two-electron exchange processes. These have been extensively reviewed (*15, 18–22*).
2. Thallium compounds have been found very useful in preparative organic chemistry: for example, thallium(I) ethoxide can be used as a strong base; thallium(III) trifluoroacetate as a good electrophilic reagent; and thallium(III) nitrate as an oxidizing agent. Such reagents are easy to make, react often at mild temperatures and offer simple one-step procedures. Several papers on this and related subjects have appeared (*13, 15, 23, 24*).
3. The extensive chemistry of organothallium compounds, a number of which are water-soluble, has been known for many years (*13, 15, 25–30*).

Except for these three topics, thallium chemistry has been explored much less than that of most elements. During the last three decades

some treatises dealing with the aqueous solution chemistry have appeared (*15, 16, 25, 30–33*). Thallium and its compounds, however, generally receive only a brief mention in the textbooks of inorganic chemistry. The book by Lee (1971) gives an excellent account of the chemistry at that time (*15*) and is briefly updated in sections of the more recent standard works *Comprehensive Coordination Chemistry* (*33a*) and *Encyclopedia of Inorganic Chemistry* (*33b*).

The increasing interest in thallium chemistry is due to several distinct applications. Besides the above-mentioned redox properties used in organic preparative chemistry and for model studies of electron transfer reactions, it can be perceived that thallium has found applications as a model for the general behavior of metal ions. For example, Tl^+ is of particular interest because of its importance as a probe for the role of alkali metal ions. The ionic radius of Tl^+, r_{Tl^+} = 1.47 Å, is only slightly larger than k_{K^+} = 1.33 Å, and approximately the same as r_{Rb^+} = 1.47 Å (*34*). Because of the ease with which Tl^+ can be monitored by spectroscopic (*35, 36*), fluorescence (*37*), polarographic (*38*), and especially nuclear magnetic resonance (NMR) methods (*39–41*), in sharp contrast to, e.g., alkali metal ions, this ion is well suited for use as a probe for potassium in biological systems (*35, 42–44*). In fact, Tl^+ has been found to activate a number of K^+-activated enzymes (*45*).

The chemistry of thallium has also been studied for its potential contribution to environmental pollution. Even though the annual world production of thallium is probably negligible in this respect (~1000 times less than mercury, and ~1,000,000 times less than lead), the element is released to the environment mainly through coal-burning power plants (*33b*). Therefore, it has been considered important to follow thallium's further fate in the natural environment, and a large number of thallium compounds have been characterized with this motivation (*46–48*).

Recent research on thallium compounds has been stimulated by the preparation of several thallium-containing high-temperature superconductors: For example, the compound with the composition $Tl_2Ca_2Ba_2Cu_3O_{10}$ becomes superconducting at temperatures as high as 125 K, which allows cooling by liquid nitrogen rather than by the expensive helium (*49*). The interest in thallium chemistry has also been fueled by several high-technology applications (*50*):

- Increasing demand for thallium as an ingredient of glass fiber in communication systems
- Photocells and other photosensitive devices utilizing the fact that

the electrical conductivity of thallium sulfide changes on exposure to light

- Discriminator circuits for γ-ray scintillators, in which the central part is an alkali halide crystal containing a minute amount of thallium
- Most recently, preparation of some Tl–oligometallic compounds for their potential use in solar energy conversion to electrical energy (photovoltaic cells)

During the last decade or two, ^{205}Tl NMR spectroscopy has become the most powerful tool for studying thallium chemistry and therefore deserves a dedicated comment. ^{205}Tl NMR has been shown to be very useful in inorganic chemistry in general, and in aqueous thallium solution chemistry in particular. Its considerable sensitivity permits investigations of dilute thallium solutions, down to micromolar concentrations. The huge ^{205}Tl NMR chemical shift region (several thousand parts per million), the high gyromagnetic ratio, and the relatively narrow signals (usually 5–35 Hz), in connection with the high magnetic fields available, have two important consequences: (1) spectral resolution is very good, and (2) many chemical systems appear in the slow exchange regime, which facilitates both kinetic studies of fast chemical reactions and investigation of thermodynamic properties of thallium solutions. The large spin–spin coupling constants (up to 57,000 Hz) (*51*) serve as a powerful structural probe. In this review, several examples of recent applications of ^{205}Tl NMR spectroscopy for studying aqueous solution chemistry will be discussed.

The current review is concerned mainly with the advances in thallium aqueous solution chemistry during the past 25 years. The chemistry of thallium in organic and organometallic chemistry has been covered by several recent review articles and book chapters (*13, 23–30, 52*); therefore, this subject will not be discussed here. The coverage of the literature will be extensive but not exhaustive. Also, since it is not possible to satisfactorily cover all work on this subject published during the time period within the scope of this review, the choice of the material is admittedly influenced by the scientific interests of the reviewer.

II. Complex Formation Equilibria

A. Thallium(I)

The aqueous chemistry of the complexes formed by the stable thallium(+) ion is relatively easy to study and, accordingly, it is quite well

known. Thallium(+) has an ionic radius and enthalpy of hydration similar to those of the large alkali metal ions potassium and rubidium. On the other hand, thallium(I) has much larger polarizability (is a softer cation) and has several properties similar to those of silver(I) and lead(II). For example, TlOH is a water-soluble base which is weaker than KOH or RbOH. Thallium(I) halides have low solubility, change their color from white to yellow in the order TlCl, TlBr, TlI, and are light-sensitive, like the silver halides. The weak complex formation with the halide ions follows the same order as that for silver(I) [cf. Table I and Lee (*15*)]. Like the (larger) alkali metal ions, Tl^+ is only weakly hydrated in aqueous solution (*53*) (see Section III,A) and its low tendency to form complexes constitutes the basis for the ^{205}Tl NMR chemical shift scale: Since the chemical shifts of aqueous solutions of different Tl(I) salts extrapolate to the same value at infinite dilution (*54*), this value corresponds to the free hydrated Tl^+ ion and is set equal to 0 ppm in ^{205}Tl NMR spectroscopy.

Most of the complexes of thallium(I) are very weak. This fact is in itself an obstacle in determining their stability constants: In order to obtain substantial complex formation, a large excess of the complexing ligand must be added. This changes the quality of the ionic medium, and thus, the activity coefficients of the studied species (see Fig. 1 below). For example, in the study of complex formation between Tl(I) and Cl^-, Nilsson (*55*) varied the chloride concentration up to 4 M, thus replacing completely the ionic medium anions (4 M $NaClO_4$). Whereas most of the equilibrium constants for thallium(I) complexes determined before 1970 were given in perchlorate medium, it has been shown that F^- is better as a noncomplexing ion (*56*). The stability constant for the species TlF is 0.00 ± 0.06 M^{-1} (*56*), whereas the stability constant calculated for the complex $TlClO_4$ in aqueous 1 M NaF is 0.32 ± 0.07 M^{-1} (*55–57*). These values are difficult to determine and thus should be treated only as estimates, since the effects caused by the changing activity coefficients (and liquid junction potential in potentiometric determinations) are not easy to assess. However, in most cases the difference in the stability constants of Tl(I) complexes determined in the two "noncomplexing" ionic media is probably negligible. A typical distribution of Tl(I) complexes in aqueous solution is shown in Fig. 1.

Even if many of the stability constants of thallium(I) complexes in aqueous solution have been determined before the time period covered by this review (*58*), a selection of constants is presented in Table I (*59–68*), since they are of interest for investigating several other properties of thallium(I) complexes (see, for example, Sections III,A, IV,A,1, and V). Most of the known stability constants for the complexes of

TABLE I

OVERALL STABILITY CONSTANTS FOR THALLIUM(I) COMPLEXES IN AQUEOUS SOLUTION AT 25°C[a]

(a) Inorganic ligands

Ligand	n	β_n	Medium	Method	Ref.
CO_3^{2-}	1	3.23 ± 0.33	I = 3.4 M (Na_2CO_3 + $NaClO_4$ + NaOH)	solubility[b]	*59*
	2	1.30 ± 0.38	same	same	*59*
CN^-	1	0	4 M $NaClO_4$	potentiometry and solubility	*55*
N_3^-	1	2.5	2 M $NaClO_4$	polarography	*60*
NH_3	1	10 ± 1	1.2 M NH_4ClO_4	potentiometry	*61*
	2	~1	same	same	*61*
NO_3^-	1	0.65 ± 0.05	1.0 M KF	polarography	*57*
NO_3^-	1	0.37 ± 0.04	4.0 M KF	same	*57*
PO_4^{3-}	1	$\log\beta$ = 2.41 ± 0.1	0.15 M $NaClO_4$	spectrophotometry	*62*
HPO_4^{2-}	1	$\log\beta$ = 0.73 ± 0.1	same	same	*62*
$P_2O_7^{4-}$	1	$\log\beta$ = 3.05 ± 0.04	same	same	*62*
$HP_2O_7^{3-}$	1	$\log\beta$ = 2.34 ± 0.1	same	same	*62*
OH^-	1	0.15	0	solubility	*63*
SCN^-	1	1.4 ± 0.3	4 M $NaClO_4$	solubility	*55*
	2	1.0 ± 0.2	same	same	*55*
	3	0.33 ± 0.06	same	same	*55*
	4	0.14 ± 0.05	same	same	*55*
SO_4^{2-}	1	2.2	2 M $NaClO_4$	polarography	*60*
F^-	1	0.00 ± 0.06	0.5 M $NaClO_4$	solubility	*56*
Cl^-	1	2.1 ± 0.1	1 M KF	polarography	*57*
Cl^-	1	1.0 ± 0.2	4 M KF	^{205}Tl NMR	*41*
	2	0.25 ± 0.05	same	same	*41*
Cl^-	1	0.8 ± 0.2	4 M $NaClO_4$	solubility	*55*
	2	0.16 ± 0.05	4 M $NaClO_4$	same	*55*
	3	0.02 ± 0.01	4 M $NaClO_4$	same	*55*
ClO_4^-	1	0.32 ± 0.07	0.5 M $NaClO_4$	solubility	*56*
Br^-	1	2.1 ± 0.4	4 M $NaClO_4$	solubility	*55*
	2	1.4 ± 0.3	same	same	*55*
	3	0.5 ± 0.2	same	same	*55*
	4	0.09 ± 0.04	same	same	*55*
Br^-	1	4.6 ± 0.3	1 M $LiClO_4$	solubility	*64*
	2	2.4 ± 0.3	same	same	*64*
Br^-	1	3.8 ± 0.2	4 M $LiClO_4$	same	*64*
	2	1.9 ± 0.2	same	same	*64*
	3	1.0 ± 0.2	same	same	*64*
I^-	1	1.4 ± 0.2	4 M $NaClO_4$	solubility	*55*
	2	1.0 ± 0.2	same	same	*55*
	3	0.35 ± 0.05	same	same	*55*
	4	0.12 ± 0.04	same	same	*55*
I_3^-	1	730	0.01 M $HClO_4$	spectrophotometry	*65*

(continues)

TABLE I (*Continued*)

(b) Organic ligands

Ligand	n	β_n	Medium	Method	Ref.
$(ADP)^{3-}$	1	1.32 ± 0.1	0.15 M $NaClO_4$	potentiometry	*62*
$(ATP)^{4}$	1	1.99 ± 0.1	0.15 M $NaClO_4$	potentiometry	*62*
L-Asparagine	1	2.50 ± 0.04	0.1 M $LiClO_4$	potentiometry	*66*
	2	4.00 ± 0.10	same	same	*66*
$(Citrate)^{3-}$	1	1.36 ± 0.1	0.15 M $NaClO_4$	spectrophotometry	*62*
Cryptate[c] (2,1,1)	1	3.19 ± 0.10	0.05 or 0.1	potentiometry[d]	*67*
(2,2,1)	1	6.8	same	same	*67*
(2,2,2)	1	5.5–6.64 ± 0.05	same	same	*67*
$(2_B,2,2)$	1	5.84 ± 0.10	same	same	*67*
$(2_B,2_B,2)$	1	4.61	same	same	*67*
$(EDTA)^{4-}$[e]	1	6.53[f]	0.1 M KNO_3	potentiometry	*68*[g]
L-Glutamine	1	2.35 ± 0.07	0.1 M $LiClO_4$	potentiometry	*66*
	2	4.05 ± 0.10	same	same	*66*
$(Malonate)^{2}$	1	0.54 ± 0.1	0.15 M $NaClO_4$	spectrophotometry	*62*
$(NTA)^{3-}$[h]	1	4.42 ± 0.04	0.15 M $NaClO_4$	spectrophotometry	*62*
$(Oxalate)^{2-}$	1	0.86 ± 0.1	0.15 M $NaClO_4$	spectrophotometry	*62*
$(Ribosephosphate)^{2-}$	1	0.87 ± 0.15	0.15 M $NaClO_4$	spectrophotometry	*62*

[a] $\beta_n = \dfrac{[TlX_n^{1-n}]}{[Tl^+][X^-]^n}$ (in molar units).

[b] 20°C, pH = 12.5 ± 0.1.

[c] Formulas of the cryptate ligands are shown in Fig. 2, Section II,A.

[d] Based on K values for Ag^+ cryptate complexes.

[e] $(EDTA)^{4-}$: ethylenediamine-*N*,*N*,*N*′,*N*′-tetraacetate^{4-}.

[f] At 20°C.

[g] Stability constants for several other polyaminocarboxylate complexes of Tl(I) have also been determined.

[h] $(NTA)^{3-}$: nitrilotriacetate^{3-}.

thallium(I) with inorganic ligands are cited in Table I; for organic ligands not mentioned in the table, the reader is referred to Refs. (*4, 5, 58, 62, 69*).

B. THALLIUM(II)

Several redox reactions involving Tl(III) in aqueous solution have been extensively studied (see Section I and IV,B). Some of these have been proposed to proceed via Tl(II) as an intermediate, e.g., the reaction with Fe(II) (*70,71*). Therefore, to understand the mechanisms of such redox reactions, it has been of interest to ascertain the chemistry of thallium(II). Thallium(II) can be produced in aqueous solution by reduction of Tl(III) with hydrogen atoms or by radiolysis of aqueous solutions

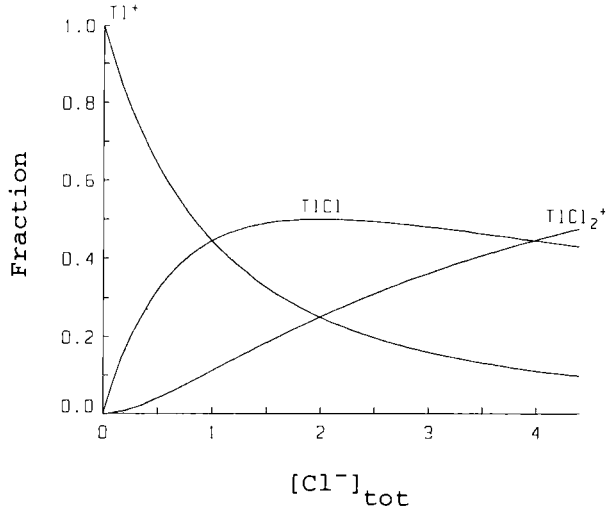

FIG. 1. Fraction of thallium(I) present in various complexes in aqueous solutions containing 1.5 mM Tl(I) and a chloride concentration varying in the range 0–4 M. Ionic medium: 4 M KF (*41*).

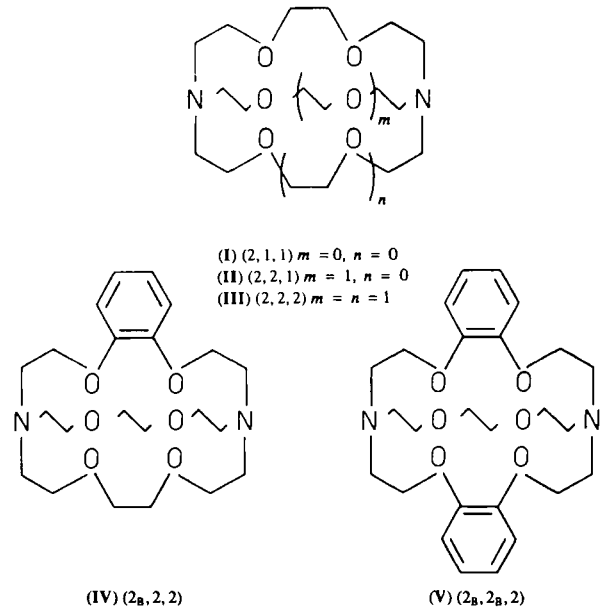

FIG. 2. Structures of some cryptate ligands (stability constants of their complexes with Tl(I) are given in Table I; ligand exchange for these complexes is discussed in Section IV,A,1). From Cox *et al.* (*67*).

of Tl(I) (*72, 73*). However, thallium(II) is a difficult ion to study: It is a very powerful oxidizing agent (standard potential +2.22 V) (*74*), and the equilibrium for the disproportionation reaction,

$$2Tl_{aq}^{2+} \rightleftharpoons Tl_{aq}^{+} + Tl_{aq}^{3+} \quad (1)$$

lies very far to the right, $K = 6.2 \times 10^{31}$ (*71*). [The redox chemistry of Tl(II) is discussed in Section IV,B.] The limited information available on Tl(II) equilibrium chemistry has been obtained from pulse radiolysis investigations, mainly by Dodson and co-workers (*71, 72, 74–83*).

The most substantial investigation of thallium(II) species in aqueous solution is that of Dodson and Schwarz, who studied equilibria and kinetics of Tl(II)–Cl^- complexes (*77*). On the basis of some (reasonable) assumptions, they have calculated the stepwise stability constants K_n for the three $TlCl_n^{2-n}$ complexes, $n = 1, 2, 3$, in 1 M $HClO_4$ and estimated $K_4 = 1\ M^{-1}$ from the ratios between the stability constants K_n for $Tl^{III}Cl_n^{3-n}$ and $Tl^{II}Cl_n^{2-n}$. The absorption spectra of the *individual* Tl(II) chloride complexes have been derived from their stability constants in combination with the experimental spectra recorded for solutions with varying composition. Absorption maxima were found at 263 and 342 nm for $TlCl^+$, at 280 and 342 nm for $TlCl_2$, and at 304 and 362 nm for $TlCl_3^-$. An interesting observation was the 10-fold increase of the extinction coefficient (at ~340 nm) of the Tl(II) solution in 1 M perchloric acid upon addition of a small amount of chloride ion ($[Cl^-] = 10^{-4}$ M) (*77*).

Farver and Nord (*84*) have found that Tl(II)-2,2′-bripyridyl is formed at a dropping mercury electrode when thallium(III)-2,2′-bipyridyl complexes in 0.1 M KNO_3 solution are reduced at low thallium concentrations (<1 mM) and pH >5. They suggested that Tl(II) complexes with other chelating agents (N and O donors) could probably also be observed polarographically.

The few known stability constants of Tl(II) complexes are collected in Table II (*85, 86*). When the values of the corresponding equilibrium constants are compared for Tl^I, Tl^{II}, and Tl^{III} (cf. Tables I–III) it can be noted that the coordination of thallium(II) is intermediate between (Tl(I) and Tl(III). The stability of the chloro complexes follows the order $Tl^ICl_n^{1-n} \ll Tl^{II}Cl_n^{2-n} \ll Tl^{III}Cl_n^{3-n}$, and the same order is valid for the acid strength of the hydrated thallium ions. Coulombic interactions of the differently charged metal ions are probably the main reason for this effect, but other properties (polarizability, lone-pair effect) certainly play a role. It is probably safe to assume also that the softness

TABLE II

OVERALL STABILITY CONSTANTS FOR THALLIUM(II) COMPLEXES IN AQUEOUS SOLUTION AT 25°C[a]

Ligand	n	$\log \beta_n$	Medium	Method	Ref.
Cl^-	1	4.8	1 M $HClO_4$	pulse radiolysis (spectrophotometry)	*77*
	2	8.1	same	same	*77*
	3	9.2	same	same	*77*
	4	~0	same	same	*77*
OH^-[b]	1	−4.6 ± 0.2	0	pulse radiolysis (conductivity, spectrophotometry)	*85*
	2	−7.7 ± 0.2	0	same	*86*

[a] $\beta_n = \dfrac{[TlX_n^{2-n}]}{[Tl^{2+}][X^-]^n}$ (in molar units).

[b] $\beta_n = \{[Tl(OH)_n^{2-n}][H^+]^n\}/[Tl^{2+}]$; 21°C.

(*87–89*) of the three thallium ions follows the trend $Tl^{3+} > Tl^{2+} > Tl^+$, contrary to the usual situation, namely that large cations are softer than small ones.

C. THALLIUM(III)

A number of equilibrium constants for complexes of thallium(III) in aqueous solution have been reported (*4, 6, 58, 64, 90–109*) and a limited selection is given in Table III (*110–114*). Studies of the chemistry of Tl(III) are difficult because of the strong hydrolytic and oxidative properties of the Tl_{aq}^{3+} ion. Despite this, most of the constants gathered in the Table are certainly reliable. However, the existence of only three azide complexes, $Tl(N_3)_n^{3-n}$, n = 1–3 (*93*) quoted in Table III, is surprising in the light of the evidence for four-coordinated ligands in complexes as $Tl(CN)_4^-$, $TlBr_4^-$, TlI_4^-, and six in $TlCl_6^{3-}$; see later discussion. In the following, only some points of interest will be discussed.

1. General Remarks

The starting solution for studies of aqueous thallium(III) compounds can be prepared by dissolving commercial Tl_2O_3 in a mineral acid. However, because of the insolubility of the oxide, this procedure may be tedious and normally works only for the preparation of dilute Tl(III)

solutions. More concentrated solutions are prepared by oxidation of thallium(I) compounds. Although the oxidation of the thallium(I) halide compounds poses no problems when oxidation is by the corresponding halogen, the preparation of noncomplexed Tl^{3+} is less straightforward. It is usually performed by anodic oxidation of Tl^{+} according to the procedure of Biedermann (*2*), or using its slightly modified version (*115*). However, in the paper of Csányi *et al.* (*116*) another procedure is outlined. Thallium(I) can be oxidized by hydrogen peroxide in weakly alkaline medium and the resulting Tl_2O_3 dissolved to the desired concentration in perchloric acid. In contrast to the material obtained with other oxidants, Tl_2O_3 prepared in this manner is readily soluble even in dilute acid. The thallium(III) perchlorate solutions obtained via the two methods (i.e., electrolysis and H_2O_2 oxidation) exhibited identical kinetic behavior (*116*).

Another observation can also be mentioned in this context. Csányi *et al.* (*116*) have observed that there was a difference in the rate of the reaction between Tl_{aq}^{3+} and H_2O_2 (a) when the $Tl(ClO)_4)_3$ stock solution was diluted simultaneously with the starting of the reaction, and (b) when the dilute solution was allowed to stand for some time. They explained this observation by the existence of an appreciable proportion of Tl(III) in form of a polynuclear complex in more concentrated (>0.1 M) $Tl(ClO_4)_3$ solutions; this complex does not break down immediately on dilution, and thus the reaction with H_2O_2 is initially slower. This is in agreement with the observations of the present author and his co-workers that the ^{205}Tl NMR line width of a freshly diluted $Tl(ClO_4)_3$ acidic aqueous solution is narrow (5–10 Hz) but broadens slowly with time and can reach up to ~70 Hz after a few months. In addition, we have observed that the mother liquor produced when the hygroscopic $Tl(ClO_4)_3 \cdot 6H_2O$ crystals (*117*) are allowed to stand at ambient atmosphere for a few minutes gives five or six ^{205}Tl NMR signals. When concentrated perchloric acid was added dropwise to this mother liquor, the signals disappeared one by one after a gradual change of their chemical shifts. This observation indicated that in very concentrated aqueous solutions of Tl_{aq}^{3+}, several polynuclear hydrolysed species exist. It would be the first observation of polynuclear thallium species in aqueous solution.

Another observation pointing in the same direction has been described in Glaser (*115*). Sometimes, during the anodic oxidation of $TlClO_4$ in acidic aqueous solution, the anode solution coagulated to a yellowish-white gel. The electrolysis was then stopped and the stopcock between the anodic and cathodic compartments was closed. After some days, the gel changed back into a clear, colorless solution. In addition,

TABLE III

OVERALL STABILITY CONSTANTS FOR THALLIUM(III) COMPLEXES IN AQUEOUS SOLUTION AT 25°C[a]

Ligand	n	log β_n	Medium	Method	Ref.
CN^-	1	13.2 ± 0.1	1 M $NaClO_4$ + 3 M $(Li^+ + H^+)ClO_4$	NMR	*97*
	2	26.5 ± 0.2	same	same	*97*
	3	35.2 ± 0.2	same	same	*97*
	4	42.6 ± 0.2	same	same	*97*
N_3^-[b]	1	3.0 ± 0.2	1 M $HClO_4$ + 1 M $NaClO_4$	potentiometry	*93*
	2	5.38	same	same	*93*
	3	6.90	same	same	*93*
OH^-[c]	1	−1.14 ± 0.08	3 M $NaClO_4$	potentiometry	*2*
	2	−2.63 ± 0.17	same	same	*2*
OH^-[d]	3	K_s = −43.8	0.5–1.2 M $HClO_4$	potentiometry	*1*
SCN^-	1	~7	3 M $(Li^+ + H^+)ClO_4$	NMR	*110*
SO_3^{2-}	4	~34?	varying	potentiometry	*111*
$S_2O_3^{2-}$	4	~41?	varying	potentiometry	*111*
Cl^-	1	7.16	3 M $HClO_4$	potentiometry	*90*
	2	12.60	same	same	*90*
	3	16.15	same	same	*90*
	4	18.32	same	same	*90*
	5	~18.02	same	^{205}Tl NMR	*112*
Br^-	1	9.28	3 M $HClO_4$	potentiometry	*103*
	2	16.7	same	same	*103*
	3	22.1	same	same	*103*
	4	25.7	same	same	*103*
	5	~24.7	same	^{205}Tl NMR	*95*
I^-	1	~11.5	3 M $HClO_4$ + 1 M $NaClO_4$	potentiometry and solubility	*99*
	2	~21	same	same	*99*
	3	~29.5	same	same	*99*
	4	35.7 ± 0.1	same	same	*99*
$(Acetate)^-$	1	6.17 ± 0.05	3 M $LiClO_4$	potentiometry	*113*
	2	11.28 ± 0.05	same	same	*113*
	3	15.10 ± 0.08	same	same	*113*
	4	18.3 ± 0.1	same	same	*113*

(*continues*)

a white, insoluble, crystalline solid precipitated [a product of Tl(III) hydrolysis?]. The solid dissolved after 2–3 days and the electrolysis could be continued.

2. *Halide Complexes*

The halide complexes of thallium(III) in aqueous solution are among the most stable of metal halide complexes, and they have been intensively studied (*3, 89–92, 103, 118–122*). There occurs a distinct break

TABLE III (*Continued*)

Ligand	n	log β_n	Medium	Method	Ref.
$(Oxalate)^{2-e}$	1	2.93	3 M $HClO_4$	spectrophotometry	*100*
$(CDTA)^{4-f}$	1	38.3[g]	1 M $NaClO_4$	potentiometry	*68*
$(DTPA)^{5-h}$	1	46.0[g]	1 M $NaClO_4$	potentiometry	*68*
$(EDTA)^{4-i}$	1	37.8[g]	1 M $NaClO_4$	potentiometry	*68*
$(EDTA)^{4-}(OH)^{-j}$	1	−6.0 ± 0.2	1 M $NaClO_4$	potentiometry	*106, 114*
$(EDTA)^{4-}Cl^{-k}$	1	2.3 ± 0.2	1 M $NaClO_4$	potentiometry	*114*
$(EDTA)^{4-}Br^{-k}$	1	3.5 ± 0.15	1 M $NaClO_4$	potentiometry	*114*
$(EDTA)^{4-}I^{-k}$	1	5.9 ± 0.2	1 M $NaClO_4$	potentiometry	*105*
	2	5.38 ± 0.2	same	same	*105*
	3	6.90 ± 0.2	same	same	*105*
$(EDTA)^{4-}(CN)^{-k}$	1	8.72 ± 0.03	1 M $NaClO_4$	^{205}Tl and ^{13}C NMR, potentiometry	*94*
$(EDTA)^{4-}(SCN)^{-k}$	1	2.70 ± 0.03	1 M $NaClO_4$	^{205}Tl and ^{13}C NMR, potentiometry	*94*
Other polydentate ligands[l]					*109*

[a] $\beta_n = \dfrac{[TlX_n^{3-n}]}{[Tl^{3+}][X^-]^n}$ (in molar units).

[b] 20°C; at higher $[N_3^-]$ concentrations Tl(III) is reduced to Tl(I); see comment in Section II,C.

[c] $\beta_n = \{[Tl(OH)_n^{3-n}][H^+]^n\}/[Tl^{3+}]$.

[d] Solubility product $K_S = [Tl^{3+}][OH^-]^3$

[e] $\beta_1 = \{[TlC_2O_4^+][H^+]^2\}/\{[Tl^{3+}][H_2C_2O_4]\}$.

[f] $(CDTA)^{4-}$: 1,2-diaminocyclohexan-*N*,*N*′-tetraacetate[4-]

[g] at 20°C

[h] $(DTPA)^{5-}$: diethylenetriamine-*N*,*N*′,*N*″-pentaacetate[5]

[i] $(EDTA)^{4-}$: ethylenediamine-*N*,*N*,*N*′,*N*′-tetraacetate[4−]; stability constants for several other polyaminocarboxylate complexes of Tl(III) have also been determined.

[j] $\beta_1 = \{[Tl(EDTA)X^{2-}][H^+]\}/[Tl(EDTA)^-]$.

[k] $\beta_1 = [Tl(EDTA)X^{2-}]/\{[Tl(EDTA)^-][X^-]\}$.

[l] A large number of stability constants for mixed complexes of the type Tl(III)LX, where L = aminocarboxylate or polyamine, have been determined by Musso (*109*).

in the stability sequence after the second complex, similar to, although less pronounced than, that found for the isoelectronic mercury(II) chloride complexes (*123*) (this matter is further discussed in Section III). The maximum number of complexes formed has been a matter of controversy. Early reports of four (*124*) and six (*118, 120*) successive complexes were based on silver chloride electrode measurements, which are of doubtful validity in the strongly oxidizing Tl(III) solutions. Potentiometric studies, using the Tl(III)/Tl(I) couple, point to a maximum coordination number of four in aqueous solution (*90–92*). However, solvent extraction data have been interpreted in terms of weak bonding of a fifth chloride (*121*), and ^{205}Tl NMR data (*119*) strongly indicate

more than four chlorides per Tl(III) at high chloride concentrations. It can be noted that there are several examples of penta- and hexachlorothallates(III) in the solid state (*45, 112, 115, 125–140*), a few of penta- and hexabromothallates (*135, 139, 141*), and not a single case where an iodo complex higher than TlI_4^- has been found. These facts, in connection with the more recent solution X-ray diffraction, ^{205}Tl NMR, and vibrational spectroscopy studies of thallium(III) halide solutions (*112, 115, 136, 142–145*), provide a convincing basis for the existence of penta- and hexachloro complexes in aqueous solution. In their ^{205}Tl NMR study (*112*), Glaser and Henriksson concluded that in aqueous thallium(III) solutions containing excess chloride, the existence of higher (than $TlCl_4^-$) chloride complexes is evident. For example, in 0.05 M thallium solutions, containing 1 M $NaClO_4$ and 3 M $HClO_4$ as ionic medium, the obtained stepwise stability constant, $K_5 = 0.3(1)$ M^{-1}, is not higher than the detection limit given by Ahrland *et al.* in their potentiometric study (*91, 92*). It is also in acceptable agreement with $K_5 = 0.8(2)$ M^{-1} obtained by spectrophotometric measurements (*146*) and $K_5 = 0.2$ M^{-1} calculated from extraction data (*121*). At higher total thallium and halide concentrations (and thus higher ionic strengths), the fifth and sixth chloride complexes are present in solution (the latter one in high concentration), whereas only minor amounts of higher bromo complexes are formed (if they are formed at all; see discussion in Section III,B). It may be noted that the stability constants of $TlCl_5^{2-}$ and $TlCl_6^{3-}$ are rather low for all three studied ionic media (*112*). However, a gradual change from only $TlCl_5^{2-}$ in 0.05 M $[Tl]_{tot}$ solutions, through both $TlCl_5^{2-}$ and $TlCl_6^{3-}$ species in 1 M, to $TlCl_6^{3-}$ solely in 2.6 M solutions could be observed. This was explained by the large variation of the $[H_2O]/[Cl^-]_{free}$ ratio: from 475 to 7 between the 0.05 and 2.6 M solutions. Even if the chloride is a strong complexing agent for Tl(III) and strives to substitute the water molecules in the first coordination sphere of the metal ion, the equilibrium

$$TlCl_6^{3-} + H_2O \rightleftharpoons TlCl_5(OH_2)^{2-} + Cl^- \qquad (2)$$

can be shifted to the right if a sufficient amount of water compared to $[Cl^-]_{free}$ is present. Alternatively, the absence of the fifth complex was explained by Spiro (*122*) in the following way (to account for his Raman results). In the $TlCl_6^{3-}$ complex, the chloride ligands are, on the average, less tightly bound than in $TlCl_4^-$. Since addition of only one chloride would destabilize the $TlCl_4^-$ structure and the addition of one more would probably lead to a slight increase in stability, it is not surprising

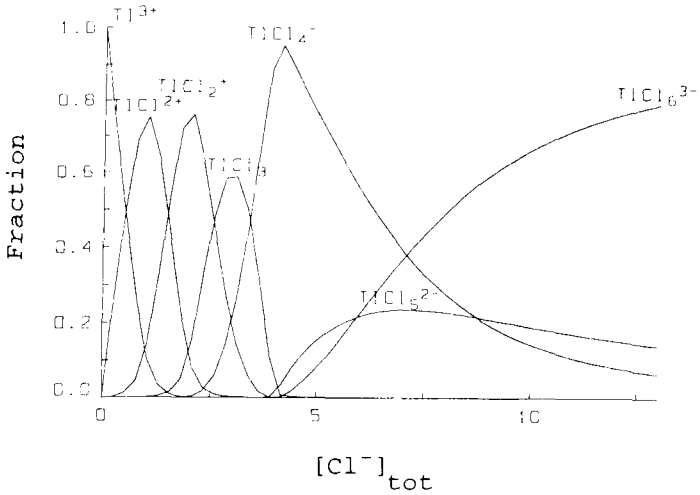

FIG. 3. Distribution of the various species in aqueous solution of 1.0 M Tl(III) containing 3 M $(H^+ + Li^+)ClO_4$ and varying molar concentrations of chloride (the ionic strength is not constant; see discussion in Glaser and Henriksson (*112*), from which the equilibrium constants are taken).

that $TlCl_5^{2-}$ does not appear to be an important species in aqueous solution. The distribution of thallium among the various chloride complexes is shown in Fig. 3. In this context, it has to be remembered that even if the existence of higher chloride complexes is evident, the calculated stability constants should be seen as rough estimates only, since (1) the chemical shifts of the solid salts were used in the calculations, and (2) at the high total thallium concentrations, the variation of the activity coefficients is certainly not negligible.

3. *Cyano Complexes*

In contrast to the general assumption in the literature (*15*), based on the redox potentials of the Tl^{3+}/Tl^+ and $(CN)_2/CN^-$ couples (see discussion in Section IV,B), it has been recently shown that thallium(III) forms very strong and kinetically stable cyanide complexes in aqueous solution (*97*). The study, performed by means of quantitative ^{205}Tl NMR and ^{13}C NMR spectroscopy in combination with pH measurements, resulted in the determination of the stability constants (Table III) and the NMR parameters (Table VI) for the four $Tl(CN)_n^{3-n}$ complexes (n = 1–4). Figure 4 displays typical ^{205}Tl NMR spectra for this

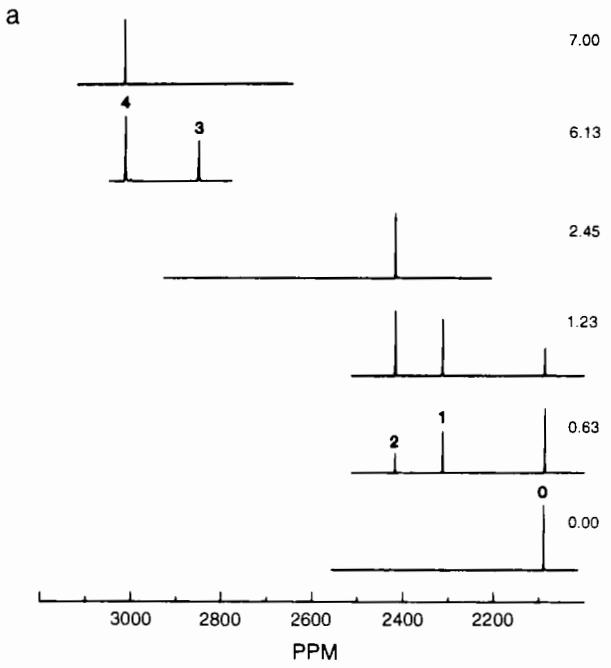
a
7.00
4
3
6.13
2.45
1.23
1
2
0.63
0
0.00
3000
2800
2600
2400
2200
PPM

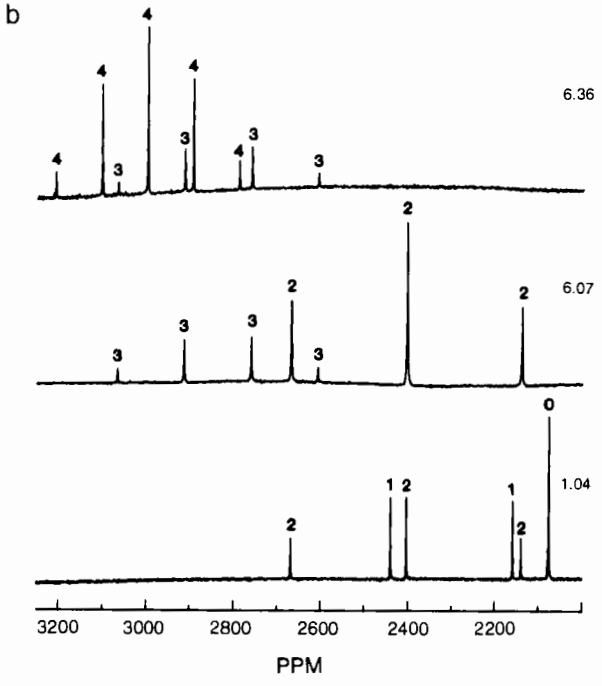
b
4
4
4
4
3
3
4
3
3
6.36
2
2
2
3
3
3
3
6.07
0
1
2
1
2
2
1.04
3200
3000
2800
2600
2400
2200
PPM

chemical system; each thallium cyanide complex gives rise to a "fingerprint" in the form of group spin–spin coupled signals (Fig. 4b).

These spectral features and other evidence presented in this paper (*97*) leave no doubt that the Tl(III) cyano complexes exist, that they have the stated composition, and that they are extremely strong and kinetically inert. In fact, the cyano complexes are stronger than any other known monodentate complexes of thallium(III). The only possible known competitor as a ligand, the iodide ion, forms the complex TlI_4^- with the overall stability constant log β_4 = 35.7 (*99*), i.e., several orders of magnitude lower than that of $Tl(CN)_4^-$ (see Table III). The distribution of thallium among the various $Tl(CN)_n^{3-n}$-species is shown in Fig. 5. Stepwise stability constants of MX_n complexes often decrease with increasing n because of statistical, steric, and coulombic factors (*147*). There are, however, some exceptions such as the cyanide complexes of the d^{10} ions copper(I), silver(I), probably gold(I), and mercury(II), where the extreme stability of the second complex, MX_2, breaks the decreasing trend. The thallium(III) ion, which is isoelectronic with Au(I) and Hg(II), behaves in a similar way (*97*) (Table III). It is certainly not a coincidence that diorganothallium(III) compounds containing the linear C–Tl–C group are also extremely stable (*15, 26*); for example, the $Tl(CH_3)_2^+$ ion is stable in aqueous solution (*148*).

There is some evidence that back-donation plays an important role in cyano complexes (*149*). For the isoelectronic Au(I), Hg(II), and Tl(III) ions, the back-donation should be most efficient (and hence the complexes should be strongest) for gold and least efficient for thallium because of the increasing charge on the metal ion. Thus, if back-donation is a major effect, the stability constants for the cyano complexes should decrease in the order Au > Hg > Tl. Unfortunately, only one stability constant, namely β_2, is (approximately) known for gold(I), but there is no doubt that the β_2-values follow the predicted trend log β_2 = 39 (for Au) > 32.7 (for Hg) > 26.5 (for Tl) (*97, 150, 151*).

The same trend can be found for the logarithms of the stability constants for the monocyano complexes of Hg(II) and Tl(III), 17.0 and 13.2, respectively. However, in the tricyano and tetracyano complexes of these two metal ions, the opposite trend is found. This might indicate

FIG. 4. ^{205}Tl(NMR spectra of acidic aqueous solutions containing 50 mM thallium(III) and varying $[CN^-]_{tot}/[Tl(III)]_{tot}$ ratios. The numbers over the peaks denote n in $Tl(CN)_n^{3-n}$. (a) Natural isotopic abundance; (b) 100% enriched in ^{13}C. Temperature = 25°C; ionic medium: $[Na^+]$ = 1 M, $[Li^+]$ + $]H^+]$ = 3M, $[ClO_4^-]$ = 4 M. The chemical shifts are given in parts per million toward higher frequency with respect to an aqueous solution of $TlClO_4$ extrapolated to infinite dilution. Reprinted from Blixt *et al.* (*97*). Copyright © 1989 American Chemical Society.

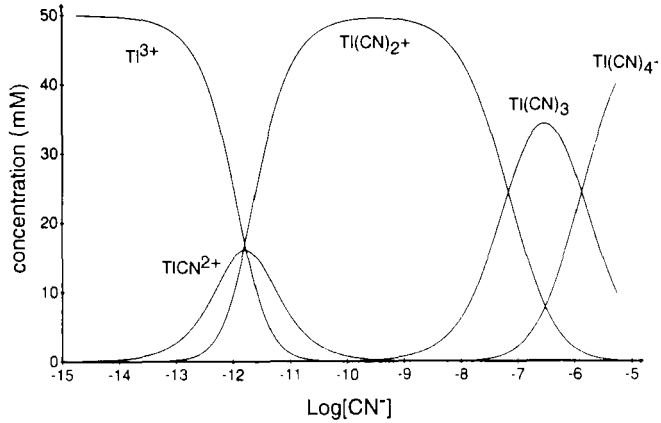

FIG. 5. Distribution of thallium(III) among the various $Tl(CN)_n^{3-n}$ complexes in acidic aqueous solution; $[Tl(III)]_{tot}$ = 50 mM. Reprinted from Blixt *et al.* (*97*). Copyright © 1989 American Chemical Society.

that in the latter two complexes back-donation is less important compared to other factors. Indeed, the enthalpy of formation of the $Hg(CN)_3^-$ and $Hg(CN)_4^-$ complexes is three times smaller than for the species $Hg(CN)^+$ and $Hg(CN)_2$ (*152*), which might be indicative of a decreasing covalent contribution for the tri- and tetracyano complexes. This is a possible explanation, but certainly not the only one [cf., eg., the discussion of the ^{13}C chemical shifts in Pesek and Mason (*153*)].

It has also been found that a number of mixed cyano–halo thallium (III) species exist in aqueous solution, of the type $Tl(CN)_nX_m^{3-m-n}$, where X = Cl, Br; n = 1–3, m = 1–3 (*108*). Whereas the cyanide–bromide system was complicated by the oxidation of Br^- by Tl(III), the chloro–cyano complexes are stable towards oxidation of chloride. The study of this complicated system comprising 18 soluble species (by means of ^{205}Tl and ^{13}C NMR in combination with potentiometry) was facilitated by the slow exchange regime regarding the cyanide exchange on the actual ^{205}Tl NMR chemical shift time scale and on the ^{205}Tl–^{13}C spin–spin coupling time scale, but rendered more difficult because of the fast chloride exchange in many of the solutions. A typical complex distribution diagram is shown in Fig. 6. Other aspects of the chemistry of the $Tl(CN)_n^{3-n}$-complexes will be discussed in Sections III,B (structure in solution) and IV,B (redox behavior).

In a discussion of the strength of the different thallium(III) complexes it can be pointed out that there are indications [based on potentiometric measurements almost one century old presented in the Ph.D. thesis of

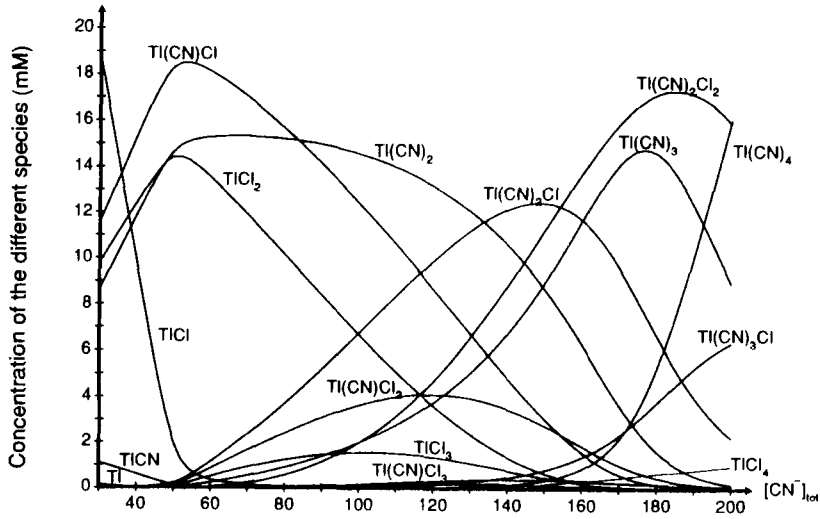

FIG. 6. Distribution of thallium(III) among the various $Tl(CN)_nCl_m^{3-m-n}$ complexes as a function of the total cyanide concentration (mM) in acidic aqueous solution (charges omitted). $[Tl(III)]_{tot}$ = 50 mM, $[Cl^-]_{tot}$ = 50 mM. From Blixt and Glaser (*108*).

Spencer (*154*)] that there is a ligand, namely thiosulfate, which can form complexes several orders of magnitude stronger than those observed for the cyanide. However, the existence of Tl(III)–$S_2O_3^{2-}$ complexes has not been proven, and this ligand might not be monodentate, as is cyanide. For polydentate ligands, the complexes $Tl(EDTA)^-$, $Tl(CDTA)^-$, and $Tl(DTPA)^{2-}$ are by far the strongest (see Table III and Fig. 12, later).

4. *Application of the Specific Interaction Theory*

The majority of equilibrium constants (including those given in Tables I–III) have been determined in solutions containing high (usually $\geq$1 M) and constant concentration of an inert electrolyte (e.g., alkali perchlorate). In this way the variation of the activity coefficients of the studied species (kept below 0.1 M) is so small that no correction factors have to be applied. The equilibrium constants, however, are strictly valid only in the ionic medium in which they have been determined. In order to avoid the burden of experimental determination of equilibrium constants in each ionic medium encountered, semi-empirical methods have been developed to recalculate the constants from one ionic medium to another. One such method is the specific interaction theory (SIT), developed by Guggenheim (*155*) and Scatchard (*156, 157*) on the basis

of Brønsted's principle of specific interactions between ions (*158*), and further advanced by Biedermann (*159*), Ciavatta (*160*), and others. This method has the advantage of simplicity and a small number of parameters and has been shown to yield equilibrium constants usually within 0.1–0.2 logarithmic units from the experimental values. According to this theory, the activity coefficient, γ_i, of an ion of charge z_i in a solution of ionic strength I (in terms of the molality, m) can be expressed by Eq. (3):

$$\log \gamma_i = -z^2 \cdot D + \sum_k \varepsilon(i,k) \cdot m_k \tag{3}$$

where $D = 0.5107\sqrt{I}\,(1 + 1.5\sqrt{I})$ represents the Debye–Hückel term at 25°C, and the summation extends over all the ions k present in solution at the molality m_k. The ε terms, called specific interaction coefficients, are set equal to zero when the charge of the ion k has the same sign as the ion i. These coefficients have to be calculated from independent measurements, usually from published equilibrium constants for at least two ionic strength values. In Table IV, the available specific interaction coefficients for thallium(III), species are given. Some of these coefficients have been used to calculate the stability constants of the $TlCl_n^{3-n}$ complexes in aqueous solution containing varying ionic media (*96*); the constants are shown in Table V, together with the experimental values. It is clear that the theory is in agreement with the experiment; interestingly, even the different experimental

TABLE IV

SPECIFIC INTERACTION COEFFICIENTS FOR THALLIUM(III) SPECIES

	$\varepsilon(i, k)$	Ref.
$\varepsilon(Tl^{3+}, ClO_4^-)$	0.66	*96*
$\varepsilon(Tl(OH)^{2+}, ClO_4^-)$	0.50	*96*
$\varepsilon(TlCl^{2+}, ClO_4^-)$	0.49	*96*
$\varepsilon(TlCl_2^+, ClO_4^-)$	0.39	*96*
$\varepsilon(TlCl_3)$	0.21	*96*
$\varepsilon(TlCl_4^-, H^+) = \varepsilon(TlCl_4^-, Li^+)$	0.22	*96*
$\varepsilon(TlBr^{2+}, ClO_4^-)$	0.54	*95*
$\varepsilon(TlBr_2^+, ClO_4^-)$	0.64	*95*
$\varepsilon(TlBr_3)$	0.57	*95*
$\varepsilon(TlBr_4^-, H^+) = \varepsilon(TlBr_4^-, Li^+)$	0.70	*95*
$\varepsilon(TlBr_4^-, Na^+)$	0.59	*95*

TABLE V

CALCULATED AND EXPERIMENTAL STABILITY CONSTANTS FOR THALLIUM(III) CHLORIDE COMPLEXES IN AQUEOUS SOLUTION AT 25°C (IN MOLAR UNITS)[a]

	3 M $NaClO_4$		3 M $HClO_4$ + 1 M $NaClO_4$		0.5 M $HClO_4$	1 M $HClO_4$	3 M $HClO_4$
	Exp. (*3*)	Calc. (*96*)	Exp. (*91*)	Calc. (*96*)	Exp. (*90*)	Calc.	Exp. (*90*)
$\log \beta_1$	7.04	6.9	7.54	7.4	6.72	6.69	7.16
$\log \beta_2$	12.32	12.1	13.38	13.1	11.82	11.79	12.60
$\log \beta_3$	15.30	15.2	16.79	16.9	14.50	14.56	16.15
$\log \beta_4$	17.36	17.4	19.58	19.2	16.31	16.43	18.32

[a] $\beta_n = \dfrac{[TlCl_n^{3-n}]}{[Tl^{3+}][Cl^-]^n}$.

values of β_4 in 3 M $HClO_4$ + 1 M $NaClO_4$ and in 3 M $NaClO_4$ are satisfactorily predicted.

In addition, in the last three columns the β_n values for the ionic medium containing varying concentration of $HClO_4$ are shown. As discussed in the preceding Section, Dodson and Schwarz (*77*) determined the stability constants for the $Tl^{III}Cl_n^{3-n}$ complexes in 1 M $HClO_4$ using the known values of β_n for $Tl^{III}Cl_n^{3-n}$ in 0.5 M $HClO_4$, since the corresponding data in 1 M $HClO_4$ were not available. As can be inferred from the table, the error introduced in this way was not serious. On the other hand, the difference in the distribution of the $TlCl_n^{3-n}$ complexes for another pair of ionic media is considerable, as is illustrated in Figs. 7a and 7b. It should be noted that the SIT method can also be used to calculate other thermodynamic parameters, such as standard redox potentials or solubilities (*159*).

5. *^{205}Tl NMR Parameters of Tl(III) Complexes*

As discussed in the introduction, during the last decade or two ^{205}Tl NMR spectroscopy has become the most versatile and powerful technique for studying thallium solution chemistry (*39, 40, 54, 161–167*). In particular, the potential of this method for studying the *aqueous* solution chemistry of thallium has been demonstrated in several papers by Glaser *et al.* (*41, 48, 51, 94, 95, 97, 98, 108, 110, 112, 115, 145, 168–174*), in which structural, kinetic, and equilibrium problems are studied. In some of these studies, the speciation of the thallium complexes could be elucidated using the *individual* chemical shifts (and coupling constants) for the studied species (*41, 94, 97, 108, 112, 171*).

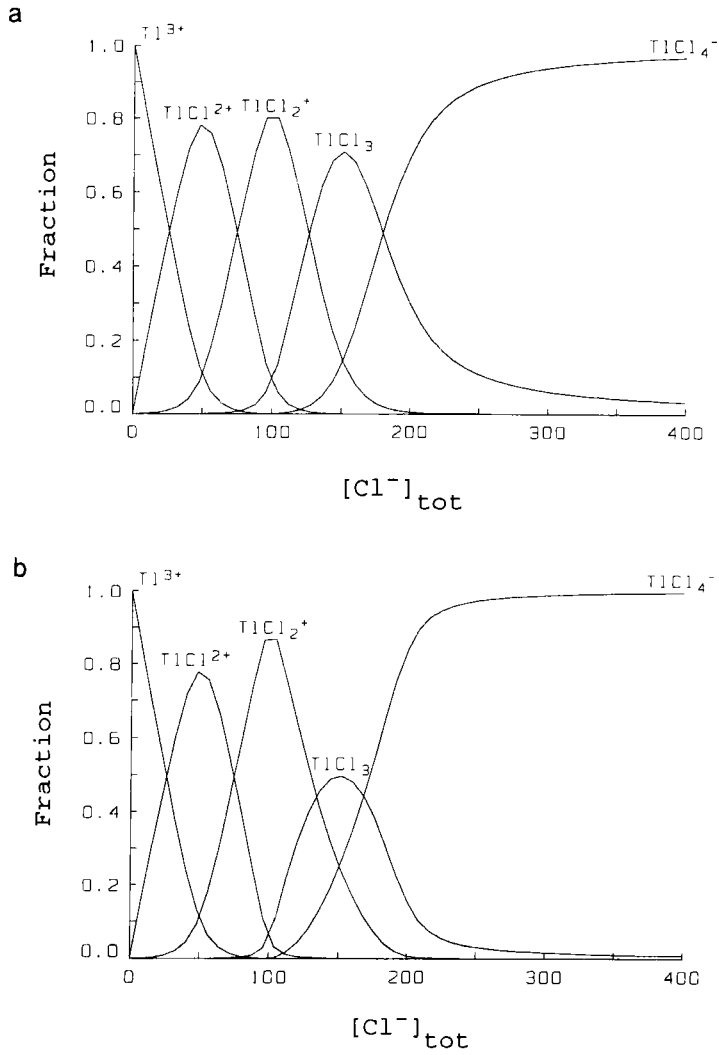

FIG. 7. Fraction of thallium(III) present in the various species in aqueous solution of 50 mM Tl(III) as a function of the total chloride concentration (mM): (a) in 3 M $HClO_4$ [equilibrium constants from Woods *et al.* (*90*)]; (b) in 3 M $HClO_4$ + 1 M $NaClO_4$ [equilibrium constants from Ahrland and Johansson (*92*)].

These shifts can, of course, also be used for direct identification of the species present in solution, and they can be either obtained directly from the NMR spectra in the case of slow exchange on the ^{205}Tl NMR chemical shift time scale, or calculated from spectra in the fast ex-

change regime (*175*). All hitherto reported values of the *individual* chemical shifts and spin–spin coupling constants for inorganic thallium complexes in aqueous solution have been collected in Table VI. It can be mentioned that the individual chemical shifts have constant values (i.e., are independent of the medium) for well-defined species, in which the thallium ion does not interact directly with the ionic medium. Therefore, these shifts are more reliable for strong complexes such as $TlCl_4^-$, $TlBr_4^-$, $Tl(CN)_2^+$, or $Tl(EDTA)^-$ (EDTA = ethylenediaminetetraacetate) than, e.g., for the usually weak complexes of thallium(I) [cf. the discussion in paper (*112*)].

III. Structure of Thallium Complexes in Aqueous Solution

Most chemical reactions in the natural surroundings and in the chemical industrial processes take place in solution, and this aggregation state constitutes the main field of interest for the majority of chemists and biochemists. However, in contrast to the large number of detailed crystal structures, the amount of available structural information for species in solution is limited. The reason for this situation is certainly the inherent disorder of the solution state, from which follows the lack of an experimental method as "hard" as the single-crystal X-ray diffraction technique. Certainly, spectroscopic methods can be used for studies of symmetry and bonding properties, but in order to obtain accurate interatomic distances diffraction techniques (or EXAFS, extended X-ray absorption fine structure) have to be used. These techniques are not always easily accessible and have some weak points; however, they are the only ones able to provide the latter type of structural data. In the following, the few reported (and one unpublished) studies of this type of thallium species in aqueous solution will be discussed.

A. Thallium(I) Compounds

For thallium(I), only three structural studies in solution are familiar to the author. The first one is an exploratory study on the structure of the hydrated Tl^+ ion in solution, performed by means of the EXAFS and X-ray diffraction techniques on concentrated TlF solutions (0.5 M and 3.0 M, respectively) in water (*53*). The EXAFS data showed no features which could be assigned to a well-structured hydration sphere around the thallium ion. The X-ray data could be explained by assuming two water molecules at about 2.74 Å and four more loosely bound

TABLE VI

INDIVIDUAL ^{205}Tl NMR PARAMETERS FOR THALLIUM COMPLEXES IN AQUEOUS SOLUTION AND IN SOME SOLID COMPOUNDS[a]

Species	^{205}Tl NMR individual chemical shift[b] (ppm)	Spin–spin coupling constant, $^1J(^{205}Tl-^{13}C)$ (Hz)	Ref.
Tl^+	0		*54, 112*
TlCl	350 ± 35[c]		*41*
$TlCl_2^-$	1200 ± 50[c]		*41*
Tl^{3+}	2093		*169*
$TlCl^{2+}$	2204[d]		*169*
$TlCl_2^+$	2199[d]		*169*
$TlCl_3$	2435		*169*
$TlCl_4^-$	2648		*169*
$TlCl_5^{2-}$	2022[e]		*112*
$TlCl_6^{3-}$	1972[f]		*112*
$TlBr^{2+}$	1575		*95*
$TlBr_2^+$	782		*95*
$TlBr_3$	1158		*95*
$TlBr_4^-$	1312		*95*
$TlBr_5^{2-}$	~−800[g]		*95*
$TlBr_6^{3-}$	−1271[h]		*112*
$Tl_2Br_9^{3-}$?	−1194[i]		*112*
TlI_4^-	−1560[j]		*112*
$Tl(CN)^{2+}$	2310.0[k]	14,636[l]	*97*
$Tl(CN)_2^+$	2414.4[k]	13,749[m]	*97*
$Tl(CN)_3$	2848.4[k]	7954	*97*
$Tl(CN)_4^-$	3010.0[k]	5436	*97*
$Tl(SCN)^{2+}$	2290	733[n]	*110*
$Tl(EDTA)^-$	2301[o]		*94*
$Tl(EDTA)(OH)^{2-}$	2313[o]		*94*
$Tl(EDTA)(Cl)^{2-}$	2308[o]		*94*
$Tl(EDTA)(Br)^{2-}$	1883[o]		*94*
$Tl(EDTA)(CN)^{2-}$	2460[o]	10,479[p]	*94*
$Tl(EDTA)(SCN)^{2-}$	2385[o]		*94*

[a] For simplicity, water molecules are omitted; see discussion in Section III. The chemical shifts are given in parts per million toward higher frequency with respect to an aqueous solution of $TlClO_4$ extrapolated to infinite dilution. The values of chemical shifts may differ, depending on the composition of the solution. This variation for a particular species is usually only a few parts per million, which is in most cases negligible compared to the large differences in the ^{205}Tl NMR chemical shifts for the different complexes. For the definition of the *individual* chemical shifts and spin–spin coupling constants, see Glaser and Henriksson (*112*).

[b] In 3 M $HClO_4$, if not stated otherwise.

[c] In 4 M KF.

[d] Note the slightly erroneous assignment in Glaser and Henriksson (*112*).

water molecules at about 3.24 Å from the Tl^+ ion, compatible with Tl(I) coordination in several crystal structures, e.g., Tl_2SnO_3 [cf. (*176*), and Table IV of (*177*)]. However, as is usual for diffraction studies of weak interactions, it is possible that other structural parameters can explain the data equally well. For example, a relatively good agreement could also be obtained by assuming three coordinated water molecules at a $Tl-OH_2$ distance of about 2.75–2.80 Å, and a number of water molecules at longer distances (>3.1 Å), similar to the Tl(I) coordination in the crystals of Tl_2O (*178*).

In any case, the hydration of Tl_{aq}^+ is very weak as compared to Tl_{aq}^{3+} (see later discussion), in agreement with the hydration enthalpies for these ions: 335 and 4117 kJ $mole^{-1}$, respectively (*15*). This difference is probably an important reason for the slow electron exchange between the two thallium ions because of the necessarily large reorganization energy of their hydration spheres (cf. Section IV,B).

The two other structural studies of Tl(I) species were performed on Tl(I)-carboxylate solutions. Almost saturated solutions of thallium(I) formate and malonate, with the very high densities of 2.8 and 3.2 g cm^{-3}, have large absorptivity for high-energy beams and good transparency for visible light. Therefore, the solutions have been examined with respect to possible applications as transparent radiation shield (*179–181*). In this context, with the intention of gaining a better understanding of the heavy solutions, Ohtaki *et al.* conducted two structural investigations of thallium(I) compounds in aqueous solution (*177, 182*). The authors used the solution X-ray diffraction technique and Raman spectroscopy to study the structure of thallium species formed in aqueous Tl(I) formate and malonate solutions with varying thallium concentrations (up to 9 M and up to 10.8 M, respectively). The ligand-to-thallium ratio was kept at 1.0 for the formate and 0.5–0.7 for the

---

[e] From the wide line ^{205}Tl NMR powder spectrum of $Cs_2TlCl_5 \cdot H_2O$.
[f] From the wide line ^{205}Tl NMR powder spectrum of $Na_3TlCl_6 \cdot 12H_2O$.
[g] Estimated value (*95*).
[h] From the wide line ^{205}Tl NMR powder spectrum of $[Co(NH_3)]TlBr_6$.
[i] From the wide line ^{205}Tl NMR powder spectrum of $CsTl_2Br_9$.
[j] From the wide line ^{205}Tl NMR powder spectrum of $[NBu_4]TlI_4$.
[k] Ionic medium: $[Na^+] = 1$ M, $[Li^+] + [H^+] = 3$ M, $[ClO_4^-] = 4$ M.
[l] The spin–spin coupling constant $^2J(^{205}Tl-^{15}N) = 54$ Hz.
[m] $^2J(^{205}Tl-^{15}N) = 108$ Hz.
[n] = $^2J(^{205}Tl-^{13}C)$. The coupling constant $^3J(^{205}Tl-^{15}N) = 143 \pm 3$ Hz.
[o] Ionic medium: 1 M $NaClO_4$.
[p] $^2J(^{205}Tl-^{15}N) = 11$ Hz.

malonate solutions. The radial distribution functions and Raman spectra of the most concentrated solutions were interpreted in terms of the polynuclear structural units shown in Fig. 8. The formate "complex" (Fig. 8a) was assumed to be tetranuclear. In addition to the three formate oxygens coordinated to Tl(I) with the Tl–O distance of 2.8 Å, one water molecule weakly associated to the metal ion, $r(\text{Tl–OH}_2)$ = 3.2 Å, was also proposed (*182*). In the malonate entity (Fig. 8b), Tl(I) is also surrounded by four oxygens atoms: two from malonate ions ($r_{\text{Tl-O}}$ = 2.62 Å) and two water oxygens ($r_{\text{Tl-OH}_2}$ = 2.96 Å), and by two oxygen atoms at a longer distance (3.66 Å). This coordination was assumed to indicate a stereochemically active lone pair of electrons of the Tl^+ ion in solution. The Tl–Tl distances in the species were determined to be 4.04 and 4.59 Å (*177*).

However, the usual skepticism concerning the solution X-ray diffraction method applied to weak interactions should be exercised, in particular in the malonate case where the temperature factors for all interactions involving thallium(I) were found to be very large. With increasing water content, and thus coming closer to what we normally mean by aqueous solution, the polynuclear units decompose. From the measured physicochemical properties, such as density, refractive index, specific

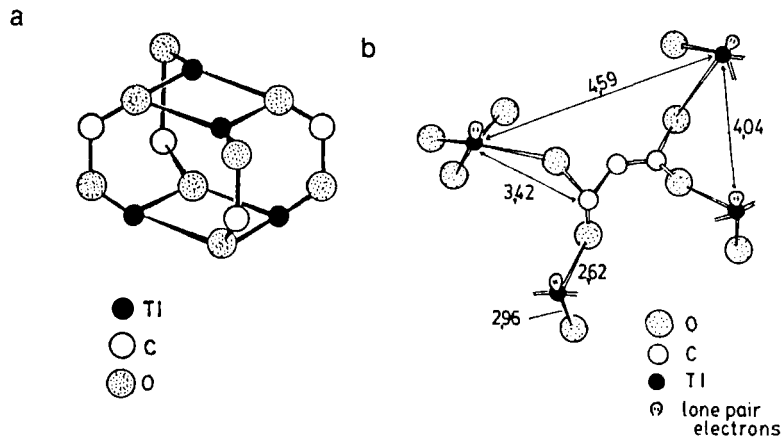

FIG. 8. Model of the structure of thallium(I) carboxylate species in highly concentrated aqueous solutions. Temperature = 25°C. (a) Formate species. $[\text{Tl}]_{\text{tot}}$ = 10.8 M, $[\text{H}_2\text{O}]/[\text{Tl(I)}]$ = 2.6, $[\text{formate}^-]/[\text{Tl(I)}]$ = 1.0. Thallium(I) ions are fourfold coordinated by three formate oxygens and one weakly bound water molecule (not shown). (b) Malonate species. $[\text{Tl}]_{\text{tot}}$ = 9.0 M, $[\text{H}_2\text{O}]/[\text{Tl(I)}]$ = 3, $[\text{malonate}^{2-}]/[\text{Tl(I)}]$ = 0.5. Fourfold oxygen coordination of thallium(I) ion is shown only for one Tl(I) atom. Some interatomic distances are given (in angstroms). From Yamaguchi *et al.* (*177*).

viscosity, and conductivity, it seems that this decomposition occurs gradually upon decrease of the concentration of the solute (*177, 182*).

B. Thallium(III) Compounds

If it is assumed that purely electrostatic interactions will determine the structures of the complexes of the spherically symmetric d^{10} ion Tl(III), then energy minima will be obtained for the following geometries (*183, 184*): linear TlX_2^+, triangular TlX_3, tetrahedral TlX_4^-, trigonal–bipyramidal TlX_5^{2-}, and octahedral TlX_6^{3-}. This assumption is often consistent with the geometries of discrete complexes found in several crystal structures (*185*), but in many cases electronic factors cause significant deviations. For instance, the isoelectronic Hg(II) shows a pronounced preference for two strong and short bonds in its halide and pseudohalide complexes (*185*).

For thallium(III) in aqueous solution, only a few structure-related studies have been reported. These have mainly dealt with tetra- and hexahalo complexes in solution and in the solid state using vibrational spectroscopy. They showed that these complexes are tetrahedral and octahedral, respectively (*122, 143, 186–190*); the characteristic vibrational frequencies were given. An outstanding exception is the Raman study of Spiro (*122*), who investigated the structural properties of thallium(III) chloride complexes in concentrated aqueous solution (Spiro's equilibrium study was discussed earlier; see Section II, C, 2). He could exclude the possibility of formation in aqueous solution of polynuclear thallium(III) species (such as $Tl_2Cl_9^{3-}$), which have previously been found in the solid state (*191, 192*) and which were forwarded by Figgis to explain his ^{205}Tl NMR data for aqueous solutions (*119*). The most interesting part of Spiro's study deals though with the hydrated Tl^{3+} ion. To start with, on the basis of his Raman data, he could rule out the possibility of complex formation between Tl_{aq}^{3+} and the perchlorate ion. Then, he assumed that the enhanced intensity and the partial polarization of the 461 cm^{-1} Raman peak of the (undistorted) perchlorate ion stems from the Tl_{aq}^{3+} ion. The enhancement decreases linearly upon addition of chloride up to Cl/Tl = 2. Thus, he concluded that the coordinated water, which gives rise to the 461 cm^{-1} peak, is replaced by chloride.

> The fact that all of the intensity enhancement is eliminated by addition of two chlorides per thallium, and half of it by one, suggests that, of the water molecules bound to Tl^{3+}, half remain bound to $TlCl^{2+}$ and none left bound to $TlCl_2^+$. Although for $Tl(OH_2)_m^{3+}$ *m*

> may on this basis be any even integer, it seems unlikely that each of the first two chlorides should displace more than one water molecule on coordination to thallium(III), i.e. that $m > 2$. The simplest interpretation of the Raman data is that only two water molecules are sufficiently strongly bound to give rise to Raman emission.[1]

As a consequence of this conclusion, Spiro proposed that there must be structural rearrangement from linear $TlCl_2^+$ to trigonal $TlCl_3$ to either tetrahedral or square-planar $TlCl_4^-$. Such a change is also suggested by the changes in the heats and entropies of formation, and in the stability constants of these complexes (*90–92, 193*).

Strong bonding of only two water molecules by Tl^{3+} is also indicated by potentiometric data. The Tl_{aq}^{3+} ion is a strong acid ($pK_a = 1.14$ in 3 M $NaClO_4$), as is its first hydrolysis product, $Tl(OH)^{2+}$ ($pK_a = 1.5$) (2) and the species $TlCl^{2+}$ [$pK_a = 1.8$, (3)]. In contrast, $TlCl_2^+$ and the higher chloride complexes do not split off further protons prior to the precipitation of Tl_2O_3. This situation could not be accounted for by considering the decreased formal charge on the thallium ion between $TlCl^{2+}$ and $TlCl_2^+$; thus, Biedermann and Spiro (*3*) suggested that "in solution which does not contain complexing agents the Tl^{3+} ion forms strong bonds with two water molecules."

In order to determine the structural properties of the thallium(III) chloride and bromide complexes in aqueous solution, two combined LAXS/Raman (LAXS = large angle X-ray scattering) studies on concentrated aqueous solutions containing the various TlX_n^{3-n} (X = Cl, Br) complexes have been accomplished (*136, 142*)]. The hydrated Tl^{3+} ion in acidic perchlorate solution was found to contain six equidistant water molecules with a Tl–O bond length of 2.235(5) Å (*115, 142*), which seems incompatible (but see the discussion later in this section), with the conclusions drawn from the Raman and potentiometric studies mentioned earlier (*3, 122*). A regular $Tl(OH_2)_6^{3+}$ unit has also been found in the crystal structure of $Tl(ClO_4)_3 \cdot 6H_2O$; the Tl–O distance in this structure, 2.23 Å, is somewhat uncertain because of the large correction for "riding" motion, from 2.17(2) Å (*117*). The structures of the $TlCl_4^-$ and $TlCl_6^{3-}$ complexes have been determined (*115, 136*) and are shown in Fig. 9 (together with the structures of the other chloride complexes discussed later). For the bromide species $TlBr_2^+$, $TlBr_3$, and $TlBr_4^-$, the interatomic distances could be refined and their structures

[1] Spiro has not completely excluded the possibility that the two strongly bound water molecules occur at equatorial positions of a distorted octahedron of water molecules, where the four axial waters would be much more weakly bound to Tl^{3+}.

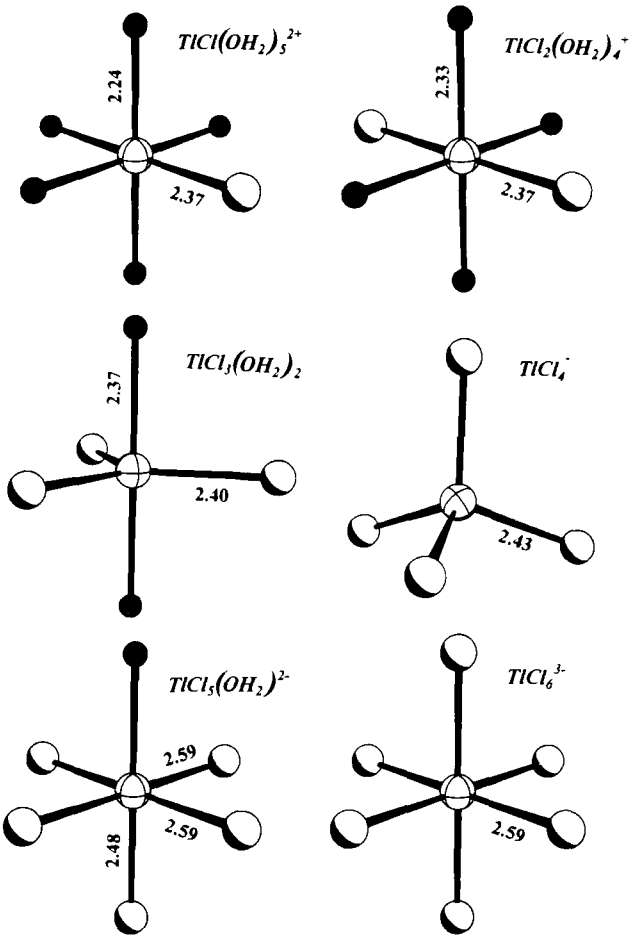

FIG. 9. Proposed structures and the determined interatomic distances (in angstroms) for thallium(III) chloro complexes in aqueous solution. The water oxygens are dark, the Cl atoms shaded. Reprinted from Blixt *et al.* (*145*). Copyright © 1995 American Chemical Society.

were determined from the (Br–Br)/(Tl–Br) distance ratio in the complexes (*142*); the structures are illustrated in Fig. 10, together with the new results (*145*) discussed later.

Very recently, an extensive structural study of Tl(III) chloride, bromide, and cyanide complexes in aqueous solution has been completed in which a combination of EXAFS, LAXS, and IR/Raman techniques were used with the aim of elucidating not only the structure of the remaining Tl(III) halide complexes, but also the number and the Tl–O

distances of the coordinated water molecules in the TlX_n^{3-n} complexes (*145*). Such information is essential for a better understanding of the chemistry of thallium(III) in general, and in particular for proposing intimate reaction mechanisms for ligand and electron exchange reactions of this metal ion (see Section IV). In addition to the chloro and bromo complexes, the recently established $Tl(CN)_n^{3-n}$ species (*97*) (see Section II,C,3) were investigated. For the latter species, no previous structural information was available, either in solution or in the solid state. In the following, a summary of the structural information on the aqua, halo, and cyano complexes of thallium(III) in aqueous solution will be given. The geometries of the complexes, including the interatomic distances, are illustrated in Figs. 9–11.

1. The Hydrated Tl^{3+} Ion

In aqueous solution not containing complexing agents, the thallium(3+) ion is hexasolvated, $Tl(OH_2)_6^{3+}$ (*115, 142, 145*). The question remains: are all six water molecules equivalent, as could be inferred

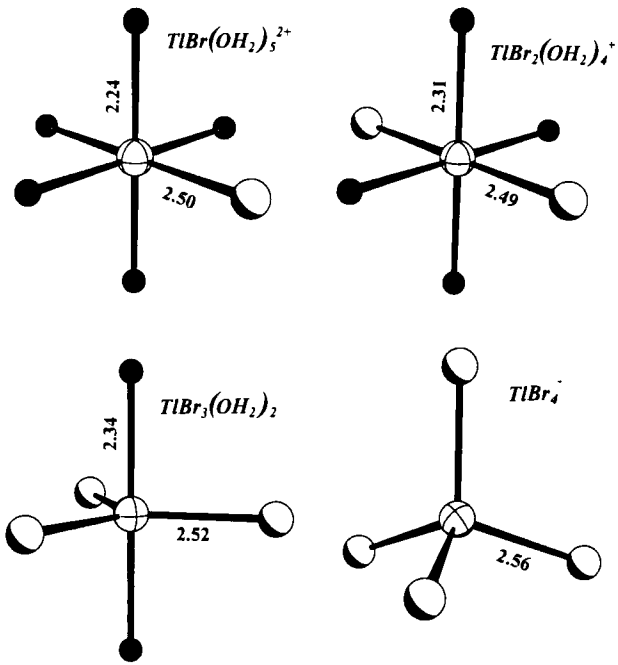

FIG. 10. Proposed structures and the determined interatomic distances (in angstroms) for thallium(III) bromo complexes in aqueous solution. The water oxygens are dark, the Br atoms are shaded. Reprinted from Blixt *et al.* (*145*). Copyright © 1995 American Chemical Society.

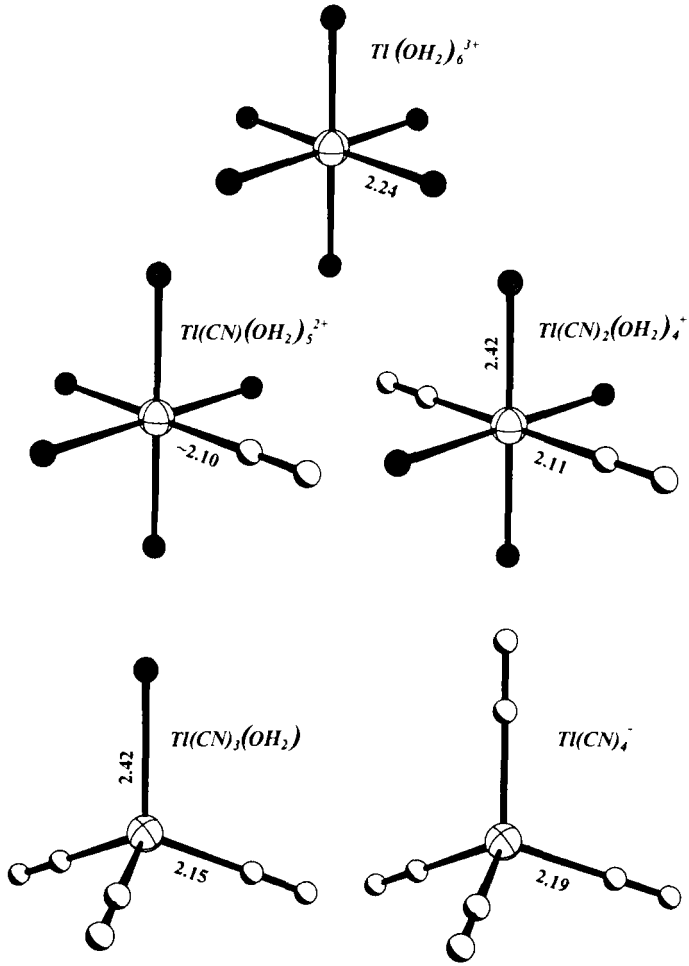

FIG. 11. Proposed structures and the determined interatomic distances (in angstroms) for thallium(III) cyano complexes in aqueous solution. The water oxygens are dark, the C and N atoms are shaded. Reprinted from Blixt *et al.* (*145*). Copyright © 1995 American Chemical Society.

from the low value of the temperature factor determined in the LAXS study (*142*), or are there two sets of coordinated water molecules, with two shorter and four longer Tl–O distances, as indicated by the Raman and hydrolysis data (*3, 122*)? The EXAFS study does not provide a direct answer to this question. However, it can be noted that the Tl–O distance obtained from the EXAFS data is 2.21(2) Å (*145*), which *may* be shorter than the corresponding distance of 2.235(5) Å from the LAXS study (*142*). If a tetragonal distortion of the octahedral geometry of

$Tl(OH_2)_6^{3+}$ is present, as has been suggested in general terms by Orgel (*194*) and Nyholm (*195*), this effect would be more pronounced for the isoelectronic Hg^{2+} ion, which has a strong preference for two strong and short bonds in its halide and cyanide complexes (*185, 196*) and which is hexasolvated in many solvents, including water (*197–200*). These observations have been ascribed to $5d_{z^2}$–6*s* mixing and second-order Jahn–Teller effects, due to the near-degeneracy of the orbitals in the valence shell (*194, 195, 200*). For mercury(II), the Hg–O bond distance in the crystal structure of $[Hg(OH_2)_6](ClO_4)_2$ is 2.341(6) Å (2.35 Å after a thermal "riding" motion correction) (*201*). The corresponding LAXS value in aqueous solution, 2.41(1) Å, is significantly larger and also shows an anomalously large Debye–Waller factor (*197, 200*). An analysis based on theoretical calculations explained these observations as being due to second-order Jahn–Teller effects, leading to dynamic distortions of the octahedral configuration (*200*). However, preliminary results from EXAFS studies on acidic mercury(II) perchlorate solutions (*202*) indicate a much shorter (ca. 0.1 Å) mean Hg–O bond than the corresponding LAXS value. A similar, but smaller, effect is observed for hexahydrated Tl^{3+} (see earlier discussion), and the different mean values obtained with the two methods may be a result of the different weighting of the contributions from the short distinct and long diffuse M–O distances in the two techniques (i.e., in EXAFS the short and strong bonds are more pronounced compared to LAXS). Thus, it is possible that there are two groups of M–O distances around the hexahydrated Hg^{2+} and Tl^{3+} ions in solution due to second-order Jahn–Teller effects, with a less pronounced splitting for the thallium(III) ion (*145*).

It can also be mentioned that the LAXS data (*142*) can be interpreted as if the $Tl(^{I}OH_2)_6^{3+}$ ion is surrounded by a second hydration sphere ($^{II}OH_2$), like many other metal ions in water (*203*). The Tl–O^{II} distance in the studied 1 M solution is about 4.1 Å, which would indicate tetrahedral bonding of $^{I}OH_2$ [a lone pair of $^{I}OH_2$ is directed towards the metal ion, while the other lone pair is accessible to accept a hydrogen bond (*203*)]. However, interpretation of longer/weaker interactions in the radial distribution curves obtained from LAXS measurements is always associated with considerable uncertainty. In the present case, the Tl–O distance could also be interpreted as originating from the second coordination sphere consisting of loosely associated perchlorate ions.

2. *TlX^{2+} Complexes*

When the first halide ligand is coordinated, five water molecules remain bonded to the thallium atom. The average Tl–O distance in-

creases slightly, ca. 0.03 Å [EXAFS data (145)], as compared to that of $Tl(OH_2)_6^{3+}$, and the Tl–O stretching vibration decreases by 30–40 cm^{-1}. Even though only a single Tl–O distance can be distinguished, it is possible that the water molecule *trans* to the halide ligand is somewhat more strongly bonded to the thallium atom (the present EXAFS data do not allow better resolution than 0.1 Å).

3. TlX_2^+ Complexes

Vibrational spectra (*115, 142, 145*) show that the XTlX unit has *trans* geometry. For the $TlBr_2^+$ complex, this is confirmed by the Br–Br distance determined from LAXS data (see earlier discussion). Four water molecules, at a Tl–O bond length of 2.3 Å, presumably complete an octahedral coordination (cf. Figs. 9–11). The Tl–X bond distance remains almost unchanged upon the formation of the TlX_2^+ complex from the TlX^{2+} (X = Cl, Br) species, and the Tl–OH_2 bond length increases considerably, to 0.1 Å. This may be due to a strong decrease of the positive charge of the metal ion upon coordination of the second X ligand. The pronounced weakening of the Tl–O bond strength is reflected in the very weak and broad IR/Raman bands. The variation of the Tl–X bond strength at the stepwise complex formation is shown in a more sensitive way by the stretching force constants than by the changes of the distances (*145*).

The linearity of the second cyano complex $Tl(CN)_2^+$ is expected, because other d^{10} metal ions—e.g., copper(I), silver(I), gold(I), and mercury(II)—also form linear dicyano complexes (*185, 204*). For the $Tl(CN)_2^+$ complex, there is strong evidence from LAXS data for a second coordination sphere comprising approximately eight water molecules at a $Tl–O^{II}$ distance of 4.3 Å. This can be rationalized by assuming two H_2O^{II} molecules hydrogen-bonded to each of the water molecules of the first hydration sphere of an assumed $Tl(CN)_2(OH_2)_4^+$ complex (*145*).

The reason for the hydration of the TlX_2^+ complexes is probably the remaining positive charge on the thallium ion, calculated to be +0.95 in $TlCl_2^+$ and +0.91 in $Tl(CN)_2^+$, whereas the corresponding values in the weakly hydrated mercury complexes are only +0.45 and +0.56, respectively (*205*). In the $Tl(CN)_2^+$ complex, the three most important contributions to the Tl-CN bonds are the coulombic energy (67% of the total binding energy), the contributions from the ligand polarizability (18%), and the σ-bonding (13%), whereas both the π-bonding (1%) and $d \rightarrow \pi^*$ back-bonding (0.5%) are relatively small, as revealed by CSOV analysis (constrained space orbital variation) (*205*).

4. TlX_3 Complexes

In the case of the bromo complex there is direct evidence of an approximately trigonal-planar $TlBr_3$ unit in solution, namely the ratio of the distances $r_{Br-Br}/r_{Tl-Br} = 1.74(\pm 0.02)$ (expected $\sqrt{3}$) obtained from LAXS data (*142*). Moreover, the IR/Raman spectra are compatible with D_{3h} symmetry for both the $TlBr_3(OH_2)_2$ and $TlCl_3(OH_2)_2$ species in solution (*145*). The Tl–O distances determined by Blixt *et al.* using EXAFS (*145*) are somewhat uncertain because of their small contribution to the EXAFS spectra. For the tricyano complex, vibrational spectra were interpreted in terms of a pseudo-tetrahedral C_{3v} symmetry, $Tl(CN)_3(OH_2)$. Although the model fitting for the EXAFS spectra could not distinguish between one and two water ligands, a distinct Tl–O bond length (2.42 Å, Fig. 11) was obtained (*145*). In the solid state, somewhat distorted trigonal-bipyramidal TlX_3O_2 units, with long (2.5–2.6 Å) Tl–O distances and the thallium atoms slightly above the X_3 plane, exist in the compounds $TlCl_3 \cdot 4H_2O$, $TlBr_3 \cdot 4H_2O$ (*206*), $TlCl_3(3\text{-}CNC_5H_4NO)_2$ (*47*), and $TlI_3(3\text{-}CH_3C_5H_4NO)_2$ (*46*).

However, a comparison between the ^{205}Tl NMR shifts for the solid compounds $TlX_3 \cdot 4H_2O$ (2051 ppm for X = Cl and 1098 ppm for X = Br) and the individual chemical shifts of the TlX_3 complexes in solution (2412 ppm for X = Cl and 1184 ppm for X = Br) (*112*) indicates a larger change in the chemical surrounding of the thallium atom in the chloride complex than in the bromide, because of its larger chemical shift difference between the solution and the solid. The vibrational spectra of this solid, $TlCl_3 \cdot 4H_2O$, also show a deviating behavior (*145*), which may be due to differences in the hydrogen bonding and the Tl–O distances for the TlX_3 species in solution and in the solid state. No solid phase containing $Tl(CN)_3$ complexes is known.

In conclusion, the available data support a trigonal-bipyramidal structure $TlX_3(OH_2)_2$ for the bromide complex and presumably also for the chloride complex in solution, while a pseudo-tetrahedral $Tl(CN)_3(OH_2)$ structure seems most likely (cf. Figs. 9–11).

5. TlX_4^- Complexes

There is a lot of convincing evidence that the tetrahalo complexes are tetrahedral in aqueous solution (*97, 112, 115, 190*), and in the solid state (*115, 117, 135, 207–210*). The Tl–X distances are 2.43, 2.56, 2.77, and 2.19 Å, for X = Cl (*112, 115, 136, 145*), Br (*142, 145*), I (*208*), and CN (*145*), respectively. For the $Tl(CN)_4^-$ complex, the tetrahedral symmetry could be expected considering that tetrahedral $M(CN)_4$ complexes are formed by many other d^{10} ions, e.g., copper(I), silver(I),

zinc(II), cadmium(II), and mercury(II) (*204, 211*). The Tl–C–N coordination is linear, as it is in all the cyano thallium(III) complexes studied (*145*). A similar coordination of the cyano ligands has been found for the tetrahedral $Hg(CN)_4^{2-}$ ion (*212*).

6. TlX_5^{2-} Complexes

In aqueous solution with a sufficiently high free chloride concentration, some amount of the $TlCl_5^{2-}$ complex is formed. The coordination geometry is probably octahedral, $TlCl_5(OH_2)^{2-}$, as indicated by the IR/Raman data (*145*); this structural unit has been found in the solid state (*115, 126, 213*). Unfortunately, the structure of this complex in aqueous solution is not accessible by X-ray diffraction/EXAFS methods, since it never exists in high enough concentration (*112*).

7. TlX_6^{3-} Complexes

The complex $TlCl_6^{3-}$ is formed both in aqueous solution and in the solid state. Its structure is octahedral, as shown from the IR/Raman and X-ray diffraction data (*115, 136*); the Tl–Cl bond distance is 2.59(1) Å. No indication of distortion of the regular octahedral geometry has been found in aqueous solution (*115, 142*). In the solid state, however, both regular and distorted $TlCl_6^{3-}$ units can exist (*132–135, 137*).

The octahedral hexabromo complex has been found in the solid state (*135, 139*), and it was proposed to exist in small amounts in aqueous solution on the basis of the changes occuring upon addition of a large amount of LiBr to a $TlBr_4^-$ solution: (a) The Tl–Br distance increased slightly (*142*); (b) the ^{205}Tl NMR chemical shift decreased 150–225 ppm (*112*); and (c) in the Raman spectrum, the symmetric stretching band shifted from 185.7 cm^{-1} to 184.5 cm^{-1} (*142*). These effects, though significant, can also be interpreted in terms of partial ion-pair formation between the $TlBr_4^-$ complex and Li^+ ions in this concentrated solution saturated with LiBr (*145*).

8. Other Thallium(III) Complexes

One more class of thallium(III) compounds has been subjected to structural investigations, namely the compounds of the type Tl(polydentate ligand)X, where the polydentate ligands were EDTA (ethylenediaminetetraacetate), DTPA (diethylenetriaminepentaacetate), TPEN (tetrakis-(2-pyridylmethyl)-ethylenediamine), NTA (nitrilotriacetate), bipy (bipyridine), terpy (2,2″:6′,2′terpyridine), pent-en (N,N,N′,N′-tetrakis-(2-aminoethyl)-ethylenediamine), and $X = OH^-, H_2O, CN^-, NO_3^-$ (*106, 109, 94*). In these compounds, thallium(III) is usually hepta- or even octa-coordinated, in contrast to monodentate ligands, where the

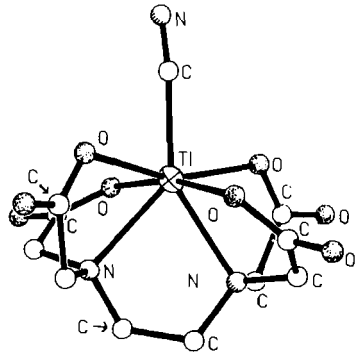

FIG. 12. The structure of the complex $Tl(EDTA)(CN)^{2-}$ as found in the solid state, but proposed to be similar in aqueous solution. The Tl–CN distance is 2.14(3) Å, and the angle Tl–C–N is 171(3)°. Reprinted from Blixt *et al.* (*94*). Copyright © 1992 American Chemical Society.

maximum coordination number is six. When the polydentate ligand occupies eight coordination sites (e.g., DTPA) (*109*), which seems to be the upper limit for thallium(III), no additional ligand X is attached to the metal ion. The decadentate ligand TTHA (triethylenetriaminehexaacetate) binds two metal ions. Strictly speaking, only the structures of several of the complexes in the solid state were determined, but in some cases the structures in aqueous solution could be inferred from their NMR and Raman spectra. An example of such a structure is shown in Fig. 12.

There is also a lot of structural information for other thallium(III) compounds (e.g., organothallium compounds), which has been obtained from the spin–spin coupling pattern of their NMR spectra. However, no interatomic distances have been obtained in this way.

IV. Dynamic Processes in Solution

A. Ligand Exchange Reactions

The kinetic characteristics of ligand exchange of thallium complexes in solution have been little explored, in contrast to the numerous equilibrium studies (*4–6, 41, 57, 61, 66, 67, 90, 92, 93, 96, 97, 112, 214–246*) and a large number of studies of redox reactions involving thallium (*81, 100, 103, 110, 246–288*).

1. Thallium(I)

For thallium(I), kinetics of only two ligand systems have been investigated hitherto: $Tl(I)–I_3^-$ (*65*) and Tl(I)–cryptates (*67, 215*). The first

kinetic study of ligand exchange on thallium(I) was reported as late as in 1975 by Purdie *et al.* (*65*). They studied the formation of the TlI_3^- complex in 0.01 M aqueous perchloric acid solution [Eq. (4)] over the temperature range +5°C to +45°C using the stopped-flow technique with spectrophotometric detection.

$$Tl^+ + I_3^- \underset{k_d}{\overset{k_f}{\rightleftharpoons}} TlI_3^- \tag{4}$$

The experiments were performed under pseudo–first-order conditions in solutions containing a large excess of Tl(I) over I_3^- ($20 \leq [Tl^+]/[I_3] \leq 1000$), so that complications due to formation of the species TlI and higher $Tl(I_3)_n^{1-n}$ complexes could be avoided. For $[Tl^+]/[I_3^-] \geq 200$, the reaction proceeds according to the second-order rate law $d[TlI_3^-]/dt = k[Tl^+][I_3]$, with the rate constant $k = (1.75 \pm 0.03) \cdot 10^4\ M^{-1}\ s^{-1}$ at 25°C, and the activation parameters $\Delta G^{\neq} = 48.8\ kJ\ mol^{-1}$, $\Delta H^{\neq} = 30.3\ kJ\ mol^{-1}$, $\Delta S^{\neq} = -61.9\ J\ mol^{-1}\ K^{-1}$. This rate constant is comparatively low for substitution reactions of univalent metal ions—e.g., the corresponding value is $2 \cdot 10^8\ M^{-1}\ s^{-1}$ for the formation of the potassium nitrilotriacetic acid complex (*289*). For the dissociation reaction of TlI_3^-, the following parameters have been calculated: $k_d = 24\ s^{-1}$ at 25°C, and the activation parameters $\Delta G^{\neq} = 64.9\ kJ\ mol^{-1}$, $\Delta H^{\neq} = 18.8\ kJ\ mol^{-1}$, $\Delta S^{\neq} = -127\ J\ mol^{-1}\ K^{-1}$. The available data did not allow any reaction mechanism to be proposed, but the strongly negative values of the activation entropies indicate an associatively activated rate-determining step, similar to the water exchange reactions on some alkali metal ions (Li^+, Na^+, K^+) (*290*).

The dissociation reactions of Tl^+ cryptates in water (and other solvents) have been followed conductimetrically in stopped-flow experiments (*67*). An equilibrium mixture of Tl^+ cryptate, with a concentration ratio of Tl^+ to cryptate > 1, was mixed with an excess of acid ($HClO_4$, CF_3SO_3H). The pseudo–first-order rate constant, k_e, was found to be linearly dependent on the acid concentration:

$$k_e = k_d + k_H[H^+]/\gamma_\pm^2. \tag{5}$$

The mean molar activity coefficients, $\gamma_\pm$, were calculated using the Davies equation (*291*). The rate constants, k_d, of the uncatalyzed dissociation were determined by extrapolation of k_e to zero acid concentration

and are listed in Table VII, together with the formation rate constants k_f, calculated using the stability constant (K_1) values given in Table I ($K_1 = k_f/k_d$). There seems to be no relation between the rate constants and the stability constants for the complexes in aqueous solution (in contrast to those in other solvents). It is suggested that water molecules may interact with the complexed Tl^+ through the space between the arms of the cryptand, and that water forms hydrogen bonds with the nitrogen and oxygen atoms of the ligand, which would explain the faster dissociation rate in aqueous solution than in other solvents.

2. Thallium(II)

Because of the instability of Tl(II) (Section II,B), only one ligand exchange reaction has been studied:

$$Tl_{aq}^{2+} + Cl^- \underset{k_{-1}}{\overset{k_1}{\rightleftharpoons}} TlCl^+ \qquad (6)$$

by means of pulse radiolysis with spectrophotometric detection (*77*). The rate constants were calculated (under certain assumptions): $k_1 = 9 \cdot 10^9\ M^{-1}s^{-1}$ and $k_{-1} = 1.4 \cdot 10^5\ M^{-1}\ s^{-1}$. The rate of the anation reaction (6) is certainly close to the diffusion limit, like the anation reactions of the Tl_{aq}^{3+} ion (*95, 169*) (see next section).

3. Thallium(III)

For thallium(III), the number of ligand exchange studies is also very limited (*94, 95, 168, 169, 173, 174, 292–295*). Fujimoto *et al.* (*293, 294*) studied the ligand exchange between thallium(III) in acidic aqueous solution and two organic ligands: 4-(2-pyridylazo)resorcinol (PAR) and semixylenol orange (SXO). The reacting thallium species were assumed to be Tl_{aq}^{3+} and $Tl(OH)(OH_2)_5^{2+}$. The reactions were found to be first-

TABLE VII

DISSOCIATION (k_d) AND FORMATION (k_f) RATE CONSTANTS FOR Tl^+ CRYPTATE COMPLEXES, EQ. (5)[a]

Ligand:	(2,2,1)	(2,2,2)	(2_B2,2)	(2_B2_B,2)
$k_d(s^{-1})$	11.0	5.99	80.6	160
$k_f(s^{-1})$	$6.9 \cdot 10^7$	$2.4 \cdot 10^7$	$5.5_8 \cdot 10^7$	$6.5 \cdot 10^6$

[a] For the stability constants of the complexes, see Table I; the structure of the ligands is shown in Fig. 2.

order both for thallium and for the entering ligand. For $Tl(OH)(OH_2)_5^{2+}$, the rate constants of the complex formation for both ligands are of the same order of magnitude: $1.8 \cdot 10^5\ M^{-1}\ s^{-1}$ for 4-(2-pyridylazo)resorcinol (H_3L^+) and $3 \cdot 10^5\ M^{-1}\ s^{-1}$ for semixylenol orange (H_4SXO^0). A reaction mechanism was proposed, involving outer-sphere complex formation and subsequent dissociation of a coordinated water molecule from the thallium species as the rate-determining step (*294*). For the complex formation reactions of the Tl_{aq}^{3+} ion, the rate constant has been calculated to be $4.1 \cdot 10^4\ M^{-1}\ s^{-1}$ for PAR as a ligand, and $7 \cdot 10^5\ M^{-1}\ s^{-1}$ for SXO (or rather, H_3SXO^-). For the latter ligand, the ligand exchange reaction was accompanied by an oxidation of SXO by Tl(III), which caused a slow decrease in absorbance.

Lincoln *et al.* (*292*) studied chloride exchange between the free chloride and probably $TlCl_6^{3-}$ (see Section II,C,2) by measuring ^{35}Cl NMR line broadening in aqueous solutions containing concentrated hydrochloric acid, [HCl] = 7 and 11 M. Under these conditions the line widths were dominated by quadrupolar relaxation. Only a lower limit for the pseudo–first-order rate constant of the exchange reaction

$$TlCl_6^{3-} + {}^*Cl^- \rightleftharpoons Tl{}^*Cl_6^{3-} + Cl^- \qquad (7)$$

could be estimated, $k \geq 1 \cdot 10^7\ s^{-1}$ at 25°C (for the rate equation rate = $k[TlCl_6^{3-}]$).

The paucity of studies concerning ligand exchange reactions for thallium may have been caused by the fact that these reactions are usually fast, not only on the traditional kinetic time scale but also on the NMR time scale of common NMR nuclei, e.g., ^1H, ^{13}C or ^{35}Cl. Towards this end, thallium NMR spectroscopy with its vast chemical shift range provides a powerful means for accessing this fast-exchange time scale (*39, 40, 163, 167*). In addition, the high sensitivity of this technique permits variation of the concentration of the studied species over a very wide range, from micromolar to molar, which is often important in kinetic measurements in general and for systems with low solubility in particular. During the last years the ^{205}Tl NMR technique has been used by the present reviewer and his co-workers to obtain a deeper insight into the kinetics and mechanisms of exchange reactions involving several thallium(III) halide and pseudohalide complexes (*95, 110, 168, 169, 174*). The initial observation of separate ^{205}Tl NMR signals of Tl_{aq}^{3+}, $TlCl^{2+}$, $TlBr^{2+}$, and $TlBr_2^+$ complexes in acidic aqueous solution (*112*) showed that at millimolar thallium concentrations, the halide exchange between these species is slow on the time scale defined by

their chemical shift differences (Fig. 13). For higher complexes only one signal was observed, but its line width was found to be controlled by chemical exchange. These observations allowed determination of the pre-exchange lifetimes for the various thallium halide complexes (*174*).

The first extensive study of ligand exchange on thallium(III) complexes comprised mutual chloride exchange between the various $TlCl_n^{3-n}$ (n = 1–4) complexes, as well as between the thallium chloro complexes and the free chloride ion in aqueous solution containing

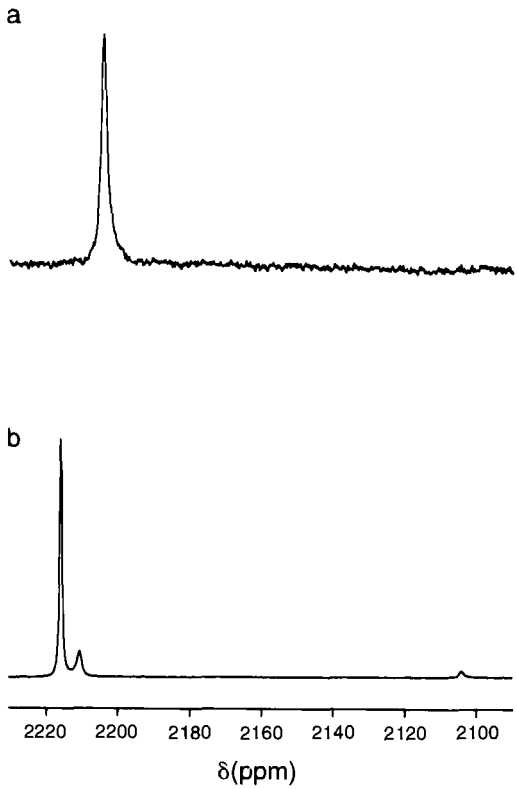

FIG. 13. ^{205}Tl NMR spectra (at 230.8 MHz) of an aqueous solution containing $[Tl(III)]_{tot}$ = 0.020 M and $[Cl^-]_{tot}$ = 0.0224 M in 3 M $HClO_4$. (a) At 25°C, one exchange-averaged signal; the spectrum exhibits fast chemical exchange between the thallium complexes on the time scale determined by the differences between their individual chemical shifts. (b) At 0°C, the ligand exchange between the complexes $Tl(OH_2)_6^{3+}$ (at 2104.0 ppm), $TlCl_2^+$ (at 2210.5 ppm), and $TlCl^{2+}$ (at 2215.8 ppm) is slow. The chemical shifts are reported in parts per million toward higher frequency with respect to an infinitely diluted aqueous solution of $TlClO_4$. Reprinted from Bányai and Glaser (*169*). Copyright © 1989 American Chemical Society.

constant ionic medium (*169*). From the line broadening of the different individual or exchange-averaged ^{205}Tl NMR signals measured at total thallium concentrations varying between 0.5 and 50 mM and a chloride/metal ratio between 0 and 7, the rate constants for all the exchange reaction pathways prevailing at chemical equilibrium have been determined. The complex formation or anation reactions,

$$TlCl_n^{3-n} + Cl^- \overset{k'_{n,n+1}}{\rightleftharpoons} TlCl_{n+1}^{2-n} \tag{8}$$

usually observed for ligand exchange on metal ion complexes in solution, have also been detected in this system for the pairs (1,2), (2,3), and (3,4). The rates of these reactions are proportional to $k'_{n,n+1}[TlCl_n^{3-n}][Cl^-]$, and the rate constants are of the order 10^8–10^9 M^{-1} s^{-1} (see Table VIII, later). An associatively activated interchange mechanism was proposed on the basis of (1) the second-order rate law; (2) the strongly negative activation entropy for the reaction represented by k'_{34}: $\Delta S^{\neq} = -107$ J mol^{-1} K^{-1}; and (3) the relatively large size of the Tl^{3+} ion as compared to the lower members of the aluminum group, considering that the solvent exchange reactions for Al^{3+}, Ga^{3+}, and In^{3+} turn from dissociative to dissociative in the named order for all studied cases (*296*).

Far more surprising was the fact that the anation reactions constituted only a minor part of the chloride exchange in this chemical system. Instead, up to the Cl/Tl ratio ≈ 3, the dynamics is dominated by a direct ligand exchange between two thallium complexes,

$$TlCl_m^{3-m} + TlCl_n^{3-n} \overset{k_{m,n}}{\rightleftharpoons} TlCl_m^{3-m} + TlCl_n^{3-n}, \tag{9}$$

where the exchanging complexes have the following number of ligands: (0,1), (1,2), (2,3), and (0,2). It would seem less probable that two positively charged species come so close to each other that a ligand exchange reaction can take place, e.g.,

$$Tl_{aq}^{3+} + {}^*TlCl_{aq}^{2+} \overset{k_{01}}{\rightleftharpoons} TlCl_{aq}^{2+} + {}^*Tl_{aq}^{3+} \tag{9a}$$

However, the obvious line broadening dependence on the total thallium concentration leaves no doubt that this is the dominating reaction path at low Cl/Tl values. Also, here the rate laws are bimolecular, rate = $k_{m,n}[TlCl_m^{3-m}][TlCl_n^{3-n}]$, but the rate constants are several orders of

magnitude lower than those for the anation reactions above (cf. Table VIII and Fig. 14a). The direct chloride exchange reactions between the thallium complexes [Eq. (9)] can be observed only because the rate of the anation reactions is decreased significantly by the low free chloride concentration, which in turn is due to the high stability of the $TlCl_n^{3-n}$ complexes (*90, 91, 112*); see Section II,C,2. For example, in an acidic solution of $[Tl(III)]_{tot} = 0.05$ M and $[Cl^-] = 0.05$ M, the free chloride concentration is less than 10^{-6} M (cf. Fig. 14b).[2] The relative contributions of the different exchange pathways to the total exchange rate as a function of the Cl/Tl ratio are shown in Fig. 14a. It can be noted that this exchange system is relatively complicated: for example, in the range $0.7 < Cl/Tl < 1.5$, six parallel paths with comparable rates coexist. Notwithstanding, the dynamics of ligand exchange could be determined because at selected solution compositions only one or two exchange reactions dominate. For the reaction type (9), an I_d mechanism was suggested. However, the kinetic and mechanistic information on ligand exchange reactions involving Tl^{3+} or other d^{10} ions is very limited or nonexistent, and the available data were not sufficient to permit definitive conclusions to be drawn on the mechanistic details.

Therefore, in order to verify the cited proposals for the mechanisms, the same authors performed a systematic ^{205}Tl NMR line broadening study of the ligand exchange dynamics of the $Tl(III)–Br^-$ system in acidic aqueous solution in the same constant ionic medium (*95*). As a result of this study, similar reaction paths were proposed for the bromide exchange between the $TlBr_n^{3-n}$ complexes, as suggested previously for the chloride system (*169*). The relative contributions of each of the 10 exchange pathways to the overall ligand exchange are shown in Fig. 15a. The dominance of the direct ligand exchange between the thallium complexes, Eq. (9), compared to the anation reactions, Eq. (8), is even more pronounced here than in the chloride case, in agreement with the larger stability constants of the $TlBr_n^{3-n}$ complexes, and hence the very low free bromide concentration (e.g., less than 10^{-8} M at Br/Tl = 1, cf. Fig. 15b). The obtained rate constants are given in Table VIII. Comparison of the rate constants for both ligands lends additional support to the proposed reaction mechanisms. Hence, for the anation reactions, which become dominating at higher X/Tl ratios (where the free halide concentration is high; see Fig. 15), the previously proposed I_a mechanism with ligand penetration as the rate-determining step is still preferred. First, the rate constants are an

[2] Note that the anation reaction k'_{01} has not been observed at all, and only the higher limit of k'_{01} could be estimated.

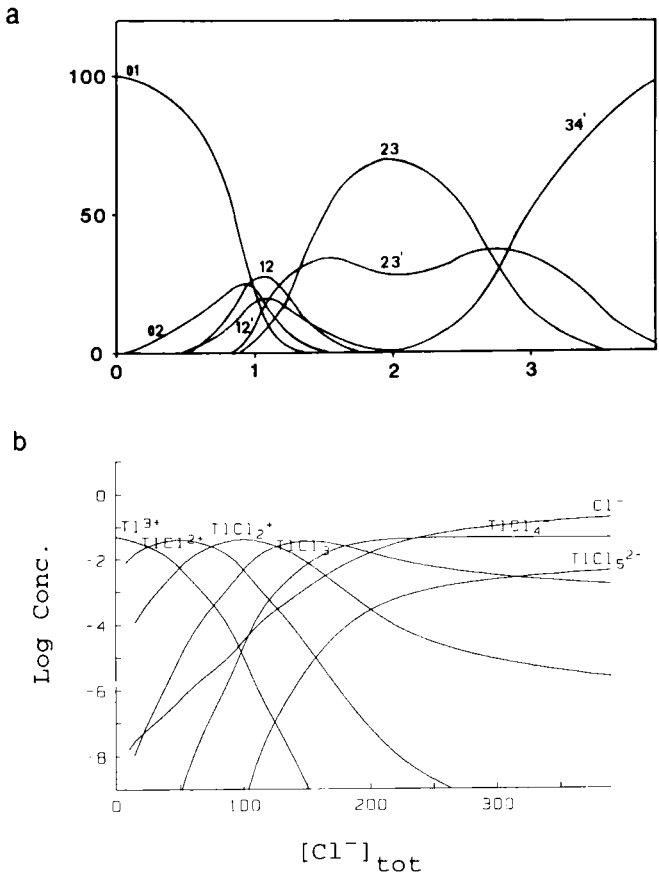

FIG. 14. (a) Percentage contribution (y-axis) of different parallel chloride exchange paths (numbered by the indices of the corresponding rate constants) to the total exchange rate $w = \Sigma_{m,n}(2k_{mn}[TlCl_m^{3-m}][TlCl_n^{3-n}] + k'_{mn}[TlCl_n^{3-n}][Cl^-])$ as a function of the $[Cl^-]_{tot}/[Tl]_{tot}$ ratio, in an aqueous solution containing $TlCl_n^{3-n}$ complexes (n = 0–5) and free chloride. T = 25°C. Reprinted from Bányai and Glaser (*169*). Copyright © 1989 American Chemical Society. (b) Distribution of the different species [log(molar concentration)] in aqueous solutions of 50 mM Tl(III) and varying concentrations of chloride (ionic medium: 3 M $HClO_4$), showing also the free chloride concentration [equilibrium constants β_1–β_4 were taken from Woods *et al.* (*90*), and β_5 from Bányai and Glaser (*169*).

order of magnitude larger in the case of bromide than in the case of chloride. Second, if water dissociation is the rate-determining step for this reaction, one would expect a rate increase in the order $TlBr(OH_2)_5^{2+} < TlBr_2(OH_2)_4^+ < TlBr_3(OH_2)_2$ because of the weakening of the thallium–water bonds (*112, 115, 142, 145*). Third, the estimated

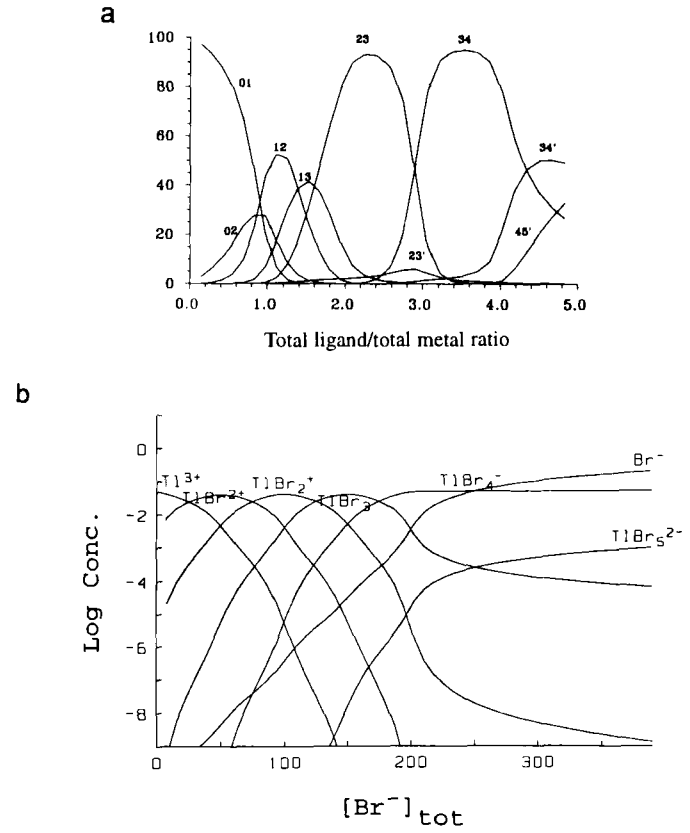

FIG. 15. (a) Percentage contribution (y-axis) of different parallel bromide exchange paths (w_{mn}, numbered by the indices of rate constants) to the total exchange rate $w = \Sigma_{m,n}(2k_{mn}[TlBr_m^{3-m}][TlBr_n^{3-n}] + k'_{mn}[TlBr_n^{3-n}][Br^-])$ as a function of the $[Br^-]_{tot}/[Tl]_{tot}$ ratio, in an aqueous solution containing $TlBr_n^{3-n}$ complexes (n = 0–5) and free bromide. T = 25°C. The contribution of the path corresponding to k'_{12} is negligible on this scale. Reprinted from Bányai and Glaser (*95*). Copyright © 1990 American Chemical Society. (b) Distribution of the different species [log(molar concentration)] in aqueous solutions of 50 mM Tl(III) and varying concentrations of bromide (ionic medium: 3 M $HClO_4$), also showing the free bromide concentration [equilibrium constants β_1–β_4 were taken from Yakovlev *et al.* (*103*) and β_5 from Bányai and Glaser (*95*).

rate constants for Reaction (8), k'_{mn}, are much higher than those suggested for the water exchange on the $TlBr_n^{3-n}$ complexes (see below). The associative mechanism for the Tl(3+) ion is compatible with the turn of the mechanism of the solvent exchange reactions from dissociative to associative when the size of the metal ion increases between Al(3+), Ga(3+), and In(3+) (*296*).

TABLE VIII

RATE CONSTANTS FOR THE VARIOUS HALIDE EXCHANGE REACTIONS BETWEEN THE TlX_n^{3-n} COMPLEXES IN AQUEOUS SOLUTION AT 25°C

For X = Br		For X = Cl	
$k_{mn}/M^{-1}s^{-1}$	k_{mn}^{rds}/s^{-1}	$k_{mn}/M^{-1}s^{-1}$	k_{mn}^{rds}/s^{-1}
Reaction type (8):			
$k'_{01} < 10^{10}$			
k'_{12} $(5.8 \pm 1.5) \times 10^9$	1×10^9	$(3.2 \pm 0.4) \times 10^8$	6×10^7
k'_{23} $(5.6 \pm 1.9) \times 10^{10}$	6×10^{10}	$(1.3 \pm 0.2) \times 10^9$	1×10^9
k'_{34} $(1.5 \pm 0.7) \times 10^9$	5×10^9	$(4.7 \pm 1.3) \times 10^8$	2×10^9
Reaction type (9):			
k_{01} $(2.8 \pm 0.5) \times 10^4$	4×10^8	$(4.5 \pm 0.4) \times 10^4$	6×10^8
k_{02} $(7.1 \pm 2.1) \times 10^5$	2×10^8	$(6.4 \pm 1.1) \times 10^5$	1×10^8
k_{11} $(6.1 \pm 1.3) \times 10^3$	—	$(9.4 \pm 2.7) \times 10^3$	—
k_{12} $(7.5 \pm 0.7) \times 10^4$	6×10^6	$(5.2 \pm 0.4) \times 10^4$	4×10^6
k_{13} $(2.4 \pm 0.6) \times 10^7$	8×10^6	—	—
k_{23} $(8.2 \pm 1.7) \times 10^6$	3×10^7	$(2.7 \pm 0.7) \times 10^7$	9×10^7
k_{34} $(2.3 \pm 0.5) \times 10^7$	8×10^7	$<3 \times 10^7$	—

For the direct exchange between the thallium complexes, Eq. (9), the dissociatively activated reaction mechanism previously proposed for the thallium chloride system (*169*) could now be confirmed and

$$Tl(OH_2)_6^{3+} + TlBr(OH_2)_5^{2+}$$

$$K_{01}^{os} \uparrow\downarrow$$

$$Tl(OH_2)_6^{3+}, BrTl(OH_2)_5^{2+}$$

$$k_{01}^{d} \uparrow\downarrow -H_2O$$

$$(H_2O)_5Tl{-}Br{-}Tl(OH_2)_5^{3+}$$

$$k_{01}^{r} \uparrow\downarrow +H_2O$$

$$(H_2O)_5TlBr^{2+}, Tl(OH_2)_6^{3+}$$

$$\uparrow\downarrow K_{01}^{os}$$

$$TlBr(OH_2)_5^{2+} + Tl(OH_2)_6^{3+}$$

SCHEME 1.

detailed. Scheme 1 exemplifies this reaction path for the complexes $Tl(OH_2)_6^{3+}$ and $TlBr(OH_2)_5^{2+}$. The scheme differs from the classical

picture of I_d-type ligand substitution processes because the entering ligand is also a complex. This means that either the dissociation of the water molecule, $k_{01}{}^{d}$, or the rearrangement of the chemical bonds in the outer-sphere complex can be the rate-determining step. The outer-sphere complex formation constant, K_{os}, could be estimated using the Bjerrum–Fuoss equation (*297, 298*), which assumes only electrostatic interactions to be present:

$$K_{os} = 4\pi Na^3/3000 \exp(-Z), \tag{10}$$

where N is Avogadro's number, a is the encounter complex separation (5 Å), and Z is the coulombic energy divided by kT. The resulting rate constants for the rate-determining step ($k_{mn}{}^{rds}$) for both the chloride and the bromide complexes are shown in Table VIII. It can be noted that for all four reactions of the type (9) in which the $Tl(OH_2)_6{}^{3+}$ species participates, namely those denoted by $k_{01}{}^{rds}$ and $k_{02}{}^{rds}$ (for X = Cl *and* Br), the rate-determining step is of the same order of magnitude. The fact that k^{rds} does not depend on the quality of the ligand can be interpreted as a confirmation of the proposed I_d mechanism in which the rate-determining step is k^d, i.e., water molecule leaving the ion pair, probably the $Tl(OH_2)_6{}^{3+}$ part of the latter. This value, $\sim 3 \cdot 10^8$ s^{-1}, can be assumed to be equal to the rate constant of water exchange for the hydrated Tl^{3+} ion, corresponding to $\sim 5 \cdot 10^7$ s^{-1} for a particular coordinated water molecule. This rate constant has been impossible to obtain by any other experimental method and is missing in all previously published books and articles on hydrated metal ions in solution (*203, 296, 299, 300*). The value previously reported by Sutin, $k \geq 3 \cdot 10^9$ s for the replacement of a particular water molecule, was calculated from data for the $Fe^{3+} + Cl^-$ reaction (*301*), and thus can be only seen as a very rough estimate. Still, it can be in agreement with the present value considering uncertainty in parameter a of Eq. (10), and that the value of K^{os} was calculated without correction for the ionic strength.

A similar situation occurs for the direct exchange reactions between the complexes where the higher $TlX_n{}^{3-n}$ species are involved (cf. Table VIII). Thus, $k_{12}{}^{rds}$ and $k_{13}{}^{rds}$ for X = Br and $k_{12}{}^{rds}$ for X = Cl are all equal to about $6 \cdot 10^6$ s^{-1}.[3] For the direct exchange reactions between the second and the third complexes, $k_{23}{}^{rds}$ is $9 \cdot 10^7$ and $3 \cdot 10^7$ s^{-1}, for X = Cl and Br, respectively. The independence of k^{rds} on the quality

[3] The reaction corresponding to k_{11} is not considered here; it is slightly different and may have another rate-determining step.

of the ligand is compatible with the suggested I_d reaction mechanism. Moreover, the water exchange rate increases slightly with the number of halide ligands between $TlX(OH_2)_5^{2+}$, $TlX_2(OH_2)_4^{+}$, and $TlX_3(OH_2)_2$ ($k^{rds} \approx 6 \cdot 10^6$, $6 \cdot 10^7$, and $8 \cdot 10^7$ s^{-1}, respectively). If this trend is significant, it would be compatible with the increasing Tl–OH_2 distance in the complexes in solution: 2.24 Å in $TlX(OH_2)_5^{2+}$, ~2.32 Å in $TlX_2(OH_2)_4^{+}$, and ~2.36 Å in $TlX_3(OH_2)_2$ (*145*). The authors were not able to explain why the water exchange rate for the hydrated Tl^{3+} ion is faster than that for the halide complexes; the Tl–OH_2 distance in $Tl(OH_2)_6^{3+}$ is relatively short, 2.21 Å (as determined by EXAFS (*145*) or 2.235 Å (from LAXS measurements) (*142*). There might be a common reason for the water lability for the hexahydrated Tl^{3+} and the Hg^{2+} ions, since they are isoelectronic and both exhibit second-order Jahn–Teller effects (*145, 200*). For the $Cu(OH_2)_6^{2+}$ ion with its first-order Jahn–Teller effect, the labilization of the coordinated water molecules has been associated with the stabilization achieved upon the formation of a five-coordinated transition state (*302*).

This reaction mechanism, where two coordinated metal ions participate in direct ligand exchange, has hitherto been reported in only a few cases. We have found only one comparable example in the literature, where the authors (*303*) have reported direct halide exchange on the coordinated indium(3+) ion in aqueous solution:

$$In(OH_2)_6^{3+} + {}^*In(OH_2)_5X^{2+} \overset{k_X}{\rightleftharpoons} In(OH_2)_5X^{2+} + {}^*In(OH_2)_6^{3+}, \quad (11)$$

where X = F, Cl, Br, or I, and determined that the rate constants decrease slightly from F to I: $k_F = 5.9 \cdot 10^4$, $k_{Cl} = 8.5 \cdot 10^3$, $k_{Br} = 8.6 \cdot 10^3$, $k_I = 2.2 \cdot 10^3$ M^{-1} s^{-1}, in parallel with the corresponding stability constants. The authors (*303*) have not obtained any additional data which would allow them to assess the reaction mechanism. These values are of the same order of magnitude as the corresponding k_{01} values for thallium(3+) (cf. Table VIII), but the rate-determining step is probably different, since the water exchange rate for the hydrated In^{3+} ion has been found to be about 10^6 s^{-1} (*296*), i.e., about two orders of magnitude smaller than that found for Tl^{3+} (*95*).

Körös and co-workers (*304, 305*) have studied the behavior of the Belousov–Zhabotinsky oscillatory reaction in the presence of thallium(III), which in this context functions as a bromide-removing agent. Körös *et al.* have explained their results by assuming that the ligand exchange occurs according to the following reactions:

$$TlBr_{n-1}^{4-n} + Br^- \overset{k_n}{\rightleftharpoons} TlBr_n^{3-n}, \qquad (12)$$

where $n = 1–4$, and assumed that these reactions occur in two steps. After the fast outer-sphere complex formation between the bromide and the hydrated thallium complex (K_{os}), the second (rate-determining) step involves replacement of a water molecule in the inner coordination sphere of the metal ion. The authors have estimated that the rate constant for the second step is $k_{H_2O} \approx 2 \cdot 10^6$ s^{-1} by assuming that it corresponds to the reaction

$$Tl(OH_2)_6^{3+} + H_2{}^*O \rightleftharpoons Tl(^*OH_2)_6^{3+} + H_2O \qquad (13)$$

and extrapolating from the known rate constants of water exchange for the hydrated metal ions Al^{3+}, Ga^{3+}, and In^{3+}. From this value of k_{H_2O} and from the estimated value for K_{os}, the rate constants for reactions (12) have been calculated: $k_1 = 10^5$, $k_2 = 10^4$, $k_3 = 2.5 \cdot 10^2$ and $k_4 = 10^2$ M^{-1} s^{-1}. These results differ from the results of Bányai and Glaser discussed earlier (*95, 169*), both concerning the reaction pathways and the value of k_{H_2O}. The reason for this discrepancy may be that the rate constant for water exchange of the Tl_{aq}^{3+} ion cannot be extrapolated from the corresponding values of the lower Group 13 elements because of the much lower $5d_{z^2}$–$6s$ energy gap for thallium and, consequently, the probable presence of the second-order Jahn–Teller effect in the latter ion, which may lead to a labilization of its coordinated water molecules (cf. the discussion in Section III). Moreover, in the solutions studied by Körös *et al.* (*304, 305*), the high sulfuric acid concentration (1 M) can lead to thallium(III)–sulfate complex formation [in fact, the authors (*304, 305*) claim that $Tl(HSO_4)_2(H_2O)_4^+$ is the predominant species], which may influence the reaction mechanism. In any case, the authors (*304, 305*) do not present any kind of evidence that Eq. (12) represents the dominating reaction pathways.

In this context it can be mentioned that the proton exchange of the $Tl(OH_2)_6^{3+}$ ion in acidic solution has been studied by means of the IQENS (incoherent quasi-elastic neutron scattering) method (*173*). The studied solution ([$Tl(ClO_4)_3$] = 1.809 M, [$HClO_4$] = 1.909 M) was placed in the fast exchange limit, i.e., the thallium to water-proton binding time is shorter than 10^{-10} s. The average proton diffusion coefficient D in this solution at 25°C was determined to $(0.52 \pm 0.02) \cdot 10^{-9}$ m^2 s^{-1}, which is comparable to the corresponding values in two other metal

ion aqueous perchlorate solutions of similar ionic strength: $0.488 \cdot 10^{-9}$ $m^2 s^{-1}$ for Cr^{3+} and $0.504 \cdot 10^{-9}$ $m^2 s^{-1}$ for Fe^{3+} (*306, 307*).

The direct ligand exchange between two complex species (as compared to anation reactions) becomes even more important for the strongest monodentate thallium(III) complexes known, namely those with cyanide (*97*). The cyanide exchange in aqueous solution containing Tl(III) and various concentrations of CN^-/HCN is currently being studied in this laboratory (*170*). The preliminary results show that the cyanide exchange reactions are much slower than those of the previously discussed halide systems (*95, 169*). As a consequence, no line broadening can be observed in NMR spectra, and the ligand exchange has to be studied with the so-called magnetization transfer techniques (*168, 308*). Moreover, for the thallium cyano complexes $Tl(CN)_n^{3-n}$ with only a few ligands ($n \leq 2$), significant exchange on the ^{205}Tl NMR T_1 time scale (*309*) occurs only at elevated temperatures, as exemplified in Fig. 16. It can be noted that the fastest cyanide exchange reaction is that between the species $Tl(OH_2)_6^{3+}$ and $Tl(CN)^{2+}$. The exchange

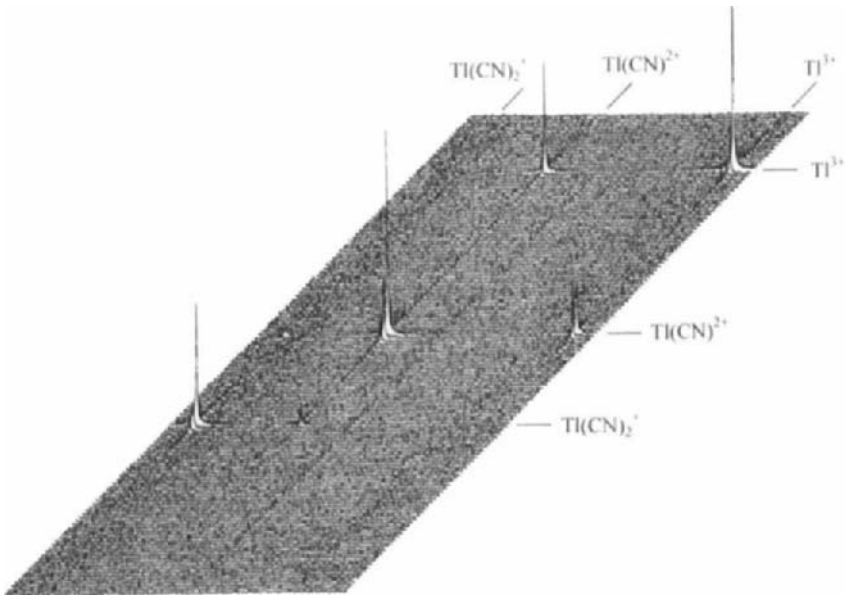

FIG. 16. ^{205}Tl NMR 2D-EXSY spectrum of an acidic aqueous solution containing the thallium species $Tl(OH_2)_6^{3+}$, $Tl(CN)^{2+}$, and $Tl(CN)_2^+$, showing the dominating cyanide exchange reactions. Temperature = 63°C. $[Tl(III)]_{tot}$ = 0.099 M, $[CN^-]_{tot}$ = 0.150 M, $[H^+]$ = 1.12 M (natural isotope composition). Spectrometer frequency 51.9 MHz, mixing time = 0.1 s.

between $Tl(CN)^{2+}$ and $Tl(CN)_2^+$ is one order of magnitude slower, but there is no observable ligand exchange between $Tl(OH_2)_6^{3+}$ and $Tl(CN)_2^+$.

Recently, a preliminary account of this study has appeared, dealing with cyanide exchange in a selected aqueous solution in which only the species $Tl(CN)_3$, $Tl(CN)_4^-$, and HCN were present (enriched to 95% in ^{13}C) (*168*). The authors showed that in this special case a combination of two-dimensional ^{205}Tl NMR and ^{13}C NMR can provide (because of the well-resolved heteronuclear spin–spin couplings) otherwise inaccessible information on the chemical (and nuclear spin) dynamics. Representative 2D-EXSY (exchange spectroscopy) spectra are shown in Fig. 17. From the ^{13}C NMR spectrum, it can be seen that the most efficient ligand exchange reaction in this solution (largest cross peaks) is the one between $Tl(CN)_3$ and $Tl(CN)_4^-$, $k_{34}^{obs} \approx 35\ s^{-1}$. From the same spectrum, the rate constants for the remaining exchange reactions could be determined:

$$Tl(CN)_4^- \rightleftharpoons HCN, \qquad k_{4,HCN}^{obs} = 3\ s^{-1}, \tag{14}$$

$$Tl(CN)_3 \rightleftharpoons HCN, \qquad k_{3,HCN}^{obs} = 1\ s^{-1}. \tag{15}$$

The ^{205}Tl NMR 2D spectrum provided additional dynamic information. For example, the peculiar appearance of the cross peak region originates from the fact that only those reactions occur which include migration of a single cyanide ion. Even if this result could be expected, since a simultaneous transfer of more than one cyanide ion is less probable, it is interesting that such information can be obtained. From the latter spectrum (Fig. 17b), the rate constants determined previously from the ^{13}C NMR EXSY could be calculated independently and led to similar results. It is remarkable that all this (and much more) dynamic information has been obtained from a single solution and, at least in principle, from only two spectra (Fig. 17).

The rate constants of the cyanide exchange reactions ($k_{34}^{obs} \approx 35\ s^{-1}$, $k_{4,HCN}^{obs} = 3\ s^{-1}$, $k_{3,HCN}^{obs} = 1\ s^{-1}$) are several orders of magnitude smaller than those for the corresponding thallium(III) halide reactions

FIG. 17. Two-dimensional exchange spectroscopy (2D-EXSY) spectra of an aqueous solution containing $Tl(CN)_3$, $Tl(CN)_4^-$, and HCN in a concentration ratio 0.021 : 0.018 : 0.166 M, enriched to 95% in ^{13}C. Temperature = 25°C. Reprinted from Batta *et al.* (*168*). Copyright © 1993 American Chemical Society. (a) ^{13}C NMR spectrum, recorded at 100 MHz, mixing time = 0.035 s. The spin–spin coupling between ^{13}C and ^1H is observed because the proton exchange between HCN and bulk water is slow (*309a*). (b) ^{205}Tl NMR spectrum, recorded at 231 MHz, mixing time = 0.020 s.

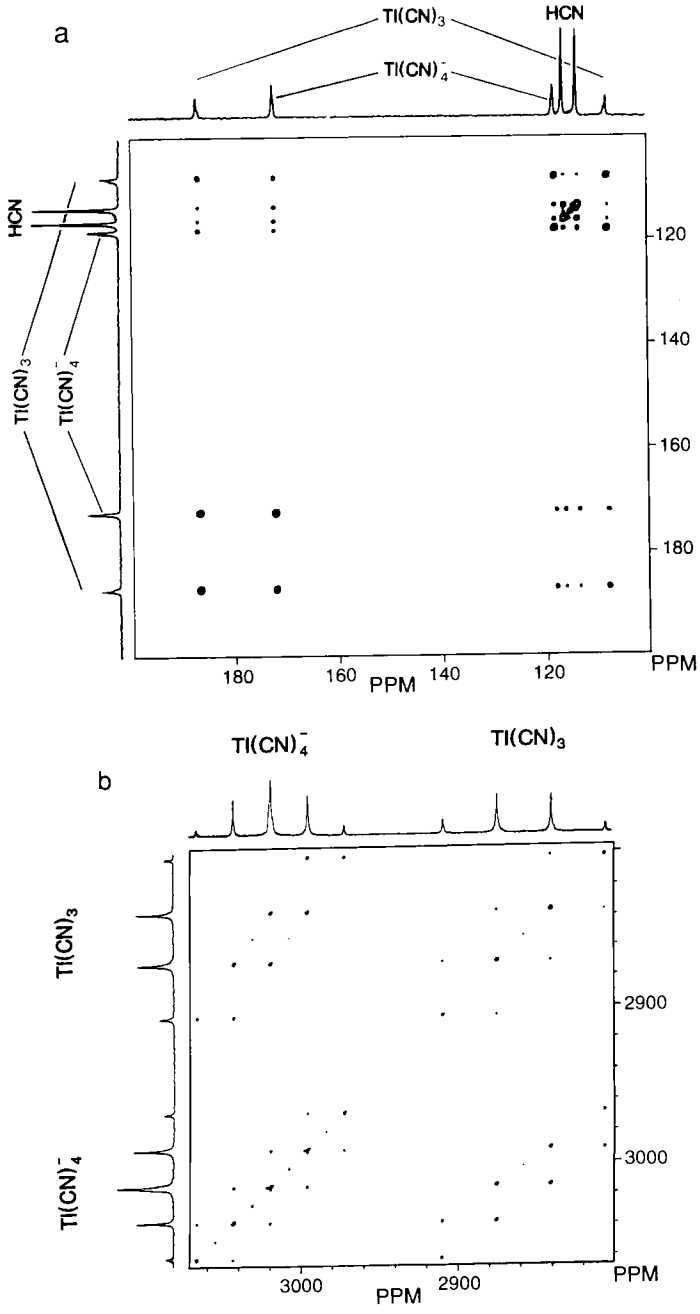
a
Tl(CN)3
HCN
Tl(CN)4−
HCN
Tl(CN)3
Tl(CN)4−
120
140
160
180
180
160
PPM
140
120
PPM
b
Tl(CN)4−
Tl(CN)3
Tl(CN)3
Tl(CN)4−
2900
3000
3000
PPM
2900
PPM

discussed earlier. For example, $k_{34}^{obs} \approx 10^6$ s^{-1} for $TlBr_n^{3-n}$ complexes in the range $3 < Br/Tl < 4$ ((*95*), Fig. 6B), where the dominating exchange reaction is

$$TlBr_3 + Tl^*Br_4^- \rightleftharpoons Tl^*Br_4^- + TlBr_3 \qquad (16)$$

(see Fig. 15). It can be concluded that the rate-determining step for the cyanide exchange reactions is much slower than the rate of water exchange estimated earlier for the halide complexes, TlX_n^{3-n} (*95*). The rds possibly involves breaking of the very strong Tl–CN bonds in the $Tl(CN)_n^{3-n}$ complex (Section II,C,3). A detailed study of the kinetics and mechanisms of ligand exchange of the latter complexes in aqueous solution is in progress in this laboratory (*170*).

No ligand exchange studied have been reported for other thallium(III) pseudohalide complexes. However, from the value of the spin–spin coupling constant $^3J(^{205}Tl-^{15}N) = 143$ Hz in the $TlSCN^{2+}$ complex (*110*), it can be estimated that the pseudo–first-order rate constant for the thiocyanate exchange on this complex is smaller than ~ 400 s^{-1}.

Thallium(III) in solution can in some cases form moieties so stable that practically no free Tl_{aq}^{3+} ion can be detected. This is, for example, the case for the previously discussed $Tl(CH_3)_2^+$ ion, the polydentate carboxylic acid complexes (TTHA, DTPA, EDTA, CDTA), and some polydentate amine complexes (TPEN, PENT-EN) (for explanation of the abbreviations, see Table III and Section III,B,8). The coordination number in the two latter types of compounds is high, up to eight (*109*). Hence, in the moiety of the type Tl(EDTA), usually not more than one additional ligand can be accommodated; the latter can be relatively labile and can undergo exchange with a free ligand. An example of such behavior is the X-ligand exchange in the $Tl(EDTA)X^{2-}$ complexes (where X = Cl, Br, CN, or SCN), which has been studied in aqueous solution (I = 1 M $NaClO_4$) by means of ^{205}Tl and ^{13}C NMR spectroscopy (*94*). For the halide complexes, only the following halide exchange reaction has been identified:

$$Tl(EDTA)X^{2-} \underset{k_f}{\overset{k_d}{\rightleftharpoons}} Tl(EDTA)_{aq}^- + X^-, \qquad (17)$$

with the rate constants shown in Table IX. It can be observed that as a result of the high stability of the $Tl(EDTA)(CN)^{2-}$ complex, the kinetics of the cyanide system differs from the kinetic behavior of the other

TABLE IX

KINETIC DATA FOR X LIGAND EXCHANGE REACTIONS INVOLVING $Tl(EDTA)X^{2-}$ IN AQUEOUS SOLUTION[a]

Complex	k_d[b] $[s^{-1}]$	k_2[d] $[M^{-1}s^{-1}]$	k_d[d] $[s^{-1}]$	k_f[e] $[M^{-1}s^{-1}]$	k_2 $[s^{-1}]$
$Tl(EDTA)Cl^{2-}$	$\geq 1.7 \cdot 10^4$			$\geq 3.4 \cdot 10^6$	$\geq 4.6 \cdot 10^7$
$Tl(EDTA)Br^{2-}$	$(2.7 \pm 0.3) \cdot 10^3$			$8.6 \cdot 10^6$	$1.2 \cdot 10^8$
$Tl(EDTA)CN^{2-}$	<3[c]	$(1.5 \pm 0.3) \cdot 10^6$	$(-1 \pm 6) \cdot 10^2$	$<1.6 \cdot 10^6$	$1.3 \cdot 10^8$
$Tl(EDTA)SCN^{2-}$	$(2.0 \pm 0.2) \cdot 10^4$	$(3.0 \pm 0.5) \cdot 10^6$	$(2.7 \pm 0.6) \cdot 10^4$	$1.0 \cdot 10^7$	$1.9 \cdot 10^8$

[a] I = 1 M $NaClO_4$; temperature = 25°C (*94*). For the definitions of the rate constants, see text.
[b] Determined from the ^{205}Tl NMR signal of $Tl(EDTA)X^{2-}$.
[c] Determined from the ^{13}C NMR carbonyl signal of $Tl(EDTA)^-$.
[d] Determined from the ^{13}C NMR signal of $^{13}CN^-$ or $S^{13}CN^-$.
[e] $k_f = k_d \cdot K_X$; k_f values measured as in notes *b* and *c* above.

complexes, $Tl(EDTA)X^{2-}$. Whereas for X = Cl, Br, and SCN the dissociation reaction (17) (k_d) is relatively fast on the actual time scale, for X = CN it is so slow that it does not influence the line widths of the actual NMR spectra.

For the pseudohalide complexes, in addition to ^{205}Tl NMR spectra, ^{13}C NMR spectra of the exchanging ligand could be recorded, which made it possible to detect the following exchange pathway, in addition to reaction (17):

$$Tl(EDTA)X^{2-} + {}^*X^- \underset{k_2}{\overset{k_2}{\rightleftharpoons}} Tl(EDTA)^*X^{2-} + X^- . \qquad (18)$$

Using the rate constants k_d of the dissociation reaction (17) and the stability constants K_X (Table III) for the mixed complexes $Tl(EDTA)Br^{2-}$ and $Tl(EDTA)SCN^{2-}$, the rate constants of the formation reaction were calculated as $k_f = k_d \cdot K_X$. The obtained values, $k_f^{Br} = 8.63(\pm 0.10) \cdot 10^6\ M^{-1}\ s^{-1}$ and $k_f^{SCN} = 1.02(\pm 0.08) \cdot 10^7\ M^{-1}\ s^{-1}$, are very close to each other. The corresponding values for k_f^{Cl} and k_f^{CN} could not be measured, but the estimated limits allow that these values also fall into the same range. Thus (at least for X = Br and SCN), the formation rate of the complexes does not depend on the quality of the entering ligand. Accordingly, and assuming that the solid-state structure of the complex $Tl(EDTA)X^{2-}$ (see Fig. 12, Section III,B,8) persists in solution, it was proposed that the rate-determining step is the water dissociation (k_w) from the intermediate:

$$\underset{H_2O}{Tl(EDTA)^-} + X^- \overset{K_{os}}{\rightleftharpoons} X^- \cdots \underset{H_2O}{Tl(EDTA)^-} \overset{k_w}{\rightleftharpoons} Tl(EDTA)X^{2-} + H_2O. \quad (19)$$

In the case of a dissociative mechanism (D or I_d), approximately the same activation parameters are expected for the formation reactions (k_f) involving different X ligands [cf. reaction (17)]. Indeed, for the two complexes $Tl(EDTA)Br^{2-}$ and $Tl(EDTA)SCN^{2-}$, $\Delta H^{\neq} = 49(\pm 2)$ and $47(\pm 2)$ kJ · mol^{-1}, and $\Delta S^{\neq} = -15(\pm 8)$ and $-6(\pm 6)$ J · mol^{-1} K^{-1}, respectively. These values are also similar to the activation parameters of the water exchange for Tl_{aq}^{3+} in 3 M $HClO_4$, $\Delta H^{\neq} = 49(\pm 2)$ kJ · mol^{-1} and $\Delta S^{\neq} = +12(\pm 0.3)$ J · mol^{-1} · K^{-1}. The estimated rate of water exchange for the hydrated Tl^{3+} ion is $3 \cdot 10^8$ s^{-1} (*95*). The corresponding rate constant for $Tl(EDTA)_{aq}^-$ could be estimated using $k_f = 9.3 \cdot 10^6$ M^{-1} as an average of the rate constants for the formation of $Tl(EDTA)Br^{2-}$ and $Tl(EDTA)SCN^{2-}$ (see Table IX). Taking into account the outer-sphere repulsion by means of the outer-sphere complex formation constant, $K_{os} = 0.074$ M^{-1} for two −1 charged ions (*298*), and $k_w = k_f/K_{os} = 1.3 \cdot 10^8$ s^{-1}.

Consequently, a dissociative mechanism was assumed, with the rate-determining step being water leaving the intermediate [see Eq. (19)]. This rate constant is of the same order of magnitude as the corresponding rate constant for Tl_{aq}^{3+}. The exchange rate for one particular water molecule could be calculated, considering the number of bound water molecules in Tl_{aq}^{3+} and $Tl(EDTA)_{aq}^-$. The hydration number of Tl^{3+} is 6 (*115, 117, 142, 145*); thus, the water exchange rate for one particular water in $Tl(OH_2)_6^{3+}$ is $k'_w = 5 \cdot 10^7$ s^{-1}. In order to calculate the corresponding constant for $Tl(EDTA)_{aq}^-$, one water molecule was assumed to be coordinated to the thallium atom in this complex, according to Eq. (19) and in agreement with the known crystal structures of the Tl(EDTA)X compounds (*94, 109, 310*). Hence, $k'_w = k_w \approx 1.3 \cdot 10^8$ s^{-1}, slightly higher than the corresponding constant for $Tl(OH_2)_6^{3+}$. The increase in the water exchange rate, if significant, was attributed to the labilization effect of the ligand, $EDTA^{4-}$. This type of labilization effect has previously been demonstrated for Fe(III) complexes on the basis of activation volumes (*311*).

It may be interesting to compare these results to the ones for another trivalent metal–aminopolycarboxylate mixed complex. For europium(III), the corresponding formation rate constant of the mixed complex has been determined via time course of luminescence emission for the $Eu(DCTA)^-$–imino-diacetate system (*312*), $k_f = 1.6 \cdot 10^7$ M^{-1} s^{-1}.

If we use this rate constant to calculate the water exchange rate following the derivation used for the $Tl(EDTA)^- - X^-$ system, we obtain $k_w = k_f/K_{os} = 1.3 \cdot 10^9\ s^{-1}$ ($K_{os} = 0.012\ M^{-1}$). This value is close to the water exchange rate for the Eu_{aq}^{3+} ion (*296*). It is possible that $Tl(EDTA)_{aq}^-$ behaves similarly to rare-earth aminopolycarboxylate complexes, in which some water molecules can also be coordinated to the metal ion.

The values of the second-order rate constants, k_2, for CN^- and SCN^- [reaction (18)] are very similar, indicating no dependence on the quality of the entering ligand. If one considers the same intermediate for these reactions as proposed earlier for reaction (17), with water exchange as the rate-determining step, then the rate constants k_1 and k_d should lead to the same k_w. In fact, since $k_2 \approx 2.3 \cdot 10^6\ M^{-1}\ s^{-1}$ (average value for k_2^{CN} and k_2^{SCN}) and $K_{os} = 0.012\ M^{-1}$, we obtain $k_w = k_2/K_{os} = 1.9 \cdot 10^8\ s^{-1}$. This value is close to the k_w value for reaction (17) (for X = SCN and Br), which would support the hypothesis of similar intermediates and rate-determining steps for the two reaction types.

A complication arises from the fact that the values of the outer-sphere complex formation constants just estimated are rough and may be quite incorrect if, for example, the real effective charge of the incoming ligand cannot be approximated to -1, but rather is lower and perhaps not equal for CN^- and SCN^-. In fact, according to different calculations, the charge of the CN^- ion is distributed nearly symmetrically over the carbon and nitrogen atoms (*313*), whereas for SCN^- most of the negative charge is located on nitrogen and only 0.25 e^- on sulfur (*314*). Moreover, both ions are elongated and not spherical, making the calculation of K_{os} more uncertain.

In conclusion, it is interesting to note that the reaction type

$$TlX_m^{3-m} + TlX_n^{3-n} \overset{k_{m,n}}{\rightleftharpoons} TlX_m^{3-m} + TlX_n^{3-n}, \qquad (20)$$

which dominates the halide exchange for $TlCl_n^{3-n}$ and $TlBr_n^{3-n}$ in a wide X/Tl range (*95, 169*) (see earlier discussion), is apparently not important for the $Tl(EDTA)X^{2-}$ species. The explanation may be that the large $Tl(EDTA)X^{2-}$ unit is not likely to approach another $Tl(EDTA)X^{2-}$ or $Tl(EDTA)^-$ complex so that a suitable geometric configuration leading to an exchange of X^- can occur.

It has to be noted that all ligand exchange reactions discussed in this section [see, for example, Eqs. (8), (9), and (12)–(18)] occur in solution in chemical equilibrium, i.e., they do not cause any macroscopic chemical change. No studies have been reported on ligand exchange

for thallium complexes on the "classical" timescale, certainly because such reactions are usually very fast.

B. Electron Exchange Reactions

$Tl^{3+} + 2e^- \rightleftharpoons Tl^+$	1.25 V	(*1*)
$Tl^{3+} + e^- \rightleftharpoons Tl^{2+}$	0.33(±0.05) V	(*259*)
$Tl^{2+} + e^- \rightleftharpoons Tl^+$	2.22(±0.05) V	(*259*)

Scheme 2. Standard redox potentials involving hydrated thallium ions.

As mentioned in the introduction, the thallium(III)/thallium(I) redox couple has been widely used as a model system for electron transfer processes. There are numerous studies of both the electron transfer between two metal ions and the redox reaction between a metal ion and another ion or molecule, usually an anion. This interest has been well documented and reviewed in the past, but also in modern books dealing with electron transfer reactions (*315, 316*). Therefore, and also because the large amount of experimental and theoretical data would call for a separate review article, this subject will not be discussed here except for a general comment and a discussion of a few very recent papers.

In particular, the electron exchange reaction between the Tl^+ and Tl^{3+} ions in aqueous solution has been intensively studied, in solutions of both complexing (OH^-, Cl^-, Br^-, CN^-, N_3^-, and other) and non-complexing anions (ClO_4^-), and is assumed now to be the best-understood two-electron transfer reaction (*13, 15, 19, 21, 22, 71, 73, 75, 76, 78, 82, 259, 315, 317–326*). However, very recently this reaction was proposed to proceed through two consecutive one-electron steps, involving the intermediate with the composition [Tl(II)–Tl(II)]. Taube (*327*) favors the formation of $[Tl_2]^{4+}$ as intermediate on the grounds that (a) postulating it is reasonable in analogy to $[Hg_2]^{2+}$; (b) simultaneous $2e^-$ transfer, which would involve a charge trapping barrier four times greater than it is for $1e^-$ exchange, can be excluded on energy grounds; (c) Tl_{aq}^{2+} as an intermediate has also been excluded on energy grounds (*72*); and (d) it offers a rationalization of the observation that Cl^- and Br^- at low concentration decrease the rate of self-exchange. As polarizable ligands, they stabilize Tl(III) and Tl(I) more than [Tl(II)–Tl(II)] (analogy to Hg_2^{2+} chemistry) (*327*).

In all studied cases, the reaction has been found to be first-order with respect to both $[Tl^+]$ and $[Tl^{3+}]$, which is compatible with the mechanism

$$Tl^{3+} + Tl^{+} \rightleftharpoons Tl^{+} + Tl^{3+}, \quad (21)$$

but also with

$$Tl^{3+} + Tl^{+} \rightleftharpoons 2Tl^{2+}. \quad (22)$$

It has been difficult to provide direct proof for either of the two reactions, but tests for thallium(II) in the reacting system have all proved negative. In itself, this is not convincing evidence that Tl(II) is not formed, and certainly is not a final argument for a simultaneous two-electron transfer according to reaction (21). However, because of several indications, this reaction is usually cited as the foremost example of a simultaneous two-electron transfer. This might be due to the lack of better examples, but also to the lack of a generally accepted definition of what is really meant by the word "simultaneous" in this context. That is, if the reaction proceeds through two consecutive one-electron steps, how short is the time between these steps before we consider the electron transfer to be simultaneous? An acceptably strict definition for a simultaneous two-electron transfer would be that "the transfer of both electrons is completed during a single vibrational transition of the activated complex, i.e., within a time span of the order of 10^{-13} seconds" (*15*). If we use this definition, the present evidence neither proves nor disproves a simultaneous two-electron transfer. Only a few experimental methods are suited to work in this time range, and it is difficult to design an experiment capable of detecting either Tl^{2+} or a free electron pair or some other effect which would be a convincing proof of the reaction mechanism.

Relatively little work has been done on the redox reaction between thallium and halide/pseudohalide ions (*75, 93, 97, 110, 328–330*). Let us consider the qualitative order of stability of thallium(III) in the form of TlX_n^{3-n} complexes, where X = Cl, Br, I, SCN, CN. Thallium(III) forms strong complexes with all these ligands; on the other hand, it can oxidize the X^- ions to X_2. It is well known that the thallium(III) chloride complexes are perfectly stable for an indefinite period of time. The corresponding bromide complexes are usually stable, but at low Br/Tl ratios Tl(III) can be reduced by Br^-; the reduction is easily prevented by adding excess of bromine. The iodo and thiocyanato complexes are approximately equally unstable toward redox reaction: Tl(III) is rapidly reduced by the anion.[4] Finally, the cyano complexes

[4] Although a large excess of I^- leads to formation TlI_4^-, and in this way protects Tl(III) (*99*).

are stable for years at room temperature. The stability of thallium(III) will certainly depend on the solution composition, but roughly these facts are in reasonable agreement with the order of the standard redox potentials for the $X_2/2X^-$ couples: +1.36, +1.09, +0.54, and +0.77 V for X = Cl, Br, I, and SCN, respectively (*34*), considering that $e^0(Tl^{3+}/Tl^+) = +1.25$ V. However, the standard potential $e^0(CN_2/(2CN^-) = 0.27$ V does not fit into this pattern. Using the two latter e^0 values, the equilibrium constant for the reaction

$$Tl^{3+} + 2CN^- \rightleftharpoons Tl^+ + (CN)_2 \tag{23}$$

can be calculated to be $10^{33.1}$. It is true that the thallium cyanide complexes are strong, but if we consider the equilibrium constant for the reduction of Tl^{3+} together with Fig. 5, it becomes clear that Tl^{3+} cannot be thermodynamically stable at any cyanide/thallium ratio. Introducing the actual Tl^{3+} and CN^- concentrations present in acidic thallium(III) cyanide solutions, the product $[Tl^{3+}][CN^-]^2$ can be calculated to vary between 10^{-31} and 10^{-25} M, which leads to 100 M $< [Tl^+][(CN)_2] < 10^8$ M. Thus, the equilibrium of reaction (23) is completely shifted to the right. Nonetheless, the actual Tr(III) solutions have proven to be stable. One could imagine that the large polarizability of the cyanide ion leads to decreased positive charge on the thallium ion, thus reducing the oxidizing power of thallium(III) to the extent that it is stable in the strong cyano complexes. However, such an effect would also lead to an increased shielding of the thallium nucleus, and hence to a decrease in the ^{205}Tl NMR chemical shifts for the cyano complexes as compared to the Tl_{aq}^{3+} ion. As can be seen from Table VI or Fig. 4a, the trend of the chemical shifts is the opposite.

Thus, the reason for the stability of the $Tl(CN)_n^{3-n}$ complexes is obviously their kinetic inertness. It is generally assumed that reduction–oxidation reactions often consist of several elementary, one-electron steps. This assumption is based on the fact that the transfer of several electrons in a single elementary discharge act is less probable than the sequential transfer through one-electron consecutive steps (however, see the discussion in the beginning of this section). In the present case, the reaction

$$Tl^{3+} + CN^- \rightleftharpoons Tl^{2+} + CN^{\cdot} \tag{24}$$

can be considered as the first step of the reduction of thallium(III). (In fact, formation of the unstable Tl(II) from Tl(III) and an aquated elec-

tron has been observed and studied [cf. Dodson and Schwarz (*77*) and Chapter V]. Now, the standard potential is +0.3 V for the couple Tl^{3+}/Tl^{2+} in 1 M $HClO_4$ (see earlier discussion) and ~+2.5 V for $CN^{\cdot}/CN^{-}$ (*331*), which recalculated to acidic solution (1 M $HClO_4$), gives ~+3.0 V [using $pK_a(HCN) = 9.0$] (*175*). This means that reaction (24) would be energetically very unfavorable. The standard potential for the couple Tl^{2+}/Tl^{+} is 2.22 V (see earlier discussion), so that here also the one-electron transfer step

$$Tl^{2+} + CN^{-} \rightleftharpoons Tl^{+} + CN^{\cdot} \qquad (25)$$

is energetically unfavorable. The stability constants for cyano complexes of Tl(II) are unknown, but are probably much smaller than those for Tl(III) [the stability constants for corresponding chloride complexes are about two orders of magnitude smaller for Tl(II) than for Tl(III); cf. Dodson and Schwarz (*77*) and Section II,B]. Thallium(I) does not form cyano complexes (see (*55*) and Section II,A). Concluding, if one of the two reactions (24) or (25) is rate-determining, the reduction of Tl(III) by CN^{-} [reaction (23)] will be kinetically hindered and, accordingly, $Tl(CN)_n^{3-n}$ complexes will be stable. This may be taken as an indication that the mechanism of reaction (23) includes two one-electron transfer steps.

In fact, after a long period of time some reduction of Tl(III) occurs in cyanide-containing solutions. After about one year at 25°C, the concentration of Tl(I) increased from 1% to between 2 and 5% in solutions with low CN/Tl ratios, and up to 12% in solutions where CN/Tl was higher than 6 and pH > 4 (*97*). These observations are in agreement with the results of Penna-Franca and Dodson (*78*), who found a drastic increase of the Tl(III)–Tl(I) exchange rate with increasing cyanide concentration.

Oxidation of the thiocyanate ion by thallium(III) has been studied by four research groups (*110, 328–330*), and two of the resulting papers were published recently (*110, 330*). The gross reaction, which is quantitative, can be written as

$$3Tl^{3+} + 4SCN^{-} + 4H_2O \rightleftharpoons 3TlSCN(s) + SO_4^{2-} + HCN + 7H^{+}. \qquad (26)$$

On the basis of their kinetic study, Gupta *et al.* (*330*) proposed the existence of a reactive complex $[Tl(SCN)]^{2+}$ and two nonreactive complexes $[Tl_2(SCN)]^{5+}$ and $[HTl(SCN)_2]^{2+}$ and determined the rate and stability constants. Polynuclear complexes $[Tl_2(SCN)_n]^{6-n}$ as intermediates in reaction (26) have also been proposed by Treindl and Fico as a

result of their polarographic kinetic study (*329*). The most recent study of this system (*110*) provided evidence that during reaction (26), which could be followed at 0°C by means of multinuclear NMR, the $Tl(SCN)^{2+}$ complex is really formed (see Fig. 18).[5] Also, $Tl(CN)^{2+}$ and $Tl(CN)_2^{+}$ complexes could be observed. In this light, the proposals forwarded in Refs. (*329, 330*) are somewhat surprising [since polynuclear thallium (III) complexes have never been reported in aqueous solution] and should most probably be modified along with their mechanistic suggestions, because the influence of the chloride, cyanide and sulfate ions present in the studied solutions was not considered.

Very recently, the redox reaction between Tl(III) and sulfite in acidic aqueous solution (0.1 M < $[H^+]$ < 1 M) was studied by stopped-flow spectrophotometry under pseudo–first-order conditions (*332*). The reaction proceeded according to

$$Tl(OH_2)_6^{3+} + SO_2(aq) + 2H_2O \rightarrow Tl_{aq}^{+} + HSO_4^{-} + 3H^+, \qquad (27)$$

in agreement with the study of Higginson and Marshall at pH = 0.5 (*333*). The rate law was found to be

$$-d[SO_2(aq)]/dt = k[S^{IV}][Tl^{III}]. \qquad (27a)$$

However, the rate increased with decreasing $[H^+]$ in the interval 0.10–1.0 M. Assuming formation of weak inner-sphere complexes between the thallium species [i.e., $Tl(OH_2)_6^{3+}$ and $Tl(OH)(OH_2)_5^{2+}$] and sulfite ligands [i.e., $SO_2(aq)$, HSO_3^-, and SO_3^{2-}], a somewhat more complicated rate law was derived (*332*). These conclusions were based on the assumption that the thallium(III) sulfito complexes are so weak that their concentrations are negligible. The previous reports on strong Tl(III)–sulfito complexes (*111, 154*) referred to chloride media, where mixed complex formation of the type $[Tl(SO_3)_mCl_n]^{(3-2m-n)+}$ could be expected to occur. Even though the existence of strong sulfito–chloro mixed complexes would probably indicate that thallium(III)–sulfito complexes are also strong [as was previously observed for $[Tl(EDTA)X]^{2-}$, X = Cl, Br, CN, and for $[Tl(CN)_mCl_n]^{3-m-n}$ complexes (*94, 108, 171*)], no definitive statement on the strength of the $[Tl(SO_3)_m]^{3-2m}$ species can be made at this point.

In conclusion, the authors of paper (*332*) proposed that sulfito complexes are formed prior to electron transfer and, even if the results

[5] The NMR parameters obtained for this complex were compared to the literature and could be interpreted in terms of S-bonded thiocyanate.

gave no decisive information about the mechanism of electron transfer, they were interpreted in terms of a simultaneous two-electron transfer or, alternatively, two consecutive one-electron transfer steps where the second step occurs very rapidly within the coordination sphere

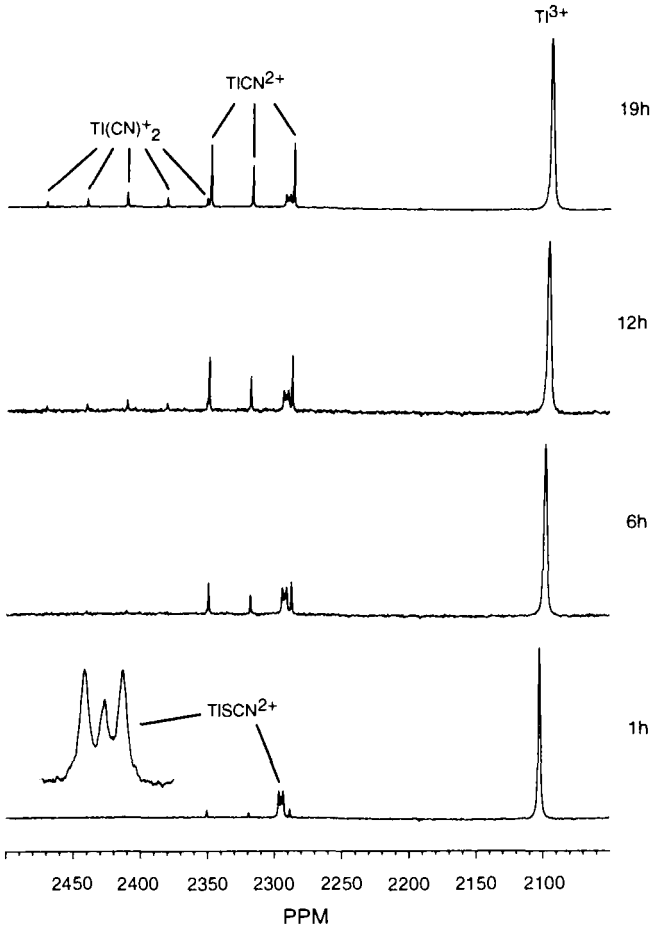

FIG. 18. ^{205}Tl NMR spectra of an aqueous solution with a starting composition [Tl(III)] = 0.17 M, [SCN^-] = 0.025 M, and [H^+] = 0.52 M (SCN enriched to ~75% in ^{13}C), as a function of the reaction time in hours [reaction (26)]. The inset shows the expansion of the peak attributed to $[Tl(SCN)]^{2+}$, with the multiplet structure caused by the spin–spin coupling between ^{205}Tl and ^{13}C in the partially enriched solution. Temperature = 0°C; spectrometer frequency 230.8 MHz; the chemical shifts are given in parts per million toward higher frequency with respect to an aqueous solution of $TlClO_4$ extrapolated to infinite dilution. Reprinted from Blixt *et al.* (*110*). Copyright © 1991 American Chemical Society.

of thallium, giving no time to release any sulfite radicals into the bulk solution.

The redox reactions where Tl(III) is an oxidant have been studied extensively (*70, 99, 100, 110, 116, 247, 260, 266, 267, 315, 328–330, 332–338*), but the corresponding studies involving Tl(I) as an electron donor are scarce (*252, 253, 255, 339*) (except for the electron exchange reaction between Tl^+ and Tl^{3+}; see earlier discussion).

One of these studies (*253*) deals with oxidation of thallium(I) by hexacyanoferrate(III) in aqueous solution. This reaction is interesting because orally or intravenously administered $K_3[Fe(CN)_6]$ (Prussian Blue) is probably the best of the hitherto tested antidotes against thallium poisoning, promoting a high patient recovery rate and no toxic side effects (*340, 341*). It has been suggested that Prussian Blue acts as an ion exchanger for univalent metal ions and its affinity increases with increasing ionic radius of the metal ion (*340*). However, in the light of the newly established, very strong complex formation between Tl(III) and cyanide ions (*97*) (cf. Section II,C,3), the action of Prussian Blue could possibly (also) be due to the oxidation of Tl(I) to Tl(III) by Fe(III), and a subsequent "masking" of thallium in the form of $Tl(CN)_n^{3-n}$. Unfortunately, this recent study (*253*) is severely complicated by the presence of concentrated (4 M) HCl and (50%) CH_3COOH in the investigated solutions. The acids are added to the solutions in order to decrease the redox potential of the Tl(III)/Tl(I) couple and to increase the potential of the $[Fe(CN)_6]^{3-}/[Fe(CN)_6]^{4-}$ couple. The addition of HCl causes the desired changes in the redox potentials and thus makes possible the oxidation of Tl(I) by $[Fe(CN)_6]^{3-}$ (probably by the formation of $Tl^{III}Cl_n^{3-n}$ complexes); the acetic acid, however, has only a minor effect. The authors (*253*) have observed a profound effect of the chloride and hydrogen ion concentrations on the rate of the reaction, which was supposed to be second-order and proceed according to

$$[Fe(CN)_6]^{3-} + Tl(I) \rightarrow [Fe(CN)_6]^{4-} + Tl(II) \qquad \text{slow}$$

$$[Fe(CN)_6]^{3-} + Tl(II) \rightarrow [Fe(CN)_6]^{4-} + Tl(III) \qquad \text{fast,} \qquad (28a)$$

in which the main active species are $Tl^ICl_2^-$ and $[H_2Fe(CN)_6]^-$. However, the complexity of the chemical system (e.g., the complex formation of thallium with chloride, cyanide, and acetate ions was not considered), in connection with some doubtful assumptions (e.g., for the stability constant of $Tl^ICl_3^{2-}$), makes the conclusions less convincing.

The rate constant for the reaction of Tl^+ with OH radicals has been

determined to be $1.0 \cdot 10^{10}$ M^{-1} s^{-1} (*74*). It has been suggested that this reaction proceeds via an electron transfer to yield Tl^{2+} (*74*):

$$Tl^+ + OH\cdot \rightarrow Tl^{2+} + OH^-, \tag{29}$$

but it appears that it goes rather via the formation of $Tl(OH)^{+}\cdot$ (*85, 86, 342*):

$$Tl^+ + OH\cdot \rightarrow Tl(OH)^{+}\cdot. \tag{30}$$

The hydrolysis products of Tl(II) exhibit different redox properties: $Tl(OH)^+$ and Tl^{2+} act as good oxidants in their reaction with methoxylated benzenes (*342, 343*) and disulfides (*344*), while $Tl(OH)_2$ can react as a reductant (towards tetranitromethane) (*86*). This is in agreement with polarographic measurements showing that Tl^{2+} is reduced over the entire potential range up to +400 mV, $Tl(OH)^+$ is reduced at potentials less than +275 mV, and $Tl(OH)_2$ shows a reduction current only at potentials below +200 mV, while at more positive potentials a much more pronounced oxidation current is observed than that for $Tl(OH)^+$ (*345*).

V. Photochemistry of Thallium Compounds in Aqueous Solution

It has been known for long time that ultraviolet irradiation of aqueous solutions of thallium(I) in the presence of excess chloride ions gives rise to a bright blue luminescence (*346*). This behavior was subsequently used as the basis for an analytical method for determining Tl(I) ion (*347*) and has been further developed (*348*). However, Tl(I) solutions not containing halide can also luminesce, although with lower quantum efficiency and shorter lifetime. Mayne and Kirkbright (*349*) studied the rates of the reactions involving the luminescent moiety of thallium(I) in 2 M NaCl, 2 M $NaClO_4$, and water [in deoxygenated solutions, because oxygen is known to react with the excited thallium(I) ion (*350*)]. They found the values of quantum efficiency and lifetime shown in Table Xa. They assumed the following processes to occur (Scheme 3):

Absorption	$Tl(I) + h\nu \rightarrow Tl(I)^*$	I_{abs}
Emission	$Tl(I)^* \rightarrow Tl(I) + h\nu$	$k_1Tl(I)^*$
Internal conversion	$Tl(I)^* \rightarrow Tl(I)$	$k_2Tl(I)^*$
Self quenching	$Tl(I)^* + Tl(I) \rightarrow 2Tl(I)$	$k_3Tl(I)^*Tl(I)$
External quenching	$Tl(I)^* + Q \rightarrow Tl(I) + Q$	$k_4Tl(I)^*Q$

SCHEME 3

TABLE X

(a) MEASURED QUANTUM EFFICIENCIES ([Tl(I)] = $5 \cdot 10^{-6}$ M) AND LIFETIMES ([Tl(I)] = 10^{-4} M) FOR Tl(I) LUMINESCENCE IN AQUEOUS SOLUTION

Solvent	2 M NaCl	2 M $NaClO_4$	Water
Quantum efficiency	0.88	0.40	0.52
Lifetime (μs)	0.62 ± 0.18	0.27 ± 0.08	0.36 ± 0.08

(b) CALCULATED PARAMETERS FOR Tl(I) LUMINESCENCE PROCESSES IN AQUEOUS SOLUTION (SCHEME 3)

Solvent	2 M NaCl	2 M $NaClO_4$	Water
Quantum efficiency at infinite dilution	0.92	0.40	0.53
k_1 (s^{-1})	$0.93 \cdot 10^6$	$1.2 \cdot 10^6$	$1.3 \cdot 10^6$
$\tau_0 = 1/k_1$ (μs)	1.07	0.83	0.77
$k_2 + k_4Q$ (s^{-1})	$8.6 \cdot 10^4$	$1.8 \cdot 10^6$	$1.2 \cdot 10^6$
k_3 ($L \cdot mole^{-1} \cdot s^{-1}$)	$6.0 \cdot 10^9$	$7.0 \cdot 10^9$	$2.8 \cdot 10^9$

They also calculated the associated rate constants (see Table Xb). From the small change of the rate constant of self-quenching, k_3, between NaCl and $NaClO_4$, and also considering that the theoretical value in water is $6.7 \cdot 10^9$ L · mole^{-1} · s^{-1} for neutral species, they concluded that the luminescent center is uncharged. It is also known that halide ions at high concentration shift the Tl(I) absorption spectrum to longer wavelengths in aqueous solution, which indicates a close approach. The well-known neutral species of the type TlCl (*4, 6, 41, 55*), which prevail in thallium(I) solutions containing excess of chloride (cf. Fig. 1, Section II,A), are possibly responsible for this effect.

Shepherd (*351*) has studied Tl^+ luminescence in aqueous solutions not containing halide ions and proposed that the previously observed large shift between the absorption (213 nm) and emission (365 nm) bands of Tl^+ in hydroxylic solvents (*349*) is a consequence of the formation of thallium–water excimers. The absorption band has been attributed to a Laporte-allowed $6s^2 \rightarrow 6s^16p^1$ transition of the free aquated Tl^+ ion (*351*).

It has also been shown (*350*) that irradiation of an acidic solution

containing oxygen and Cl^- ions by UV light leads to photo-oxidation of Tl(I) to Tl(III), and to the production of H_2O_2 according to the reaction

$$Tl(I) + 2H^+ + O_2 \overset{h\nu}{\rightleftharpoons} Tl(III) + H_2O_2 \tag{31}$$

Complete oxidation of thallium(I) usually took about 20 minutes. The solution, which contained $4 \cdot 10^{-4}$ M Tl(I) and more than 3 M Cl^-, was saturated in oxygen: In solutions deoxygenated by blowing nitrogen gas for one hour, no oxidation of thallium(I) could be observed. Chloride ions are necessary for the reaction which is assisted by Tl(III); the redox potential of the thallium(III)/thallium(I) couple is reduced at high chloride concentration, and this explains why the oxidation does not occur in the absence of chloride.

In another study (*352*), irradiation of aqueous O_2-free $Tl^I(SO_4)_2$ solutions by 10 MeV electron pulses resulted in luminescence, in which the excitation of Tl_{aq}^+ was produced via the reactions

$$Tl_{aq}^+ + OH \rightarrow Tl_{aq}^{2+} + OH^-, \tag{32}$$

followed by

$$Tl_{aq}^{2+} + e_{aq}^- \rightarrow {}^*Tl_{aq}^+. \tag{33}$$

From the decay of the luminescence obtained with low doses of radiation, the half-life of the ${}^*Tl_{aq}^+$ emission was calculated to be $T_{1/2} = 4.2 \cdot 10^{-7}$ s. It was also observed that 3 μs after the electron pulse, the intensity of the luminescence was strongly enhanced by increasing the H^+ concentration. This pH dependence was explained by the reaction of OH radicals with Tl_{aq}^+ ions to yield the long-lived $TlOH^+$ intermediate, which is converted by a fast reaction with H^+ to Tl_{aq}^{2+}. Also, the total yield of the luminescence per pulse increased strongly from neutral to alkaline solutions, which was assumed to be due to the following sequence of reactions:

$$Tl^+OH + OH^- \rightarrow Tl^{2+}O^{2-} + H_2O, \tag{34}$$

$$Tl^+ + O^{2-} \rightarrow Tl^{2+}O^{2-}, \tag{35}$$

$$Tl^{2+}O^{2-} + e_{aq}^- \rightarrow {}^*Tl^+O^{2-}. \tag{36}$$

Dissolution of crystalline TlBr, TlI, and their solid mixtures was investigated in aqueous solution at 25, 35, and 45°C (*353*), both in the

presence of air and daylight and under argon in dark. It was found that TlI is more soluble in the former case (0.180 g Tl^+ per liter at 25°C, ΔH = 27.2 kJ/mol) than in the latter case (0.055 g Tl^+ per liter, ΔH = 29.3 kJ/mol). This effect was ascribed to photolysis. The solubility of TlBr was the same in both cases, 0.396 g Tl^+ per liter, ΔH = 25.9 kJ/mol.

Thallium(III) in acidic aqueous solution can also undergo photochemically induced reactions. For example, the observed high-yield photoinduced exchange between Tl(III) and Tl(I) was explained (*323*) by a chain mechanism initiated by the reaction

$$Tl(III)_{aq} \overset{h\nu}{\rightleftharpoons} Tl(II)_{aq} + H^+ + OH. \tag{37}$$

The same pathway was assumed to be responsible for the reduction of Tl(III) and the oxidation of 2-propanol to acetone in deaerated aqueous perchloric acid solution, where the UV-light–initiated formation of Tl(II) in the primary process was demonstrated by flash photolysis (*354*). This pathway was shown to have a kinetic form similar to the γ-irradiation–induced oxidation of alcohols by Tl(III) (*256*). The primary quantum yield of Tl(III) reduction was estimated to be 0.36 ± 0.07.

Within the main group metals of the first three columns of the periodic table, only thallium forms stable complexes exhibiting charge-transfer photochemistry with active participation of the metal center (*355*). So far, only the complexes of the metal in the 3+ oxidation state have been photochemically studied. Because of the s^0 configuration of thallium(III), the only electron transition involving the metal concerns the ligand-to-metal charge transfer (LMCT). The quantum yield for converting the light into electrochemical energy in such processes can be high; for example, it is equal to 0.54 for λ = 254 nm for the reaction

$$[Tl^{III}(bipy)_2I_2]^+ \overset{h\nu}{\rightleftharpoons} Tl^+ + 2\,bipy + I_2 \tag{38}$$

in acetonitrile (*355*).

Another type of thallium compounds which have potential applications in converting light into electrochemical energy are the bi- or oligometallics of the type shown in Fig. 19. Similar compounds, such as $(CN)_5$-$\mathbf{Fe^{II}}$-(μ-CN)-$\mathbf{Pt^{IV}}(NH_3)_4$-(μ-NC)-$\mathbf{Fe^{II}}$-$(CN)_5$, have recently been shown to undergo redox reaction when irradiated by visible light (*356*). Research in this field has been active during the last few years, and

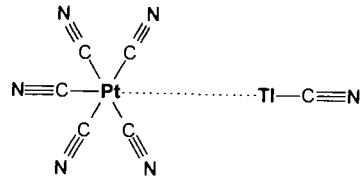

FIG. 19. Partial structure of a bimetallic Tl–Pt compound in aqueous solution, deduced from a combination of multinuclear NMR and Raman spectra (*51*).

some solid compounds of this type containing thallium and a transition metal ion have been prepared and their properties studied (*357–361*).

A somewhat different, but very interesting, study on the chemical properties of colloidal thallium(0) in aqueous solution has been reported recently by Ershov and Henglein (*362*). When a deaerated 0.1 mM $TlClO_4$ aqueous solution was γ-irradiated, its absorption spectrum changed as shown in Fig. 20. The solution contained also 0.1 M 2-propanol as a scavenger for OH radicals, and $4 \cdot 10^{-4}$ M poly(ethyleneimine) as stabilizer of the colloid. The sharp band at about 216 nm, which belongs to the Tl^+ ion, disappeared almost completely after 30 minutes. The spectrum of the formed Tl^0 colloid, with a maximum at about 340 nm, shifted to longer wavelengths during the first 2–3 hours of irradiation and finally covered a large part of the visible wavelengths. After longer irradiation time, the spectrum did not change. The experiments were interpreted in terms of the very fast reaction ($k = 3 \cdot 10^{10}$ M^{-1} s^{-1}) (*363*)

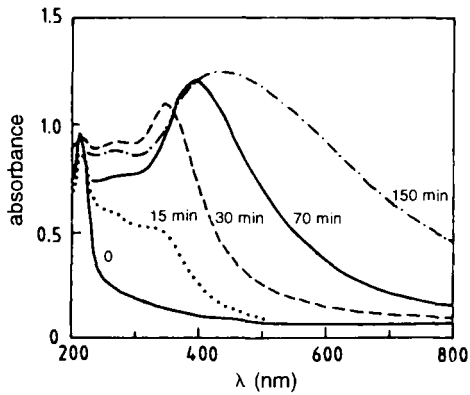

FIG. 20. Absorption spectra of a deaerated aqueous solution of 0.1 mM $TlClO_4$ before and at various times of γ-irradiation. Reprinted from Ershov and Henglein (*362*). Copyright © 1993 American Chemical Society.

$$e^- + Tl^+ \rightarrow Tl^0, \tag{39}$$

leading to formation of small Tl^0 particles, about 20–30 Å in diameter, after 10 minutes of irradiation (*362*). When irradiation was continued, the particles formed larger aggregates: 60–80 Å in diameter after 40 minutes and 100–200 Å after 2 hours of irradiation, as shown by electron micrographs.

The thallium colloids were immediately oxidized to Tl^+ upon exposure to air. When Tl^+ ions were formed, the particles that constituted an aggregate became positively charged and disintegrated by the repulsive Coulomb forces. However, when certain electrolytes were added after the colloid had formed, the properties of the colloid were changed. For example, after addition of NaOH or $Ba(ClO_4)_2$, no Tl^+ ions were formed; thus, the changes in the absorption band were entirely due to changes in the structure of the particles and not to the consumption of the reduced thallium. Similar disintegration effects have previously been observed in the oxidation of cadmium particle clusters (*364*). Generally speaking, the absorption spectrum of metallic particles which are substantially smaller than the wavelength of light is not dependent on the particle size (*365*), but it is strongly dependent on the aggregation of the particles. Since the tendency to agglomerate is quite different for different metals and depends on the method of preparation, the possibility of preparing light-absorbing devices with selected wavelength characteristics can be envisaged.

VI. Applications: Concluding Remarks

The redox properties of thallium are important in preparative organic and organometallic/inorganic chemistry. For this reason, studies of redox behavior and the thermodynamics and kinetics of complexing processes are likely to remain relevant. The employment of the Tl^+ ion as a probe for K^+ in biological systems will no doubt continue, because of the easy detection of the former. For the same reason, thallium(III) can be used as a representative for several other metal ions in solution.

Interest in the chemistry of thallium may be enhanced by the development of molecular devices with specific functionalities, such as superconductors, photosensitive devices, solar energy "light-harvesting" compounds, and ingredients in glass-fiber communication systems. Because of the potential applications, and for fundamental chemical reasons, the chemistry of thallium will continue to attract the attention of (and puzzle) chemists.

REFERENCES

1. Sherrill, M. S.; Haas, A. J. *J. Am. Chem. Soc.* **1936,** *58,* 952.
2. Biedermann, G. *Ark. Kemi* **1953,** *5,* 441.
3. Biedermann, G.; Spiro, T. G. *Chem. Scr.* **1971,** *1,* 155.
4. Sillén, L. G.; Martell, A. E. "Stability Constants of Metal-Ion Complexes" Spec. Publ. No. 25; Chemical Society: London, 1971.
5. Smith, R. M.; Martell, A. E. "Critical Stability Constants"; Plenum: New York, 1977; Vol. 4.
6. Högfeldt, E. "Stability Constants for Metal-Ion Complexes"; Pergamon: Oxford, United Kingdom, 1982.
7. Christie, A. "The Pale Horse"; Harper Collins: London, 1961.
8. Emsley, J. *New Sci.* **1978,** *August 10,* 392.
9. Westmar, B. *Dagens Nyheter (Swedish daily newspaper, Stockholm)* **1988,** *Nov. 2,* 5.
10. Michelsen, T. *Dagens Nyheter* **1991,** *Febr. 8,* 8.
11. Reed, D.; Crawley, J.; Faro, S. N.; Pieper, S. J.; Kurland, L. T. *J. Amer. Med. Assoc.* **1963,** *183,* 516.
12. Picchioni, A. L. *Am. J. Hosp. Pharm.* **1965,** *22,* 352.
13. Downs, A. J., Ed.; "Chemistry of Aluminium, Gallium, Indium and Thallium"; Blackie: London, 1993.
14. Kemper, F. H.; Bertram, H. P. In "Metals and Their Compounds in the Environment"; Merian, E. Ed.; VCH: Weinheim, 1991; p. 1227.
15. Lee, A. G. "The Chemistry of Thallium"; Elsevier: Amsterdam, 1971.
16. Bailar, J. C. "Comprehensive Inorganic Chemistry"; Pergamon: Oxford, United Kingdom, 1973; p. 1124.
17. Sax, N. I. "Dangerous Properties of Industrial Materials"; 5th ed., Van Nostrand-Reinhold: New York, 1979.
18. Basolo, F.; Pearson, R. G. "Mechanisms of Inorganic Reactions"; Wiley: New York, 1967.
19. Rossotti, F. J. C. *J. Inorg. Nucl. Chem.* **1954,** *1,* 159.
20. Sutin, N. *Annu. Rev. Nucl. Sci.* **1962,** *12,* 285.
21. Sykes, A. G. *Adv. Inorg. Chem. Radiochem.* **1967,** *10,* 153.
22. Taube, H. *Adv. Inorg. Chem. Radiochem.* **1959,** *1,* 1.
23. Zweifel, G. In "Comprehensive Organic Chemistry"; Barton, D. H. R., and Ollis, W. D., Eds.; Pergamon: Oxford, 1979; Vol. 3, 1013.
24. McKillop, A.; Taylor, E. C. In "Organic Synthesis by Oxidation with Metal Compounds"; Mijs, W. J., and de Jonge, C. R. H. I., Eds.; Plenum: New York, 1986; p. 695.
25. Kurosawa, H. *J. Organomet. Chem.* **1978,** *158,* 221.
26. Kurosawa, H. In "Comprehensive Organometallic Chemistry"; Wilkinson, G., Ed.; Pergamon: Oxford, 1982; Vol. 1, 725.
27. Negishi, E. "Organometallics in Organic Synthesis"; Wiley: New York, 1980.
28. McKillop, A.; Taylor, E. C. In "Comprehensive Organometallic Chemistry"; Pergamon: Oxford, 1982; Vol. 7, 465.
29. Uemura, S. In "The Chemistry of the Metal-Carbon Bond"; Hartley, F. R., Ed.; Wiley: Chichester, 1987; p. 473.
30. McKillop, A.; Smith, J. D. In "Dictionary of Organometallic Compounds"; Chapman and Hall: London, 1984–1989; p. 2271.
31. Kul'ba, F. Y.; Mironov, V. E. "Khimija Tallija (Komplexnoje Sojedinienja)"; Gosud. Naychno-techn. Izdat. Khim. Liter.: Leningrad, 1963.

32. Smith, I. C.; Carson, B. L. "Trace Metals in the Environment"; 1st ed., Ann Arbor Science Publ: Ann Arbor, MI, 1977; Vol. 1, 394.
33. (a) Tuck, D. G. In "Comprehensive Coordination Chemistry"; Wilkinson, G., Ed., Pergamon: Oxford, 1987; Vol. 3, 167–175. (b) Tóth, I.; Györi, B. In "Encyclopedia of Inorganic Chemistry"; King, R. B., Ed.; Wiley: Chichester, 1994; Vol. 8, 4134–4142.
34. Weast, R. C., Ed.; "Handbook of Chemistry and Physics"; CRC Press: Cleveland, OH, 1975, F209.
35. Senge, M. O.; Ruhland-Senge, K.; Regli, K. J.; Smith, K. M. *J. Chem. Soc., Dalton Trans.* **1993,** 3519.
36. Gresser, R.; Boyd, D. W.; Albrecht-Gary, A. M.; Schwing, J. P. *J. Am. Chem. Soc.* **1980,** *102,* 651.
37. Cornelius, G.; Gärtner, W.; Haynes, D. H. *Biochemistry* **1974,** *13,* 3053.
38. Lee, E. L.; Tabib, J.: Weaver, M. J. *J. Electroanal. Chem.* **1979,** *96,* 241.
39. Hinton, J. F.; Metz, K. R.; Briggs, R. W. In "Progress in Nuclear Magnetic Resonance Spectroscopy"; Emsley, J. W., Feeney, J., and Sutcliffe, L. H., Eds.; Pergamon: Oxford, 1988; Vol. 20, part 5., 423.
40. Hinton, K. R.; Metz, K. R. In "NMR of Newly Accessible Nuclei"; Laszlo, P., Ed.; Academic Press: New York, 1983; Vol. 2, 367.
41. Glaser, J.; Henriksson, U.; Klason, T. *Acta Chem. Scand.* **1986,** *A40,* 344.
42. Sueltor, C. H. In "Metal Ions in Biological Systems"; Sigel, H., Ed.; Dekker: New York, 1974; Vol. III, 201.
43. Williams, R. J. P. *Q. Rev. Chem. Soc.* **1970,** *24,* 331.
44. Krasne, S.; Eisenman, G. In "Membranes, A Series of Advances"; Eisenman, G., Ed.; Dekker: New York, 1973; Vol. 2, 277.
45. Davies, E. D.; Long, D. A. *J. Chem. Soc.* **1968,** 2050.
46. Bermejo, M. R.; Castineiras, A.; Gayoso, M.; Hiller, W.; Englert, U.; Strähle, J. *Z. Naturforsch., B: Anorg. Chem., Org. Chem.* **1984,** *39,* 1159.
47. Gutiérrez-Puebla, E.; Vegas, V. *Acta Crystallogr.* **1980,** *B36,* 145.
48. Castano, M. V.; Sánchez, A.; Casas, J. S.; Sordo, J.; Brianso, J. L.; Piniella, J. F.; Solans, X.; Germain, G.; Debaerdemaeker, T.; Glaser, J. *Organometallics* **1988,** *7,* 1897.
49. Downs, A. J., Ed.; "Chemistry of Aluminium, Gallium, Indium and Thallium"; Blackie: London, 1993; p. 108.
50. Downs, A. J., Ed.; "Chemistry of Aluminium, Gallium, Indium and Thallium"; Blackie: London, 1993; p. 488.
51. (a) Berg, K.; Glaser, J.; Read, M. *Eur. Exp. NMR Conf., 12th,* Oulu, Finland, 1994; p. 184. (b) Berg, K.; Glaser, J.; Read, M.; Toth, I. *J. Am. Chem. Soc.* 1995, *117.*
52. Wade, K.; Banister, A. J. "The Chemistry of Aluminium, Gallium, Indium and Thallium"; Pergamon: Oxford, 1975.
53. Persson, I.; Glaser, J., unpublished.
54. Dechter, J. J.; Zink, J. I. *J. Am. Chem. Soc.* **1975,** *97,* 2937.
55. Nilsson, R. O. *Ark. Kemi* **1956,** *10,* 363.
56. Johansson, L. *Coord. Chem. Rev.* **1974,** *12,* 241.
57. Bond, A. M. *J. Phys. Chem.* **1970,** *74,* 331.
58. Lee, A. G. *Coord. Chem. Rev.* **1972,** *8,* 289.
59. Fedorenko, A. M.; Perekhod, A. F.; Bobryshev, V. G.; Shul'gin, V. F. *Russ. J. Inorg. Chem.* **1980,** *25,* 518.
60. Banerjea, D.; Singh, I. P. *J. Indian Chem. Soc.* **1962,** *39,* 353.
61. Stupko, T. V.; Isaev, I. D.; Mironov, V. E. *Zh. Neorg. Khim.* **1989,** *34,* 2441.
62. Manners, J. P.; Morallee, K. G.; Williams, R. J. P. *J. Inorg. Nucl. Chem.* **1971,** *33,* 2085.

63. Bell, R. P.; Panckhurst, M. H. *J. Chem. Soc.* **1956,** 2836.
64. Fedorov, V. A.; Robov, A. M.; Isaev, I. D.; Alekseeva, A. D. *Zh. Neorg. Khim.* **1974,** *19,* 1466.
65. Purdie, N.; Farrow, M. M.; Steggall, M.; Eyring, E. M. *J. Am. Chem. Soc.* **1975,** *97,* 1078.
66. Kul'ba, F. Y.; Ushakova, V. G.; Yakovlev, Y. B. *Zh. Neorg. Khim.* **1975,** *20,* 79.
67. Cox, B. G.; Stroka, J.; Schneider, I.; Schneider, H. *J. Chem. Soc., Faraday Trans. I.* **1989,** 187.
68. Anderegg, G.; Bottari, E. *Helv. Chim. Acta* **1967,** *50,* 2341.
69. Perrin, D. D. "Stability Constants for Metal-Ion Complexes"; Pergamon: Oxford, 1983; Vol. B.
70. Dhas, T. P. A.; Mishra, D. K.; Mittal, R. K.; Gupta, Y. K. *Indian J. Chem., Sect. A* **1991,** *30A,* 340.
71. Dodson, R. W. *J. Radioanal. Chem.* **1976,** *30,* 245.
72. Schwarz, H. A.; Cornstock, D.; Yandell, J. K.; Dodson, R. W. *J. Phys. Chem.* **1970,** *78,* 448.
73. Cercek, B.; Ebert, M.; Swallow, A. J. *J. Chem., Soc. A* **1966,** 612.
74. Schwarz, H. A.; Comstock, D.; Yandell, J. K.; Dodson, R. W. *J. Phys. Chem.* **1974,** *78,* 488.
75. Carpenter, L. G.; Ford-Smith, M. H.; Bell, R. P.; Dodson, R. W. *Discuss. Faraday Soc.* **1960,** *29,* 92.
76. Dodson, R. W. *J. Am. Chem. Soc.* **1953,** *75,* 1795.
77. Dodson, R. W.; Schwarz, H. A. *J. Phys. Chem.* **1974,** *78,* 892.
78. Penna-Franca, E.; Dodson, R. W. *J. Am. Chem. Soc.* **1955,** *77,* 2651.
79. Roig, E.; Dodson, R. W. *J. Phys. Chem.* **1961,** *65,* 2175.
80. Schwarz, H. A.; Dodson, R. W. *J. Phys. Chem.* **1976,** *80,* 2543.
81. Schwarz, H. A.; Dodson, R. W. *J. Phys. Chem.* **1984,** *88,* 3643.
82. Warnqvist, B.; Dodson, R. W. *Inorg. Chem.* **1971,** *10,* 2624.
83. Widmer, H. M.; Dodson, R. W. *J. Phys. Chem.* **1970,** *74,* 4289.
84. Farver, O.; Nord, G. *J. Chem. Soc., Chem. Commun.* **1967,** *15,* 736.
85. O'Neill, P.; Schulte-Frohlinde, D. *J. Chem. Soc., Chem. Commun.* **1975,** 387.
86. Bonifacic, M.; Asmus, K.-D. *J. Chem. Soc., Dalton Trans.* **1976,** 2074.
87. Pearson, R. G. *J. Chem. Ed.* **1968,** *45,* 643.
88. Pearson, R. G. *J. Chem. Ed.* **1968,** *45,* 581.
89. Ahrland, S. *Helv. Chim. Acta* **1967,** *50,* 306.
90. Woods, M. J. M.; Gallagher, P. K.; Z. Z. Hugus, J.; King. E. L. *Inorg. Chem.* **1964,** *3,* 1313.
91. Ahrland, S.; Grenthe, I.; Johansson, L.; Norén, B. *Acta Chem. Scand.* **1963,** *17,* 1567.
92. Ahrland, S.; Johansson, L. *Acta Chem. Scand.* **1964,** *18,* 2125.
93. Vogt, G. *Ber. Bunsenges. Phys. Chem.* **1965,** *69,* 648.
94. Blixt, J.; Glaser, J.; Solymosi, P.; Tóth, I. *Inorg. Chem.* **1992,** *31,* 5288.
95. Bányai, I.; Glaser, J. *J. Am. Chem. Soc.* **1990,** *112,* 4703.
96. Biedermann, G.; Glaser, J. *Acta Chem. Scand.* **1986,** *A40,* 331.
97. Blixt, J.; Györi, B.; Glaser, J. *J. Am. Chem. Soc.* **1989,** *111,* 7784.
98. Györi, B.; Sánchez, A.; Glaser, J. *J. Organomet. Chem.* **1989,** *361,* 1.
99. Johansson, L. *Acta Chem. Scand.* **1966,** *20,* 2156.
100. Moensted, L. B.; Moensted, O.; Nord, G. *Trans. Faraday Soc.* **1970,** *66,* 936.
101. Yakovlev, Y. B.; Ravlenko, L. I. *Zh. Neorg. Khim* **1979,** *24,* 2107.
102. Yakovlev, Y. B.; Ravlenko, L. I. *Zh. Neorg. Khim* **1982,** *27,* 1157.
103. Yakovlev, Y.; Kul'ba, F. Y.; Mironov, U. E. *Zh. Neorg. Khim.* **1967,** *12,* 3283.

104. Biryuk, E. A.; Nazarenko, V. A.; Liam-Ngong T. *Zh. Neorg. Khim.* **1969,** *14,* 714.
105. Veksin, V.; Tóth, I; Zékány, L.; Brucher, E. *Magy. Kém. Foly.* **1984,** *90,* 207.
106. Anderegg, G. "Critical Survey of Stability Constants of EDTA Complexes"; Pergamon: 1977; Vol. 14.
107. Saito, K.; Terrey, H. *J. Chem. Soc.* **1956,** 4701.
108. Blixt, J.; Glaser, J. *Int. Conf. Solution Chem. 20th,* Jerusalem, Israel, August 6–11 1989; p. 107.
109. Musso, S. Ph.D. thesis, ETH, Zurich, 1993.
110. Blixt, J.; Dubey, R. K.; Glaser, J. *Inorg. Chem.* **1991,** *30,* 2824.
111. Sillén, L. G.; Martell, A. E. "Stability Constants of Metal-Ion Complexes"; Spec. Publ. No. 17, Chemical Society: London, 1964.
112. Glaser, J.; Henriksson, U. *J. Am. Chem. Soc.* **1981,** *103,* 6642.
113. Kul'ba, F. Y.; Yakovlev, Y. B.; Mironov, V. E. *Russ. J. Inorg. Chem.* **1965,** *10,* 886.
114. Tóth, I.; Brucher, E.; Zékány, L.; Veksin, V. *Polyhedron* **1989,** *8,* 2057.
115. Glaser, J. Ph.D. thesis, KTH (The Royal Institute of Technology), Stockholm, Sweden, 1981.
116. Böti, Z.; Horváth, I.; Szil, Z.; Csányi, L. J. *J. Chem. Soc., Dalton Trans.* **1978,** 1012.
117. Glaser, J.; Johansson, G. *Acta Chem. Scand.* **1981,** *A35,* 639.
118. Peschanski, D.; Valladas-Dubois, S. *Bull. Soc. Chim. Fr.* **1956,** 1170.
119. Figgis, B. N. *Trans. Faraday Soc.* **1959,** *55,* 1075.
120. Busev, A. I.; Tiptsova, V. G.; Sokolova, T. A. *Vestnik Moskov. Univ. Khim.* **1960,** *11,* 6.
121. Horrocks, D. L.; Voigt, A. F. *J. Am. Chem. Soc.* **1957,** *79,* 2440.
122. Spiro, T. G. *Inorg. Chem.* **1965,** *4,* 731.
123. Sillén, L. G. *Acta Chem. Scand.* **1949,** *3,* 539.
124. Benoit, R. *Bull. Soc. Chim. Fr.* **1949,** 518.
125. Wallace, R. C. *Z. Kristallogr. Mineral.* **1910–1911,** *49,* 417.
126. Watanabé, T.; Atoji, M. *J. Am. Chem. Soc.* **1950,** *72,* 3819.
127. Millikan, M. B.; James, B. D. *Inorg. Chim. Acta* **1980,** *44,* L93.
128. Joy, G.; Jr., P. G.; Wharf, I.; Shriver, D. F.; Dougherty, J. P. *Inorg. Chem.* **1975,** *14,* 1795.
129. Bell, J. D.; Gainsford, A. R.; Golding, B. T.; Herlt, A. J.; Sargeson, A. M. *J. Chem. Soc., Chem. Commun.* **1974,** 980.
130. Grunwald, B. Ph.D. thesis, Erlangen-Nurnberg, 1977.
131. Hoard, J. L.; Goldstein, L. *J. Chem. Phys* **1935,** *3,* 645.
132. Böhme, R.; Rath, J.; Grunwald, B.; Thiele, G. *Z. Naturforsch., B: Anorg. Chem.* **1980,** *35,* 1366.
133. Brodersen, K.; Rath, J.; Thiele, G. *Z. Anorg. Allg. Chem.* **1972,** *894,* 13.
134. Rath, H. J. Ph.D. thesis, Nurnberg, 1972.
135. Glaser, J. Ph.D. thesis, Paper No. 10, KTH (The Royal Institute of Technology), Stockholm, Sweden, 1981.
136. Glaser, J. *Acta Chem. Scand.* **1982,** *A36,* 451.
137. Glaser, J. *Acta Chem. Scand.* **1980,** *A34,* 141.
138. Linhard, M.; Manthey, W.; Plieth, K. *Z. Elektrochem.* **1953,** *57,* 862.
139. Watanabé, T.; Atoji, M.; Okazaki, C. *Acta Crystallogr.* **1950,** *3,* 405.
140. Spiro, T. G. *Inorg. Chem.* **1965,** *4,* 1290.
141. Pratt, J. H. *Am. J. Sci.* **1895,** *49,* 397.
142. Glaser, J.; Johansson, G. *Acta Chem. Scand.* **1982,** *A36,* 125.
143. Carr, C.; Goggin, P. L.; Sandström, M. *J. Chem. Soc., Chem. Commun.* **1981,** 772.
144. Blixt, J. Ph.D. thesis, KTH (The Royal Institute of Technology), Stockholm, Sweden, 1993.

145. Blixt, J.; Glaser, J.; Mink, J.; Persson, I.; Persson, P.; Sandström, M. *J. Am. Chem. Soc.* **1995,** *117,* 5089.
146. Schmidt, K. W. *J. Inorg. Nucl. Chem.* **1970,** *32,* 3549.
147. Cotton, F. A.; Wilkinson, G. "Advanced Inorganic Chemistry"; Wiley: New York, 1988; 42.
148. Coates, G. E.; Mukherjee, R. N. *J. Chem. Soc.* **1963,** 229.
149. Wilkinson, G. "Comprehensive Coordination Chemistry"; Pergamon: Oxford, 1987; Vol. 2, 7.
150. Skibsted, L. H.; Bjerrum, J. *Acta Chem. Scand. Ser. A* **1977,** *A31,* 155.
151. Beck, M. T. *Pure Appl. Chem.* **1987,** *59,* 1703.
152. Christensen, J. J.; Izatt, R. M.; Eatough, D. *Inorg. Chem.* **1965,** *4,* 1278.
153. Pesek, J. J.; Mason, W. R. *Inorg. Chem.* **1979,** *18,* 924.
154. Spencer, J. F.; Abegg, R. *Z. Anorg. Chem.* **1905,** *44,* 379.
155. Guggenheim, E. A. "Application of Statistical Mechanics"; Oxford Univ. Press (Clarendon): Oxford, 1966.
156. Scatchard, G. *J. Am. Chem. Soc.* **1968,** *90,* 3124.
157. Scatchard, G. *Chem. Rev.* **1936,** *19,* 309.
158. Brönsted, J. N. *J. Am. Chem. Soc.* **1922,** *90,* 3124.
159. Biedermann, G. "Ionic Media"; Dahlem Konf.: Berlin, 1975, p. 339.
160. Ciavatta, L. *Ann. Chim. (Rome)* **1990,** *80,* 255.
161. Hinton, J. F.; Briggs, R. W. *J. Magn. Reson.* **1975,** *19,* 393.
162. Hoad, C. S.; Matthews, R. W.; Thakur, M. M. *J. Organomet. Chem.* **1977,** *124,* C31.
163. Hinton, J. F.; Metz, K. R.; Briggs, R. W. *Ann. Rep. NMR Spectrosc.* **1982,** *13,* 211.
164. Briggs, R. W.; Hinton, J. F. *J. Solution Chem.* **1977,** *6,* 827.
165. Briggs, R. W.; Hinton, J. F. *J. Solution Chem.* **1978,** *7,* 1.
166. Gudlin, D.; Schneider, H. *Inorg. Chim. Acta* **1979,** *33,* 205.
167. Hinton, J. F.; Briggs, R. W. In "NMR and the Periodic Table"; Harris, R. K., and Mann, B. E., Eds.; Academic Press: London, 1978; p. 279.
168. Batta, G.; Bányai, I.; Glaser, J. *J. Am. Chem. Soc.* **1993,** *115,* 6782.
169. Bányai, I.; Glaser, J. *J. Am. Chem. Soc.* **1989,** *111,* 3186.
170. Bányai, I.; Glaser, J.; Loszonczy, J., *to be published.*
171. Berg, K.; Blixt, J.; Glaser, J., *submitted for publication.*
172. Glaser, J.; Tóth, I. *J. Chem. Soc., Chem. Commun.* **1986,** 1336.
173. Salmon, P.; Glaser, J. *ILL Rep. 6-05-191* **1989.**
174. Henriksson, U.; Glaser, J. *Acta Chem. Scand.* **1985,** *A39,* 355.
175. Bányai, I.; Blixt, J.; Glaser, J.; Tóth, I. *Acta Chem. Scand.* **1992,** *46,* 138.
176. Verbaere, A.; Dion, M.; Tournoux, M. *J. Solid State Chem.* **1974,** *11,* 184.
177. Yamaguchi, T.; Tanaka, Y.; Ozutsumi, K.; Ohtaki, H.; Kusumegi, A. *Nippon Kagaku Kaishi* **1986,** *11,* 1484.
178. Sabrowsky, H. *Z. anorg. allg. Chem.* **1971,** *381,* 266.
179. Kusumegi, A.; Kondo, K.; Watase, Y.; Yoshimura, Y.; Miyake, K.; Hemmi, Y.; Haba, J.; Hara, K. *Nucl. Instrum. Methods* **1982,** *196,* 231.
180. Kusumegi, A. *Bull. Inst. Chem. Res., Kyoto Univ.* **1982,** *60,* 234.
181. Kusumegi, A.; Kondo, K.; Watase, Y.; Yoshimura, Y.; Miyake, K. *Nucl. Instrum. Methods* **1981,** *185,* 83.
182. Ozutsumi, K.; Ohtaki, H.; Kusumegi, A. *Bull. Chem. Soc. Jpn.* **1984,** *57,* 2612.
183. Hanic, F. In "Coordination Chemistry of Solutions"; Högfeldt, E., Ed.; The Royal Institute of Technology (KTH): Stockholm, 1972; p. 472.
184. Deacon, G. B. *Rev. Pure Appl. Chem.* **1963,** *13,* 189.
185. Wells, A. F. "Structural Inorganic Chemistry"; 5th ed., Oxford Univ. Press (Clarendon): Oxford, 1984; Chapters 7, 26.

186. Delwaulle, M.-L. *C. R. Acad. Sci. Fr.* **1954,** *238,* 2522.
187. Cotton, F. A.; Johnson, B. F. G.; Wing, R. M. *Inorg. Chem.* **1965,** *4,* 502.
188. Carty, A. J. *Coord. Chem. Rev.* **1969,** *4,* 29.
189. Andrews, S. P.; Badger, P. E. R.; Goggin, P. L.; Hurst, N. W.; Rattray, A. J. M. *J. Chem. Res. Synop.* **1978,** 94.
190. Carr, C. Ph.D. thesis, University of Bristol, United Kingdom, 1984.
191. Hoard, J. L.; Gordstein, L. *J. Chem. Phys* **1935,** *3,* 199.
192. Powell, H. M.; Wells, A. F. *J. Chem. Soc.* **1935,** 1008.
193. Leden, I.; Ryhl, T. *Acta Chem. Scand.* **1964,** 1196.
194. Orgel, L. E. *J. Chem. Soc.* **1958,** 4186.
195. Nyholm, R. S. *J. Chem. Soc., Proc.* **1961,** 273.
196. Persson, I.; Sandström, M.; Goggin, P. *Inorg. Chim. Acta* **1987,** *129,* 183.
197. Sandström, M.; Persson, I.; Ahrland, S. *Acta Chem. Scand.* **1978,** *A32,* 607.
198. Åkesson, R.; Sandström, M.; Stålhandske, C.; Persson, I. *Acta Chem. Scand.* **1991,** *45,* 165.
199. Bergström, P.-Å.; Lindgren, J.; Sandström, M.; Zhou, Y. *Inorg. Chem.* **1992,** *31,* 150.
200. Strömberg, D.; Sandström, M.; Wahlgren, U. *Chem. Phys. Lett.* **1990,** *172,* 49.
201. Johansson, G.; Sandström, M. *Acta Chem. Scand.* **1978,** *A32,* 109.
202. Persson, I.; Sandström, M., personal communication.
203. Friedman, H. L. *Chem. Scr.* **1985,** *25,* 42.
204. Jones, L. H. "Inorganic Vibration Spectroscopy"; Dekker: New York, 1971; Chapter 4.
205. Åkesson, R.; Persson, I.; Sandström, M.; Wahlgren, U. *Inorg. Chem.* **1994,** *33,* 3715.
206. Glaser, J. *Acta Chem. Scand.* **1979,** *A33,* 789.
207. Glaser, J. *Acta Chem. Scand.* **1980,** *A34,* 157.
208. Glaser, J.; Goggin, P. L.; Sandström, M.; Lutsko, V. *Acta Chem. Scand.* **1983,** *A37,* 437.
209. Hazell, A. C. *J. Chem. Soc.* **1963,** 3459.
210. Spiro, T. G. *Inorg. Chem.* **1967,** *6,* 569.
211. Sharpe, A. G. In "Comprehensive Coordination Chemistry"; Wilkinson, G., Gillard, R. D., and McCleverty, J. A., Eds.; Pergamon: Oxford, 1987; Vol. 2, 10.
212. Brodersen, K.; Beck, I.; Beck, R.; Hummel, H. U.; Liehr, G. *Z. Anorg. Allg. Chem.* **1984,** *516,* 30.
213. Watanabé, T.; Atoji, M. *J. Am. Chem. Soc.* **1950,** *13,* 338.
214. Chantooni, M. K. J.; Kolthoff, I. M. *Proc. Natl. Acad. Sci. USA* **1981,** *78,* 7245.
215. Cox, B. G.; Stroka, J.; Schneider, H. *Inorg. Chim. Acta* **1988,** *147,* 9.
216. Johansson, L. *Acta Chem. Scand.* **1973,** *27,* 1832.
217. Kamnev, A. A.; Ezhov, B. B. *Koord. Khim.* **1990,** *16,* 764.
218. Kodama, M.; Kimura, E. *Bull. Chem. Soc. Jpn.* **1976,** *49,* 2465.
219. Kutuzova, M. Y.; Kuznechikhina, M. A.; Chernikova, G. E.; Isaev, I. D.; Shishin, L. P.; Bol'shakova, I. M.; Shmyd'ko, L. I.; Kalosh, T. N.; Robov, A. M.; Fedorov, V. A. *Tezisy Dokl. Vses. Chugaevskoe Soveshch. Khim. Kompleksn. Soedin., 12th* **1975,** *1.*
220. Lada, E.; Lei, X.; Kalinowski, M. K. *Monatsh. Chem.* **1992,** *123,* 425.
221. Maslowska, J.; Wojtysiak, K. *Zesz. Nauk. Politech. Lodz: Technol. Chem. Spozyw.* **1988,** *508,* 47.
222. Rabinovich, V. A.; Galesnik, N. Y. *Izv. Vyssh. Uchebn. Zaved., Khim. Khim. Tekhnol.* **1975,** *18,* 486.
223. Roesch, F.; Tran, K. H.; Milanov, M.; Khalkin, V. A. *Isotopenpraxis* **1988,** *24,* 386.
224. Sasaki, Y.; Takizawa, M.; Umemoto, K.; Matsuura, N. *Electrochim. Acta* **1981,** *26,* 185.
225. Sasaki, Y.; Inaba, M.; Ikegami, T. *Nippon Kagaku Kaishi* **1989,** *807.*

226. Schramm, C.; Zink, J. I. *J. Am. Chem. Soc.* **1979,** *101,* 4554.
227. Sohn, S. C.; Eom, T. Y.; Suh, M. Y.; Jung, K. S. *J. Korean Chem. Soc.* **1991,** *35,* 288.
228. Stary, J.; Kratzer, K.; Leseticky, L.; Svata, V.; Vrbska, T. *J. Radioanal. Nucl. Chem.* **1992,** *157,* 295.
229. Stupko, T. V.; Isaev, I. D.; Mironov, V. E. *Koord. Khim.* **1987,** *13,* 1467.
230. Toropova, V. F.; Garifzyanov, A. R.; Panfilova, I. E. *Talanta* **1987,** *34,* 211.
231. Tsyplyakova, V. A.; Migal, P. K.; Solomon, L. S.; Vylkova, E. S. *Nov. Polyarogr. Tezisy Dokl. Vses. Soveshch. Polyarogr.* **1975,** *6,* 36.
232. Zaitsev, V. M.; Mishin, V. Y.; Kirin, I. S.; Gusel'nikov, V. S.; Kolyadin, A. B. *Izv. Akad. Nauk SSSR, Neorg. Mater.* **1969,** *5,* 778.
233. Bashilova, N. I.; Nelyapina, N. I. *Zh. Neorg. Khim.* **1976,** *21,* 2525.
234. Busev, A. I.; Filip, V. Z. *Zh. Neorg. Khim.* **1969,** *14,* 3221.
235. Busev, A. I.; Filip, V. Z. *Anal. Lett.* **1969,** *2,* 175.
236. Chuchalin, L. K.; Peshchevitskii, B. I.; Kuzin, I. A. *Zh. Neorg. Khim.* **1969,** *14,* 1785.
237. Dement'eva, M. I.; Podchainova, V. N. *Zavod. Lab.* **1975,** *41,* 1319.
238. Ignaczak, M.; Andrijewski, G. *Pol. J. Chem.* **1980,** *54,* 171.
239. Kornev, V. I. *Zh. Fiz. Khim.* **1971,** *45,* 2510.
240. Pechurova, N. I.; Trubacheva, L. V. *Vestn. Mosk. Univ., Ser. 2:Khim.* **1982,** *23,* 260.
241. Ulstrup, J. *Acta Chem. Scand.* **1969,** *23,* 3091.
242. Yakovlev, Y. B.; Kul'ba, F. Y.; Mironov, V. E. *Probl. Sovrem. Khim. Koord. Soedin.* **1968,** *241.*
243. Yakovlev, Y. B.; Kul'ba, F. Y.; Ushakova, V. G. *Tezisy Dokl—Vses. Chugaevskoe Soveshch. Khim. Kompleksn. Soedin., 12th* **1975,** *1.*
244. Yakovlev, Y. B.; Kul'ba, F. Y.; Ushakova, V. G.; Vitkauskaite, I. *Zh. Neorg. Khim* **1977,** *22,* 87.
245. Yakovlev, Y. B.; Ushakova, V. G.; Vitkauskaite, I. *Zh. Neorg. Khim.* **1980,** *25,* 3241.
246. Zamashchikov, V. V.; Chanysheva, I. R.; Bobrov, O. I. *Dopov. Akad. Nauk Ukr. RSR, Ser. B: Geol., Khim. Biol. Nauki* **1976** p. 1097.
247. Prasada Rao, M. S.; Mohan Rao, A. R.; Kalavathi, R.; Siva Rao, T.; Vani, P. *J. Chem. Soc., Dalton Trans.* **1993,** 2283.
248. Ahmad, F.; Kumar, S.; Baswani, V. S. *J. Inorg. Nucl. Chem.* **1980,** *42,* 999.
249. Ignaczak, M.; Andrijewski, G. *Pol. J. Chem.* **1980,** *54,* 1343.
250. Pechurova, N. I.; Vekshin, V. V.; Zhaboedova, L. A.; Spitsyn, V. i. *Izv. Akad. Nauk SSSR, Ser. Khim.* **1977,** p. 1972.
251. Ignaczak, M.; Andrijewski, G. *Pol. J. Chem.* **1981,** *55,* 2613.
252. Gokavi, G. S.; Raju, J. R. *Indian J. Chem., Sect. A* **1988,** *27,* 494.
253. Gokavi, G. S.; Raju, J. R. *Int. J. Chem. Kinet.* **1988,** *20,* 365.
254. Kimura, M.; Akazome, T.; Takenaka, K.; Kobayashi, A. *Bull. Chem. Soc. Jpn.* **1980,** *53,* 1271.
255. Balasubramanian, R.; Sinha, B. P. *Indian J. Chem., Sect. A* **1977,** *15,* 413.
256. Burchill, C. E.; Hickling, G. G. *Can. J. Chem.* **1970,** *48,* 2466.
257. Chimatadar, S. A.; Nandibewoor, S. T.; Raju, J. R. *Indian J. Chem., Sect. A* **1987,** *26,* 255.
258. Chimatadar, S. A.; Hiremath, S. C.; Raju, J. R. *Indian J. Chem., Sect. A* **1991,** *30,* 190.
259. (a) Falcinella, B.; Felgate, P. D.; Laurence, G. S. *J. Chem. Soc., Dalton Trans.* **1974,** 1367. (b) *idem,* **1975,** 1.
260. Farver, O.; Nord, G. *Acta Chem. Scand, Ser. A* **1978,** *A32,* 963.
261. Gupta, K. S.; Grupta, Y. K. *Indian J. Chem.* **1970,** *8,* 1001.
262. Nord, G. *Inorg. Chem.* **1976,** *15,* 1921.
263. Srinivasan, V. S.; Venkatasubramanian, N. *Curr. Sci.* **1970,** *39,* 254.

264. Srinivasan, V. S.; Venkatasubramanian, N. *Proc.—Indian Acad. Sci., [Ser.]: Chem. Sci.* **1982,** *91,* 371.
265. Ahmad, F.; Kumar, S. *Indian J. Chem., Sect. A* **1982,** *21,* 567.
266. Kyrd, J. E.; Halpern, J. *J. Amer. Chem. Soc.* **1973,** *95,* 2586.
267. Fadnis, A. G.; Shrivastava, S. K. *An. Quim., Ser. A* **1986,** *82,* 5.
268. Giraudi, G.; Baiocchi, C. *Atti Accad. Sci. Torino, Cl. Sci. Fis., Mat. Nat.* **1975,** *109,* 603.
269. Gupta, K. S.; Saxena, S. D.; Swarup, R. *Indian J. Chem., Sect. A* **1980,** *19,* 336.
270. Hirose, I.; Funabashi, K.; Kawajiri, K.; Kobayashi, T. *Nippon Kagaku Kaishi* **1989,** p. 826.
271. Ignaczak, M.; Scholl, H.; Andrijewski, G.; Kasprzak, J.; De, I. J. I. M. *Pol. J. Chem.* **1986,** *60,* 3.
272. Mentasti, E.; Pramauro, E.; Carlotti, M. E.; Pelizzetti, E. *Atti Accad. Sci. Torino, Cl. Sci. Fis., Mat. Nat.* **1974,** p. 667.
273. Mohanty, S. B.; Acharya, R. C.; Nanda, C. N.; Rout, M. K. *Indian J. Chem., Sect. A* **1976,** *14,* 42.
274. Pechal, M.; Cvengrosova, Z.; Hrusovsky, M. *Chem. Prum.* **1981,** *31,* 525.
275. Pechal, M.; Holotik, S.; Strasak, M.; Hrusovsky, M. *Chem. Zvesti* **1983,** *37,* 159.
276. Pelizzetti, E.; Mentasti, E.; Baiocchi, C.; Carlotti, M. E. *Atti Accad. Sci. Torino, Cl. Sci. Fis., Mat. Nat.* **1974,** p. 279.
277. Pelizzetti, E.; Mentasti, E.; Pramauro, E.; Carlotti, M. E. *Gazz. Chim. Ital.* **1975,** *105,* 307.
278. Pelizzetti, E.; Mentasti, E.; Pramauro, E. *Gazz. Chim. Ital.* **1975,** *105,* 403.
279. Pramauro, E.; Baiocchi, C. *Atti Accad. Sci. Torino, Cl. Sci. Fis., Mat. Nat.* **1974,** p. 367.
280. Radhakrishnamurti, P. S.; Panda, R. K.; Panigrahi, J. C. *Indian J. Chem., Sect. A* **1987,** *26,* 124.
281. Satyanarayana, P. V. V.; Rao, B. N. M.; Ramana, G. V. *J. Indian Chem. Soc.* **1989,** *66,* 198.
282. Srinivasan, V. S.; Venkatasubramanian, N. *Indian J. Chem.* **1970,** *8,* 57.
283. Strasak, M.; Hrusovsky, M.; Urbanec, J.; Vojtko, J.; Gregus, S. *Chem. Zvesti* **1976,** *30,* 553.
284. Strasak, M. *React. Kinet. Catal. Lett.* **1977,** *7,* 387.
285. Subramanian, P. V.; Paul, R.; Subrahmanyan, V. *Indian J. Chem.* **1973,** *11,* 1074.
286. Tret'yakov, V. P. *React. Kinet. Catal. Lett.* **1982,** *21,* 49.
287. Urbanec, J.; Strasak, M.; Vojtko, J.; Hrusovsky, M. *Collect. Czech. Chem. Commun.* **1976,** *41,* 611.
288. Urbanec, J.; Strasak, M.; Repasova, I.; Hrusovsky, M. *Chem. Prum.* **1977,** *27,* 346.
289. Eigen, M.; Maass, G. *Z. Phys. Chem. (Wiesbaden)* **1966,** *49,* 163.
290. Rode, B. M.; Reibnegger, G. J.; Fujiwara, S. *J. Chem. Soc., Faraday Trans. 2* **1980,** *76,* 1268.
291. Davies, C. W. "Ion Association"; Butterworths: London, 1962.
292. Lincoln, S. F.; Sandercock, A. C.; Stranks, D. R. *Aust. J. Chem.* **1975,** *28,* 1901.
293. Kawai, Y.; Takahashi, T.; Hayashi, K.; Imamura, T.; Nakayama, H.; Fujimoto, M. *Bull. Chem. Soc. Jpn.* **1972,** *45,* 1417.
294. Funada, R.; Imamura, T.; Fujimoto, M. *Bull. Chem. Soc. Jpn.* **1979,** *52,* 1535.
295. Qadeer, A. *Z. Phys. Chem. (Frankfurt am Main)* **1974,** *88,* 160.
296. van Eldik, R., Ed.; "Inorganic High Pressure Chemistry Kinetics and Mechanisms"; Elsevier: Amsterdam, 1986.
297. Bjerrum, N.,; *Kgl. Danske Videnskab. Selskab* **1926,** *7,* 9.

298. Fuoss, R. M. *J. Am. Chem. Soc.* **1958,** *80,* 5059.
299. Jordan, R. B. "Reaction Mechanisms of Inorganic and Organometallic Systems"; Oxford Univ. Press: New York, 1991.
300. Ohtaki, H.; Radnai, T. *Chem. Rev.* **1993,** *93,* 1157.
301. Sutin, N. *Ann. Rev. Phys. Chem.* **1966,** *17,* 119.
302. Åkesson, R.; Pettersson, L. G. M.; Sandström, M.; Wahlgren, U. *J. Am. Chem. Soc.* **1994,** *116,* 8705.
303. Cannon, T. H.; Richards, R. E. *J. Chem. Soc., Faraday Trans. 1* **1966,** *62,* 1378.
304. Körös, E.; Varga, M. *J. Phys. Chem.* **1984,** *88,* 4116.
305. Varga, M.; Györgyi, L.; Körös, E. *J. Phys. Chem.* **1985,** *89,* 1019.
306. Easteal, A. J.; Price, W. E.; Woolf, L. A. *J. Phys. Chem.* **1989,** *93,* 7517.
307. Easteal, A. J.; Mills, R.; Woolf, L. A. *J. Phys. Chem.* **1989,** *93,* 4968.
308. Sanders, J. K. M.; Hunter, B. K. "Modern NMR Spectroscopy"; 2nd ed.; Oxford Univ. Press: Oxford, 1993.
309. Sandström, J. "Dynamic NMR Spectroscopy"; Academic Press: London, 1982.
309a. Bányai, I.; Blixt, J.; Glaser, J.; Tóth, I. Acta Chem. Scand. **1992,** *46,* 142.
310. Bommeli, H. P. Ph.D. thesis, ETH, Zurich, 1992.
311. Mizunu, M.; Funahashi, S.; Nakasuka, N.; Tanaka, M. *Inorg. Chem.* **1991,** *30,* 1550.
312. Horrocks, W. d. W., Jr.; Arkle, V. K.; Liotta, F. J.; Sudnick, D. R. *Inorg. Chem.* **1983,** *8,* 3455.
313. Golub, A. M.; Köhler, H.; Skopenko, V. V. "Chemistry of Pseudohalides"; Elsevier: Amsterdam, 1986; 85.
314. Jörgensen, K. A.; Lawesson, S. O. *J. Am. Chem. Soc.* **1984,** *106,* 4687.
315. Cannon, R. D. "Electron Transfer Reactions"; Butterworths: London, 1980.
316. Lappin, A. G. "Redox Mechanisms in Inorganic Chemistry"; Ellis Horwood: New York, 1994.
317. Challenger, G. E.; Masters, B. J. *J. Am. Chem. Soc.* **1956,** *78,* 3012.
318. Schafer, H. *Z. Anorg. Allg. Chem.* **1960,** *307,* 7.
319. Schafer, H. *Z. Anorg. Allg. Chem.* **1960,** *305,* 64.
320. Waind, G. M. *Proc. Symp. Coord. Chem.,* Tihany, Hungary, 1964; pp 453.
321. Adamson, M. G.; Stranks, D. R. *J. Chem. Soc., Chem. Commun.* **1967,** 648.
322. Gelsema, W. J.; De, L. C. L.; Blijleven, H. A.; Hendriks, E. J. *Rec. Trav. Chim, Pays Bas* **1969,** *88,* 110.
323. Stranks, D. R.; Yandell, Y. K. *J. Phys. Chem.* **1969,** *73,* 840.
324. Sykes, A. G. *Chemistry in Britain* **1970,** *6,* 159.
325. Solomatin, V. T.; Rzhavichev, S. P. *Zh. Anal. Khim.* **1976,** *31,* 2345.
326. Ershov, B. G. *Russ. Chem. Revs.* **1981,** *50,* 1119.
327. Taube, H., private communication.
328. Taimni, I. K. *J. Chem. Soc.* **1931,** 2433.
329. Treindl, L.; Fico, M. *Collection Czechoslov. Chem. Commun.* **1969,** *34,* 2873.
330. Gupta, Y. K.; Kumar, D.; Jain, S.; Gupta, K. S. *J. Chem. Soc., Dalton Trans.* **1990,** 1915.
331. Pearson, R. G. *J. Am. Chem. Soc.* **1986,** *108,* 6109.
332. Berglund, J.; Werndrup, P.; Elding, L. I. *J. Chem. Soc., Dalton Trans.* **1994,** 1435.
333. Higginson, W. C. E.; Marshall, J. W. *J. Chem. Soc.* **1957,** 477.
334. Mentasti, E.; Pelizzetti, E.; Pramauro, E.; Giraudi, G. *J. Inorg. Nucl. Chem.* **1975,** *37,* 537.
335. Goyal, M. R.; Mittal, R. K.; Gupta, Y. K. *Indian J. Chem., Sect. A* **1988,** *27,* 487.
336. Imamura, T.; Fujimoto, M. *Bull. Chem. Soc. Jpn.* **1972,** *45,* 442.
337. Gupta, K. S.; Gupta, Y. K. *J. Chem. Soc. A* **1970,** 25.

338. Nord, G. *Inorg. Chem.* **1977,** *16,* 201.
339. Rosseinsky, D. R.; Hill, R. J. *J. Chem. Soc., Dalton Trans.* **1972,** 715.
340. Heydlauf, H. *Eur. J. Pharmacol.* **1969,** *6,* 340.
341. Tilson, H. A. *Fundam. Appl. Toxicol.* **1987,** *9,* 601.
342. O'Neill, P.; Steenken, S.; Schulte, F. D. *Angew. Chem.* **1975,** *87,* 417.
343. O'Neill, P.; Steenken, S.; Schulte-Frohlinde, D. *J. Phys. Chem.* **1975,** *79,* 2773.
344. Bonifacic, M.; Asmus, K.-D. *J. Phys. Chem.* **1976,** *80,* 2426.
345. Asmus, K.-D.; Bonifacic, M.; Toffel, P.; O'Neill, P.; Schulte-Frohlinde, D.; Steenken, S. *J. Chem. Soc., Faraday Trans. I* **1978,** 1820.
346. Pringsheim, P.; Vogels, H. *Physica* **1940,** *7,* 225.
347. Sill, G. W.; Peterson, H. E. *Anal. Chem.* **1949,** *21,* 1266.
348. Kirkbright, G. F.; West, T. S.; Woodward, C. *Talanta* **1965,** *12,* 517.
349. Mayne, P. J.; Kirkbright, G. F. *J. Inorg. Nucl. Chem.* **1975,** *37,* 1527.
350. Kirkbright, G. F.; Mayne, P. J.; West, T. S. *J. Chem. Soc., Dalton Trans.* **1972,** 1918.
351. Shepherd, T. M. *J. Chem. Soc., Faraday Trans* **1979,** *2,* 644.
352. Steffen, G.; Cercek, B. *Biophysik* **1969,** *6,* 137.
353. Zhukova, L. V.; Kitaev, G. A.; Kozlov, F. N. *Zh. Fiz. Khim.* **1978,** *52,* 1692.
354. Burchill, C. E.; Wolodarsky, W. H. *Can. J. Chem.* **1970,** *48,* 2955.
355. Horváth, O.; Stevenson, K. L. "Charge Transfer Photochemistry of Coordination Compounds"; VCH: New York, 1993; and references therein.
356. Pfennig, B. W.; Bocarshy, A. B. *Coord. Chem. Revs.* **1991,** *111,* 91.
357. Weissbart, B.; Balch, A. L.; Tinti, D. S. *Inorg. Chem.* **1993,** *32,* 2096.
358. Renn, O., Lippert, B. *Inorg. Chim. Acta* **1993,** *208,* 219.
359. Balch, A. L.; Davis, B. J.; Fung, E. Y.; Olmstead, M. M. *Inorg. Chim. Acta* **1993,** *212,* 149.
360. Balch, A. L.; Rowley, S. P. *J. Am. Chem. Soc.* **1990,** *112,* 6139.
361. Nagle, J. K.; Balch, A. L. *J. Am. Chem. Soc.* **1988,** *110,* 319.
362. Ershov, B. G.; Henglein, A. *J. Phys. Chem.* **1993,** *97,* 3434.
363. Anbar, M.; Bambenek, M.; Ross, A. B. NSRDS-NBS, Report no. 43, 1973.
364. Henglein, A.; Gutiérrez, M.; Janata, E.; Ershov, B. G. *J. Phys. Chem.* **1992,** *96,* 4598.
365. Mie, G. *Ann. Phys.* **1908,** *25,* 377.

ADVANCES IN INORGANIC CHEMISTRY, VOL. 43

CATALYTIC STRUCTURE–FUNCTION RELATIONSHIPS IN HEME PEROXIDASES

ANN M. ENGLISH and GEORGE TSAPRAILIS

Department of Chemistry and Biochemistry, Concordia University, Montreal, Quebec, Canada H3G 1M8

I. Introduction

Heme peroxidases were reviewed in a related series in 1984 (*1*). At that time many heme peroxidases were known, but only one X-ray structure was available, that of cytochrome *c* peroxidase (CCP)[1] (*2*). In

[1] Abbreviations: ARP = *Arthromyces ramosus* peroxidase; BHA = benzhydroxamic acid; CCP = cytochrome *c* peroxidase; CIP = *Coprinus cinereus* peroxidase; CMP = *Coprinus macrorhizus* peroxidase; cyt *c* = cytochrome *c*; ENDOR = electron–nuclear double resonance; EPO = eosinophil peroxidase; EPR = electron paramagnetic resonance; HRP = horseradish peroxidase; LIP = lignin peroxidase; LPO = lactoperoxidase; MnP = manganese peroxidase; MPO = myeloperoxidase; PGHS = prostaglandin H synthase; RR = resonance Raman; TPO = thyroid peroxidase; VA = veratryl alcohol.

Copyright © 1995 by Academic Press, Inc.
All rights of reproduction in any form reserved.

the interim there have been significant advances in our understanding of structure–function relationships in heme peroxidases and in the elucidation of peroxidase mechanisms. This is in large part due to the application of site-directed mutagenesis to the unraveling of the roles of specific residues surrounding the heme (*3*). One advantage of structure–function studies on heme proteins and heme enzymes is that the relatively rigid heme provides a well-defined active-site cavity. Many heme proteins with diverse functions (myoglobin, cytochrome P_{450}, peroxidases) share the same heme prosthetic group, which necessitates that the biological activity be governed by the polypeptide.

In addition to site-directed mutagenesis, the recent explosion in protein X-ray structure determinations has provided us with many new heme protein structures. Notable among these are the structures of the enzymes, cytochrome P_{450} (*4*), lignin peroxidase (*5*), *Coprinus cinereus* peroxidase (*6*), myeloperoxidase (*7*), and prostaglandin H synthase (*8*). In addition, structures of mutants of CCP have been numerous (*3, 9*). Also of benefit in understanding structure–function relationships in heme peroxidases has been the wealth of information published on mutants of myoglobin (*10*). Comparisons of the effects of mutations in the heme cavities of the peroxidases and myoglobin serve to highlight the different structural requirements for efficient peroxidase activity and reversible O_2 binding, which are the biological functions of peroxidases and O_2 storage proteins, respectively.

Peroxidases catalyze the oxidation of a wide variety of organic and inorganic substrates by hydrogen peroxide: $H_2O_2 + 2AH \rightarrow 2H_2O + 2A$. Following a description of heme peroxidases of known structure in Section II, details of the enzyme intermediates formed during catalysis will be discussed in Sections III and IV, and substrate specificity will be discussed in Section V. Catalases react by a mechanism similar to that of peroxidases, but the reaction catalyzed is the disproportionation of peroxide: $2H_2O_2 \rightarrow 2H_2O + O_2$. The biological function of catalases appears to be the prevention of peroxide buildup, but as can be seen from Section V, peroxidases have a variety of roles, including biosynthesis and defense.

The peroxidase field was reviewed in depth in two volumes published in 1991 (*11*). Enzymes belonging to the superfamily of plant, fungal, and bacterial peroxidases were reviewed in Volume II and additionally in two other texts (*12, 13*). General reviews on heme peroxidases since 1992 include those published by Poulos and Fenna (*14*) and Poulos (*15*), which highlight structural comparisons and potential biotechnological applications of peroxidases, respectively. One of the present authors also surveyed the heme peroxidase literature in a review published in

1994 (*16*). The goal of this review is to focus on very recent research on heme peroxidases which has altered to some extent our views on the detailed mechanisms of peroxidase catalysis. While the literature published over the last few years will receive more attention, the reader will be directed to appropriate reviews for background data.

II. Crystal Structures of Heme Peroxidases

A. Cytochrome *c* Peroxidase

The first crystal structure obtained for a heme enzyme was that of CCP, published in 1980 (*2*). This was some 20 years following the determination of the X-ray structures of myoglobin and hemoglobin (*17*). A 1.7-Å resolution structure of CCP appeared in 1984 (*18*), and structures of liganded forms (CO, NO, CN^-, F^-) (*19–22*), as well as that of the stable intermediate compound I, have been published (*23*). Numerous structures of wild-type proteins and mutants expressed in *E. coli* have also been determined (*3, 9, 24–26*). Figure 1 depicts the polypeptide backbone of the yeast enzyme, indicating the position of the heme, and the proximal and distal histidine residues. The structure can be divided into N- and C-terminal domains, and the heme is in a cavity at the domain interface. The substrate access channel is also at the domain interface and is discussed in Section V. The secondary structure is dominated by α-helices with only a small amount of β-sheet in the proximal domain. The refined structures of the recombinant wild-type enzymes are essentially identical to that of the yeast enzyme, but small differences are observed in the mutants around the mutated residues (*3*).

The active site of CCP with its important catalytic residues is shown in Fig. 2. On the distal side of the heme, where H_2O_2 and other exogenous ligands bind, Arg48, Trp51, and His52 extend from helix B and form the distal heme pocket. H-bonding between Asn82 and His52 ensures that the nonionized imidazole ring exists as the tautomer with the H atom on N1 and not N3, which is important in H_2O_2 activation (Section III). The N3 atom of the proximal His175 from helix F is coordinated to the heme iron, and N1 of this residue is H-bonded to the carboxylate side chain of Asp235. This strong H-bond imparts considerable anionic character to His175, which is assumed to be important in stabilizing the high oxidation state of iron generated on peroxide binding (Section III). In van der Waals contact with the heme and the

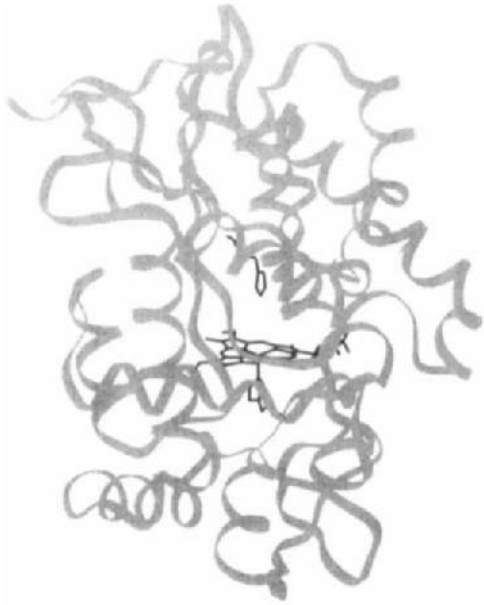

FIG. 1. Schematic diagram of yeast cytochrome *c* peroxidase C_α backbone generated from the X-ray coordinates (*18*) using Insight II (v. 2.3.0) software (BIOSYM Technologies Inc., San Diego). The heme, the distal His52, and the proximal His175 are shown in bold.

proximal His175 is Trp191, which is redox-active during the turnover of CCP (Sections III, IV, and V,A).

B. LIGNIN AND MANGANESE PEROXIDASES

Lignin is a major component of woody plant cell walls, and lignin biodegradation is important in the carbon cycle. White-rot fungi, which are the most effective organisms at lignin degradation, secrete two heme peroxidases, LIP and MnP. The crystal structure of LIP refined to 2 Å was published in 1993 (*5*). A comparison of the CCP and LIP structures (*5, 14*) confirmed proposals of similar structures for heme peroxidases of fungal and plant origin (*27, 28*) (Section II,G). Figure 3 shows the α-carbon backbone for LIP, and a comparison with Fig. 1 reveals that CCP and LIP possess remarkably similar 3D structures despite <20% sequence homology (*5, 27, 28*). However, unlike CCP, LIP contains two tightly bound Ca^{2+} ions and four disulfide bridges per molecule, the locations of which are also indicated in Fig. 3.

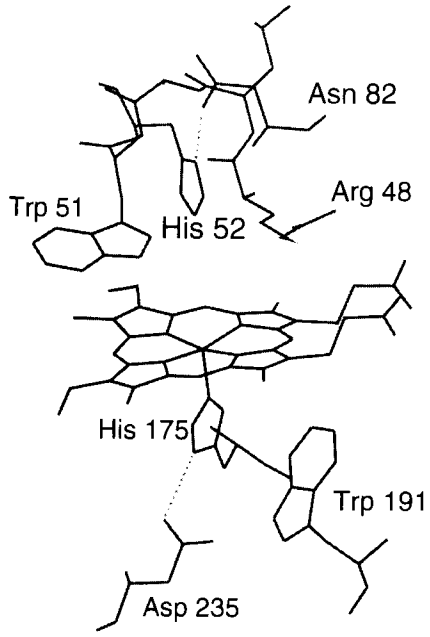

FIG. 2. Active-site structure of yeast cytochrome *c* peroxidase. The dashed lines represent H-bonds between N1 of the distal His52 and the side-chain carbonyl of Asn82, and N1 of the proximal His175 and the side-chain carboxylate of Asp235. This diagram was generated using the X-ray coordinates for the 1.7-Å structure of CCP (*18*).

The active-site structures of CCP and LIP are also very similar. Figure 4 reveals that the three key catalytic residues in the distal cavity of LIP which extend from helix B, Arg43, Phe46, and His47, correspond to Arg48, Trp51, and His52 of CCP. His176, which extends from the proximal helix F, is bonded to the iron and H-bonded to the carboxylate of Asp238. One notable difference in the active sites of CCP and LIP is the presence of tryptophan residues (51 and 191) in the former and phenylalanine residues (46 and 193) in the same locations in the latter. Possible consequences of these substitutions are discussed in Sections III and IV. Veratryl alcohol, a metabolite excreted by the fungus, is believed to be a substrate for LIP, and a possible binding site for the alcohol within 7 Å of the heme has been proposed (*5, 14*) (Section V,B).

Preliminary X-ray data have been published on MnP (*29*). This heme

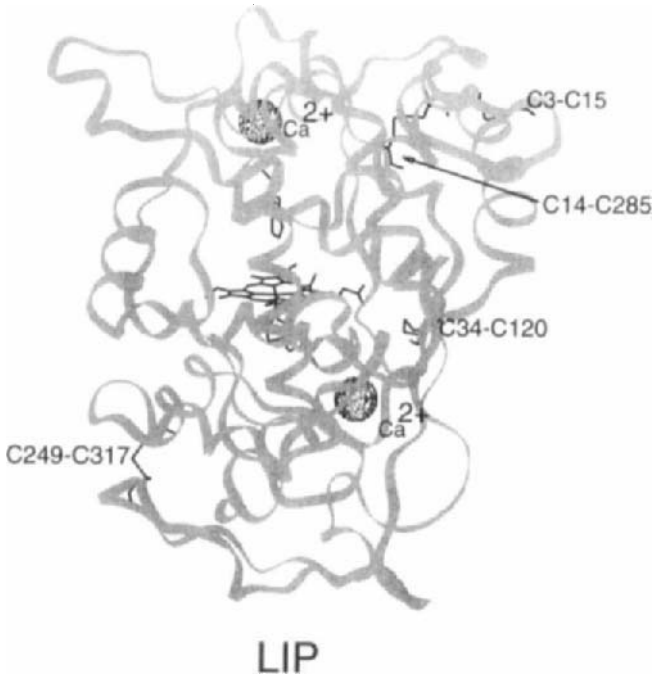

FIG. 3. Schematic diagram of lignin peroxidase C_α backbone generated from the X-ray coordinates (*5*). The heme, the distal His47, the proximal His176, the four disulfide bridges, and the van der Waals radii of the two Ca^{2+} ions are shown in bold.

enzyme has physical characteristics very similar to those of LIP, but utilizes mononuclear Mn^{II} complexes as reducing substrates instead of veratryl alcohol (Section V,B).

C. *Arthromyces ramosus* AND *Coprinus cinereus* PEROXIDASES

The addition of two new fungal peroxidase structures in 1994 (*6, 30*) further underscores the structural similarities in the plant peroxidase superfamily (*27, 28*) (Section II,G). The 3D structure of ARP has been refined to 1.9 Å (*30*), and its polypeptide fold (Fig. 5) is similar to that of LIP and CCP. ARP has four disulfide bridges, two tightly bound Ca^{2+} ions, and an N-glycosylation site, features it shares with LIP. In fact, the Ca^{2+} binding sites correspond to those identified in LIP and are believed to be important in the stabilization of the structure. ARP is an extracellular enzyme secreted by the fungus *A. ramosus,* and a considerable amount of the enzyme is nicked at Asn304 in cultures of

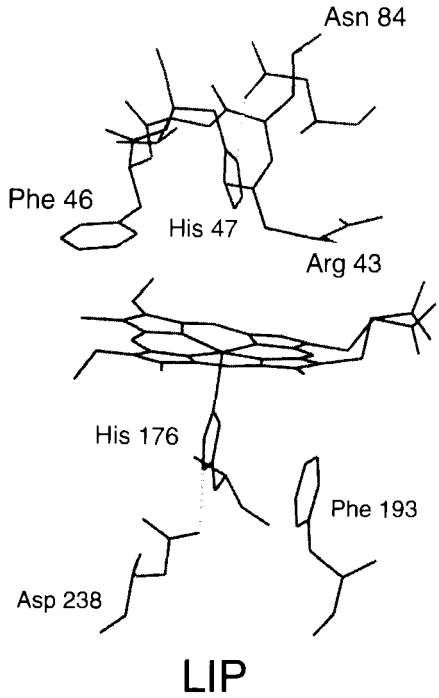

FIG. 4. Active-site structure of lignin peroxidase. The dashed lines represent H-bonds between N1 of the distal His47 and the side-chain carbonyl of Asn84, and N1 of the proximal His176 and the side-chain carboxylate of Asp238. This diagram was generated using the X-ray coordinates for the 2.0-Å structure of LIP (*5*).

the fungus. The peptide segment containing the protease-susceptible site is solvent-exposed, but nicking does not alter the activity of the enzyme.

In the ARP numbering scheme, the catalytically important residues are Arg52, Phe55, His56, His184, and Asp246. The active sites of ARP (Fig. 6) and LIP (Fig. 4) are remarkably similar with respect to the location and H-bonding of the active-site residues. The proximal His184 is coordinated to the iron and H-bonded to the carboxylate side chain of Asp246. The N1 of the distal His56 is H-bonded to Asn93, which is also H-bonded to the main-chain carbonyl group of Glu87. However, replacement of Ala105 in helix C of ARP by proline in LIP may result in the deviation of Asn93 by ~1 Å, which in turn may lead to the rotation of the distal His56 observed in ARP relative to LIP (*30*). H-bonding between the heme propionates and the polypeptide also differs in ARP and LIP. The main-chain NH group of Gly191 is directly

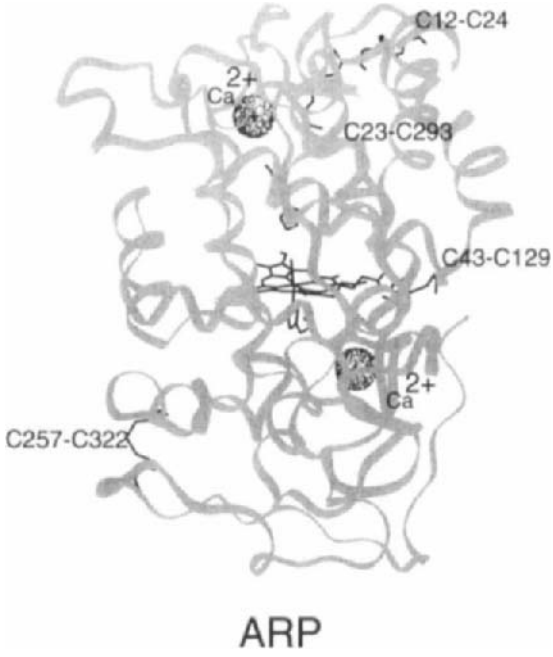

FIG. 5. Schematic diagram of *Arthromyces ramosus* peroxidase C_α backbone generated from the X-ray coordinates (*30*). The heme, the distal His56, the proximal His184, the four disulfide bridges, and the van der Waals radii of the two Ca^{2+} ions are shown in bold.

H-bonded to a propionate in ARP, but in LIP Asp183 H-bonds via its carboxylate side chain. It has been proposed that this carboxylate-carboxylate H-bond may give rise to the low pH optimum found for the reduction of substrates by LIP (Section V,B). Also, the distal Arg43 H-bonds directly with a propionate in LIP, but in ARP and CCP, a water molecule links the distal arginine to both propionate groups via H-bonds.

The 3D structure of recombinant CIP has been reported to 2.6-Å resolution (*6*). Recombinant CIP (expressed in the fungus *Aspergillus oryzae*) is identical to the wild type from *C. cinereus,* and both are identical in primary structure and enzymic properties to ARP and to the commercial *Coprinus macrorhizus* peroxidase (CMP) (*31*). The identity of CIP and ARP was confirmed by X-ray crystallography, because the 3D structure of CIP (*6*) is the same as that described earlier for ARP (*30*). However, an additional glycine residue was reported at the N-terminal of ARP, so that the CIP residue numbers are one lower

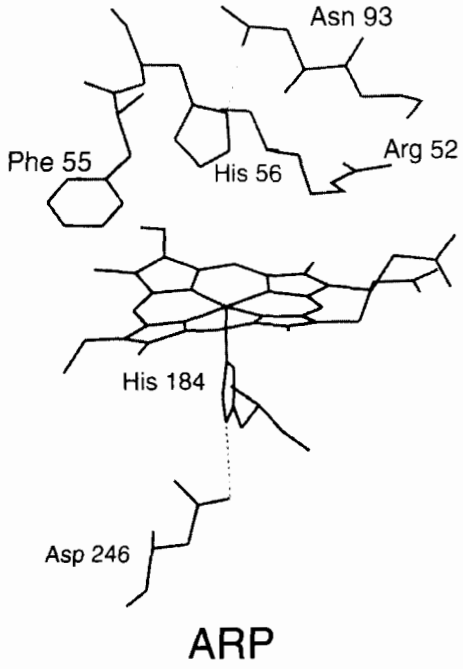

FIG. 6. The active-site structure of *Arthromyces ramosus* peroxidase. The dashed lines represent H-bonds between N1 of the distal His56 and the side-chain carbonyl of Asn93, and N1 of the proximal His184 and the side-chain carboxylate of Asp246. This diagram was generated using the X-ray coordinates for the 1.9-Å structure of ARP (*30*).

than those given earlier for ARP. The resonance Raman spectrum of CIP indicates that the ferric heme is mainly 5-coordinate, high-spin like CCP (*32*). The X-ray data for ARP reveal that a distal water molecule (Wat 415) is 2.96 Å from the heme, which is not within bonding distance, consistent with the RR results. The physiological functions of ARP, CIP, and CMP are not known, but these peroxidases exhibit similar substrate specificity to HRP.

D. PLANT PEROXIDASES

A 3-Å structure has been published for isoenzyme E5 of HRP (*33*), but no high-resolution X-ray structure is yet available for a plant peroxidase. It is anticipated that over the next few years structural data will be available for a number of plant peroxidases. Crystallographic studies on recombinant HRP isoenzyme *c* (HRP-C) (*34*), barley peroxi-

dase (*34, 35*), and cytosolic pea ascorbate peroxidase (*36*) are under way. Despite the fact that HRP-C is the most studied of heme peroxidases, its high degree of glycosylation has been an obstacle in obtaining suitable crystals for X-ray structure determination. Expression of proteins in *E. coli* yields nonglycosylated forms (*37*), on which the preliminary X-ray data for the plant peroxidases were obtained.

E. Myeloperoxidase

A number of heme peroxidases defend organisms against infection. Neutrophils, which are specialized white blood cells that play a key role in combating infection, contain high peroxidase activity. These cells are directed to the site of microbial invasion and sequester the invader in an intracellular vacuole or phagosome. Phagocytosis triggers a respiratory burst resulting in the production of superoxide, which dismutates to H_2O_2. MPO present in the neutrophils produces HOCl (hypochlorous acid) from chloride and H_2O_2, and HOCl nonenzymatically chlorinates a number of biomolecules, which accounts for the potent antimicrobial activity of MPO (*38*).

The crystal structure of canine MPO has recently been determined to 3-Å resolution (*7, 14*). This mammalian enzyme is a covalently linked dimer of molecular weight 140 kDa that can be cleaved into two identical halves by reduction of a single disulfide bond. Each half of the dimer, termed hemi-MPO, has the same optical properties and catalytic activity as the parent. Hemi-MPO consists of two polypeptides of 466 and 108 amino acid residues, and a heme-type prosthetic group is covalently bound to the larger polypeptide in a crevice ~15 Å below the protein surface. Like CCP and LIP, the secondary structure of MPO is dominated by α-helices with relatively little β-sheet structure (Fig. 7). There are five intrachain disulfide bridges in the large polypeptide, and a single Ca^{2+} ion; there is also a disulfide bridge in the small polypeptide (Fig. 7). Like LIP, MPO is a glycoprotein, and four potential N-linked glycosylation sites have been identified in the larger subunit. Sugar residues at the dimer interface play a role in dimer stabilization, in addition to the lone interchain disulfide bridge (*7*).

The key active-site residues in MPO are shown in Fig. 8. The N3 atom of the proximal His336, which extends from helix H8C, is coordinated to the iron, and the N1 atom forms a H-bond with the side chain of Asn421. In the distal heme pocket, His95 is located 5.7 Å from the iron, a separation similar to that found in CCP (5.5 Å) (*18*) and LIP (5.3 Å) (*5*), and Arg239 is also in an equivalent position to the distal arginines in CCP, LIP, and ARP (Figs. 2, 4, and 6). Thus, it appears that a number

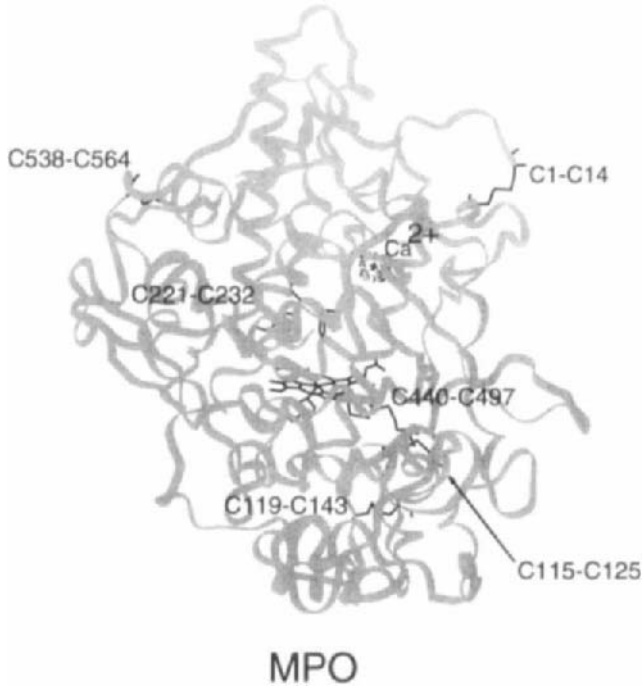

FIG. 7. Schematic diagram of canine myeloperoxidase C_α backbone generated from the X-ray coordinates (*7*). The heme, the distal His95, the proximal His336, the six disulfide bridges, and the van der Waals radius of the Ca^{2+} ion are shown in bold. Cys1–Cys14 is the single disulfide bridge in the small polypeptide (see text).

oxidase, or as a dihydroporphyrin (chlorin). The nature of the heme was not unambiguously determined in the 3-Å crystal structure, but a protoporphyrin IX heme covalently linked to the polypeptide by an ester bond formed between one of the methyl groups and the side chain of Glu242 would yield a structure that is consistent with the X-ray results (*7*) and recent spectroscopic studies (*40, 41*). A higher resolution structure (2.28 Å) of MPO revealed covalent bonds between Glu242 and Asp94 and modified methyl groups on pyrrole rings A and C, and also beween the vinyl group on ring A and Met243 (*41a*).

The green chromophore of MPO has received considerable attention because its visible absorption bands are red-shifted from those of most other heme proteins (*39*). Based on its spectroscopic properties, the chromophore has been identified as a high-spin ferric heme with formyl and vinyl porphyrin peripheral substituents, as in heme *a* of cytochrome

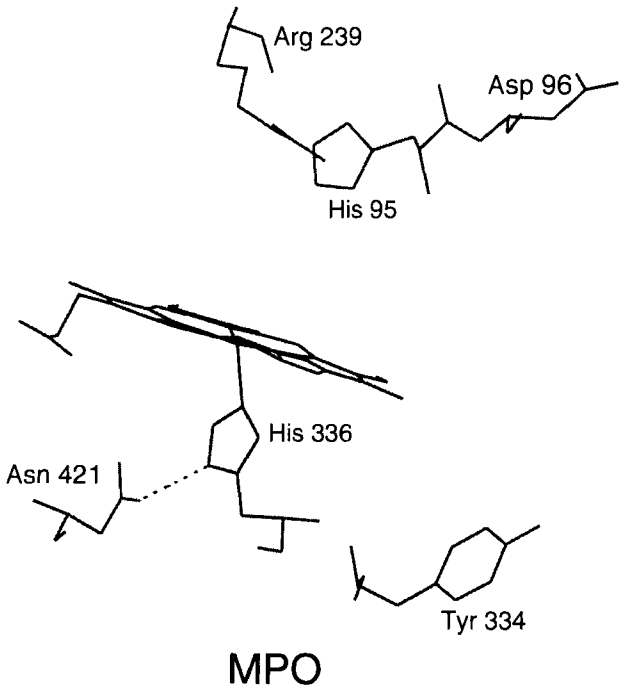

FIG. 8. Active-site structure of canine myeloperoxidase. The dashed line shows the H-bond between N1 of the proximal His336 and the side-chain carbonyl of Asn421. This diagram was generated using the X-ray coordinates for the 3-Å structure of MPO (*7*).

oxidase, or as a dihydroporphyrin (chlorin). The nature of the heme was not unambiguously determined in the 3-Å crystal structure, but a protoporphyrin IX heme covalently linked to the polypeptide by an ester bond formed between one of the methyl groups and the side chain of Glu242 would yield a structure that is consistent with the X-ray results (*7*) and recent spectroscopic studies (*40, 41*). A higher resolution structure (2.28 Å) of MPO revealed covalent bonds between Glu242 and Asp94 and modified methyl groups on pyrrole rings A and C, and also beween the vinyl group on ring A and Met243 (*41a*).

F. PROSTAGLANDIN H SYNTHASE

PGHS, which catalyzes the first two steps in the biosynthesis of prostaglandins (fatty acid derivatives with hormonal or regulatory properties), has been the subject of a number of recent reviews (*42–45*).

The enzyme is a homodimer of molecular weight 140 kDa, including 3.5% carbohydrate, and is widely distributed in animal tissues. PGHS exhibits both peroxidase and cyclooxygenase activities (Section V,C), and the most common substrate for the cyclooxygenase activity is the fatty acid arachidonic acid, which is oxidized to the hydroperoxy endoperoxide, PGG_2. The peroxidase activity of the enzyme can effectively utilize a variety of peroxides, but is most reactive towards fatty acid hydroperoxides, such as PGG_2, produced in the cyclooxygenase cycle. Recently it has been established that there are constitutive and inducible isoenzymes (*46*); these are designated PGHS-1 and PGHS-2, respectively.

The relationship between the peroxidase and cyclooxygenase activities of PGHS has received much attention (*42–45, 47*). The heme is essential for both, and the recent X-ray structure of PGHS-1 (*8, 48*) revealed that the peroxidase and cyclooxygenase active sites are different but adjacent to each other. Consistent with the X-ray data, inhibition studies have shown that arachidonic acid and PGG_2 do not bind at the same site on the enzyme. The peroxidase activity of PGHS is believed to have two functions. It reduces PGG_2 produced in the cyclooxygenase reaction to prostaglandin H_2 (PGH_2) (Section V,C), and it activates the cyclooxygenase reaction. Thus, PGG_2, the product of the cyclooxygenase activity (or some other hydroperoxide) is required for its own synthesis. The peroxidase active site is found in a shallow cleft, and a large part of the heme is exposed to the solvent, which may be necessary to accommodate a large hydroperoxide substrate such as PGG_2. The proximal iron ligand is His388, and the distal His207 extends from helix 2 into the distal cavity. However, there is no distal arginine in PGHS-1, unlike the other peroxidases whose X-ray structures have been obtained to date. Gln203 in the distal cavity may fulfill the catalytic role of the distal arginine, as is observed in heme catalases (*8, 48*).

PGHS-1 has a membrane binding domain, and the cyclooxygenase active site is at the top of a long narrow channel ($\sim 8 \times 25$ Å), which extends from the membrane-binding surface to the heme (*8, 48*). The cyclooxygenase substrate, arachidonic acid, fits into this site with its C-13 close to Tyr385 and its carboxylate group close to Arg120. Such substrate docking is consistent with the proposed cyclooxygenase mechanism, which involves abstraction of a H atom from C-13 of arachidonic acid by a tyrosyl radical generated in the peroxidase cycle. Tyr385 is close to the heme edge (*8*), so that oxidation of this residue in the peroxidase cycle is not unlikely. In support of this mechanism, the Y385F mutant of PGHS-1 exhibits no cyclooxygenase activity (*49*). The

Tyr385 radical (or other radical species) acts as a catalyst since it is regenerated following converison of arachidonic acid to PGG_2, so that high peroxidase activity is not required for high cyclooxygenase activity. However, recent studies failed to show good correlation between cyclooxygenase activity and the appearance of the tyrosyl radical (*45*); thus, the detailed mechanism of hydroperoxide-dependent activation of the cyclooxygenase activity of PGHS has not yet been fully resolved.

As well as having intriguing biochemical properties, PGHS plays a critical role in physiological and pathophysiological processes (43, 44). The enzyme has been the target for a large number of nonsteroidal anti-inflammatory drugs (NSAIDs), including aspirin (*50*). Ser530, which is acetylated by aspirin, is close to the top of the cyclooxygenase channel, and aspirin probably inhibits the enzyme by preventing access of arachidonic acid to the active site (*8*). With the identification of an inducible form, PGHS-2, the emphasis in NSAID development has shifted to the selective inhibition of this isoform, which is believed to be induced as part of the inflammatory response mechanism (*50–52*). Studies to date have indicated that selective inhibition of PGHS-2 is possible *in vitro* (*45*); thus, PGHS-2 has become a key enzyme from pharmacological and economical viewpoints (*43, 44*).

G. Plant and Mammalian Peroxidase Superfamilies

The plant peroxidase superfamily consists of evolutionarily related heme peroxidases from bacteria, fungi, and plants (*28*). The superfamily can be divided into three classes based on amino acid sequence (*28*). CCP and plant cytosolic ascorbate peroxidase fall into class I, and the main role of peroxidases in this class appears to be the removal of H_2O_2. Class II comprises the extracellular peroxidases such as lignin-degrading LIP and MnP; CIP and ARP also belong to class II, but their function is unknown. Class III peroxidases include the classical plant secretory peroxidases such as HRP and its isoenzymes, and barley peroxidase.

Although there is little overall sequence homology within the plant peroxidase superfamily, the tertiary structures obtained to date (CCP, LIP, ARP, and CIP), display considerable structural similarity. All possess 10 major α-helices (A–J) and little β-structure. The connecting loops between the helices vary greatly in length, and LIP, ARP, and CIP have 50 additional residues at what corresponds to the C-terminal of CCP, which has 294 residues. CCP and other class I peroxidases do not contain the four disulfide bridges, the two structural Ca^{2+} ions, or the glycosylation sites found in class II and III peroxidases. Neither

does CCP possess an aromatic substrate binding site adjacent to its heme like the class II and III enzymes (Section V,B). The substrate for CCP is ferrocyt *c*, which binds at the surface of the protein (Section V,A). Thus, although CCP was originally used as a paradigm for the plant peroxidase superfamily (*13, 27*) because its X-ray structure was the first to be determined, LIP, ARP, and CIP share greater structural similarities with each other and with HRP than with CCP (*5, 6, 30*), and so are likely to be better structural models for the plant peroxidases.

There are nine invariant residues in the plant peroxidase superfamily (*28*). Five of these are involved in catalysis and are shown in Fig. 2 for CCP. The other conserved residues play important structural roles, such as a buried salt bridge between Asp106 and Arg130 (CCP numbering) (*28*).

As with the plant peroxidase superfamily and other families of homologous enzymes (*27, 28*), it is to be anticipated that the 3D structures of the mammalian peroxidases will be shown to be very similar. A comparison of the sequences of MPO, TPO, EPO, and LPO reveals that the residues surrounding the heme are highly conserved (*7, 14*), suggesting a common heme environment for these four mammalian peroxidases. Furthermore, all 12 cysteines involved in the six disulfide bridges in MPO (Fig. 7) are conserved in the four mammalian peroxidases. Thus, if the pattern of disulfide bonds seen in MPO is also conserved, the 3D structures are likely to be very similar (*14*).

Although there is little sequence homology (~20%) between PGHS-1 and MPO, the fold of the catalytic domain of PGHS-1 is very similar to that of MPO (*8, 48*). In addition, spatial superposition of CCP, LIP, MPO, and PGHS-1 revealed that the arrangement of the helices making up the heme pocket in all four peroxidases is very similar, suggesting a peroxidase fold (*8*). However, there are differences in the catalytic residues between the mammalian peroxidases (Sections II,E and II,F) and the plant peroxidase superfamily, showing that peroxidase activity can be supported by different combinations of active-site residues, as discussed in the next section.

III. Mechanisms of Compound I Formation

The first step in peroxidase catalysis is the formation of a two-electron oxidized enzyme intermediate on reaction of peroxide (ROOH, R = H, alkyl, or aryl) with the resting ferric form of the enzyme. This intermediate, which stores the two oxidizing equivalents of the peroxide, is termed compound I. An Fe^{III}-OOH intermediate, or ES complex,

has not been observed for heme peroxidases, perhaps with the exception of HRP at low temperature (*53*). This indicates that rapid cleavage of the O–O bond occurs once peroxide binds to the heme iron.

Following elucidation of the X-ray structure of CCP (*18*), a detailed mechanism for the formation of compound I in CCP was proposed (*54*). As shown schematically in Fig. 9, this involved binding of H_2O_2 to the heme iron, with the concomitant donation of a proton to the distal His52 from the α-oxygen atom. The positively charged guanidinium side chain of Arg48 moved to directly interact with the anionic peroxide ligand, thus promoting the buildup of negative charge on the β-oxygen atom. Reorientation of Arg48, coupled with proton transfer from His52 to the β-oxygen, resulted in general acid-catalyzed heterolytic cleavage of the O–O bond, and the formation of H_2O and Fe^{V}=O. Rapid intramolecular electron transfer from an amino acid residue reduced the

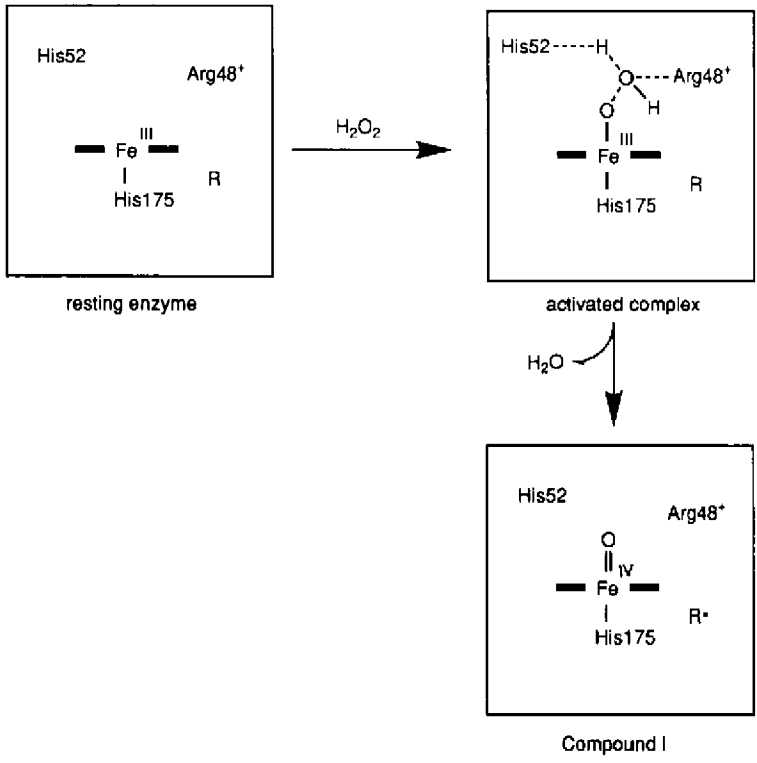

FIG. 9. Schematic representation of the formation of compound I in CCP [adapted from Poulos and Fenna (*14*)] based on the first proposed mechanism (*54*) (see text).

$Fe^{V}=O$ moiety to $Fe^{IV}=O$; thus, one oxidizing equivalent remained at the heme iron and one was stored on the polypeptide as an amino acid radical in CCP compound I. The formation of $Fe^{V}=O$ has not been validated experimentally for CCP, or any other heme peroxidase, possibly because of its rapid intramolecular reduction to $Fe^{IV}=O$. The formation of $Fe^{V}=O$ is not, however, a requirement in the mechanisms of compound I formation discussed later, because the porphyrin or protein (via the porphyrin, Section IV) could directly donate an electron to the peroxide.

Similar mechanisms of compound I formation are believed to hold for plant and fungal peroxidases. Five of the nine conserved residues in the plant peroxidase superfamily (Section II,G) are at the active site, and these residues in CCP (Arg48, His52, Asn82, His175, Asp235) are shown in Fig. 2. Elucidation of the X-ray structures of LIP (Fig. 4), CIP, and ARP (Fig. 6) confirmed that the key catalytic residues were indeed in equivalent positions in these proteins and CCP. However, the second oxidizing equivalent in compound I of the plant and fungal peroxidases is stored as a porphyrin cation radical, rather than as an amino acid radical as in CCP. (The transfer of oxidizing equivalents between the heme and the protein moiety in various peroxidases is discussed in Section IV.) Consistent with the role assigned to the distal histidine as a general acid–base catalyst in peroxide turnover, mutation of His52 to Leu in CCP resulted in a 10^5-fold decrease in the rate of compound I formation (*55, 56*). Despite the key role proposed for the mobile positive charge on the distal Arg48, mutation of this residue to lysine led to only a two-fold decrease in the rate of compound I formation (*55, 57*).

The Fe^{III}–OOH, or ES, complex of CCP is not stable, so its X-ray structure cannot be determined. However, the Fe^{II}–O_2 adduct of the Phe191 mutant of CCP is stable, and its X-ray structure has been determined as a model for the ES complex (*58*). The refined structure reveals two distinct binding sites for oxygen atoms close to the iron. These are stabilized by H-bonding between the O_2 ligand and Trp51 and His52, but no interaction between the distal Arg48 and the bound O_2 is observed (*58*). Extrapolation of this structural information to the ES complex led to a revised mechanism for compound I formation in CCP. Peroxide binds to the Fe^{III} ion, and a proton is transferred from the α-oxygen to His52 to generate the activated complex as described in the original mechanism (*54*). However, as shown in Fig. 10A, there is no direct interaction between Arg48 and the peroxy anion in this revised mechanism (*58*). His52 donates the proton to the β-oxygen, giving rise to a water molecule as leaving group, which is dispelled

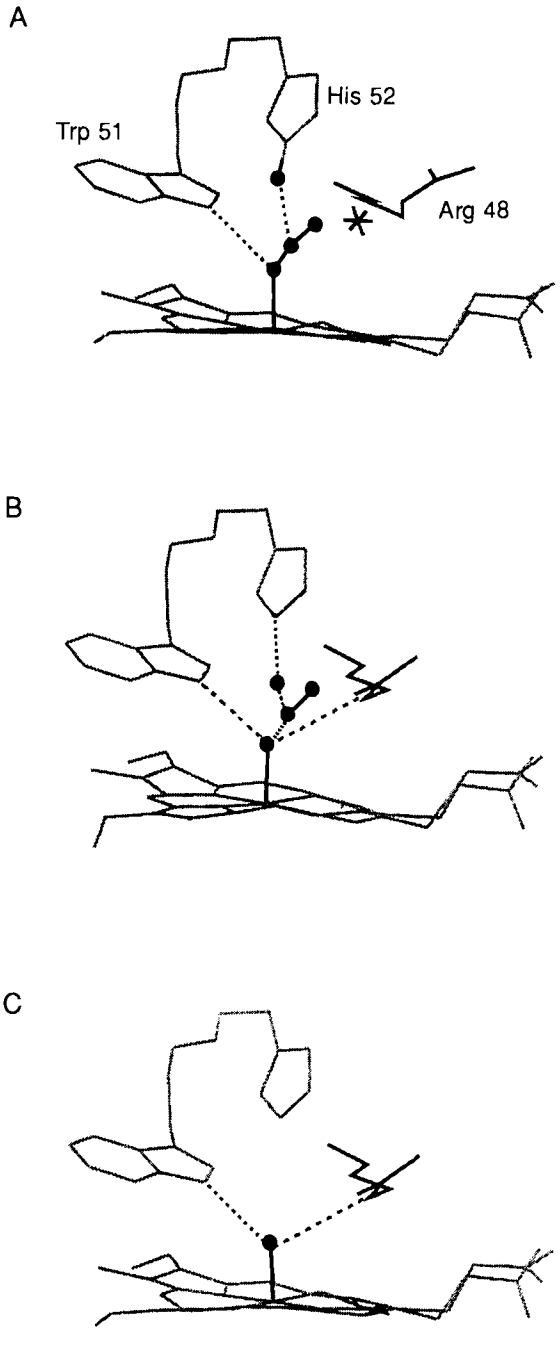
A
His 52
Trp 51
Arg 48
B
C

from the heme pocket by nonbonded interactions with the nascent oxene ligand. As the O–O bond is cleaved, Arg48 moves toward the iron and H-bonds to the oxene atom, displacing an active-site water molecule (Wat648) (Fig. 10B) and leading to compound I formation (Fig. 10C). The original model required an Fe–OOH bond length of 3.2 Å to optimize interaction between Arg48 and the peroxide, which was poorly oriented for proton transfer between the α-oxygen and His52 (*58*). Thus, the model in Fig. 10 of the Fe^{III}–OOH complex is in better agreement with the relative importance of His52 and Arg48 observed experimentally for CCP compound I formation (*55–57*). H-bonding between Asn82 and N1 of His52 (Fig. 2) forces N3 of His52 to serve as a H-bond acceptor from H_2O_2 and other heme ligands (*14*). Asn82 is conserved in the plant peroxidase superfamily (*28*) and as expected the distal histidine has a similar H-bonding pattern in LIP (Fig. 4), CIP, and ARP (Fig. 6).

In contrast to CCP, the R38K mutant of HRP-C exhibited a 500-fold decrease in the rate of compound I formation, indicating that the distal Arg → Lys substitution is not tolerated to the same degree in both enzymes (*59, 60*). Aromatic peracids, such as *m*-chloroperbenzoic acid (compound I in Scheme 1), react with HRP to form compound I at

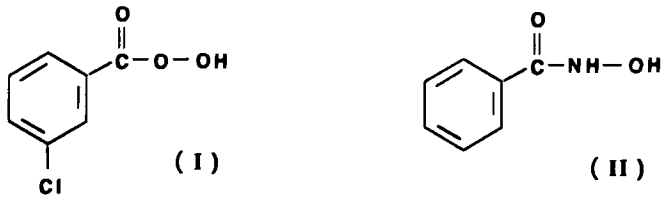

SCHEME 1

FIG. 10. The Fe^{III}–OOH (ES) complex of CCP and its decay to compound I. (A) The proposed structure of the ES complex, showing H-bonding between the α-oxygen and Trp51, and the β-oxygen and His52. The active-site water molecule (Wat 648) is depicted as an asterisk. (B) The activated complex, showing proton donation from His52 to the β-oxygen, partial cleavage of the O–O bond, and the reorientation of Arg48, which dispels Wat 648 from the active site, to H-bond donate to the nascent oxene ligand. (C) The oxyferryl center of compound I, showing H-bonding between the oxene ligand and Trp51 and Arg48. This diagram was generated using the X-ray coordinates for the 2.2-Å structure of the O_2 adduct of CCP(W191F) (*58*), which were kindly provided by Mark Miller, UCSD.

diffusion-controlled rates (*61*). The interaction of the aromatic peracid substrate analogue benzhydroxamic acid (BHA) (compound II in Scheme 1), with HRP (*62, 63*) and other peroxidases (*63–65*) has been studied extensively. Upon docking of the aromatic ring of BHA in the proposed aromatic substrate-binding site of HRP (Section V,B), it was noted that the hydroxamic acid side chain H-bonded exclusively with Arg38 (*59*). Furthermore, the R38K mutant of HRP appears to have lost the ability to bind BHA, suggesting that H-bonding to the distal Arg38 stabilizes the HRP–BHA complex (*59, 66*). The aromatic residue immediately adjacent to the distal histidine in plant peroxidases is highly conserved and is always phenylalanine (*13*). Thus, the distal Trp51, which H-bonds to the α-oxygen in the Fe^{II}–O_2 adduct and presumably the ES complex of CCP (Figure 10A), is replaced by Phe41 in HRP. This elimination of a distal H-bond may lead to different orientations of the bound peroxide anion in HRP and CCP, and thus to altered roles for the distal arginine in the catalysis of O–O bond cleavage in the two peroxidases. Although no X-ray data are yet available for HRP, detailed NMR studies suggest that the distal histidine and arginine residues have similar positions in the heme cavities of HRP and CCP (*67*).

Mutation in the proximal heme cavity of CCP has also led to some surprising results. Asp235 accepts a H-bond from the proximal His175 and imparts to this residue imidazolate character, which was proposed to be important in the activation of H_2O_2 (*54*). However, mutation of Asp235 to Asn led to only a fivefold decrease in the rate of compound I formation compared to that for the wild-type enzyme (*55, 68*). Similarly, it has been reported that the D235A mutant rapidly forms compound I (*69*). Thus, electron donation to the heme iron via His175 does not significantly accelerate compound I formation, indicating that Asp235 is not important in peroxide activation. Furthermore, mutation of His175 to Gln, Glu, or Cys resulted in proximal-ligand mutants that all react with H_2O_2 as fast as the wild-type enzyme (*25*). Hence, the mutagenesis work on CCP to date reveals that the distal pocket, especially the distal His52, is responsible for the high reactivity with H_2O_2 and that the nature of the proximal ligand is unimportant in this respect. Mutation of Asp235 does, however, alter the redox and ligation properties of ferric CCP and diminishes its ferrocyt *c* oxidizing activity (*24, 68, 69*).

Given that the distal His52 is a key residue in the rapid formation of compound I, then why does metmyoglobin, which also possesses a distal histidine residue, react with H_2O_2 much more slowly than CCP? The rate constants for the bimolecular reaction of CCP and metmyo-

globin with H_2O_2 are $\sim 10^7$ and $10^2\ M^{-1}s^{-1}$, respectively (*70*). In myoglobin, Phe43 takes the place of Arg48, and the proximal His93 is weakly H-bonded to a carbonyl group of the peptide backbone (*54*). If strong proximal H-bond donation and the presence of Arg48 are not necessary for rapid H_2O_2 activation in CCP, then why is the reaction of H_2O_2 with metmyoglobin 10^5-fold slower than that for CCP? It has been reported that ~30% of the peroxide bond-breaking reaction occurs via homolytic cleavage in sperm whale myoglobin, compared to 100% heterolytic cleavage in peroxidases (*71*). This suggests that the more polar pocket of CCP promotes charge separation, as is required for heterolytic cleavage, whereas in the nonpolar heme cavity of myoglobin, $OH^{\cdot}$ radical formation may be competitive with deprotonation of H_2O_2, the first step in heterolytic cleavage.

The mammalian peroxidases also react rapidly with H_2O_2 to form a compound I intermediate. Complete formation of MPO compound I requires a large excess of peroxide, and binding of H_2O_2 to the ferric enzyme appears to be reversible (*39*). Peroxide binds to the deprotonated form; the reactivity is controlled by a group on the enzyme with a pK_a of ~4 that is assigned to the distal histidine (*39*). The X-ray structure of MPO reveals that Asn421 (*8, 48*) takes the place of Asp235 in CCP (Fig. 8), and a histidine residue (M. Garavito, personal communication) is found in the same location in PGHS-1. Furthermore, no distal arginine is present in the heme pocket of PGHS-1 (Section II,F). A comparison of the active sites of peroxidases and catalases illustrates that efficient activation of H_2O_2 at a heme center can be achieved by different combinations of active-site residues. Compound I formation in catalase is believed to follow a mechanism similar to that in peroxidases (*72*). The distal His74 and Asn147, and the proximal Tyr357 (*73*) carry out equivalent roles to the corresponding distal (His52 and Arg48) and proximal (His175) residues shown in Fig. 2 for CCP.

IV. Endogenous Reduction of Peroxidase Intermediates

As discussed in Section III, the classical peroxidase cycle results in the transfer of the two oxidizing equivalents of H_2O_2 to the protein to yield compound I. In the absence of added or exogenous electron donors, compound I loses its oxidizing ability over time and the UV-vis absorption spectrum typically returns to one similar to the resting ferric enzyme. This indicates that in the peroxidases there are endogenous donors to the oxidizing centers first formed on reaction with H_2O_2.

In most heme peroxidases the two oxidizing equivalents are initially

stored at the heme. These are in form of Fe^{IV}=O and a porphyrin cation radical. HRP is archetypical of such enzymes, and the spectrum of HRP compound I is shown in Fig. 11. LIP, ARP, and CIP possess compound I spectra almost identical to that shown in Fig. 11, consistent with the formation of Fe^{IV}=O and a porphyrin cation radical on their reaction with H_2O_2 (*74–76*). Endogenous reduction of the porphyrin radical occurs in the absence of added electron donors, and the initial green compound I is converted to a brown species, compound II, which has a spectrum like that shown in Fig. 11 for HRP. Similar behavior is observed for the mammalian peroxidases that have been studied. Compound I–type spectra are initially observed for MPO, LPO, and PGHS, but rapid conversion to compound II–type spectra is observed, indicating that the porphyrin cation radical rapidly oxidizes the protein (Section V,C).

The UV-vis spectra of CCP compounds I and II are almost identical and resemble that of HRP compound II (Fig. 11). This clearly indicates that the second oxidizing equivalent is not located on the porphyrin in CCP. The storage site of this equivalent has been the focus of much attention. The crystal structure of CCP reveals two tryptophan residues in close proximity to the heme (Trp51 and Trp191; Fig. 2). Trp51 was initially considered to be the likely site of oxidation (*77*), because the

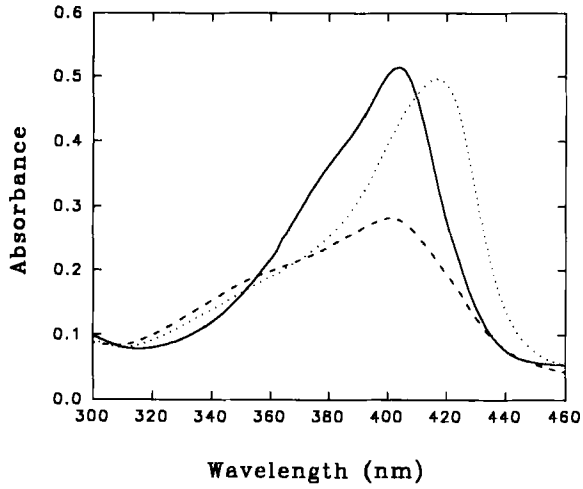

FIG. 11. Soret absorption at pH 7.0 of 5 μM ferric HRP (solid line), HRP compound I immediately following addition of 1.2 molar equivalents of H_2O_2 (dashed line), and HRP compound II (dotted line).

corresponding residue is phenylalanine in plant and fungal peroxidases (*13*). However, the W51F mutant exhibits an identical EPR spectrum to wild-type CCP, whereas the W191F mutant possesses a narrow EPR signal typical of tyrosyl radicals (*78*). Subsequent ENDOR studies on mutants containing perdeuterated tryptophan residues confirmed that Trp191 was the locus of the second oxidizing equivalent in wild-type CCP compound I (*79*). Since the indole ring of Trp191 and the proximal His175 are in van der Waals contact (Fig. 2), one of the oxidizing equivalents generated on the reduction of peroxide is rapidly transferred to the proximal domain. Mutation of Trp191 to Phe allowed detection, following rapid mixing with H_2O_2, of a porphyrin cation radical with a half-life of ~14 ms (*80*). In LIP (Fig. 4), where Phe193 takes the place of Trp191, the radical resides on the porphyrin. Since it is harder to oxidize the side chain of phenylalanine than the indole side chain of tryptophan (*81*), the radical is not rapidly transferred from the porphyrin to the polypeptide as in CCP.

The rate of intramolecular oxidation of the protein in compound I will depend on the separation between oxidizable residues and the heme. The most likely electron donors in the protein are the side chains of tryptophan, tyrosine, and methionine residues (*81*), and the locations of these residues relative to the heme are shown in Fig. 12 for CCP, LIP, ARP, and MPO. From this figure it can be clearly seen that CCP and MPO contain many more oxidizable residues than the two fungal peroxidases. Consistent with this observation is the fact that CCP can reduce up to 10 molar equivalents of H_2O_2 in the *absence* of exogenous donors (*82*). Amino acid analysis (*83*) and fluorescence studies on CCP (*84*) have revealed the loss of 3–4 tyrosine and 3–4 tryptophan residues after oxidation of the enzyme with 10 molar equivalents of H_2O_2. This ability of CCP to store a large number of reducing equivalents on its polypeptide may be related to its biological function as an antioxidant in yeast mitochondria. Yeast presumably undergo oxidative stress when they convert from anaerobic to aerobic metabolism, and the ability of CCP to reduce more than one molar equivalent of H_2O_2 in the absence of its reducing substrate, ferrocyt *c*, may be important under certain physiological conditions. Furthermore, the oxidized enzyme retains ~15–85% activity, depending on the extent of oxidation (*84*).

CCP provided the first example of a redox-active tryptophan residue in enzyme catalysis (*85*), and a second example has just been proposed in ribonucleotide reductase turnover (*86*). The long half-life of the Trp191 radical in CCP compound I ($t_{1/2}$ ~3 h) (*87*), despite the presence of neighboring tyrosine residues (*84*) which rapidly reduce $Trp^{\cdot}$ in aqueous solution (*88*), suggests a special radical-stabilizing environ-

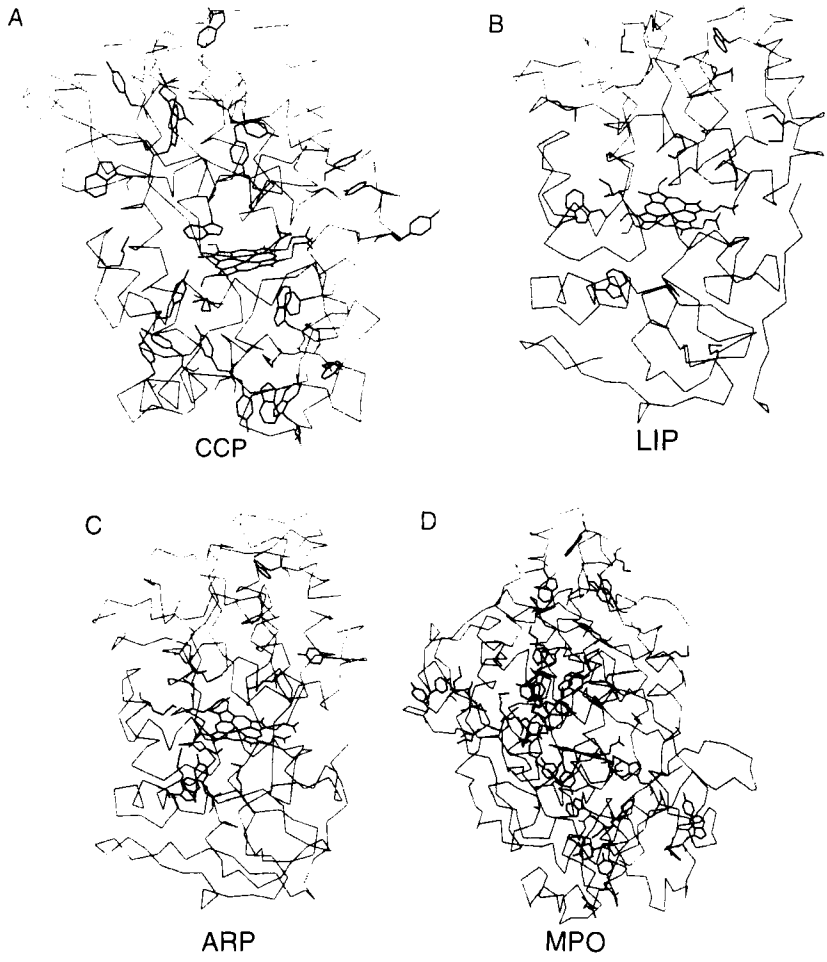

FIG. 12. The C_α backbones of CCP, LIP, ARP, and MPO, showing the location of the methionine, tryptophan, and tyrosine residues relative to the heme.

ment around Trp191. Electrostatic potential calculations revealed that a region of strong negative potential surrounds the Trp191 side chain, which is sufficient to stabilize the radical by 7.8 kcal/mol relative to a free indolyl radical in solution (*89*).

Although ARP, CIP, LIP, and HRP all possess a paucity of oxidizable residues (Fig. 12), spontaneous decay of LIP compound I to compound II is reported to be much faster (*90, 91*) than that for CIP (*76*) or HRP (*92*). The closest oxidizable residues to the heme of LIP are Met172

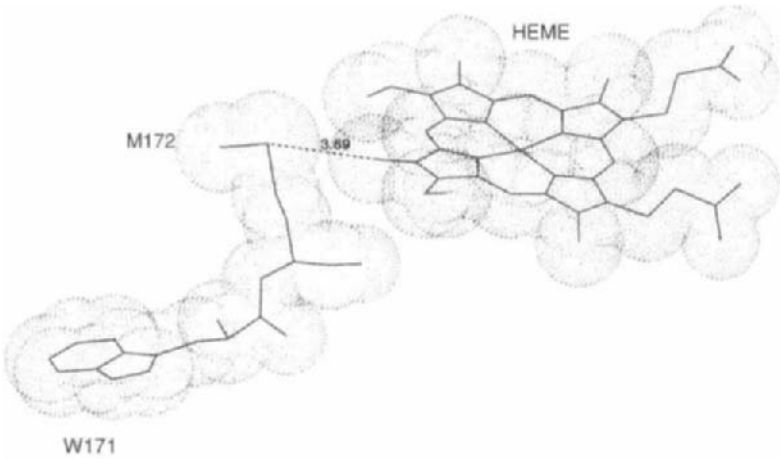

FIG. 13. The van der Waals surfaces of the heme, Met172, and Trp171 residues of LIP.

(~3.7 Å) and the neighboring Trp171 (Fig. 13). This region of the polypeptide may be a radical storage site similar to Trp191 of CCP, which is surrounded by Met230 and Met231 (*93*). The rapid spontaneous conversion of MPO compound I to compound II (*39*) is not surprising given the large number of potential endogenous donors surrounding the heme (Fig. 12). Likewise, PGHS-1 compound I, which initially possesses a porphyrin cation radical, rapidly converts to compound II. An EPR signal with $g = 2.005$ and hyperfine splitting typical of a tyrosyl radical appears at the same time as the growth of the Soret compound II absorbance (*94*). This suggests that a tyrosine residue donates an electron to the porphyrin cation radical and Tyr385, which is close to the heme edge (*8*), is assumed to be the donor. The tyrosyl radical thus generated presumably abstracts a H atom from arachidonic acid in the cyclooxygenase cycle of PGHS (Section II,F).

There is currently much interest in the roles played by amino acid radicals, such as tyrosyl radicals, in many enzymes (*95*). Thus, further examination of the radicals generated in plant and fungal peroxidases should provide important insight into the reactivity of protein radicals in redox enzymes. CCP in particular provides an ideal system to study the generation, stabilization, storage, translocation, and quenching of amino acid radicals in a protein matrix because of the large number of endogenous donors in its polypeptide (Fig. 12) (*84*).

Endogenous reduction of the Fe^{IV}=O heme is generally observed on longer time scales (minutes to hours) than the radicals. However, mutation of the distal Arg48, His52 (*55*), or Trp51 (*96*) residues, and

proximal His175 (*25*) or Asp235 (*55*) residues in CCP, resulted in large decreases in the stability of the oxyferryl heme species of these mutants. Clearly, new pathways for compound I decay are available to the mutants. It is of interest, however, that the oxyferryl heme of the W191F mutant exhibits essentially the same stability as that of the wild-type enzyme (*55, 97*).

V. Exogenous Reduction of Peroxidase Intermediates

A. Cytochrome *c* Peroxidase and Cytochrome *c*

Peroxidases utilize a large variety of substrates to reduce compound I (Fe^{IV}=O, $P^{\cdot+}$) back to the resting, ferric state:

$$(Fe^{IV}{=}O, P^{\cdot+}) + A_{Red} \rightarrow (Fe^{IV}{=}O, P) + A_{ox}, \quad (1)$$

$$(Fe^{IV}{=}O, P) + A_{Red} \rightarrow (Fe^{III}, P) + A_{ox} + H_2O. \quad (2)$$

As indicated by Eqs. (1) and (2), most peroxidases undergo one-electron reductions to generate the intermediate compound II (Fe^{IV}=O, P), with a single oxidizing equivalent stored as Fe^{IV}=O. Reduction of compound II leads to formation of the resting ferric enzyme and a water molecule. Yeast CCP, and also bacterial CCP from *Pseudomonas* (*98*), are unique among known heme peroxidases in that their reducing substrate is the macromolecule, ferrocyt *c*. The reaction catalyzed by CCP is the following:

$$2\ \text{cyt}\ c^{II} + H_2O_2 + 2H^+ \rightarrow 2\ \text{cyt}\ c^{III} + 2H_2O. \quad (3)$$

Reduction of compounds I and II by ferrocyt *c* involves complex formation between the two proteins. Since the X-ray structure of yeast CCP (*18*) and also those of cyts *c* from a number of species (*99*) are known, complex formation and electron transfer between CCP and cyt *c* has been the focus of intense research. The CCP–cyt *c* complex is a paradigm for protein–protein recognition, complex formation, and intracomplex electron transfer. Research on the structure and stability of this complex published before 1990 has been excellently reviewed (*93*), and a number of reviews of electron transfer between the two proteins have also appeared (*93, 100*). Thus, the discussion here will focus mainly on very recent results.

A highlight of current work in this area has been the elucidation of

the X-ray structure of the CCP–cyt *c* complex (*101*). Cocrystals of CCP were grown with 1:1 yeast cyt *c* and 2:1 horse cyt *c* under high- and low-salt conditions, respectively. The structures of the two complexes are very similar, and that with yeast cyt *c* is shown in Fig. 14. The X-ray data on the cocrystals will be used as the structural basis for discussions of the complexes.

The refined structure of the CCP–cyt *c* complex is remarkably different from the electrostatic model generated by visually optimizing interactions between the lysine residues surrounding the heme of cyt *c* and surface carboxylates on CCP (*54*). This latter approach placed the cyt *c* molecule at the arrow in Fig. 14. Mapping of the binding domain on horse cyt *c* for CCP has been carried out experimentally by examining the activities of cyts *c* singly modified at specific lysines, or by differential chemical modification in the presence and absence of CCP. A con-

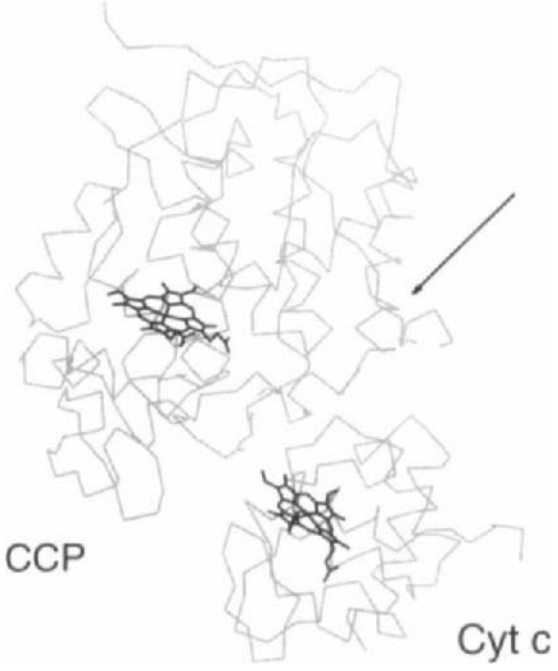

FIG. 14. Structure of the CCP-yeast iso-1 cyt *c* complex based on the X-ray coordinates (*101*). The hemes of the two molecules are shown in bold. A previous model of the complex, based on optimizing electrostatic interactions between surface residues (*54*), placed the cyt *c* molecule at the arrow.

sensus map of the key lysines involved in CCP–cyt *c* interaction (*102*) includes Lys8, 13, 27, 72, 79, 86, and 87 on the front surface of cyt *c* (Fig. 15). Lys73, 86, and 87 are shown to be involved in complex formation in the CCP–yeast cyt *c* structure, and Lys8, 72, and 87 in the horse cyt *c* complex (*101*). The model building study predicted the involvement of Lys8, 13, 72, and 87 on cyt *c*, which is highly consistent with the experimental consensus data (*102*). Differential chemical modification of carboxylate groups in free CCP and in its complex with horse cyt *c* revealed that Asp33, 34, 37, 221, and 224 were found to be protected in the complex (*103*). The electrostatic model predicts contacts between the three N-terminal aspartates (33, 34, 37) and cyt *c*, whereas only Asp34 is listed as a contact from the X-ray data. Neither the model nor the X-ray structure predict involvement of Asp221 or 224 in the interaction domain. Discrepancies between the model building, X-ray, and chemical modification results would arise if the CCP–cyt *c* interaction were dynamic with interconversion between different binding modes. More recent work, which utilized site-specific mutants of key lysines in cyt *c* (*104*) and aspartates in CCP (*26, 105*) identified in the electrostatic model, is not consistent with a single complex. A strict lock-and-key model would require that stereospecific H-bonding inter-

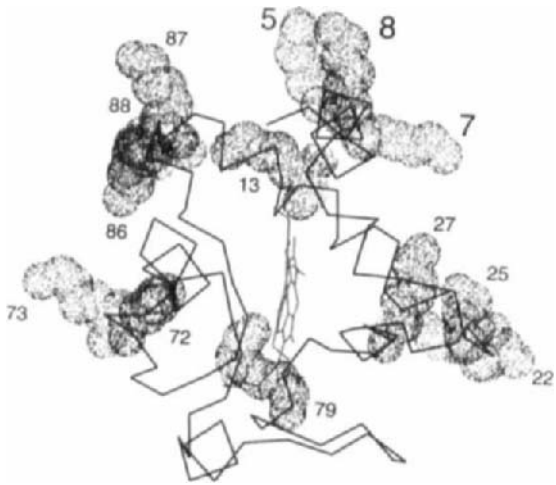

FIG. 15. The C_α backbone of horse heart cyt *c*, showing the location of the heme and the van der Waals surfaces of the 13 lysine residues surrounding the heme edge. The consensus map of the key lysines involved in CCP–cyt *c* interaction includes Lys8, 13, 27, 72, 79, 86, and 87. The van der Waals surfaces of these lysines are shown in bold. This diagram was generated using the X-ray coordinates of horse heart cyt *c* (*162*).

actions stabilize the complex, which would then be subject to significant destabilization on mutation of the residues involved. NMR experiments (*106*), using hydrogen exchange of the backbone amides of horse cyt *c* as a probe, clearly define a number of areas of interaction, including those predicted by the electrostatic model, but also a much wider area encompassing essentially all the consensus lysines in cyt *c* (Fig. 15).

Consistent with strong experimental support for multiple forms of the CCP–cyt *c* complex, a Brownian dynamics simulation (*107*) predicted a number of electrostatically stable encounter complexes between CCP and cyt *c*. This led McLendon and coworkers to propose the "Velcro" model for binding between soluble redox proteins such as CCP and cyt *c* (*106*). This model proposes that the reaction partners recognize each other by complementary-charged patches, which can interact in a variety of orientations like Velcro. Charge complementarity is involved in alignment, whereas the binding free energy derives mainly from hydrophobic and van der Waals interactions. Such was observed in the crystal structure of the CCP–yeast cyt *c* complex obtained at high salt (150 mM NaCl), since only one weak intermolecular H-bond was observed in the complex (*101*). The CCP–horse cyt *c* complex obtained at low ionic strength revealed three intermolecular H-bonding interactions, compatible with the greater electrostatic stabilization observed for the complex at low ionic strength (*93*).

As a basis for discussion of electron transfer in the CCP–cyt *c* complex, the electron-transfer pathway between the two hemes predicted from the structure of the CCP–yeast cyt *c* complex is shown in Fig. 16. Noteworthy is the presence in this pathway of Trp191, which is the center of radical formation in CCP compound I as discussed in Section IV. Using flash photolysis it has been possible to directly observe *intracomplex* electron transfer from ferrocyt *c* to compounds I and II of CCP in the preformed complexes. In one set of experiments (*108*), cyt *c* was covalently derivatized at surface lysine residues with a Ru–polypyridine photoredox reagent (Ru). Photoinduced intracomplex electron transfer was observed following rapid reduction of cyt *c* by *Ru:

$$\text{compound I}\text{–}{}^{*}\text{Ru}^{\text{II}}\text{cyt } c^{\text{III}} \rightarrow \text{compound I}\text{–}\text{Ru}^{\text{III}}\text{cyt } c^{\text{II}}, \tag{4}$$

$$\text{compound I}\text{–}\text{Ru}^{\text{II}}\text{cyt } c^{\text{II}} \rightarrow \text{compound II}\text{–}\text{Ru}^{\text{II}}\text{cyt } c^{\text{III}}. \tag{5}$$

The Ru^{III} generated in reaction (4) is rapidly reduced by a sacrificial donor such as EDTA to prevent back electron transfer and allow Ru^{II}cyt c^{II} to transfer an electron to compound I [Eq. (5)]. At low ionic strength (2 mM) and a 1 : 1 ratio of compound I to horse cyt *c*, reduction of the

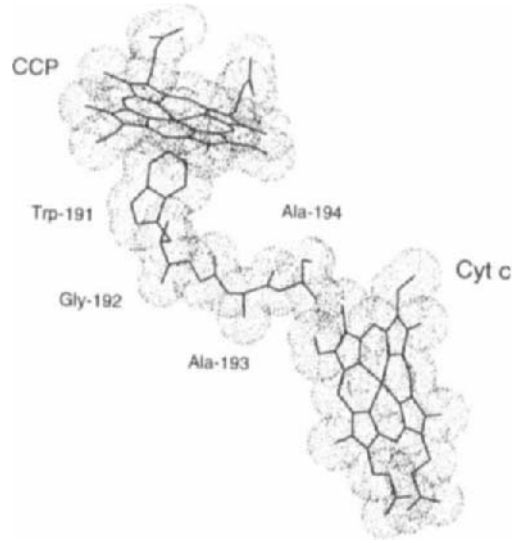

FIG. 16. The proposed electron-transfer pathway between CCP and yeast iso-1 cyt *c*. Adapted from Pelletier and Kraut (*101*).

Trp191 radical was observed at pH 7. The reaction was biphasic, and the rate constants depended on the location of the Ru label on cyt *c*. The fast rate constants varied from 5,000 to 55,000 s^{-1}, and the slow rate constants from 200 to 520 s^{-1}, suggesting two binding orientations for Rucyt *c* on CCP (*108*). At higher ionic strength, the rate of interconversion of the fast and slow binding orientations increased, and a single electron-transfer rate constant of 2,800 s^{-1} was observed for the Ru–Lys72 derivative of cyt *c* (*108*). Subsequent experiments revealed that at pH 5 and 6, following reduction of the Trp191 radical by Rucyt *c*, intramolecular electron transfer to the Fe^{IV}=O center occurred (*109*). The rate and extent of Trp191 → Fe^{IV}=O electron transfer decreased with increasing pH and was not observed at pH 7, in agreement with the pH-dependent equilibration of the single oxidizing equivalent between the heme and Trp191 in compound II (*110*).

Reduction of the radical first in reaction (5) is consistent with the proposed electron-transfer pathway between the hemes in the CCP–yeast cyt *c* complex (Fig. 16). However, flash photolysis experiments involving rapid bimolecular reduction of *native* cyts *c* by *free* flavin semiquinones ($FH^{\cdot}$) gave different results (*111*). The reactions monitored were the following:

$$FH^{\cdot} + \text{compound I–cyt } c^{III} \rightarrow F + \text{compound I–cyt } c^{II} + H^{+}, \quad (6)$$

$$\text{compound I–cyt } c^{II} \rightarrow \text{compound II–cyt } c^{III}. \quad (7)$$

$FH^{\cdot}$ selectively reduces cyt *c*, so that intramolecular electron transfer from ferrocyt *c* (cyt c^{II}) to compound I [Eq. (7)] was observed following a 1-μs flash. Monophasic reduction of the Fe^{IV}=O center was seen with native tuna (920 s^{-1}), horse (730 s^{-1}), and yeast (150 s^{-1}) cyts *c* at low ionic strength (*111*). In marked contrast to the reduction of compound I by the Rucyts *c*, no reduction of the Trp191 radical was observed (*111*). Furthermore, no intramolecular electron transfer from Fe^{III} to the Trp191 radical was observed on a 1-s time scale following the flash, suggesting that the ferric heme does *not* transfer an electron to the radical site during the catalytic turnover of CCP (*112*).

Stopped-flow studies carried out under different conditions yielded results that are compatible with *both* flash photolysis studies. A salt-dependent switch in the sites reduced by *native* horse cyt *c* has been reported by Erman and co-workers (*113*). At low ionic strength ($\leq$10 mM), the Fe^{IV}=O center is preferentially reduced by ferrocyt *c*, in agreement with the flash results using native cytochromes [Eq. (7)]. At high ionic strength (200 mM) the radical is preferentially reduced (*112*). Furthermore, Hahm *et al.* have shown that *both* the radical and heme are reduced from the same site at high ionic strength, which necessitates intramolecular electron transfer from Trp191 to the Fe^{IV}=O heme (*114*). Thus, the electron-transfer pathway between compound I and Rucyts *c* at low ionic strength may be similar to that with native cyts *c* at high ionic strength.

Figure 17 shows the proposed electron-transfer pathway in the CCP–horse cyt *c* complex based on the X-ray results (*101*). The slightly different orientation of the horse cytochrome in the complex results in poorer access of the horse cyt *c* heme to the Ala193–Ala194 loop of CCP. From Fig. 17, it is conceivable that an electron-transfer pathway not involving Trp191 may be more efficient, and that this could lead to direct reduction of the Fe^{IV}=O center at low ionic strength. However, mutation of Trp191 $\rightarrow$ Phe would also have to interfere with electron transfer via this pathway, since the Phe191 mutant does not demonstrate single turnover with native cyt *c* following its reduction by $FH^{\cdot}$ at low ionic strength (*97*). Amazingly, the H175Q/W191F double mutant of CCP possesses cyt *c* oxidizing activity, suggesting that a new electron-transfer pathway opens up this mutant (*25*).

It is important to evaluate the data from the single turnover experiments discussed earlier together with the steady-state turnover data

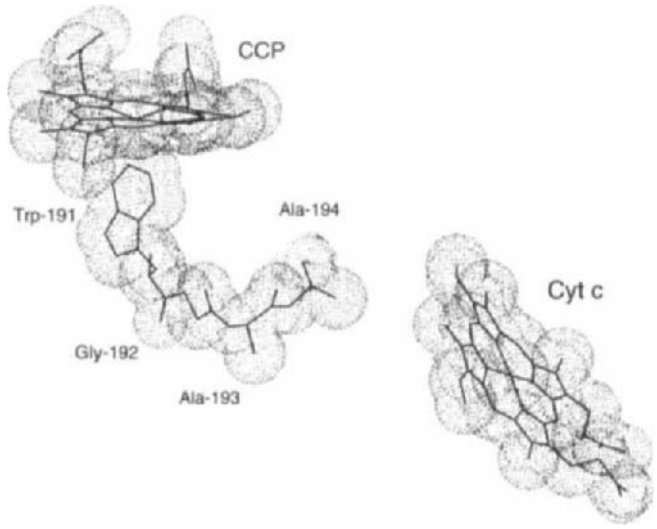

FIG. 17. The proposed electron-transfer pathway beween CCP and horse cyt *c*. Adapted from Pelletier and Kraut (*101*).

for CCP. Because it has been shown that $Fe^{III} \rightarrow Trp191^{\cdot}$ electron transfer does *not* occur in compound II in ≤ 1 s (*112*), both electrons *cannot* be transferred to compound I via the heme during steady-state turnover. Although $Trp191 \rightarrow Fe^{IV}{=}O$ electron transfer is observed with a rate constant of 150 s^{-1} at pH 6.0 (*109*), a turnover number of 1450 s^{-1} has been reported for CCP with yeast cyt *c* at pH 6 (*115*). Clearly, under optimal turnover conditions, direct electron transfer from ferrocyt *c* to the heme and to the radical site of compound I must occur. Consistent with this requirement, both the single turnover experiments (*111, 116, 117*) and the maximum turnover number under steady-state conditions (*115*) depend strongly on ionic strength, pH, buffer ions, and the source of cyt *c*.

Extensive studies on nonphysiological electron transfer using zinc-substituted CCP (*118*) or cyt *c* (119) have also been reported. The reaction scheme using ZnCCP is the following:

$$\text{ZnCCP–cyt } c^{III} \xrightarrow{h\nu} {}^{*}\text{ZnCCP–cyt } c^{III} \xrightarrow{k_f} Zn^{+}\text{CCP–cyt } c^{II}, \quad (8)$$

$$Zn^{+}\text{CCP–cyt } c^{II} \xrightarrow{k_b} \text{ZnCCP–cyt } c^{III}. \quad (9)$$

Photoexcitation of ZnCCP yields an excited triplet, which is a strong reductant, that transfers an electron to ferricyt *c* [Eq. (8)]. Back electron transfer from ferrocyt *c* to Zn^{+}CCP [Eq. (9)] regenerates the reactants in a step that resembles electron transfer from ferrocyt *c* to the Fe^{IV}=O heme of compounds I and II. Back electron transfer is very efficient with yeast cyt *c* as a donor ($k_b \sim 10^4\ s^{-1}$), but much less efficient when tuna cyt *c* ($12\ s^{-1}$) is the donor (*120*). The much more pronounced species dependency of reaction (9) compared to that of the physiological reaction [Eq. (7)] (*111*) is noteworthy.

From the many different investigations of the CCP–cyt *c* complex, it was generally concluded that the binding stoichiometry was 1 : 1 (*93*). However, potentiometric titrations, which assess the net change in protonation on binding of the two proteins, revealed the presence of high- and low-affinity binding sites with micromolar and millimolar dissociation constants at low ionic strength (*121*). Furthermore, the kinetics of quenching of the zinc porphyrin triplet in both the ZnCCP–cyt *c* and CCP–Zncyt *c* complexes (*118, 119, 122*) also revealed two binding sites with *simultaneous* occupancy of both. In these unnatural complexes, electron transfer occurs only between the prosthetic groups, since no protein radical is generated, and efficient transfer was observed *only* from the low-affinity site. Given that the Fe^{IV}=O center of compound I is preferentially reduced by native cyt *c* at low ionic strength as discussed earlier, this heme-to-heme electron transfer might occur from the low-affinity site of CCP, as in the artificial systems. Nonetheless, the relationship among the high- and low-affinity binding sites, the sites from which reduction of the radical and Fe^{IV}=O centers can occur, and the crystallographically identified binding site remains to be fully elucidated.

B. Plant and Fungal Peroxidases

In contrast to CCP, many plant and fungal peroxidases seem to be designed to oxidize small aromatic substrates (*13, 63*). However, the variety of electron-donor substrates used by peroxidases is certainly at odds with the notion of enzyme specificity. The vast array of oxidizable substrates includes high–molecular-weight organic polymers and simple inorganic ions, as well as redox proteins. MnP, like LIP, is involved in lignin degradation by white-rot fungi (*123*). It provides an intriguing example of peroxidase donor–substrate utilization. Mn^{II} is oxidized to Mn^{III} by the enzyme intermediates, and it is assumed that Mn^{III} assists in the oxidative degradation of lignin. A recent study (*123*) of the

reduction of MnP compound II to the ferric state by Mn^{II} in the presence of various chelators led to the following proposed mechanism:

$$\text{compound II} + Mn^{II}L \rightarrow MnP^{III} + Mn^{III}L, \quad (10)$$

$$Mn^{III}L + L \rightarrow Mn^{III}L_2. \quad (11)$$

The monochelated form $Mn^{II}L$, where L is probably oxalate under physiological conditions (*123*), reduces compound II in a slow step [Eq. (10)]. Rapid formation of the dichelated form, $Mn^{III}L_2$ [Eq. (11)], precedes release of Mn^{III} into the medium. Once the X-ray structure of MnP is completed (*29*), it will be possible to ascertain if the proposed mechanism is reasonable on structural grounds.

The recent availability of the X-ray structures of LIP (*5*) and ARP (*30*) revealed significant differences in the size of the substrate-access channel to the heme in peroxidases. Figure 18 compares the van der Waals surfaces around the access channels in CCP, LIP, ARP, and HRP. The last was constructed by substituting HRP residues for ARP residues using the published sequence alignments (*28, 124*). The amino acid residues surrounding the entrance are not well conserved. A larger number of residues make up the channel in ARP than in LIP, resulting in the formation of a wider channel in the former. The CCP heme pocket is also larger than that of LIP, and it has been shown that small substrates, such as guaiacol and ferrocyanide, are primarily oxidized at the heme edge of CCP (*125*). The relative accessibility of the heme explains the relative ease of formation of δ-meso-substituted heme adducts in chemical inactivation studies with highly reactive substrates such as phenylhydrazine (*126*). As anticipated from Fig. 18, LIP is less susceptible to δ-meso heme additions (*127*) than the other peroxidases. Heme modification generally occurs at the δ-meso position, suggesting that substrates have access to the heme edge only (*126*). However, CCP has a sufficiently open active site to allow formation of a phenyl–iron complex, and substrates such as styrene can access the oxene ligand, which results in monooxygenase activity (*128*).

It has been pointed out that plant and fungal peroxidases share a conserved segment (I/L/V-**P**-X-**P**-X-X-; **IPGPGN** in ARP; **LPAPFF** in HRP; **VPEPFH** in LIP) that is very close to the heme edge (<5 Å) and just before helix E (*63, 129*). Phe142 and Phe143 form part of this segment in HRP and have been implicated by NMR to be involved, together with the heme 8-methyl, in the binding of aromatic substrates (*63, 130*). Veratryl alcohol, a substrate for LIP (see later discussion), has been modeled into the heme pocket. Phe148, which follows the

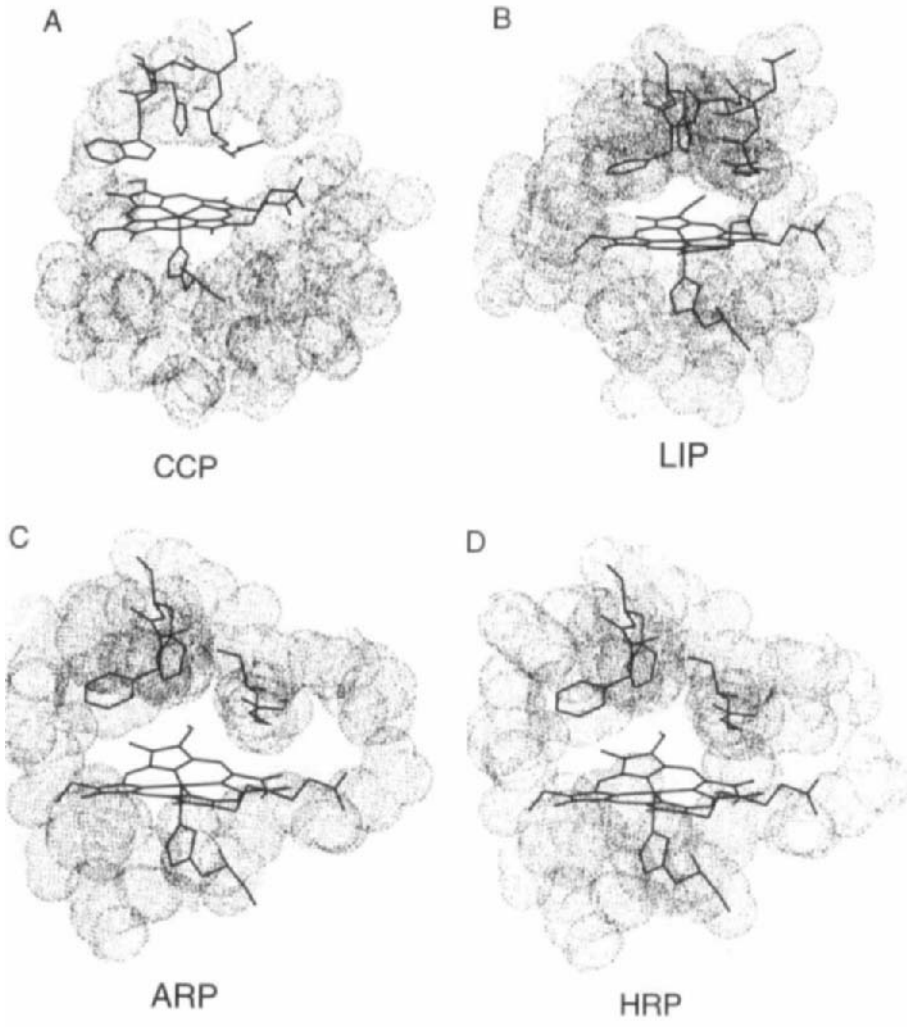

FIG. 18. Substrate access channel leading to the distal heme cavity in CCP, LIP, ARP, and HRP. The HRP diagram was generated by replacement of the ARP residues with the corresponding residues in HRP (see text). The residues surrounding the channels are represented by their van der Waals surfaces. Adapted from Poulos and Fenna (*14*) and Kunishima *et al.* (*30*).

VPEP motif in LIP, forms a primary contact with the alcohol in the model (*5, 14*). The G156F/N157F double mutant of CIP (Gly156 and Asn157 follow the IPGP motif) shows altered substrate specificity compared to the wild-type enzyme (*130*). These observations have led to

the proposal that this segment of the proteins may be important in the control of peroxidase specificity (*63, 129*).

Substrate specificity is also controlled by the oxidizing power of compounds I and II. Using a series of substituted aromatic amines and phenols, Dunford and co-workers have shown that the rate constants for the reduction of HRP compounds I and II by these substrates increased with the electron-donating power of the substituents (*131–133*). Correlation of the rate constants with Hammett σ parameters, rather than σ^+ parameters, revealed concerted electron and proton transfer from the substrate in the rate-determining step. A similar study showed that CCP is a much less efficient oxidant of aromatic substrates than HRP, and the rate constants are better correlated with σ^+ than with σ, indicating the development of positive charge on the substrate in the transition state (*134*). Hence, it appears that the heme cavity of CCP, unlike that of HRP, is not optimally designed to promote rapid oxidation of small aromatic substrates.

LIP, which is involved in lignin degradation by white-rot fungi (*135*), also oxidizes small aromatic substrates. The X-ray structure revealed a binding site for veratryl alcohol (VA) close to the heme 8-methyl

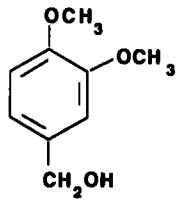

Veratryl Alcohol

SCHEME 2

group. This alcohol, shown in Scheme 2, is a metabolite produced by the fungus and is oxidized by LIP compound I to $VA^{\cdot+}$. It is proposed that in the presence of lignin, $VA^{\cdot+}$ abstracts a H atom from the polymer, assisting in its radical breakdown (*136*). Neither ARP (*137*) nor HRP (*138*) compound I will oxidize VA, as they are not strong enough oxidants to remove an electron from nonphenolic substrates (*138*). The high oxidizing power of LIP compound I is of considerable interest (*139*), but the X-ray structure (*5, 14*) and NMR studies (*140*) reveal no obvious features of the LIP active site that would impart such strong oxidizing power to its compound I. It is noteworthy that the reduction of LIP compound I is optimal at pH 3 (*141*), and disruption of the carboxylate–carboxylate H-bond between a heme propionate and Asp183 (Section II,B), which is not present in CCP or ARP, may increase

the oxidizing power of LIP compound I at low pH (*5, 14*). However, it has been observed that the rate of oxidation of $Fe(CN)_6^{4-}$ and other substrates by HRP increases at low pH (*142*), indicating that compound I may be a better oxidant under these conditions. Thus, LIP may be able to catalyze the oxidation of VA at low pH, since it can form a stable compound I at low pH.

Little is known in general about what controls the oxidizing power of compounds I and II of heme peroxidases. Protonation of the distal histidine and heme propionates at low pH should increase the net positive charge in the heme pocket and increase the reduction potential of the porphyrin cation radical and the oxyferryl ion. Reduction of the latter also requires protonation of the oxene ligand to form H_2O, and protonation should be more favorable at low pH. In fact, it has been suggested that under certain conditions, proton transfer to the oxene atom is rate-limiting in CCP compound I reduction (*143*). In myoglobin, reduction of the oxyferryl ion by a surface bond Ru^{II} complex is orders of magnitude slower than predicted (*144*), and it was proposed that proton transfer to the oxene atom is rate-limiting. A recent study of the pH dependence of this electron-transfer step (C. Fenwick and A. English, unpublished results) supports this view, which is not surprising given that the role of the polypeptide in myoglobin is to provide a nonpolar environment for heme-bound O_2 (*10*).

To fully investigate H-bonding between distal residues and heme-bound ligands such as the oxene ligand, IR and resonance Raman (RR) studies have proven to be particularly useful (*145*). Using a combination of IR and RR, Smulevich *et al.* (*146*) have shown that heme-bound CO in CCP can adopt linear and tilted conformations, with the latter strongly H-bonded to a distal residue. Because CCP–CO exhibits an acid–based transition with a pK_a of 7.5 (*147*), it was originally assumed that the CO was H-bonded to the distal His52. Recently, however, it has been shown that the CO adduct of the Leu52 mutant undergoes a similar acid–base transition, thereby implicating Arg48 in distal H-bonding (*148*). An IR examination of the pH dependence of the CO stretching vibrations of HRP–CO in the authors' laboratory yielded results consistent with H-bonding between CO and the distal Arg38 in HRP (*148a*). RR studies on the ferric HRP–CN conformers (*149*) also implicated the distal Arg38 as a H-bond donor, whereas NMR studies suggest that the CN^- ligand is H-bonded to His42 (*62*). Crystal structures of liganded forms of CCP (*19–22*) reveal that Arg48 has considerable conformational flexibility. Binding of fluoride to the heme causes a dramatic change in the position of Arg48, which allows it to interact with the F^- ligand, and smaller changes are observed on CO,

CN^-, and NO binding. However, the recent X-ray structure of the O_2 complex of the Phe191 mutant of CCP (Section III) showed that the O_2 ligand is H-bonded to His52, and not to Arg48. Taken as a whole, these studies indicate that a heme-bound ligand in either CCP or HRP (and presumably other peroxidases) can adopt a number of conformations, suggesting that the distal heme cavity can accommodate a variety of heme ligands.

Despite conflicting results over distal H-bond donors, particularly with respect to the diatomic ligands, there is solid structural evidence that Arg48 H-bonds to the oxene ligand in CCP compound I (*23, 150*). The low RR frequencies observed for the Fe^{IV}=O stretching vibrations of compound II of CCP and HRP (753 and 779 cm^{-1}) compared to ferrylmyoglobin (797 cm^{-1}) (*151*) indicate strong H-bond donation to the oxene atom from distal residues in the peroxidases. Strong H-bond donation from Arg38 to the hydroxide complex of ferric HRP has been proposed based on recent RR results (*152*), suggesting that the distal arginine may also interact with monatomic ligands in HRP, and possibly with the oxene ligand. We propose that the distal arginine controls protonation of the oxene ligand, which serves to stabilize compound I in the absence of electron donors, and to regulate oxyferryl heme reduction in the presence of donors. As discussed earlier, replacement of Arg48 in CCP leads to rapid decay of the oxyferryl center (*55, 57*) (Section IV).

C. Mammalian Peroxidases

The reactions catalyzed by PGHS are the following:

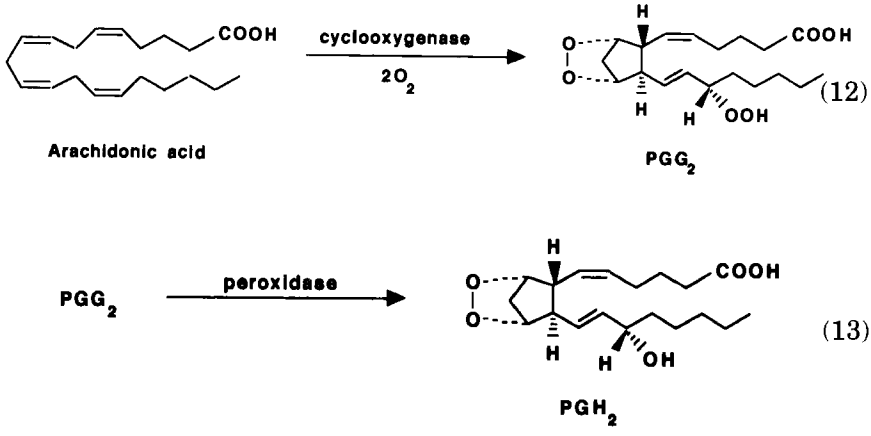

While most peroxidases appear to use H_2O_2 as an acceptor substrate and the biochemical transformations of interest are carried out on the donor substrates, this is not the case for PGHS. Since PGH_2 produced in the peroxidase step is a key intermediate in prostaglandin biosynthesis, its synthesis has been the focus of attention rather than transformations of PGHS electron-donor substrates. However, a wide range of species will act as donor substrates (*43*), consistent with the relatively exposed heme of PGHS-1 (*8, 48*), and the physiological reducing substrate may vary with tissue (*43*).

The *in vivo* electron-donor substrate of MPO is generally regarded to be Cl^-, which is converted to HOCl by compound I. Since the reactivities of a large number of compounds towards HOCl and the product of the MPO peroxidase reaction are identical, HOCl (pK_a 7.5) is believed to diffuse from the active site of the enzyme; therefore, MPO could simply be a physiological source of free HOCl, which is a potent microbicide (*39*). MPO is one of only three known heme-containing proteins that can efficiently oxidize chloride to hypochlorite. The other two proteins are eosinophil peroxidase (*153*) and chloroperoxidase (*154*). From active-site comparisons with CCP, ARP, and LIP, structural reasons for the unusual catalytic properties of MPO are not obvious except for the structural differences in the heme macrocycle (Section II,E). However, the ferric/ferrous reduction potentials at pH 7.0 are 24, −135, and −194 mV for MPO, LIP, and CCP, respectively (*139*), suggesting a more electron deficient heme in MPO. A decrease in electron density at the heme iron could arise from an electron-withdrawing substituent on the heme and/or reduced basicity of the proximal histidine. MPO undergoes rapid spontaneous conversion to compound II ($t_{1/2} \leq 7$ s) (*39*), a form of the enzyme that is unreactive towards Cl^-. Compound II may arise from the endogenous reduction of the porphyrin cation radical in compound I by Tyr334, which is only 5 Å from the heme (Fig. 8).

As discussed in Section II,G, the key residues for peroxidase catalysis identified in the heme cavity of MPO (Fig. 8) are present in LPO and TPO (*7, 14*). Ferric LPO, which has a Soret maximum at 412 nm, reacts with H_2O_2 to give compound I. In the absence of electron-donor substrates, compound I is converted to a species that exhibits a compound II-type spectrum (Fig. 11), but which accepts two electrons from ferrocyanide. An amino acid residue has been proposed as the storage site for one of the two oxidizing equivalents (*155*), so that endogenous reduction of LPO results in an intermediate analogous to compound I of CCP. The physiological role of LPO appears to be the use of H_2O_2 produced by microorganisms to oxidize SCN^- to $OSCN^-$, which inhibits microbial growth (*156*):

$$LPO^{III} + H_2O_2 \rightarrow \text{compound I} + H_2O, \qquad (14)$$

$$\text{compound I} + SCN^- \rightarrow LPO^{III} + OSCN^-. \quad (15)$$

The properties of SCN^- are similar to those of the halides, and LPO compound I also catalyzes the oxidation of I^- to HOI. The LPO/H_2O_2/I^- system is used to introduce the radiolabel ^{125}I into exposed tyrosine residues in proteins and membranes (*155*). There is evidence for both free and enzyme-bound iodinating species (*157, 158*).

TPO is found in the thyroid gland, where it is involved in the synthesis of the thyroid hormones thyroxine (T_4) and triiodothyronine (T_3) (*159*). The synthesis of these hormones involves the iodination of tyrosine residues in the protein thyroglobulin (Tg), which is present in high concentration in the thyroid gland and contains more than 40 tyrosine residues. Iodide is actively transported into the thyroid, and TPO catalyzes the iodination and coupling of Tg-bound tyrosines. Proteolysis of Tg leads to the release of free T_3 and T_4 into the blood. To function as an iodinating reagent, I^- is oxidized from -1 to $+1$, and the proposed mechanism is similar to that just given for LPO [Eqs. (14) and (15)]. TPO compound I reacts with I^- to give a hypoiodite intermediate, Fe^{III}–OI^-. It is not known whether iodination is catalyzed by TPO-bound hypoiodite [Eq. (16)] or whether free HOI ($pK_a = 10.64$) is released from the enzyme's active site [Eqs. (17) and (18)]. The latter would explain the low substrate specificity of TPO, analogous to LPO.

$$Fe^{III}\text{–}OI^- + RH + H^+ \rightarrow TPO^{III} + RI + H_2O, \quad (16)$$

$$Fe^{III}\text{–}OI^- \rightarrow TPO^{III} + HOI, \quad (17)$$

$$HOI + RH \rightarrow RI + H_2O. \quad (18)$$

The mechanism of coupling of two Tg-bound iodotyrosines to yield Tg-bound iodothyronine requires H_2O_2, but not I^-. Both free radical and ionic mechanisms would explain the catalysis of coupling by TPO compound I (*160*). A free radical mechanism would involve the formation of two tyrosyl radicals which undergo coupling. In an ionic mechanism, two-electron oxidation would yield a reactive tyrosyl cation. When a stoichiometric amount of H_2O_2 is added to ferric TPO in the absence of an electron-donor substrate, an HRP compound II–type spectrum (Fig. 11) is observed. Like LPO, this form of TPO contains two oxidizing equivalents and can catalyze the iodotyrosine coupling reaction, but not the iodination reaction (*161*). An HPR-like compound I (Fig. 11) has been observed during the iodination reaction, suggesting that TPO compound I must accept two electrons from I^- or donate the

oxene atom to I^- to form hypoiodite at the heme (*159*). The observation of two types of compound I for TPO and LPO with different substrate specificities suggests that porphyrin–protein radical exchange may play a role in controlling peroxidase activity and substrate specificity.

VI. Outlook

Our understanding of structure–function relationships in heme peroxidases will continue to advance primarily because of progress in structural work and protein engineering. A number of crystal structures are in preparation, including those for MnP, HRP, and barley peroxidase, which will result in the availability of a large number of structures. Site-directed mutagenesis, which permits the preparation of mutants almost at will, should provide answers to the many features of heme peroxidase structure–function relationships that are not currently understood. For example, do the identified key distal and proximal residues play similar roles in all heme peroxidases? What variation can be tolerated at the active site before enzyme activity is lost? Also, designing greater substrate specificity into heme peroxidases may allow their use in synthesis. Interest in substrate binding to peroxidases has increased in recent years: Now that many peroxidases have been expressed in *E. coli,* it may be possible to design mutants with high selectivity for a given substrate and effect synthesis of specific target molecules. Undoubtedly, future mechanistic and structural studies on mutant proteins will substantially increase our understanding of active-site control of peroxidatic and catalactic activity, and heme protein chemistry in general.

References

1. Frew, J. E.; Jones, P. In "Advances in Inorganic and Bioinorganic Mechanisms", Sykes, A. G., Ed.; Academic Press: London, 1984; Vol. 3, 175–212.
2. Poulos, T. L.; Freer, S. T.; Alden, R. A.; Edwards, S. L.; Skogland, U.; Takio, K.; Eriksson, B.; Xuong, N. H.; Yonetani, T.; Kraut, J. *Biochemistry* **1980,** *255,* 575.
3. Mauro, J. T.; Miller, M. A.; Edwards, S. L.; Wang, J.; Fishel, L. A.; Kraut, J. in "Metal Ions in Biological Systems: Exploring Structure-Function Relationships in Yeast Cytochrome c Peroxidase Using Mutagenesis and Crystallography", Sigel, H.; Sigel, A., Eds.; Dekker: New York, 1989; Vol. 27, 477–503.
4. Poulos, T. L.; Finzel, B. C.; Howard, A. J. *Biochemistry* **1986,** *25,* 5314.
5. Poulos, T. L.; Edwards, S. L.; Wariishi, H.; Gold, M. H. *J. Biol. Chem.* **1993,** *268,* 4429.

6. Peterson, J. F. W.; Kadziola, A.; Larsen, S. *FEBS Lett.* **1994,** *339,* 291.
7. Zeng, J.; Fenna, R. E. *J. Mol. Biol.* **1992,** *226,* 185.
8. Picot, D.; Loll, P. J.; Garavito, M. *Nature (London)* **1994,** *367,* 243.
9. Wang, J.; Mauro, J. M.; Edwards, S. L.; Oatley, S. L.; Fishel, L. A.; Ashford, V. A.; Xuong, N.; Kraut, J. *Biochemistry* **1990,** *29,* 7160.
10. Springer, B. A.; Sliger, S. G.; Olson, J. S.; Phillips, G. N., Jr. *Chem. Rev.* **1994,** *94,* 699.
11. Everse, J.; Everse, K. E.; Grisham, M. B. "Peroxidases in Chemistry and Biology"; CRC Press: Boca Raton, FL, 1991; Vol. I & II.
12. Gaspar, T.; Penel, C.; Greppin, H. "Plant Peroxidases 1980–1990: Progress and Prospects in Biochemistry and Physiology"; University of Geneva: Geneva, 1992.
13. Welinder, K. G. In "Plant Peroxidases 1980–1990: Topics and Detailed Literature on Molecular, Biochemical, and Physiological Aspects", Penel, C.; Gaspar, T.; Greppin, H., Eds.; University of Geneva: Geneva, 1992; 1–24.
14. Poulos, T. L.; Fenna, R. E. In "Metal Ions in Biological Systems: Metalloenzymes Involving Amino Acid-Residue and Related Radicals", Sigel, H.; Sigel, A., Eds.; Dekker: New York, 1994; Vol. 30, 25–75.
15. Poulos, T. L. *Curr. Opin. Biotech.* **1993,** *4,* 484.
16. English, A. M. In "Encyclopedia of Inorganic Chemistry: Iron: Heme Protein, Peroxidases, & Catalases", King, R. B., Ed.; Wiley: Chistester, 1994; Vol. 4, 1682–1697.
17. Kendrew, J. C.; Dickerson, R. E.; Strandberg, B. E.; Hart, R. G.; Davis, D. R.; Phillips, D. C.; Shore, V. C. *Nature (London)* **1960,** *185,* 422.
18. Finzel, B. C.; Poulos, T. L.; Kraut, J. *J. Biol. Chem.* **1984,** *259,* 13027.
19. Edwards, S. L.; Poulos, T. L. *J. Biol. Chem.* **1990,** *265,* 2588.
20. Edwards, S. L.; Kraut, J.; Poulos, T. L. *Biochemistry* **1988,** *27,* 8074.
21. Poulos, T. L.; Freer, S. T.; Alden, R. A.; Xuong, N. H.; Edwards, S. L.; Hamlin, R. C.; Kraut, J. *J. Biol. Chem.* **1978,** *253,* 3730.
22. Edwards, S. L.; Poulos, T. L.; Kraut, J. *J. Biol. Chem.* **1984,** *259,* 12984.
23. Edwards, S. L.; Xuong, N. H.; Hamlin, R. C.; Kraut, J. *Biochemistry* **1987,** *26,* 1503.
24. Goodin, D. B.; McRee, D. E. *Biochemistry* **1993,** *32,* 3313.
25. Choudhury, K.; Sundaramoorthy, M.; Hickman, A.; Yonetani, T.; Woehl, E.; Dunn, M. F.; Poulos, T. L. *J. Biol. Chem.* **1994,** *269,* 20239.
26. Corin, A. F.; McLendon, G.; Zhang, Q.; Hake, R. A.; Falvo, J.; Lu, K. S.; Ciccarelli, R. B.; Holzschu, D. *Biochemistry* **1991,** *30,* 11585.
27. Welinder, K. G. In "Biochemical, Molecular and Physiological Aspects of Plant Peroxidases", Lobarzewski, J.; Creppin, H.; Penel, C.; Gaspar, T., Eds.; University of Geneva: Geneva, 1991; 3–13.
28. Welinder, K. G. *Curr. Opin. Struct. Biol.* **1992,** *2,* 388.
29. Sundaramoorthy, M.; Kishi, K.; Gold, M. H.; Poulos, T. L. *J. Mol. Biol.* **1994,** *238,* 845.
30. Kunishima, N.; Fukuyama, K.; Matsubara, H.; Hatanaka, H.; Shibano, Y.; Amachi, T. *J. Mol. Biol.* **1994,** *235,* 331.
31. Kjalke, M.; Andersen, M. B.; Schneider, P.; Christensen, B.; Schülein, M.; Welinder, K. G. *Biochim. Biophys. Acta* **1992,** *1120,* 248.
32. Smulevich, G.; Feis, A.; Focardi, C.; Tams, J.; Welinder, K. G. *Biochemistry* **1994,** *33,* 15425.
33. Morita, Y.; Mikami, B.; Yamashita, H.; Lee, J. Y.; Aibara, S.; Sato, M.; Katsube, Y.; Tanaka, N. In "Biochemical, Molecular and Physiological Aspects of Plant Peroxidases", Lobarzewski, J.; Creppin, H.; Penel, C.; Gaspar, T., Eds.; University of Geneva: Geneva, 1991; 81–88.
34. Henriksen, A.; Svensson, L. A.; Smith, A. T.; Burke, J. E.; Thorneley, R. N. F.;

Welinder, K. G.; Gajhede, M. In "Plant Peroxidases: Biochemistry and Physiology", Welinder, K. G.; Rasmussen, S. K.; Penel, C. T.; Greppin, H., Eds.; University of Geneva: Geneva, 1993; 5–8.
35. Henriksen, A.; Petersen, J. F. W.; Svennson, A.; Hejgaard, J.; Welinder, K. G.; Galhede, M. *J. Mol. Biol.* **1992,** *228,* 690.
36. Patterson, W. R.; Poulos, T. L. *J. Biol. Chem.* **1994,** *269,* 17020.
37. Smith, A. T.; Santama, N.; Dacey, S.; Edwards, M.; Bray, R. C.; Thorneley, R. N. F.; Burke, J. F. *J. Biol. Chem.* **1990,** *265,* 13335.
38. Klebanoff, S. J. In "Peroxidases in Chemistry and Biology", Everse, J.; Everse, K. E.; Grisham, M. B., Eds.; CRC Press: Boca Raton, FL, 1991; Vol. I, 1–35.
39. Hurst, J. K. In "Peroxidases in Chemistry and Biology", Everse, J.; Everse, K. E.; Grisham, M. B., Eds.; CRC Press: Boca Raton, FL, 1991; Vol. I, 37–62.
40. Hori, H.; Ikeda-Saito, M. *Biochemistry* **1990,** *29,* 7106.
41. Sono, M.; Bracete, A. M.; Huff, A. M.; Ikeda-Saito, M.; Dawson, J. H. *Proc. Natl. Acad. Sci. USA* **1991,** *88,* 11148.
41a. Fenna, R.; Zeng, J.; Davey, C. *Arch. Biochem. Biophys.* **1995,** *316,* 653.
42. Smith, W. L.; Marnett, L. J. In "Metal Ions in Biological Systems: Prostaglandin Endoperoxidase Synthase", Sigel, H.; Sigel, A., Eds.; Dekker: New York, 1994; Vol. 30, 163–199.
43. Marnett, L. J.; Maddipati, K. R. In "Peroxidases in Chemistry and Biology", Everse, J.; Everse, K. E.; Grisham, M. B., Eds.; CRC Press: Boca Raton, FL, 1991; Vol. I, 293–334.
44. Smith, W. L; Marnett, L. J. *Biochim. Biophys. Acta* **1991,** *1083,* 1.
45. Smith, W. L.; Eling, T. E.; Kulmacz, R. J.; Marnett, L. J.; Tsai, A. *Biochemistry* **1992,** *31,* 3.
46. Xie, W.; Chipman, J. G.; Robertson, D. L.; Erikson, R. L.; Simmons, D. L. *Proc. Natl. Acad. Sci. USA* **1991,** *88,* 2692.
47. Kulmacz, R. J.; Pendleton, R. B.; Lands, W. E. M. *J. Biol. Chem.* **1994,** *269,* 5527.
48. Garavito, R. M.; Picot, D.; Loll, P. J. *Curr. Opin. Struct. Biol.* **1994,** *4,* 529.
49. Tsai, A.; Hsi, L. C.; Kulmacz, R. J.; Palmer, G.; Smith, W. L. *J. Biol. Chem.* **1994,** *269,* 5085.
50. Vane, J. *Nature (London)* **1994,** *367,* 215.
51. Meade, E. A.; Smith, W. L.; DeWitt, D. L. *J. Biol. Chem.* **1993,** *268,* 6610.
52. Mitchell, J. A.; Akarasereenont, P.; Thiemermann, C.; Flower, R. J.; Vane, J. R. *Proc. Natl. Acad. Sci. USA* **1993,** *90,* 11693.
53. Baek, H. K.; Van Wart, H. E. *J. Am. Chem. Soc.* **1992,** *114,* 718.
54. Poulos, T. L.; Finzel, B. C. In "Peptide and Protein Reviews", Hearn, M. T. L., Eds.; Dekker: New York, 1984; Vol. 4, 115–171.
55. Erman, J. E.; Vitello, L. B. *J. Am. Chem. Soc.* **1992,** *114,* 6592.
56. Erman, J. E.; Vitello, L. B.; Miller, M. A.; Shaw, A.; Brown, K. A.; Kraut, J. *Biochemistry* **1993,** *32,* 9798.
57. Vitello, L. B.; Erman, J. E.; Miller, M. A.; Wang, J.; Kraut, J. *Biochemistry* **1993,** *32,* 9807.
58. Miller, M. A.; Shaw, A.; Kraut, J. *Nature Struct. Biol.* **1994,** *1,* 524.
59. Smith, A. T.; Sanders, S. A.; Sampson, C.; Bray, R. C.; Burke, J. F.; Thorneley, R. N. F. In "Plant Peroxidases: Biochemistry and Physiology", Welinder, K. G.; Rasmussen, S. K.; Penel, C. T.; Greppin, H., Eds.; University of Geneva: Geneva, 1993; 159–168.
60. Smith, A. T.; Sanders, S. A.; Greschik, H.; Thorneley, R. N. F.; Burke, J. F.; Bray, R. C.; *Biochem. Soc. Trans.* **1992,** *20,* 340.

61. Dunford, H. B.; Hewson, W. D. *Biochemistry* **1977,** *16,* 2949.
62. La Mar, G. N.; Hernandez, G.; de Ropp, J. S. *Biochemistry* **1992,** *31,* 9158.
63. Veitch, N. C. In "Plant Peroxidases: Biochemistry and Physiology", Welinder, K. G.; Rasmussen, S. K.; Penel, C. T.; Greppin, H., Eds.; University of Geneva: Geneva, 1993; 57–64.
64. Hori, H.; Fenna, R. E.; Kimura, S.; Saito-Ikeda, M. *J. Biol. Chem.* **1994,** *269,* 8388.
65. Hosoya, T.; Sakurada, J.; Kurokawa, C.; Toyoda, R.; Nakamura, S. *Biochemistry* **1989,** *28,* 2639.
66. Smulevich, G.; Paoli, M.; Burke, J. F.; Sanders, S. A.; Thorneley, R. N. F.; Smith, A. T. *Biochemistry* **1994,** *33,* 7398.
67. Chen, Z.; de Ropp, J. S.; Hernandez, G.; La Mar, G. N. *J. Am. Chem. Soc.* **1994,** *116,* 8772.
68. Vitello, L. B.; Erman, J. E.; Miller, M. A.; Mauro, J. M.; Kraut, J. *Biochemistry* **1992,** *31,* 11524.
69. Ferrer, J. C.; Turano, P.; Banci, L.; Bertini, I.; Morris, I. K.; Smith, K. M.; Smith, M.; Mauk, A. G. *Biochemistry* **1994,** *33,* 7819.
70. Yonetani, T.; Schleyer, H. *J. Biol. Chem.* **1967,** *242,* 1974.
71. Allentoff, A. J.; Bolton, J. L.; Wilks, A.; Thompson, J. A.; Ortiz de Montellano, P. R. *J. Am. Chem. Soc.* **1992,** *114,* 9744.
72. Poulos, T. L. In "Advances in Inorganic Biochemistry: Heme Proteins", Eichhorn, G. L.; Marzilli, L. G., Eds.; Elsevier: New York, 1988; Vol. 7(1), 1–36.
73. Murthy, M. R. N.; Reid, T. J., III; Sicignano, A.; Tanaka, N.; Rossmann, M. G. *J. Mol. Biol.* **1981,** *152,* 465.
74. Andrawis, A.; Johnson, K. A.; Tien, M. *J. Biol. Chem.* **1988,** *263,* 1195.
75. Farhangrazi, Z. S.; Copeland, B. R.; Nakayama, T.; Amachi, T.; Yamazaki, I.; Powers, L. S. *Biochemistry* **1994,** *33,* 5647.
76. Andersen, M. B.; Hsuanyu, Y.; Welinder, K. G.; Schneider, P.; Dunford, H. B. *Acta Chem. Scand.* **1991,** *45,* 1080.
77. Poulos, T. L.; Kraut, J. *J. Biol. Chem.* **1980,** *255,* 8199.
78. Scholes, C. P.; Liu, Y.; Fishel, L. A.; Farnum, M. F.; Mauro, J. M.; Kraut, J. *Isr. J. Chem.* **1989,** *29,* 85.
79. Sivaraja, M.; Goodin, D. B.; Smith, M.; Hoffman, B. M. *Science* **1989,** *245,* 738.
80. Erman, J. E.; Vitello, L. B.; Mauro, J. M.; Kraut, J. *Biochemistry* **1989,** *28,* 7992.
81. Isied, S. S. In "Metal Ions in Biological Systems: Electron Transfer Reactions in Metalloproteins", Sigel, H.; Sigel, A., Eds.; Dekker: New York, 1991; Vol. 27, 1–56.
82. Erman, J. E.; Yonetani, T. *Biochim. Biophys. Acta* **1975,** *393,* 343.
83. Coulson, A. F. W.; Yonetani, T. *Biochem. Biophys. Res. Commun.* **1972,** *49,* 391.
84. Fox, T.; Tsaprailis, G.; English, A. M. *Biochemistry* **1994,** *33,* 186.
85. Prince, R. G.; George, G. N. *Trends Biochem. Sci.* **1990,** *15,* 170.
86. Bollinger, J. M., Jr.; Tong, W. H.; Ravi, N.; Huynh, B. H.; Edmondson, D. E.; Stubbe, J. *J. Am. Chem. Soc.* **1994,** *116,* 8024.
87. Erman, J. E.; Yonetani, T. *Biochim. Biophys. Acta* **1975,** *393,* 350.
88. Jovanovic, S. V.; Harriman, A.; Simic, M. G. *J. Phys. Chem.* **1986,** *90,* 1935.
89. Miller, M. A.; Han, G. W.; Kraut, J. *Proc. Natl. Acad. Sci. USA* **1994,** *91,* 11118.
90. Renganathan, V.; Gold, M. H. *Biochemistry* **1986,** *26,* 1626.
91. Harvey, P. J.; Palmer, J. M.; Schoemaker, H. E.; Dekker, H. L.; Wever, R. *Biochim. Biophys. Acta* **1989,** *994,* 59.
92. Schonbaum, G. R.; Lo, S. *J. Biol. Chem.* **1972,** *247,* 3353.
93. Bosshard, H. R.; Anni, H.; Yonetani, T. In "Peroxidases in Chemistry and Biology", Everse, J.; Everse, K. E.; Grisham, M. B., Eds.; CRC Press: Boca Raton, FL, 1991; Vol. II, 51–84.

94. Tsai, A. L.; Back, H.; Van Wart, H. E.; Palmer, G.; Kulmacz, R. J. *Biophys. J.* **1992,** *61,* A205.
95. Sigel, H.; Sigel, A. "Metal Ions in Biological Systems: Metalloenzymes Involving Amino Acid-Residue and Related Radicals"; Dekker: New York, 1994; Vol. 30.
96. Fishel, L. A.; Villafranca, J. E.; Mauro, J. M.; Kraut, J. *Biochemistry* **1987,** *26,* 351.
97. Mauro, J. M.; Fishel, L. A.; Hazzard, J. T.; Meyer, T. E.; Tollin, G.; Cusanovich, M. A.; Kraut, J. *Biochemistry* **1988,** *27,* 6243.
98. Ellfolk, N.; Rönnberg, M.; Österlund, K. *Biochim. Biophys. Acta* **1991,** *1080,* 68.
99. Moore, G. R.; Pettigrew, G. W. "Cytochrome c: Evolutionary Structural and Physiological Aspects"; Springer–Verlag: Berlin, 1990.
100. McLendon, G.; Hake, R. *Chem. Rev.* **1992,** *92,* 481.
101. Pelletier, H.; Kraut, J. *Science* **1992,** *258,* 1748.
102. Pettigrew, G. W.; Moore, G. R. "Cytochromes c: Biological Aspects", Springer–Verlag: Berlin, 1987.
103. Bechtold, R.; Bosshard, H. R. *J. Biol. Chem.* **1985,** *260,* 5191.
104. Das, G.; Hickey, D. R.; Principio, L.; Conklin, K. T.; Short, J.; Miller, J. R.; McLendon, G.; Sherman, F. *J. Biol. Chem.* **1988,** *263,* 18290.
105. Zhang, Q.; Hake, R.; Billstone, V.; Simmons, J.; Falvo, J.; Holzchu, D.; Lu, K.; McLendon, G.; Corin, A. *Mol. Cryst. Liq. Cryst.* **1991,** *194,* 343.
106. McLendon, G. In "Metal Ions in Biological Systems: Electron Transfer Reactions in Metalloproteins", Sigel, H.; Sigel, A., Eds.; Dekker: New York, 1991; Vol. 27, 183–198.
107. Northrup, S. H.; Boles, J. O.; Reynolds, J. C. L. *Science* **1988,** *241,* 67.
108. Hahm, S.; Durham, B.; Millett, F. *Biochemistry* **1992,** *31,* 3472.
109. Liu, R. Q.; Miller, M. A.; Han, G. W.; Hahm, S.; Geren, L.; Hibdon, S.; Kraut, J.; Durham, B.; Millet, F. *Biochemistry* **1994,** *33,* 8678.
110. Coulson, A. F. W.; Erman, J. E.; Yonetani, T. *J. Biol. Chem.* **1971,** *246,* 917.
111. Hazzard, J. T.; Poulos, T. L.; Tollin, G. *Biochemistry* **1987,** *26,* 2836.
112. Hazzard, J. T.; Tollin, G. *J. Am. Chem. Soc.* **1991,** *113,* 8956.
113. Nuevo, M. R.; Chu, H. H.; Vitello, L. B.; Erman, J. E. *J. Am. Chem .Soc.* **1993,** *115,* 5873.
114. Hahm, S.; Miller, M. A.; Geren, L.; Kraut, J.; Durham, B.; Millet, F. *Biochemistry* **1994,** *33,* 1473.
115. Kang, C. H.; Fergusson-Miller, S.; Margoliash, E. *J. Biol. Chem.* **1977,** *252,* 919.
116. Hazzard, J. T.; McLendon, G.; Cusanovich, M. A.; Tollin, G. *Biochem. Biophys. Res. Commun.* **1988,** *151,* 429.
117. Corin, A. F.; Hake, R. A.; McLendon, G.; Hazzard, J. T.; Tollin, G. *Biochemistry* **1993,** *32,* 2756.
118. Stemp, E. D. A.; Hoffman, B. M. *Biochemistry* **1993,** *32,* 10848.
119. Zhou, J. S.; Hoffman, B. M. *J. Am. Chem. Soc.* **1993,** *115,* 11008.
120. Liang, N.; Kang, C. H.; Ho, P. S.; Margoliash, E.; Hoffman, B. M. *J. Am. Chem. Soc.* **1986,** *108,* 4665.
121. Mauk, M. R.; Ferrer, J. C.; Mauk, A. G. *Biochemistry* **1994,** *33,* 12609.
122. Zhou, J. S.; Hoffman, B. M. *Science* **1994,** *265,* 1693.
123. Kishi, K.; Wariishi, H.; Marquez, L.; Dunford, H. B.; Gold, M. H. *Biochemistry* **1994,** *33,* 8694.
124. Baunsgaard, L.; Dalbøge, H.; Houen, G.; Rasmussen, E. M.; Welinder, K. G. *Eur. J. Biochem.* **1993,** *213,* 605.
125. DePillis, G. D.; Sishta, B. P.; Mauk, A. G.; Ortiz de Montellano, P. R. *J. Biol. Chem.* **1991,** *266,* 19334.

126. Ortiz de Montellano, P. R. In "Annual Review of Pharmacology and Toxicology: Catalytic Sites of Hemoprotein Peroxidases", Cho, A. K.; Blaschke, T. F.; Loh, H. H.; Way, J. L., Eds.; Annual Reviews Inc.: Palo Alto, CA, 1992; Vol. 32, 89–107.
127. DePillis, G. D.; Wariishi, H.; Gold, M.H.; Ortiz de Montellano, P. R. *Arch. Biochem. Biophys.* **1990,** *280,* 217.
128. Miller, V. P.; DePillis, G. D.; Ferrer, J. C.; Mauk, A. G.; Ortiz de Montellano, P. R. *J. Biol. Chem.* **1992,** *267,* 8936.
129. Veitch, N. G.: Tams, J. W.; Vind, J.; Dalbøge, H.; Welinder, K. G. *Eur. J. Biochem.* **1994,** *222,* 909.
130. Tams, J. W.; Vind, J.; Welinder, K. G. In "Plant Peroxidases: Biochemistry and Physiology", Welinder, K. G.; Rasmussen, S. K.; Penel, C. T.; Greppin, H., Eds.; University of Geneva: Geneva, 1993; 143–148.
131. Job, D.; Dunford, H. B. *Eur. J. Biochem.* ***1976,*** *66,* 607.
132. Dunford, H. B.; Adeniran, A. J. *Arch. Biochem. Biophys.* **1986,** *251,* 536.
133. Huang, J.; Dunford, H. B. *Can. J. Chem.* **1990,** *68,* 2159.
134. Roe, J. A.; Goodin, D. B. *J. Biol. Chem.* **1993,** *268,* 20037.
135. Hammel, K. E.; Jensen, K. A., Jr.; Mozuch, M. D.; Landucci, L. L.; Tien, M.; Rease, E. A. *J. Biol. Chem.* **1993,** *268,* 12274.
136. Harvey, P. J.; Floris, R.; Lundell, T.; Palmer, J. M.; Schoemaker, H. E.; Wever, R. *Biochem. Soc. Trans.* **1992,** *20,* 345.
137. Andersen, M. B.; Johansson, T.; Nyman, P. O.; Welinder, K. G. In "Biochemical, Molecular and Physiological Aspects of Plant Peroxidases", Lobarzewski, J.; Creppin, H.; Penel, C.; Gaspar, T., Eds.; University of Geneva: Geneva, 1991; 169–174.
138. Hammel, K. E.; Kalyanaraman, B.; Kirk, T. K. *J. Biol. Chem.* **1986,** *261,* 16948.
139. Millis, C. D.; Cai, D.; Stankovich, M. T.; Tien, M. *Biochemistry* **1989,** *28,* 8484.
140. Banci, L.; Bertini, I.; Turano, P.; Tien, M.; Kirk, T. K. *Proc. Natl. Acad. Sci. USA* **1991,** *88,* 6956.
141. Wariishi, H.; Huang, J.; Dunford, H. B.; Gold, M. H. *J. Biol. Chem.* **1991,** *266,* 20694.
142. Dunford, H. B.; Stillman, J. S. *Coord. Chem. Rev.* **1976,** *19,* 187.
143. Yandell, J, K.; Yonetani, T. *Biochim. Biophys. Acta* **1983,** *748,* 263.
144. Fenwick, C.; Marmor, S.; Govindaraju, K.; English, A. M.; Wishart, J. F.; Sun, J. *J. Am. Chem. Soc.* **1994,** *116,* 3169.
145. Smulevich, G. In "Advances in Spectroscopy: Biomolecular Spectroscopy, Part A", Clark, R. J. H.; Hester, R. E., Eds.; Wiley: Chistester, 1993; Vol. 20, 163–193.
146. Smulevich, G.; Mauro, J. M.; Fishel, L. A.; English, A. M.; Kraut, J.; Spiro, T. G. *Biochemistry* **1987,** *27,* 5486.
147. Izuka, T.; Makino, R.; Ishimura, Y.; Yonetani, T. *J. Biol. Chem.* **1985,** *260,* 1407.
148. Smulevich, G.; Miller, M. A.; Kraut, J.; Spiro, T. G. *Biochemistry* **1991,** *30,* 9546.
148a. Holzbaur, I. E.; English, A. M.; Ismail, A. A., to be submitted.
149. Al-Mustafa, J.; Kincaid, J. Biochemistry **1994,** *33,* 2191.
150. Fülöp, V.; Phizackerley, R. P.; Soltis, S. M.; Clifton, I. J.; Wakatsuki, S.; Erman, J.; Hajdu, J.; Edwards, S. L. *Structure* **1994,** *2,* 201.
151. Reczek, C. M.; Sitter, A. J.; Terner, J. *J. Mol. Struc.* **1989,** *214,* 27.
152. Feis, A.; Marzocchi, M. P.; Paoli, M.; Smulevich, G. *Biochemistry* **1994,** *33,* 4577.
153. Henderson, W. R., Jr. In "Peroxidases in Chemistry and Biology", Everse, J.; Everse, K. E.; Grisham, M. B., Eds.; CRC Press: Boca Raton, FL, 1991; Vol. I, 105–121.
154. Griffin, B. W. In "Peroxidases in Chemistry and Biology", Everse, J.; Everse, K. E.; Grisham, M. B., Eds.; CRC Press: Boca Raton, FL, 1991; Vol. II, 85–137.
155. Thomas, E. L.; Bozeman, P. M.; Learn, D. B. In "Peroxidases in Chemistry and Biology", Everse, J.; Everse, K. E.; Grisham, M. B., Eds.; CRC Press: Boca Raton, FL, 1991; Vol. I, 123–142.

156. Reiter, B.; Perraudin, J.-P. In "Peroxidases in Chemistry and Biology", Everse, J.; Everse, K. E.; Grisham, M. B., Eds.; CRC Press: Boca Raton, FL, 1991; Vol. I, 143–180.
157. Huber, R. E.; Edwards, L. A.; Crane, T. J. *J. Biol. Chem.* **1989,** *264,* 1381.
158. Sun, W.; Dunford, H. B. *Biochemistry* **1993,** *32,* 1324.
159. Magnussen, R. P. In "Peroxidases in Chemistry and Biology", Everse, J.; Everse, K. E.; Grisham, M. B., Eds.; CRC Press: Boca Raton, FL, 1991; Vol. I, 199–219.
160. Garavet, J. M.; Cahnmann, H. J.; Nunez, J. *J. Biol. Chem.* **1981,** *256,* 9167.
161. Virion, A.; Courtin, F.; Deme, D.; Michot, J. L.; Kaniewski, J.; Pommier, J. *Arch. Biochem. Biophys.* **1985,** *242,* 41.
162. Bushnell, G. W.; Louie, G. V.; Brayer, G. D. *J. Mol. Biol.* **1990,** *214,* 585.

ADVANCES IN INORGANIC CHEMISTRY, VOL. 43

ELECTRON-, ENERGY-, AND ATOM-TRANSFER REACTIONS BETWEEN METAL COMPLEXES AND DNA

H. HOLDEN THORP

Department of Chemistry, University of North Carolina, Chapel Hill, North Carolina 27599-3290

I. Introduction

Nucleic acids are structurally diverse polymeric materials. From the perspective of a polymer chemist, nucleic acids can be synthesized by organisms with very high ($>10^6$) molecular weights, perfect monodispersity, high water solubility, perfect isotacticity, and exquisite control over the sequence of four monomer units (*1*). Even with the best living catalysts, achieving these goals with conventional polymers is impossible. (Too bad you can't make a plastic bag out of DNA!) Using PCR and combinatorial approaches, this structural diversity can be

Copyright © 1995 by Academic Press, Inc.
All rights of reproduction in any form reserved.

exploited to engineer desirable functions into nucleic acid polymers by selecting single macromolecules from astounding 4^n numbers of possibilities (*2–4*). These approaches have been used to select aptamers with high affinities for small molecules (*5–9*), to design hydrolytic catalysts with high specificities for substrates or metal cofactors (*10–13*), and to perform molecular computing (*14*). These exciting areas provide a new impetus for detecting nucleic acid structures and understanding how nucleic acids can promote chemical reactions.

With all of the excitement over nucleic acid engineering, there is a new tendency to forget that DNA also has a rather significant biological function in the flow of genetic information in living organisms. The reactivity of DNA toward both redox chemistry and hydrolysis is important in nucleotide biosynthesis and metabolism (*1*). Nucleic acids are excellent targets for anticancer and antiviral therapies, and nucleotide reactivity plays an important role in the design of specific nucleic acid damage agents and the understanding of natural products that cleave nucleic acid polymers (*15–20*). Likewise, ionizing radiation treatment leads to nucleic acid oxidation (*21*). Finally, there is a great deal of interest in using redox and hydrolytic chemistry (*22*) to probe structures and manipulate sequences of complex nucleic acid polymers using targeted cleavage agents (*23–25*).

What are the roles of metal complexes in the frontiers of nucleic acid chemistry? On the surface, a number of roles are apparent. The catalytic activity of ribozymes is dependent on metal ions, such as Mg^{2+} and Mn^{2+}, that initiate the hydrolytic reaction (*12, 26–28*). Cationic metal ions compensate the negative charges of the sugar phosphate backbone, and the nature of these cations can play important roles in the folding of RNA (*29–32*) and in the formation of unusual DNA structures, such as Z-DNA, G quartets, and cruciforms (*33*). Metal complexes that bind covalently to DNA can act as antitumor agents (*34–37*), as does the naturally occurring metal-binding bleomycin, which is thought to exert its chemotherapeutic activity through DNA (or RNA) oxidation (*17, 38*).

Beyond these obvious roles, the spectroscopic and electrochemical signatures of metal complexes can be used to understand DNA reactivity and to detect DNA structures. In this review, efforts to exploit the redox and photophysical properties of metal complexes to understand DNA reactivity will be discussed (*23, 39*). Metal complexes provide a special opportunity for these studies, because they exhibit well-defined redox states that can be correlated with redox changes in nucleic acids and nucleotides. In metal complexes, changes in these redox states are coupled to changes in the optical spectroscopy of the metal center,

which can be used to track the redox state of DNA. In addition, these spectroscopic signatures can also be used to determine DNA binding.

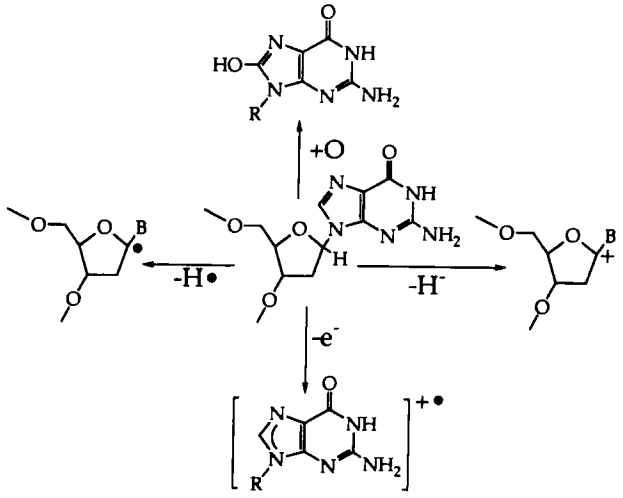

SCHEME 1

What redox changes of DNA are of interest? Shown in Scheme 1 is a guanosine nucleotide, which can react via four redox pathways. The sugar functionality can react via activation of C–H bonds (*17, 39*). These reactions can be both heterolytic (hydride transfer) and homolytic (hydrogen atom transfer) to generate either a carbocation or a radical, respectively. The reaction shown in Scheme 1 is for activation of the 1′ C–H bond (*25*), but activation of all four other sites has now been observed (*15, 16, 40, 41*). These C–H activations usually lead to strand scission either directly after breaking the C–H bond (frank strand scission) or after base treatment of the generated lesion. The bases of DNA are also reactive, although the guanine base is significantly more reactive than adenine, thymine, and cytosine (*24, 42*). Guanine can react either by an oxo-transfer type pathway to generate 8-oxo-guanine, or through outer-sphere electron transfer to generate a radical cation. Hydration of the radical cation has been shown to produce 8-oxo-guanine (as shown in Scheme 1), which produces a base-labile lesion in DNA (*43*). Recently, oxidation of guanine at the C1 position has been suggested as a parallel (and perhaps more prominent) pathway (*44*).

In our laboratory, we have developed metal complexes that allow us to study all of the pathways shown in Scheme 1 with the goal

of understanding the fundamental aspects (driving force, activation barriers, reaction probabilities) of these pathways. Both homolytic and heterolytic C–H activation are relevant to DNA cleavage by iron bleomycin (FeBLM) (*17, 18*), and homolytic activation is seen in DNA cleavage by the enediyne antibiotics (*19, 20*). Homolytic C–H bond scission is also the first step in the reduction of ribonucleotides to deoxyribonucleotides by ribonucleotide reductases (*45*). Guanine oxidation by outer-sphere electron transfer is seen during ionizing radiation treatment (*21*). Oxo transfer from a metal complex is thought to occur during the oxidation of xanthine, a metabolic product of guanine hydrolysis, to uric acid by the enzyme xanthine oxidase (*46*). The proposed mechanism for xanthine oxidase adapted from a recent volume (*47*) is

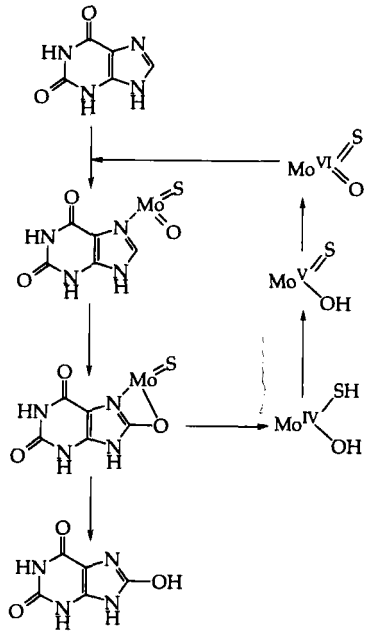

SCHEME 2

shown in Scheme 2. In this review, each of the four pathways shown in Scheme 1 will be discussed, as well as the associated biological relevances from the standpoint of mechanistic inorganic chemistry. First, a brief introduction to DNA structure will be given to introduce a general reader to the important elements of DNA structure and reactivity.

II. DNA Fundamentals

The structure of the DNA double helix is shown in Fig. 1 (*1*). Each strand is composed of sugar–phosphate monomeric units (nucleotides). The familiar form of DNA, the B-helix, is shown in Fig. 1 (*48, 49*). An important feature of the B-DNA structure as far as inorganic chemistry is concerned is that the winding of the double helix creates both a major groove and a minor groove. In the minor groove, the anionic phosphate groups are much closer together than in the major groove, so cation binding is much more favorable in the minor groove (*50–52*). When electrostatic interactions dominate the binding affinity, as occurs for all hydrated metal ions and many metal complexes, binding occurs primarily in the minor groove. The amino group of guanine projects into the minor groove, and since this group is partially positive, the electrostatic attractions between cations and DNA are somewhat attenuated near GC base pairs in the minor groove (*53*). Thus, electrostatic binding in the minor groove is usually somewhat more favorable for AT sequences than for CG sequences.

The binding of cations to DNA can be described by polyelectrolyte theory, as developed by Manning and Record (*51, 52*). This theory states that the observed binding constant is a function of the charge

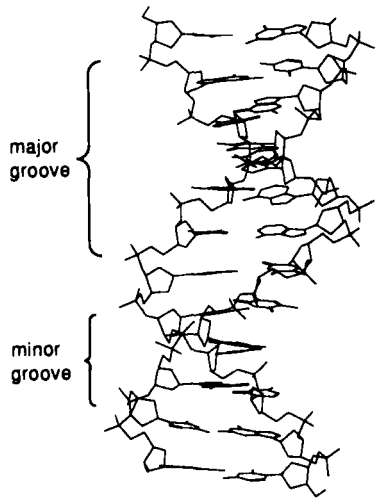

FIG. 1. X-ray crystal structure of the DNA duplex d[(5′-CGCAAATTTGCG-3′)]$_2$. From Coll *et al.* (*49*). The closer proximity of phosphates in the minor groove compared to the major groove provides a highly anionic template for the binding of cations.

on the cation (Z), the degree to which the DNA charge must be compensated before unwinding occurs (Ψ), and the concentration of the buffer cation ($[M^+]$):

$$\ln K_B = \ln K_t^\circ - Z\Psi \ln[M^+] - \text{activity term}, \quad (1)$$

where K_t° is the binding constant in the absence of electrostatics, which comprise van der Waals, hydrophobic, and hydrogen-bonding interactions. The activity term is generally negligible under common buffer conditions (*54*). Plots of $\ln K_B$ versus $\ln[M^+]$ yield straight lines with slopes of $Z\Psi$. The quantity Ψ is generally 0.88 for calf thymus DNA when monovalent cations are bound; however, the value of $Z\Psi$ can be somewhat variable for cations with charges of +2 and higher (*54–57*). These variations are due to coupled release of monocations when polycation binding occurs (*57*).

While electrostatic interactions often provide the baseline affinity for metal complexes to DNA, other interactions can contribute to the binding affinity via the $\ln K_t^\circ$ term. Complexes with ligands that are hydrogen-bond donors can form hydrogen bonds to phosphate oxygens, as seen in crystal structures of hydrated cations with DNA and nucleotides (Fig. 2) (*58–60*). Methyl groups from metal complexes can interact with thymine methyl groups that project into the major groove via hydrophobic methyl–methyl interactions (*61, 62*). An interaction that has received a great deal of interest is intercalation, which occurs when a planar aromatic ligand is accommodated between DNA base pairs. For this reaction to occur, the DNA must unwind somewhat to produce

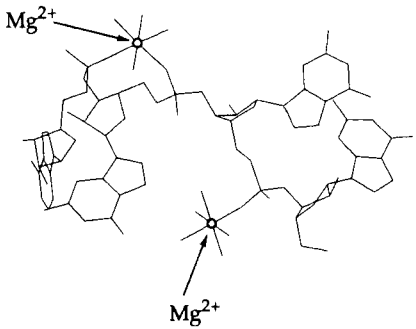

FIG. 2. View of Mg^{2+} bound to $tRNA^{phe}$. Cations can associate with nucleic acids via hydrogen bonding of waters of hydration to phosphate oxygens or via replacement of a water of hydration by phosphate oxygen. Structure data taken from Jack *et al.* (*67*).

a void that can accommodate the binding functionality (*23*). These interactions impart high binding affinities (10^6 M^{-1}) to the metal complex (*55, 63*). In these cases, the electrostatic term becomes small compared to K_t°, so there is no longer as strong a preference for binding in the minor groove as is seen with electrostatic binders. In fact, many octahedral metallointercalators appear to bind in the major groove (*64–66*).

While B-form DNA is certainly the most familiar DNA structure, there are many other DNA structures, such as G quartets, Z-DNA, Holladay junctions, and cruciforms, that play important roles in gene processing and DNA recognition (*33*). RNA polymers are considerably more diverse structurally than DNA (*32*). Thus far, the only known crystal structure of a large RNA polymer is that of tRNA, shown in Fig. 3 (*30, 67*). Comparison of the tRNA structure with that of the B-helix illustrates that RNA polymers are considerably more complicated structurally. Unraveling the complex structures of RNA polymers is fertile ground for developing metal complexes that target particular RNA substructures, such as loops, helices, and pseudoknots (*29, 32,*

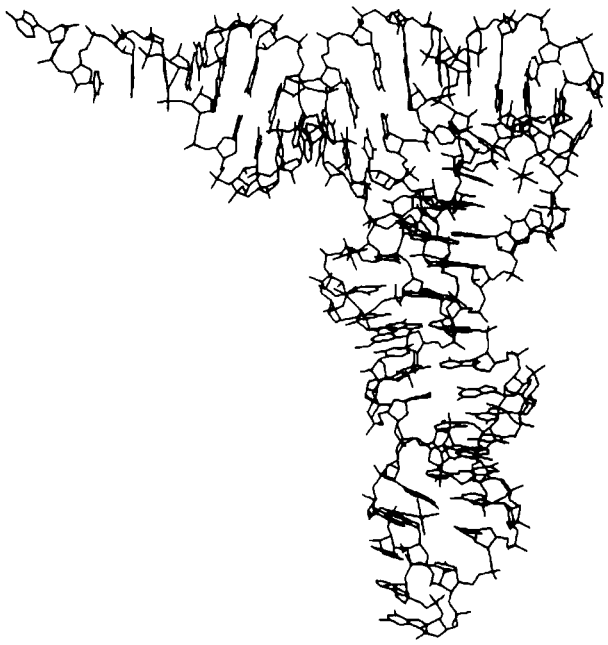

FIG. 3. Structure of tRNA taken from Jack *et al.* (*67*).

68–72). In particular, binding of metal cations at phosphate–phosphate contacts is vital to folding of RNA polymers. Cationic metal complexes may have the ability to target these important cation binding sites and reveal important phosphate–phosphate contacts. However, the different reactivities of DNA and RNA toward oxidation by metal complexes must also be considered (*73–75*), as will be discussed in some detail later.

A point that is often mysterious to inorganic chemists is the means by which the loci of cleavage events are determined in large nucleic acid polymers: high-resolution gel electrophoresis (*1*). In this experiment, a DNA (or RNA) polymer is labeled at one end with ^{32}P in the phosphate group. Using enzymes, the oligomers can be labeled selectively at either the 3′ or 5′ end. When this labeled oligomer is cleaved, any fragments generated that still contain the ^{32}P label can be imaged on a sequencing

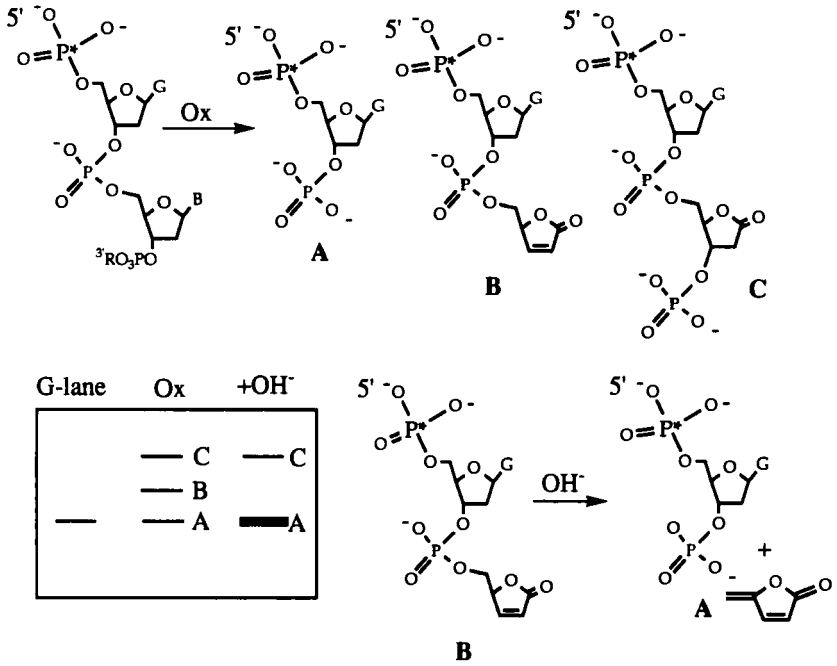

SCHEME 3

gel using autoradiography. As shown in Scheme 3, fragments that do not contain the label are not imaged. When subjected to electrophoresis, the labeled DNA fragments can be separated on the basis of molecular weight. Using the Maxam–Gilbert reactions, the fragments can be

cleaved on purpose at specific bases, which allows the experimenter to calibrate the gel to the known sequence. The Maxam–Gilbert reactions generate fragments that terminate in phosphate groups. A powerful feature of this technique is that the nature of the terminus of the DNA fragment can be assessed. For example, if additional sugar functionality is still attached to a phosphate, that fragment will migrate behind the Maxam–Gilbert product, since the modified fragment is slightly heavier. Treatment with base usually generates a phosphate terminus.

III. Metal Complexes in Metal–DNA Chemistry

Now that some of the fundamentals of the DNA chemistry have been presented, attention can be turned to the other players in metal–DNA chemistry. Much of the early metal–DNA chemistry involved targeting covalent binding interactions using metal complexes with labile coordination sites. Cisplatin, $Pt(NH_3)_2Cl_2$, binds to DNA via replacement of the labile chloride ligands by basic nitrogens in adenine and guanine from DNA (*76*). Clarke *et al.* have observed similar chemistry for $Ru(NH_3)_5$ fragments (*37, 77*). Covalent binding of related ruthenium polypyridyl complexes, such as $Ru(bpy)_2(OH_2)_2^{2+}$ and $Ru(tpy)(bpy)OH_2^{2+}$, has also been observed (tpy = 2,2′,2″-terpyridine, bpy = 2,2′-bipyridine (*78–80*). (See chart of structural functions.) A model complex for these latter interactions, $Ru(bpy)_2(EtG)Cl^+$ (EtG = 9-ethylguanine), has recently been prepared by Reedijk *et al.* (Fig. 4) (*81*). A related model complex is $Re(bpy)(CO)_3(EtG)^+$ (Fig. 5), which exhibits a long-lived excited state [τ(600 nm) = 170 ns, ϕ = 0.05] (*82*). This long-lived emission is sensitive to guanine coordination and may provide a means for detecting covalent binding by emission spectroscopy.

The DNA chemistry of tris complexes of bidentate polypyridyl ligands has been studied extensively (*23*). The advantages here are that the tris complexes are coordinatively saturated, and when ruthenium(II) is the central metal, there is no opportunity for reactions other than electron and energy transfer. Thus, cleavage of DNA by complicated hydrogen atom or oxo transfer pathways is unlikely, and the binding modes of the complexes can be studied exclusively. The ruthenium(II) tris chelate complexes exhibit long-lived, emissive MLCT states in the visible region of the spectrum (*83–85*), and the effect of DNA on these properties provides a means of characterizing the DNA–metal interactions (*56, 57, 63, 86, 87*). Quenching of the emission by energy or electron transfer also provides information on the binding interaction. When the ruthenium(II) center is replaced by rhodium(III), there are

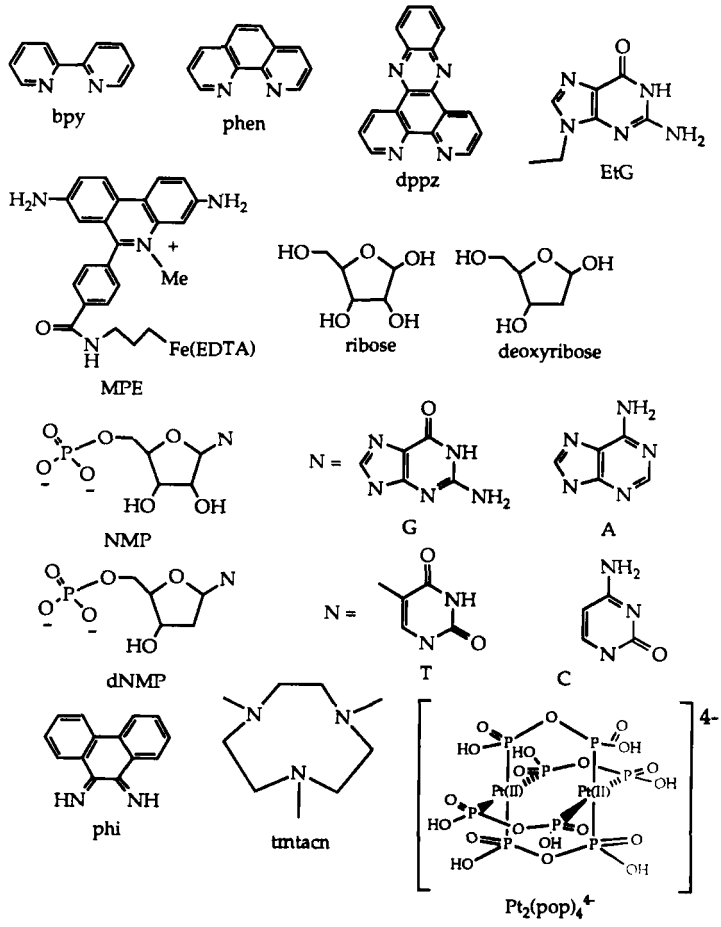

CHART 1. Chart of structural functions.

no low-lying excited states in the visible, and the lowest excited state is localized on the coordinated ligand (*42, 88, 89*). These states effect strand scission via hydrogen abstraction upon photolysis at 300 nm of a DNA-bound complex (*61, 62, 64, 65, 90–94*).

A. Iron Bleomycin

1. Natural Bleomycin

Iron bleomycin (FeBLM) is a natural product with anticancer activity that is thought to arise from nucleic acid damage and has been termed

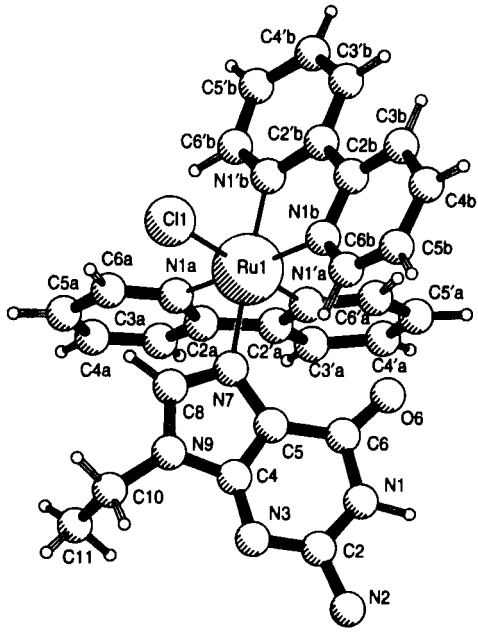

FIG. 4. X-ray crystal structure of $Ru(bpy)_2(EtG)Cl^+$ reprinted with permission from van Vliet *et al.* (*81*). Copyright © 1994 American Chemical Society.

the "prototypic DNA cleaver" (*17*). The bleomycin molecule is a large peptide (Fig. 6) that has a metal-binding domain and presents a number of nitrogen donors to bound metal ions, such as Fe, Cu, and Co (*17, 18, 95, 96*). Recent NMR studies have established a working structure for the metal-containing peptide bound to DNA (*97, 98*). The binding affinity of FeBLM is relatively modest, $1 \times 10^5\ M^{-1}$ (*17*). The activated form is generated by reduction of Fe^{3+}–BLM in the presence of oxygen, which produces a reactive species whose precise chemical nature (Fe^{3+}–OOH, $Fe(V)O^{3+}$, $Fe(IV)O^{2+}$) is still a subject of debate (*99*), although recent evidence supports the Fe^{3+}–OOH formulation (*100*). Activated BLM is a broad-spectrum oxidant that is capable of oxidizing substrates both by hydrogen-atom transfer, as in the oxidation of ribose and deoxyribose, and by oxo transfer, as in the oxidation of styrene to styrene oxide and phosphine to phosphine oxide (*17, 101, 102*). The bleomycin molecule itself consists of a metal-binding domain and peptide and sugar domains that contain many readily oxidizable groups. As a result, activated BLM is capable of self-inactivation, as indicated by the fact that repeated electrochemical activation in the absence of

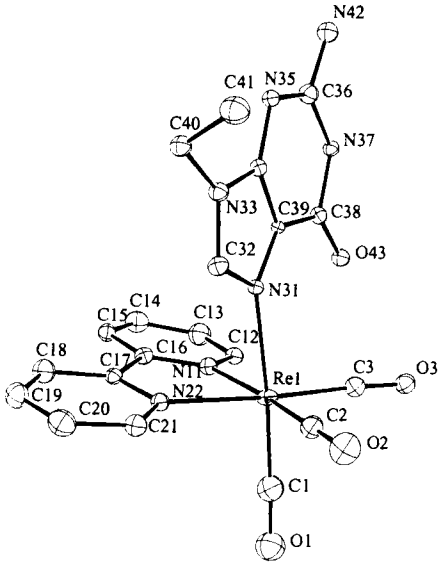

FIG. 5. X-ray crystal structure of $Re(bpy)(CO)_3(EtG)^+$ reprinted with permission from Oriskovich *et al.* (*82*). Copyright © 1995 American Chemical Society.

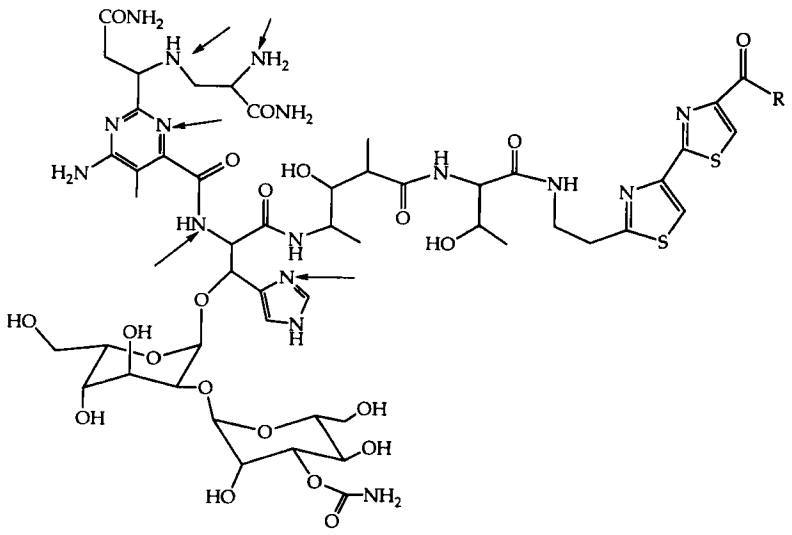

FIG. 6. Structure of bleomycin. Suspected metal-binding groups are indicated by arrows.

DNA leads to a dramatic loss in the ability of BLM to degrade DNA (*99*). The presence of DNA protects BLM from self-inactivation, leading to catalytic DNA damage; however, electrochemical experiments show a decrease in catalytic current during electrochemically activated DNA degradation (*99*), indicating that self-inactivation does compete with DNA cleavage to some extent. The mechanism of degradation of DNA by FeBLM involves abstraction of the 4′-hydrogen, as shown in Scheme 1, although oxidation at the 1′ position is observed in ara- and ribo-containing nucleotides (*103*). No guanine oxidation has been observed in DNA or RNA.

Recent studies have shown that sequence-specific isotope effects are observed for cleavage by FeBLM (*104, 105*). The isotope effects are observed by selective incorporation of 4′-deuterated nucleotides in restriction fragments and comparison of the extent of cleavage for the deuterated and unlabeled sites. The observation of such a net isotope effect is revealing with regard to the cleavage mechanism. The first step in cleavage of DNA by activated FeBLM involves binding of the

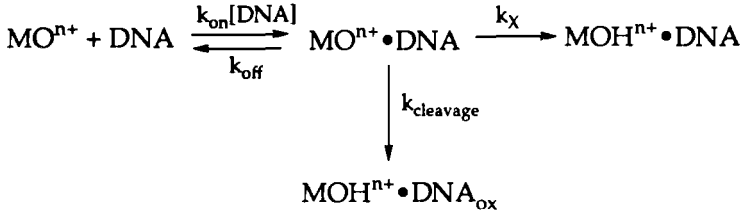

SCHEME 4

activated complex to DNA. As shown in Scheme 4, the bound complex can then either cleave DNA ($k_{cleavage}$), dissociate (k_{off}), or undergo other nonproductive processes such as self-inactivation (k_X) that lead to metal reduction but no DNA oxidation. The observation of a significant isotope effect on cleavage demonstrates that cleavage must be much slower than the other processes ($k_X + k_{off}$) (*105*). If this was not the case, then cleavage would be observed regardless of whether a hydrogen or deuterium was abstracted. Thus, the isotope effect must be considered in light of selection against other processes, so the apparent isotope effect is equal to the true kinetic isotope effect scaled by the rates of competing processes:

$$^{D}(V/K) = (k_H/k_D)[(k_D + k_X + k_{off})/(k_H + k_X + k_{off})]. \quad (2)$$

The observed isotope effects are sequence-specific, which could result

either from different transition-state geometries for hydrogen abstraction at different sites (i.e., different k_H/k_D) or from a dependence of k_X on the DNA sequence.

A number of studies have attempted to address the origins of sequence specificity for DNA and RNA cleavage by FeBLM. Many studies have indicated that the metal-binding region is primarily responsible for the observed selectivity for GC and GT sites. The cleavage patterns of models based only on the metal-binding domain are identical to those of actual bleomycin (see later discussion) (*106*), suggesting that the metal complex itself is responsible for the sequence specificity. In contrast, recent experiments by Hecht and co-workers show that removal of one or both thiazoles from FeBLM dramatically alters the specificity (*107*), implying a more complicated mechanism of specificity involving the entire molecule.

Studies of cleavage of RNA by FeBLM have also provided new insight into the mechanism of specificity (*38*). In general, many fewer sites are observed for cleavage of RNA than for cleavage of DNA. For cleavage of tRNA and an analogous tDNA, the same principal site is observed in each; however, at high FeBLM concentrations, many more sites are observed in the tDNA than in the analogous tRNA (*73*). Interestingly, this effect does not arise from the binding thermodynamics, because FeBLM binds to both tDNA and tRNA with equal affinity, implying that efficient binding of activated FeBLM does not guarantee that cleavage will occur. This result is consistent with the finding that FeBLM cleaves a natural double helix containing D-deoxyribose, but does not cleave the corresponding unnatural L-deoxyribose oligomer, even though both are bound with equal affinity (*108*). The observation of binding of activated FeBLM with no cleavage implies that the complex is reduced via self-inactivation (k_X).

2. *Bleomycin Models*

Mascharak and co-workers have developed a synthetic analogue system for bleomycin (*106, 109–112*). In this system, the coordinating functions of BLM (alkyl amines, pyrimidine, peptide nitrogen, and imidazole) are combined in a minimal configuration for modeling BLM within a ligand termed PMA^-. In addition to iron, bleomycin also coordinates copper and cobalt, and studies of these forms have been pursued as a source of new information on the physiologically relevant mechanism (*17, 18 96*). The $Cu(PMA)^+$ complex has been structurally characterized (Fig. 7) (*109, 111*), and its electronic properties mimic well those of Cu–BLM (*113*). As with Cu–BLM, a pH-dependent conformational equilibrium exists that interconverts $Cu(PMA)^+$ with a di-

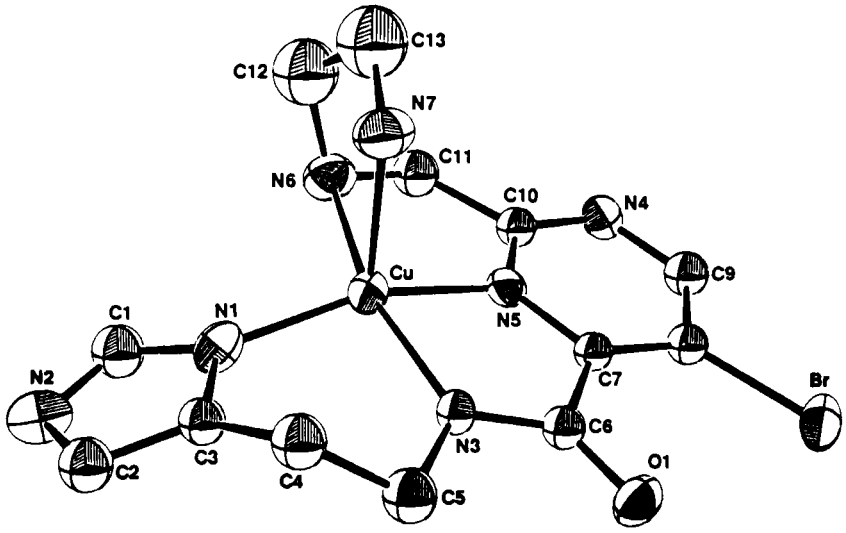

FIG. 7. X-ray crystal structure of $Cu(PMA)^+$ reprinted with permission from Brown *et al.* (*111*). Copyright © 1989 American Chemical Society.

nuclear form that has also been structurally characterized. Upon treatment with dithiothreitol in the presence of oxygen, Cu–BLM induces DNA strand breaks (*114*). Similar behavior is observed with $Cu(PMA)^+$, and scavenging studies implicate the intervention of hydroxyl radical (*111*).

Aerobic oxidation of Co(II)–BLM affords a number of strongly colored Co(III) products (*115, 116*). The origin of the different colors is still under investigation; however, the synthetic analogue approach has led to several different $[Co(PMA)X]^{n+}$ complexes (X = OH_2, Cl^-, *N*-methylimidazole) that mimic these color changes (*112*). Irradiation of Co–BLM leads to strand breaks in DNA (*117*), as does $Co(PMA)(OH_2)^{2+}$ (Fig. 8) (*110, 112*).

As alluded to earlier, a very exciting result has emerged from the synthetic analogue studies for Fe–BLM. As with copper and cobalt, $Fe(PMA)^{2+}$ and $Fe(PMA)^+$ are good spectroscopic analogues of Fe(III)–BLM and Fe(II)–BLM (*106*), and the Fe(II) model complex binds NO and CO in a manner similar to Fe–BLM to give EPR and vibrational spectra similar to those of the natural system (*113, 118*). Reaction of the Fe(II) complex with O_2 generates a species that gives an EPR spectrum very similar to that of the Fe(III)OOH species obtained during oxygen activation by FeBLM (*100*). The PMA complex hydroxylates

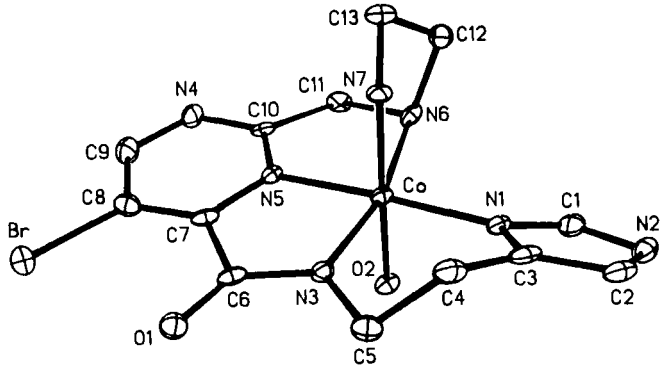

FIG. 8. X-ray crystal structure of $Co(PMA)(OH_2)^{2+}$ reprinted with permission from Tan *et al.* (*112*). Copyright © 1992 American Chemical Society.

and epoxidizes hydrocarbons both with oxygen and with shunt oxidants such as PhIO and H_2O_2, and the product profiles are very similar to those obtained with FeBLM (*101, 102*). The most stunning result is that in two different restriction fragments, the sequence specificity of cleavage by $Fe(PMA)^{2+}$ is very similar to that of FeBLM. This result strongly suggests that the sequence specificity of FeBLM is a result of the properties of the metal-binding domain and not a function of the rest of the rather large bleomycin molecule. As stated earlier, other recent results argue to the contrary (*107*).

B. OXORUTHENIUM(IV)

Metal–oxo complexes are effective oxidizing agents via both hydrogen abstraction and oxo transfer (*46, 119*). Meyer *et al.* have developed a series of oxo complexes that can be isolated in the oxidized form (*120*). These complexes are prepared by changing one pyridyl nitrogen from a tris-chelate type complex to a water molecule, as in $Ru(tpy)(bpy)OH_2^{2+}$ or $Ru(bpy)_2(py)OH_2^{2+}$. Upon oxidation at moderate potentials, the coordinated aqua ligands deprotonate to provide successive hydroxo and oxo complexes:

$$Ru^{II}(tpy)(bpy)OH_2^{2+} \rightarrow Ru^{III}(tpy)(bpy)OH^{2+} + H^+ + e^-, \quad (3)$$

$$Ru^{III}(tpy)(bpy)OH^{2+} \rightarrow Ru^{IV}(tpy)(bpy)O^{2+} + H^+ + e^-. \quad (4)$$

The deprotonation of the aqua ligands is primarily responsible for stabilizing the high oxidation state; at pH 7 the relevant potentials

are only 0.49 V for the (III/II) couple and 0.62 V for the (IV/III) couple (*120*). A crystal structure of a derivative of the oxo form, Ru(damp)(bpy)O^{2+}, has been shown to have a Ru–O bond length of 1.80 Å (Fig. 9) (*121*). A similar bond length was observed in the crystal structure of Ru(tmtacn)(bpy)O^{2+} by Cheng and co-workers (Fig. 10) (*122*). Oxoruthenium(IV) structures are rare; to our knowledge these are the only two examples. In several related examples of reduced aquaruthenium(II) complexes, the average Ru–OH_2 bond length is 2.2 Å (*122–126*). Careful inspection of the Ru–N bond lengths reveals that there is very little change upon oxidation of the ruthenium center (Ru^{II}–N_{avg} = Ru^{IV}–N_{avg} = 2.1 Å). Thus, the higher oxidation is stabilized solely by the anionic charge on the oxo ligand and by π-donation from the oxo ligand (*125*).

Because of the proximity of the (IV/III) and (III/II) couples, the Ru(IV)O^{2+} complex is nearly as good a two-electron oxidant as it is a one-electron oxidant (*119*). Therefore, C–H bond activation usually proceeds via hydride transfer (*127*). The complex is also reactive toward electron transfer and oxo transfer, as shown in Scheme 5 (*128*). The

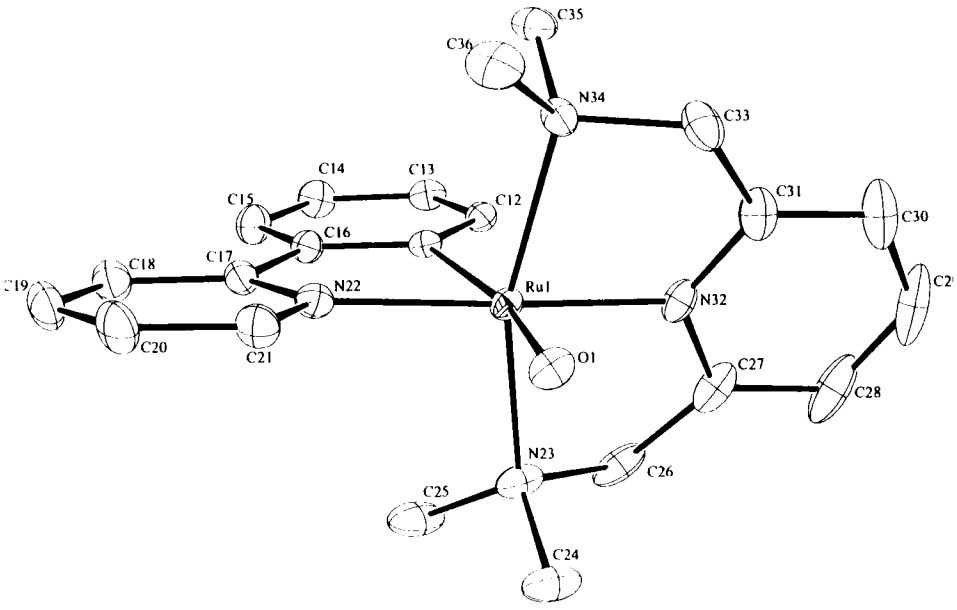

FIG. 9. X-ray crystal structure of Ru(damp)(bpy)O^{2+}.

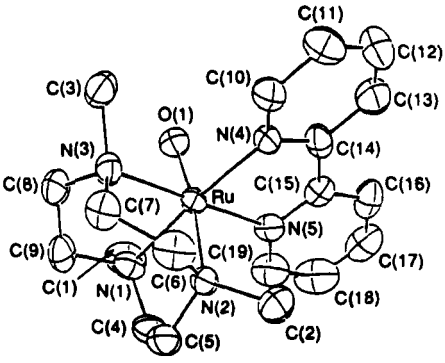

FIG. 10. X-ray crystal structure of Ru(tmtacn)(bpy)O^{2+} taken from Cheng *et al.* (*122*). Copyright © 1994 Royal Society of Chemistry.

Ru(III)OH^{2+} state, which is present at long times during oxidation, reacts via hydrogen-atom transfer, although at a rate that is three orders of magnitude slower than hydride transfer by Ru(IV)O^{2+} (*127*). Finally, the complex undergoes self-reduction analogous to that seen for FeBLM, where 10% of the ruthenium complexes are sacrificed to regenerate 90% of the original Ru(II)OH_2^{2+} (*129*). Since all of the *reversible* redox potentials and pK_a's of the Ru(IV), Ru(III), and Ru(II) states are known, the thermodynamics of each redox pathway shown in Scheme 5 can be precisely determined. The relevant thermodynamic parameters are not available for many oxidants because of a catalytic mechanism involving an intermediate that cannot be isolated.

One of the attractive features of the Ru(IV)O^{2+} system is that the Ru(IV), Ru(III), and Ru(II) forms all have readily distinguishable optical spectra (*120*). The mechanism of oxidation on the metal end of the

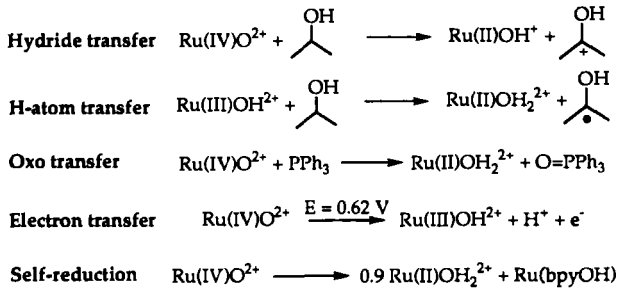

SCHEME 5

reaction can therefore be studied in detail. One complication of these reactions is that once Ru(II) is generated, comproportionation with Ru(IV) occurs to generate Ru(III):

$$Ru^{IV}O^{2+} + Ru^{II}OH_2^{2+} \rightarrow 2\,Ru^{III}OH^{2+}. \quad (5)$$

The Ru(III) state is usually also reactive, either through a direct one-electron mechanism or through unfavorable disproportionation according to the reverse of Eq. (5). These pathways are at least three orders of magnitude slower than the Ru(IV) pathways (*127*), so the contributions of Ru(IV) and Ru(III) can be separated in product analysis studies. In kinetic studies, if modern rapid-scanning stopped-flow spectrometers are used, then fitting is based on authentic spectra of the Ru(IV), Ru(III), and Ru(II) forms and calculated spectra of any observed colored intermediates (*75, 130*). These spectrometers allow scanning of a 200 nm wavelength range every millisecond, allowing detailed mechanistic investigations.

C. DIPLATINUM(II)

Dinuclear complexes that bring square-planar d^8 centers into a face-to-face orientation lead to an electronic structure shown in Scheme 6

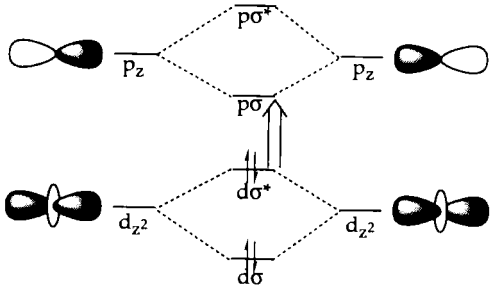

SCHEME 6

(*131, 132*). Specifically, the filled d_{z^2} orbitals interact to form bonding ($d\sigma$) and antibonding ($d\sigma^*$) combinations. The low-lying p_z orbitals interact similarly to form $p\sigma$ and $p\sigma^*$ combinations. For a d^8–d^8 system, these levels are populated such that the HOMO is the $d\sigma^*$ level. Thus, the bond order in the ground state is zero, and the lowest-energy absorption corresponds to the spin- and symmetry-allowed $(d\sigma^*)^2 \rightarrow (d\sigma^*)^1(p\sigma)^1$ transition. The energies of this transition are strongly

dependent on the metal–metal separation, and hence on the nature of the bridging ligand (*132*).

When pyrophosphite is the bridging ligand, the complex $Pt_2(pop)_4^{4-}$ exhibits the $d\sigma^* \rightarrow p\sigma$ transition at 368 nm, and the emissive excited state is long-lived [τ(513 nm) = 10 μs, ϕ = 0.5] (pop = $P_2O_5H_2^{2-}$) (*133*). The excited state therefore exhibits a metal–metal bond order of 0.5, which is evident in resonance Raman and low-temperature absorption spectra (*132*). This excited state is a powerful outer-sphere electron- and energy-transfer agent, owing to the high excitation energy and facile reduction and oxidation potentials (*131*). Of more interest is the ability of the complex to accept hydrogen atoms to form a hydridoplatinum(III) linkage (*134, 135*):

$$Pt_2^{II4-*} + R\text{–}H \rightarrow [H\text{–}Pt^{III}Pt^{II}]^{4-} + R\cdot. \tag{6}$$

The (III,II) dimer is prone to disproportionation to produce a (III,III) dihydride and $Pt_2(pop)_4^{4-}$:

$$2[H\text{–}Pt^{III}Pt^{II}]^{4-} \rightarrow [H\text{–}Pt^{III}Pt^{III}\text{–}H]^{4-} + Pt_2^{4-}. \tag{7}$$

The dihydride complex exhibits a $d\sigma \rightarrow d\sigma^*$ absorbance, and photolysis into this band liberates dihydrogen and $Pt_2(pop)_4^{4-}$ to complete a catalytic cycle (*135*). The radical can either dimerize, as in $PhCH_2\cdot$,

$$2\,PhCH_2\cdot \rightarrow PhCH_2CH_2Ph, \tag{8}$$

or lose another hydrogen atom to another equivalent of $Pt_2(pop)_4^{4-*}$, as with $(CH_3)_2C\cdot OH$:

$$(CH_3)_2C\cdot OH \rightarrow (CH_3)_2C{=}O. \tag{9}$$

The rate constants for hydrogen atom transfer can be measured by Stern–Volmer quenching and have been studied for a wide range of substrates, such as alcohols, hydrocarbons, and tin hydrides (*134*). The rate constants fall in the range 10^4–10^6 M^{-1} s^{-1} and qualitatively follow the C–H bond strength (*131*). The radical reactivity is entirely consistent with homolytic scission and not heterolytic hydride transfer.

D. Other Systems

There are many other metal complexes that have been developed for studying DNA chemistry that will not be discussed in this review. In

most cases, they have been discussed in other recent reviews (*23, 39, 136, 137*). The iron complexes $Fe(EDTA)^{2-}$ and MPE are excellent agents for hydroxy radical footprinting (*138, 139*), and Riordan and Wei have recently developed related methods for generation of methyl radicals from photolysis (*140*). Nickel macrocycle complexes effect DNA and RNA cleavage via catalysis of the oxidation of guanine by persulfate (*24, 141*). Porphyrin complexes cleave DNA via sugar oxidation upon treatment with persulfate, light, or oxygen (*142–144*). Treatment of Cu–phen with hydrogen peroxide effects strand scission (*25, 145*), and is discussed extensively here (phen = 1,10-phenanthroline).

IV. Electron- and Energy-Transfer Reactions Involving Bound Complexes

The foregoing discussion shows why metal complexes are so well suited for mapping the innate reactivity of biological substrates. For each foreseeable reaction pathway, there is a matched metal complex that can readily be studied in real time using spectroscopic signatures. For hydride transfer and oxo transfer, $Ru(IV)O^{2+}$ complexes allow for mechanistic investigations using stopped-flow spectrophometry (*119*). For hydrogen atom transfer, Stern–Volmer quenching and other photophysical measurements can be used in conjunction with $Pt_2(pop)_4^{4-}$ (*131*). For electron transfer, tris chelate complexes such as $Ru(bpy)_3^{2+}$ can be followed using electrochemistry or stopped-flow (*83*). In each of these cases, the reactivity patterns have been studied extensively using simple organic molecules, so there is a vast library of information to use in understanding reactions with complicated substrates such as nucleic acids.

Electron and energy transfer reactions where one or both partners are bound to DNA are now considered. While these reactions do not directly reveal aspects of DNA reactivity, an understanding of how DNA can modulate the reactions of bound complexes is important in understanding how to probe DNA reactivity using metal complexes. The idea that DNA would provide a novel reaction medium for redox reactions of metal complexes stems perhaps initially from the observation that DNA binding enhances the emission intensity of the MLCT state of complexes based on $Ru(bpy)_3^{2+}$ (*86, 146–156*). This effect apparently arises because the metal complex is bound in a relatively nonpolar environment compared to water, which leads to a red shift in the MLCT absorption maximum (*157, 158*). An increase in the emission polarization of the bound complex also suggests that the complex is held more rigidly when bound, which could account for the emission enhancement

(*86*). Complexes with higher binding affinities, such as $Ru(phen)_3^{2+}$, show larger enhancements in intensity and exhibit biphasic emission decays where one component is long-lived compared to the free solution lifetime (*57, 146, 147, 149*). Recently, the Barton group reported the complex $Ru(bpy)_2(dppz)^{2+}$, which is not emissive in fluid solution but is emissive when bound to DNA via intercalation of the planar dppz ligand (*159, 160*). This occurs because of the effects mentioned earlier and also because the dppz nitrogens are much more basic in the excited state than in the ground state. Protection of the dppz ligand from water by intercalation prohibits full or partial protonation from deactivating the excited state. This phenomenon has been termed the "molecular light switch" effect (*159*).

When bound to DNA, metal complexes can participate in bimolecular quenching reactions. When the quencher is not bound to DNA, as with $Fe(CN)_6^{3-}$, the quenching rate constant is decreased relative to the solution rate constant, because the anionic charge on the DNA prohibits collisions between bound ruthenium and the anionic quencher (*86, 160*). Conversely, when cationic electron-transfer quenchers such as $Co(bpy)_3^{3+}$ are used, quenching rate constants are accelerated, because of the increased local concentration of metal complexes bound to the double helix (*151, 161, 162*). These effects are worth a factor of 5–20 in bimolecular rate constant. Similar effects have been observed for the covalent labeling of DNA by catonic platinum complexes (*163*). In the bimolecular reactions, Stern–Volmer plots remain linear for $Ru(phen)_3^{2+}$ as the donor, so statistical mixing of the donor and acceptor must occur (*161, 162*). Thus, these rate accelerations must be due to increased concentration effects. However, when the excited state is strongly bound, as for $Ru(bpy)_2(dppz)^{2+}$, quenching plots are no longer linear, but instead exhibit an exponential dependence consistent with the Perrin "sphere of action" formalism (*164*).

The "sphere of action" interpretation suggests that long-range electron transfer through the double helix occurs and that the π-stack of the double helix provides a particularly "friendly" medium for electron transfer (*164*). This suggestion can be tested by studying electron transfer through DNA between two complexes held fixed at a well-defined distance. Immobilization of both partners by covalent attachment to oligonucleotides has been accomplished by two groups (*165, 166*). Though there is disagreement on the degree to which the electron transfer is enhanced, in both cases it is clear that the π stack of the nucleic acid bases in the double helix provides an effective conduit for electron transfer where reaction is at least as efficient as through protein interiors (*167–170*). The difference in rate in the two systems

may be a result of different orientations of the attached metal complexes to the π stack. This exciting area of research will provide insight into hole and electron migration through DNA, which is important in understanding the mechanisms of DNA damage by ionizing radiation (*21*).

Studies of similar reactions provide a new twist to understanding the thermodynamics of binding of metal complexes to DNA. These studies have centered on $Pt_2(pop)_4^{4-}$, which exhibits a long-lived (π = 10 μs) excited state in aqueous solution. As discussed earlier, this excited state is reactive toward energy and electron transfer with a variety of quenchers, including metal complexes (*131*). Since $Pt_2(pop)_4^{4-}$ is a tetraanion, it does not bind to DNA; however, many metal complexes that quench $Pt_2(pop)_4^{4-*}$ bind to DNA (*55*). Shown in Fig. 11 is the emission spectrum of $Pt_2(pop)_4^{4-}$ in buffer, with $Co(phen)_3^{3+}$ in buffer, and with the same concentration of $Co(phen)_3^{3+}$ in the presence of DNA. As shown, the cobalt complex is a much more efficient quencher in the absence of DNA when there is significant ion pairing between $Co(phen)_3^{3+}$ and $Pt_2(pop)_4^{4-*}$. In the presence of DNA, the cationic cobalt complex is now bound to DNA while $Pt_2(pop)_4^{4-*}$ is repelled from the double helix. When the ionic strength is increased, the buffer rate constant decreases, because high ionic strength discour-

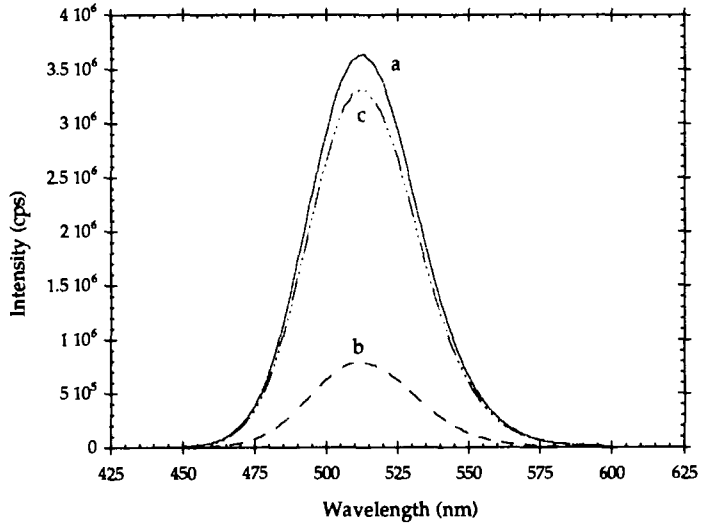

FIG. 11. Emission spectra of (a) 10 μM $Pt_2(P_2O_5H_2)_4^{4-}$ in pH 7 buffer, (b) with 60 μM $Co(phen)_3^{3+}$, and (c) with 5 mM calf thymus DNA and 60 μM $Co(phen)_3^{3+}$.

ages ion pairing of the two metal complexes. Similarly, the DNA rate constant increases because the repulsion of the $Pt_2(pop)_4^{4-}$ from the double helix is not as great.

Such quenching reactions where the excited state is in solution and the quencher is bound to DNA can be used to determine the binding constants of the metal complex quenchers. These determinations are performed by measuring the degree of quenching shown in Fig. 11. For low-affinity complexes ($K < 10{,}000\ M^{-1}$), we have successfully fit titrations using (*55, 56*)

$$\frac{(k_a - k_f)}{(k_b - k_f)} = \frac{K[\text{DNA}]}{K[\text{DNA}] + 1}, \tag{10}$$

where k_a is the Stern–Volmer rate constant observed for the absorbance band at a particular DNA concentration, k_b is the rate constant in excess DNA, k_f is the rate constant in the absence of DNA, and K is the binding constant of the complex to DNA. For complexes with binding constants greater than $10{,}000\ M^{-1}$, it is necessary to apply

$$\frac{(k_a - k_f)}{(k_b - k_f)} = \frac{b - \left(b^2 - \dfrac{2K^2C_t[\text{DNA}]}{s}\right)^{1/2}}{2KC_t}, \tag{11a}$$

$$b = 1 + KC_t + \frac{K[\text{DNA}]}{2s}, \tag{11b}$$

where C_t is the total concentration of the metal complex, and s is the binding site size in base pairs. Equation (11) is derived from an equation developed by Carter *et al.* based on neighbor-exclusion binding (*171*). The results obtained from Eq. (11) are identical to those obtained using a more typical Scatchard analysis, since both equations are based on the same binding model (*171*); however, Eq. (11) in the form shown here is more convenient both computationally and in terms of displaying the data.

With the ability to measure high and low binding constants accurately, it is possible to assess carefully the effects of ionic strength on the binding constants of metal complexes to DNA. This analysis is of interest in cases where the binding constant is high, as with octahedral metallointercalators (*40, 152*). For example, the binding affinity of

$Ru(tpy)(dppz)OH_2^{2+}$ (Fig. 12) decreases as the concentration of the buffer cation is increased (*55*). From Eq. (1), we can determine the binding parameters for comparison to those of classical intercalators, such as ethidium bromide. The measured values for K_t°, which reflect the contribution to the binding affinity that does not arise from electrostatic forces, are essentially identical for ethidium ($\Delta G_t^\circ = -6.5$ kcal/mol) and $Ru(tpy)(dppz)OH_2^{2+}$ (−5.9 kcal/mol). Thus, this experiment shows rigorously that the intercalation ability of the coordinated dppz ligand is the same as for a traditional intercalator.

Related questions arise in considering complexes with very low affinities. For example, one goal in such a research program is to develop complexes that have binding affinities similar to hydrated cations so

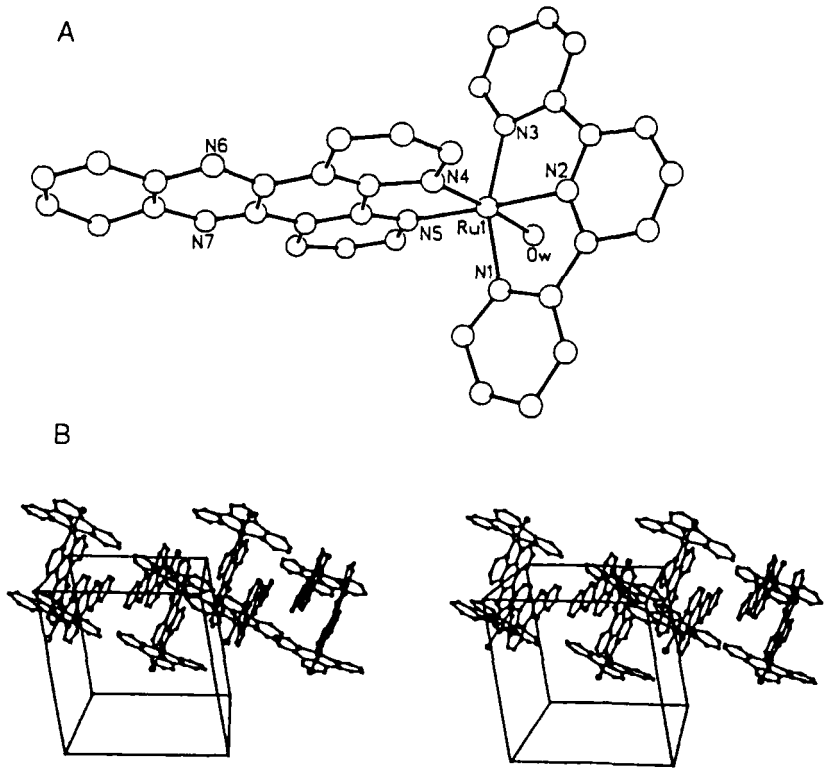

FIG. 12. (A) X-ray crystal structure of $Ru(tpy)(dppz)OH_2^{2+}$ taken from Gupta *et al.* (*123*). Copyright © 1992 VCH Publishers. (B) The dppz ligands undergo extensive π-stacking in the crystal, which is consistent with the high affinity of $Ru(tpy)(dppz)OH_2^{2+}$ for intercalation.

that it is possible to target cation binding sites that are important in RNA folding (*30, 67*). The complex $Ru(tpy)(bpy)OH_2^{2+}$ has a very low binding affinity that is the same as for $Ru(bpy)_3^{2+}$, which appears to bind primarily by electrostatics (*55, 152*). To investigate this hypothesis, the dependence of the DNA binding of $Ru(tpy)(bpy)OH_2^{2+}$ on the salt concentration has been examined. The non-electrostatic binding energy is −0.8 kcal/mol, which is significantly smaller than that of $Ru(phen)_3^{2+}$ and $Ru(tpy)(dppz)OH_2^{2+}$ (*55, 57*) and only a factor of 2 higher than that for those systems which no longer give a meaningful measurement (*54*). This result strongly supports the idea that complexes of bpy, such as $Ru(tpy)(bpy)OH_2^{2+}$, bind to DNA almost solely by means of electrostatic interactions. Similar conclusions have been drawn from similar experiments on the binding of $Co(NH_3)_6^{3+}$ (*172*).

During these experiments, it was observed that in a tris-HCl buffer system [tris = tris(hydroxymethyl)aminomethane], the DNA binding constant of $Ru(tpy)(bpy)OH_2^{2+}$ is somewhat higher than in potassium phosphate buffer of the same cation concentration. The DNA binding constants are indeed consistently larger in tris than in phosphate buffer, and plots of the binding constant versus salt concentration gave a slope of −1.2 that is similar to those observed for nearly all of the divalent ruthenium complexes studied so far. In fact, the slopes observed for all the divalent ruthenium complexes studied thus far fall in the range of 1.35 ± 0.15, which indicates a very similar contribution to the binding affinity from electrostatics for all the complexes. Equation (1) can be used to calculate a non-electrostatic binding energy for tris buffer of −2.3 kcal/mol, which is considerably larger than the value calculated for potassium phosphate solution. Therefore, subtle changes in the binding affinity of the buffer cation can modulate the determined binding affinity of the metal complex of interest.

V. DNA Cleavage by Hydrogen-Atom Abstraction

The sugar functionality of nucleotides contains a number of activated C–H bonds that can be cleaved via hydrogen atom transfer (*17*). Cleavage of DNA by activated FeBLM has been shown to lead to scission of the 4′ C–H bond to produce a radical that can react with oxygen or undergo one-electron oxidation and hydration (Scheme 7) (*17, 173*). Nucleic acid cleavage reactions produce two types of products. Small molecules, such as bases, modified bases, or sugar fragments, can be detected by techniques such as HPLC and GC-MS. For bleomycin, the carbocation pathway gives the free nucleic acid bases (adenine,

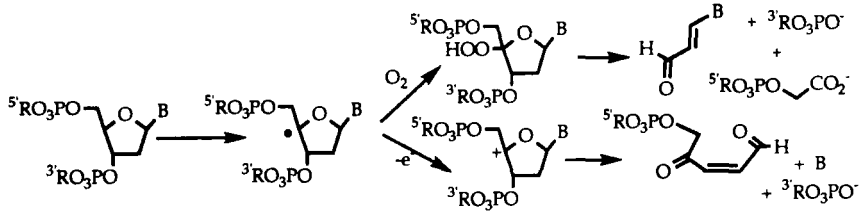

SCHEME 7

thymine, guanine, and cytosine), and the radical pathway gives the base proposals. The second type of product, the nucleic acid fragments, can be detected by high-resolution electrophoresis (*105*).

In addition to the 4′ chemistry observed for FeBLM, activation of the other four positions has been observed. The enediynes cleave the 5′ C–H bond to produce a radical that is further oxidized to a ketone and leads directly to strand scission (*19, 20*). Photolytic oxidation by $Rh(phen)_2(phi)^{3+}$ cleaves the 3′ C–H bond to produce a radical that can partition in the same manner as the 4′ radical produced by FeBLM

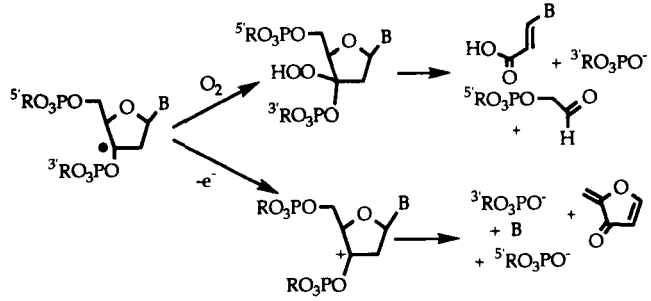

SCHEME 8

(Scheme 8) (*40*). The products are either free bases or base propenoic acids. Substitution of uracil at the 5 position with bromine produces a duplex that damages itself upon photolysis via cleavage of the 2′ C–H bond (*174*).

The final position that can be oxidized is the 1′ C–H bond. In oligomers containing 2′-hydroxy sugars, Hecht and co-workers have observed oxidation at the 1′ position by FeBLM (*103*). The Cu–phenanthroline complex oxidizes DNA at the 1′ position upon treatment with hydrogen peroxide (*25*). The reaction mechanism, shown in

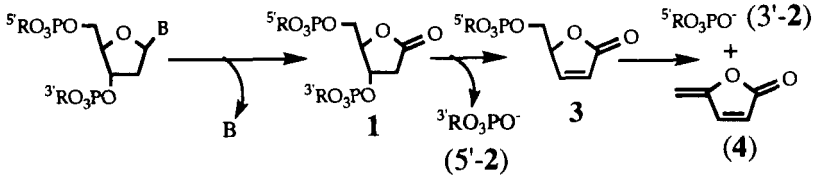

SCHEME 9

Scheme 9, produces a 1′ radical that undergoes further oxidation to produce a ribonolactone (**1**) and free base. For some sequences, the ribonolactone residue is stable, and no frank scission is observed. For other sequences, the ribonolactone undergoes elimination at neutral pH to produce a 3′ phosphate and a derivatized 5′ terminus (**3**) that migrates behind 5′-phosphate termini on high-resolution gels of 5′-labeled oligomers. For still other sequences, the furanone fragment is also eliminated to produce a 5′-phosphate terminus and 5-MF (**4**), which can be detected by HPLC. Upon treatment with piperidine, all of the intact ribonolactone linkages and modified phosphate termini are hydrolyzed to phosphate termini and 5-MF.

The $Pt_2(pop)_4^{4-}$ complex offers a unique opportunity for studying hydrogen transfer reactivity of nucleotides and DNA. The DNA cleavage reactions are unique in that the tetraanionic platinum complex is repelled from DNA, so if hydrogen abstraction does occur, it must proceed via an unfavorable "binding" equilibrium:

$$Pt_2(pop)_4^{4-} + DNA \rightleftharpoons Pt_2(pop)_4^{4-} \cdot DNA. \qquad (12)$$

Once a collision has occurred, $Pt_2(pop)_4^{4-*}$ should be capable of abstracting hydrogen atoms. We have demonstrated that photolysis of $Pt_2(pop)_4^{4-}$ in the presence of plasmid DNA leads to strand scission as monitored by agarose electrophoresis (*175*). In this experiment, supercoiled DNA is converted to a nicked form that can be detected by simple electrophoresis and staining with ethidium bromide. Only one cleavage event in the entire plasmid (up to 4000 base pairs) is required to visualize cleavage, so this is a very sensitive assay (*176*). Cleavage with $Pt_2(pop)_4^{4-}$ is observed upon photolysis at only 450 nm, where the triplet $d\sigma^* \rightarrow p\sigma$ absorption occurs. The extent of cleavage increases with increasing ionic strength, which would be expected to shift the binding equlibrium in Eq. (12) to the right.

If $Pt_2(pop)_4^{4-}$ is a photolytic cleavage reagent, then it can be reasoned that it must be competent to perform hydrogen abstraction in aqueous

solution. As described earlier, the complex is known to mediate these reactions catalytically in nonaqueous solution, but DNA studies motivated an increased understanding of the complexes catalytic properties in water. Roundhill *et al.* had reported previously that the complex was somewhat unstable in aqueous solution (*177*). As a model for the DNA reaction, the photooxidation of 1-phenylethanol to acetophenone by $Pt_2(pop)_4^{4-}$ has been investigated in H_2O (*178*). The final concentration of acetophenone after photolysis at pH 7 was found to range from 20 to 40 times the amount of $Pt_2(pop)_4^{4-}$ initially present. Photolysis of aqueous buffer solutions containing 1-phenylethanol produced no conversion to acetophenone in the absence of the metal complex. Thus, the oxidation is photocatalytic, and while fewer turnovers are observed in water than in aqueous solution, the stability of the complex in water is sufficient to realize catalysis. An interesting feature of the system is that photocatalytic oxidation of alcohols can be accomplished using the d^7–d^7 dimer, $Pt_2(pop)_4Cl_2^{4-}$. This reaction was attempted because $Pt_2(pop)_4Cl_2^{4-}$ is considerably more stable in buffer solution than $Pt_2(pop)_4^{4-}$, showing no decomposition when allowed to stand in the dark for several hours (*179*). While use of the oxidized $Pt_2(pop)_4Cl_2^{4-}$ complex does not lead to additional turnovers, it does provide the ability to store the catalyst in buffer solution for extended periods, which may be useful in certain applications. In related studies, Cl^- ion suppressed catalytic activity. The number of turnovers was a maximum at pH 3 and decreased at both higher and lower values.

One reaction scheme that accounts for the pH dependence of the turnover number is shown in Fig. 13. In this scheme, the $Pt_2(pop)_4Cl_2^{4-}$ is photoconverted to $Pt_2(pop)_4^{4-}$, which is the photocatalytic species.

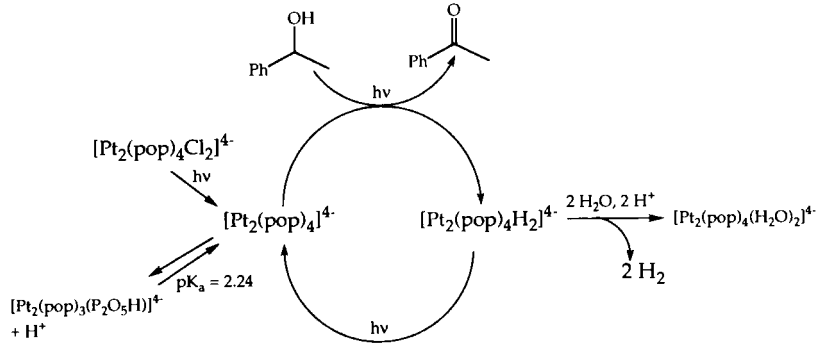

FIG. 13. Possible reaction scheme for the photocatalytic oxidation of 1-phenylethanol by $Pt_2(pop)_4^{4-}$ and $Pt_2(pop)_4Cl_2^{4-}$.

The $Pt_2(pop)_4^{4-}$ oxidizes the alcohol and is converted to $Pt_2(pop)_4H_2^{4-}$. This species can be photoconverted back to $Pt_2(pop)_4^{4-}$, or it can undergo a known reaction with water to form dihydrogen and $Pt_2(pop)_4(H_2O)_2^{4-}$ (*135*). Thus, at high pH, the catalyst is deactivated by deprotonation of the pop ligand (*177*), and at low pH, the catalyst is deactivated by protonation of the hydride complex to form the inactive aqua complex. Both of these reactions reduce the efficiency of the catalytic reaction, and at pH 3, these two side reactions are minimized, allowing for the greatest numbers of turnovers.

To determine the fundamental photoreactions of $Pt_2(pop)_4^{4-}$ with DNA, it was possible to determine the Stern–Volmer rate constant for quenching of the $Pt_2(pop)_4^{4-*}$ emission by ribose sugars, the DNA bases, and several mononucleotides (*178*). Quenching rate constants could not be obtained for any of the DNA bases; the free bases are only slightly soluble in both water and nonaqueous solvents, and no quenching of $Pt_2(pop)_4^{4-*}$ was observed. Quenching is observed for deoxyribose, and the quenching rate constant obtained from a least-squares fit, 3.4×10^5 M^{-1} s^{-1}, is similar to those obtained with alcohols (*180*), which have been shown to quench $Pt_2(pop)_4^{4-*}$ by hydrogen abstraction. This rate constant is 3–4 orders of magnitude less than those obtained for electron- or energy-transfer quenching (*55, 181*), implicating hydrogen abstraction as the quenching mechanism for ribose. Shown in Table I are quenching rate constants obtained for several mononucleotides. These rate constants are all quite similar to that of deoxyribose, indicating that a hydrogen atom is abstracted from the sugar in each case.

TABLE I

RATE CONSTANTS FOR OXIDATION OF SUGARS AND NUCLEOTIDES BY OXORUTHENIUM(IV) AND DIPLATINUM(II)

Substrate	$Ru(tpy)(bpy)O^{2+}$ $k(M^{-1}\ s^{-1})$	$Pt_2(pop)_4^{4-}$ $k(M^{-1}\ s^{-1})$
Ribose	0.029	5.1×10^4
Deoxyribose	0.082	3.4×10^5
TMP	0.39	6.5×10^5
CMP	0.10	—
dCMP	0.59	1.3×10^5
AMP	0.39	1.7×10^5
dAMP	2.5	6.2×10^6
dGMP	—	2.2×10^6

Further support for this idea comes from the similarity of the quenching rate constants for the various mononucleotides. There appears to be no preference for nucleotides of any one base, and if base oxidation occurred, a significantly faster rate constant would be expected for more reactive bases, such as guanine (*75*).

An intriguing observation in Table I is that the rate constant for quenching by deoxyribose is nearly an order of magnitude faster than that for ribose. This observation appears to be general, because an even larger difference in quenching rate constants is observed for 5′-AMP and 5′-dAMP. This trend has been observed in related reactions, and the implications and possible origins will be discussed later. In actual DNA or RNA, the nucleic acid structure will dictate which hydrogen atoms are available for abstraction by $Pt_2(pop)_4^{4-}$. Since all the hydrogen atoms are available in reactions with free nucleotides and sugars, this experiment gives the *upper limit* for the intrinsic rate constant for reaction of $Pt_2(pop)_4^{4-*}$ with a nucleotide within a DNA or RNA strand. Of interest here is how the polymer structure and charge will affect the rate constant for abstraction of hydrogen atoms from polynucleotides. Thus, these upper limits for reaction with the monomers will provide useful information for probing quantitatively the attenuation by nucleic acid charge and structure of the kinetics of DNA and RNA damage by $Pt_2(pop)_4^{4-*}$.

VI. DNA Cleavage by Hydride and Oxo Transfer

A. Hydride Transfer

Initial studies of the sequence specificity of cleavage by Ru(tpy)(bpy)O^{2+} centered on single-stranded oligomers that exhibit only a random-coil structure in solution (*182*) to maximize the probability of reaction with the metal complex. It was necessary therefore to keep structural complexity from interfering with the intrinsic reactivity of various sites on the oligomer toward the cleavage agent. Frank scission is observed that must arise from sugar oxidation, because isolated cytosine and adenine are not reactive toward oxidation by Ru(tpy)(bpy)O^{2+} (*75*) and because base oxidations usually produce only piperidine-labile cleavages (*182, 183*). The product bands are indicative of 1′-oxidation, as observed with Cu–phen (Scheme 9) (*25*), because some lesions migrate between the phosphate-terminated bands and with the phosphate-terminated bands following piperidine treatment. These termini must be derivatized phosphates (**3**) that are hydrolyzed to au-

thentic phosphates (3′-**2**) upon piperidine treatment. Following piperidine treatment, many more DNA lesions are apparent. This observation is also suggestive of 1′ oxidation, which generates a ribonolactone residue (**1**) that often requires base treatment to induce strand scission but does give immediate base release (*25, 41, 103*). Also consistent with 1′ chemistry is the observation that depletion of oxygen from the cleavage reaction solution does not alter the results. Labeling the 3′ end produces only phosphate termini, also consistent with 1′ oxidation.

The released products in Scheme 9 are the free nucleic acid bases (adenine, thymine, guanine, and cytosine) and the furanone 5-methylene-2,5-H-furanone (5-MF, **4**) derived from the sugar ring. Analysis of solutions of DNA oxidized with $Ru(tpy)(bpy)O^{2+}$ directly by reverse-phase HPLC shows the formation of all four bases in roughly equal amounts (*184*). Quantitation of the released bases gives a yield of 10% based on the metal concentration (*185*). Extraction of the reaction mixture with chloroform produces a solution that by HPLC and GC—MS can be shown to contain the furanone **4** (*186*). The detected species gives retention times, optical absorption, and mass spectra identical to an authentic sample, so the species in the chromatograms is **4** and not an isomeric furanone that can arise from 3′ oxidation (*40*). All of the expected products for 1′ sugar oxidation have therefore been detected.

The observation of 1′ oxidation implicates binding and reaction of the complex in the minor groove (*25, 41, 103, 187*). In related cleavage reactions, inhibition of cleavage by distamycin and other groove binders has been used to support action of small molecules in the minor groove (*50*), since distamycin is known to bind to the minor groove of duplex DNA. In fact, the crystal structure of distamycin bound to a double-stranded oligomer has been determined (*48, 49*) and shows binding of the drug to the central AAATTT segment (Fig. 14). Oxidation of the duplex by $Ru(tpy)(bpy)O^{2+}$ in the presence of distamycin leads to protection of the duplex from oxidation, as indicated in the figure. Further, the protection occurs specifically in the AAATTT segment and not on the ends, in accordance with the known distamycin binding locus. This experiment further confirms binding and reaction of the complex in the minor groove and is consistent with the observation of 1′ oxidation.

B. Oxo Transfer

In addition to the sugar oxidations at A, T, and C, the guanine sites show enhanced cleavage upon piperidine treatment. This result is consistent with a second pathway involving oxidation of the guanine

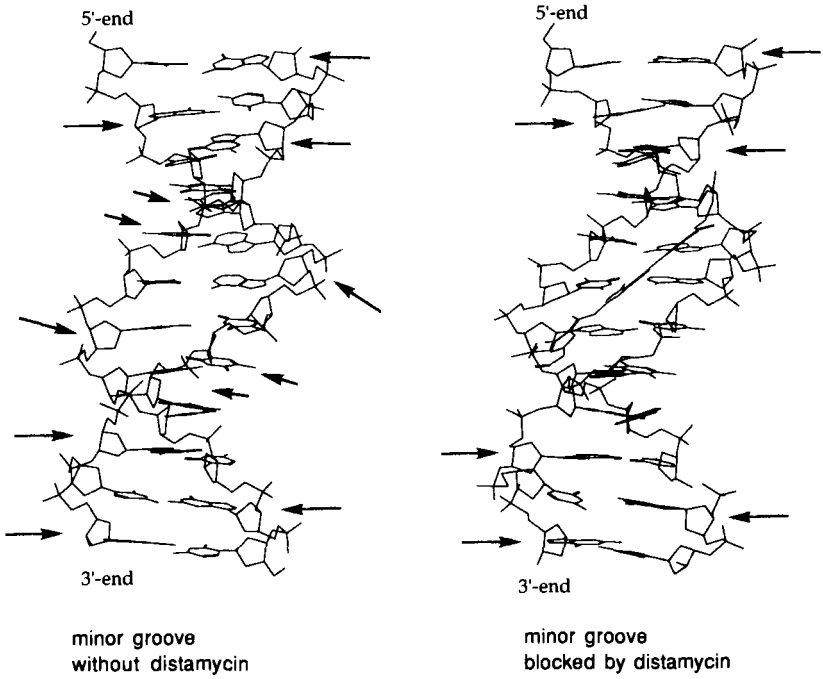

FIG. 14. Crystal structure of d[(5′-CGCAAATTTGCG)]$_2$ showing sites of cleavage (arrows) by Ru(tpy)(bpy)O^{2+} with (left) and without (right) distamycin. No cleavage is observed in the crystallographic distamycin binding site in the presence of the drug. Crystal structures taken from Coll *et al.* (*49*).

base, which is known to produce a piperidine-labile lesion (*182, 183*). After base treatment, the extent of cleavage at guanine is considerably greater than that observed at the other sites. Some of the cleavage at guanine may arise from sugar oxidation; indeed, oxidation of calf thymus DNA by Ru(tpy)(bpy)O^{2+} does lead to the release of free guanine (*184*), which must arise from oxidation of guanine sugars. Nonetheless, the amount of guanine released is similar to that of the other bases, which suggests that most of the cleavage at G arises from base oxidation. Quantitation of the yield of cleavage at each site by densitometry shows that following piperidine treatment, the yield of cleavage at G is about seven times larger than at A, T, and C on a per nucleotide basis.

C. Model Studies

The rate constants for oxidation of model mononucleotides and sugars are set out in Table I. The rate constants were measured under

pseudo–first-order conditions and, in most cases, were first-order in both nucleotide and ruthenium (*75*). In the slower reactions, the concentration of nucleotide was large enough that significant electrostatic binding of the complex to the dianionic nucleotide occurred, leading to saturation kinetics. These data were analyzed using double-reciprocal plots, and second-order rate constants were calculated for comparison to the other cases. Reactions at different ionic strengths and with trianionic diphosphate nucleotides confirmed that the binding equilibrium was electrostatic.

As shown in Table I, the A, C, and T nucleotides all behave via simple kinetics and give rate constants and activation parameters (not shown) consistent with heterolytic activation of C–H bonds. Product analyses are consistent with 1′ oxidation, as seen in polymeric DNA; however, the yield of base release is much higher for mononucleotides. An 80% yield of thymine based on ruthenium is observed for TMP oxidation, and a quantitative yield is observed for cytosine based on total CMP consumed. As discussed earlier for $Pt_2(pop)_4^{4-}$, the site of oxidation in model sugars and mononucleotides cannot be regulated by the polymer structure, as can occur in studies of natural DNA and RNA. Thus, the extent of oxidation of any particular C–H bond is controlled only by the relative reactivity of each site. Oxidation of the 1′, 4′, and 5′ hydrogens has been observed for small molecules that bind in the minor groove (*17, 19, 20, 25, 103*), so selection of the 1′ position by $Ru(tpy)(bpy)O^{2+}$ must occur partly because of the innate reactivity of the site. Since the 5′ position is a CH_2 site, it is likely to be more difficult to oxidize. In fact, recent theoretical studies have suggested that the C–H bond strengths at the 1′, 3′, and 4′ positions in deoxyribose are significantly lower than for the 2′ and 5′ positions, with the 1′ position slightly lower than for 3′ and 4′ (*188*). If the nucleic acid base is more electron-releasing than hydroxyl, the 1′ position may become significantly more reactive in nucleotides compared to deoxyribose.

The kinetic studies also argue strongly for 1′ oxidation. First, all of the nucleotides are more reactive than deoxyribose and ribose. This result can be ascribed to more effective activation of the 1′ position by the nucleic acid base compared to hydroxyl, which is likely to be less electron-donating. This trend is evident even after correction of rate constants for the electrostatic binding preequilibrium. In fact, this same trend is evident in the $Pt_2(pop)_4^{4-}$ rate constants. Since $Pt_2(pop)_4^{4-}$ is a tetraanion, the reactions of nucleotides are actually discouraged electrostatically relative to those of the neutral sugars—yet nucleotides are more reactive by about an order of magnitude in rate constant.

Second, the lower reactivity of the 2′-oxy nucleotides and sugars toward $Ru(tpy)(bpy)O^{2+}$ can be ascribed to deactivation of the 1′-position by the 2′-hydroxyl (*189*), which also argues primarily for oxidation at the 1′ position. This observation has also been made for quenching of $Pt_2(pop)_4^{4-}$.

Absorbance vs time curves for guanosine-5′-monophosphate (GMP) are not monoexponential, as observed with the other substrates. The decay curves for GMP oxidation are sigmoidal in shape, as shown in Fig. 15. This behavior is consistent with formation of a bound, colored intermediate and eventual overoxidation of the substrate where the first step is much slower than the subsequent steps. Thus, initial oxidation of GMP produces a species that is oxidized more rapidly than GMP itself. Oxidation of *trans*-stilbene by $Ru(IV)O^{2+}$ occurs with an initial rate-determining step corresponding to the formation of a bound epoxide complex $Ru(III)(epoxide)^{3+}$, and other oxo-transfer reactions of $Ru(IV)O^{2+}$ proceed via similar initial steps (*130, 190*). These bound

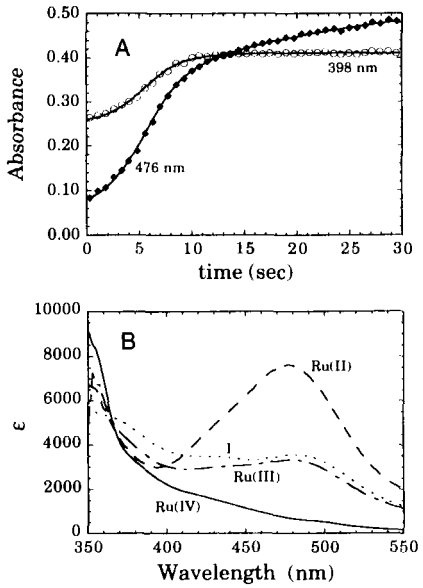

FIG. 15. (A) Absorbance vs time traces at 398 nm (open circles) and 476 nm (closed diamonds) for the oxidation of GMP (3.8 mM) by $Ru(tpy)(bpy)O^{2+}$ (0.12 mM) in 50 mM phosphate buffer (pH 7.1). Solid lines are the single-wavelength decays calculated using SPECFIT from fitting the change in the entire spectrum from 350 nm to 550 nm over the indicated time range. (B) Spectra calculated from the fitting procedure.

complexes are then oxidized rapidly by an additional equivalent of oxidized ruthenium.

A global fit was performed to the following kinetic model:

$$\mathrm{Ru(IV)O^{2+}} + \mathrm{GMP} \xrightarrow{k_1} \mathbf{I}, \quad (13)$$

$$\mathrm{Ru(IV)O^{2+}} + \mathbf{I} \xrightarrow{k = 50{,}000\ \mathrm{M^{-1}\,s^{-1}}} \mathrm{Ru(III)OH^{2+}} + \mathrm{Ru(II)OH_2^{2+}} + \mathrm{P1}, \quad (14)$$

$$\mathrm{Ru(III)OH^{2+}} + \mathbf{I} \xrightarrow{k = 50{,}000\ \mathrm{M^{-1}\,s^{-1}}} 2\mathrm{Ru(II)OH_2^{2+}} + \mathrm{P1}, \quad (15)$$

$$\mathrm{Ru(IV)O^{2+}} + \mathrm{Ru(II)OH_2^{2+}} \underset{k = 3000\ \mathrm{M^{-1}\,s^{-1}}}{\overset{k = 2 \times 10^5\ \mathrm{M^{-1}\,s^{-1}}}{\rightleftharpoons}} 2\mathrm{Ru(III)OH^{2+}}, \quad (16)$$

$$\mathrm{Ru(III)OH^{2+}} + \mathrm{P1} \xrightarrow{k = 7000\ \mathrm{M^{-1}\,s^{-1}}} \mathrm{Ru(II)OH_2^{2+}} + \mathrm{P2}, \quad (17)$$

$$\mathrm{Ru(III)OH^{2+}} + \mathrm{P2} \xrightarrow{k = 7000\ \mathrm{M^{-1}\,s^{-1}}} \mathrm{Ru(II)OH_2^{2+}} + \mathrm{P3}, \quad (18)$$

where P1, P2, and P3 are noncolored guanine oxidation products and **I** is a bound Ru(III)–O–GMP adduct similar to the bound epoxide produced during olefin oxidation. The results of the global fitting of the complete time-dependent spectra are shown as both sample kinetic traces (Fig. 15A) and the calculated spectra of the absorbing species (Fig. 15B). The simulation produces the calculated spectra of $Ru(IV)O^{2+}$, $Ru(III)OH^{2+}$, and $Ru(II)OH_2^{2+}$, which all agree well with the known spectra (*120*). The only calculated spectrum that is not known explicitly from independent experiments is that of **I**, but this spectrum strongly resembles the calculated spectra of complexes of Ru(III) with bound oxidized substrates, especially bound epoxides (*130, 190*). The rate constants for the comproportionation equilibrium [Eq. (10)] are known (*127*). The determination of k_1 using this model and time window is well defined: Experiments conducted over the concentration ranges of 0.03 to 0.23 mM $Ru(tpy)(bpy)O^{2+}$ and 1 to 33 mM GMP give $k_1 = 9 \pm 2\ \mathrm{M^{-1}\,s^{-1}}$.

The $Ru(tpy)(bpy)O^{2+}$ complex cleaves DNA by oxidation of guanine as well as by sugar oxidation, and the guanine reaction is significantly more efficient (*186*). The kinetic studies are consistent with the DNA results, because oxidations of the A, T, and C deoxynucleotides all exhibit single-exponential kinetics with rate constants in the same range ($0.4–2\ \mathrm{M^{-1}\,s^{-1}}$), and the guanine reaction is mechanistically more complicated and more efficient. A likely site of initial oxidation is C8 to form 8-oxoguanine (*43, 44, 191*), suggesting that species **I** has the structure:

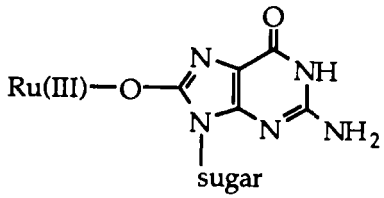

Oxidation of guanine at the C8 position has received the most attention; however, Cadet *et al.* have recently shown that oxidation at C1 may be more important (*44*). The steric demands of forming a bound intermediate at either position may have profound implications for the sequence and structural selectivity of guanosine oxidation (*182, 183, 192*). They suggest that the sugar/guanine oxidation ratio might be controlled by modulating the accessibility of the oxo ligand in Ru(tpy)(bpy)O^{2+}. Indeed, oxidation of DNA by Ru(tpy)(bpy)O^{2+} produces high–molecular-weight bands on sequencing gels consistent with the formation of **I** that yield scission at guanine upon piperidine treatment (*193*).

D. Partitioning between the Two Pathways

It is possible to view the cleavage reaction in broad terms using the model shown in Scheme 10. Binding of Ru(IV)O^{2+} to DNA occurs via

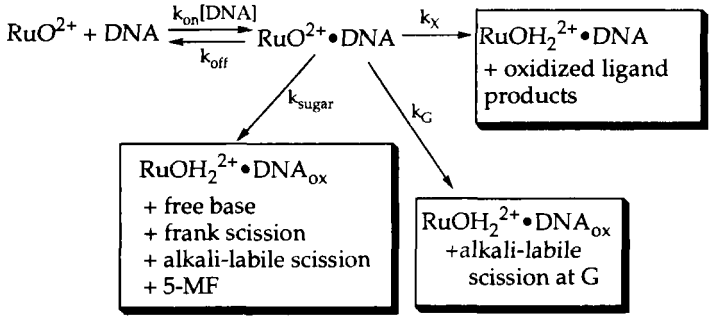

Scheme 10

a weak binding equilibrium with K_b = 660 M^{-1}. Even though this implies a relatively fast k_{off}, earlier kinetic studies demonstrated that the metal complex is always reduced prior to dissociation (*184*). The yield of oxidation at guanine is seven times that at the other nucleo-

tides. Since we know that the yield of base release is 10% based on total ruthenium (*185*), we can estimate that base oxidation consumes an additional 15% after making corrections for the extent of sugar oxidation at G. By estimating the yields of both sugar and base oxidation, we can account for about 25% of the total ruthenium based on $Ru(tpy)(bpy)O^{2+}$ by a two-electron process. However, we must consider the comproportionation reaction [Eq. (16)]. The base release measurements and the sequencing gel experiments are performed after all of the $Ru(IV)O^{2+}$ has been reduced, but long before an appreciable amount of $Ru(III)OH^{2+}$ has been reduced. Thus, a yield of 25% of DNA oxidation based on $Ru(tpy)(bpy)O^{2+}$ actually corresponds to a yield of 50%.

Accounting for half of the oxidizing equivalents based on $Ru(tpy)(bpy)O^{2+}$ implies that about 50% of the total $Ru(IV)O^{2+}$ reacts via a self-inactivation pathway (k_X), which has been demonstrated for polypyridyl oxidants (*129*). This self-inactivation pathway results from the bimolecular reaction of two oxoruthenium complexes to produce Ru(II) and oxidized polypyridyl ligands, as discussed earlier and shown in Scheme 5. Thus, observations imply that in terms of Scheme 10, $k_X > k_G > k_{sugar}$ for $Ru(IV)O^{2+}$. This ordering makes the prediction that a less powerful oxidant will be reduced via the k_X and k_G pathways, but not via k_{sugar}, as long as the rates of the various processes are directly related to the thermodynamic driving force. The $Ru^{III}(tpy)(bpy)OH^{2+}$ complex is isostructural with $Ru(tpy)(bpy)O^{2+}$, but is a much weaker oxidant that cleaves DNA only by sugar oxidation (*186*). The rate of k_X compared to k_G must also be increased, because densitometry shows that the yield of base oxidation from $Ru(III)OH^{2+}$ is only 14% of that realized with $Ru(IV)O^{2+}$.

From the model in Scheme 10, a further prediction can be made that an even weaker oxidant than $Ru(III)OH^{2+}$ should be reduced efficiently in the presence of DNA with no detectable damage to the nucleic acid—i.e., only the k_X pathway is operative. This prediction is confirmed by the results on $Os(tpy)(bpy)O^{2+}$. It has been shown by X-ray crystallography that $Os(tpy)(bpy)OH_2^{2+}$ is structurally identical to the ruthenium analogue (Fig. 16), so the only difference in the complexes is the weaker oxidizing power of the osmium complex. Nevertheless, $Os(tpy)(bpy)O^{2+}$ does not damage DNA as assessed by high-resolution electrophoresis, even though it is reduced efficiently in DNA (*186*). Thus, reduction of $Os(tpy)(bpy)O^{2+}$ occurs via the k_X pathway, and it is possible to use the time dependence of osmium reduction to measure k_X directly. These studies show that self-inactivation of $Os(tpy)(bpy)O^{2+}$ is catalyzed by DNA (Fig. 17). The extent of catalysis is a function of the square of the concentration of osmium bound to DNA calculated

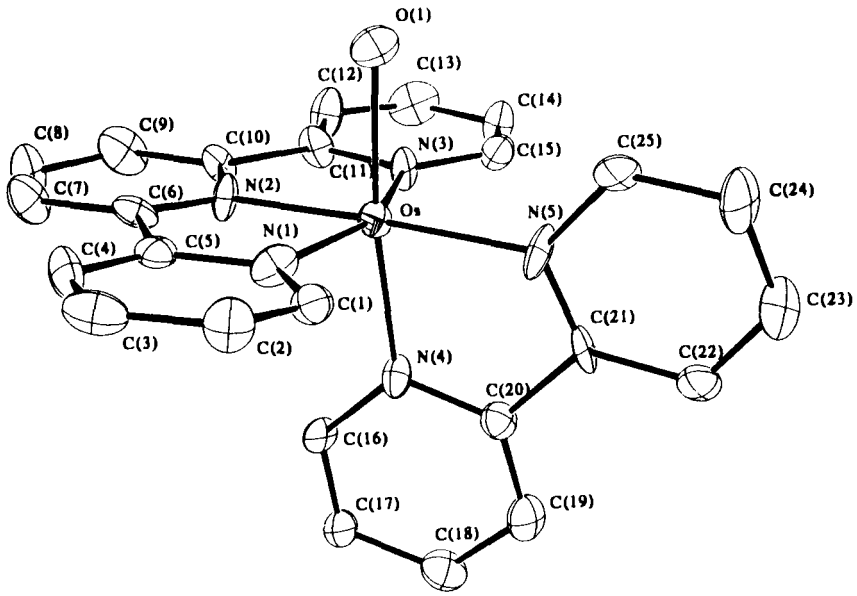

FIG. 16. X-ray crystal structure of $Os(tpy)(bpy)OH_2^{2+}$ taken from Cheng *et al.* (*186*). Copyright © 1995 American Chemical Society.

from a binding isotherm determined in a separate experiment (*55*). This analysis therefore supports the idea that DNA catalyzes the bimolecular self-inactivation reaction by condensing $Os(tpy)(bpy)O^{2+}$ on the double helix. An important feature of this catalysis is that the rate enhancement is sequence-specific, with AT polymers more efficient catalysts than GC (Table II). This effect probably arises from a higher binding affinity of the complex for the more open minor groove of the AT polymer (*53*).

Kinetic results on the reduction of $Os(IV)O^{2+}$ clearly show that k_X is catalyzed by DNA for this particular oxidant. For the $Ru(IV)O^{2+}$ experiments, it is not possible to show directly that this pathway is catalyzed relative to homogeneous solution. However, inspection of the relative yields of oxidation in DNA and in homogeneous oxidations of small molecules reveals that catalysis must occur. Oxidation of substrates such as 2-propanol and activated hydrocarbons proceeds in many cases with quantitative yields of oxidized products based on total $Ru(IV)O^{2+}$ (or on applied current in electrolytic oxidations) (*194*). Thus, a conversion of only 50% of the total $Ru(IV)O^{2+}$ into DNA oxidation implies that self-inactivation competes much more effectively with sub-

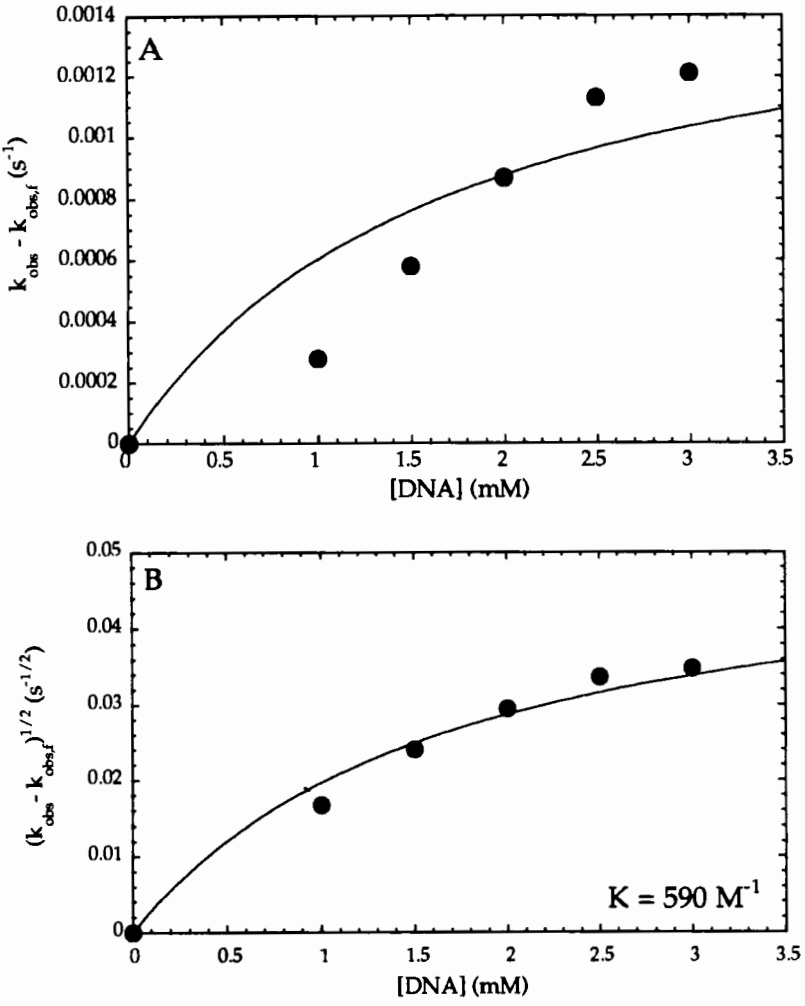

FIG. 17. (A) Plot of the observed rate of Os(tpy)(bpy)O^{2+} reduction in the presence of DNA (k_{obs}) minus the rate in the absence of DNA ($k_{obs,f}$) vs DNA concentration. The solid line is the best fit to Eq. (5). (B) Plot of $(k_{obs} - k_{obs,f})^{1/2}$ vs DNA concentration. The solid line is the best fit to the binding isotherm with the indicated K_B [Eq. (10)].

strate oxidation in DNA than in homogeneous solution. This implies either that DNA catalyzes the self-inactivation or that the substrate oxidation is much slower in the polymer. Based on our observations on Os(IV)O^{2+}, catalysis of k_X seems more likely, especially in single-

TABLE II

RATE ENHANCEMENT FOR Os(tpy)(bpy)O^{2+} REDUCTION IN THE PRESENCE OF NUCLEIC ACID POLYMERS

Polymer	k_{cat}/k_{uncat}
DNA	13.1 ± 1.4
poly(dA)·poly(dT)	44 ± 6
poly(dG)·poly(dC)	10.4 ± 0.6

stranded oligomers where a complex structure is not likely to obstruct oxidation sites.

Because the reaction appears to be controlled by the relative potentials of k_X, k_G, and k_{sugar}, it should be possible to predict the yield of these pathways on a sequencing gel from the relative rate constants in the mononucleotides. From densitometry of sequencing gels, it has been observed previously that the ratio of cleavage at G to cleavage at any of the other nucleotides is about 7 : 1 on a per nucleotide basis, i.e., $k_G/k_{sugar} = 7$ (*186*). This ratio was obtained in single-stranded DNA, where very little control of the cleavage pattern by the oligomer structure would be expected—i.e., the reactivity should largely control the extent of cleavage at each site. From the data in Table I, an average k_{sugar} for TMP, dCMP, and dAMP of 1.2 M^{-1} s^{-1} can be calculated. Using the value of $k_G = 9$ M^{-1} s^{-1} obtained from the analysis in Fig. 9, *the ratio calculated from the kinetic data is* $k_G/k_{sugar} = 7.5$, *which is in excellent agreement with the ratio calculated from densitometry of sequencing gels of single-stranded DNA*. Thus, it is possible to make predictions about the cleavage pattern based on the kinetic studies. In future experiments, it will be possible to understand when the DNA structure is in control of the cleavage pattern by understanding when the cleavage ratios do not match the kinetic data on the mononucleotides.

VII. DNA Cleavage by Electron Transfer

The remaining pathway shown in Scheme 1 is outer-sphere electron transfer to produce the guanine radical cation. This reaction appears ideally suited to study by voltammetric techniques, which has been a goal of the author's research group for some time. Electrochemistry

has been applied to detecting DNA and RNA and to studying guanine oxidation. However, low diffusion coefficients of DNA polymers and irreversible redox couples complicate the analysis (*195–197*). Despite the suitability of $Ru(tpy)(bpy)O^{2+}$ for nucleic acid oxidation, cyclic voltammograms of $Ru(tpy)(bpy)OH_2^{2+}$ in the presence of DNA show only a barely detectable amount of catalytic enhancement in the Ru(IV/III) wave that is attributable to DNA oxidation (*125*). There are two principal difficulties with observing such an enhancement in these voltammograms. The first is that the bound complex has a diffusion coefficient that is two orders of magnitude lower than that of the free complex, and current due to bound complex is therefore difficult to observe (*99, 171, 198*). The second difficulty is that the rate of hydrogen and hydride abstraction is too slow (10^{-2} M^{-1} s^{-1}) (*75, 127, 184*) to regenerate the reduced form of the metal complex during a voltammetric scan. Thus, a low binding affinity and a high rate of reaction are crucial in designing efficient electrocatalytic DNA cleavage agents whose reaction mechanisms are amenable to study using voltammetric methods.

It has been shown that complexes that participate only in outer-sphere electron transfer oxidize guanine electrocatalytically if the potential of the metal complex is greater than 0.9 V (*199*). Shown in Fig. 18 are cyclic voltammograms of $Ru(bpy)_3^{2+}$ with and without calf thymus DNA (*200*). The catalytic enhancement is observed for calf thymus DNA, poly(GC), or oligomers containing G, but not for poly(AT).

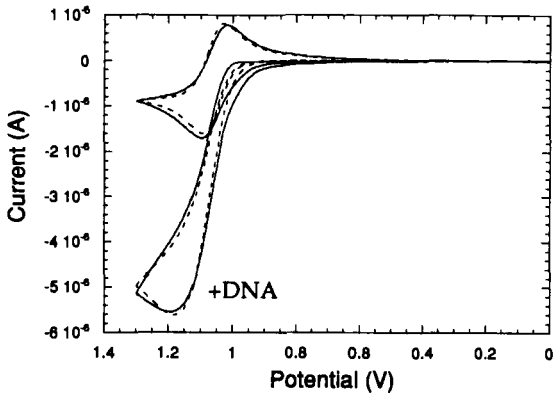

FIG. 18. Cyclic voltammograms of $Ru(bpy)_3^{2+}$ with and without calf thymus DNA. The dashed lines show theoretical voltammograms calculated using DigiSim for an EC′ mechanism. Data were taken at high ionic strength so that binding of the metal complex to DNA did not complicate the kinetic analysis. From Johnston *et al.* (*200*). Copyright © 1995 American Chemical Society.

Electrolysis of the solution beyond the $Ru(bpy)_3^{3+/2+}$ potential produces base-labile lesions specifically at G. Thus, the chemical reaction that leads to cycling of the metal complex is oxidation of guanine to the radical cation. Using digital simulation, the rate constant for the chemical reaction can be measured from the data shown in Fig. 18. When the potential of the mediator is varied, a Marcus plot can be constructed. If Marcus theory is obeyed, the rate constant should vary linearly with the driving force with a slope of 1/2. Such a dependence is observed for oxidation of guanine by $Ru(bpy)_3^{2+}$ and derivatives (Fig. 19).

VIII. Conclusions

Correlating nucleotide reactivity with studies on oligomers and polymers leads to several new fundamental principles concerning nucleic acid oxidation. First, if the oxidant is weak enough, model studies can be used to understand cleavage patterns for complex polymers. In the case of $Ru(tpy)(bpy)O^{2+}$, the rate constants for mononucleotide oxidation can be used to predict the cleavage pattern in single-stranded oligomers. This situation obtains because the oxidant is only capable of oxidizing the 1′ position.

Second, the relative reactivities of $Ru(IV)O^{2+}$, $Ru(III)OH^{2+}$, and $Os(IV)O^{2+}$ show that guanine oxidation is much more facile than sugar oxidation. This observation suggests that all oxidants that cleave DNA

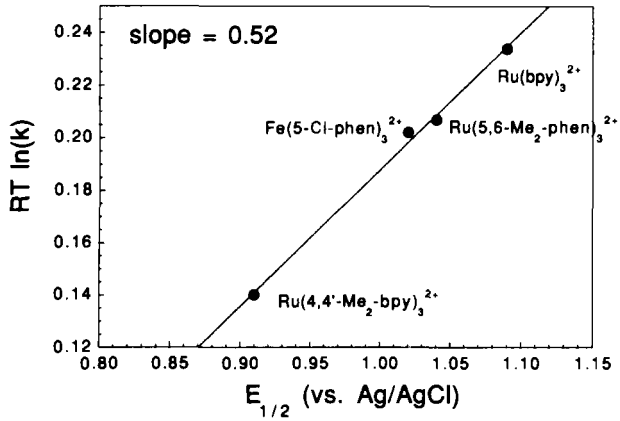

FIG. 19. Plot of RT in k for the rate of oxidation of guanine in calf thymus DNA by the indicated metal complexes against the $E_{1/2}$ of the complexes. From Johnston *et al.* (*200*). Copyright © 1995 American Chemical Society.

by sugar oxidation should also oxidize guanine. For Cu–phen, guanine oxidation has been observed (*191, 201*). Guanine has also been shown to quench the excited state of $Rh(phen)_2Cl_2^+$ (*42*), which is related to the photocleaving excited state of $Rh(phen)_2(phi)^{3+}$. The only cleavage mechanism demonstrated thus far for $Rh(phen)_2(phi)^{3+}$ is hydrogen abstraction (*40*); however, it is possible that guanine oxidation would not lead to cleavage if back electron transfer from the reduced rhodium complex to $G^{\cdot+}$ is fast. Rapid back electron transfer would in fact be expected for a photoinduced reaction where the driving forces for recombination are generally very high (*202*). An interesting question involves why no guanine oxidation is observed for FeBLM, which is an excellent catalyst for reactions such as hydroxylation and epoxidation (*101, 102*). These oxidations would appear comparatively more difficult than guanine oxidation based on the results described here. It may be worthwhile to consider that guanine oxidation is generally an inner-sphere reaction, which for $Ru(tpy)(bpy)O^{2+}$ actually proceeds through a bound intermediate. These reactions may therefore be highly sensitive to the accessibility of the guanine, as observed for nickel macrocycles (*24*). A large molecule such as FeBLM may not be capable of accessing guanine residues that are buried in the interior of helices, or the steric constraints of the bleomycin chains may altogether prohibit formation of a bound Fe–O–guanine adduct (*97, 98*).

Third, findings on the relative rates of sugar oxidation suggest that RNA cleavage is significantly more difficult than DNA cleavage. The rate data are consistent with the observation of many more cleavages in a DNA hairpin than in an analogous RNA hairpin (*75*). Related observations have been made for analogous tRNAs and tDNAs for FeBLM and $Rh(phen)_2(phi)^{3+}$ (*73, 74*), and the relatively higher reactivity of DNA has been noted in other systems (*25, 68*). Our observations suggest that this phenomenon arises from the polar effect of the 2′ hydroxyl group on the resulting 1′ radical or carbocation (*189*). Analogous effects could occur at other positions.

It is possible to use these new principles to target important sites in biopolymers. As discussed earlier, it has been shown using the $Pt_2(pop)_4^{4-}$ binding assay and polyelectrolyte theory that the $Ru(tpy)(bpy)OH_2^{2+}$ complex binds to DNA solely via electrostatics. This observation suggests that the oxidized form might cleave specifically at cation binding sites that are important in nucleic acid folding. Such binding sites have been crystallographically characterized in tRNA (*30, 31, 67*). The $Ru(tpy)(bpy)O^{2+}$ complex does, in fact, cleave tRNA specifically at two sites, both of which correspond to Mg^{2+} binding sites (Fig. 20). These cleavage sites are observed when the tRNA is folded

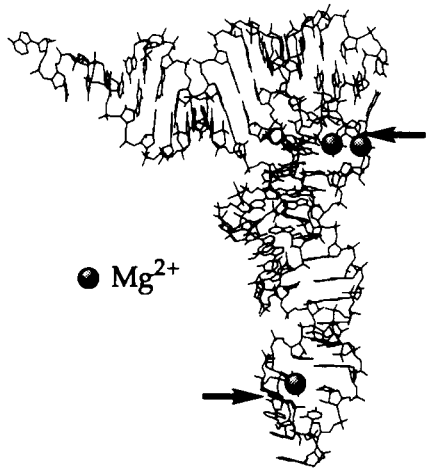

FIG. 20. Two of the Mg^{2+} binding sites that are important in folding of $tRNA^{phe}$ are targeted by $Ru(tpy)(bpy)O^{2+}$, as indicated by the solid arrows. Crystal structure of $tRNA^{phe}$ taken from Jack et al. (*67*).

in high Na^+, and Mg^{2+} is an excellent inhibitor of cleavage. Within the two cleavage sites, the primary oxidations are at guanine, but sugar cleavage occurs at sites that are adjacent to the primary site. No general sugar cleavage is observed as with DNA, which is consistent with the lower reactivity of ribose sugars compared to deoxyribose. This example illustrates how a knowledge of the intimate mechanism of oxidation can lead to useful new methods for determining structures. It is our hope that this work will lead to related advances in targeting DNA with pharmaceutical products, in sensing DNA secondary and tertiary structures, and in understanding mutagenesis and nucleotide metabolism.

ACKNOWLEDGMENTS

For their persistence, creativity, and hard work, I thank current and former undergraduates, graduate students, postdoctorals, and collaborators whose names appear in the citations, especially Greg Neyhart, C.-C. Cheng, Bill Kalsbeck, Tom Welch, Neena Grover, Jim Goll, Suzie Ciftan, Pam Carter, Dean Johnston, Nishi Gupta, Tracy Oriskovich, Klaus Breiner, and Sheila Smith. I also thank the Camille and Henry Dreyfus Foundation, the North Carolina Biotechnology Center, the Burroughs-Wellcome Co., the National Science Foundation, and the David and Lucile Packard Foundation for supporting this work.

References

1. Adams, R. L. P.; Knowler, J. T.; Leader, D. P. "The Biochemistry of the Nucleic Acids"; Chapman & Hall: London, 1992.
2. Smith, M. *Angew. Chem., Int. Ed. Engl.* **1994,** *33,* 1214.
3. Sanger, F. *Annu. Rev. Biochem.* **1988,** *57,* 1.
4. Mullis, K. B. *Angew. Chem., Int. Ed. Engl.* **1994,** *33,* 1209.
5. Feigon, J. *Clin. Chem.* **1994,** *40,* 647.
6. Ellington, A. D. *Curr. Biol.* **1994,** *4,* 427.
7. Lorsch, J. R.; Szostak, T. W. *Biochemistry* **1994,** *33,* 973.
8. Burgstaller, P.; Famulok, M. *Angew. Chem., Int. Ed. Engl.* **1994,** *33,* 1084.
9. Wang, K. Y.; Krawczyk, S. H.; Bischofgerger, N. *Biochemistry* **1993,** *32,* 11285.
10. Uhlenbeck, O. C. *Nature (London)* **1991,** *328,* 596.
11. Piccirilli, J. A.; McConnell, T. S.; Zaug, A. J.; Noller, H. F.; Cech, T. R. *Science* **1992,** *256,* 1420.
12. Piccirilli, J. A.; Vyle, J. S.; Caruthers, M. H.; Cech, T. R. *Nature (London)* **1993,** *361,* 85.
13. Pan, T.; Dichtl, B.; Uhlenbeck, O. C. *Biochemistry* **1994,** *33,* 9561.
14. Adelman, L. M. *Science* **1994,** *266,* 1021.
15. Myers, A. G.; Cohen, S. B.; Kwon, B. M. *J. Am. Chem. Soc.* **1994,** *116,* 1670.
16. Myers, A. G.; Cohen, S. B.; Kwon, B. M. *J. Am. Chem. Soc.* **1994,** *116,* 1255.
17. Stubbe, J.; Kozarich, J. W. *Chem. Rev.* **1987,** *87,* 1107.
18. Hecht, S. M. *Acc. Chem. Res.* **1986,** *19,* 83.
19. Lee, M. D.; Ellestad, G. A.; Borders, D. B. *Acc. Chem. Res.* **1991,** *24,* 235.
20. Nicolaou, K. C.; Smith, A. L. *Acc. Chem. Res.* **1992,** *25,* 497.
21. Steenken, S. *Chem. Rev.* **1989,** *89,* 503.
22. Burstyn, J. N.; Deal, K. A. *Inorg. Chem.* **1993,** *32,* 3585.
23. Pyle, A. M.; Barton, J. K. *Prog. Inorg. Chem.* **1990,** *38,* 413.
24. Burrows, C. J.; Rokita, S. E. *Acc. Chem. Res.* **1994,** *27,* 295.
25. Sigman, D. S. *Acc. Chem. Res.* **1986,** *19,* 180.
26. Pyle, A. M. *Science* **1993,** *261,* 709.
27. Dahm, S. C.; Uhlenbeck, O. C. *Biochemistry* **1991,** *30,* 9464.
28. Dahm, S. C.; Derrick, W. B.; Uhlenbeck, O. C. *Biochemistry* **1993,** *32,* 13040.
29. Quigley, G. J.; Teeter, M. M.; Rich, A. *J. Mol. Biol.* **1978,** *75,* 64.
30. Jack, A.; Ladner, J. E.; Rhodes, D.; Brown, R. S.; Klug, A. *J. Mol. Biol.* **1977,** *111,* 315.
31. Reid, S. S.; Cowan, J. A. *Biochemistry* **1990,** *29,* 6025.
32. Chastain, M.; Tinoco, I., Jr. *Prog. Nucleic Acids Res. Mol. Biol.* **1991,** *41,* 131.
33. Palecek, E. *Crit. Rev. Biochem. Mol. Biol.* **1991,** *26,* 151.
34. Lippard, S. J. *Science* **1993,** *261,* 699.
35. Brown, S. J.; Kellett, P. J.; Lippard, S. J. *Science* **1993,** *261,* 603.
36. Pil, P. M.; Lippard, S. J. *Science* **1992,** *256,* 234.
37. Clarke, M. J. *Met. Ions Biol. Syst.* **1980,** *11,* 231.
38. Holmes, C. E.; Carter, B. J.; Hecht, S. M. *Biochemistry* **1993,** *32,* 4293.
39. Neyhart, G. A.; Kalsbeck, W. A.; Welch, T. W.; Grover, N.; Thorp, H. H. *Adv. Chem. Ser.* **1995,** in press.
40. Sitlani, A.; Long, E. C.; Pyle, A. M.; Barton, J. K. *J. Am. Chem. Soc.* **1992,** 114, 2303.
41. Sugiyama, H.; Tsutsumi, Y.; Fujimoto, K.; Saito, I. *J. Am. Chem. Soc.* **1993,** *115,* 4443.
42. Billadeau, M. A.; Wood, K. V.; Morrison, H. *Inorg. Chem.* **1994,** *33,* 5780.
43. Kasai, H.; Yamgizumi, Z.; Berger, M.; Cadet, J. *J. Am. Chem. Soc.* **1992,** *114,* 9692.

44. Cadet, J.; Berger, M.; Buchko, G. W.; Joshi, P. C.; Raoul, S.; Ravanat, J.-L. *J. Am. Chem. Soc.* **1994,** *116,* 7403.
45. Stubbe, J. *J. Biol. Chem.* **1990,** *265,* 5329.
46. Holm, R. H. *Chem. Rev.* **1987,** *87,* 1401.
47. Lippard, S. J.; Berg, J. M. "Principles of Bioinorganic Chemistry"; University Science Books: Mill Valley, CA, 1994.
48. Kennard, O.; Hunter, W. N. *Angew. Chem., Int. Ed. Engl.* **1991,** *30,* 1254.
49. Coll, M.; Frederick, C. A.; Wang, A. H.-J.; Rich, A. *Proc. Natl. Acad. Sci. USA* **1987,** *84,* 8385.
50. Kuwabara, M.; Yoon, C.; Goyne, T.; Thederahn, T.; Sigman, D. S. *Biochemistry* **1986,** *25,* 7401.
51. Record, M. T., Jr.; Anderson, C. F.; Lohman, T. M. *Q. Rev. Biophys.* **1978,** *11,* 103.
52. Manning, G. S. *Q. Rev. Biophys.* **1978,** *11,* 179.
53. Jayaram, B.; Sharp, K. A.; Honig, B. *Biopolymers* **1989,** *28,* 975.
54. Kalsbeck, W. A.; Thorp, H. H. *Inorg. Chem.* **1994,** *33,* 3427.
55. Kalsbeck, W. A.; Thorp, H. H. *J. Am. Chem. Soc.* **1993,** *115,* 7146.
56. Smith, S. R.; Neyhart, G. A.; Kalsbeck, W. A.; Thorp, H. H. *New J. Chem.* **1994,** *18,* 397.
57. Satyanarayana, S.; Dabrowiak, J. C.; Chaires, J. B. *Biochemistry* **1992,** *31,* 9319.
58. Gessner, R. V.; Quigley, G. J.; Wang, A. H.-J.; van der Marel, G. A.; van Boom, J. H.; Rich, A. *Biochemistry* **1985,** *24,* 237.
59. Sigel, H. *ACS Symp. Ser.* **1989,** *402,* 159.
60. Sigel, H.; Massoud, S. S.; Corfu, N. A. *J. Am. Chem. Soc.* **1994,** *116,* 2958.
61. Krotz, A. H.; Hudson, B. P.; Barton, J. K. *J. Am. Chem. Soc.* **1993,** *115,* 12577.
62. Campisi, D.; Morii, T.; Barton, J. K. *Biochemistry* **1994,** *33,* 4130.
63. Hiort, C.; Lincoln, P.; Nordén, B. *J. Am. Chem. Soc.* **1993,** *115,* 3448.
64. David, S. S.; Barton, J. K. *J. Am. Chem. Soc.* **1993,** *115,* 2984.
65. Collins, J. G.; Shields, T. P.; Barton, J. K. *J. Am. Chem. Soc.* **1994,** *116,* 9840.
66. Dupureur, C. M.; Barton, J. K. *J. Am. Chem. Soc.* **1994,** *116,* 10286.
67. Jack, A.; Ladner, J. E.; Klug, A. *J. Mol. Biol.* **1976,** *108,* 619.
68. Celander, D. W.; Cech, T. R. *Science* **1991,** *251,* 401.
69. Puglisi, J. D.; Wyatt, J. R.; Tinoco, I., Jr. *Acc. Chem. Res.* **1991,** *24,* 152.
70. Puglisi, J. D.; Wyatt, J. R.; Tinoco, I., Jr. *J. Mol. Biol.* **1990,** *214,* 437.
71. Sharp, K. A.; Honig, B.; Harvey, S. C. *Biochemistry* **1990,** *29,* 340.
72. Wyatt, J. R.; Puglisi, J. D.; Tinoco, I., Jr. *J. Mol. Biol.* **1990,** *214,* 455.
73. Holmes, C. E.; Hecht, S. M. *J. Mol. Biol.* **1993,** *268,* 25909.
74. Lim, A. C.; Barton, J. K. *Biochemistry* **1993,** *32,* 11029.
75. Neyhart, G. A.; Cheng, C.-C.; Thorp, H. H. *J. Am. Chem. Soc.* **1995,** *117,* 1463.
76. Lippard, S. J. *Acc. Chem. Res.* **1978,** *11,* 211.
77. Clarke, M. J.; Taube, H. *J. Am. Chem. Soc.* **1974,** *96,* 5413.
78. Grover, N.; Gupta, N.; Thorp, H. H. *J. Am. Chem. Soc.* **1992,** *114,* 3390.
79. Grover, N.; Welch, T. W.; Fairley, T. A.; Cory, M.; Thorp, H. H. *Inorg. Chem.* **1994,** *33,* 3544.
80. Barton, J. K.; Lolis, E. *J. Am. Chem. Soc.* **1985,** *107,* 708.
81. van Vliet, P. M.; Haasnoot, J. G.; Reedijk, J. *Inorg. Chem.* **1994,** *33,* 1934.
82. Oriskovich, T. A.; White, P. S.; Thorp, H. H. *Inorg. Chem.* **1995,** *34,* 1629.
83. Krause, R. A. *Struct. Bonding (Berlin)* **1987,** *67,* 1.
84. Meyer, T. J. *Pure Appl. Chem.* **1986,** *58,* 1193.
85. Kalyanasundaram, K. *Coord. Chem. Rev.* **1982,** *46,* 159.
86. Kumar, C. V.; Barton, J. B.; Turro, N. J. *J. Am. Chem. Soc.* **1985,** *107,* 5518.

87. Baker, A. D.; Morgan, R. J.; Strekas, T. C. *J. Am. Chem. Soc.* **1991,** *113,* 1411.
88. Watts, R. J.; Van Houten, J. *J. Am. Chem. Soc.* **1978,** *100,* 1718.
89. Creutz, C.; Keller, A. D.; Sutin, N.; Zipp, A. P. *J. Am. Chem. Soc.* **1982,** *104,* 3618.
90. Chow, C. S.; Behlen, L. S.; Uhlenbeck, O. C.; Barton, J. K. *Biochemistry* **1992,** *31,* 972.
91. Kirshenbaum, M. R.; Tribolet, R.; Barton, J. K. *Nucleic Acids Res.* **1988,** *16,* 7943.
92. Krotz, A. H.; Kuo, L. Y.; Barton, J. K. *Inorg. Chem.* **1993,** *32,* 5963.
93. Pyle, A. M.; Long, E. C.; Barton, J. K. *J. Am. Chem. Soc.* **1989,** *111,* 4520.
94. Sitlani, A.; Dupureur, C. M.; Barton, J. K. *J. Am. Chem. Soc.* **1993,** *115,* 12589.
95. Hecht, S. M., ed.; "Bleomycin: Chemical, Biochemical and Biological Aspects"; Springer–Verlag: New York, 1979.
96. Dabrowiak, J. C. *Adv. Inorg. Biochem.* **1983,** *4,* 69.
97. Wu, W.; Vanderwall, D. E.; Stubbe, J.; Kozarich, J. W.; Turner, C. J. *J. Am. Chem. Soc.* **1994,** *116,* 10843.
98. Manderville, R. A.; Ellena, J. F.; Hecht, S. M. *J. Am. Chem. Soc.* **1994,** *116.*
99. Van Atta, R. B.; Long, E. C.; Hecht, S. M.; van der Marel, G. A.; van Boom, J. H. *J. Am. Chem. Soc.* **1989,** *111,* 2722.
100. Sam, J. W.; Tang, X.-J.; Peisach, J. *J. Am. Chem. Soc.* **1994,** *116,* 5250.
101. Murugesan, N.; Hecht, S. M. *J. Am. Chem. Soc.* **1985,** *107,* 493.
102. Heimbrook, D. C.; Mulholland, R. L.; Hecht, S. M. *J. Am. Chem. Soc.* **1986,** *108,* 7839.
103. Duff, R. J.; de Vroom, E.; Geluk, A.; Hecht, S. M.; van der Marel, G. A.; van Boom, J. H. *J. Am. Chem. Soc.* **1993,** *115,* 3350.
104. Kozarich, J. W.; Worth, L., Jr.; Frank, B. L.; Christner, D. F.; Vanderwall, D. E.; Stubbe, J. *Science* **1989,** *245,* 1396.
105. Worth, J. L.; Frank, B. L.; Christner, D. F.; Absalon, M. J.; Stubbe, J.; Kozarich, J. W. *Biochemistry* **1993,** *32,* 2601.
106. Guajardo, R. J.; Hudson, S. E.; Brown, S. J.; Mascharak, P. K. *J. Am. Chem. Soc.* **1993,** *115,* 7971.
107. Hamamichi, N.; Natrajan, A.; Hecht, S. M. *J. Am. Chem. Soc.* **1992,** *114,* 6278.
108. Urata, H.; Ueda, Y.; Usami, Y.; Akagi, M. *J. Am. Chem. Soc.* **1993,** *115,* 7135.
109. Brown, S. J.; Mascharak, P. K.; Stephan, D. W. *J. Am. Chem. Soc.* **1988,** *110,* 1996.
110. Brown, S. J.; Hudson, S. E.; Mascharak, P. K.; Olmstead, M. M. *J. Am. Chem. Soc.* **1989,** *111,* 6446.
111. Brown, S. J.; Hudson, S. E.; Stephan, D. W.; Mascharak, P. K. *Inorg. Chem.* **1989,** *28,* 468.
112. Tan, J. D.; Hudson, S. E.; Brown, S. J.; Olmstead, M. M.; Mascharak, P. K. *J. Am. Chem. Soc.* **1992,** *114,* 3841.
113. Sugiura, Y.; Suzuki, T.; Otsuka, M.; Kobayashi, S.; Ohno, M.; Takita, T.; Umezawa, H. *J. Biol. Chem.* **1983,** 258.
114. Ehrenfeld, G. M., *et al. Biochemistry* **1987,** *26,* 931.
115. Albertini, J. P.; Garner-Suillerot, A. *Biochemistry* **1982,** *21,* 6777.
116. Sugiura, Y. *J. Am. Chem. Soc.* **1980,** *102,* 5216.
117. Chang, C. H.; Meares, C. F. *Biochemistry* **1982,** *21,* 6332.
118. Sugiura, Y.; Kuwahara, J.; Suzuki, T. *FEBS Lett.* **1985,** *182,* 39.
119. Meyer, T. J. *J. Electrochem. Soc.* **1984,** *131,* 221C.
120. Takeuchi, K. J.; Thompson, M. S.; Pipes, D. W.; Meyer, T. J. *Inorg. Chem.* **1984,** *23,* 1845.
121. Welch, T. W.; Thorp, H. H., submitted for publication.
122. Cheng, W.-C.; Yu, W.-Y.; Cheung, K.-K.; Che, C.-M. *J. Chem. Soc., Dalton Trans.* **1994,** 57.

123. Gupta, N.; Grover, N.; Neyhart, G. A.; Liang, W.; Singh, P.; Thorp, H. H. *Angew. Chem., Int. Ed. Engl.* **1992,** *31,* 1048.
124. Gupta, N.; Grover, N.; Neyhart, G. A.; Singh, P.; Thorp, H. H. *Inorg. Chem.* **1993,** *32,* 310.
125. Grover, N.; Gupta, N.; Singh, P.; Thorp, H. H. *Inorg. Chem.* **1992,** *31,* 2014.
126. Seok, W. K., Ph. D. thesis, University of North Carolina at Chapel Hill, 1988.
127. Thompson, M. S.; Meyer, T. J. *J. Am. Chem. Soc.* **1982,** *104,* 4106.
128. Dobson, J. C.; Seok, W. K.; Meyer, T. J. *Inorg. Chem.* **1986,** *25,* 1513.
129. Roecker, L.; Kutner, W.; Gilbert, J. A.; Simmons, M.; Murray, R. W.; Meyer, T. J. *Inorg. Chem.* **1985,** *24,* 3784.
130. Stultz, L. K.; Binstead, R. A.; Reynolds, M. S.; Meyer, T. J. *J. Am. Chem. Soc.* **1995,** *117,* 2520.
131. Roundhill, D. M; Gray, H. B; Che, C.-M. *Acc. Chem. Res.* **1989,** *22,* 55.
132. Stiegman, A. E.; Rice, S. F.; Gray, H. B. *Inorg. Chem.* **1987,** *26,* 1112.
133. Sperline, R. P.; Dickson, M. K.; Roundhill, D. M. *J. Chem. Soc. Chem. Commun.* **1977,** *62.*
134. Vlcek, A. A.; Gray, H. B. *J. Am. Chem. Soc.* **1987,** *109,* 286.
135. Harvey, E. L.; Stiegman, A. E.; Vlcek, A. A.; Gray, H. B. *J. Am. Chem. Soc.* **1987,** *109,* 5233.
136. Theil, E. C. *New J. Chem.* **1993,** *18,* 435.
137. Barton, J. K. In "Bioinorganic Chemistry"; Bertini, I., Gray, H. B., Lippard, S. J., Valentine, J. S. Eds.; University Science Books: Mill Valley, CA, 1994; 505–584.
138. Tullius, T. D. *Annu. Rev. Biophys. Biophys. Chem.* **1989,** *18,* 213.
139. Dervan, P. B. *Science* **1986,** *232,* 464.
140. Riordan, C. G.; Wei, P. *J. Am. Chem. Soc.* **1994,** *116,* 2189.
141. Muller, J. G.; Chen, X.; Dadiz, A. C.; Rokita, S. E.; Burrows, C. J. *J. Am. Chem. Soc.* **1992,** *114,* 6407.
142. Groves, J. T.; Farrell, T. P. *J. Am. Chem. Soc.* **1989,** *111,* 4998.
143. Bernadou, J.; Pratviel, G.; Bennis, F.; Girardet, M.; Meunier, B. *Biochemistry* **1989,** *28,* 7268.
144. Pitié, M.; Casas, C.; Lacey, C. J.; Pratviel, G.; Bernadou, J.; Meunier, B. *Angew. Chem., Int. Ed. Engl.* **1993,** *32,* 557.
145. Sigman, D. S.; Bruice, T. W.; Mazumder, A.; Sutton, C. L. *Acc. Chem. Res.* **1993,** *26,* 98.
146. Barton, J. K. *J. Biomol. Struct. Dyn.* **1993,** *1,* 621.
147. Barton, J. K.; Danishefsky, A. T.; Goldberg, J. M. *J. Am. Chem. Soc.* **1984,** *106,* 2172.
148. Barton, J. K. *Comments Inorg. Chem.* **1985,** *3,* 321.
149. Barton, J. K.; Goldberg, J. M.; Kumar, C. V.; Turro, N. J. *J. Am. Chem. Soc.* **1986,** *108,* 2081.
150. Goldstein, B. M.; Barton, J. K.; Berman, H. M. *Inorg. Chem.* **1986,** *25,* 842.
151. Orellana, G.; Kirsch-De Mesmaeker, A.; Barton, J. K.; Turro, N. J. *Photochem. Photobiol.* **1991,** *54,* 499.
152. Pyle, A. M.; Rehmann, J. P.; Meshoyrer, R.; Kumar, C. V.; Turro, N. J.; Barton, J. K. *J. Am. Chem. Soc.* **1989,** *111,* 3051.
153. Tysoe, S. A.; Morgan, R. J.; Baker, A. D.; Strekas, T. C. *J. Phys. Chem.* **1993,** *97,* 1707.
154. Lecomte, J.-P.; Kirsch-De Mesmaeker, A.; Orellana, G. *J. Phys. Chem.* **1994,** *98,* 5382.
155. Barton, J. K.; Basile, L. A.; Danishefsky, A.; Alexandrescu, A. *Proc. Natl. Acad. Sci. USA* **1984,** *81,* 1961.
156. Kelly, J. M.; Tossi, A. M.; McConnell, D. J.; OhUigin, C. *Nucleic Acids Res.* **1985,** *13,* 6017.

157. Meyer, T. J. *Chem. Rev.* **1995,** in press.
158. Kalyanasundaram, K. "Photochemistry in Microheterogeneous Systems"; Academic Press: London, 1987.
159. Friedman, A. E.; Chambron, J. C.; Sauvage, J. P.; Turro, N. J.; Barton, J. K. *J. Am. Chem. Soc.* **1990,** *112,* 4960.
160. Jenkins, Y.; Friedman, A. E.; Turro, N. J.; Barton, J. K. *Biochemistry* **1992,** *31,* 10809.
161. Barton, J. K.; Kumar, C. V.; Turro, N. J. *J. Am. Chem. Soc.* **1986,** *108,* 6391.
162. Purugganan, M. D.; Kumar, C. V.; Turro, N. J.; Barton, J. K.; *Science* **1988,** *241,* 1645.
163. Elmroth, S. K. C.; Lippard, S. J. *J. Am. Chem. Soc.* **1994,** *117,* 3633.
164. Murphy, C. J.; Arkin, M. R.; Ghatalia, N. D.; Bossman, S.; Turro, N. J.; Barton, J. K. *Proc. Natl. Acad. Sci. USA* **1994,** *91,* 5315.
165. Murphy, C. J.; Arkin, M. R.; Jenkins, Y.; Ghatlia, N. D.; Bossmann, S. H. Turro, N. J.; Barton, J. K. *Science* **1993,** *262,* 1025.
166. Meade, T. J.; Kayyem, J. F. *Angew. Chem., Int. Ed. Engl.* **1995,** *34,* 352.
167. Moser, C. C.; Keske, J. M.; Warncke, K.; Farid, R. S.; Dutton, P. L. *Nature (London)* **1992,** *355,* 796.
168. Wuttke, D. S.; Gray, H. B. *Curr. Opin. Struct. Biol.* **1993,** *3,* 555.
169. Risser, S. M.; Beratan, D. N.; Meade, T. J. *J. Am. Chem. Soc.* **1993,** *115,* 2508.
170. McLendon, G.; Hake, R. *Chem. Rev.* **1992,** *92,* 481.
171. Carter, M. T.; Rodriguez, M.; Bard, A. J. *J. Am. Chem. Soc.* **1989,** *111,* 8901.
172. Braunlin, W. H.; Anderson, C. F.; Record, M. T. *Biochemistry* **1987,** *26,* 7724.
173. Sugiyama, H.; Xu, C.; Murugesan, N.; Hecht, S. M.; van der Marel, G. A.; van Boom, J. H. *Biochemistry* **1988,** *27,* 58.
174. Sugiyama, H.; Tsutsumi, Y.; Saito, I. *J. Am. Chem. Soc.* **1990,** *112,* 6720.
175. Kalsbeck, W. A.; Grover, N.; Thorp, H. H. *Angew. Chem., Int. Ed. Engl.* **1991,** *30,* 1517.
176. Sehlstedt, U.; Kim, S. K.; Carter, P.; Goodisman, J.; Vollano, J. F.; Nordén, B.; Dabrowiak, J. C. *Biochemistry* **1994,** *33,* 417.
177. Bryan, S. A.; Dickson, M. K.; Roundhill, M. D. *Inorg. Chem.* **1987,** *26,* 3878.
178. Kalsbeck, W. A.; Gingell, D. M.; Malinsky, J. E. *Inorg. Chem.* **1994,** *33,* 3313.
179. Che, C. M.; Mak, T. C. W.; Miskowski, V. M.; and Gray, H. B. *J. Am. Chem. Soc.* **1986,** *108,* 7840.
180. Yam, V. W.-W.; Che, C.-M.; Tang, W.-T. *J. Chem. Soc., Chem. Commun.* **1988,** 100.
181. Peterson, J. R.; Kalyanasundaram, K. *J. Phys. Chem.* **1985,** *89,* 2486.
182. Chen, X.; Burrows, C. J.; Rokita, S. E. *J. Am. Chem. Soc.* **1992,** *114,* 322.
183. Chen, X.; Burrows, C. J.; Rokita, S. E. *J. Am. Chem. Soc.* **1991,** *113,* 5884.
184. Neyhart, G. A.; Grover, N.; Smith, S. R.; Kalsbeck, W. A.; Fairley, T. A.; Cory, M.; Thorp, H. H. *J. Am. Chem. Soc.* **1993,** *115,* 4423.
185. Welch, T. W.; Neyhart, G. A.; Goll, J. G.; Ciftan, S. A.; Thorp, H. H. *J. Am. Chem. Soc.* **1993,** *116,* 9311.
186. Cheng, C.-C; Goll, J. G.; Neyhart, G. A.; Welch, T. W.; Singh, P.; Thorp, H. H. *J. Am. Chem. Soc.* **1995,** *117,* 2970.
187. Goyne, T. E.; Sigman, D. S. *J. Am. Chem. Soc.* **1987,** *109,* 2846.
188. Miaskiewicz, K.; Osman, R. *J. Am. Chem. Soc.* **1993,** *116,* 232.
189. Giese, B. *Angew. Chem., Int. Ed. Engl.* **1983,** *22,* 753.
190. Dovletoglou, A.; Meyer, T. J. *J. Am. Chem. Soc.* **1994,** *116,* 215.
191. Pavlov, Y. I.; Minnick, D. T.; Izuta, S.; Kunkel, T. A. *Biochemistry* **1994,** *33,* 4695.
192. Chen, X.; Woodson, S. A.; Burrows, C. J.; Rokita, S. E. *Biochemistry* **1993,** *32,* 7610.

193. Cheng, C.-C.; Thorp, H. H. **1994,** unpublished results.
194. Thompson, M. S.; DeGiovani, W. F.; Moyer, B. A.; Meyer, T. J. *J. Org. Chem.* **1984,** *49,* 4972.
195. Subramanian, P.; Dryhurst, G. *J. Electroanal. Chem.* **1987,** *224,* 167.
196. Palecek, E.; Fojta, M. *Anal. Chem.* **1994,** *66,* 1566.
197. Federova, O. S.; Podust, L. M. *J. Inorg. Biochem.* **1988,** *34,* 149.
198. Carter, M. J.; Bard, A. J. *J. Am. Chem. Soc.* **1987,** *109,* 7528.
199. Johnston, D. H.; Cheng, C.-C.; Campbell, K. J.; Thorp, H. H. *Inorg. Chem.* **1994,** *33,* 6388.
200. Johnston, D. H.; Glasgow, K. C.; Thorp, H. H. *J. Am. Chem. Soc.,* in press.
201. Aruoma, O. I.; Halliwell, B.; Gajewski, E.; Dizdaroglu, M. *Biochem. J.* **1991,** *273,* 601.
202. McCleskey, T. M.; Winkler, J. R.; Gray, H. B. *J. Am. Chem. Soc.* **1992,** *114,* 6935.

ADVANCES IN INORGANIC CHEMISTRY, VOL. 43

MAGNETISM OF HETEROBIMETALLICS: TOWARD MOLECULAR-BASED MAGNETS

OLIVIER KAHN

Laboratoire de Chimie Inorganique, URA CNRS n° 420, Université de Paris-Sud, 91405 Orsay, France[1]

[1] Present address: Institut de Chimie de la Matière Condensée de Bordeaux, Laboratoire des Sciences Moléculaires, avenue du Docteur Schweitzer, 33608 Pessac, France.

Copyright © 1995 by Academic Press, Inc.
All rights of reproduction in any form reserved.

I. Introduction

Molecular magnetism has emerged as a novel field of research over the last two decades. This field concerns the chemistry and the physics of open-shell molecules and molecular assemblies containing open-shell units. The first textbook devoted entirely to this subject was published in 1993 (*1*). In 1975, the main facets of molecular magnetism may be summarized as follows:

(i) Design of open-shell molecules, the main emphasis being on molecules containing at least two magnetic centers. These spin carriers may be transition metal ions as well as purely organic radicals.

(ii) Determination of the spectra of the low-lying states for such open-shell molecules, using various techniques such as magnetic susceptibility and magnetization measurements, EPR and optical spectroscopies, or inelastic neutron scattering.

(iii) Determination of spin density maps through polarized neutron diffraction.

(iv) Theoretical interpretation of the experimental data concerning both low-lying state spectra and spin density maps.

(v) Chemistry and physics of transition metal compounds exhibiting a spin conversion or spin transition between two different spin states.

(vi) The relations among magnetic properties, structure, and reactivity of metalloenzymes and model compounds. This facet may be defined as biomagnetism.

(vii) Three-dimensional effects in molecular assemblies containing open-shell units. The main issues deal with molecular-based compounds exhibiting a spontaneous magnetization below a critical temperature T_c, and spin-transition compounds exhibiting abrupt transitions with hysteresis effects. Both types of compounds may potentially be used for storing information.

(viii) Incorporation of such magnetic molecular assemblies in genuine devices, or for a first time in demonstrators.

What characterizes molecular magnetism is its interdisciplinary nature. It has already been pointed out that molecular magnetism has common frontiers with quite a few other area such as supramolecular chemistry, theoretical chemistry and physics, material and life sciences, and molecular electronics (*1*).

Among all molecules and molecular assemblies relevant to molecular magnetism, those containing two (or possibly more) kinds of metal ions have played a particularly important role. Two facts, at least, justify this situation. First, the types of interactions between two spin carriers A and B within a molecular unit are much more diverse when A and B are different. For instance, the strict orthogonality of the magnetic orbitals leading to the stabilization of the molecular state of highest spin multiplicity is much easier to achieve in heterobimetallic than in homobimetallic species (*2*). Secondly, with several kinds of magnetic centers, it is possible to design molecular lattices showing quite peculiar spin topologies. In particular, the case of ferrimagnetic lattices will be much discussed in this article.

In 1987 we published the first review on the magnetism of heteropolymetallic systems (*3*). This article was largely devoted to the mechanism of the interaction in heterobinuclear complexes. The field of heteropolymetallic compounds was covered up to the first attempts to obtain molecular-based magnets. The very last sentence of this article was: "One may anticipate that in a few years another review will be necessary, and that its main emphasis will be on systems of higher nuclearity and extended systems with subtle spin orders." In the present case, our prediction was quite correct, which is not so frequent in science. The field of heterobimetallic systems has developed tremendously since 1987, particularly in relation to the synthesis of molecular-based magnets. It is now timely to write a second review concerning this topic.

This new review does not follow the same plan as the former one, but is organized around the central theme of bimetallic magnets. The next section reviews some key concepts in molecular magnetism, such as spin delocalization and spin polarization, and then treats of the interaction between two spin carriers. Each subsequent section, from III to VII, is devoted to one type of bridge. Within a given section, the various compounds are presented in order of increasing nuclearity and dimensionality—i.e., binuclear, trinuclear, . . . , one-, two-, and three-dimensional structures. The goal of this paper is not at all to be exhaustive, but rather to focus on the bridges which have already allowed the

design of molecular-based magnets. To date, these bridges are oxamato, oxamido, oxalato, dithiooxalato, oximato, and cyano. The final section is a brief perspective on this field of research.

II. Interaction between Metal Ions in Polynuclear Molecules

The mechanism of the interaction between two metal ions within a binuclear molecule has been discussed in several review articles and books, which we invite the reader to refer to if necessary (*1, 4–10*). We restrict ourselves here to a brief review of some key concepts.

A. Spin Delocalization and Spin Polarization in Molecules with a Unique Spin Carrier

Before considering polymetallic molecules, it is interesting to take a quick look to molecules containing a unique magnetic ion. Let us assume that this metal ion carries n unpaired electrons. In molecular orbital theory, at the self-consistent field (SCF) level, these unpaired electrons in the ground state are described by the n highest occupied molecular orbitals, assuming that there is no orbital degeneracy. These orbitals may be partially delocalized toward the ligands, which accounts for spin delocalization. The spin density is positive not only on the metal ion, but also in some regions of space surrounding this metal ion. Let us present an example of spin delocalization, concerning a dianion, $[Cu(pbaOH)]^{2-}$ [pbaOH = 2-hydroxy-1,3-propylenebis(oxamato)] which we will discuss again later. The Cu(II) ion is surrounded

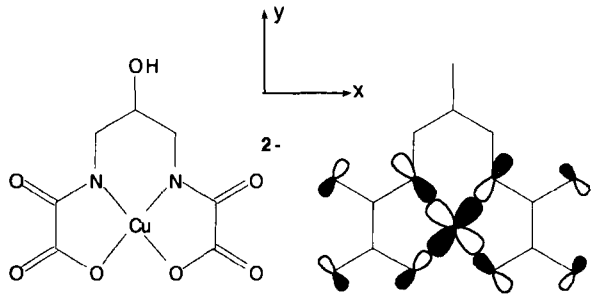

by two nitrogen and two oxygen atoms belonging to oxamato groups. The unpaired electron arising from the Cu(II) ion in such planar surroundings occupies an xy-type orbital pointing toward the Cu–N and

Cu–O directions. Moreover, the N–C–O and O–C–O linkages are conjugated. It follows that the spin density is delocalized not only toward the four atoms bound to Cu(II), but also along the N–C–O and O–C–O bonds. This delocalization is a bit more pronounced along the N–C–O than along the O–C–O linkages; the $2p$ valence orbitals of nitrogen are more diffuse than the $2p$ valence orbitals of oxygen, so that the $3d_{xy}$(Cu)–$2p$(N) overlaps are more pronounced than the $3d_{xy}$–$2p$(O) overlaps (*11*).

At the SCF level, the spin density for open-shell molecules carrying n unpaired electrons is positive or zero in any point of space; it cannot be negative. However, it is well known from magnetic resonance spectroscopies (EPR and NMR) or polarized neutron diffraction studies that the spin density in some regions of space may be negative. This phenomenon is called spin polarization; its theoretical interpretation requires going beyond the SCF approximation and taking into account the electron correlation in a more rigorous manner. One of the ways to do so is to perform a configuration interaction, i.e., to mix the SCF ground state with excited states of the same symmetry (*1, 12*). Theoretical calculations beyond the SCF approximation on $[Cu(pbaOH)]^{2-}$ predict negative spin densities around the carbon atoms of the oxamato groups. Such negative spin densities were found through polarized neutron diffraction in the trivalent hexacyanometallates $[M(CN)_6]^{3-}$ (*13–15*).

When the number n of unpaired electrons is greater than 1, the local spin S is larger than $\frac{1}{2}$, and another phenomenon must be considered: the local anisotropy which partially removes the $2S + 1$ degeneracy of the spin state in zero applied magnetic field. This zero-field splitting gives rise to Kramers doublets when S is a half integer, and to nondegenerate levels when S is an integer, provided that the local symmetry is low enough. The origin of the phenomenon is the synergistic effect between spin–orbit coupling and distortion around the metal ion. The phenomenological Hamiltonian accounting for this zero-field splitting is

$$\mathbf{H}_{ZFS} = \mathbf{S} \cdot \mathbf{D} \cdot \mathbf{S}, \tag{1}$$

where $\mathbf{S}$ is the spin operator and $\mathbf{D}$ is traceless tensor.

B. The Concept of the Magnetic Orbital and of Overlap Density in an A–B Binuclear Molecule

Let us consider an A–B binuclear molecule where A and B stand for metal ions carrying n_A and n_B unpaired electrons, respectively. The

local spins are $S_A = n_A/2$ and $S_B = n_B/2$. At first we neglect the interaction between A and B. The n_A unpaired electrons occupy n_A orbitals, noted a_μ, centered on A, and partially delocalized toward the terminal and bridging ligands surrounding A. Similarly the n_B unpaired electrons occupy n_B orbitals, noted b_ν, centered on B, and partially delocalized toward the terminal and bridging ligands surrounding B. The indices μ and ν refer to the site symmetries. These orbitals a_μ and b_ν, which are neither molecular nor atomic orbitals, are called "natural magnetic orbitals" (*1*). What is crucial is that two magnetic orbitals a_μ and b_ν in general are delocalized toward the same bridging network, so that they may overlap. In other terms, the overlap density $\rho_{\mu\nu}(i)$, defined by

$$\rho_{\mu\nu}(i) = a_\mu(i)b_\nu(i), \tag{2}$$

may be important in the bridging region. The interaction between A and B is governed by the overlap densities between pairs of magnetic orbitals, as expressed in Eq. (2).

C. Isotropic Interaction in an A–B Binuclear Molecule

The isotropic interaction between A and B gives rise to low-lying pair states characterized by a molecular spin S varying from $|S_A - S_B|$ to $S_A + S_B$ by an integer value. The spin Hamiltonian accounting for this isotropic interaction may be written as

$$\mathbf{H} = -J\mathbf{S}_A \cdot \mathbf{S}_B, \tag{3}$$

where J is the isotropic interaction parameter. Positive J corresponds to an antiferromagnetic interaction; the ground state is characterized by $S = |S_A - S_B|$, and the most excited state by $S = S_A + S_B$. Negative J corresponds to a ferromagnetic interaction; the spectrum of the low-lying states is inverted, the ground state having the highest spin. J in (3) may be expressed as (*16*)

$$J = \frac{2}{n_A n_B} \sum_{\mu,\nu} J_{\mu\nu}, \tag{4}$$

where the $J_{\mu\nu}$'s are contributions involving pairs of magnetic orbitals. Ignoring the spin polarization results in the expression of $J_{\mu\nu}$:

$$J_{\mu\nu} = 2k_{\mu\nu} + 4\beta_{\mu\nu}S_{\mu\nu}, \tag{5}$$

with

$$\begin{aligned} k_{\mu\nu} &= \langle a_\mu(i)b_\nu(j)|1/r_{ij}|a_\mu(j)b_\nu(i)\rangle, \\ S_{\mu\nu} &= \langle a_\mu(i)|b_\nu(i)\rangle, \\ \beta_{\mu\nu} &= \langle a_\mu(i)|\mathbf{h}(i)|b_\nu(j)\rangle. \end{aligned} \tag{6}$$

$\mathbf{h}(i)$ is a one-electron Hamiltonian taking into account the kinetic energy of electron i and its interaction with the nuclei and the core electrons. Equation (5) is valid when the square of the overlap integral, $S_{\mu\nu}{}^2$, is neglected as compared to unity. The two-electron exchange integral, $k_{\mu\nu}$, is always positive, or zero when the overlap density $\rho_{\mu\nu}(i)$ is vanishingly small in any point of space, so that the first term in the right-hand side of Eq. (5) is a ferromagnetic contribution. In contrast, $\beta_{\mu\nu}$ and $S_{\mu\nu}$ have opposite signs, so that the second term of Eq. (5) is an antiferromagnetic contribution. When a_μ and b_ν have the same symmetry, the term $4\beta_{\mu\nu}S_{\mu\nu}$ most often dominates, and $J_{\mu\nu}$ is negative. The reverse situation holds when a_μ and b_ν do not transform as the same irreducible representation of the point group describing the symmetry properties of A–B. $S_{\mu\nu}$ and $\beta_{\mu\nu}$ are then zero; the two magnetic orbitals are said to be orthogonal. The magnitude of $J_{\mu\nu}$ then depends on the extrema of the overlap density $\rho_{\mu\nu}(i)$.

This model of the isotropic interaction in A–B, based on the concepts of natural magnetic orbitals and overlap densities between pairs of such orbitals, allows to analyze most of the situations. It is utilized extensively in the remainder of this paper.

D. Interaction between Heterobinuclear Molecules

Until now, we have focused on the intramolecular interaction within an A–B heterobinuclear molecule. In this section we present briefly some fundamental ideas concerning the interaction between two such heterobinuclear units within a crystal lattice. There are numerous applications of these ideas in the remainder of this article.

In molecular magnetism we are concerned not only with local spins associated with metal ions (or organic radicals), but also with molecular spins associated with open-shell molecular units as a whole. It turns out that the interaction between two such molecular units may not be of the same nature as the interaction between two metal ions, one

belonging to a molecular unit, the other one belonging to the other molecular unit. Figure 1 illustrates this situation in the simple case of two adjacent binuclear units A–B, with local spins $S_A > S_B$. The intramolecular interaction is assumed to be antiferromagnetic with a $S_g = S_A - S_B$ ground state, and to be much larger than the intermolecular interactions noted A---A, B---B, or A---B. This latter assumption is in line with the concept of assemblies of open-shell molecules in which the intramolecular effects are more pronounced than the intermolecular ones. In the low-temperature range where kT is much smaller than the absolute value of the intramolecular interaction parameter J, only the $S = S_g$ ground state is thermally populated. If the intermolecular interactions were negligibly weak, the magnetic behavior of A–B for $kT \ll |J|$ would be that of a $S = S_g$ isolated local spin. Non-negligible intermolecular interactions may modify this situation.

In Fig. 1a, the antiferromagnetic (AF) interaction A---A favors the AF interaction between the S_g molecular spins. In 1b, the AF interaction A---B favors a ferromagnetic (F) interaction between the molecular spins. In 1c, the F interaction A---A favors an F interaction between the molecular spins. In 1d, finally, the F interaction A---B favors the AF interaction between the molecular spins. The situation in Fig. 1b is by far the most interesting. We have seen that it is much easier to create an antiferro- than a ferromagnetic interaction between two spin carriers. This is true for both intra- and intermolecular interactions.

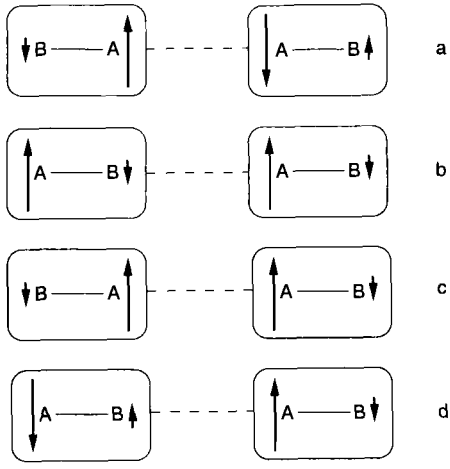

FIG. 1. Spin interactions between two heterobinuclear units. From Baron *et al.* (*24*).

The spin topology schematized in Fig. 1b suggests a strategy to realize the parallel alignment of molecular spins at the scale of a lattice.

To finish this short discussion, we stress that the extremely simple ideas visualized in Fig. 1 sometimes quite surprise solid-state chemists or physicists who do not feel that the presence of molecules gives rise to original situations.

The presence of a large positive spin density around A and a weaker (in absolute value) negative spin density around B in the A–B molecule schematized in Fig. 1 was assumed to arise from an intramolecular antiferromagnetic interaction. In some molecules containing a unique spin carrier, large positive and weak negative spin densities may arise from spin polarization effects (see Section II,A). Ferromagnetic intermolecular interactions may again be achieved if the weak negative spin density of a molecule interacts preferably with the large positive spin density of the nearest neighbor molecule. Such a mechanism of intermolecular ferromagnetic interaction was first proposed by McConnell (*17*), and then invoked for several compounds containing organic radicals (*18–21*).

III. Oxamato-Bridged Heterobimetallic Compounds

The first oxamato-bridged compounds were mentioned in the review article of 1987 (*3*). Since then, quite a few other compounds have been described, including several molecular-based magnets. All those compounds were synthesized from the copper(II) precursors $[Cu(pba)]^{2-}$, $[Cu(pbaOH)]^{2-}$, and $[Cu(opba)]^{2-}$ shown in Fig. 2; pba stands for 1,3-propylenebis(oxamato), pbaOH stands for 2-hydroxy-1,3-propylenebis(oxamato), and opba stands for *ortho*-phenylenebis(oxamato).

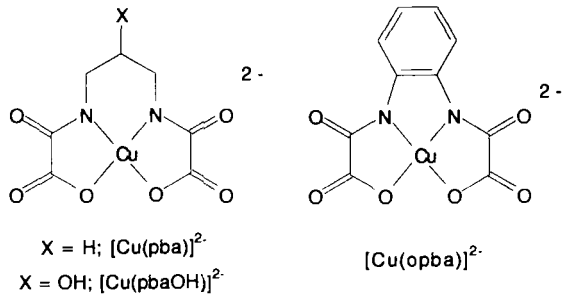

FIG. 2. Copper(II) precursors for oxamato-bridged polynuclear species.

A. Ni(II)Cu(II) Binuclear and Ni(II)Cu(II)Ni(II) Trinuclear Species

To our knowledge, there is only one report of an oxamato-bridged heterobinuclear compound, and its structure has not been determined (*22*). Its formula is $[Ni(bapa)(H_2O)Cu(pba)] \cdot 2H_2O$, with bapa = bis(3-aminopropyl). Its magnetic properties are characteristic of a Ni(II)-Cu(II) pair with a doublet ground state and a quartet excited state, and doublet-quartet energy gap being equal to $3J/2 = -141.9\ cm^{-1}$.

The reaction of $[Cu(pba)]^{2-}$ with Ni(II) perchlorate in the presence of bapa also affords a trinuclear species of formula $\{[Ni(bapa)(H_2O)]_2Cu(pba)\}(ClO_4)_2$. The structure of the trinuclear cation is shown in Fig. 3. The nickel atoms are in a distorted octahedral environment, and the copper atom in an environment markedly distorted from square planar to tetrahedral. The average value of the Cu---Ni separation through the oxamato bridge is equal to 5.31 Å.

The magnetic susceptibility data of the compound are represented in Fig. 4 in the form of the $\chi_M T$ vs T plot, χ_M being the molar magnetic susceptibility and T the temperature. The curve exhibits a rounded minimum around 100 K.

The spin Hamiltonian appropriate to interpret the magnetic data is

$$\mathbf{H} = -J\mathbf{S}_{Cu} \cdot (\mathbf{S}_{Ni1} + \mathbf{S}_{Ni2}) + \mathbf{S}_{Ni1} \cdot \mathbf{D}_{Ni} \cdot \mathbf{S}_{Ni1} + \mathbf{S}_{Ni2} \cdot \mathbf{D}_{Ni} \cdot \mathbf{S}_{Ni2} + \beta[g_{Ni}(\mathbf{S}_{Ni1} + \mathbf{S}_{Ni2}) + g_{Cu}\mathbf{S}_{Cu}] \cdot H, \quad (7)$$

where J is the isotropic interaction parameter between nearest-neighbor Cu(II) and Ni(II) ions, $\mathbf{D}_{Ni}$ is the local anisotropy tensor for the

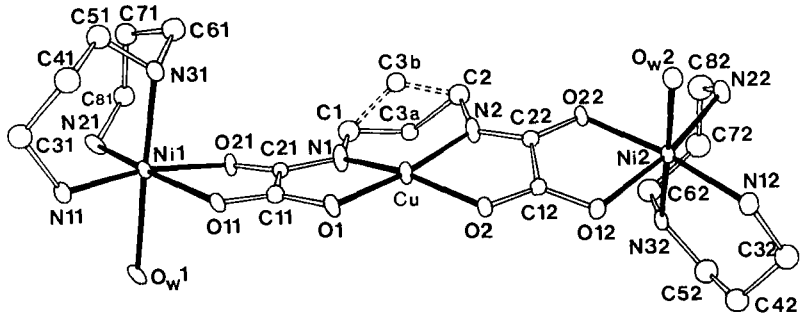

FIG. 3. Structure of the trinuclear cation $\{[Ni(bapa)(H_2O)]_2Cu(pba)\}^{2+}$, with bapa = bis(3-aminopropyl). Reprinted from Ribas *et al.* (*22*). Copyright © 1990 American Chemical Society.

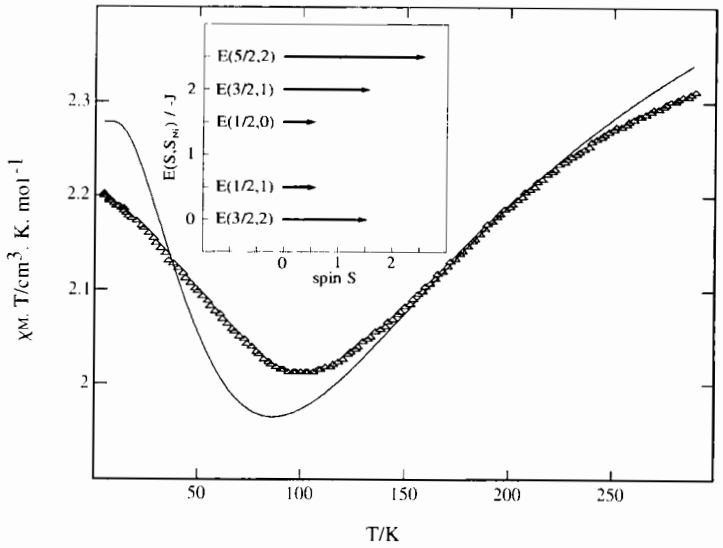

FIG. 4. $\chi_M T$ vs T curve and spin state structure for $\{[Ni(bapa)(H_2O)]_2Cu(pba)\}(ClO_4)_2$; ($\triangle$) experimental data, (—) calculated curve. In the spin state structure, each low-lying state is represented by an arrow, the length of which is equal to the spin S. Reprinted from Ribas *et al.* (*22*). Copyright © 1990 American Chemical Society.

Ni(II) ions, and g_{Ni} and g_{Cu} are the local Zeeman factors for Ni(II) and Cu(II) ions, respectively, assumed to be isotropic. The energies $E(S, S_{Ni})$ of the low-lying spin states depend on the quantum numbers S and S_{Ni} associated with the spin operators:

$$\mathbf{S}_{Ni} = \mathbf{S}_{Ni1} + \mathbf{S}_{Ni2},$$
$$\mathbf{S} = \mathbf{S}_{Ni} + \mathbf{S}_{Cu}. \tag{8}$$

They are found as shown in Fig. 4, where each spin state is represented by an arrow of which the length is equal to the spin S. The spin state structure is irregular in the sense that the energy of the states does not vary linearly with the spin. The ground state is the quartet $E(\frac{3}{2}, 2)$. When going up in energy, the spin S first decreases, then increases, the most excited state being the state with the highest spin. This irregularity of the spin state structure leads to the minimum observed in the $\chi_M T$ vs T plot (*23*). The fitting of the magnetic data leads to $J = -90.3$ cm^{-1}, which seems to be a classical value for the Ni(II)–Cu(II) interaction through the oxamato bridge. In the present case, the $\chi_M T$

vs T plot is weakly sensitive to the Ni(II) local anisotropy, which consequently cannot be determined from the magnetic data.

B. Mn(II)Cu(II) Chain Compounds

We will speak first of the compounds obtained with the [Cu(pbaOH)]$^{2-}$ precursor, then of those obtained with [Cu(opba)]$^{2-}$.

1. *Mn(II)Cu(II) Chain Compounds Obtained from the [Cu(pbaOH)]$^{2-}$ Precursor*

Three compounds have been obtained in the Mn(II)–[Cu(pbaOH)]$^{2-}$ system. The slow diffusion of two aqueous solutions containing Na_2[Cu(pbaOH)] and Mn(II) perchlorate, respectively, affords two kinds of crystals, of which the formulas are MnCu(pbaOH)$(H_2O)_3 \cdot 2H_2O$ and MnCu(pbaOH)$(H_2O)_3$, respectively (*24–26*). The structure of both compounds consists of oxamato-bridged Mn(II)Cu(II) linear chains, as shown in Fig. 5. The difference between the two structures concerns the interchain interactions, as emphasized in Fig. 6. In the former compound, the chains run along the a axis of a monoclinic lattice. Along the other two crystallographic directions, the shortest interchain metal---metal separations involve metal ions of the same nature. In the latter compound, crystallizing in an orthorhombic lattice, along one of the crystallographic directions perpendicular to the chain axis,

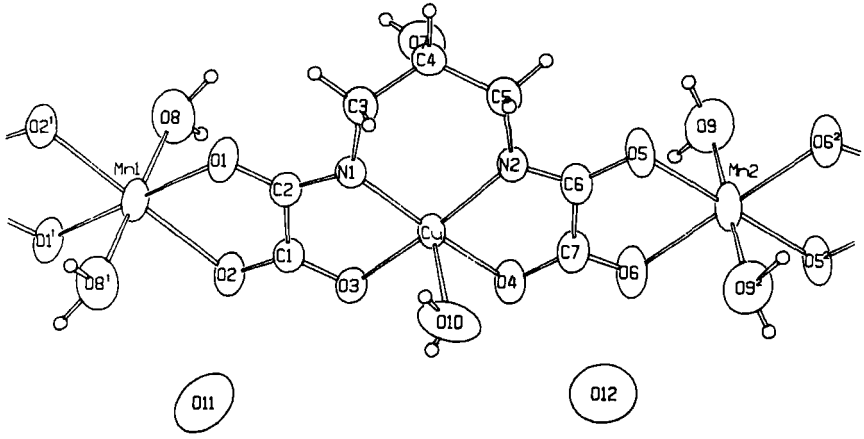

FIG. 5. Structure of the chain compound MnCu(pbaOH)$(H_2O)_3 \cdot 2H_2O$. The structure of the chain in MnCu(pbaOH)$(H_2O)_3$ is essentially the same. From Baron *et al.* (*24*).

the chains are related by a unit cell translation, so that the shortest metal---metal separations again involve metal ions of the same kind. On the other hand, along the other direction perpendicular to the chain axis, the shortest metal---metal separations are of the Mn---Cu type.

Down to ca. 30 K, the magnetic behaviors of the two compounds are identical. At room temperature, $\chi_M T$ is equal to 4.2 cm^3 K mol^{-1}, which is slightly lower than expected for uncorrelated Mn(II) and Cu(II) ions. As T is lowered, $\chi_M T$ decreases, reaches a rounded minimum around 115 K, then increases more and more rapidly. Such a behavior is characteristic of a Mn(II)Cu(II) ferrimagnetic chain compound (*27*) and may be interpreted as arising from a Mn(II)–Cu(II) antiferromagnetic interaction characterized by $J = -24.5$ cm^{-1}. The fitting of the magnetic susceptibility data above 30 K is performed using a model where the $S_{Mn} = \frac{5}{2}$ local spin is assumed to be large enough to be treated as a classical spin, and the $S_{Cu} = \frac{1}{2}$ local spin is treated as a quantum spin (*1, 28, 29*). On the other hand, the structural differences induce dramatic differences as far as the low-temperature magnetic properties are concerned. $\chi_M T$ for $MnCu(pbaOH)(H_2O)_3 \cdot 2H_2O$ displays a sharp maximum at 3 K associated with a maximum of χ_M at 2.4 K (see Fig. 7). This behavior reveals a three-dimensional antiferromagnetic ordering of the ferrimagnetic chains at $T_c = 2.4$ K. This maximum of χ_M disappears when the applied magnetic field is larger than 0.9 kOe (see Fig. 8). Such a field is sufficient to overcome the weak interchain antiferromagnetic interactions. The compound may be described as a metamagnet built from ferrimagnetic chains. The value of the critical field, H_c, for which the intermolecular antiferromagnetic interactions are overcome may be determined more accurately from the field dependence of the magnetization at 1.7 K, i.e., below T_c. The curve also shown in Fig. 8 presents a change of sign of the second derivative $\partial^2 M/\partial H^2$ around 1 kOe, corresponding to the field-induced transition from an antiferromagnetic to a ferromagnetic-like state. We use the expression "ferromagnetic-like" because a genuine ferromagnetic state corresponds to a parallel alignment of the spins in zero field. From the $M = f(H)$ curve of Fig. 8, it is possible to plot the field dependence of the differential magnetic susceptibility, $\partial M/\partial H$, also shown in Fig. 8. This differential magnetic susceptibility displays a maximum at $H_c = 0.9$ Oe (*24*).

As far as $MnCu(pbaOH)(H_2O)_3$ is concerned, $\chi_M T$ increases very rapidly as T is lowered below ca. 30 K, reaches extremely high values, and becomes strongly field dependent around 5 K, which suggests that a three-dimensional ferromagnetic ordering of the ferrimagnetic chains takes place. The temperature dependence of the magnetization for the

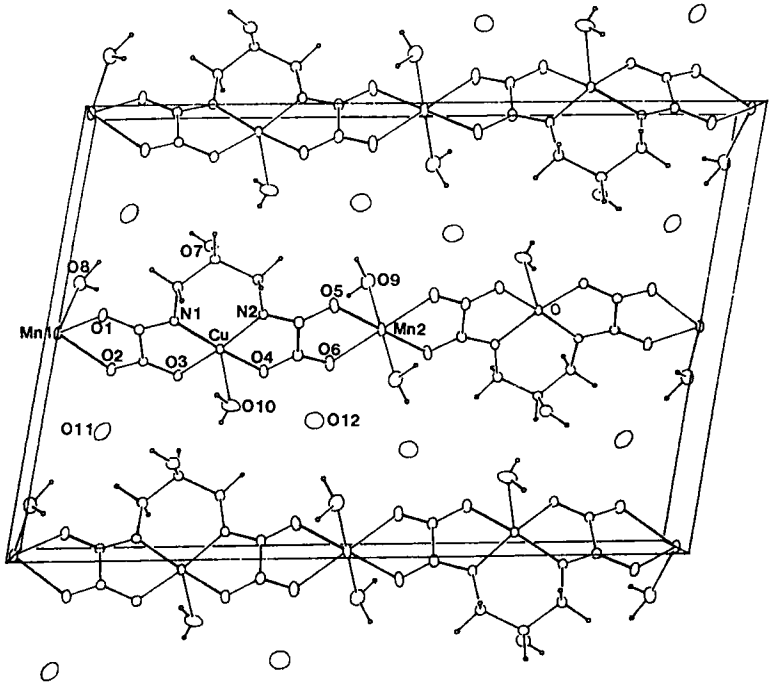
O7
O8
N1
N2
O5
O9
Mn1
O1
Cu
Mn2
O2
O3
O4
O6
O10
O11
O12

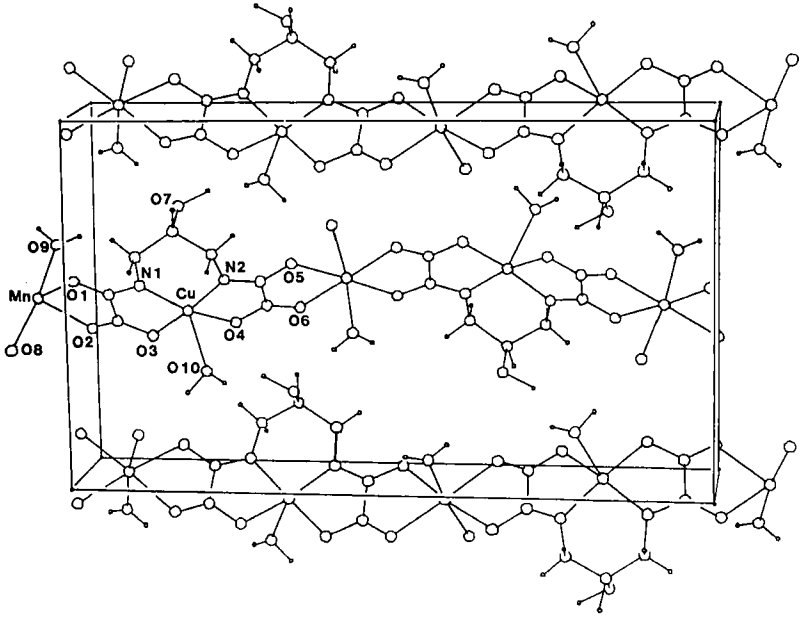
O7
O9
N1
N2
O5
Mn
O1
Cu
O6
O4
O2
O3
O8
O10

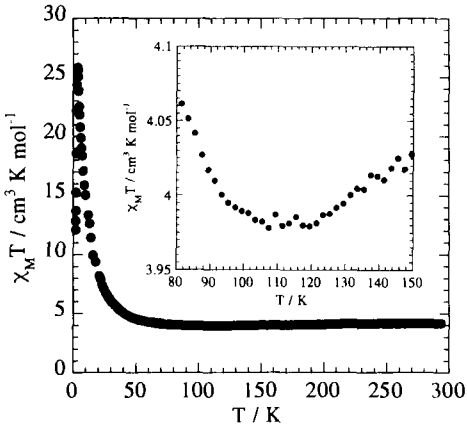

FIG. 7. $\chi_M T$ vs T curve for MnCu(pbaOH)$(H_2O)_3 \cdot 2H_2O$. From Baron *et al.* (*24*).

polycrystalline sample within a field of 3×10^{-2} Oe shown in Fig. 9 confirms the onset of a ferromagnetic ordering. The field-cooled magnetization (FCM) obtained in cooling within the field displays the typical features of a ferromagnetic transition, i.e., a rapid increase in M when T decreases below 5 K, then a break in the curve at $T_c = 4.6$ K, and finally the beginning of saturation when T is lowered further. If the field is switched off below T_c, then a remnant magnetization is observed. The zero-field–cooled magnetization (ZFCM) is obtained by cooling below T_c, and then applying the field and heating up. At any temperature below T_c, the ZFCM is lower than the FCM, because in this low-temperature range the applied field is too weak to move the domain walls. The ZFCM merges with the FCM at T_c. The field dependence of the magnetization below T_c displays a very large zero-field susceptibility $(\partial M/\partial H)_{H=0}$, as expected for a magnet, then a rapid saturation with a saturation magnetization value of $4\,N\beta$ mol^{-1}. This value exactly corresponds to what is expected for all the $S_{Mn} = \frac{5}{2}$ local spins aligned along the field direction and the $S_{Cu} = \frac{1}{2}$ local spins aligned along the opposite direction. MnCu(pbaOH)$(H_2O)_3$ also exhibits a hysteresis loop $M = f(H)$. The coercive field, however, remains weak; it is of the order of 50 Oe at 1.7 K (*25, 26*).

FIG. 6. Perspective views of three neighboring chains in MnCu(pbaOH)$(H_2O)_3 \cdot 2H_2O$ (top) and MnCu(pbaOH)$(H_2O)_3$ (bottom). From Baron *et al.* (*24*).

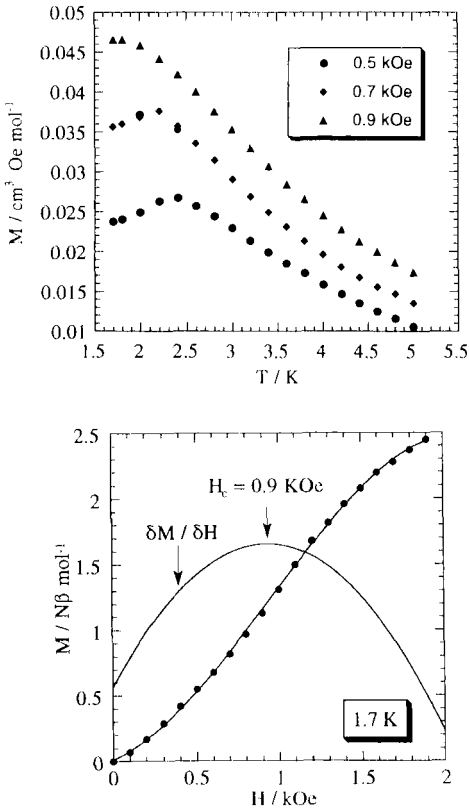

FIG. 8. Magnetization vs temperature curves for three values of the applied magnetic field (top), and field dependence of the magnetization at 1.7 K (bottom) for $MnCu(pbaOH)(H_2O)_3 \cdot 2H_2O$. In the bottom diagram the black points represent the experimental data, and the solid lines represent the fitting of the experimental data and the differential magnetic susceptibility $\partial M/\partial H$. From Baron *et al.* (*24*).

Magnetic anisotropy and single-crystal EPR measurements have provided some information concerning the relation between the interchain interactions and the three-dimensional magnetic orderings (*26, 30*). In both compounds, along one of the crystallographic directions the chains are related by a unit cell translation, with Cu---Cu = Mn---Mn = 5.03 Å as the shortest metal---metal separations. Along this direction, the dominant interchain interactions are probably ferromagnetic and of dipolar origin. On the other hand, along another crystallographic direction, the chains are related by an axial glide plane with the shortest Mn---Mn and Cu---Cu metal---metal separations for

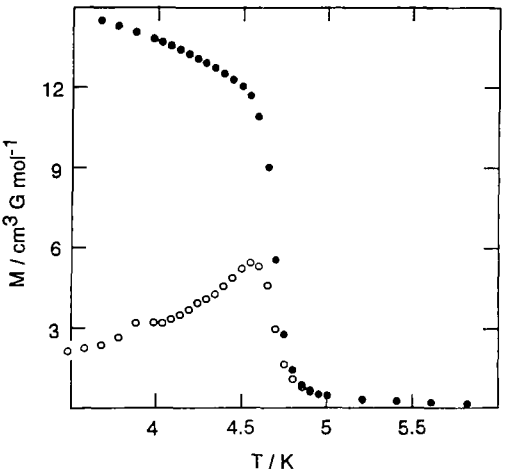

FIG. 9. Magnetization vs temperature curves for MnCu(pbaOH)$(H_2O)_3$ within a field of 3×10^{-3} Oe; (●) FCM, (○) ZFCM. Reprinted from Pei *et al.* (*25*). Copyright © 1986 American Chemical Society.

MnCu(pbaOH)$(H_2O)_3 \cdot 2H_2O$, and by a screw axis with the shortest Mn---Cu metal---metal separations for MnCu(pbaOH)$(H_2O)_3$. Along that direction the interactions between nearest-neighbor metal ions are probably antiferromagnetic, and of exchange (i.e., orbital) origin. Mn---Mn and Cu---Cu interchain antiferromagnetic interactions favor an antiparallel alignment of the chain spins for MnCu(pbaOH)$(H_2O)_3 \cdot 2H_2O$. In contrast, Mn---Cu interchain antiferromagnetic interactions favor a parallel alignment of the chain spins for MnCu(pbaOH)$(H_2O)_3$. This example emphasizes the role of the topology of the spin carriers in the three-dimensional magnetic effects.

A third compound has been obtained in the Mn(II)–$[Cu(pbaOH)]^{2-}$ system, through partial dehydration in mild conditions of MnCu(pbaOH)$(H_2O)_3$. Its formula is MnCu(pbaOH)$(H_2O)_2$. The water molecule occupying the apical position in the copper coordination sphere is selectively removed, which most likely brings the ferrimagnetic chains closer to each other and increases the interchain interactions. This compound also exhibits a three-dimensional ferromagnetic ordering of the ferrimagnetic chains, but at a significantly higher temperature; T_c is found to be equal to 30 K (*31*).

2. *Mn(II)Cu(II) Chain Compounds Obtained from the $[Cu(opba)]^{2-}$ Precursor*

Two Mn(II)Cu(II) chain compounds have been obtained with the precursor $[Cu(opba)]^{2-}$. The first is MnCu(opba)$(H_2O)_2 \cdot$ DMSO, with

DMSO = dimethylsulfoxide (*32*). Its structure consists of oxamato-bridged Mn(II)Cu(II) linear chains running along the *b*-axis of a triclinic lattice with an intrachain Mn---Cu distance of 5.387 Å (see Fig. 10). The chains pack above each other along the *a*-axis, forming bimetallic layers with Mn---Mn = 5.03 Å as the shortest metal---metal interchain separation. The layers are separated by noncoordinated DMSO molecules along the *c*-axis. The magnetic properties are characteristic of one-dimensional ferrimagnetism, with a minimum $\chi_M T$ around 130 K, and a maximum at 8 K associated with a three-dimensional antiferromagnetic ordering of the ferrimagnetic chains occurring at T_c = 5 K. The Mn–Cu intrachain interaction parameter, $J = -32.1$ cm^{-1}, is larger in absolute value than for the compounds described in the previous section. Both the temperature dependence at various fields and the field dependence below T_c of the magnetization reveal a field-induced transition from an antiferromagnetic to a ferromagnetic-like state, as observed for $MnCu(pbaOH)(H_2O)_3 \cdot 2H_2O$. The field necessary to align the chain spins, however, is larger; H_c is found as 5.0 kOe (instead of 0.9 kOe).

The formula of the second Mn(II)Cu(II) chain compound is MnCu(opba)$(DMSO)_3$ (*33*). In contrast with all the systems described so far, the manganese atom has a *cis* configuration, as shown in Fig. 11, instead of a *trans* configuration, so that the chains run in a zigzag and not a ribbonlike fashion. Two DMSO molecules are bound to the manganese atom in a *cis* position, and the third occupies the apical position in the copper coordination sphere. Because of the bulkiness of the DMSO molecules, the chains are very well separated from each other, the shortest metal---metal interchain separations being as large as Mn---Mn = 7.21 Å and Mn---Cu = 7.505 Å. The magnetic susceptibility very closely follows the behavior expected for a perfect one-dimen-

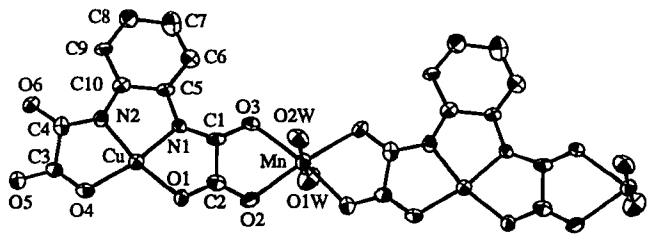

FIG. 10. Structure of the linear chain compound $MnCu(opba)(H_2O)_2 \cdot DMSO$. Reprinted from Stumpf *et al.* (*32*). Copyright © 1993 American Chemical Society.

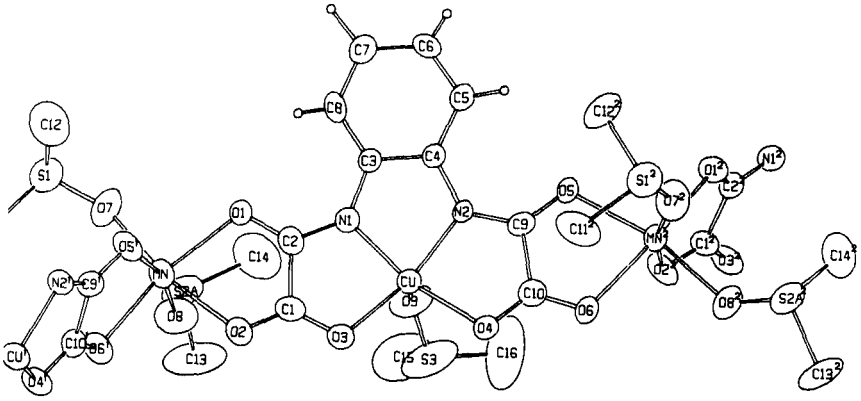

FIG. 11. Structure of the zigzag chain compound MnCu(opba)(DMSO)$_3$. Reprinted from Stumpf *et al.* (*33*). Copyright © 1993 American Chemical Society.

sional ferrimagnet. It is remarkable that down to 1.7 K there is no indication of three-dimensional ordering. MnCu(opba)(DMSO)$_3$ may be considered as a quasi-perfect one-dimensional ferrimagnet; the interchain interactions are negligibly small. It follows that the external field necessary to align the chain spins in parallel is negligibly small as well.

Heating MnCu(opba)(DMSO)$_3$ to 140° under vacuum results in a product of which the stoichiometry is MnCu(opba) · 0.7DMSO. This product behaves as an amorphous magnet below T_c = 6.5 K.

C. OTHER BIMETALLIC CHAIN COMPOUNDS

The compounds of formula ACu(pbaOH)$(H_2O)_3 \cdot 2H_2O$ with A = Fe, Co, Ni, and Zn have also been prepared (*34*). They are isomorphous with MnCu(pbaOH)$(H_2O)_3 \cdot 2H_2O$. The two noncoordinated water molecules, however, are more difficult to remove than for the manganese derivative. The magnetic behavior of ZnCu(pbaOH)$(H_2O)_3 \cdot 2H_2O$ is that of isolated Cu(II) ions; the magnetic susceptibility follows the Curie law $\chi_M T$ = 0.39 cm^3 K mol^{-1} down to low temperature. All the other compounds of this family exhibit one-dimensional ferrimagnetic behavior, with a minimum in the $\chi_M T$ vs T plot. This minimum occurs around 95 K for A = Fe, 53 K for A = Co, and 80 K for A = Ni. The metal ions of NiCu(pbaOH)$(H_2O)_3 \cdot 2H_2O$ have no first-order orbital momen-

tum. The magnetic susceptibility data in the temperature range where the three-dimensional effects may be ignored have been interpreted with an $S_{Ni} = 1$, $S_{Cu} = \frac{1}{2}$ ring-chain approach (*1*, *35–37*), which leads to $J = -81.4$ cm^{-1}. The Fe(II) and Co(II) ions, on the other hand, are orbitally degenerate, which makes it extremely difficult to interpret the magnetic data quantitatively.

The cobalt and nickel derivatives exhibit a long-range antiferromagnetic ordering at 3.4 and 2.9 K, respectively. For the iron derivative, the situation is a bit more complex. The spins of the ferrimagnetic chains do not cancel exactly on the scale of the lattice; there is a canting, which leads to a weak ferromagnetism and a remnant magnetization below a critical temperature $T_c = 10$ K. To finish this section, let us mention that the ACu(pbaOH)$(H_2O)_3$ compounds in which the noncoordinated water molecules are removed have not yet been investigated. It would be quite interesting to see whether these compounds exhibit a 3D ferromagnetic ordering of the ferrimagnetic chains, as MnCu(pbaOH)$(H_2O)_3$ does.

D. Two-Dimensional Mn(II)Cu(II) Compounds

The zigzag chain structure of MnCu(opba)$(DMSO)_3$ resulting from the *cis* coordination of the DMSO molecules around manganese may suggest a strategy to increase the dimensionality of the system. This strategy consists of replacing the DMSO molecules bound to the manganese atom with the bisbidentate ligands $[Cu(opba)]^{2-}$, which results in a cross-linking of the chains, as schematized in Fig. 12. The reaction of a Mn(II) salt with $(NBu_4)_2[Cu(opba)]$ in the $\frac{2}{3}$ stoichiometry affords a compound of formula $(NBu_4)_2Mn_2[Cu(opba)]_3 \cdot 6DMSO \cdot H_2O$ (*33*). Up to now, it has not been possible to solve the crystal structure. However, it is most likely that this structure consists of layers with Mn_6Cu_6 edge-sharing hexagons. The manganese atom would be surrounded by three Cu(opba) groups. Such an arrangement, shown in Fig. 13, has actually been found in a related compound in which the tetra-*n*-butylammonium cation is replaced by a radical cation (see Section II,E). The NBu_4^+ cations and noncoordinated DMSO molecules are probably located between the honeycomb layers.

The $\chi_M T$ vs T plot for $(NBu_4)_2Mn_2[Cu(opba)]_3 \cdot 6DMSO \cdot H_2O$ presents a minimum around 120 K, characteristic of a ferrimagnetic behavior with Mn–Cu antiferromagnetic interactions and noncompensation of the local spins in the ground state. As T is lowered below 120 K, $\chi_M T$ increases more and more rapidly and eventually becomes field-dependent. The temperature dependence of the FCM, ZFCM, and REM

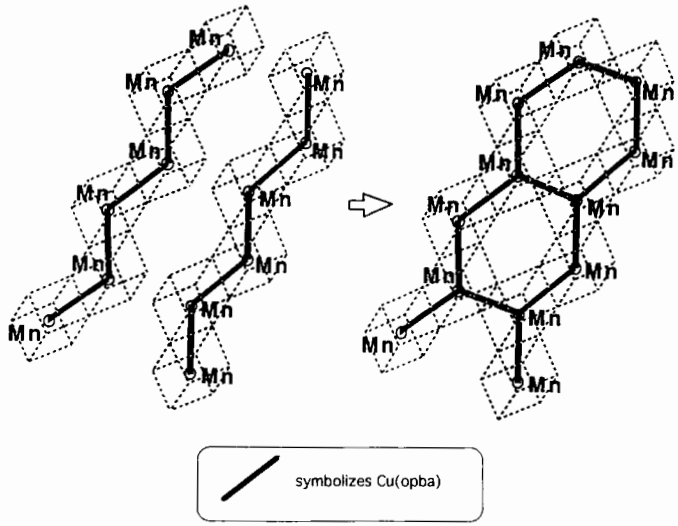

FIG. 12. Formation of a honeycomb two-dimensional lattice through crosslinking of zigzag chains.

(remnant magnetization) curves confirms that the compound presents a 3D magnetic ordering at $T_c = 15$ K with a spontaneous magnetization below this temperature. The field dependence of the magnetization at 5 K, shown in Fig. 14, reveals a saturation magnetization of 7 Nβ mol^{-1}, which confirms that in the magnetically ordered state all the $S_{Mn} = \frac{5}{2}$ local spins are aligned along the field direction, and the $S_{Cu} = \frac{1}{2}$ local spins along the opposite direction.

Heating $(NBu_4)_2Mn_2[Cu(opba)]_3 \cdot 6DMSO \cdot H_2O$ at 170°C under vacuum results in a compound of formula $(NBu_4)_2Mn_2[Cu(opba)]_3$. All the solvent molecules are removed. This compound exhibits a spontaneous magnetization below $T_c = 22$ K.

E. A Molecular-Based Magnet Containing Three Spin Carriers with a Fully Interlocked Structure

The anionic copper(II) precursor $[Cu(opba)]^{2-}$ can be prepared with almost all kinds of countercations, including radical cations. One of them, denoted rad^+, is 2-(1-methylpyridinium-4-yl)-4,4,5,5-tetramethylimidazoline-1-oxyl-3-oxide:

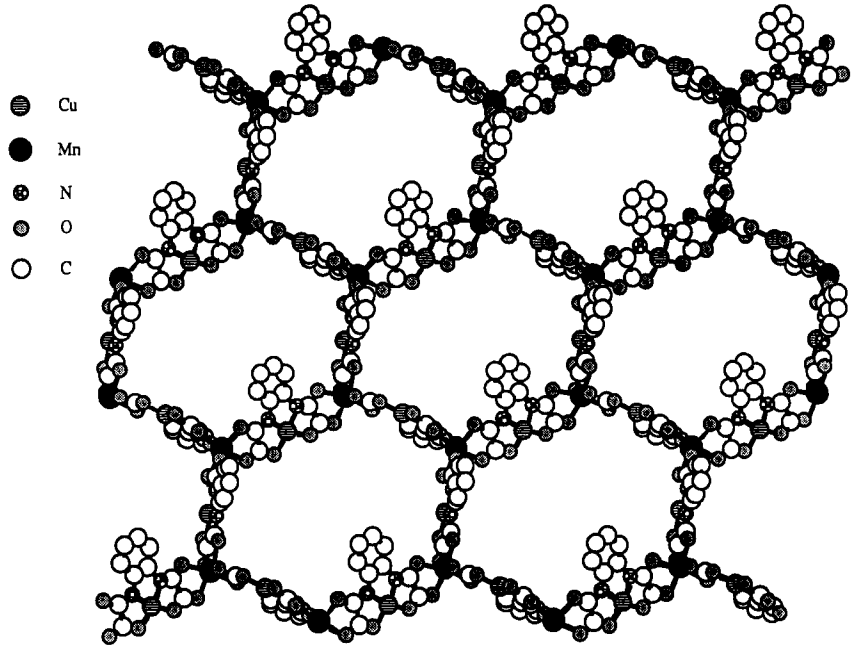

FIG. 13. Structure of a layer in $(rad)_2Mn_2[Cu(opba)]_3(DMSO)_2 \cdot 2H_2O$, with rad^+ = 2-(1-methylpyridinium-4-yl)-4,4,5,5-tetramethylimidazoline-1-oxyl-3-oxide. Reprinted from Stumpf *et al.* (*38*). Copyright © 1993 American Association for the Advancement of Science.

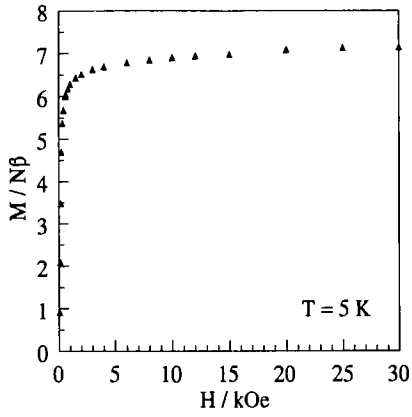

FIG. 14. Field dependence of the magnetization at 5 K for $(NBu_4)_2Mn_2[Cu(opba)]_3 \cdot 6DMSO \cdot H_2O$. Reprinted from Stumpf *et al.* (*33*). Copyright © 1993 American Chemical Society.

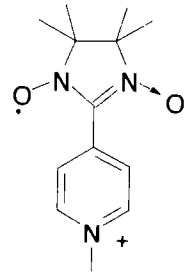

where the unpaired electron is equally shared between the two N–O groups. The reaction of Mn(II) chloride with a large excess of $(rad)_2$[Cu(opba)] in DMSO affords well-shaped single crystals of a compound of formula $(rad)_2Mn_2[Cu(opba)]_3(DMSO)_2 \cdot 2H_2O$ (*38, 39*). The structure of this compound is quite amazing. There are two equivalent two-dimensional networks, denoted A and B. Each network consists of honeycomb layers as shown in Fig. 13. These layers stack above each other in a graphitelike fashion. The A and B networks are quasi-perpendicular and interpenetrate each other with a full interlocking of the Mn_6Cu_6 hexagons, as shown in Fig. 15. The topology is that of a wire netting. The hexagons are further connected through the radical cations which bridge two copper atoms belonging to networks A and B, respectively. This affords Cu_A–rad–Cu_B–rad chains. Another peculiarity of this structure concerns the chirality of the manganese sites. A manganese atom surrounded by three bidentate ligands is obviously chiral. In the structure there is a perfect alternation of Λ and Δ sites occupying the adjacent corners of a hexagon; two such sites are linked by a Cu(opba) group.

The $\chi_M T$ vs T plot for $(rad)_2Mn_2[Cu(opba)]_3(DMSO)_2 \cdot 2H_2O$ is rather similar to that observed for $(NBu_4)_2Mn_2[Cu(opba)]_3 \cdot 6DMSO \cdot H_2O$, with a minimum $\chi_M T$ around 115 K. The FCM, ZFCM, and REM curves shown in Fig. 16 reveal that a 3D magnetic ordering with the appearance of a spontaneous magnetization occurs at T_c = 22.5 K. The field dependence of the magnetization at 4.2 K, represented in Fig. 17, deserves to be discussed; the $M = f(H)$ curve is significantly different from that obtained for $(NBu_4)_2Mn_2[Cu(opba)]_3 \cdot 6DMSO \cdot H_2O$. As expected for a magnet, the zero-field susceptibility $(\partial M/\partial H)_{H=0}$ is very high, and the magnetization reaches 4.2 $N\beta$ mol^{-1} within a few tens of oersteds. When the field is increased further, M increases rather smoothly, reaching 6.5 $N\beta$ mol^{-1} at 200 kOe. Even with such a very high field, the magnetization is lower than the saturation observed for

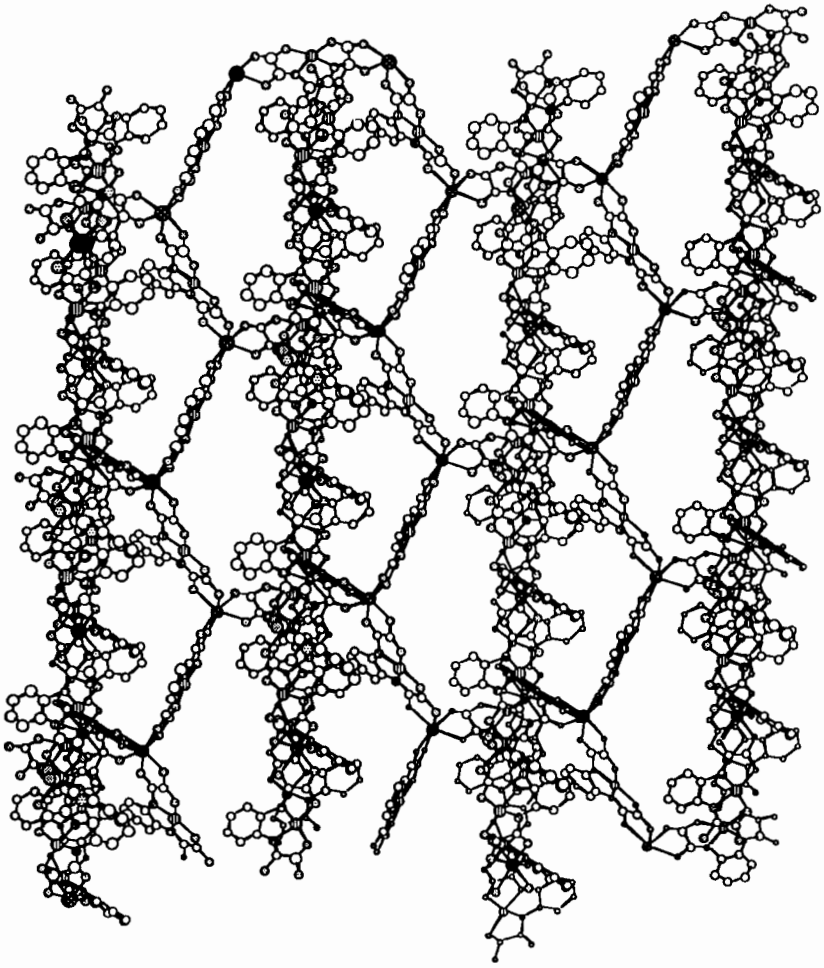

FIG. 15. Interpenetration of the two quasi-perpendicular networks in $(rad)_2Mn_2[Cu(opba)]_3(DMSO)_2 \cdot 2H_2O$. Reprinted from Stumpf *et al.* (*39*). Copyright © 1994 American Chemical Society.

$(NBu_4)_2Mn_2[Cu(opba)]_3 \cdot 6DMSO \cdot H_2O$. This behavior is due to the fact that the radical cations interact ferromagnetically with the Cu(II) ions along the Cu_A–rad–Cu_B–rad chains (*40*). Since the S_{Mn} spins align along the direction of the applied field and the S_{Cu} spins along the opposite direction, the radical spins, S_{rad}, also align in the direction opposite to that of the applied field, which diminishes the magnetization with regard to the $Mn_2[Cu(opba)]_3$ skeleton. When the field increases,

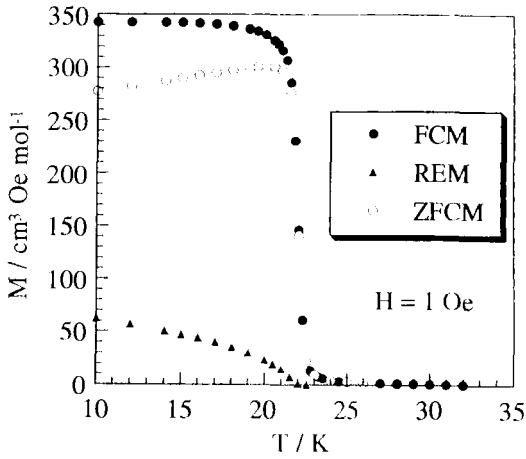

FIG. 16. Magnetization vs temperature curves for $(rad)_2Mn_2[Cu(opba)]_3(DMSO)_2 \cdot 2H_2O$. Reprinted from Stumpf *et al.* (39). Copyright © 1994 American Chemical Society.

a progressive spin decoupling between the radicals and the anionic skeleton happens, and the S_{rad} spins tend to orient along the field direction. From the profile of the $M = f(H)$ curve, it has been possible to estimate the magnitude of the Cu–rad ferromagnetic interaction; the J parameter has been found to be equal to 11.5 cm^{-1}.

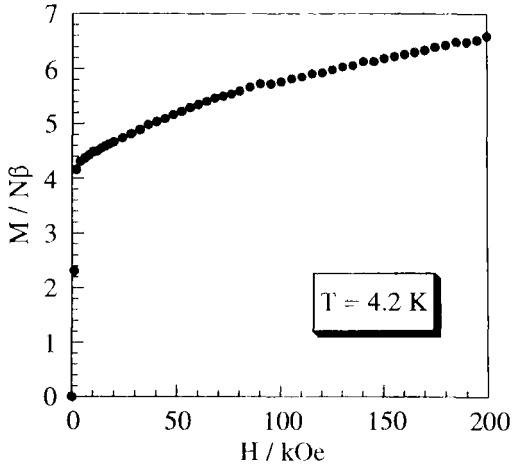

FIG. 17. Field dependence of the magnetization at 4.2 K for $(rad)_2Mn_2[Cu(opba)]_3(DMSO)_2 \cdot 2H_2O$. Reprinted from Stumpf *et al.* (39). Copyright © 1994 American Chemical Society.

In the magnetically ordered state, $(rad)_2Mn_2[Cu(opba)]_3(DMSO)_2 \cdot 2H_2O$ presents an extremely narrow magnetic hysteresis loop. The coercive field is inferior to 10 Oe.

F. Co(II)Cu(II) Two-Dimensional Molecular-Based Magnets with Large Coercive Fields

All the Mn(II)Cu(II) molecular-based magnets we have spoken about thus far present a magnetic hysteresis loop with a weak coercive field, of a few tens of oersteds at the most. When manganese is replaced by cobalt in the two-dimensional compounds $(cat)_2Mn_2[Cu(opba)]_3 \cdot S$, with cat^+ standing for a cation and S for solvent molecules, a large coercive field is obtained (*41*). Let us describe the magnetic properties of one of these compounds, of formula $(rad)_2Co_2[Cu(opba)]_3 \cdot 0.5DMSO \cdot 3H_2O$. The FCM, ZFCM, and REM curves are displayed in Fig. 18. The FCM shows a break around T_c = 34 K. The REM obtained in switching off the field at 2 K, and warming in zero field, is strictly equal to the FCM below T_c. All the information induced by the field is retained. As for the ZFC, it is negligibly small up to 15 K. The magnetic domains are randomly oriented, and the domain walls do not move. The ZFCM increases slightly as T increases above 15 K, because of the thermal agitation which displaces the domain walls. FCM and ZFCM merge at

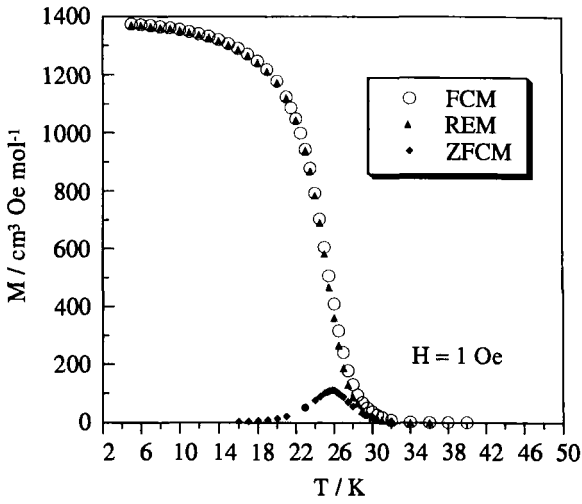

FIG. 18. Magnetization vs temperature curves for $(rad)_2Co_2[Cu(opba)]_3 \cdot 0.5DMSO \cdot 3H_2O$. Reprinted from Stumpf *et al.* (*41*). Copyright © 1994 American Chemical Society.

T_c. The field dependence of the magnetization at 1.7 K, shown in Fig. 19, reveals a hysteresis loop with a coercive field as large as 3.0 kOe and a remnant magnetization of about 7×10^3 cm^3 Oe mol^{-1}.

The strong coercivity observed in these Co(II)Cu(II) compounds is most probably due to the unquenched orbital momentum of the Co(II) ion in octahedral surroundings.

G. Lanthanide(III)Cu(II) One- and Two-Dimensional Compounds

The most powerful magnets known to date are transition metal–rare earth intermetallics (*42*). The archetype of compounds of this kind is $Nd_2Fe_{14}B$, which exhibits a coercive field of the order of 10 kOe at room temperature (*43*). In molecular chemistry, the lanthanide–transition metal species are still rather rare, and only in a few cases have the magnetic properties been investigated in a thorough fashion. In Kahn (*3*) a section was devoted to Cu(II)Gd(III)Cu(II) trinuclear species. Irrespective of the details of the molecular architecture, the Gd(III)–Cu(II) interaction is found to be ferromagnetic, the interaction parameter between Gd(III) and Cu(II) ions bridged by two phenolato bridges of the order of $J = 3$ cm^{-1} (*44–46*). This result at the first view is surprising; indeed, owing to the $4f^7$ configuration of Gd(III), the orthogonality of the magnetic orbitals may not be invoked. Moreover, the $4f$ singly

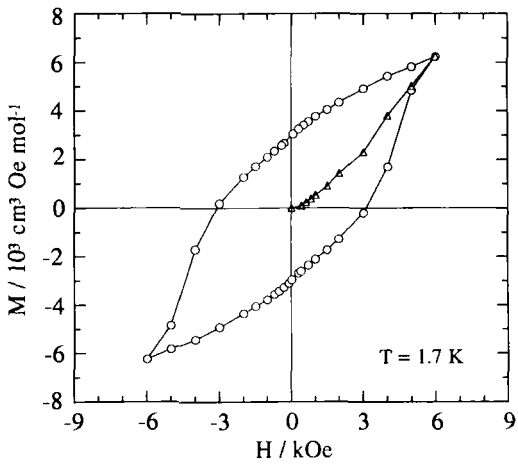

FIG. 19. Magnetic hysteresis loop at 1.7 K for $(rad)_2Co_2[Cu(opba)]_3 \cdot 0.5DMSO \cdot 3H_2O$. Reprinted from Stumpf *et al.* (*41*). Copyright © 1994 American Chemical Society.

occupied orbitals are contracted around the nucleus and efficiently shielded by the outer 5*s* and 5*d* occupied orbitals. It follows that these 4*f* orbitals are very weakly delocalized toward the bridges. As a consequence, all the integrals involving 4*f*(Gd)–3*d*(Cu) overlap densities may be assumed to be negligibly small, and the corresponding $J_{\mu\nu}$ contributions defined in Eq. (5) may be assumed to vanish. At this level of approximation, the $S = 3$ and $S = 4$ low-lying states for a Gd(III)-Cu(II) pair are accidentally degenerate. The ferromagnetic nature of the interaction is attributed to the coupling between the $S = 3,4$ low-lying states and the $S = 3,4$ excited states arising from the charge-transfer configuration associated with the 3*d*(Cu) → 5*d*(Gd) process. The 5*d* lanthanide orbitals are much more diffuse than the 4*f* orbitals, and the transfer integrals β_{5d-3d} may be rather large. Because of Hund's rule, the $S = 4$ excited state is lower in energy than the $S = 3$ excited state, and the coupling between low-lying and excited states stabilizes the low-lying parallel spin state (*47, 48*), as schematized in Fig. 20. This mechanism, implying an electron transfer from a singly occupied orbital on one site to an empty orbital on the other site, was first introduced by Goodenough (*49*).

Let us turn back to the Ln(III)Cu(II) oxamato-bridged compounds. To date, only the Ln(III)–$[Cu(pba)]^{2-}$ system has been explored, and three families of compounds have been characterized, depending on the synthesis method and/or the nature of the trivalent lanthanide Ln(III) (*50*). The first family corresponds to the formula $Ln_2[Cu(pba)]_3 \cdot 23H_2O$, with Ln going from Tb to Yb, and Y. The structure is the simplest one; it consists of discrete and infinite ladder motifs, the edges made of LnCu(pba) units, and the rungs of Cu(pba) units linking two Ln(III) ions, as shown in Fig. 21 (*50*). The magnetic properties of these compounds have not yet been investigated in detail. The second family also corresponds to the formula $Ln_2[Cu(pba)]_3 \cdot 23H_2O$, but with Ln going from La to Gd. The structure consists of discrete and infinite tubelike motifs with a pseudo-fourfold symmetry, resulting from the condensation of two ladderlike motifs associated with a rearrangement of the rungs, as schematized in Fig. 22 (*51*). The third and final family consists of ladder motifs which are not isolated, but linked together by oxalato groups, affording a double-sheet two-dimensional pattern. In addition, this structure contains discrete $[Cu(H_2O)_5]^{2+}$ cations interspersed between the layers. Its formula is $\{Ln_2(ox)[Cu(pba)]_3\}[Cu(H_2O)_5] \cdot 20H_2O$, with ox = oxalato and Ln going from La to Gd (*52*).

As for the Cu(II)Gd(III)Cu(II) trinuclear species mentioned at the beginning of this section, the magnetic properties of these Ln(III)Cu(II) materials essentially depend on the nature of Ln, and not much on the

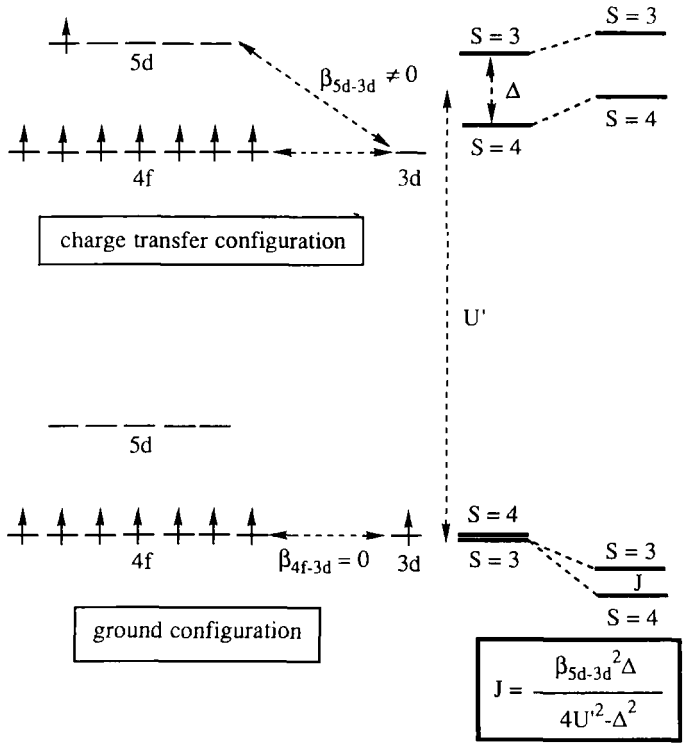

FIG. 20. Schematic representation of the orbital mechanism explaining the ferromagnetic nature of the Gd(III)–Cu(II) interaction; $\beta_{4f\text{-}3d}$ and $\beta_{5d\text{-}3d}$ are one-electron transfer integrals, and U' is the energy of the charge-transfer configuration arising from the $3d$(Cu) → $5d$(Gd) process. Reprinted from Andruh *et al.* (*47*). Copyright © 1993 American Chemical Society.

details of the structure. So, for all the Gd(III)Cu(II) compounds $\chi_M T$ increases more and more rapidly as T is lowered, revealing ferromagnetic Gd(III)–Cu(II) interactions through the oxamato bridge. Field dependences of the magnetization confirm that all the local spins tend to align along the field direction. Actually, heat capacity measurements on both $Gd_2[Cu(pba)]_3 \cdot 23H_2O$ and $\{Gd_2(ox)[Cu(pba)]_3\}[Cu(H_2O)_5] \cdot 20H_2O$ have revealed a three-dimensional ferromagnetic ordering at $T_c = 1$ K, with a characteristic λ peak, as shown in Fig. 23 (*53*). These compounds may be considered as the first molecular-based ferromagnets involving lanthanide ions. To evaluate the magnitude of the Gd(III)–Cu(II) interaction, a theoretical model has been constructed in which the $S_{Gd} = \frac{7}{2}$ and $S_{Cu} = \frac{1}{2}$ local spins of a ladder are treated as classical and quantum spins, respectively (*54*). Assuming that the

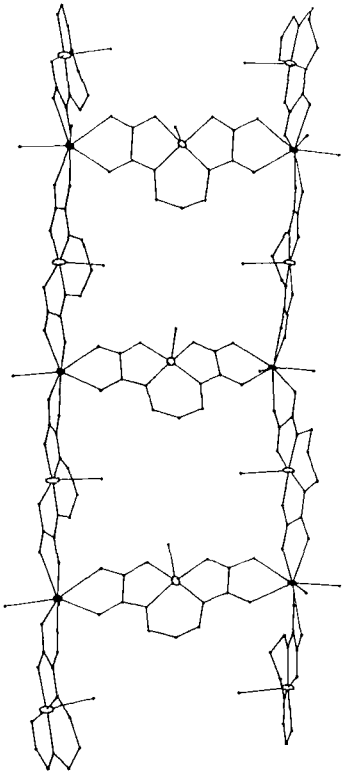

FIG. 21. Structure of a ladderlike motif in $Dy_2[Cu(pba)]_3 \cdot 23H_2O$; the black points represent the dysprosium atoms, and the white points the copper atoms. From Guillou *et al.* (*50*).

Gd(III)–Gd(III) interaction through the oxalato bridge of $\{Gd_2(ox)[Cu(pba)]_3\}[Cu(H_2O)_5] \cdot 20H_2O$ is negligible, the model may be applied to this compound. It leads to an excellent fitting of the $\chi_M T$ vs T plot for $J = 0.28\ cm^{-1}$ (see Fig. 24).

The magnetic properties of the Nd(III)Cu(II) compounds have also been studied in some detail. Let us focus on the compound $Nd_2[Cu(pba)]_3 \cdot 23H_2O$, with a structure containing tubelike motifs as shown in Fig. 22. The magnetic susceptibility of this compound presents a rounded maximum around 2.5 K, as shown in Fig. 25; $\chi_M T$ tends to zero as T approaches absolute zero. Heat capacity and ac susceptibility measurements do not indicate any sign of long-range antiferromagnetic ordering. It follows that the maximum of χ_M indicates that the ground

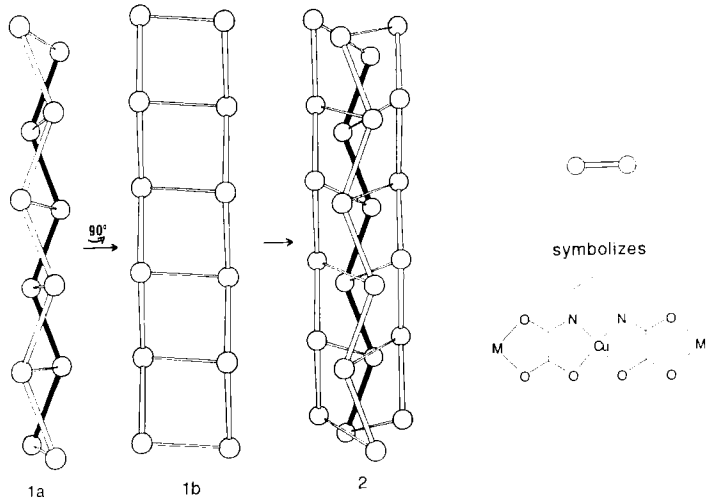

FIG. 22. Condensation of two ladderlike motifs are shown in Fig. 21 along with the redistribution of the ladder rungs to achieve the tubelike motif found in $Sm_2[Cu(pba)]_3 \cdot 23H_2O$. From Guillou *et al.* (*51*).

state of the compound is nonmagnetic, which at the first view is quite an unexpected result. This situation has been attributed to a compensation at low temperature between the local magnetic moments of two Nd(III) ions on the one hand and of three Cu(II) ions on the other hand. This idea has been tested with a theoretical model in which the local Kramers doublets for Nd(III) and Cu(II) interact antiferromagnetically.

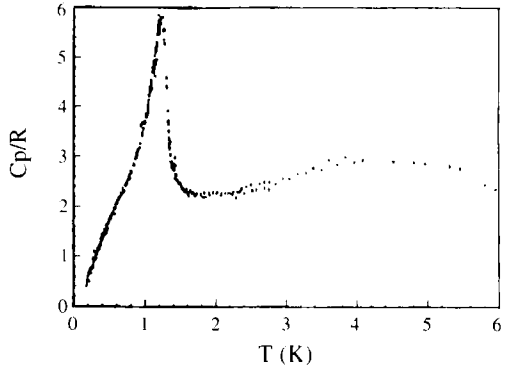

FIG. 23. Temperature dependence of the heat capacity for $Gd_2[Cu(pba)]_3 \cdot 23H_2O$.

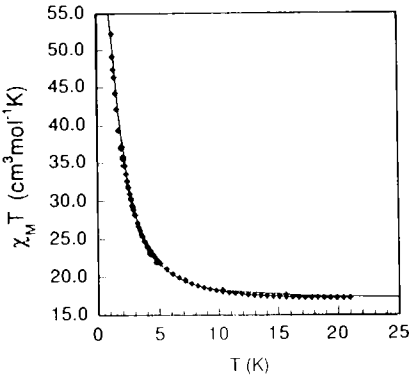

FIG. 24. $\chi_M T$ vs T plot for $\{Gd_2(ox)[Cu(pba)]_3\}[Cu(H_2O)_5] \cdot 20H_2O$; (◆) experimental data, (—) theoretical curve. From Georges *et al.* (*54*).

A compensation of the magnetic moments may be expected in a ladderlike motif for a value of the ratio g_{Nd}/g_{Cu} close to 2, g_{Nd} and g_{Cu} being the Zeeman factors for the ground Kramers doublets of Nd(III) and Cu(II), respectively (*55*).

IV. Oxamido-Bridged Heterobimetallic Compounds

The heterobimetallic compounds containing oxamido bridges are at least as numerous as those containing oxamato bridges. To our knowl-

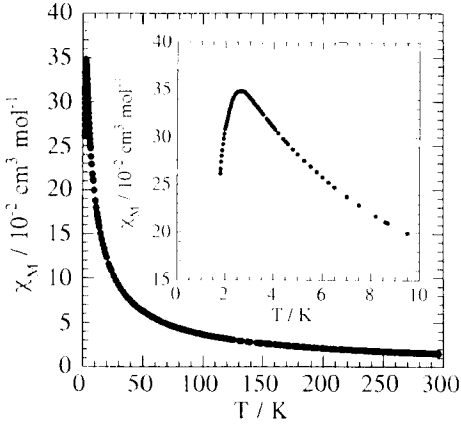

FIG. 25. χ_M vs T curve for $Nd_2[Cu(pba)]_3 \cdot 23H_2O$. From Kahn *et al.* (*55*).

edge, in all cases one of the metal ions is Cu(II). The other metal ion is often Mn(II), but it may be any other ion as well. The various Cu(II) precursors together with their abbreviations are gathered in Fig. 26. One of them, Cu(oxpn) with oxpn = *N*,*N*′-bis(3-aminopropyl)oxamido, is neutral; the others are dianions, namely $[Cu(obp)]^{2-}$ with obp = oxamidobis(*N*,*N*′-propionato), $[Cu(obbz)]^{2-}$ with obbz = oxamidobis (*N*,*N*′-benzoato), $[Cu(X_4obbz]^{2-}$ with X_4obbz = oxamidobis(*N*,*N*′-3,5-dihalogenobenzoato), $[Cu(obzp)]^{2-}$ with obzp = oxamidobis(*N*-benzoato-*N*′-propionato), and $[Cu(obze)]^{2-}$ with obze = oxamidobis(*N*-benzoato-*N*′-ethanoato).

A. Binuclear Compounds

Two Mn(II)Cu(II) oxamido-bridged binuclear compounds have been reported. The formula of the former is [Mn(Me_6-[14]ane-N_4)Cu(oxpn)]

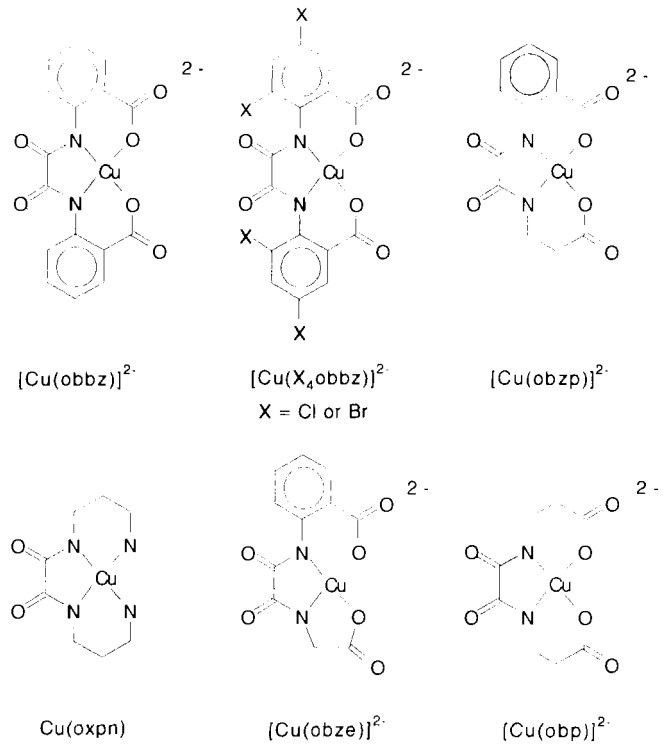

FIG. 26. Copper(II) precursors for oxamido-bridged polynuclear species.

$(CF_3SO_3)_2$, with Me_6-[14]ane-N_4 = (±)-5,7,7,12,14,14-hexamethyl-1,4,8,11-tetraazacyclotetradecane (*56*). The structure of the bimetallic cation is shown in Fig. 27. The intramolecular Mn---Cu distance is 5.436 Å.

The magnitude of the intramolecular interaction has been deduced from the temperature dependence of both the magnetic susceptibility and the optical absorption spectrum. The $\chi_M T$ vs T curve of Fig. 28 is characteristic of an antiferromagnetically coupled Mn(II)Cu(II) pair with an $S = 2$ ground state and an $S = 3$ excited state. The fitting of this curve with the theoretical expression (*1*)

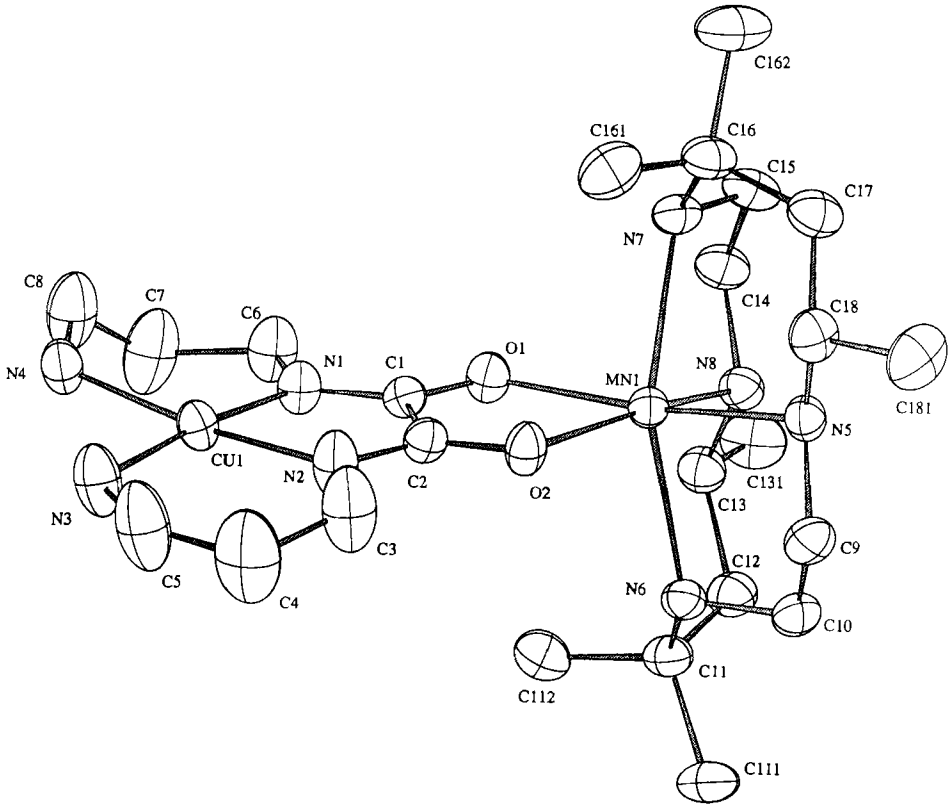

FIG. 27. Structure of the binuclear cation $[Mn(Me_6\text{-}[14]ane\text{-}N_4)Cu(oxpn)]^{2+}$, with Me_6-[14]ane-N_4 = (±)-5,7,7,12,14,14-hexamethyl-1,4,8,11-tetraazacyclotetradecane. Reprinted from Mathonière *et al.* (*56*). Copyright © 1993 American Chemical Society.

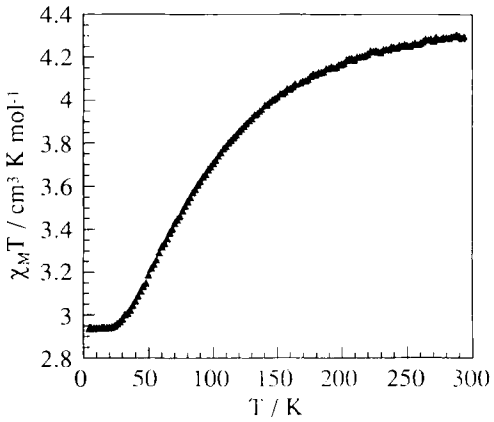

FIG. 28. $\chi_M T$ vs T curve for [Mn(Me$_6$-[14]ane-N$_4$)Cu(oxpn)](CF$_3$SO$_3$)$_2$. Reprinted from Mathonière *et al.* (*56*). Copyright © 1993 American Chemical Society.

$$\chi_M T = \frac{2N\beta^2}{k} \frac{5g_2^2 + 14g_3^2 \exp\left(\frac{3J}{kT}\right)}{5 + 7\exp\left(\frac{3J}{kT}\right)} \tag{9}$$

leads to a quintet–septet energy gap of $3J = -93.9$ cm^{-1}; g_2 and g_3 in Eq. (9) are the Zeeman factors associated with the $S = 2$ and $S = 3$ states, respectively, and are related to the local Zeeman factors g_{Mn} and g_{Cu} through (*1, 10, 57*)

$$g_2 = (7g_{Mn} - g_{Cu})/6,$$
$$g_3 = (5g_{Mn} + g_{Cu})/6. \tag{10}$$

The fact that $\chi_M T$ is constant in the temperature range where only the quintet ground state is thermally populated indicates that the zero-field splitting within this $S = 2$ state is very weak, which is confirmed by the EPR spectrum. Let us point out that this Mn(II)Cu(II) binuclear cation may be viewed as a molecular unit with a large positive spin density in the Mn(II) region and a small negative spin density in the

Cu(II) region. Such a view is supported by the spin density map of Fig. 29, deduced from a polarized neutron diffraction investigation (*58*).

The absorption spectrum of $[Mn(Me_6\text{-}[14]ane\text{-}N_4)Cu(oxpn)](CF_3SO_3)_2$ is shown in Fig. 30. The main feature of this spectrum is a sharp and intense band at 23,700 cm^{-1} corresponding formally to the $^6A_1 \rightarrow {}^4A_1 + {}^4E$ spin-forbidden transition for Mn(II); this transition is activated by the magnetic interaction (*59*). Actually, the interaction between the $S^*_{Mn} = \frac{3}{2}$ local excited state for Mn(II) and the $S_{Cu} = \frac{1}{2}$ local ground state for Cu(II) gives rise to $S^* = 1$ and 2 pair excited states, and the band at 23,700 cm^{-1} corresponds to the $S = 2 \rightarrow S^* = 2$ transition. Therefore, the intensity of this band is proportional to the population of the $S = 2$ pair ground state. The temperature dependence of the intensity represented in Fig. 31 offers an alternative method of determining the quintet–septet energy gap.

The second binuclear compound is $MnCu(obze)(H_2O)_4 \cdot 2H_2O$, the structure of which is represented in Fig. 32. This compound behaves

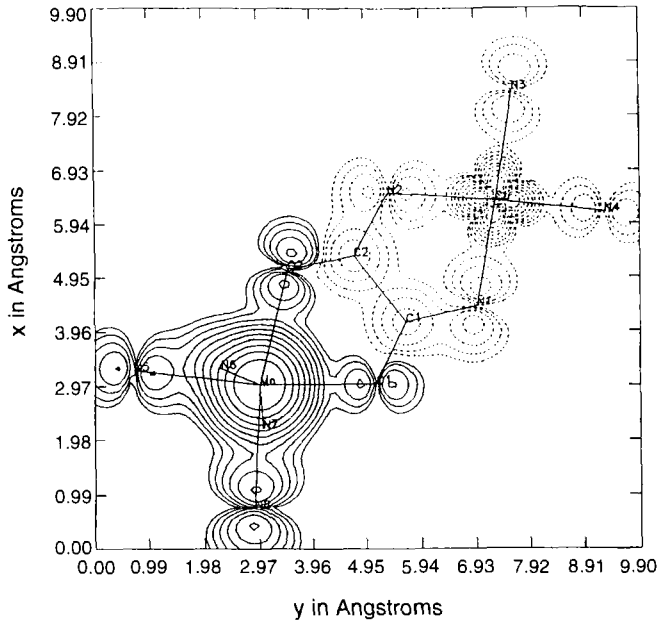

FIG. 29. Spin density map within the bridging network of $[Mn(Me_6\text{-}[14]ane\text{-}N_4)Cu(oxpn)](CF_3SO_3)_2$ as deduced from a polarized neutron diffraction investigation; solid and dotted lines are used for positive and negative spin densities, respectively. From Baron *et al.* (*58*).

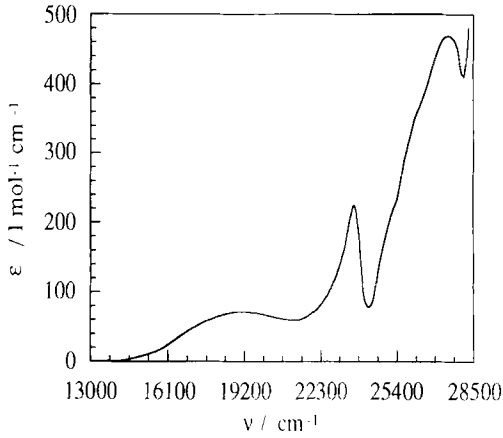

FIG. 30. Absorption spectrum in acetonitrile solution of [Mn(Me$_6$-[14]ane-N$_4$)Cu(oxpn)](CF$_3$SO$_3$)$_2$. Reprinted from Mathonière *et al.* (*56*). Copyright © 1993 American Chemical Society.

magnetically as [Mn(Me$_6$-[14]ane-N$_4$)Cu(oxpn)](CF$_3$SO$_3$)$_2$, the quintet–septet energy gap being $3J = -100.8$ cm^{-1}. The interest of this compound comes from the fact that it may polymerize through very mild conditions to afford a compound of formula MnCu(obze)(H$_2$O)$_2$, the magnetic properties of which are dramatically modified (*60*). Indeed, MnCu

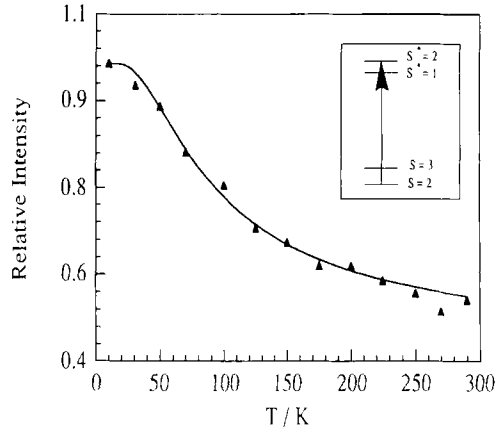

FIG. 31. Temperature dependence of the intensity of the formally spin-forbidden absorption band $^6A_1 \rightarrow {}^4A_1 + {}^4E$ for Mn(II) in [Mn(Me$_6$-[14]ane-N$_4$)Cu(oxpn)](CF$_3$SO$_3$)$_2$; (▲) experimental data, (—) calculated curve. Reprinted from Mathonière *et al.* (*56*). Copyright © 1993 American Chemical Society.

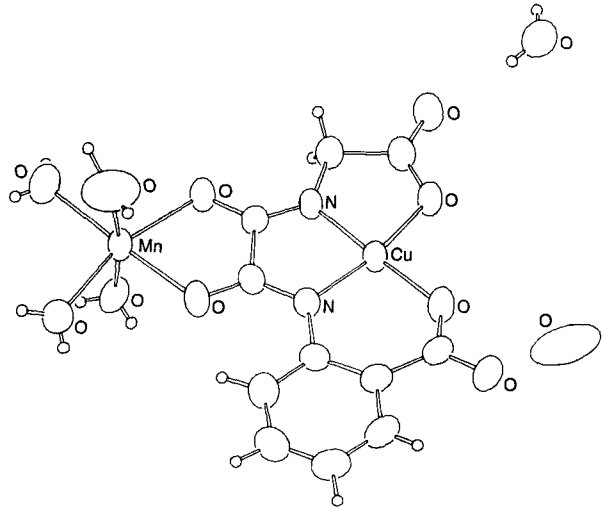

FIG. 32. Structure of the binuclear compound $MnCu(obze)(H_2O)_4 \cdot 2H_2O$. Reprinted from Pei *et al.* (*60*). Copyright © 1991 American Chemical Society.

$(obze)(H_2O)_2$ shows a three-dimensional magnetic ordering with a spontaneous magnetization below T_c = 4.6 K. The electronic spectrum of this polymeric compound strongly suggests that the Mn(II) ion retains an octahedral environment, and therefore is bound to the oxygen atoms of the carboxylato groups. This provides an interaction pathway between the negative spin density associated with Cu(II) of a Mn(II)Cu(II) unit and the positive spin density associated with Mn(II) of an adjacent unit, as schematized:

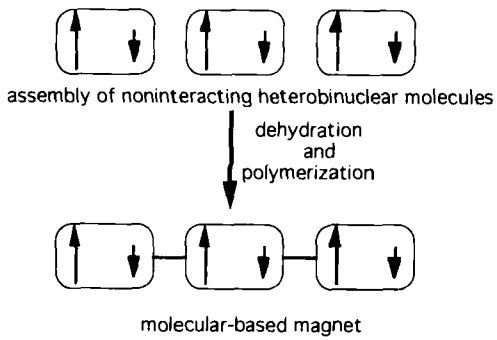

In addition to these two Mn(II)Cu(II) binuclear species, two Ni(II)-Cu(II) species have also been described. Their formulas are NiCu(obp)

$(H_2O)_5$ (*61*) and NiCu(obbz)$(H_2O)_4 \cdot H_2O$ (*62*). The magnetic properties are typical of Ni(II)Cu(II) pairs with a doublet ground state and a quartet excited state. The $3J/2$ energy gaps between the two low-lying states are of the order of -150 cm^{-1}.

B. M(II)Cu(II)$_3$ (M = Mn, Ni) Tetranuclear Species

A series of tetranuclear compounds where a divalent ion M is surrounded by three Cu(oxpn) ligands have been synthesized. The general formula is $\{M[Cu(oxpn)]_3\}(ClO_4)_2 \cdot 2H_2O$, with M = Mn, Ni, and Cd. Figure 33 represents schematically the structure of the tetranuclear dication (*63*). The magnetic susceptibility for M = Mn and Ni has been interpreted with a spin Hamiltonian of the form

$$\mathbf{H} = -J\mathbf{S}_M \cdot \mathbf{S}_{Cu} + \beta[g_M\mathbf{S}_M + g_{Cu}(\mathbf{S}_{Cu1} + \mathbf{S}_{Cu2} + \mathbf{S}_{Cu3}) \cdot H, \quad (11)$$

with

$$\mathbf{S}_{Cu} = \mathbf{S}_{Cu1} + \mathbf{S}_{Cu2} + \mathbf{S}_{Cu3},$$
$$\mathbf{S} = \mathbf{S}_M + \mathbf{S}_{Cu}. \quad (12)$$

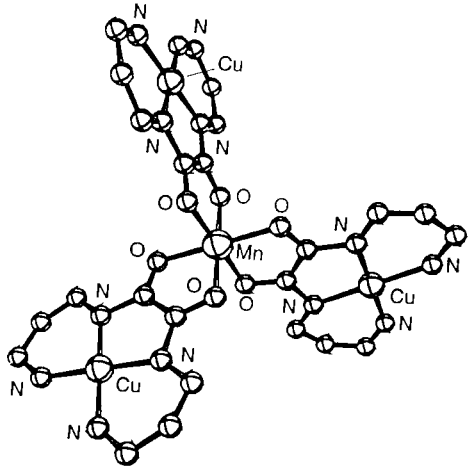

FIG. 33. Schematic representation of the tetranuclear cation $\{Mn[Cu(oxpn)]_3\}^{2+}$. From Lloret *et al.* (*63*).

As expected, the Mn–Cu and Ni–Cu interactions are antiferromagnetic, so that the ground state is characterized by $S = 1$, $S_{Cu} = \frac{3}{2}$ for M = Mn, and $S = \frac{1}{2}$, $S_{Cu} = \frac{3}{2}$ for M = Ni. The Cu(II) local spins tend to align in parallel owing to the M–Cu antiferromagnetic interactions.

C. Mn(II)Cu(II) Alternating Bimetallic Chain Compounds

The anionic copper(II) precursors drawn in Fig. 26 may in principle link metal ions through both the oxamido and one of the carboxylato groups. The simultaneous presence of the two kinds of coordination leads to alternating bimetallic chain compounds. Alternating here means that there is a double alternation, of the spin carriers, Mn(II) and Cu(II), and of the interaction pathways, the oxamido and carboxylato bridges.

In fact, two types of Mn(II)Cu(II) alternating-chain compounds have been obtained, depending on the coordination around the carboxylato bridge. This coordination may be *syn–anti* or *anti–anti:*

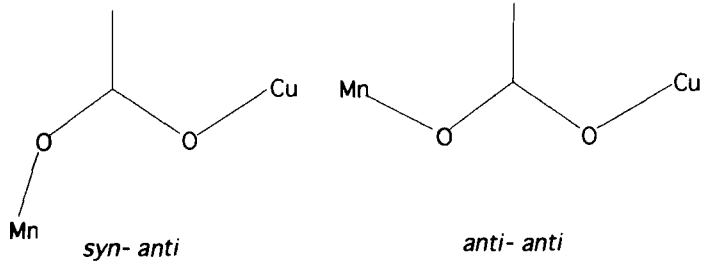

An example of *syn–anti* configuration is provided by MnCu(obzp)$(H_2O)_3$ (*64*). The Mn---Cu separations are 5.438 Å through the oxamido bridge, and 5.367 Å through the carboxylato bridge. The magnetic behavior of such compounds with a *syn–anti* configuration is that of oxamido-bridged Mn(II)Cu(II) binuclear species. The temperature dependence of the magnetic susceptibility may be fitted with Eq. (9). The Mn–Cu interaction through the carboxylato bridge is negligibly small. The same situation holds for the compound MnCu(Br_4obbz)$(H_2O)_3 \cdot 2.5H_2O$ (*65*). Interestingly, when Br_4obbz is replaced by Cl_4obbz, a compound of formula MnCu(Cl_4obbz)$(H_2O)_3$ is obtained, the structure of which consists of binuclear units in which the Mn(II) and Cu(II) ions are only bridged by a carboxylato group, with a *syn–anti* coordination. The Mn(II)–Cu(II) interaction is then found to be negligibly small (*65*).

An example of *anti–anti* configuration is provided by MnCu(obp)

$(H_2O)_3$, the structure of which is shown in Fig. 34 (*66, 67*). The Mn---Cu separations are 5.452 Å through the oxamido bridge and 6.066 Å through the carboxylato bridge. Despite the larger separation, the Mn(II)–Cu(II) interaction through the carboxylato bridge is no longer negligible. The magnetic behavior has a one-dimensional ferrimagnetic character, with a rounded minimum in the $\chi_M T$ vs T plot, and a rapid increase of $\chi_M T$ as T is lowered further. A theoretical expression for the magnetic susceptibility of such systems has been derived; it depends on two interaction parameters, J_1 and J_2, and is based on a model where one of the local spins (S_{Mn} in the present case) is asumed to be high enough to be treated as a classical spin, the other local spin (S_{Cu} in our case) being treated as a quantum spin. This expression is a bit too complicated to be reproduced here. It is given in several review papers and books (*1, 68*). The $\chi_M T$ vs T plot for MnCu(obp)$(H_2O)_3$ is represented in Fig. 35. The minimum of $\chi_M T$ is observed around 40 K. Three-dimensional effects occur in the low-temperature range; $\chi_M T$ shows a sharp maximum at 2.9 K, associated with a three-dimensional antiferromagnetic ordering of the ferrimagnetic chains and a maximum of χ_M at T_c = 2.31 K. The fitting of the susceptibility data leads to J_1 (through oxamido) = -32 cm^{-1}, and J_2 (through carboxylato) = -6.8 cm^{-1}.

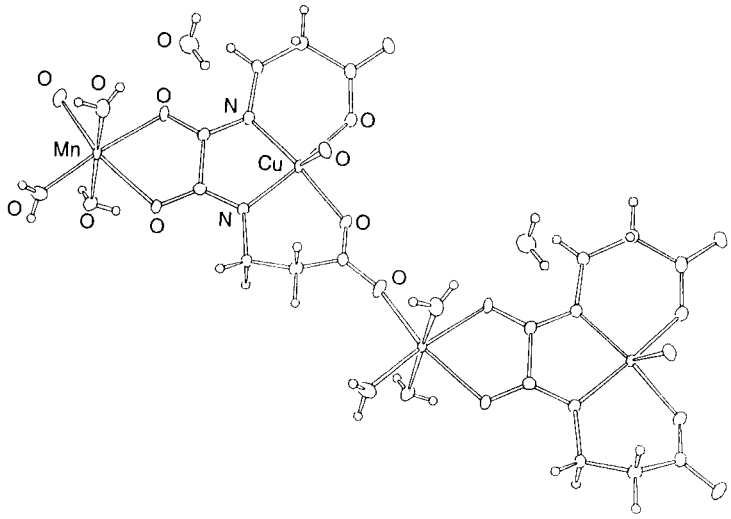

FIG. 34. Structure of the alternating-chain compound MnCu(obp)$(H_2O)_3$. Reprinted from Pei *et al.* (*66*). Copyright © 1988 American Chemical Society.

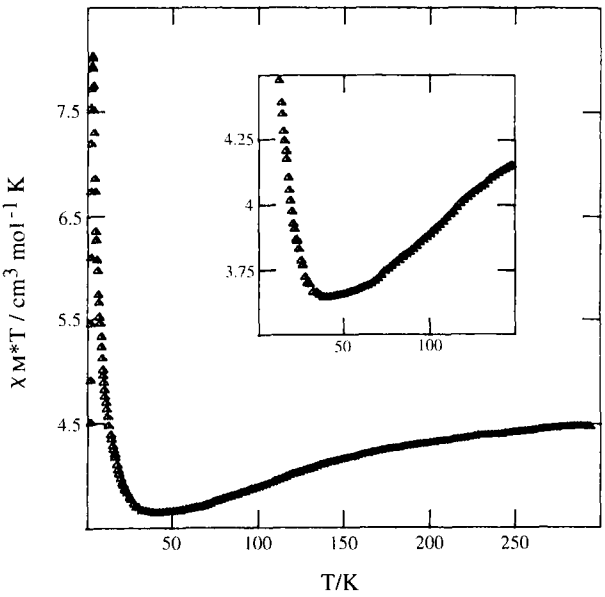

FIG. 35. $\chi_M T$ vs T curve for MnCu(obp)$(H_2O)_3$. Reprinted from Pei *et al.* (*66*). Copyright © 1988 American Chemical Society.

The reason the *anti–anti* configuration is more favorable for transmitting the interaction through the carboxylato bridge than the *syn–anti* one may be understood as follows: The magnetic orbitals mainly involved in the Mn–Cu interaction are of the x^2-y^2 type with a lobe pointing along the Mn–O(carboxylato) or Cu–O(carboxylato) bond. These orbitals are partially delocalized toward the 2*p* orbitals centered on the carboxylato oxygen atoms in a σ-type fashion, as shown in Fig. 36. The 2*p* oxygen orbitals are much more favorably oriented to overlap in the *anti–anti* than in the *syn–anti* configuration. It can also be seen that these 2*p* oxygen orbitals may overlap with the same 2*p* carbon orbital in the *anti–anti* case, and with different 2*p* carbon orbitals in the *syn–anti* case.

D. A Mn(II)Cu(II) Molecular-Based Magnet and Its Precursors

The reaction of the $[Cu(obbz)]^{2-}$ precursor with Mn(II) ions affords two phases, the formulas of which are MnCu(obbz) · $5H_2O$ and MnCu (obbz) · H_2O (*62*). Four of the water molecules of the pentahydrated phase may be very easily removed, which probably indicates that these molecules are noncoordinated. To date it has not been possible to grow

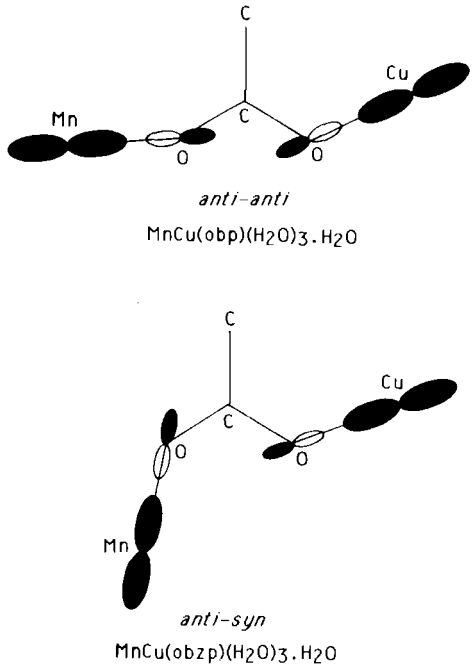

FIG. 36. Orbital interaction between Mn(II) and Cu(II) ions through the carboxylato bridge with *anti–anti* and *anti–syn* configurations. Reprinted from Pei *et al.* (*64*). Copyright © 1989 American Chemical Society.

single crystals of X-ray quality of these phases, and information concerning the structure was deduced from XANES and EXAFS spectroscopies at both the Mn and the Cu edges. For both phases, Cu(II) is in elongated tetragonal surroundings and Mn in distorted octahedral surroundings. The XANES and EXAFS data are consistent with the following description of the structures:

We first consider alternating bimetallic chains with both oxamido and carboxylato bridges. Mn(II) is surrounded by six oxygen atoms; two of them belong to the oxamido bridge, one to the carboxylato bridge, and one to a water molecule. The other two oxygen atoms would belong to carboxylato groups of adjacent chains, so that the structure as a whole would have a two- or three-dimensional character.

The magnetic properties of MnCu(obbz) · $5H_2O$ are very similar to those of MnCu(obp)$(H_2O)_3$, with a long-range antiferromagnetic ordering around 2.3 K. On the other hand, the magnetic properties of MnCu (obbz) · H_2O reveal the onset of a spontaneous magnetization at T_c =

14 K. Figure 37 shows the FCM, ZFCM, and REM curves. The field dependence of the magnetization below T_c gives a saturation magnetization of ca. 4 Nβ mol^{-1}, which agrees with an alignment of the S_{Mn} local spins along the field direction, and an alignment of the S_{Cu} local spins along the opposite direction. As for the other Mn(II)Cu(II) magnets, the coercive field for MnCu(obbz) · H_2O is weak, of the order of 50 Oe at 4.2 K.

More recently, another precursor of the magnet MnCu(obbz) · H_2O has been obtained. Its formula is MnCu(obbz)$(H_2O)_3$ · DMF with DMF = dimethylformamide, and its crystal structure has been solved (*69*). This structure is shown in Fig. 38. It consists of alternating bimetallic chains with oxamido and carboxylato bridges. MnCu(obbz)$(H_2O)_3$ · DMF presents a long-range antiferromagnetic ordering at T_c = 2.3 K. This compound may be transformed into MnCu(obbz) · H_2O either under vacuum at ambient temperature, or under ambient pressure at 60°C. The crucial question concerns the structural modifications accompanying this transformation. Most likely, when two water and one DMF molecules are removed, the Mn(II) ion completes its octahedral surroundings by binding to two carboxylato oxygen atoms belong-

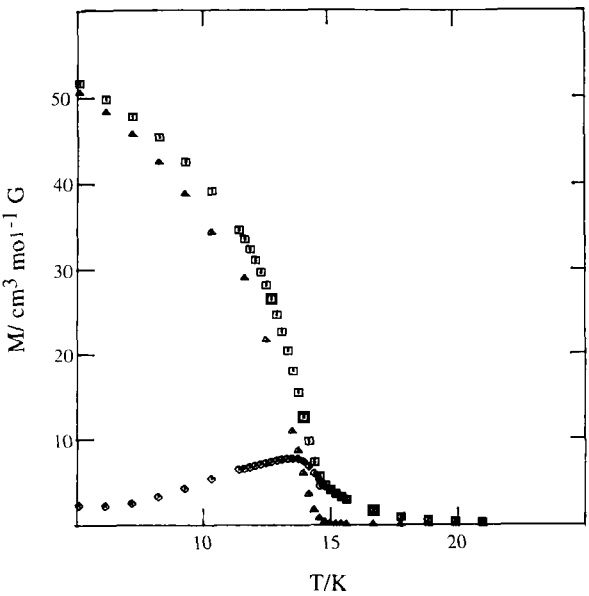

FIG. 37. Magnetization versus temperature curves for MnCu(obbz) · H_2O; (⊡) FCM, (◇) ZFCM, (▲) REM. Reprinted from Nakatani *et al.* (*62*). Copyright © 1989 American Chemical Society.

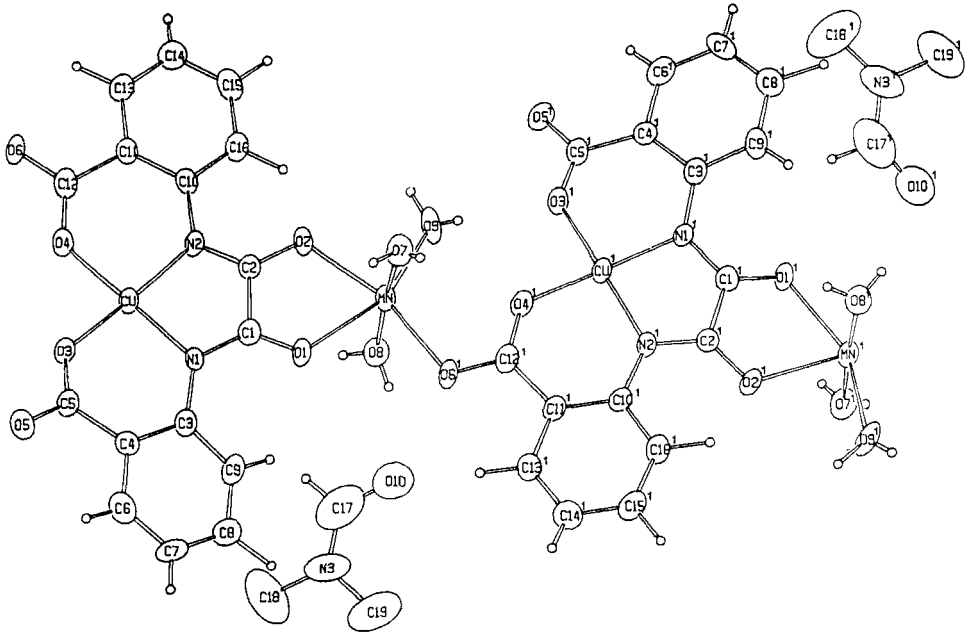

FIG. 38. Structure of MnCu(obbz)$(H_2O)_3$ · DMF. Reprinted from Lloret *et al.* (*69*). Copyright © 1993 American Chemical Society.

ing to adjacent chains within the lattice. A two-dimensional association of chains has been postulated for the structure of MnCu(obbz) · H_2O.

V. Oxalato- and Dithiooxalato-Bridged Heterobimetallic Compounds

In 1990, Okawa and co-workers reported on a very interesting series of oxalato-bridged bimetallic compounds with a polymeric structure, exhibiting three-dimensional magnetic ordering, with critical temperatures ranging from 4 to 45 K (*70*). Subsequently, some of these compounds were structurally characterized. In parallel with the investigation of these molecular-based magnets, some oxalato-bridged bi-, tri-, and tetranuclear species were prepared, in order to characterize the nature of the interaction through the oxalato bridge.

A. HETEROBINUCLEAR COMPOUNDS

Three oxalato-bridged Cr(III)Cu(II) binuclear species have been described, of general formula (salen)Cr(ox)CuL, with salen = *N*,*N*′-ethyl-

enebis(salicylidenaminato), ox = oxalato, and HL = *N*-acetylacetonylidene-*N*-(2-pyridylethyl)amine, *N*-salicylidene-*N*-(2-pyridylethyl)amine, or *N*-salicylidene-*N*,*N*′-diethylamine (*71*, *72*). The first of these compounds has been structurally characterized (in the form of a solvate with DMF and methanol molecules). Its structure is shown in Fig. 39. Cr(III) is in distorted octahedral surroundings and Cu(II) in square pyramidal surroundings with the two oxalato oxygen atoms in the basal plane. The interaction between the local spins $S_{Cr} = \frac{3}{2}$ and $S_{Cu} = \frac{1}{2}$ gives rise to $S = 1$ and $S = 2$ pair states, with a $2J$ energy gap between them. The theoretical expression for $\chi_M T$ is

$$\chi_M T = \frac{2N\beta^2}{k} \frac{g_1^2 + 5g_2^2 \exp\left(\frac{2J}{kT}\right)}{3 + 5\exp\left(\frac{2J}{kT}\right)}, \tag{13}$$

where the Zeeman factors associated with the spin states are related to the local Zeeman factors g_{Cr} and g_{Cu} through (*1*, *10*, *57*)

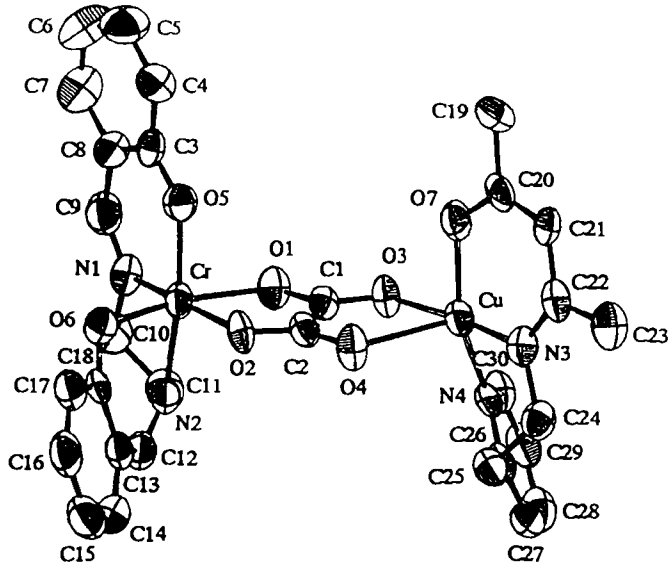

FIG. 39. Structure of the binuclear compound (salen)Cr(ox)CuL with salen = *N*,*N*′-ethylenebis(salicylidenaminato), ox = oxalato, and HL = *N*-acetylacetonylidene-*N*-(2-pyridylethyl)amine. Reprinted from Ohba *et al.* (*72*). Copyright © 1993 American Chemical Society.

$$g_1 = (5g_{Cr} - g_{Cu})/4,$$
$$g_2 = (3g_{Cr} + g_{Cu})/4. \quad (14)$$

In Eq. (13), both Cr(III) local anisotropy and anisotropic interaction are neglected. For the three compounds, $\chi_M T$ slightly increases as T is lowered, which indicates that the interaction is ferromagnetic with a $S = 2$ pair ground state. The triplet–quintet energy gaps, $2J$, were found in the range 8.8–11.4 cm^{-1}. The ferromagnetic nature of the interaction may be easily understood from symmetry arguments. The three unpaired electrons arising from Cr(III) occupy the t_{2g} orbitals, which transform as the $a_1 + a_2 + b_2$ irreducible representations of the C_{2v} idealized symmetry. The unpaired electron arising from Cu(II) occupies an orbital pointing toward the four nearest neighbors in the basal plane and transforming as b_1. The strict orthogonality of the four magnetic orbitals involved in the problem is achieved, and the interaction is expected to be ferromagnetic (*1, 2*).

In addition to the Cr(III)Cu(II) binuclear compounds, Okawa synthesized a series of compounds of formula [(salen)Cr(ox)M(taea)](BPh_4), with M = Mn, Fe, Co, and Ni, and taea = tris(2-aminoethyl)amine (*72*). For all the compounds the Cr(III)–M(II) interaction is found to be ferromagnetic, the interaction parameters being 1.0 cm^{-1} for M = Mn, 1.6 cm^{-1} for M = Fe, 2.6 cm^{-1} for M = Co, and 9.2 cm^{-1} for M = Ni. These J values were obtained by describing the low-lying pair states with the isotropic spin Hamiltonian $-J\mathbf{S}_{Cr}\cdot\mathbf{S}_M$. The validity of such a model might be questionable for M = Fe and Co. Indeed, the Fe(II) and Co(II) ions in distorted octahedral surroundings have a large local anisotropy. The ferromagnetic nature of the interaction has been rationalized as follows: The configurations of the unpaired electrons for the M(II) ions in octahedral surroundings are $t_{2g}^3 e_g^2$ for M = Mn, $t_{2g}^2 e_g^2$ for M = Fe, $t_{2g}^1 e_g^2$ for M = Co, and e_g^2 for M = Ni. The interactions between t_{2g}(Cr) and e_g(M) electrons are strictly ferromagnetic, providing positive $J_{t_{2g}e_g}$ contributions to J, whereas the overall interaction between t_{2g} electrons would be antiferromagnetic, providing a negative contribution to J. For Mn(II), Fe(II), and Co(II), the t_{2g}^3(Cr)–e_g^2(M) contributions would predominate over those of t_{2g}^3(Cr)–t_{2g}^n(M).

Another ferromagnetically coupled oxalato-bridged binuclear species has been obtained. Its formula is [terpy)Cu(ox)VO(ox)(H_2O)]·H_2O, with terpy = 2,2′:6′,2″-terpyridine. The triplet ground state has been reported to be stabilized by about 1 cm^{-1} with respect to the excited singlet (*73*). In principle, the Cu(II)VO(II) pair offers a clear-cut example of strict orthogonality of the magnetic orbitals. In the present case, how-

ever, the very low symmetry of the Cu(ox)V bridging network might have destroyed this orthogonality.

B. Compounds of Higher Nuclearity

A few trinuclear and tetranuclear μ-oxalato and μ-dithiooxalato heterobimetallic compounds are known. Two $Cu(II)_2VO(II)$ species have been described. The former has already been mentioned in Kahn (*3*). The latter is $[(terpy)Cu(ox)VO(H_2O)(ox)Cu(terpy)](ClO_4)\cdot H_2O$. The exact structure is not known, and the magnetic susceptibility data do not reveal any interaction (*73*).

A μ-oxalato $Cr(III)Ni(II)_3$ tetranuclear compound is known. Its formula is $\{Cr[(ox)Ni(Me_6\text{-}[14]ane\text{-}N_4)]_3\}(ClO_4)_3$. A central Cr(III) ion in distorted octahedral surroundings is linked through oxalato bridges to three Ni(II) ions, also in distorted octahedral surroundings (*74*). The magnetic properties of this $Cr(III)Ni(II)_3$ compound are discussed in detail in Kahn (*1*). We restrict ourselves here to pointing out that along the three Cr(ox)Ni linkages the interaction is ferromagnetic, because of the orthogonality between the t_{2g}^3(Cr) and e_g^2(Ni) orbitals. It turns out that the ground state is $S = S_{Cr} + 3S_{Ni} = \frac{9}{2}$.

The very similar compound in which the oxalato bridges are replaced by dithiooxalato bridges with the sulfur atoms bound to the central Cr(III) ion has also been described. Its formula is $\{Cr[(C_2O_2S_2)Ni(Me_6\text{-}[14]ane\text{-}N_4)]_3\}(ClO_4)_3$, and the structure of the tetranuclear cation is shown in Fig. 40 (*75, 76*). Again, the ground state has the highest spin, $S = \frac{9}{2}$. The magnitude of the coupling, however, is more than twice as large in the dithiooxalato derivative as in the oxalato derivative (J = 11.8 and 5.2 cm^{-1}, respectively). This difference may be attributed to the fact that the spin density arising from the Cr(III) ion is more delocalized toward the dithiooxalato than the oxalato bridges, owing to the more covalent character of the Cr–S bonds. It is interesting to note here that the presence of sulfur-containing bridges usually favors the antiferromagnetic interaction, while in the present case it favors the ferromagnetic interaction. There is nothing mysterious behind that. Owing to the diffuseness of the 3*s* and 3*p* valence orbitals of sulfur as compared to the 2*s* and 2*p* valence orbitals of oxygen, the replacement of oxygen by sulfur atoms in the bridging networks increases the overlap densities between magnetic orbitals. When these magnetic orbitals are not orthogonal, the overlap integrals between magnetic orbitals are enhanced, which favors the antiferromagnetic contributions. On the other hand, when these magnetic orbitals are orthogonal, they are the

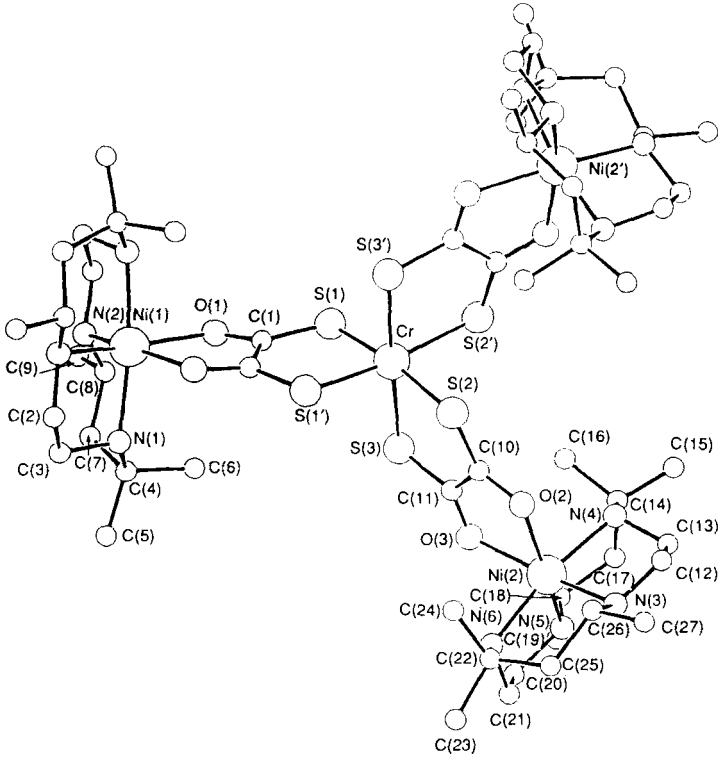

FIG. 40. Structure of the tetranuclear cation $\{Cr[(dto)Ni(Me_6\text{-}[14]ane\text{-}N_4)]_3\}^{3+}$, with dto = dithiooxalato. From Mitsumi *et al.* (*75*).

two-electron exchange integrals which are enhanced, and this favors the ferromagnetic contributions.

C. Long-Range Ordering in Polymeric Compounds

1. *Oxalato-Bridged Two-Dimensional Magnets Obtained from* $[Cr(ox)_3]^{3-}$

In 1990, Okawa and co-workers reported on the first oxalato-bridged bimetallic assemblies exhibiting long-range ferromagnetic ordering. The reaction of equimolar aqueous solutions of $K_3[Cr(ox)_3]\cdot 3H_2O$ and $Cu(NO_3)_2\cdot 3H_2O$ in the presence of tetra-*n*-butylammonium bromide affords an insoluble powder of formula $(NBu_4)[CuCr(ox)_3]$. The $\chi_M T$ vs T plot for this compound down to 30 K reveals a Curie–Weiss behavior

with a Weiss temperature $\theta = 14$ K, indicating ferromagnetic interactions beween the spin carriers. As T is decreased further below 30 K, $\chi_M T$ increases more and more rapidly, then diverges. The FCM curve recorded with a field of 2 Oe shows a break at $T_c = 7$ K, characteristic of a long-range magnetic ordering (*70*).

Subsequently, a series of related compounds of formula $(NBu_4)[MCr(ox)_3]$ with M = Mn, Fe, Co, Ni, and Zn were obtained by the same group (*77, 78*). All these compounds, except the last one, exhibit a three-dimensional magnetic ordering. The critical temperatures were found to be 6 K for M = Mn, 12 K for M = Fe, 10 K for M = Co, and 14 K for M = Ni. Below T_c, the compounds behave as soft magnets with rather weak coercive fields. The largest coercitivity was found for the Fe(II)Cr(III) derivative; the coercive field at 5 K is reported as 320 Oe.

These results raise two quite important questions. The first concerns the nature, ferro- or antiferromagnetic, of the M(II)–Cr(III) interaction. The second concerns the architecture of the compounds. Concerning the nature of the interaction, the field dependence of the magnetization gives a saturation magnetization corresponding to the parallel alignment of the S_{Cr} and S_M local spins. However, the magnetic field necessary to reach this saturation is larger than expected for a genuine ferromagnet. The profile of the $M = f(H)$ curves in the low magnetic field range suggests some spin decoupling. It is probable that in zero-field the local spins are not rigorously parallel, but canted, and the magnetic field overcomes this canting. If it is so, the compounds should be described as weakly canted ferromagnets. It may be noticed that the ferromagnetic nature of the M(II)–Cr(III) interactions in the $(NBu_4)_2[MCr(ox)_3]$ polymeric compounds is in line with what has been found in the binuclear species [(salen)Cr(ox)M(taea)](BPh$_4$) (see Section V,A).

Information on the structure of $(NBu_4)[MnCr(ox)_3]$ has been obtained by Atovnyan *et al.*, who succeeded in growing single crystals of the compound (*79*). The structure analysis reveals an anionic two-dimensional network with layers consisting of edge-sharing Mn(II)Cr(III) hexagons, and NBu_4^+ cations located between the layers. The separation between two adjacent layers is 8.95 Å. Shortly thereafter, Decurtins and co-workers grew single crystals of $(PPh_4)[MnCr(ox)_3]$ (*80*), the structure of which is very similar to that of $(NBu_4)[MnCr(ox)_3]$. Each metal site surrounded by three oxalato groups is chiral. In both compounds the two-dimensional network is generated by a perfect alternation of Λ and Δ chiral sites, as shown in Fig. 41. Using only one type, Λ or Δ, of chiral sites would result in a three-dimensional assembly. We will come back to this point in the next section. Three-dimensional

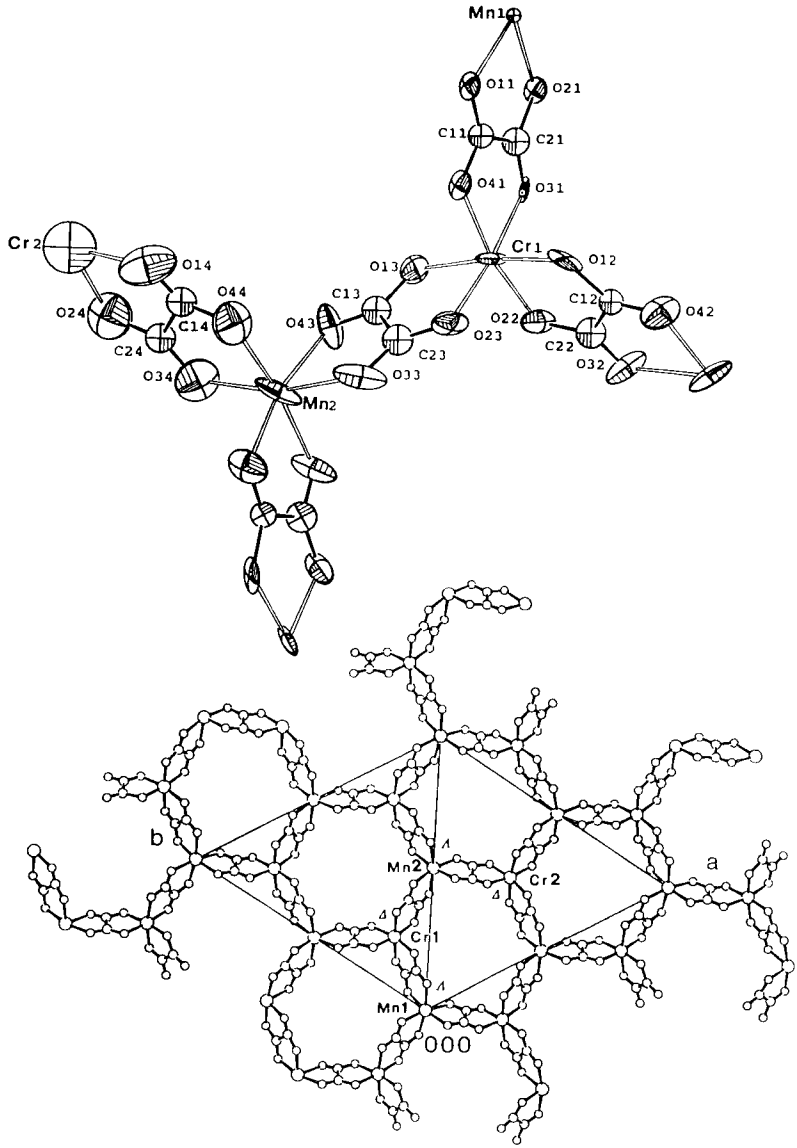

FIG. 41. Structure of the two-dimensional anionic network $[MnCr(ox)_3]^-$ in $(PPh_4)_2[MnCr(ox)_3]$. From Decurtins *et al.* (*80*).

ferromagnetic ordering in $(PPh_4)[MnCr(ox)_3]$ has been observed at $T_c = 5.9$ K. Decurtins also investigated the optical properties of $(PPh_4)[MnCr(ox)_3]$. The absorption spectrum is characteristic of the $Cr(ox)_3$ chromophore with an enhancement of the $^4A_2 \rightarrow {}^2E$, $^4A_2 \rightarrow$

$^2T_1$, and $^4A_2 \rightarrow {}^2T_2$ spin-forbidden transitions. A strong site-selective luminescence from the ^2E states of Cr(III) is also observed at low temperature.

2. *Dithiooxalato-Bridged Magnets Obtained from $[Cr(dto)_3]^{3-}$*

Okawa and co-workers have also reported on dithiooxalato-bridged bimetallic assemblies of the formula $(NPr_4)[MCr(dto)_3]$, with NPr_4^+ = tetra-*n*-propylammonium, dto = dithiooxalato, and M = Fe, Co, and Ni (*81*). No structure is available yet, but the architecture is assumed to be the same as that of the oxalato-bridged compounds, with dto bridging through the sulfur atoms to Cr(III) and through the oxygen atoms to M(II). For the three compounds, $\chi_M T$ continuously increases as T is lowered, revealing ferromagnetic Cr(III)–M(II) interactions. The compounds exhibit a long-range ferromagnetic ordering at T_c = 8, 16, and 23 K for M = Fe, Co, and Ni, respectively. The FCM, ZFCM, and REM curves for one of these compounds, $(NPr_4)[FeCr(dto)_3]$, are shown in Fig. 42. The critical temperatures for the oxalato- and dithiooxalato-bridged M(II)Cr(III) materials as reported by Okawa are com-

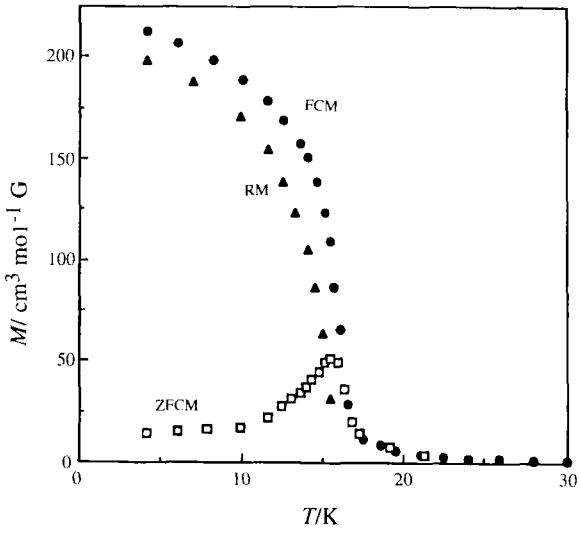

FIG. 42. Magnetization vs temperature curves for $(NPr_4)_2[FeCr(dto)_3]$. RM stands for remnant magnetization. From Okawa *et al.* (*81*).

pared in Table I. Okawa attempted to deduce the values of the M(II)–Cr(III) interaction parameters from the T_c values, using a mean-field approximation. Actually, the oxalato-bridged compounds, and probably also the dithiooxalato-bridged ones, have a two-dimensional structure, and T_c is governed not only by the J interaction parameter within a layer, but also by the interlayer interactions.

3. Oxalato-Bridged Magnets Obtained from $[Fe(ox)_3]^{3-}$

Okawa *et al.* have also reported on bimetallic assemblies of formula $(NBu_4)[MFe(ox)_3]$ prepared from $K_3[Fe(ox)_3]\cdot 3H_2O$, with M = Ni, Fe, Mn, and Zn (*82–84*). For the first two compounds, $(NBu_4)[NiFe(ox)_3]$ and $(NBu_4)[FeFe(ox)_3]$, the M(II)–Fe(III) interactions are antiferromagnetic as indicated by the magnetic susceptibility data above ca. 80 K; χ_M follows Curie–Weiss laws with negative Weiss temperatures, −80 K for M = Ni, and −95 K for M = Fe. The temperature dependence of the magnetization for both compounds reveals a magnetic transition with T_c = 28 K and 43 K, respectively. These compounds may be described as ferrimagnets. The magnetic behavior below T_c is not yet perfectly clear. It has been suggested that a spin-glass–like behavior was observed. In fact, it seems that the situation for $(NBu_4)[FeFe(ox)_3]$ is even more original (*85*). The FCM curve (see Fig. 43) reveals a large negative magnetization below T_c. Surprisingly, this diamagnetism in the magnetically ordered phase is not observed when the tetra-*n*-butylammonium cation is replaced by tetra-*n*-propylammonium or tetraphenylphosphonium. $(NBu_4)[FeFe(ox)_3]$ was also investigated by Mössbauer spectroscopy (*84*). Nuclear Zeeman splittings in zero applied field are observed below T_c = 43 K, which confirms that the compound possesses a spontaneous magnetization. As far as $(NBu_4)[MnFe(ox)_3]$ is concerned, the antiferromagnetic interaction between $S_{Fe(III)} = \frac{5}{2}$ and

TABLE I

COMPARISON OF THE T_c VALUES FOR THE $(NBu_4)[MCr(ox)_3]$ AND $(NPr_4)[MCr(dto)_3]$ COMPOUNDS[a]

M	$(NBu_4)[MCr(ox)_3]$ T_c	$(NPr_4)[MCr(dto)_3]$ T_c
Fe	8 K	12 K
Co	16 K	10 K
Ni	23 K	14 K

[a] From Okawa *et al.* (*81*).

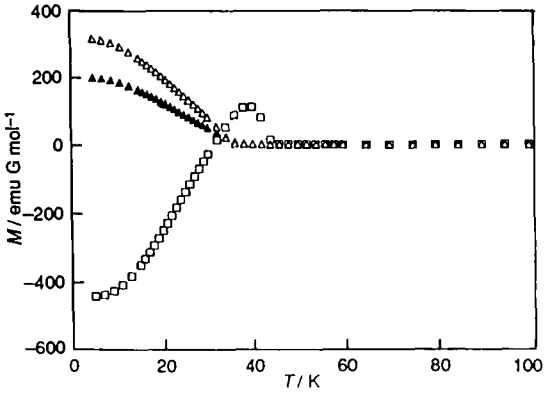

FIG. 43. Field-cooled magnetization vs temperature curves for the (cat)$[Fe_2(ox)_3]$ compounds with cat = NPr_4 (△), PPh_4 (▲), and NBu_4 (□). From Mathonière *et al.* (*85*).

$S_{Mn(II)} = \frac{5}{2}$ local spins results in a three-dimensional antiferromagnetic ordering.

D. Chirality and Dimensionality in Oxalato-Bridged Polymeric Compounds

We mentioned earlier (see Section V,C,1) that for the two-dimensional compounds of formula (cat)$[MnCr(ox)_3]$, with cat^+ standing for a monovalent cation, each metal site of a given chirality (Λ or Δ) is surrounded by three metal sites of the opposite chirality (Δ or Λ), so that within a layer all the Mn(II) sites have the same chirality and all the Cr(III) sites have the other chirality. If the Mn(II) and Cr(III) sites had the same chirality, the hexagons of the honeycomb structure could no longer be closed, and the structure would be three- instead of two-dimensional. This structure as a whole would obviously be chiral (*86*).

Such a chiral three-dimensional (3D) structure has been reported for the first time by Decurtins and co-workers (*87*). These authors first discovered that an aqueous solution of $(bipyH)^+[Fe^{III}(ox)_2(H_2O)_2]$ turns red with exposure to UV light, indicating the formation of the $[Fe(bipy)_3]^{2+}$ cation. Slow evaporation affords crystals of $[Fe(bipy)_3][Fe^{II}_2(ox)_3]$ crystallizing in the cubic and noncentrosymmetric space group $P4_321$. The structure consists of an open three-connected anionic network in which all the $Fe^{II}(ox)_3$ chromophores have the same chirality, and $[Fe(bipy)_3]^{2+}$ cations with the same chirality fill the vacancies. This structure is reminiscent of that of diamond (*88*). A projection of

the anionic network onto the [100] plane (see Fig. 44) shows octagons and squares, with fourfold helicoidal axes passing through the centers of the squares and turning all clockwise (or all counterclockwise). The same compound can be obtained in a slightly more rational way by directly reacting $[Fe(bipy)_3]^{2+}$, Fe(II), and ox^{2-} species (*89*). Similar compounds have been obtained by replacing Fe(II) in the tris(2,2′-bipyridine) cation by Co(II) and Ni(II), and Fe(II) in the anionic network by Mn(II). Compounds with essentially the same 3D structure, of formula $[Fe(bipy)_3][A^{I}B^{III}(ox)_3]$, have also been synthesized with, for instance, A = Li and B = Cr.

Despite the 3D structure, the magnetic properties of all these compounds are not very appealing. Indeed, for the $[A^{II}_2(ox)_3]^{2-}$ networks, the A(II) ions interact antiferromagnetically through the oxalato bridge, resulting in a long-range antiferromagnetic ordering. For the $[A^{I}B^{III}(ox)_3]^{2-}$ networks, the interaction between two B(III) ions through the

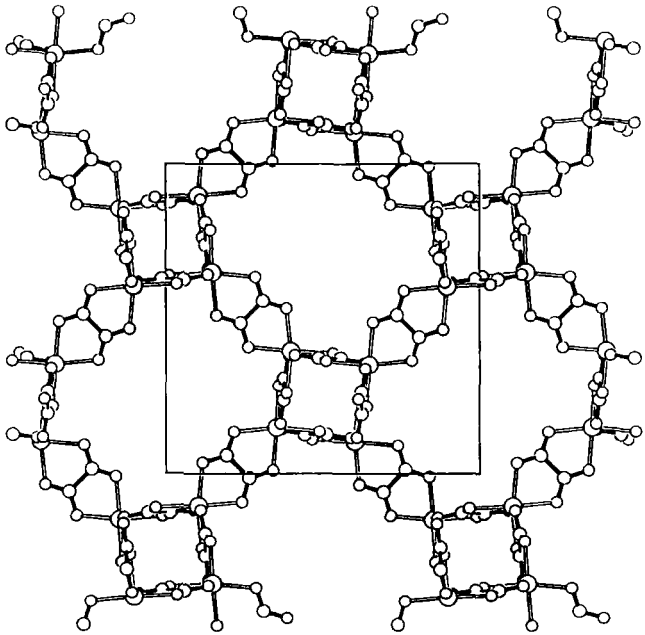

FIG. 44. Projection onto the [100] plane of the three-dimensional anionic network $[Fe_2(ox)_3]^{2-}$ in $[Fe(bipy)_3][Fe_2(ox)_3]$; the large balls stand for iron atoms, and the small balls stand for the oxygen and carbon atoms of the oxalato bridges. From Collin (*86*) and reprinted from Decurtins *et al.* (*87*). Copyright © 1993 American Chemical Society.

diamagnetic ox–A–ox linkage is negligibly small. On the other hand, it would be extremely interesting to obtain oxalato-bridged bimetallic compounds with a 3D structure, involving A and B magnetic metal ions with different local spins. The stoichiometry $(cat)[A^{II}B^{III}(ox)_3]$ seems to be particularly appropriate. The problem we are faced with is to favor the 3D structure with respect to the 2D one. For $[Fe(bipy)_3][Fe_2(ox)_3]$, the driving force leading to the 3D structure seems to be the charge, the size, and the symmetry of the cation. The process may be described as follows: When reacting $[Fe(bipy)_3]^{2+}$, Fe(II), and ox^{2-} species, 2D and 3D structures in principle can be obtained. The size of the cation closely fits the vacancies of the anionic framework in the case of the 3D structure, which favors this structure. In turn, the formation of the noncentrosymmetric 3D network provokes the enantiomeric separation of $[Febipy)_3]^{2+}$. At this writing, Decurtins is attempting to synthesize 3D $(cat)[A^{II}B^{III}(ox)_3]$ phases, with $cat^+ = [Rh^{III}(ppy)_2(bipy)]^+$ ('ppy = 2-phenylpyridine).

VI. Oximato-Bridged Heterobimetallic Compounds

The oximato group, $N{=}O^-$, can bridge two metal ions through both the imino nitrogen and the deprotonated oxygen atoms, thus affording polymetallic species. For a long time it has been known that this oximato bridge propagates a very strong antiferromagnetic interaction. In bis(oximato)-bridged copper(II) binuclear species, the interaction can be so pronounced that even at room temperature the compound is almost diamagnetic (*90, 91*). The singlet–triplet energy gap may be as large as $-1000\ cm^{-1}$ (*92–94*). Similarly, in copper(II) trinuclar species, the excited quartet state may be almost entirely depopulated in the whole 300–4 K temperature range (*94–96*). It turns out that the bis(oximato) bridge is one of the most efficient extended antiferromagnetic couplers. Such a situation incited several groups to investigate bis(oximato)-bridged heterobimetallic species, from binuclear discrete units up to one-dimensional compounds. At this stage it is probably worthwhile to stress that the ferrimagnetic strategy to obtain magnets is more efficient when (i) the difference $|S_A - S_B|$ between the local spins is larger on the one hand, and (ii) the magnitude of the A–B antiferromagnetic interaction is more pronounced on the other hand. Therefore, bis(oximato)-bridged Mn(II)Cu(II) compounds are good candidates for novel molecular-based magnets.

A. Heterobinuclear Compounds

Lloret, Julve, and co-workers investigated two Mn(II)Cu(II) binuclear species, one with an oxamido bridge, the other one with a bis(oximato) bridge, and compared the magnitudes of the interaction (*97*). The two species, schematized below, are $[Mn(bipy)_2Cu(oxpn)]^{2+}$ and $[Mn(bipy)_2Cu(pdmg)]^{2+}$, with pdmg = 3,9-dimethyl-4,8-diazaundeca-3,8-diene-

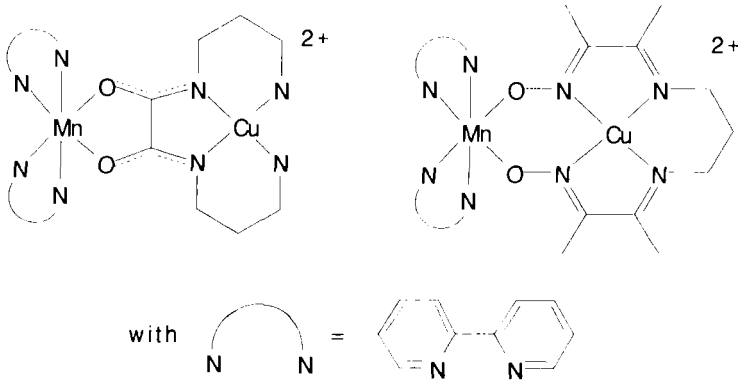

2,10-dione-bis(oximato). Lloret *et al.* found $J = -24.5$ cm^{-1} for the former compound, and $J = -50.3$ cm^{-1} for the latter, which confirms the efficiency of the bis(oximato) bridge in transmitting an antiferromagnetic interaction. Such a situation may be easily understood when we realize that the magnitude of the interaction is governed by the overlap between the two *xy*-type magnetic orbitals centered on Mn(II) and Cu(II) ions, respectively (*1*). Each magnetic orbital is partially delocalized toward the nearest neighbor atoms of the metal ion on which this orbital is centered. The overlap occurs on both sides of the bridge, as shown below, and is obviously more pronounced in the case where the bridging nitrogen and oxygen atoms are directly bound than in the case where they are separated by a carbon atom.

A bis(oximato)-bridged Ni(II)Cu(II) related compound has also been described (*98*). Its formula is $[Ni(cyclam)Cu((pdmg)](ClO_4)$, with cyclam = 1,4,8,11-tetraazacyclotetradecane. The energy gap between ground doublet and excited quartet states was found to be $3J/2 = -306$ cm^{-1}. More interesting, probably, is the nature of the interaction in the Cr(III)Cu(II) binuclear cation of formula $[Cr(salen)Cu(pdmg)]^+$. The temperature dependence of the magnetic susceptibility reveals a $S = 2$ parallel spin ground state, and a $S = 1$ excited state, the energy gap between these two states being found to be $2J = 23.6$ cm^{-1} (*99*). The

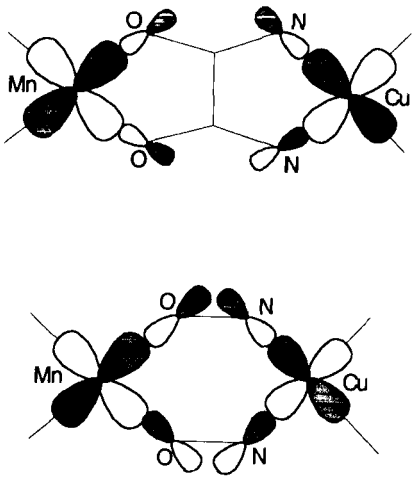

ferromagnetic nature of the Cr(III)–Cu(II) interaction obviously arises from the orthogonality of the four magnetic orbitals involved in this case (see Section V,A).

Quite an interesting series of bis(oximato)-bridged heterobinuclear compounds were synthesized and investigated by Chaudhuri and coworkers (100). These compounds are obtained by the reaction of $[Cu(Hpdmg)]^+$ with a salt of a divalent, trivalent, or tetravalent metal ion in the presence of the cyclic triamine L = 1,4,7-trimethyl-1,4,7-triazacyclononane. The general formula of the binuclear cations may be written as $[LXM(pdmg)Cu(H_2O)_x]^{+,\text{ or } 2+}$, with M = Cr(III), Mn(III), Mn(II), Fe(III), Co(II), Ni(II), and Cu(II), X = Cl^-, CH_3O^-, or $CH_3CO_2^-$, and x = 1 or 0. The structures of two of these binuclear cations are shown in Fig. 45, namely $[L(CH_3O)Cr(pdmg)Cu(H_2O)]^{2+}$ and $[LMn(\mu\text{-}CH_3CO_2)(pdmg)Cu]^{2+}$. One will note that for the latter compound the two metal ions are bridged by the acetato ligand in addition to the two oximato groups. The magnetic properties of all these MCu(II) compounds have been studied and interpreted. The values of the interaction parameter J occuring in the isotropic spin Hamiltonian $H = -J\mathbf{S}_M \cdot \mathbf{S}_{Cu}$, together with the ground state spins, are given in Table II.

Once again, the orthogonality of the magnetic orbitals in the Cr(III) Cu(II) compound leads to a ferromagnetic interaction. The same situation holds for the Mn(III)Cu(II) compound. The authors of this work proposed a rationalization of their findings in terms of interaction pathways along each of the M–O–N–Cu linkages. It must be stressed again that when two spin carriers are bridged by several groups, identical

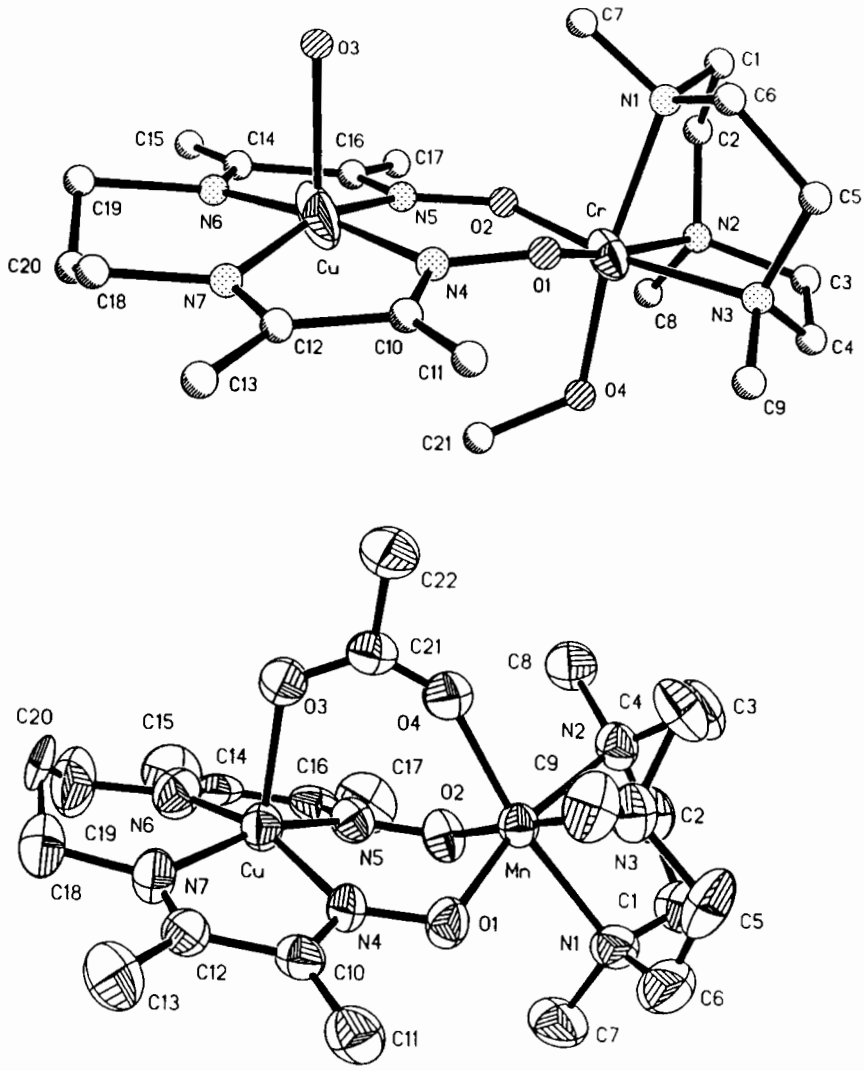

FIG. 45. Structure of the binuclear cations $[L(CH_3O)Cr(pdmg)Cu(H_2O)]^{2+}$ (top) and $[LMn(\mu\text{-}CH_3CO_2)(pdmg)Cu]^{2+}$ (bottom), with pdmg = 3,9-dimethyl-4,8-diazaundeca-3,8-diene-2,-10-dione-bis(oximato) and L = 1,4,7-trimethyl-1,4,7-triazacyclononane. Reprinted from Birkelbach *et al.* (*100*). Copyright © 1994 American Chemical Society.

or different, it is not possible to analyze the interaction parameter deduced from the magnetic data without taking into account the phase relations between the bridges. In other terms, what is crucial for predicting the nature of the interaction is not the symmetry of each of the

TABLE II

VALUES OF THE INTERACTION PARAMETER IN THE $[LXM(pdmg)Cu(H_2O)_x]^{1+,\,or\,2+}$ HETEROBINUCLEAR CATIONS[a]

Compound	J/cm^{-1}	Ground state spin
$(CH_3O)Cr(III)Cu(II)$	39	2
$(CH_3CO_2)Mn(III)Cu(II)$	109	$\frac{5}{2}$
$(CH_3CO_2)Mn(II)Cu(II)$	−83	2
$(Cl)Fe(III)Cu(II)$	−78	2
$(CH_3CO_2)Fe(III)Cu(II)$	−90	2
$(CH_3CO_2)Ni(II)Cu(II)$	−198	$\frac{1}{2}$

[a] The compounds are abbreviated as XMCu(II).

bridges, but the symmetry of the bridging network as a whole. In Table II, the case of the (Cl)Co(II)Cu(II) compound has been omitted. Indeed, the orbital degeneracy of the Co(II) ion in octahedral surroundings forbids interpretation of the magnetic data with an isotropic spin Hamiltonian. In the low-temperature range—say, below 30 K—only the local Kramers doublet of the Co(II) ion is thermally populated, and the interaction between this Kramers doublet and the $S_{Cu} = \frac{1}{2}$ local ground state of Cu(II) may lead to a singlet pair state, separated by several tens of wavenumbers of the first excited states.

Two bis(oximato)-bridged Ni(II)Cu(II) species of another type have been described by Colacio and co-workers (*101*). These authors started from the polydentate ligand ω,ω'-bis((1,3-dimethyl-5-nitrosouracil-6-yl)amine)propane, here denoted H_2L, shown below:

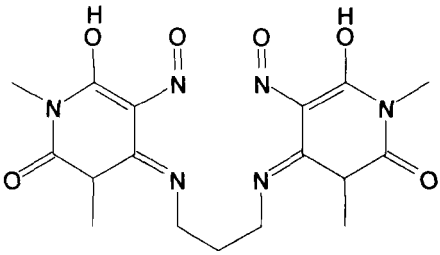

They prepared the copper(II) precursor $[CuL(H_2O)]\cdot 3H_2O$, in which the metal ion occupies the N_4- central cavity. The reaction of this precursor with $[Ni(Me_6\text{-}[14]ane\text{-}N_4)](ClO_4)_2$ affords the compound of formula

$[Ni(Me_6\text{-}[14]ane\text{-}N_4)(\mu\text{-}L)Cu(ClO_4)](ClO_4)\cdot H_2O$. The structure of the heterobinuclear cation is rather unexpected. As a matter of fact, the coordination of CuL to the $[Ni(Me_6\text{-}[14]ane\text{-}N_4)]^{2+}$ moiety takes place through an exocyclic oxygen atom of the uranyl cycle and a *syn–anti* oximato group. The Ni---Cu separation is equal to 4.792 Å. Curiously, the basal plane of the Cu(II) ion comprises two amino and oximato nitrogen atoms, and either an oxygen (occupancy 0.78) or a nitrogen atom (occupancy 0.22) from the other oximato group. This structure is shown in Fig. 46. The energy gap between ground doublet and excited quartet states is found to be $3J/2 = -185\ cm^{-1}$. The EPR spectrum below ca. 50 K is typical of a doublet pair state. When the temperature is increased above 50 K, a signal at $g = 4$ is detected, corresponding to the $M_S = \pm\frac{1}{2}$ Kramers doublet arising from the quartet excited state.

When the copper(II) precursor $[CuL(H_2O)]$ reacts with another Ni(II) species, namely $[Ni(Me_3\text{-}[12]\text{-}N_3)](ClO_4)_2$, with $Me_3\text{-}[12]\text{-}N_3$ = 2,4,4-

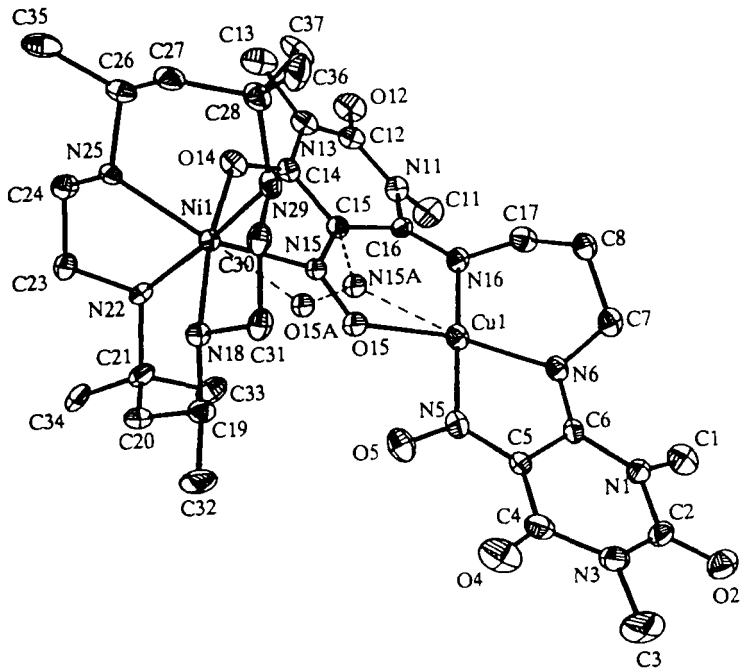

FIG. 46. Structure of the binuclear cation $[Ni(Me_6\text{-}[14]ane\text{-}N_4)(\mu\text{-}L)Cu(ClO_4)]^+$, with H_2L = ω,ω′-bis((1,3-dimethyl-5-nitrosouracil-6-yl)amine)propane and $Me_6\text{-}[14]ane\text{-}N_4$ = (±)-5,7,7,12,14,14-hexamethyl-1,4,8,11-tetraazacyclotetradecane. Reprinted from Colacio *et al.* (*101*). Copyright © 1994 American Chemical Society.

trimethyl-1,5,9-triazacyclododec-1-ene, an elimination of one CO molecule from a pyrimidine ring of a ligand L^{2-} occurs, leading to an imidazole ring (the new ligand is then denoted L'^{2-}). The Cu(II) and Ni(II) ions are bridged by one N–O oximato group in a *syn–syn* fashion on the one hand, and one oxygen atom of a nitroso-oximato group from the pyrimidine and imidazole rings on the other hand, as shown in Fig. 47. The Ni---Cu separation is equal to 2.45 Å, i.e., much shorter than in the previous example. In this compound the Ni(II)–Cu(II) interaction is so large that only the ground doublet state is populated up to room temperature, and the EPR spectrum does not display any signal at $g = 4$, assignable to the $M_S = \pm\frac{1}{2}$ Kramers doublet belonging to the quartet excited state.

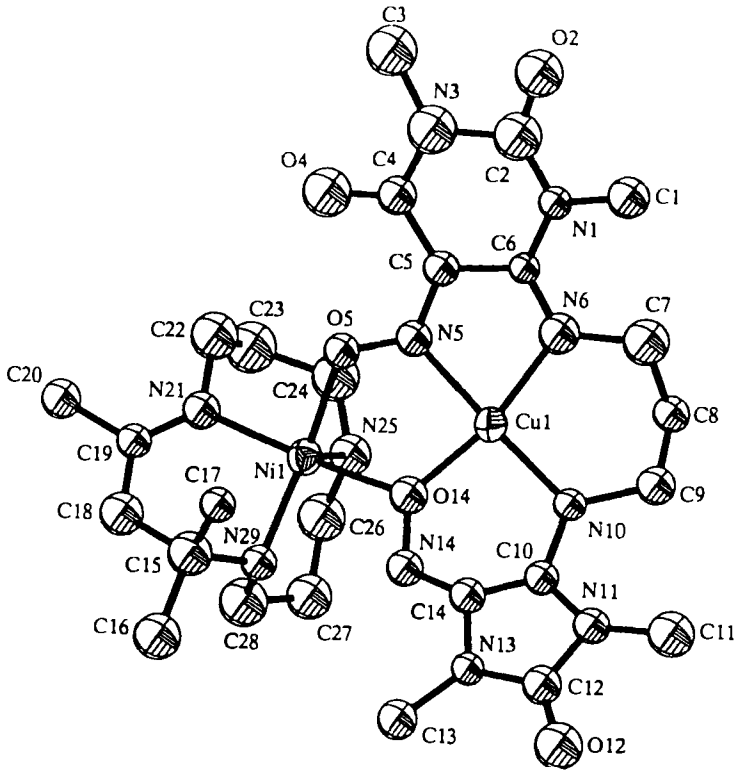

FIG. 47. Structure of the binuclear cation $[Ni(Me_3\text{-}[12]\text{-}N_3)(\mu\text{-}L')Cu(ClO_4)]^+$ where L'^{2-} is the ligand derived from L^{2-} after elimination of one CO molecule from a pyrimidine ring, and $Me_3\text{-}[12]\text{-}N_3$ = 2,4,4-trimethyl-1,5,9-triazacyclododec-1-ene. Reprinted from Colacio *et al.* (*101*). Copyright © 1994 American Chemical Society.

B. Heterotrinuclear Compounds

Two types of ABA symmetrical heterotrinuclear compounds have been reported thus far. The former type involves the central core $[Cu(dmg)_2]^{2-}$ shown below, where Hdmg is dimethylglyoxime:

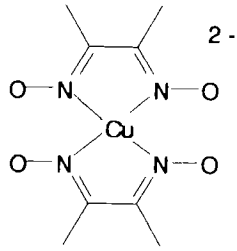

The most interesting compound of this kind is probably $[(salen)Cr]_2Cu(dmg)_2$, where two Cr(III) ions are linked by the $[Cu(dmg)_2]^{2-}$ core (99). As pointed out earlier, the Cr(III)–Cu(II) interaction is expected to be ferromagnetic, because of the orthogonality of the magnetic orbitals, and the ground state has actually been found to be the state of highest spin, $S = \frac{7}{2}$; $\chi_M T$ for this compound continously increases as T is lowered and tends to a low-temperature limit $\chi_M T = 21N\beta^2 g^2/4k \approx 7.9$ cm^3 K mol^{-1}. The fitting of the $\chi_M T$ vs T curve leads to $J_{CrCu} = 13$ cm^{-1}. The spectrum of the low-lying states $E(S,S_{Cr})$, with

$$\mathbf{S}_{Cr} = \mathbf{S}_{Cr1} + \mathbf{S}_{Cr2},$$
$$\mathbf{S} = \mathbf{S}_{Cr} + \mathbf{S}_{Cu}, \tag{15}$$

is displayed in Fig. 48, where each state is represented by an arrow, the length of which is equal to S.

The latter type of heterotrinuclear compounds involves the central core $[B(dmg)_3]^{4-}$, where B is a divalent metal ion. The general formula of these compounds is $[(LA)_2B(dmg)_3]^{n+}$, where L is 1,4,7-trimethyl-1,4,7-triazacyclononane, with $n = 2$ when A is a trivalent ion, and $n = 4$ when A is tetravalent. The first reported compound of this family is $[(LFe)_2Cu(dmg)_3](ClO_4)_2$ (*102*). The structure of the Fe(III)Cu(II)-Fe(III) cation is shown in Fig. 49. The dominant interaction, occurring between adjacent Fe(III) and Cu(II) ions, is antiferromagnetic. The ground state is then characterized by $S = \frac{9}{2}$, $S_{Fe} = 5$. When going up in energy, the spin S diminishes, reaches the value $\frac{1}{2}$, then increases

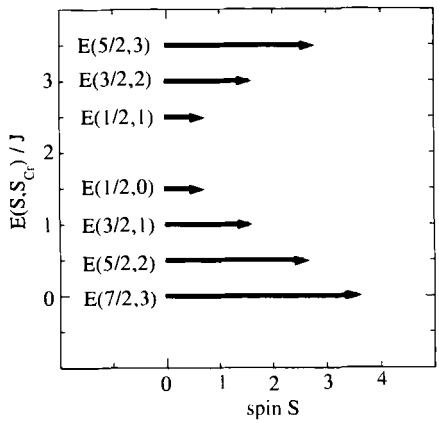

FIG. 48. Spin-state structure for a Cr(III)Cu(II)Cr(III) trinuclear compound with ferromagnetic Cr(III)–Cu(II) interactions; each low-lying state is represented by an arrow, the length of which is equal to the spin S.

to $S = \frac{11}{2}$ for the most excited state (*23*). The spin-state structure is irregular. Consequently, the $\chi_M T$ vs T curve should exhibit a minimum, which in the present case cannot be observed. As a matter of fact, the interaction parameter between Fe(III) and Cu(II) ions is reported to be equal to $J = -84\ cm^{-1}$, so that the minimum in the $\chi_M T$ vs T plot is expected to occur around 408 K. Another heterotrinuclear compound

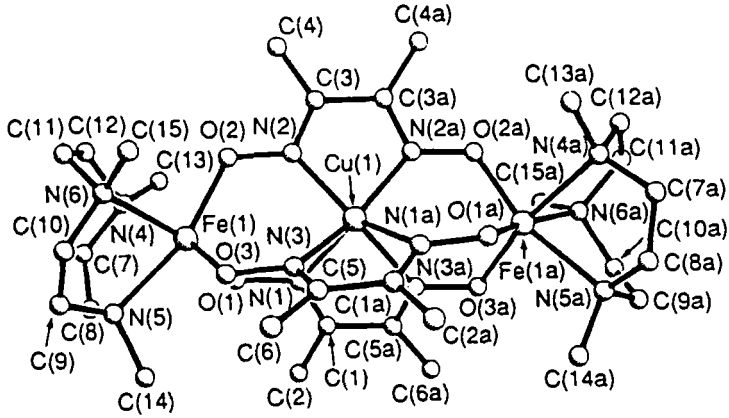

FIG. 49. Structure of the trinuclear cation $[(LFe)_2Cu(dmg)_3]^{2+}$, with dmg = dimethylglyoximato and L = 1,4,7-trimethyl-1,4,7-triazacyclononane. From Chaudhuri *et al.* (*102*).

with an irregular spin-state structure is $[(LFe)_2Ni(dmg)_3](PF_6)_2$ (*103*). The Fe (III)–Ni(II) antiferromagnetic interaction leads to a ground state characterized by $S = 4$, $S_{Fe} = 5$. In the present case, the minimum in the $\chi_M T$ vs T plot is observed around 130 K. The interaction parameter between Fe(III) and Ni(II) ions is found to be $J = -64\ cm^{-1}$. Interestingly, when the central ion is Zn(II) with a zero local spin, a noticeable antiferromagnetic interaction between terminal spin carriers is observed, which confirms the efficiency of the oximato bridge as magnetic coupler (*104*).

C. Long-Range Ordering of Chain Compounds

The $[Cu(dmg)_2]^{2-}$ core shown earlier is obviously a very appealing precursor for the design of chain compounds. The chemistry of this precursor, however, is more difficult than one might anticipate. As a matter of fact, the starting material is the neutral species $[Cu(Hdmg)_2]$, and the double deprotonation is rather difficult to achieve, so that unexpected results can be obtained. For instance, the reaction of $[Cu(Hdmg)_2]$ with Mn(II) carboxylate affords the bis(oximato)-bridged Mn(III)Cu(II) compound schematized in Fig. 50, of formula $[MnCu(dmg)_2(H_2O)_2(CH_3CO_2)]$ (*105*). The magnetic properties of this chain compound actually are quite interesting. Indeed, the $\chi_M T$ vs T plot shown also in Fig. 50 reveals a one-dimensional ferromagnetic behavior; $\chi_M T$ continuously increases from 4.44 $cm^3\ K\ mol^{-1}$ up to 23.5 $cm^3\ K\ mol^{-1}$ as T is lowered from room temperature to 14 K. At that temperature, $\chi_M T$ presents a sharp maximum, associated with a maximum of χ_M at 12 K. The magnetic susceptibility data above ca. 30 K may be interpreted with the classical spin–quantum spin model (*28, 29*). The Mn(III)–Cu(II) interaction parameter is then found to be equal to $J = 52\ cm^{-1}$. The ferromagnetic nature of the interaction may again be attributed to the orthogonality between the four Mn(III) magnetic orbitals, transforming as the $2a_1 + a_2 + b_1$ irreducible representations of the C_{2v} symmetry group, and the Cu(II) magnetic orbital, transforming as b_2. The maximum of the susceptibility is due to a long-range antiferromagnetic ordering of the ferromagnetic chains. The antiferromagnetic interchain interactions are overcome when the applied magnetic field reaches 4.5 kOe. $[MnCu(dmg)_2(H_2O)_2(CH_3CO_2)]$ may then be considered as a metamagnet.

When the precursor $[Cu(dmg)]^{2-}$ is replaced by $[Cu(chd)_2]^{2-}$, chd being 1,2-cyclohexanedioneoximato, the ferromagnetic chains interact within the lattice in a ferromagnetic fashion, and the compound exhibits a long-range ferromagnetic ordering at $T_c = 9$ K (*106*).

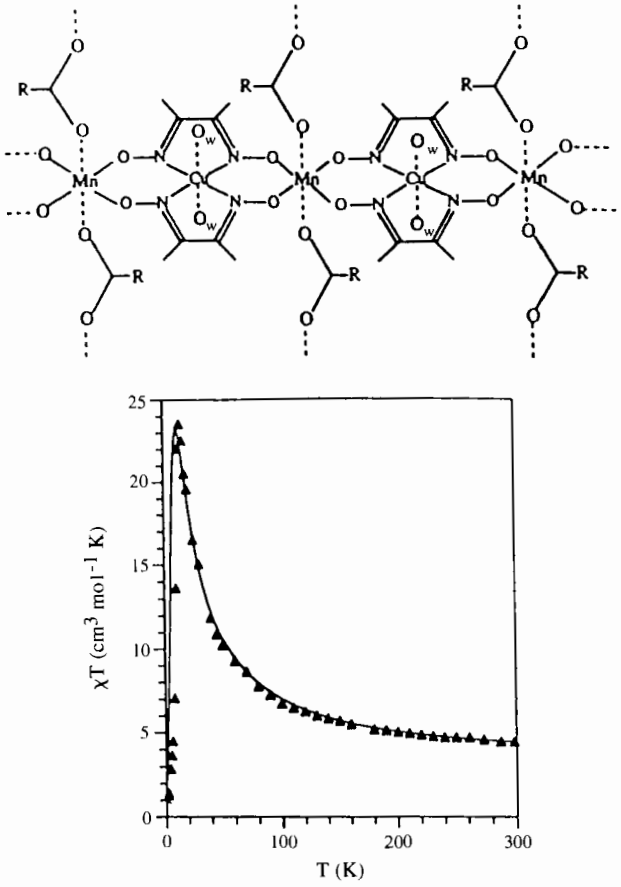

FIG. 50. Schematic representation of the chain compound $[MnCu(dmg)_2(H_2O)_2(CH_3CO_2)]$, and $\chi_M T$ vs temperature curve for this compound; (▲) experimental data, (—) calculated curve. Reprinted from Lloret *et al.* (*105*). Copyright © 1992 American Chemical Society.

The compound $[FeCu(chd)_2(H_2O)_2(CH_3CO_2)]$ has also been reported. The Fe(III)Cu(II) chains are ferrimagnetic and order antiferromagnetically within the lattice at 7.5 K.

VII. Cyano-Bridged Bimetallic Compounds

The hexacyanometalate anions $[B(CN)_6]^{n-}$ have long been known to be flexible building blocks for obtaining polymetallic compounds. These

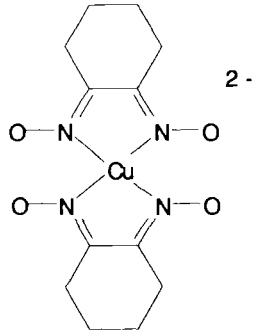

building blocks have been utilized to synthesize Prussian Blue-like phases which occupy a peculiar situation at the frontier between molecular and solid-state chemistry. They may also be utilized to obtain bimetallic compounds with a more molecular character.

A. Prussian Blue-like Phases

One of the very first synthetic coordination compounds ever reported (in 1710) is the Prussian Blue obtained by reaction of the diamagnetic $[Fe(CN)_6]^{4-}$ complex anion with Fe(III) (*107*). This compound, of formula $Fe_4[Fe(CN)_6]_3 \cdot 15H_2O$, exhibits a long-range ferromagnetic ordering at $T_c = 5.6$ K (*108, 109*). Prussian Blue belongs to a vast family of Prussian Blue-like bimetallic phases with the general formula $A_k[B(CN)_6]_l \cdot nH_2O$, where A is high spin and B is low spin. For $k = l$, the basic structure schematized in Fig. 51 is face-centered cubic with

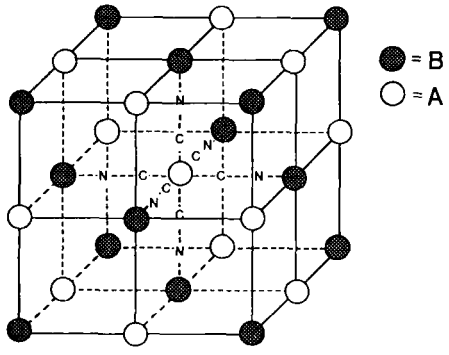

FIG. 51. Face-centered cubic structure of the $A[B(CN)_6]$ Prussian Blue-like phases. From Ludi and Güdel (*110*).

A–C–N–B linear linkages along three perpendicular directions (*110*). Alkaline cations such as Cs^+ may occupy A_4 or B_4 tetrahedral sites. For $k > l$, some $B(CN)_6$ motifs are missing, which creates a local breaking of the three-dimensional periodicity. The vacant sites are usually occupied by water molecules coordinated to the adjacent A atoms. For instance, when A is divalent and B trivalent, compounds with the $A_3[B(CN)_6]_2 \cdot nH_2O$ stoechiometry are obtained. One-third of the $B(CN)_6$ sites are vacant; on average, each A atom is then surrounded by four nitrogen atoms from cyano groups and two oxygen atoms from water molecules in order for the octahedral coordination to be retained. The minimal number of water molecules per A_3B_2 unit is then six.

In Prussian Blue itself, only the Fe(III) ions carry a local spin, and the interaction occurs between next-nearest neighbors. Much higher ordering temperatures may be anticipated when both A and B are magnetic centers. The compounds may then be three-dimensional ferri- or ferromagnets, depending on the nature of the A–B interaction. Owing to the high symmetry of the metal sites and of the lattice as a whole, the symmetry rules between magnetic orbitals recalled in Section II,C apply in a particularly heuristic fashion. The electronic configuration of the high-spin site A is $t_{2g}^{x}e_g^{y}$ and that of the low-spin site B is t_{2g}^{z}. The A–B interaction parameter may be written as a sum of $J_{\mu\nu}$ contributions involving pairs of magnetic orbitals. The $J_{t_{2g}t_{2g}}$ contributions involving t_{2g}-type orbitals centered on both A and B favor an antiferromagnetic (AF) interaction; the $J_{e_gt_{2g}}$ contributions involving e_g-type orbitals on A and t_{2g}-type orbitals on B favor a ferromagnetic interaction. When both types of contributions are present, the AF contributions usually dominate, and the interaction parameter is larger in absolute value when the number of $J_{e_gt_{2g}}$ contributions is smaller. Antiferromagnetic interactions may give rise to either a long-range antiferromagnetic ordering when the local spins S_A and S_B are equal, or a long-range ferrimagnetic ordering when there is no compensation of the local spins. The various possibilities for magnetic ordering according to the electronic configurations of the high-spin A and low-spin B sites in Prussian Blue-like phases are gathered in Table III. All the examples we will discuss here obey the predictions of Table III. This table, however, does not provide any information on the magnitude of the A–B interaction. Some qualitative remarks, however, may allow optimization of the materials. The t_{2g}-type magnetic orbitals of the $B(CN)_6$ motifs are delocalized toward the empty π^* orbitals of the cyano ligands, as schematized below:

TABLE III

NATURE OF THE MAGNETIC ORDERING IN PRUSSIAN BLUE-LIKE PHASES ACCORDING TO THE ELECTRONIC CONFIGURATIONS OF THE HIGH-SPIN A AND LOW-SPIN B IONS[a]

A B	t_{2g}^1 and t_{2g}^5	t_{2g}^2 and t_{2g}^4	t_{2g}^3
$t_{2g}^1e_g^0$	AF	FI	FI
$t_{2g}^2e_g^0$	FI	AF	FI
$t_{2g}^3e_g^0$	FI	FI	AF
$t_{2g}^3e_g^1$	FI	FI	FI
$t_{2g}^3e_g^2$	FI	FI	FI
$t_{2g}^4e_g^2$	FI	FI	FI
$t_{2g}^5e_g^2$	FI	FI	FI
$t_{2g}^6e_g^2$	F	F	F
$t_{2g}^6e_g^3$	F	F	F

[a] AF stands for antiferromagnetic, F for ferromagnetic, and FI for ferrimagnetic ordering.

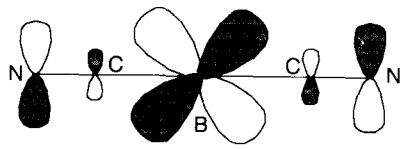

This delocalization is more pronounced as the energies of the 3*d* metal and π^* ligand orbitals are closer. Therefore, increasing the t_{2g}(A)–t_{2g}(B) contributions can be achieved by using low-spin B sites with high-energy 3*d* orbitals, viz. early transition metal in a lower oxidation state (*111, 112*). Maximizing the A–B antiferromagnetic interaction may also result in decreasing or eliminating the $J_{e_gt_{2g}}$ ferromagnetic contributions. The latter occurs when the A site has no unpaired electrons in e_g orbitals. Finally, for the same pair of A and B sites, the ferro- or ferrimagnetic ordering temperature is higher when there is no rupture in the three-dimensional periodicity, i.e., when the stoichiometry between these A and B ions is 1/1.

The first magnetic studies concerning Prussian Blue–like phases were performed by Bozorth and co-workers three decades ago. They reported on magnetic ordering temperatures as high as 50 K (*108*).

Unfortunately, these authors did not properly characterize their compounds. At the beginning of the eighties, Klenze and co-workers (*113*), then Babel and co-workers (114–117) characterized several phases with magnetic ordering temperatures up to 90 K. More recently, two groups led by Verdaguer (*118–120*) and Girolami (*111, 112, 121*), respectively, initiated a thorough and systematic investigation of these Prussian Blue-like phases and obtained compounds showing "high critical temperatures." Quite recently, Verdager and co-workers reported on a phase of formula $V^{II}_{0.4}V^{III}_{0.6}[Cr(CN)_6]_{0.86}\cdot 3H_2O$ ordering ferrimagnetically at 310 K, i.e., above room temperature (*120*). The results obtained to date are gathered in Table IV (*122–124*), which is organized from top to bottom according to the low-spin B site. This table is largely borrowed from Girolami and co-workers (*112*).

The nature, ferro- or ferrimagnetic, of the magnetic ordering can be

TABLE IV

MAGNETIC PROPERTIES OF PRUSSIAN BLUE-LIKE COMPOUNDS[a]

Compound	T_c/K	Ordering	Ref.
$(NEt_4)_{0.5}Mn^{II}_{1.25}[V^{II}(CN)_5]\cdot 2H_2O$	230	FI	*111*
$Cs_2Mn^{II}[V^{II}(CN)_6]$	125	FI	*111*
$Cr^{II}_3[Cr^{III}(CN)_6]_2\cdot 10H_2O$	240	FI	*119*
$V^{II}_{0.4}V^{III}_{0.6}[Cr(CN)_6]_{0.86}\cdot 3H_2O$	310	FI	*120*
$Cs_{0.75}Cr^{II}_{1.125}[Cr^{III}(CN)_6]\cdot 5H_2O$	190	FI	*119*
$CsMn^{II}[Cr^{III}(CN)_6]\cdot H_2O$	90	FI	*114*
$CsNi^{II}[Cr^{III}(CN)_6]\cdot 2H_2O$	90	F	*118*
$Mn^{II}_3[Cr^{III}(CN)_6]_2\cdot 15H_2O$	66	FI	*122*
$Ni^{II}_3[Cr^{III}(CN)_6]_2\cdot 15H_2O$	53	F	*122*
$Cu^{II}_3[Cr^{III}(CN)_6]_2\cdot 15H_2O$	66	F	*122*
$(NMe_4)Mn^{II}[Cr^{III}(CN)_6]\cdot 4H_2O$	59	FI	*115*
$K_2Mn^{II}[Mn^{II}(CN)_6]$	41	FI	*121*
$CsNi^{II}[Mn^{III}(CN)_6]\cdot H_2O$	42	F	*112*
$Ni^{II}_3[Mn^{III}(CN)_6]_2\cdot 12H_2O$	30	F	*112*
$CsMn^{II}[Mn^{III}(CN)_6]\cdot 1/2H_2O$	31	FI	*121*
$Mn^{II}_3[Mn^{III}(CN)_6[_2\cdot 11H_2O$	37	FI	*121*
$(NMe_4)Mn^{II}[Mn^{III}(CN)_6]\cdot 8H_2O$	29	FI	*115*
$Mn^{II}[Mn^{IV}(CN)_6]\cdot xH_2O$	49	FI	*113*
$Fe^{III}_4[Fe^{II}(CN)_6]_3\cdot xH_2O$	5.6	F	*108, 123*
$Co^{II}_3[Fe^{III}(CN)_6]_2\cdot 14H_2O$	14	FI	*124*
$Ni^{II}_3[Fe^{III}(CN)_6]_2\cdot 14H_2O$	23	F	*124*
$Cu^{II}_3[Fe^{III}(CN)_6]_2\cdot 12H_2O$	14	FI	*124*
$Mn^{II}_3[Fe^{III}(CN)_6]_2\cdot 15H_2O$	9	FI	*124*

[a] F and FI stand for ferro- and ferrimagnetic ordering, respectively. The first compound on this list is not cubic.

determined through both the temperature dependence of the magnetic susceptibility and the field dependence of the magnetization below T_c. For a ferromagnet, $\chi_M T$ increases continuously as T is lowered to T_c. On the other hand, for a ferrimagnet, $\chi_M T$ presents a minimum in the paramagnetic range, above T_c. When the critical temperature is close to room temperature, this minimum may occur far above 300 K and therefore cannot be detected. That is what happens for $(NEt_4)_{0.5}Mn^{II}_{1.25}[V^{II}(CN)_5]\cdot 2H_2O$, $Cr^{II}_3[Cr^{III}(CN)_6]_2\cdot 10H_2O$, and $V^{II}_{0.4}V^{III}_{0.6}[Cr(CN)_6]_{0.86}\cdot 3H_2O$ (*111, 119*). As far as the field dependence of the magnetization is concerned, the saturation magnetization value, M_S, immediately indicates whether the S_A and S_B local spins are aligned along the same direction or along opposite directions. In the former case, one has $M_S = Ng\beta(S_A + S_B)$; in the latter, $M_S = Ng\beta(|S_A - S_B|)$.

We have already pointed out that a magnet is characterized not only by its critical temperature, but also by its hysteresis loops conferring a memory effect on the system. For the Prussian Blue-like phases, as expected, the largest coercive fields are obtained when the ground state of A and/or B is an orbital triplet, i.e., possesses an orbital momentum. Such a requirement is fulfilled for $CsMn^{II}[Mn^{III}(CN)_6]\cdot\frac{1}{2}H_2O$; indeed, the ground state of the low-spin Mn(III) ion is $^3T_{1g}$, and the cooercive field at 4.5 K is found equal to 1150 Ce (*121*).

B. Molecular Cyano-Bridged Bimetallic Species

The hexacyanometalate anions may be used as bricks to design a large variety of bimetallic compounds with a symmetry lower than that of the Prussian Blue-like phases. To date, one compound of that kind has been described by Okawa and co-workers (*125*). Its formula is $[Ni(en)_2]_3[Fe(CN)_6]_2\cdot 2H_2O$, with en = ethylenediamine. The structure of this compound is quite original; it consists of zigzag chains formed by the alternate array of $[Fe(CN)_6]^{3-}$ and *cis* $[Ni(en)_2]^{2+}$ units. In addition, two zigzag chains of that kind are combined by *trans* $[Ni(en)_2]^{2+}$, providing a kind of rope-ladder chain. In the lattice the chains assemble to form two-dimensional sheets (see Fig. 52). Preliminary magnetic measurements suggest that the compound orders ferromagnetically below $T_c = 18.6$ K.

VIII. Conclusion and Outlook

Our objective in writing this review article was not to speak of all the heterobimetallic compounds with magnetic centers, but to restrict

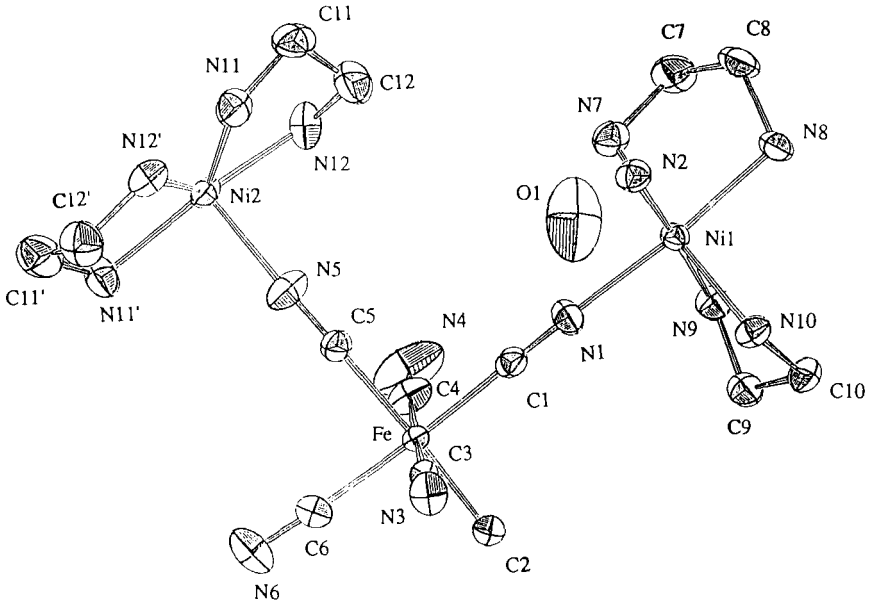

FIG. 52. Asymmetric unit for $[Ni(en)_2]_3[Fe(CN)_6]_2 \cdot 2H_2O$ (top) and projection of the polymeric structure onto the *ab* plane (bottom). For clarity, the en = ethylenediamine groups have been omitted in the projection. Reprinted from Ohba *et al.* (*125*). Copyright © 1994 American Chemical Society.

ourself to those which in one way or another are relevant to the field of molecular-based magnets. This field has been astonishingly active in the last decade, and it seemed to us that it was timely to stop for a short while to establish the state of the art.

Heterobimetallic species are of interest to other areas. They are present in some metalloenzymes, and mimicking the structure and, if possible, the reactivity of these enzymes is also an active field of research. A good example of biological heteropairs is provided by the Fe(III)–Cu(II) active site of cytochrome *c* oxidase. For a long time, attempts have been made to obtain synthetic analogues of this metalloenzyme, and significant results were recently reported (*126, 127*). Heterobimetallic compounds with μ-oxo-di-μ-carboxylato bridges have also been investigated, in particular by Wieghardt and co-workers, who reported on interesting results in terms of molecular magnetism (*128, 129*). These authors, however, did not attempt to design compounds exhibiting bulk magnetic properties.

We also ignored in this paper the bimetallic compounds in which all the interactions are intermolecular, occurring between anionic and

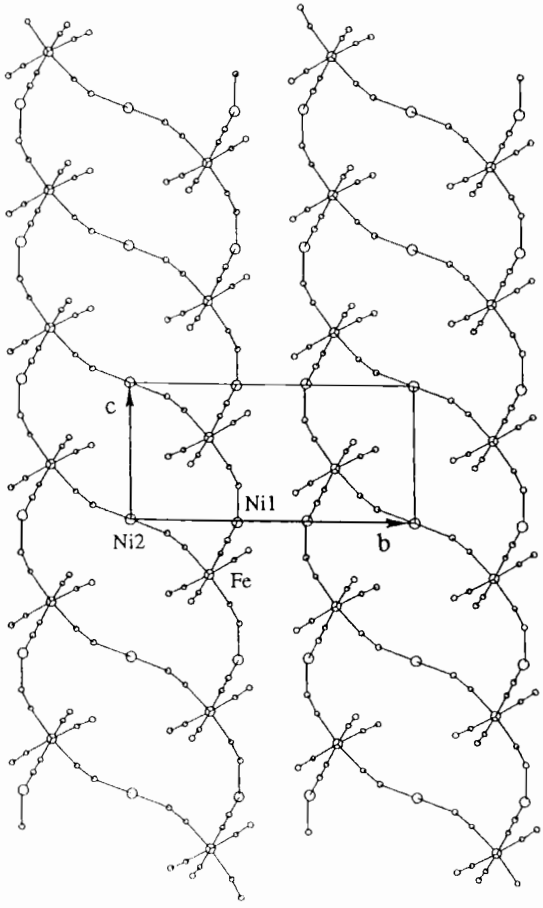

FIG. 52. *Continued.*

cationic mononuclear species. Compounds of that kind have been extensively investigated by Palacio, Carlin, and co-workers (*130–133*). In some cases, long-range ferrimagnetic orderings have been characterized. However, because of the weakness of the intermolecular interactions, the critical temperatures are always very low. For instance, $[Cr(en)_3][FeCl_6]Cl_6 \cdot H_2O$ orders ferrimagnetically at $T_c = 0.9$ K (*133*). An interesting aspect of these compounds is the role of the hydrogen bonds in the propagation of the magnetic interactions.

The field of molecular-based magnets is obviously not limited to heterobimetallics. Great activity is devoted to compounds incorporating

both metal ions and organic radicals. One- (*40, 134–137*), two- (*138, 139*), and three-dimensional (*140*) compounds of that kind exhibiting a spontaneous magnetization below a certain temperature have been obtained, with critical temperatures increasing as the dimensionality increases. This aspect of molecular magnetism probably deserves to be the subject of another review article. In a certain sense the heterobimetallics and the metal ion–organic radical compounds could be gathered together under the name of "heteromagnetics." The Mn(II)Cu(II) and Mn(II)–organic radical ferrimagnetic chain compounds have many similarities from the point of view of physics. The same holds for the oxamato-bridged two-dimensional compounds mentioned in section III,C and the compounds recently described by Iwamura and co-workers (*138, 139*).

The first molecular-based magnets were described by 1986. After a decade of activity in this field, we would like to sum up briefly the main pieces of information arising from all the results obtained so far, then suggest some perspectives.

Probably the most important information is that the critical temperature below which spontaneous magnetization is observed depends dramatically on the structural dimensionality. Critical temperatures above room temperature have been observed for three-dimensional lattices (*120, 140*). This information is far from being a surprise; however, it raises a problem. Fundamentally, molecular chemistry is a zero-dimensional chemistry. It is this zero-dimensionality which confers its specificity, in particular the solubility. When the dimensionality is increased, the molecular character tends to vanish, or at least to diminish. Is there much difference between Prussian Blue-like phases and ferrimagnetic oxides such as garnets, except that the bridges are CN^- in the former case and O^{2-} in the latter? Actually, there is another significant difference; the Prussian Blue-like phases are prepared at room temperature from solution chemistry, while the ferrimagnetic oxides are prepared at high temperature. In that sense, the Prussian Blue-like phases retain some molecular character.

The second piece of information, closely related to the first one, is that the intramolecular interactions (those through bonds) are much more efficient than the intermolecular interactions (those through space). Therefore, a polymeric lattice most often will lead to a higher critical temperature than an assembly of separated open-shell units of the same dimensionality.

The third piece of information concerns the coercivity which confers a memory effect on the system. The value of the coercive field at a given temperature for a polycrystalline magnet depends both on the

chemical nature of the compound and on some extrinsic factors such as the size and the shape of the microcrystallites. Concerning the chemical nature of the compound, the key role is played by the magnetic anisotropy of the spin carriers, which prevents the domains from rotating freely when the field is applied. For instance, replacing Mn(II) with an orbital singlet ground state ($^6A_1$) by Co(II) with an orbital triplet ground state ($^4T_1$) in the oxamato-bridged Mn(II)Cu(II) magnets dramatically increases the coercivity. The purely organic magnets with very isotropic spin carriers probably cannot display significant coercivity.

The fourth piece of information worth mentioning is that the nature of the interaction between two magnetic ions is rather well understood. By far the most efficient strategy to obtain a ferromagnetic interaction is to achieve strict orthogonality of the magnetic orbitals. Only a few pairs of metal ions, such as Cr(III)Ni(II) or Cr(III)Cu(II), are appropriate for that. Most often the interaction is antiferromagnetic. It turns out that the ferrimagnetic approach seems to be easier to apply than the ferromagnetic one. For genuine molecular-based magnets, as well as for Prussian Blue-like phases, the compounds exhibiting the highest critical temperatures are actually ferrimagnets.

The fifth and last piece of information we would like to point out deals with the synthesis of the compounds. To the best of our knowledge, all the heterobimetallic magnets are synthesized using the "complex as ligand" approach. In this chemistry the ligands which can be both terminal and bridging play a fundamental role. That is why we decided to organize this article around the various ligands of that kind. A step forward in this field of research would be to synthesize and utilize novel ligands possessing this versatility.

Up to now, most of the efforts in the field of molecular-based magnets have dealt with the synthesis and the characterization of new compounds on the one hand, and the study of their magnetic properties on the other hand. Our opinion is that quite a few other physical properties deserve to be investigated. We have in mind first the spectroscopic properties. EPR and NMR studies, both in the paramagnetic and the magnetically ordered phases, might provide original insights. The observation of ferromagnetic resonance in EPR below T_c is spectacular (*39*). Even if the interpretation of the findings seems to be complicated, more colleagues should attempt to record the EPR spectra of their magnets below T_c. The optical spectroscopies also deserve to be more systematically utilized. Most of the heterobimetallic magnets are weakly colored. The absorpton spectrum in the UV–visible range is not at all the simple superposition of what belongs to each chromophore. The magnetic interaction results in giant enhancements of formally

spin-forbidden transitions, and the intensity of these bands depends dramatically upon temperature (*56, 141*). Some magnets may also present interesting luminescence properties with peculiar energy transfer processes between the different metal sites (*80, 89*). As far as the physical studies are concerned, we also have in mind the polarized neutron diffraction. In the paramagnetic phase, this technique leads to spin density maps and therefore provides unique information on the mechanism of the interaction between magnetic centers. In particular, it allows one to distinguish between spin delocalization and spin polarization (*58, 142, 143*). In the magnetically ordered phase, polarized neutron diffraction leads to the magnetic structure of the material.

Suggesting some perspectives in a field of research is always dangerous. The future may be cruel for those who make such an attempt. Our opinion—but it is only our opinion, the reflection of our subjectivity—is that the molecular character may open new doors. What is important in our mind is not so much to obtain molecular-based magnets reproducing the magnetic properties of conventional magnets, but to combine magnetic and other physical (or mechanical) properties. The molecular approach allows us to associate bricks providing the magnetic character with other bricks providing optical, electron-transfer, or even bistability properties. We recently synthesized a Mn(II)Cu(II) molecular magnet incorporating the $[Ru(bipy)_3]^{2+}$ chromophore (*144*); it is a first step in this direction. We intend to increase our effort along this line.

ACKNOWLEDGMENTS

A part of the work described in this article was performed in Orsay by my co-workers and colleagues. Their names appear in the references listed. To all of them I express my deepest gratitude. I also express my gratitude to the colleagues from other groups who collaborated with me on this subject. Finally, it is both a pleasure and a duty for me to specify that a significant part of the results reported here were obtained in various groups of the network "Magnetic Molecular Materials" in the frame of the Human Capital and Mobility Program of the European Union, contract n° ERBCHRXCT920080.

REFERENCES

1. Kahn, O. "Molecular Magnetism"; VCH: New York, 1993.
2. Kahn, O.; Galy, J.; Journaux, Y.; Jaud, J.; Morgenstern-Badarau, I. *J. Am. Chem. Soc.* **1982,** *104,* 2165.
3. Kahn, O. *Struct. Bonding (Berlin)* **1987,** *68,* 89.

4. Anderson, P. W. In "Magnetism"; Rado, G. T.; Suhl, H. Eds.; Academic Press: New York, 1963; Vol. 1, 25.
5. Ginsberg, A. P. *Inorg. Chim. Acta Rev.* **1971,** *5,* 45.
6. Doedens, R. J. *Prog. Inorg. Chem.* **1975,** *19,* 173.
7. O'Connor, C. J. *Prog. Inorg. Chem.* **1982,** *29,* 203.
8. Kahn, O. *Angew. Chem., Int. Ed. Engl.* **1985,** *24,* 834.
9. Willet, R. D.; Gatteschi, O.; Kahn, O. Eds., "Magneto-Structural Correlations in Exchange Coupled Systems", NATO ASI Series C; Reidel: Dordrecht, 1985; Vol. 140.
10. Bencini, A.; Gatteschi, D. "EPR of Exchange Coupled Systems", Springer–Verlag: Berlin, 1989.
11. Kahn, O. *Comments Condens. Mater. Phys.* **1994,** *17,* 39.
12. Kollmar, C.; Kahn, O. *Acc. Chem. Res.* **1993,** *26,* 259.
13. Figgis, B. N.; Reynolds P. A. *J. Chem. Soc., Dalton Trans.* **1987,** *1,* 747.
14. Figgis, B. N.; Forsyth, J. B.; Reynolds, P. A. *Inorg. Chem.* **1987,** *26,* 101.
15. Figgis, B. N.; Kucharski, E. S.; Vrtis, M. *J. Am. Chem. Soc.* **1993,** *115,* 176.
16. Van Vleck, J. H. "The Theory of Electric and Electric Susceptibilities", Oxford Univ. Press: Oxford, 1932.
17. McConnell, H. M. *J. Chem. Phys.* **1963,** *39,* 1910.
18. Izuoka, A.; Murata, S.; Sagawara, T.; Iwamura, H. *J. Am. Chem. Soc.* **1987,** *109,* 2631.
19. Kollmar, C.; Couty, M.; Kahn, O. *J. Am. Chem. Soc.* **1991,** *113,* 7994.
20. Kollmar, C.; Kahn, O. *J. Chem. Phys.* **1993,** *98,* 453.
21. Lanfranc de Panthou, F.; Luneau, D.; Laugier, J.; Rey, P. *J. Am. Chem. Soc.* **1993,** *115,* 9095.
22. Ribas, J.; Diaz, C.; Costa, R.; Journaux, Y.; Mathonière, C.; Kahn, O.; Gleizes, A. *Inorg. Chem.* **1990,** *29,* 2042.
23. Pei, Y.; Journaux, Y.; Kahn, O. *Inorg. Chem.* **1988,** *27,* 399.
24. Baron, V.; Gillon, B.; Sletten, J.; Mathonière, C.; Codjovi, E.; Kahn, O. *Inorg. Chim. Acta,* **1995,** *235,* 69.
25. Pei, Y.; Verdaguer, M.; Kahn, O.; Sletten, J.; Renard, J. P. *J. Am. Chem. Soc.* **1986,** *108,* 7428.
26. Kahn, O.; Pei, Y.; Verdaguer, M.; Renard, J. P.; Sletten, J. *J. Am. Chem. Soc.* **1988,** *110,* 782.
27. Pei, Y.; Verdaguer, M. Kahn, O.; Sletten, J.; Renard, J. P. *Inorg. Chem.* **1987,** *26,* 138.
28. Seiden, J.; *J. Phys., Lett.* **1983,** *44,* L947.
29. Verdaguer, M.; Gleizes, A.; Renard, J. P.; Seiden, J. *Phys. Rev. B.* **1986,** *29,* 5144.
30. Gatteschi, D.; Guillou, O.; Zanchini, C.; Sessoli, R.; Kahn, O.; Verdaguer, M.; Pei, Y. *Inorg. Chem.* **1989,** *28,* 287.
31. Nakatani, K.; Bergerat, P.; Codjovi, E.; Mathonière, C.; Pei, Y.; Kahn, O. *Inorg. Chem.* **1991,** *30,* 3977.
32. Stumpf, H. O.; Pei, Y.; Ouahab, L.; Le Berre, F.; Codjovi, E.; Kahn, O. *Inorg. Chem.* **1993,** *32,* 5687.
33. Stumpf, H. O.; Pei, Y.; Kahn, O.; Sletten, J.; Renard, J. P. *J. Am. Chem. Soc.* **1993,** *115,* 6738.
34. van Koningsbruggen, P. J.; Kahn, O.; Nakatani, K.; Pei, Y.; Renard, J. P.; Drillon, M.; Legoll, P. *Inorg. Chem.* **1990,** *29,* 3325.
35. Verdaguer, M.; Julve, M.; Michalowicz, A.; Kahn, O. *Inorg. Chem.* **1983,** *22,* 2624.
36. Drillon, M.; Gianduzzo, J. C.; Georges, R. *Phys. Lett. A* **1983,** *96,* 413.
37. Drillon, M.; Coronado, E.; Georges, R.; Gianduzzo, J. C.; Curely, J. *Phys. Rev. B* **1989,** *40,* 10992.

38. Stumpf, H. O.; Ouahab, L.; Pei, Y.; Grandjean, D.; Kahn, O. *Science* **1993,** *261,* 447.
39. Stumpf, H. O.; Ouahab, L.; Pei, Y.; Bergerat, P.; Kahn, O. *J. Am. Chem. Soc.* **1994,** *116,* 3866.
40. Caneschi, A.; Gatteschi, D.; Sessoli, R.; Rey, P. *Acc. Chem. Res.* **1989,** *22,* 392.
41. Stumpf, H. O.; Pei, Y.; Michaut, C.; Kahn, O.; Renard, J. P.; Ouahab, L. *Chem. Mater.* **1994,** *6,* 257.
42. Rauluszkiewicz, J.; Szymczak, H.; Lachowicz, H. K. Eds., "Physics of Magnetic Materials"; World Scientific: Singapore, 1985.
43. Sagawa, M.; Fujimura, S.; Togawa, M.; Yamamoto, H.; Matsnura, Y.; *J. Appl. Phys.* **1984,** *55,* 2083.
44. Bencini, A.; Benelli, C.; Caneschi, A.; Carlin, R. L.; Dei, A.; Gatteschi, D. *J. Am. Chem. Soc.* **1985,** *107,* 8128.
45. Bencini, A.; Benelli, C.; Caneschi, A.; Gatteschi, D. *Inorg. Chem.* **1986,** *25,* 572.
46. Benelli, C.; Caneschi, A.; Gatteschi, Guillou, O.; Pardi, L. *Inorg. Chem.* **1990,** *29,* 1750.
47. Andruh, M.; Ramade, I.; Codjovi, E.; Guillou, O.; Kahn, O.; Trombe, J. C. *J. Am. Chem. Soc.* **1993,** *115,* 1822.
48. Kahn, O.; Guillou, O. In "New Frontiers in Magnetochemistry"; O'Connor, C. J., Ed.; World Scientific: Singapore, 1993; p. 179.
49. Goodenough, J. B. "Magnetism and the Chemical Bond"; Wiley-Interscience: New York, 1963.
50. Guillou, O.; Kahn, O.; Oushoorn, R. L.; Boubekeur, K.; Batail, P. *Inorg. Chim. Acta* **1992,** *198–200,* 119.
51. Guillou, O.; Oushoorn, R. L.; Kahn, O.; Boubekeur, K.; Batail, P. *Angew. Chem. Int. Ed. Engl.* **1992,** *31,* 626.
52. Guillou, O.; Bergerat, P.; Kahn, O.; Bakalbassis, E.; Boubekeur, K.; Batail, P.; Guillot, M. *Inorg. Chem.* **1991,** *31,* 110.
53. Bartolomé, F.; Bartolomé, J.; Oushoorn, R. L.; Guillou, O.; Kahn, O. *J. Magn. Magn. Mater.* **1995,** *140,* 1711.
54. Georges, R.; Kahn, O.; Guillou, O. *Phys. Rev. B* **1994,** *49,* 3235.
55. Kahn, O.; Guillou, O.; Oushoorn, R. L.; Drillon, M.; Rabu, P.; Boubekeur, K.; Batail, P. *New J. Chem.* **1995,** *19,* 655.
56. Mathoniére, C.; Kahn, O.; Daran, J. C.; Hilbig, H.; Köhler, F. H. *Inorg. Chem.* **1993,** *32,* 4057.
57. Scaringe, R. P.; Hodgson, D.; Hatfield, W. E. *Mol. Phys.* **1978,** *35,* 701.
58. Baron, V.; Gillon, B.; Kahn, O.; Mathonière, C.; Grand, A.; Öhrström, L.; Tellgren, R., unpublished results.
59. Ferguson, J.; Guggenheim, H. J.; Tanabe, Y. *J. Phys. Soc. Jpn.* **1966,** *21,* 692.
60. Pei, Y.; Kahn, O.; Nakatani, K.; Codjovi, E.; Mathonière, C.; Sletten, J. *J. Am. Chem. Soc.* **1991,** *113,* 6558.
61. Gulbrandsen A.; Sletten J.; Nakatani, K.; Pei, Y.; Kahn, O. *Inorg. Chim. Acta* **1993,** *212,* 271.
62. Nakatani, K.; Carriat, J. Y.; Journaux, Y.; Kahn, O.; Lloret, F.; Renard, J. P.; Pei, Y.; Sletten, J.; Verdaguer, M. *J. Am. Chem. Soc.* **1989,** *111,* 5739.
63. Lloret, F.; Journaux, Y.; Julve, M. *Inorg. Chem.* **1990,** *29,* 3967.
64. Pei, Y.; Nakatani, K.; Kahn, O.; Sletten, J.; Renard, J. P. *Inorg. Chem.* **1989,** *28,* 3170.
65. Nakatani, K.; Sletten, J.; Halut-Desportes, S.; Jeannin, S.; Jeannin, Y.; Kahn, O. *Inorg. Chem.* **1991,** *30,* 164.
66. Pei, Y.; Kahn, O.; Sletten, J.; Renard, J. P.; Georges, R.; Gianduzzo, J. C.; Curely, J.; Xu, Q. *Inorg. Chem.* **1988,** *27,* 47.

67. Gatteschi, D.; Zanchini, C.; Kahn, O.; Pei, Y. *Chem. Phys. Lett.* **1989,** *160,* 157.
68. Kahn, O.; Pei, Y.; Nakatani, K.; Journaux, Y. *New J. Chem.* **1992,** *16,* 269.
69. Lloret F.; Julve, M.; Ruiz, R.; Journaux, Y.; Nakatani, K.; Kahn, O.; Sletten, J. *Inorg. Chem.* **1993,** *32,* 27.
70. Zhong, Z. J.; Matsumoto, N.; Okawa, H.; Kida, S. *Chem. Lett.* **1990,** 87.
71. Ohba, M.; Tamaki, H.; Matsumoto, N.; Okawa, H.; Kida, S. *Chem. Lett.* **1991,** 1157.
72. Ohba, M.; Tamaki, H.; Matsumoto, N.; Okawa, H. *Inorg. Chem.* **1993,** *32,* 5385.
73. Cortes, R.; Urtiaga, M. K.; Lezama, L.; Arriortua, M. I.; Rojo, T. *Inorg. Chem.* **1994,** *33,* 829.
74. Pei, Y.; Journaux, Y.; Kahn, O. *Inorg. Chem.* **1989,** *28,* 100.
75. Mitsumi, M.; Okawa, H.; Sakiyama, H.; Ohba, M.; Matsumoto, N.; Kurisaki, T.; Wakita, H. *J. Chem. Soc., Dalton Trans.* **1993,** 2991.
76. Matsumoto, N.; Ohba, M.; Mitsumi, M.; Inoue, K.; Hashimoto, Y.; Okawa, H. *Mol. Cryst. Liq. Cryst.* **1993,** *233,* 299.
77. Tamaki, H.; Zhong, Z. J.; Matsumoto, N.; Kida, S.; Koikawa, M.; Achiwa, N.; Hashimoto Y.; Okawa, H. *J. Am. Chem. Soc.* **1992,** *114,* 6974.
78. Okawa, H.; Matsumoto, N.; Tamaki, H.; Ohba, M. *Mol. Cryst. Liq. Cryst.* **1993,** *233,* 257.
79. Atovmyan, L. O.; Shilov, G. V.; Lyubovskaya, R. N.; Zhilyaeva, E. I.; Ovanesyan, N. S.; Pirumova, S. I.; Gusakovskaya, I. G.; Morozov, Y. G. *JETP Lett.* **1993,** *58,* 766.
80. Decurtins, S.; Schmalle, H. W.; Oswald, H. R.; Linden, A.; Ensling, J.; Gütlich, P.; Hauser, *A. Inorg. Chim. Acta* **1994,** *216,* 65.
81. Okawa, H.; Mitsumi, M.; Ohba, M.; Kodera, M.; Matsumoto, N. *Bull Chem. Soc. Jpn.* **1994,** *67,* 2139.
82. Tamaki, H.; Mitsumi, M.; Nakamura, K.; Matsumoto, N.; Kida, S.; Okawa, H.; Iijima, S. *Chem. Lett.* **1992,** 1975.
83. Okawa, H.; Matsumoto, N.; Tamaki, H.; Ohba, M. *Mol. Cryst. Liq. Cryst.* **1993,** *233,* 257.
84. Iijima, S.; Katsura, T.; Tamaki, H.; Mitsumi, M.; Matsumoto, N.; Okawa, H. *Mol. Cryst. Liq. Cryst.* **1993,** *233,* 263.
85. Mathonière C.; Carling, S. G.; Yusheng, D.; Day, P. *J. Chem. Soc., Chem. Commun.* **1994,** 1551.
86. Collin, J. C. Ph.D. thesis, University of Paris South, Orsay, 1994.
87. Decurtins, S.; Schmalle, H. W.; Schneuwly, P.; Oswald, H. R. *Inorg. Chem.* **1993,** *32,* 1888.
88. Wells, A. F. "Structural Inorganic Chemistry", Clarendon Press: Oxford, 1984.
89. Decurtins, S.; Schmalle, H. W.; Schneuwly, P.; Ensling, J.; Gütlich, P. *J. Am. Chem. Soc.* **1994,** *116,* 9521.
90. Mohanty, G.; Baral, S.; Singh, R. P.; Chakravorty, A. *Inorg. Nucl. Chem. Lett.* **1974,** *10,* 655.
91. Bertrand, A.; Smith, J. H.; Eller, P. G. *Inorg. Chem.* **1974,** *13,* 1649.
92. Luneau, D.; Oshio, H.; Okawa, H.; Koikawa, M.; Kida, S. *Bull. Chem. Soc. Jpn.* **1990,** *63,* 2212.
93. Ruiz, R.; Sanz, J.; Cervera, B.; Lloret, F.; Julve, M.; Bois, C.; Faus, J.; Munoz, M. C. *J. Chem. Soc., Dalton Trans.* **1993,** 1623.
94. Ruiz, R.; Sanz, J.; Lloret, F.; Julve, M.; Faus, J.; Bois, C.; Munoz, M. C. *J. Chem. Soc., Dalton Trans.* **1993,** 3035.
95. Okawa, H.; Koikawa, M.; Kida, S. *J. Chem. Soc., Dalton Trans.* **1990,** 469.
96. Luneau, D.; Oshio, H.; Okawa, H.; Kida, S. *J. Chem. Soc., Dalton Trans.* **1990,** 2283.
97. Ruiz, R.; Lloret, F.; Julve, M.; Faus, J.; Munoz, M. C.; Solanz, X. *Inorg. Chim. Acta* **1993,** *213,* 261.

98. Ruiz, R.; Lloret, F.; Julve, M.; Munoz, M. C.; Bois, C. *Inorg. Chim. Acta* **1994,** *219,* 179.
99. Zhong, Z. J.; Okawa, H.; Matsumoto, N.; Sakiyama, H.; Kida, S. *J. Chem. Soc., Dalton Trans.* **1991,** 497.
100. Birkelbach, F.; Winter, M.; Flörke, U.; Haupt, H. J.; Butzlaff, C.; Lengen, M.; Bill, E.; Trautwein, A. X.; Wieghardt, K.; Chaudhuri, P. *Inorg. Chem.* **1994,** *33,* 3990.
101. Colacio, E.; Dominguez-Vera J. M.; Escuer, A.; Kivekas, R.; Romerosa, A. *Inorg. Chem.* **1994,** *33,* 3914.
102. Chaudhuri, P.; Winter, M.; Fleischhauer, P.; Haase, W.; Flörke, U.; Haupt, H. J. *J. Chem. Soc. Chem. Commun.* **1990,** 1728.
103. Chaudhuri, P.; Winter, M.; Della Vedova, B. P. C.; Fleischhauer, P.; Haase, W.; Flörke, U.; Haupt, H. J. *Inorg. Chem.* **1991,** *30,* 4777.
104. Chaudhuri, P.; Winter, M.; Birkelbach, F.; Fleischhauer, P.; Haase, W.; Flörke, U.; Haupt, H. J. *Inorg. Chem.* **1991,** *30,* 4291.
105. Lloret, F.; Ruiz, R.; Julve, M.; Faus, J.; Journaux, Y.; Castro, I.; Verdaguer, M. *Chem. Mater.* **1992,** *4,* 1150.
106. Lloret, F.; Ruiz, R.; Cervera, B.; Castro, I.; Julve, M.; Faus, J.; Real, A.; Sapina, F.; Journaux, Y.; Colin, J. C.; Verdaguer, M. *J. Chem. Soc. Chem. Commun.* **1994,** 2615.
107. Anonymous, *Misc. Berolinensia ad Incrementum Sci (Berlin)* **1710,** *1,* 377.
108. Bozorth, R. M.; Williams, H. J.; Walsh, D. E. *Phys. Rev.* **1956,** *103,* 572.
109. Holden, A. N.; Matthias, B. T.; Anderson, P. W.; Lewis, H. W. *Phys. Rev.* **1956,** *102,* 1463.
110. Ludi, A.; Güdel, H. U. *Struct. Bonding (Berlin)* **1973,** *14,* 1.
111. Entley, W. R.; Girolami, G. S. *Science,* in press.
112. Entley, W. R.; Treadway, C. R.; Girolami, G. S. *Mol. Cryst. Liq. Cryst.,* in press.
113. Klenze, R.; Kanellakopoulos, B.; Trageser, G.; Eysel, H. H. *J. Chem. Phys.* **1980,** *72,* 5819.
114. Griebler, W. D.; Babel, D. Z. *Z. Naturforsch., B: Anorg. Chem., Org. Chem.* **1982,** *37,* 832.
115. Babel, D. *Comments Inorg. Chem.* **1986,** *5,* 285.
116. Babel, D.; Kurtz, W. In "Solid State Chemistry 1982", Metselaar, R.; Heijligers, H. J. M.; Schoonman, J., Eds.; Elsevier: Amsterdam, 1983.
117. Kurtz, W.; Babel, D. *Solid State Commun.* **1983,** *48,* 277.
118. Gadet, V.; Mallah, T.; Castro, I.; Verdaguer, M. *J. Am. Chem. Soc.* **1992,** *114,* 9213.
119. Mallah, T.; Thiébaut, S.; Verdaguer, M.; Veillet, P. *Science* **1993,** *262,* 1554.
120. Mallah, T.; Ferlay, S.; Auberger, C.; Helary, C.; L'Hermite, F.; Ouahès, R.; Vassermann, J.; Verdaguer, M.; Veillet, P. *Mol. Cryst. Liq. Cryst.,* in press.
121. Entley, W. R.; Girolami, G. S. *Inorg. Chem.* **1994,** *33,* 5165.
122. Gadet, V. Ph.D. thesis, University of Paris VI, 1992.
123. Herren, F.; Fischer, P.; Ludi, A.; Hälg, W. *Inorg. Chem.* **1980,** *19,* 956.
124. Gadet, V.; Bujoli-Doeuff, M.; Force, L.; Verdaguer, M.; Malkhi, K. E.; Deroy, A.; Besse, J. P.; Chappert, C.; Veillet, P.; Renard, J. P.; Beauvillain, P. In "Magnetic Molecular Materials", NATO ASI Series E, Gatteschi, D.; Kahn, O.; Miller, J. S.; Palacio, F., Eds.; Plenum: New York, 1991; Vol. 198.
125. Ohba, M.; Maruono, N.; Okawa, H. *J. Am. Chem. Soc.* **1994,** *116,* 11566.
126. Lee, S. C.; Holm, R. H. *J. Am. Chem. Soc.* **1993,** *115,* 11789.
127. Karlin, K. D.; Nanthakumar, A.; Fox, S.; Murthy, N. N.; Ravi, N.; Huynh, B. H.; Orosz, R. D.; Day, E. P. *J. Am. Chem. Soc.* **1994,** *116,* 4753.
128. Bossek, U.; Weyhermüller, T.; Wieghardt, K.; Bonvoisin, J.; Girerd, J. J. *J. Chem. Soc., Chem. Commun.* **1989,** 633.

129. Hotzelmann, R.; Wiegardt, K.; Flörke, U.; Haupt, H. J.; Weatherburn, D. C.; Bonvoisin, J.; Blondin, G.; Girerd, J. J. *J. Am. Chem. Soc.* **1992,** *114,* 1681.
130. Carlin, R. L. *Comments Inorg. Chem.* **1991,** *11,* 215.
131. Moron, M. C.; Palacio, F.; Navarro, R.; Pons, J.; Casabo, J.; Carlin, R. L. *Inorg. Chem.* **1990,** *29,* 842.
132. Moron, M. C.; Palacio, F.; Pons, J.; Casabo, J.; Carlin, R. L. *Eur. J. Solid State Inorg. Chem.* **1991,** *28,* 431.
133. Moron, M. C.; Palacio, F.; Pons, J.; Casabo, J.; Solans, X.; Merabet, K. E.; Huang, D.; Shi, X.; Teo, B. K.; Carlin, R. L. *Inorg. Chem.* **1994,** *33,* 746.
134. Miller, J. S.; Calabrese, J. C.; Rommelmann, H.; Chittipeddi, S. R.; Zhang, J. H.; Reiff, W. M.; Epstein, A. J. *J. Am. Chem. Soc.* **1987,** *109,* 769.
135. Broderick, W. E.; Thomson, J. A.; Day, E. P.; Hoffman, B. M. *Science,* **1990,***249,* 401.
136. Caneschi, A.; Gatteschi, D.; Renard, J. P.; Rey, P.; Sessoli, R. *Inorg. Chem.* **1989,** *28,* 1976, 3314.
137. Miller, J. S.; Calabrese, J. C.; McLean, R. S.; Epstein, A. J. *Adv. Mater.* **1992,** *4,* 498.
138. Inoue, K.; Iwamura, H. *J. Am. Chem. Soc.* **1994,** *116,* 3173.
139. Inoue K.; Hayamizu, T.; Iwamura, H. *Mol. Cryst. Liq. Cryst.,* in press.
140. Manriquez, J. M.; Yee, G. T.; McLean, R. S.; Epstein, A. J.; Miller, J. S. *Science* **1991,** *252,* 1415.
141. Mathonière, C.; Kahn, O. *Inorg. Chem.* **1994,** *33,* 2103.
142. Gillon, B.; Cavata, C.; Schweiss, P.; Journaux, Y.; Kahn, O.; Schneider, D. *J. Am. Chem. Soc.* **1989,** *111,* 7124.
143. Ressouche, E.; Boucherle, J. X.; Gillon, B.; Rey, P.; Schweizer, J. *J. Am. Chem. Soc.* **1993,** *115,* 3610.
144. Turner, S. S.; Michaut, C.; Kahn, O.; Ouahab, L.; Lecas, A.; Amouyal, E. *New J. Chem.,* in press.

ADVANCES IN INORGANIC CHEMISTRY, VOL. 43

THE MAGNETOCHEMISTRY OF HOMO- AND HETERO-TETRANUCLEAR FIRST-ROW *d*-BLOCK COMPLEXES

KEITH S. MURRAY

Chemistry Department, Monash University, Clayton, Victoria 3168, Australia

I. Introduction

There has been a great resurgence of interest in the magnetochemical properties of polynuclear *d*-block metal complexes in recent years. This is, in part, due to the intrinsic interest in relating structures to magnetic exchange effects, so-called magnetostructural correlations (*1*), and to more topical interests in determining the properties of paramagnetic clusters in the active sites of metal–proteins and enzymes (*2, 3*)

Copyright © 1995 by Academic Press, Inc.
All rights of reproduction in any form reserved.

and the construction of small building blocks as possible precursors for making new molecular- or bulk-magnetic materials (*4*). The availability of automated variable-field/temperature Squid and Faraday instruments, incorporating superconducting magnets and devices, has made the measurement of magnetochemical detail on a variety of materials, both solid and liquid (e.g., protein solutions), much easier than before (*5*). However, capital and liquid helium costs, and theoretical interpretation, still place such instrumentation in the specialized category, somewhat akin to electron spin resonance (ESR) spectroscopy. Indeed, as pointed out recently by Trautwein *et al.* (*6*), the ideal way to approach problems dealing with the electronic structures of chemical, biochemical or "new" materials of the polynuclear type just mentioned is to use a combination of physicochemical techniques, each of which might probe a different spectroscopic time scale or part of a spin Hamiltonian or set of energy levels. These techniques include magnetic susceptibility, ESR spectroscopy, Mössbauer effect spectroscopy (e.g., for ^{57}Fe compounds), magnetic circular dichroism spectroscopy (MCD), nuclear magnetic resonance spectroscopy (NMR), and resonance Raman spectroscopy. In the present article, emphasis will be placed on magnetic susceptibility data and their interpretation, particularly from a structure-chemical viewpoint, the results of the other techniques only being mentioned where appropriate.

Two new books on molecular magnetism, by Kahn (*7*) and O'Connor (*8*), have appeared recently, as well as various monographs (*2*) and reviews (*9, 10*), many having some emphasis on exchange-coupled clusters. All this activity points up the vitality and importance of magnetochemistry in modern-day chemistry, biochemistry, and materials science. The subject is a very wide and active one and, therefore, only specialized aspects can be covered here. A review of current knowledge in the magnetochemistry of homo- and hetero-tetranuclear clusters is presented. Even within this subarea, it is impossible to be absolutely comprehensive. Apologies are offered in advance to those whose work may not be included. Further, in the case of tetranuclear systems, which have recently seen major advances being made, e.g., mixed-valent $Fe_4S_4(SR)_4$–cubane clusters and double-exchange effects (*10*), or spin-frustration effects in butterfly-shaped Mn_4 and Fe_4 clusters (*7, 11, 12*), a limited but reasonably comprehensive treatment will be given. There are a number of reasons for choosing tetranuclear rather than, say, di- or trinuclear species: (i) The design and synthesis, sometimes accidental, but often very ingenious, of such clusters, and of their attendant ligand frameworks, has grown apace and needs pulling together. (ii) Tetranuclear clusters, or four-metal combinations (i.e.,

those with different intermetallic distances) are important active-site entities in certain metalloproteins, particularly those involved in functions such as multielectron transfer (e.g., Fe_4 ferredoxins) (*13*), small-molecule binding and reactivity [e.g., N_2-binding to molybdenum–iron sulfur clusters in nitrogenase (*14*), O_2-binding to Cu_4 combinations in copper oxidases (*15, 16*) or {Cu–Fe, $Cu_{2(?)}$, Fe} combinations in cytochrome *c* oxidase (*17–20*)] or water oxidation [e.g., Mn_4 site in photosystem II (*21, 22*)]. Many model systems have been constructed in attempts to mimic some aspects of the biomolecules; emphasis will be given here to structure/magnetism relations. (iii) Tetranuclear clusters, both homo- and heteronuclear in makeup, form part of higher-nuclearity cluster design studies aimed at obtaining "high-spin" ground states, via intramolecular ferromagnetic or ferromagnetic-like coupling effects (*4, 7, 8, 23–27*). The understanding gained in molecular design and data interpretation should aid in building more extended frameworks which will, it is hoped, display spontaneous magnetization effects such as three-dimensional ferromagnetic ordering.

One of the main aims of the present review, in Section III, is to allow readers to look up what is known, for example, on the magnetic exchange features of structurally characterized tetranuclear manganese species, in various oxidation states and in various topological arrangements—e.g., Mn_4 squares, rectangles, chains, tetrahedra, or cubes—so that the readers can compare their own data in a reasonably quantitative fashion. In so doing, a structural postulation may be corroborated or a new tetranuclear motif identified. From a historical and parochial point of view, it is interesting to note that some of the earliest structure/magnetism correlations in tetranuclear clusters were made in, or partly in, Australia (*28–30*). Martin (*31*) and Sinn (*32*) summarized these and other studies in two excellent early reviews. Other more recent reviews (*33–38*) and monographs (*39, 40*), including those cited earlier, can be consulted for studies on polynuclear exchange-coupled compounds, some of which contain short sections on tetranuclear species. A recent large review worthy of mention, by Guerriero *et al.* (*40a*), contains a detailed summary of the structures of tetranuclear (and other polynuclear) complexes formed with acyclic and macrocyclic Schiff-base ligands. The appropriate Heisenberg theory of spin coupling has been dealt with in many of these articles; thus, only a concise treatment, relevant to Section III, is presented in Section II. Some secondary aims of this theoretical section are to point out when, or when not, to make various common assumptions or approximations in theory and practice; to provide a set of computer subroutines which are hoped to be of use to practicing magneto chemists; and to give an

example of spin frustration in a heterotetranuclear mixed-spin cluster, the treatment of which contains some of the present day modus operandi in regard to ground-state variability, energy vs J/J' plots, etc.

II. Notes on the Heisenberg Theory of Spin Coupling in Tetranuclear Clusters[1]

A. Preamble

There are three mathematical methods for calculating the effect of a Heisenberg Hamiltonian and hence the magnetic susceptibilities in clusters such as tetranuclear species:

Vector coupling (VC)
Irreducible tensor operators (ITO)
Full matrix diagonalization (FMD)

The VC method, originating with Kambe (*41*), is the easiest of the three to set up and use, and it can result in the evaluation of closed-form expressions for the susceptibility, which chemists feel comfortable working with. Some articles dealing with the VC method are included in the references (*1, 7, 8, 12, 29, 31–35, 37–40*). This method is limited by the symmetry of the cluster system: since one has to be able to obtain appropriate and unique combinations of spin operators, it can therefore be used only for certain symmetries. In the case of tetranuclear symmetries, those appropriate for VC treatment will be highlighted here and throughout the survey in Section III. Departure from these symmetries leads to the Hamiltonian with Eq. (1), which is given later and which can allow for up to six different J values, some of which may be equal. ITO or FMD methods must then be used. FMD has a major drawback in that it can result in very large matrices requiring long diagonalization times, and thus long computing times (*42, 43*). The ITO method reduces the size of the matrices, thereby reducing the computation times dramatically. Its drawback is that it is a bit more difficult to set up in the first case and requires a considerable degree of sophisticated mathematics (*7, 25, 26, 33, 42–50*). It is difficult to include the single-ion effects in the ITO calculations such as zero-field splitting (ZFS). In contrast, it is relatively easy to set up the matrix in FMD and to include effects such as ZFS (*43*). So the decision must

[1] Written in conjunction with Mr. Kevin J. Berry, Western Port Secondary College, Hastings, Victoria 3915, Australia. Any queries on the subroutines in B. should be addressed to him.

be made as to what precisely needs to be done for the case in hand and which effects are likely to be dominant. In general, because of the size of the respective matrices (see Table I), FMD would usually be limited to $S = 1$ or $S = \frac{1}{2}$ systems. However, there are examples of its use for higher spin systems.

Another interesting decision which has to be made concerns the use of Van Vleck's equation (11) or the thermodynamic equation (12) for calculating the susceptibility, the latter containing the field term, H (*51*). The Van Vleck equation (*52*) is appropriate for low applied fields and relatively low spin states at all temperatures. For higher spin states (e.g., $S_T \geq \frac{3}{2}$) and magnetic fields larger than, say, 0.5 tesla, the thermodynamic expression should be used to calculate susceptibilities in the region of less than ca. 50 K because of the thermal depopulation of the upper Zeeman sublevels deriving from the lowest S_T states. The Van Vleck equation can be used for data measured at temperatures greater than 50 K, and its use is quicker in terms of computation speeds. It should be noted that variations in susceptibility and moment with temperature, at high fields and low temperatures, may also be influenced by physical effects such as crystallite orientation (so-called torquing), which needs to be eliminated, for instance, by dispersing the powdered sample in Vaseline or trapping it in a polymer film (*12, 53*). Large magnetic anisotropy often gives rise to this effect (e.g., Mn^{III} or Co^{II} mononuclear compounds), but anisotropy in exchange-coupled clusters is not yet well recognized, except by chance, or by checking. There is future scope for single-crystal studies of anisotropy in clusters.

B. Heisenberg Exchange Coupling in Tetranuclear Species (Including a Useful Set of Microsoft BASIC Subroutines for Calculating Coupled Spin States, Energies, and Susceptibilities)

Exchange coupling between four paramagnetic centers M_1, M_2, M_3, and M_4, with spins S_1, S_2, S_3, and S_4, respectively, is given by the general Hamiltonian in Eq. (1), where J_{12} is the exchange coupling constant between centers 1 and 2, J_{13} is between centers 1 and 3, etc. This Hamiltonian introduces six exchange constants, which may all be equal, all nonequal, or various combinations of equality due to the available exchange pathways and inherent symmetry of the system. Some typical shapes of four-metal cores are shown in Fig. 1: tetrahedral (found in tetrahedral, cubane, or adamantane clusters), square, and rhomboidal (found also in "butterfly" cores). As indicated earlier, calculation of the magnetic susceptibility from Hamiltonian (1) requires use

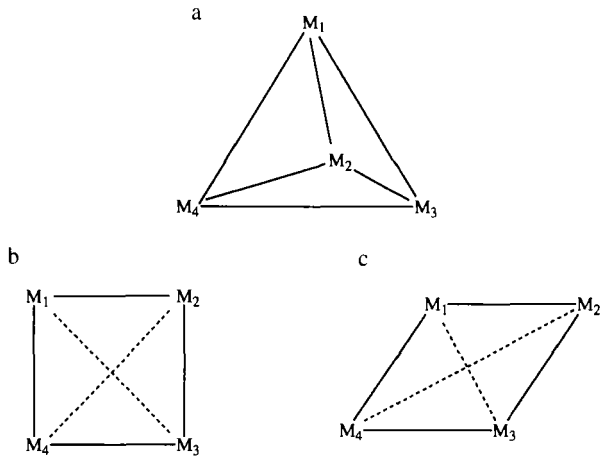

FIG. 1. Shapes of tetranuclear cores: (a) tetrahedron, (b) square, (c) rhombus.

of either matrix diagonalization methods or irreducible tensor operators. The matrix diagonalization method can result in the need to diagonalize sizeable matrices, and the latter method reduces the size of these. The sizes of the matrices for situations where all the individual spin states are the same are given in Table I.

$$\mathcal{H}_{ex} = -2J_{12}\mathbf{S}_1 \cdot \mathbf{S}_2 - 2J_{13}\mathbf{S}_1 \cdot \mathbf{S}_3 - 2J_{14}\mathbf{S}_1 \cdot \mathbf{S}_4 - 2J_{23}\mathbf{S}_2 \cdot \mathbf{S}_3 - 2J_{24}\mathbf{S}_2 \cdot \mathbf{S}_4 - 2J_{34}\mathbf{S}_3 \cdot \mathbf{S}_4 \quad (1)$$

When all six exchange constants are equal, the Hamiltonian reduces to Eq. (2). The expression for the magnetic susceptibility is readily

TABLE I

SIZES OF MATRICES FOR HOMO-TETRANUCLEAR SPECIES [I.E., $(2S + 1)^4$]

Spin state	Matrix size
$\frac{1}{2}$	16
1	81
$\frac{3}{2}$	256
2	625
$\frac{5}{2}$	1296

determined and, as indicated in Section II, has been published for a variety of systems with common spin states (*7, 31, 32–34*). Tetrahedral (T_d) symmetry is such a case.

$$\mathcal{H}_{ex} = -2J(\mathbf{S}_1 \cdot \mathbf{S}_2 + \mathbf{S}_1 \cdot \mathbf{S}_3 + \mathbf{S}_1 \cdot \mathbf{S}_4 + \mathbf{S}_2 \cdot \mathbf{S}_3 + \mathbf{S}_2 \cdot \mathbf{S}_4 + \mathbf{S}_3 \cdot \mathbf{S}_4) \tag{2}$$

Various other symmetries of the tetranuclear species give rise to different Hamiltonians. One particularly useful Hamiltonian, which essentially results from rhomboidal symmetry, is in Eq. (3). In this Hamiltonian, the diagonal exchange constants are nonequal and different from the exchange between the ions around the periphery.

$$\mathcal{H}_{ex} = -2J(\mathbf{S}_1 \cdot \mathbf{S}_2 + \mathbf{S}_2 \cdot \mathbf{S}_3 + \mathbf{S}_3 \cdot \mathbf{S}_4 + \mathbf{S}_1 \cdot \mathbf{S}_4) - 2J_{13}\mathbf{S}_1 \cdot \mathbf{S}_3 - 2J_{24}\mathbf{S}_2 \cdot \mathbf{S}_4 \tag{3}$$

This three-J value Hamiltonian can be reduced to that of expression (2) by allowing the values for the diagonal exchange parameters to be equal to J.

In the square symmetry, where the diagonal exchange constants are equal and may be different from that of the periphery, it is possible to satisfy this requirement by allowing $J_{13} = J_{24} = J'$ in Eq. (3). In planar parallelograms, the first term in (3) requires two J values, since $\mathbf{S}_1 \cdot \mathbf{S}_2 = \mathbf{S}_3 \cdot \mathbf{S}_4 \neq \mathbf{S}_2 \cdot \mathbf{S}_3 = \mathbf{S}_1 \cdot \mathbf{S}_4$.

Hamiltonian (3) can be readily solved and provides a good basis for the determination of the magnetic susceptibility of many tetranuclear species. The solution for this Hamiltonian is as follows:

Three parameters are defined by vector coupling in Eqs. (4) to (6).

$$\mathbf{S}_{13} = \mathbf{S}_1 + \mathbf{S}_3 \tag{4}$$

$$\mathbf{S}_{24} = \mathbf{S}_2 + \mathbf{S}_4 \tag{5}$$

$$\mathbf{S}_T = \mathbf{S}_{13} + \mathbf{S}_{24} \tag{6}$$

The values for $\mathbf{S}_{13}$, $\mathbf{S}_{24}$, $\mathbf{S}_{24}$ are given by relationships (7) to (9).

$$|\mathbf{S}_1 - \mathbf{S}_3| \leq \mathbf{S}_{13} \leq \mathbf{S}_1 + \mathbf{S}_3 \tag{7}$$

$$|\mathbf{S}_2 - \mathbf{S}_4| \leq \mathbf{S}_{24} \leq \mathbf{S}_2 + \mathbf{S}_4 \tag{8}$$

$$|\mathbf{S}_{13} - \mathbf{S}_{24}| \leq \mathbf{S}_T \leq \mathbf{S}_{13} + \mathbf{S}_{24} \tag{9}$$

These definitions of spin parameters allow the computation of the various different coupled states present for any set of four individual spin states under the Hamiltonian (3), and the energies of these are given by Eq. (10).

$$E(S_{13}, S_{24}, S_T) = -J(S_T(S_T + 1) - S_{13}(S_{13} + 1) - S_{24}(S_{24} + 1)) - J_{13}(S_{13}(S_{13} + 1)) - J_{24}(S_{24}(S_{24} + 1)) \quad (10)$$

These definitions can be easily incorporated into a computer program which will generate the appropriate coupled spin states and energies, and then used to calculate the magnetic susceptibility under Van Vleck's equation (11). The more complete thermodynamic equation for χ is given in Eq. (12).

$$\chi = \frac{N\beta^2 g^2}{3kT} \frac{\sum_i S_T(S_T + 1)(2S_T + 1)\exp(-E_i/kT)}{\sum_i (2S_T + 1)\exp(-E_i/kT)} \quad (11)$$

$$\chi = -\frac{N}{H} \frac{\sum_i \left(\frac{\delta E_i}{\delta H}\right)\exp(-E_i/kT)}{\sum_i \exp(-E_i/kT)} \quad (12)$$

The routines, given later, have been written in Microsoft BASIC and use arrays to store the calculated parameters. In these subroutines, the variables CO and NALPHA are given by $N\beta^2/3k$ and χ(TIP) (temperature-independent paramagnetism), respectively. These subroutines can be used in conjunction, for instance, with a spreadsheet to quickly work out a new system or to check out one in the literature. As an example of the latter, we take a very recent case of rhomboidal symmetry found by Chaudhuri *et al.* (*54*) in a "butterfly" complex in which the body ions are Mn^{III}, with $S_1 = S_3 = 2$, and the wing-tips are Cr^{III}, with $S_2 = S_4 = \frac{3}{2}$. The lowest two coupled states found for best fit and given in Fig. 4 of Chaudhuri *et al.* (*54*) are $|3, 3, 0\rangle$ (ground) and $|2, 3, 1\rangle$ separated by 15.8 cm^{-1}. Use of Eq. (10) shows the following:

$$E(3, 3, 0) = 24J - 12J_{13} - 12J_{24}$$

$$E(2, 3, 1) = 16J - 6J_{13} - 12J_{24}$$

The authors assume J_{24} is zero, and thus that the energy separation

between these two states is $-8J + 6J_{13}$. Taking the published best-fit antiferromagnetic values of $J = -11.7$ cm^{-1} and $J_{13} = -13$ cm^{-1} yields a separation of 15.6 cm^{-1}, close to that quoted. The energies of all 60 states (including S_{24} terms) can be rapidly checked and degeneracies noted. The highest-lying state in this example has $S_T = 7$ with $E(4, 3, 7) = 665.6$ cm^{-1}. The susceptibility equation was not given in Chaudhuri *et al.* (*54*) because of its length, i.e., some 44 terms, even with J_{24} = zero, but it can be rapidly checked using the subroutine SUSCEPT, which follows.

```
SUBROUTINE Spin States:
INPUT "Type in the four spin states S1,S2,S3,S4";
S1,S2,S3,S4
S13=S1+S3:S24=S2+S4
S31=ABS(S1-S3):S42=ABS(S2-S4)
FOR I=S31 TO S13 STEP 1
FOR J = S42 TO S24 STEP 1
X=ABS(I-J);Y=I+J
FOR K = X TO Y STEP 1
L=L+1
ST(L)=K
EJ(L)=-((K*(K+1))-(I*(I+1))-(J*(J+1)))
EJ13(L)=-((I*(I+1)))
EJ24(L)=-((J*(J+1)))
NEXT
NEXT
NEXT
N=L
RETURN

SUBROUTINE Energy:
FOUR I=1 TO N
E(I)=EJ(I)*J12+EJ13(I)*J13+EJ24(I)*J24
NEXT
EMIN=E(1)
FOR I=2 TO N
IF E(I)<EMIN THEN EMIN=E(I)
NEXT
FOR I=1 TO N
E(I)=E(I)-EMIN
NEXT
RETURN
```

```
SUBROUTINE Suscept:
S=0:SS=0
FOR I=1 TO N
EX=EXP(-E(I)/KT)
S=S+(ST(I)*(ST(I)+1)*(2*ST(I)+1)*EX)
SS=SS+((2*ST(I)+1)*EX)
NEXT
CHI=(G*G*CO*S/(SS*T)) + NALPHA
RETURN
```

C. A Hetero-tetranuclear Square Complex Showing Spin Frustration Features Which Sensitively Influence the Ground-State Properties

As a further example of exploring more subtle aspects of Heisenberg theory, consider the square core in Fig. 1 in conjunction with the Hamiltonian in Eq. (3) such that $S_1 = S_3 = \frac{5}{2}$ (e.g., Fe^{III}) and $S_2 = S_4 = \frac{1}{2}$ (e.g., Cu^{II}). Furthermore, let $J \neq J_{13} = J_{24} = \alpha J$. This is an example of two competing exchange pathways with "edge" constants J assumed equal and diagonal constant J_{13}, with the ratio J_{13}/J equal to α. For antiferromagnetic coupling, i.e., J negative, and with $J_{13} = J_{24}$ zero, a spin-frustration situation exists and the ground state S_T is equal to 4; see Eqs. (7) to (9). The simple spin picture appropriate to this situation is shown in Fig. 2. As J_{13} is increased from zero, the S_T value for the ground state will change from 4 to zero with changes occurring at the following points:

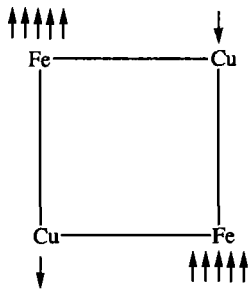

FIG. 2. Spin structure for square $\{Fe^{III}Cu^{II}Fe^{III}Cu^{II}\}$ complex assuming $J_{13} = J_{24} = 0$.

$$
\begin{aligned}
S_T = 4 &\qquad \alpha \leq 0.2 \\
S_T = 3 &\qquad 0.2 \leq \alpha \leq 0.25 \\
S_T = 2 &\qquad 0.25 \leq \alpha \leq 0.33 \\
S_T = 1 &\qquad 0.33 \leq \alpha \leq 0.5 \\
S_T = 0 &\qquad \alpha \geq 0.5
\end{aligned}
$$

These changeover positions can be clearly seen in the correlation diagram shown in Fig. 3, in which E/J is plotted against α. (Related kinds of correlation diagrams are referred to on many occasions in Section

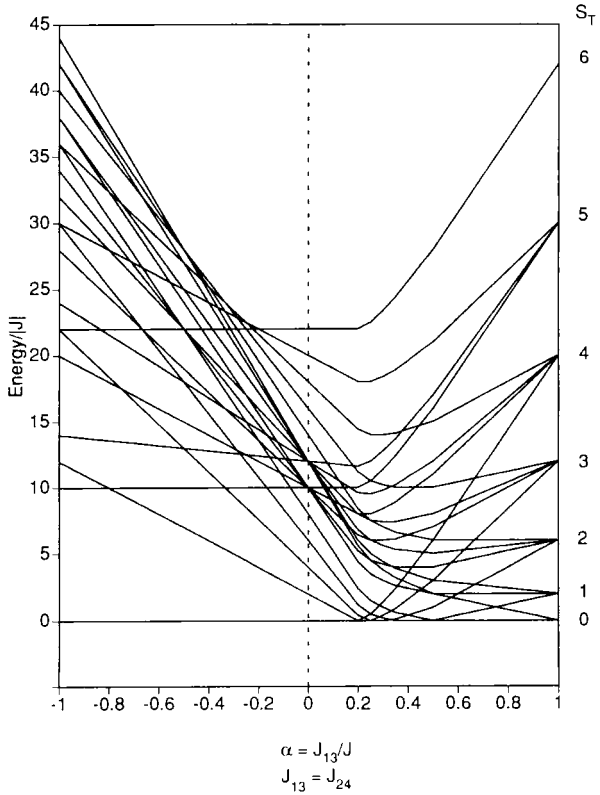

FIG. 3. Energy correlation diagram showing $E/|J|$ vs J_{13}/J for states arising from a square array of $\{S_1 = \frac{5}{2}; S_2 = \frac{1}{2}; S_3 = \frac{5}{2}; S_4 = \frac{1}{2}\}$. $J < 0$.

III.) Use of Van Vleck's equation (11) with J assumed equal to -100 cm^{-1}, and taking steps in α of 0.1, from $\alpha = 0$ to $\alpha = 1$, yields the plots of susceptibility and moment vs temperature shown in Figs. 4 and 5. As anticipated, there are some dramatic changes in magnetic behavior in both the limiting values and the temperature variations. For example, with a ground state $S_T = 4$, μ levels off below ca. 60 K at a value of $\sqrt{80}$ $\mu_B = 8.94$ μ_B (for $g = 2.0$). In contrast, for $\alpha = 0.3$, the low temperature limit for $S_T = 2$ of μ is 4.87 μ_B. Thermally accessible states having higher values of S_T than 2 make the 300 K value of μ in the latter case ca. 6.2 μ_B. For α greater than 0.5, the μ values

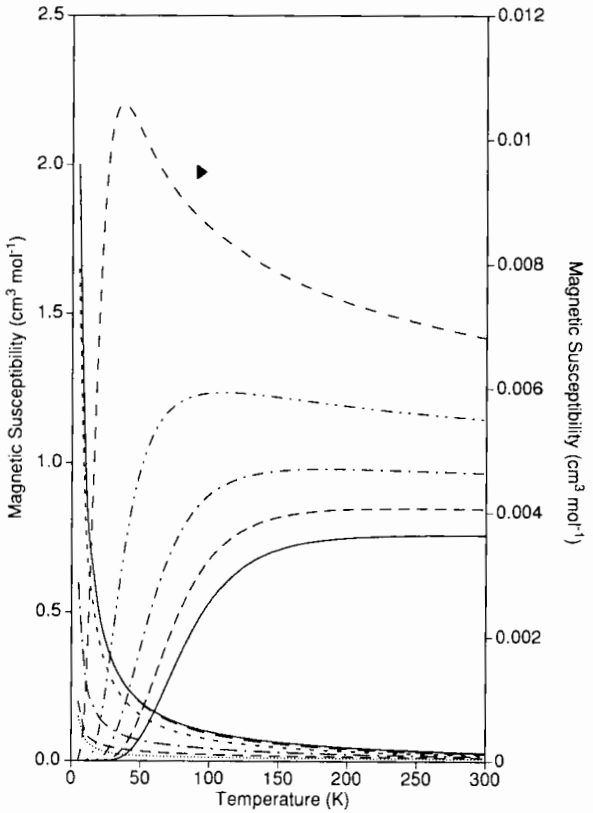

FIG. 4. Calculated χ vs T plots for $J = -100$ cm^{-1}, $J_{13} = J_{24}$. Starting from top right-hand curve, α varies from 0.6 (– – –) to 1.0 (—) in steps of 0.1. Starting from top L.H.S. curve, α varies from 0 (—) to 0.5 (·····) in steps of 0.1.

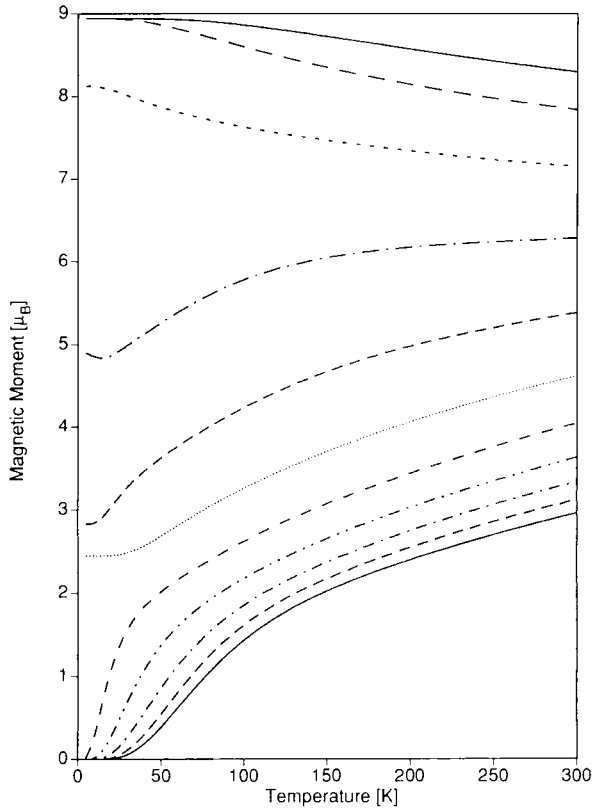

FIG. 5. Calculated μ vs T plots for the values of α ranging from 0 (top curve), in steps of 0.1, to 1.0 (bottom curve). $J = -100$ cm^{-1}, $J_{13} = J_{24}$. (Note that the $S_T = 3$ ground-state situation is not included here.)

decrease towards zero at low temperatures and start from room-temperature values of between 3 and 4 μ_B.

In extrapolating such effects in tetranuclear species toward the design of extended arrays which might display very high magnetic moments, one would aim for designs which would either have small α values, for J negative and J_{13} negative, or would have ferromagnetic J and J_{13} values. The first alternative is, of course, the essence of ferrimagnetism, much exploited in oxamido-bridged $\{Mn^{II}(\frac{5}{2})\ Cu^{II}(\frac{1}{2})\}$ chain compounds by Kahn *et al.* (*7, 35, 55, 56*). The second is the essence of the more elusive ferromagnetic ordering in molecular magnetic materials (*4, 7, 8, 24, 57*).

III. A Survey of Magnetochemical Data on First-Row *d*-Block Transition-Metal Tetranuclear Cluster Complexes

A. Titanium

There are no well-established tetranuclear Ti(II) or Ti(III) complexes. Cubane-shaped Ti(IV)–alkoxo (*58*) and adamantane $[Ti_4O_6]^{4+}$ clusters (*59*) are known, but these are diamagnetic d^0 systems.

B. Vanadium

Only limited magnetic data are available for the few exchange-coupled tetranuclear vanadium species that have been structurally characterized. Magnetic studies carried out by Kakos and Winter (*60*) in the range 300–77 K, combined with other data, suggested that the mixed chloro–alkoxo vanadium(III) complex, $V^{III}Cl(OCH_3)_2 \cdot CH_3OH$, had a rhomboidal structure involving μ-methoxo bridges. Fitting of the data to Dubicki's calculations (*28*) of χ (per V) for a $S = 1$ rhombus, assuming the absence of any orbital degeneracy for these distorted octahedral $V^{III}(d^2)$ centers, yielded the parameters shown in Fig. 6. The exchange Hamiltonian used in Eq. (13) is a recast of Eq. (3):

$$\begin{aligned}\mathcal{H}_{ex} = &-2J_A(\mathbf{S}_1 \cdot \mathbf{S}_2 + \mathbf{S}_2 \cdot \mathbf{S}_3 + \mathbf{S}_3 \cdot \mathbf{S}_4 + \mathbf{S}_4 \cdot \mathbf{S}_1) \\ &- 2J_B(\mathbf{S}_2 \cdot \mathbf{S}_4) - 2J_C(\mathbf{S}_1 \cdot \mathbf{S}_3)\end{aligned} \tag{13}$$

These air-sensitive complexes require further structural characterization and more detailed magnetic study, as Lippard *et al.* (*61*) are presently doing in the case of iron and manganese alkoxo β-diketonato clusters.

Recently Leigh *et al.* (*62*) have synthesized an interesting series of μ-oxo vanadium(IV) salen complexes, including those which contain a linear $[V_4^{IV}O_3]^{10+}$ core within complexes such as [V(salen)OV(salen)

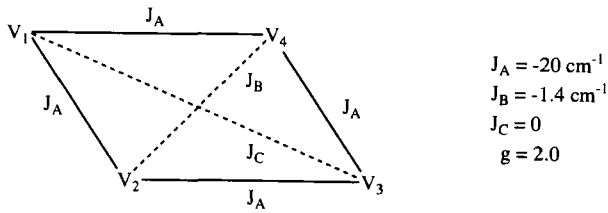

FIG. 6. The coupling model for a V^{III}_4 rhombus showing best-fit parameter values (*60*).

OV(salen)OV(salen)](BF$_4$)$_2$ (Fig. 7). The uneven bridge-bonding is of the type (V=O → V–O–V ← O=V). The magnetic moment (per V) decreases from 1.53 μ_B at 294 K to 1.33 μ_B at 90 K, due to antiferromagnetic coupling, with hints of a ground state S_T 1 (per V_4) or two uncoupled spin $\frac{1}{2}$ "end" groups being responsible for Curie-like dependence below ca. 100 K. These compounds deserve further study of their susceptibilities, at lower temperatures and in variable fields.

C. Chromium

Some of the chelating ligands used to form chromium clusters are shown in Fig. 8.

1. Chromium(III) Clusters

a. Planar Rhomboidal Shape. When one thinks of Cr(III) one thinks of Denmark and then Switzerland and Germany. Historically, these were some of the first tetranuclear clusters to receive detailed

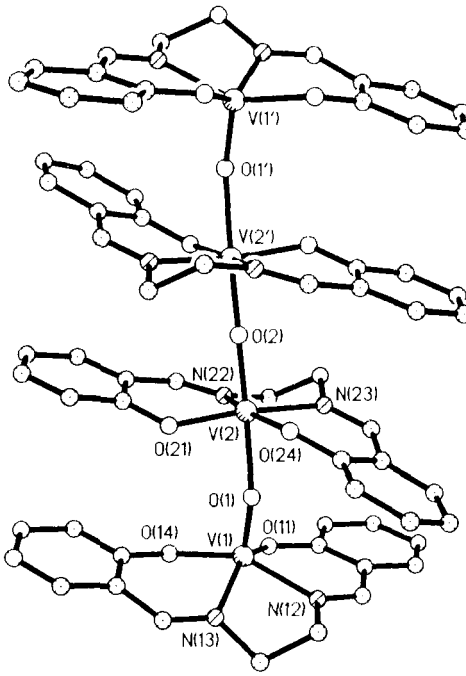

FIG. 7. The structure of [V(salen)OV(salen)OV(salen)OV(salen)]$^{2+}$ (62).

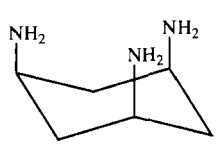

tach

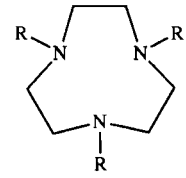

R_3-tacn

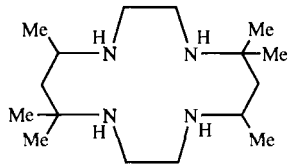

Me_6-[14]ane-N_4

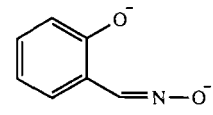

$salox^{2-}$

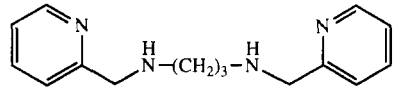

bispictn

FIG. 8. Ligands used to form tetranuclear Cr^{III} complexes.

magnetochemical attention. Earlier magnetic analyses on the "Pfeiffer" complex cation $[Cr^{III}_4en_6(\mu\text{-}OH)_6]^{6+}$, made in the U.S. (*63*), were revised by Gray, Barraclough, and Dubicki in 1969 (*64*, 65) in terms of a planar-rhomboidal geometry after the crystal structure of the azide salt became available (*66*). Cr···Cr separations were 3.606 Å (edge), 2.929 Å (short diagonal), and 6.554 Å (long diagonal). A first-order Heisenberg Hamiltonian was solved by the Kambe vector coupling model, and the long diagonal interaction was assumed to be zero. The eigenvalue energies were inserted into Van Vleck's susceptibility equation. Fitting to this equation yielded $g = 2.0$, $J = -7.3\ cm^{-1}$, and $J' = -14\ cm^{-1}$, the latter interaction being appropriate to the short $Cr(\mu\text{-}OH)_2Cr$ (diagonal) pathway with the former to the $Cr(\mu\text{-}OH)Cr$ (edge) pathway. The ratio of J/J' was 0.52.

Some four years later Jezowcka-Trebiatowska *et al.*, in a rather obscure journal (*67*), reported a similar fit for the Pfeiffer-Cl^- salt and extended the range of compounds to include the Br^-, I^-, SO_4^{2-}, and

$S_2O_6^{2-}$ salts. The J and J' values for the I^- salt, while having $J' > J$, were much smaller than those for the Cl^- and Br^-.

In 1979, Güdel and Hauser made a detailed magnetochemical (*68, 69*) and neutron scattering (*70, 71*) study of a range of salts of the Pfeiffer cation and of the structurally related "rhodoso" cation, $[Cr_4^{III}(NH_3)_{12}(\mu\text{-}OH)_6]^{6+}$. It is interesting to note that this Swiss group was one of the first (*31, 71*) to use theoretical and graphical techniques which have, quite correctly, become more commonly used over the years for clusters that display competing exchange interactions. These techniques included matrix diagonalization and tensor operator methods [based on Griffiths (*33*)], zero-field spin-level energy "ladders," spin-level correlation diagrams (i.e., E vs J/J' ratio, the latter diagrams equivalent to and the precursor to spin-frustration arguments). Consideration was also given to the use of Van Vleck's susceptibility equation vs the thermodynamic form under conditions of low temperatures and high fields; see also Section II,A. The limitations of using best fits of susceptibility data in multiparameter models were also discussed. The symmetry of the rhomboidal Pfeiffer and rhodoso salts was assumed to be D_{2h} and, as in the earlier treatment (*64*), the edge interactions, J, were assumed equal. However, biquadratic (second-order) exchange terms were included with each of the bilinear (first-order) terms, the latter including a long-diagonal J'' term; see Fig. 9. The exchange Hamiltonian was that in Eq. (14).

$$\begin{aligned}\mathcal{H}_{ex} = &-2J(\mathbf{S}_1\cdot\mathbf{S}_3 + \mathbf{S}_1\cdot\mathbf{S}_4 + \mathbf{S}_2\cdot\mathbf{S}_3 + \mathbf{S}_2\cdot\mathbf{S}_4)\\ &- 2J'\,\mathbf{S}_1\cdot\mathbf{S}_2 - 2J''\mathbf{S}_3\cdot\mathbf{S}_4\\ &+ 2j\{(\mathbf{S}_1\cdot\mathbf{S}_3)^2 + (\mathbf{S}_1\cdot\mathbf{S}_4)^2 + (\mathbf{S}_2\cdot\mathbf{S}_3)^2 + (\mathbf{S}_2\cdot\mathbf{S}_4)^2\}\\ &+ 2j'(\mathbf{S}_1\cdot\mathbf{S}_2)^2 + 2j''(\mathbf{S}_3\cdot\mathbf{S}_4)^2 \qquad (14)\end{aligned}$$

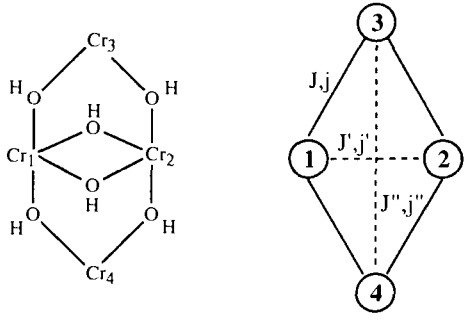

FIG. 9. The coupling model used for a Cr^{III}_4 rhombus in Pfeiffer and rhodoso salts (*42, 68*).

[N.B. Eq. (14) has been converted from the original $J\mathbf{S}_i \cdot \mathbf{S}_j$ Hamiltonian (*50*). Note also a sign difference in biquadratic terms in Andersen *et al.* (*42*).]

Each coupled spin level in the zero-field or correlation diagram had energy $E(S_{12}, S_{34}, S)$ for each wave function $|S_{12}, S_{34}, S, M\rangle$. The coupling scheme adopted was $\mathbf{S}_{12} = \mathbf{S}_1 + \mathbf{S}_2$; $\mathbf{S}_{34} = \mathbf{S}_3 + \mathbf{S}_4$; $\mathbf{S} = \mathbf{S}_{12} + \mathbf{S}_{34}$. Since the matrix of Eq. (14) cannot be diagonalized, matrix elements were worked out by tensor operator methods (*50, 68*).

The plots of μ^2 (per Cr_4) were similar for the seven salts, although some differences were noted in the low-temperature region (<40 K). The rhodoso chloride, for instance, showed a gradual decrease from $43(\mu_B)^2$ at 270 K to $2(\mu_B)^2$ at 1.7 K, in a field of 1 tesla. Magnetization data at 4.2 K were linear in fields up to 2–3 tesla. The best-fit parameters are shown in Table II, that for the neutron scattering analysis providing a "true" reference for the non-unique fits obtained from the magnetic data. Inclusion of biquadratic j values improved the fitting process. The parameter sets given in Table II lead to the low-lying spin-level energies being separated by tens of wavenumbers, with either the $|330\rangle$ spin-singlet or the $|231\rangle$ spin-triplet levels providing the ground

TABLE II

BEST-FIT EXCHANGE PARAMETERS (cm^{-1}) FOR THE RHOMBUS-SHAPED $[Cr_4(NH_3)_{12}(OH)_6](Y)_6 \cdot xH_2O$ (RHODOSO) AND $[Cr_4en_6(OH)_6](Y)_6 \cdot xH_2O$ (PFEIFFER) SALTS[a]

Complex	Y^-	J	j	J'	j'	J''	J/J'
$[Cr_4(NH_3)_{12}(OH)_6]^{6+}$	Cl^- (deut.)[b]	−8.7	−0.05	−12.5	−0.80	−0.85	0.69
	Cl^- (deut.)	−8.3	+0.11	−11.2	−0.82	—	0.74
	Cl^-	−9.8	−0.32	−12.5	−1.06	—	0.78
	Cl^-[c]	−9.5	−0.30	−12.2	−1.0	—	0.78
	Br^-	−6.7	−0.17	−10.8	−0.58	−1.65	0.62
	N_3^-	−7.5	—	−14.6	—	−1.0	0.51
$[Cr_4(en)_6(OH)_6]^{6+}$	Cl^-	−7.0	−0.33	−10.9	−0.38	+2.9	0.64
	Br^-	−8.8	−0.56	−15.2	−0.62	+2.9	0.58
	N_3^-	−7.8	−0.38	−14.0	−0.62	—	0.56
	N_3^-[d]	−7.3	—	−14.0	0	0	0.52

[a] See (*68*) for errors in J and j and temperature interval used. deut = fully deuterated $[Cr_4(ND_3)_{12}(OD)_6](Cl)_6 \cdot 4D_2O$; g = 1.98 throughout.

[b] From inelastic neutron scattering data (*50*).

[c] Taken from second column of Table 7 of Andersen *et al.* (*42*); note that the sign of the j_{kl} $(S_k \cdot S_l)^2$ terms in Andersen *et al.* (*42*) and Güdel and Hauser (*68*) are different. See Eq. (14) for convention used in the present table.

[d] From Flood *et al.* (*64*).

level. For example, in the deuterated rhodoso-chloride, the $|330\rangle \rightarrow |231\rangle$ separation is only 3.25 cm^{-1} (Fig. 10), and this is manifest in a sharp decrease in μ^2, toward zero, below 10 K. It is even sharper in the rhodoso-bromide, since the $|330\rangle$ to $|231\rangle$ separation is less than 1 cm^{-1}. The azide salts of both cations have lower J/J' values, compatible with them being on the $|231\rangle$ side of the $|330\rangle$ $|231\rangle$ crossover region within the E vs J/J' correlation diagrams (*50, 70*). Interestingly, the similarities in the ordering and separation of the very lowest levels, noted in pairs of common-anion salts, was ascribed to the effect which hydrogen-bonding between that anion and the hydroxo-bridging OH groups had on the respective Cr–OH–Cr super exchange pathways. Crystal packing differences were felt not to be responsible for these similarities, but could be responsible for the small differences within the rhodoso or Pfeiffer series. The effects of hydrogen-bonding on intra- and intermolecular exchange interactions in other Cr^{III} clusters have been observed in other studies (*72*).

Andersen *et al.* (*42*) later reported a similar magnetic study on the rhodoso-chloride. After exploration of various parameter combinations, they came to similar conclusions to those deduced by Güdel and Hauser

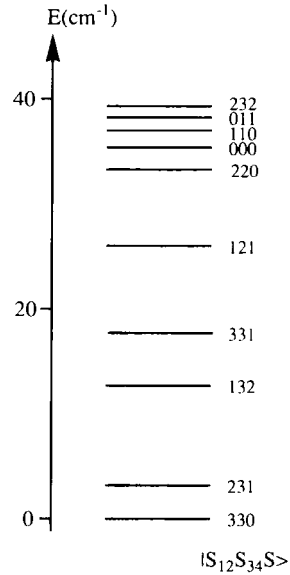

FIG. 10. Zero-field energy ladder for deuterated rhodoso-chloride, $[Cr_4(ND_3)_{12}(OD)_6]Cl_6$, calculated from best-fit parameters in Güdel and Hauser (*68*).

(Table II), although they noted that zero-field splitting of the |231⟩ state could well influence the shape of μ^2/T data below 4.2 K. While the J and J' values were generally of the size and sign anticipated for Cr–OH–Cr and Cr–$(OH)_2$–Cr bridges (*73*, *74*), Andersen *et al.* (*42*) found that calculations of J' for the Cr–$(OH)_2$–Cr moiety of the rhodosochloride using the Glerup–Hodgson–Pedersen (GHP) dimer model (*75*), in combination with accurate crystallographic data, gave a value half of that observed, possibly because of neglect of the extra edge pathway existing in the rhombus. A nice summary of aspects of the magnetism of these rhomboidal Cr^{III} clusters was given by Carlin in his 1986 book (*40*). Contemporaneous with the early studies on the Pfeiffer cation was one carried out in Melbourne by Dubicki, Kakos, and Winter (*29*) on the mixed chloro–alkoxo complex $Cr^{III}(OCH_3)Cl_2 \cdot CH_3OH$. The susceptibilities were obtained only in the range 300–96 K, and it was found that μ (per Cr) decreased from 3.66 μ_B to 3.32 μ_B. A rhomboidal structure, rather like that found by X-ray crystallography in Ti^{IV} alkoxides (*59*), was proposed and thought to involve μ-OCH_3 and μ-Cl bridging groups. A first-order Heisenberg model of the type shown in Fig. 6 for the V^{III} analogue was employed, in conjunction with a χ equation derived using Van Vleck's equation. A number of parameter combinations were found to fit the limited set of data. Low-temperature measurements, combined with magnetization data, would be required in order to reach a definitive answer. The parameters found were $g = 2.0$, $J_A = -5$ to -6 cm^{-1}, $J_B = -1$ to -5 cm^{-1}, and $J_C = 0$ to -1 cm^{-1}, which are, in sign and magnitude, those anticipated for these kinds of bridging groups.

b. Adamantane-like Structure. The $[Cr_4{}^{III}(\mu\text{-}OH)_6]^{6+}$ cation in the mixed salt $[tach_4Cr_4(OH)_6](ClO_4)_{3.57}(SO_3CF_3)_{2.43}$, shown in Fig. 11, has an average Cr···Cr separation of 3.668(9) Å between the tetrahedral

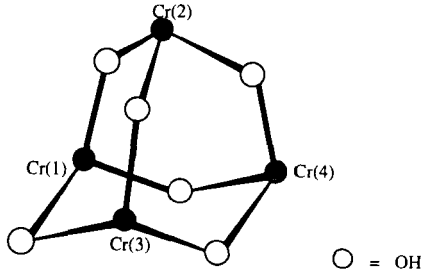

FIG. 11. Adamantane core in $[tach_4Cr_4(OH)_6]^{6+}$ (*76*).

array of distorted octahedral Cr^{III} centers (*76*). The μ (per Cr_4) value of 6.9 μ_B at 295 K compares to an uncoupled value of 7.75 μ_B and decreases gradually to 1.5 μ_B at 4.5 K, while the corresponding χ plot has a maximum at 14 K. This antiferromagnetic behavior is indicative of a $S_T = 0$ ground state. It has been simulated using a one-J Heisenberg exchange model. A best-fit using the thermodynamic χ expression in Eq. (12) yielded the parameters $J = -4.5\ cm^{-1}$, $g = 1.95$. Glerup *et al.* (*76*) gave quantitative and qualitative explanations for the low value of J found in this tetranuclear μ-hydroxo complex compared to those found in tri-μ-hydroxo-bridged "triol" dimers. Angular overlap model (AOM) calculations of matrix elements between ground-state levels and charge-transfer levels in multiples of $e_{\pi(OH)}$, the π-interaction to the bridging oxygen p orbitals (those at 90° to the CrOCr plane), ultimately yielded the ratio $J_{triol}/J_{adamantane} = 18$, in reasonable agreement with the experimental ratio of 16.5. Qualitatively, it was noted that one should be very cautious in comparing J values between complexes with similar bridges but a different number of interacting metal atoms—e.g., dimer, trimer, tetramer—because comparison should be made to the energy gains *per metal atom* resulting from antiferromagnetic coupling. Alternatively, calculations should be made on the basis of the interacting orbitals in the cluster of interest. One can think of other well-known examples of such differences in J, e.g., $Cr^{III}OCr^{III}$ vs triangular $Cr^{III}_3(\mu_3\text{-}O)$, and the Fe^{III} congeners (*77–79*).

c. Cubanes. The cubane-like cluster $[Cr_4(OH)_4$ (6-methyl-2-hydroxypyridinate$)_8]$ showed a steady decrease in μ (per Cr) from 3.18 μ_B at 298 K to 2 μ_B at 100 K due to antiferromagnetic coupling (*80*).

d. "Linear" Tetramer. A thorough study of χ (per Cr) vs temperature on the centrosymmetric di-μ-hydroxo complex $[(en)_2Cr(\mu\text{-}OH)_2Cr(en)(\mu\text{-}OH)_2Cr(en)(\mu\text{-}OH)_2Cr(en)_2](Br)_6 \cdot 2H_2O$ (Fig. 12) showed a

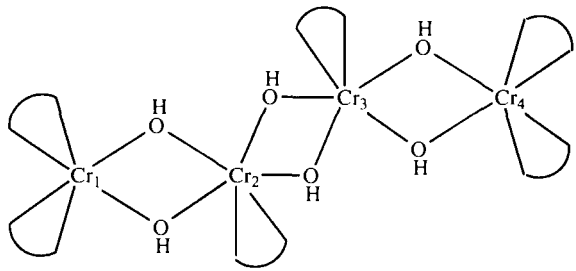

FIG. 12. Structural representation and coupling model for $[(en)_2Cr(OH)_2Cr(en)(OH)_2Cr(en)(OH)_2Cr(en)_2]^{6+}$ (*81*).

maximum at ca. 37 K, the corresponding μ_{Cr} values decreasing from 3.6 μ_B at 300 K to 0.5 μ_B at 4.2 K (*81*).

In order to interpret these data, Damhus and Pedersen, in 1984 (*42*), developed a general computer program capable of diagonalizing a matrix of Heisenberg operators containing first- and second-order (biquadratic) exchange constants. The energy eigenvalues from this program were then read into a second program which calculated susceptibilities by use of the thermodynamic expression given in Eq. (12). The program was capable of calculating any combination of spin value, J, and j. Specifically, for this linear Cr_4^{III} complex, the Hamiltonian shown in Eq. (15) was explored.

$$\mathcal{H}_{ex} = \sum_{k<l}^{n} - 2[J_{kl}\mathbf{S}_k \cdot \mathbf{S}_l + j_{kl}(\mathbf{S}_k \cdot \mathbf{S}_l)^2] \tag{15}$$

Small additive Curie monomer and χ (TIP) terms were included in the χ expression as adjustable parameters. With g fixed at 1.98, five different fitting procedures were adopted allowing for various combinations of nearest-neighbor and more distant exchange interactions occurring between the four Cr^{III} centers. It emerged that a simple pairwise first-order model, the same as that used by Güdel and Hauser (*82*) for $Cr_2Cl_9^{3-}$ "pair" interactions (see later discussion), was adequate, viz., $-2J(\mathbf{S}_1 \cdot \mathbf{S}_2 + \mathbf{S}_3 \cdot \mathbf{S}_4) - 2J'\mathbf{S}_2 \cdot \mathbf{S}_3$, where $J = -9.5$ cm^{-1}, $J' = -7$ cm^{-1}. These values of the exchange parameters could be reproduced quite well by incorporating the structural data for the central and end "dimer" fragments into the GHP dimer model (*75*). A spin-correlation energy plot of E/J vs α ($= J'/J$) was presented, from which the best fit α value of 0.74 corresponded to a set of low-lying spin states having energies of 0 cm^{-1} ($S_T = 0$), 10 cm^{-1} ($S_T = 1$), and 32 cm^{-1} ($S_T = 2$). The first 10 levels were all within 80 cm^{-1} of the ground state.

e. Planar Trigonal Shape in Homo- and Heteronuclear Species. The groups from Berne (*83*) and Copenhagen (*42*) involved in the rhomboidal systems also studied, respectively, the trigonally shaped complexes $[Cr\{(OH)_2Cr(en_2\}_3](S_2O_6)_3 \cdot 8H_2O$ and $[Cr\{(OH)_2Cr(NH_3)_4\}_3](Br)_6 \cdot nH_2O$. It can be seen in Fig. 13 that the central octahedrally coordinated Cr^{III} ion forms three equivalent di-μ-hydroxo bridges to the terminal $Cr^{III}L_4$ fragments (L = NH_3 or L_2 = en). The magnetization of the $S_2O_6^{2-}$ salt at 4.2 K was linear in fields up to ca. 1 tesla, so χ data were measured in fields of $\leq$1 tesla. Both complexes showed similarly shaped μ^2/T plots, with a gradual decrease occurring between 300 and 40 K followed by a minimum in μ^2, then a rise to a limiting value of μ^2 (per Cr_4) of

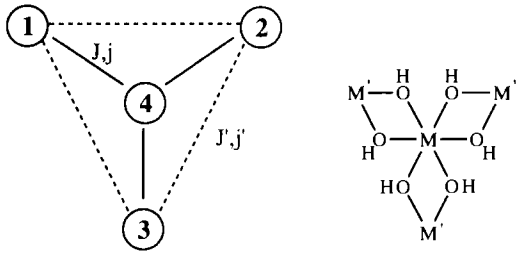

FIG. 13. Structural representation of trigonal core in $[Cr\{(OH)_2Cr(NH_3)_4\}_3]^{6+}$ (*42*, *83*).

ca. 44 ($S_2O_6^{2-}$) and 41(Br^-), indicative of a ground spin state $S_T = 3$ in both cases. A simple one-J Heisenberg Hamiltonian approach, ignoring any edge interactions, was compared to a more complete Hamiltonian, the latter including "spoke," J, and edge, J', interactions, together with their biquadratic j and j' terms (*83*). Zero-field splitting and intercluster interactions were neglected. The best-fit parameter values are given in Table III. The corresponding zero-field spin-level energy diagrams showed the $|S_{12}S_{123}S\rangle$ septet ground level, $|3, 4.5, 3\rangle$, to be separated by ca. 18 cm^{-1} from the degenerate spin quintets $|2, 3.5, 2\rangle$ and $|3, 3.5, 2\rangle$, where $\mathbf{S}_{12} = \mathbf{S}_1 + \mathbf{S}_2$, $\mathbf{S}_{123} = \mathbf{S}_{12} + \mathbf{S}_3$, $\mathbf{S} = \mathbf{S}_{123} + \mathbf{S}_4$. The correlation diagram of E vs J'/J showed that the ground state in these trigonal tetramers can have $S = 3$, 2, 1, or 0, depending on J'/J_3, the $S = 3$ being lowest when J'/J is < 0.3. The strength of coupling within the planar $Cr(OH)_2Cr$ spokes was found to be in agreement with GHP calculations (*75*).

The Copenhagen and Wyoming groups have recently extended this trigonal tetranuclear design to include a range of mixed-metal combinations $[M^{II}\{(OH)_2Cr^{III}L_4\}_3]^{5+}$, where M = Co, Ni, Mn, Zn, Mg and L_4 =

TABLE III

BEST-FIT EXCHANGE PARAMETERS (cm^{-1}) FOR TRIGONAL CLUSTERS IN $[Cr\{(OH)_2Cr\ en_2\}_3](S_2O_6)_3 \cdot 8H_2O$ (**A**) AND $[Cr\{(OH)_2Cr(NH_3)_4\}_3](Br)_6 \cdot nH_2O$ (**B**)

Complex	J^a	J^b	J'	j	j'	g	J'/J
A (*83*)	−8.1	−9.9	−0.7	+0.05	—	2.04	0.07
B (*42*)	−4.7	−5.4	−0.5	+0.21	—	2.0	0.09

[a] From one-J model.

[b] Three-parameter fit from complete Hamiltonian.

$(NH_3)_4$, $(en)_2$, bispictn (*84*). All show net antiferromagnetic coupling such that the μ values at 2 K for the bispictn series level off to values compatible with a ground level S ($=S_1 + S_2 + S_3 + S_4$) of 2 for M^{II} = Mn, 3 for M^{II} = Co, and $\frac{7}{2}$ for M^{II} = Ni. The J_{MCr} values obtained for best fit were -2.8 cm^{-1} (Mn), -0.5 cm^{-1} (Co), and -2.5 cm^{-1} (Ni). J'(edge) values in these and in the M^{II} = Zn complex [and a $La^{III}Cr^{III}_4$ analogue (*85*)] were much smaller, 0 to -0.5 cm^{-1}. The corresponding spin energy levels showed, in all cases, that the ground level had a larger S value than the nearest excited state, the latter being generally less than 10 cm^{-1} away. Unusually shaped μ/T plots are possible in such situations, the precise shape depending also on the sign of J.

Interestingly, when the Cr^{III} ion was placed in the center of a trigonal array of Ni^{II} ions, in a μ-oxalato bridged complex $[Cr^{III}\{(C_2O_4)Ni(Me_6\text{-}[14]ane\text{-}N_4\}_3](ClO_4)_3$ (Fig. 14), net ferromagnetic coupling was observed. This resulted in an $S = \frac{9}{2}$ ground state (*7, 86*). The J_{CrNi} value was $+2.6$ cm^{-1}, and the moment, per tetramer, increased gradually from 6.6 μ_B at 295 K to 9.5 μ_B at 6 K, before leveling off. Ferromagnetic coupling in the $Cr^{III}(C_2O_4)Ni^{II}$ fragments was ascribed to orthogonality of the $Cr(t_{2g})$ and $Ni(e_g)$ orbitals. In a corresponding μ-thiooxalato bridged tetranuclear complex, the structure of which showed Cr–S bonding and Cr···Ni separations of 5.98 Å, J_{CrNi} was again found to be ferromagnetic and bigger ($+5.9$ cm^{-1}) than in the μ-oxalate complex (*87*).

Extension of these tris-μ-oxalato-bridged designs to produce polymeric complexes of the type $\{(Bu_4N)[M^{II}Cr^{III}(C_2O_4)_3]\}_x$, where M^{II} = Mn, Fe, Co, Ni, Cu, Zn, has yielded some novel molecular-based ferromagnets with T_c values occurring in the range 6 and 14 K (*88*). Other related designs have recently been reported (*89–91*) in new molecular-magnetic materials.

f. Tetrahedral $Cr_4(\mu_4$-S) Core. An interesting μ_4-sulfido bridged

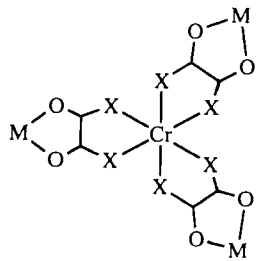

FIG. 14. Trigonal array in $Cr\{(C_2O_4)Ni(Me_6\text{-}[14]ane\text{-}N_4\}_3]^{3+}$ (*7, 86*).

cluster $[Cr^{III}_4(\mu_4\text{-}S)(\mu\text{-}CH_3CO_2)_8(H_2O)_4]^{2+}$, which contains an inner Cr_4S core of T_d symmetry and peripheral bridging acetates, also showed intramolecular ferromagnetic coupling between the four octahedral Cr^{III} ions (*92*). Pertinent distances and angles include Cr···Cr = 3.71–3.91 Å and Cr–S–Cr = 104.7–112.7°. χ/T and magnetization data (up to 4 tesla at 1.27 and 4.22 K), in combination with Brillouin function and Heisenberg Hamiltonian calculations [Eqs. (2) and (11)], confirmed the $S_T = 6$ ground state and yielded a J value of $+10.1 \pm 0.2$ cm^{-1}, for $g = 2.0$. Weak antiferromagnetic intercluster ordering occurred below 0.17 K. Various uses for this material were envisaged within the areas of biology and NMR imaging.

g. Butterfly Structures: $[Cr^{III}_4O_2]^{8+}$, $[Cr^{III}_2Fe^{III}_2O_2]^{8+}$, *and* $[Cr^{III}_2Mn^{III}_2O_2]^{8+}$. Discovery of the tetranuclear "butterfly" $Cr^{III}_4(\mu_3\text{-}O)_2$ within $[Cr_4O_2(O_2CCH_3)_7(bipy)_2]PF_6$ came some years after those of the Fe^{III} and Mn^{III} analogues. The synthesis involved use of a mononuclear Cr^{III} precursor rather than di- or trinuclear units (*93*). The core structure, shown in Fig. 15, is similar to the Mn^{III} analogue. It has a "body" $Cr_1\cdots Cr_3$ distance of 2.783 Å and "body–wingtip" distances of $Cr_1\cdots Cr_4$ = 3.316 Å and $Cr_3\cdots Cr_4$ = 3.427 Å.

The susceptibility data did not show a maximum, but were clearly indicative of antiferromagnetic coupling (μ per Cr_4 = 6.04 μ_B at 281.5 K, μ = 2.44 μ_B at 2.0 K, cf. uncoupled μ per Cr_4 = 7.4 μ_B). The χ data were fitted to the thermodynamic expression in Eq. (12) using energies of the components of the ground-state manifold obtained by diagonalization of the isotropic Heisenberg Hamiltonian given in Eq. (1). Biquadratic j terms were not included. After applying various assumptions on the choice of coupling parameter equalities and then exploring wide ranges of parameters, two equally acceptable fits were obtained, both assuming three variable parameters: $J_{12} = J_{23} = J_{34} = J_{41}$; J_{13}; J_{24}, one allowing for an add-on temperature-independent susceptibility term, the latter fit yielded:

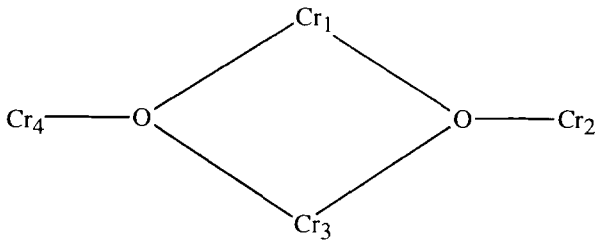

FIG. 15. "Butterfly" core and numbering scheme in $[Cr_4O_2]^{8+}$ (*93*).

$J_{12} = -14.7\ cm^{-1}$ $J_{13} = -24.7\ cm^{-1}$ $J_{12}/J_{13} = 0.59$ $J_{24} = -3.4\ cm^{-1}$

$\chi_{TIP} = 180 \times 10^{-6}$ cgs. $g = 1.98$

The corresponding zero-field energy levels showed a ground state spin triplet, $S_T = 1$, with $S_T = 2$ above at 18.9 cm^{-1} and other levels, including $S_T = 0$ at 30–46 cm^{-1}, up to 648.3 cm^{-1} (for $S_T = 6$). The J_{12} value is a little larger than in the triangular $Cr_3(\mu_3\text{-}O)$ basic carboxylates (ca. $-11\ cm^{-1}$) (*78*).

Vincent *et al.* (*94*) have recently synthesized, in good yield, a range of butterfly complexes of the type $[Cr_4O_2(O_2CR)_7(L)_2]^+$ by reacting the trinuclear basic carboxylate with the chelating ligand, L, in benzonitrile solution. They used R = CH_3 and C_6H_5 and L = bipy, phen, picolinate and structurally characterized the phen complex. From the room temperature μ(per Cr_4) values of ca. 5.4 μ_B for the phen and picolinate complexes, it is possible that these two are slightly more strongly coupled than the bipy complex (see earlier discussion). Further work is needed, however.

Chaudhuri and co-workers (*54, 95*) have made some very interesting mixed-metal butterfly cores in isostructural complexes of the type $[L_2Cr^{III}_2(\mu\text{-}OCH_3)_2(\mu_3\text{-}O)_2(salox)_2M^{III}_2](ClO_4)_2 \cdot 3H_2O$, where M = Mn (*54*), Fe (*95*); L = 1,4,7-trimethyl-1,4,7-triazacyclononane; and $salox^{2-}$ = salicylaldehyde oxime dianion. In contrast to the peripheral carboxylate-bridging in the Cr_4 complex, described earlier, methoxo and oximato (Cr–O–N–M) bridging occurs here. The octahedral Cr^{III} ions are on the wingtip positions with square-pyramidal Mn^{III} (or Fe^{III}) ions on the body positions. The spin-coupling model employed was similar to that used for the Cr_4 complex (Fig. 16), except that the long $Cr_2 \cdots Cr_4$ interaction was assumed to be zero. Thus, a two-J model was adequate.

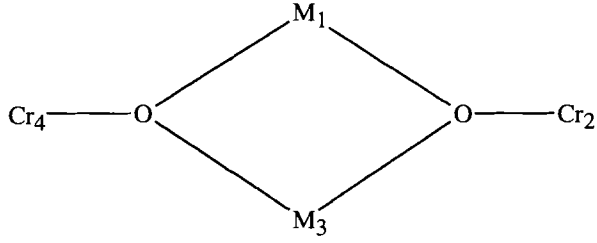

FIG. 16. "Butterfly" core and numbering scheme in $[Cr_2M_2O_2]^{8+}$ where M = Mn^{III} or Fe^{III} (*54, 95*).

Low-temperature turnover in the susceptibility curves required incorporation of a $(T - \theta)$ term in Van Vleck's equation (11), as well as a small component of paramagnetic impurity. Use of variable field experimental data in this low-temperature region, combined with the thermodynamic form of χ, Eq. (12), would have been desirable. Exploration of wide parameter space in the fitting process and use of best-fit contour maps of J_{MM} vs J_{CrM} yielded the following parameter values:

$Cr_2Mn_2O_2$: $J_{CrMn} = -11.7$ cm^{-1}, $J_{MnMn} = -13.0$ cm^{-1}, $J_{CrMn}/J_{MnMn} = 0.9$, $g = 1.71$, $\theta = -3.0$ K; ground state, $S_T = S_{Mn(1)} + S_{Mn(3)} + S_{Cr(2)} + S_{Cr(4)} = 0$

$Cr_2Fe_2O_2$: $J_{CrFe} = -7.5$ cm^{-1}, $J_{FeFe} = -5.3$ cm^{-1}, $J_{CrFe}/J_{FeFe} = 1.42$, $g = 2.0$, $\theta = -14.2$ K; ground state, $S_T = 1$

The zero-field energy level diagrams for both systems show that the low-energy states are close to the ground state but closer in the $Cr_2Fe_2O_2$ system than in the $Cr_2Mn_2O_2$, the first excited state in the former being only 2.6 cm^{-1} away. The J_{CrM} and J_{MM} values are similar in size in each case, but the ratios are a little different. The ratios of these two antiferromagnetic interactions influence the nature of the ground state, and the smallest possible S_T value is achieved. This is compatible with spin–spin frustration occurring. In the $Cr_2Mn_2O_2$ case, the body Mn spins are frustrated, while in the $Cr_2Fe_2O_2$ case, the Fe···Fe spin interaction is frustrated. Goodenough–Kanamori rules for superexchange were involved to explain trends in the size of the "body" J_{MnMn} values compared to those in the $Mn_4^{III}O_2$ analogue (see Section III,D,2,a), the latter having a larger Mn–Mn separation and MnOMn angle. Antiferromagnetic π pathways, between Mn^{III} $(d_{yz}, d_{xz})^2$ orbitals and bridging-oxygen p orbitals, and antiferromagnetic σ pathways, involving Mn^{III} $(d_{xy})^1$, together compete with ferromagnetic {$Mn^{III}(d_{z^2})^1$–oxygen $2p$ (orthogonal)} pathways, thus yielding net weak antiferromagnetic J_{MnMn} values. The only weakness with this argument is that it ignores any effect that the Cr wingtip ions have on the Mn_2O_2 unit. The reader is referred to a paper on mixed-metal basic carboxylate compounds for possible alternative reasons for smaller-than-expected J values occurring in μ-oxo pathways (*79*).

h. "Pair-of-Dimer" Effects: Interactions between Cr^{III} Dimers. The Cr^{III} example, $Cs_3Cr_2Cl_9$, is not a designed "pair-of-dimer" structure of the types we see later in the Mn, Fe, Ni, and Cu sections, but is one which exhibits interdimer interactions noticeable in neutron scattering experiments at low temperatures (*82*). We have already seen that a common way to qualitatively treat such effects, which are often mani-

fest in rapid decreases in magnetic moments at very low temperatures, is to incorporate $(T - \theta)$ terms into Van Vleck's equation (*37*). Alternatively, molecular field terms can be added to the intramolecular exchange term. Hauser and Güdel adopted the approach of a "supercluster" consisting, in the case of $Cs_3Cr_2Cl_9$, of four identical dimers (*82*). A Heisenberg exchange Hamiltonian was sequentially diagonalized for a dimer, tetramer, and octamer model. Matrix elements were deduced by tensor-operator mathematics, and a symmetrical 44 × 44 matrix resulted in the tetramer case. The exchange model in the tetramer was essentially that of a parallelogram, shown in Fig. 17, but with only one edge (J_{ab}) and one diagonal (J_{ad}) interaction being considered. It is not unlike the model adopted for tetranuclear copper (II) chelates which are formed from two weakly coupled dinuclear structures; see Section III,H.

The tetramer ground state is $|000\rangle$ when J_{ad} is zero, since both dimers are in their ground states. A correlation diagram of J_{ad}/J_{ab} vs E, for tetramer states of lowest energy, shows that a J_{ad}/J_{ab} value of $\frac{1}{6}$ was appropriate to the energy splitting obtained from inelastic neutron scattering data, and this corresponded to a 3% mixing of the $|110\rangle$ state into the ground $|000\rangle$ state. The $|110\rangle$ corresponded to a situation in which the nearest-neighbor dimers, both in their first excited $S = 1$ states, coupled antiferromagnetically. Using $J_{ab} = -6$ cm^{-1} and $J_{ad} = -1$ cm^{-1}, the zero-field energy splitting pattern showed the $|101\rangle$ and $|011\rangle$ states some 15 cm^{-1} above $|000\rangle$, with $|110\rangle$ and two others some 25 cm^{-1} above. Related effects were noted in the octamer model, with a high density of states above 20 cm^{-1} from the ground, with excited cluster states being highly mixed and with a 9% mixing of $S = 1$ excited states into the ground state. Thus, this cluster approach provided valuable insight into the origin of cooperative effects and extended interac-

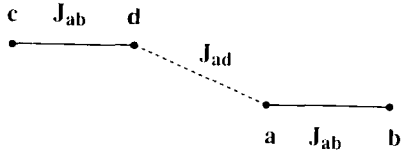

$$\mathcal{H} = -2J_{ab}(\mathbf{S}_a.\mathbf{S}_b + \mathbf{S}_c.\mathbf{S}_d) - 2J_{ad}\mathbf{S}_a.\mathbf{S}_d$$

$$\mathbf{S}_1 = \mathbf{S}_a + \mathbf{S}_b \qquad \mathbf{S}_2 = \mathbf{S}_c + \mathbf{S}_d \qquad \mathbf{S} = \mathbf{S}_1 + \mathbf{S}_2$$

Function $|S_1,S_2,S\rangle$

FIG. 17. The coupling model for a pair-of-Cr(III) dimers (*82*).

tions, particularly in relation to the contribution of excited configurations to the cluster ground state. It is a pity the authors did not compute $\mu/T/H$ curves for low T and high H. The physical origin of the J_{ad} interactions between $Cr_2Cl_9^{3-}$ dimers was not discussed.

D. MANGANESE

Recent years have witnessed great activity in studies of tetranuclear Mn compounds, largely because of their possible relevance to the putative Mn_4 cluster at the water oxidation center (WOC) of photosystem II (*9, 21, 22, 96–99*) and because of their use as high-nuclearity cluster building blocks, the latter forming the basis of possible molecular magnetic materials (*11, 12, 24, 27*).

Among the recent reviews and book chapters dealing with aspects of tetranuclear Mn species, Hendrickson has reviewed the magnetism of butterfly $[Mn^{III}_4O_2]^{8+}$ and cubane $[Mn^{IV}Mn^{III}_3O_3Cl]^{6+}$ clusters with emphasis on spin frustration effects (*11, 12*). Kahn has described the theory for a triangular mixed-metal $[Mn^{II}(Cu^{II}\ \text{oxamide})_3]^{2+}$ complex in his recent book (*7*). This section is arranged in order of increasing Mn oxidation state, with mixed-valence species placed before Mn_4^{IV}. Some of the ligands used in Mn complexation are shown in Fig. 18.

1. Manganese(II)

a. Cubanes. Alkoxide-briged $[Mn^{II}_4(\mu\text{-OR})_4]^{4+}$ moieties have been structurally characterized with (4 + 4) macrocyclic (*40a, 99, 100*) and simple alkoxide cubes (*61*). Variations are found in such features as the symmetry of the Mn^{II}_4 core, the coordination number and geometry of the Mn centers, and the $Mn^{II}\cdots Mn^{II}$ separations, 3.15–3.45 Å. A detailed analysis of the magnetic data is only available, to date, on one of McKee's macrocyclic systems (*99*). In this analysis, Tuchagues *et al.* (*101*) carried out diagonalization of the spin Hamiltonian in the 1296 uncoupled spin-states basis set. The Hamiltonian contained isotropic exchange, axial, and rhombic zero-field terms and Zeeman terms. Calculated plots of χT vs T were presented for a variety of parameter sets. Systematic variations were made in the signs and sizes of g and, sequentially, of one J value (assuming T_d symmetry of the Mn_4 cluster), two independent J values (assumed for S_4 symmetry), or three J values (assumed for C_{2v} symmetry). The J values were limited to the range -2.5 to $0.25\ cm^{-1}$. We had made similar calculations and parameter variations for $S = \frac{5}{2}$ and $S = 2$ dimers some years earlier (*43, 53*). In fitting the observed data for the complex $[Mn_4(L^A)(ClO_4)_4]2H_2O$, where L^A is the 4 + 4 macrocycle formed from 1,3-diamino-2-hydroxy-

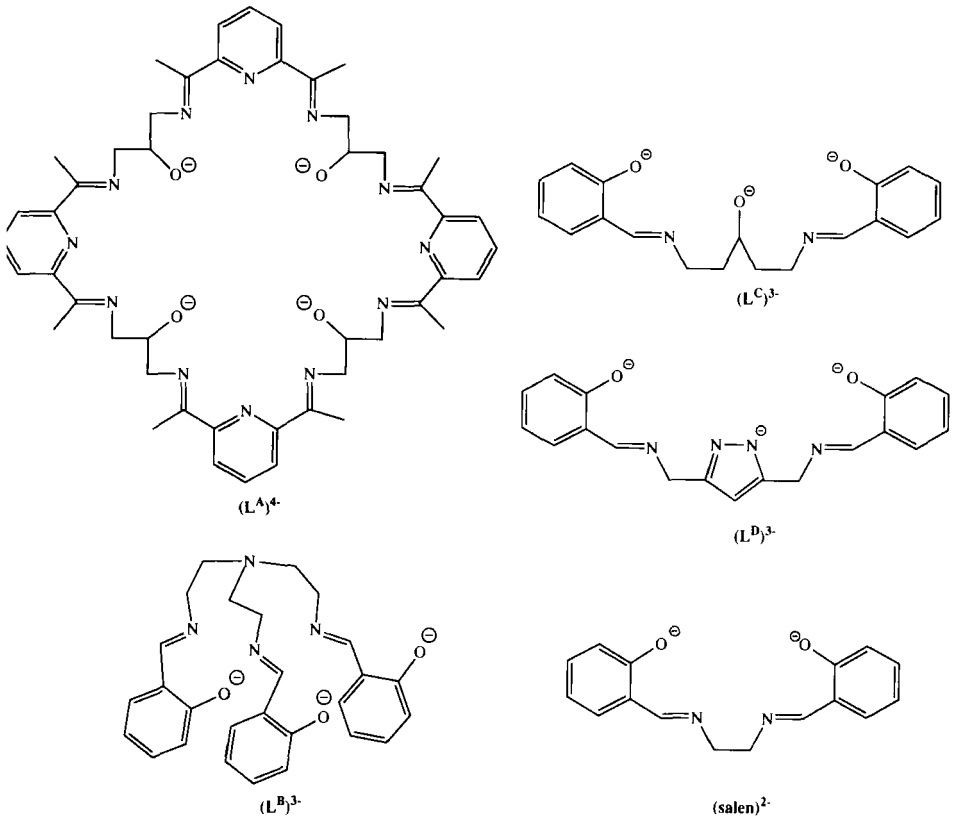

FIG. 18. Ligands used to form tetranuclear Mn complexes.

propane and 2,6-diacetylpyridine, a one-J (T_d) model with no ZFS was found to be adequate, despite the small structural distortions toward S_4. Ironically, the diagonalization approach was not required. A very small negative value of J was obtained, i.e., $g = 1.954$, $D = 0$, $J = -0.51$ cm^{-1}.

The fluoride-bridged cube $[Mn^{II}_4(\mu\text{-}F)_4(\text{N-Et-imidazole})_4](BF_4)_4$ yielded a reasonable fit to a Heisenberg model [Eq. (2)] when susceptibility values obtained above ca. 40 K were used. The six Mn–Mn exchange constants were assumed to be equal. J was very small, estimated to be -0.8 ± 0.3 cm^{-1}. A "twist" in the high-field magnetization data was ascribed to a two-step process involving spin-flop (*102*). Swapping 5-Me-pyrazole for N-Et-imidazole gave a similar value for J (*103*).

A rare example of a chalcogenide cubane cluster containing a diva-

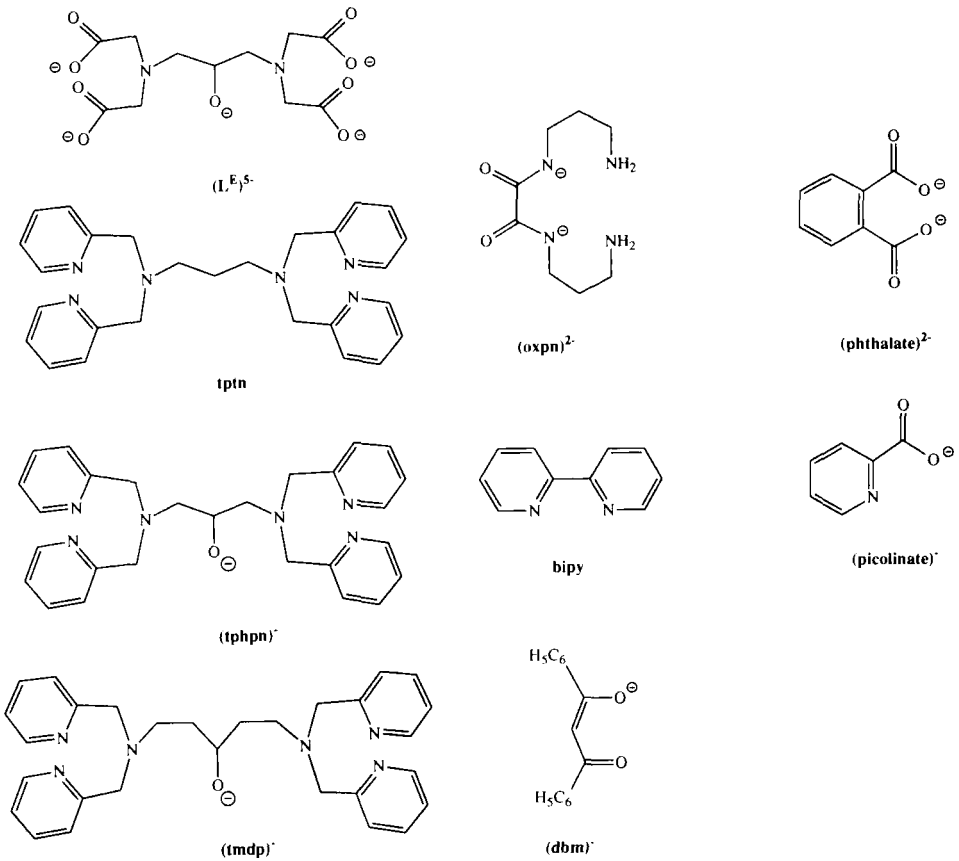

FIG. 18. *Continued.*

lent ion, $(Me_4N)_4(Mn^{II}{}_4(\mu\text{-}Te)_4(TePr^i)_4]MeCN$, with Mn···Mn distances nearly identical (3.275 Å), showed stronger antiferromagnetic coupling than the μ-fluoro or μ-alkoxo species. Thus, analysis using a one-J "tetrahedral" model and Eq. (2) yielded $J = -21.7$ cm^{-1} and $g = 2.0$ (*104*).

b. Rhomboidal Geometry. The heteropolyanion $Mn^{II}{}_4(H_2O)_2(PW_9O_{34})_2]^{10-}$ encapsulates a planar rhomboid Mn_4O_{16} core which contains four $Mn^{II}O_6$ octahedra edge-bridged by oxide groups. Coronado *et al.* (*105*) used a two-J isotropic Heisenberg Hamiltonian appropriate to Fig. 19. This yielded $g = 2.0$, $J = -1.7$ cm^{-1}, $J' = -0.3$ cm^{-1}, and $J'/J = 0.18$. The ratio is compatible with a ground-state S' value of 0 separated by only 3.4 cm^{-1} from an $S' = 1$ state. In the Cu^{II} analogue,

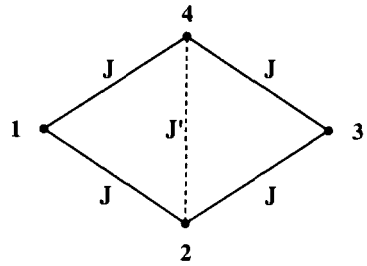

FIG. 19. The coupling model for M_4O_{16} rhomb-like cores in $[M_4(H_2O)_2(PW_9O_{34})_2]^{10-}$ (*105*).

a ratio of $J'/J = 3.6$ leads to spin frustration and a $S' = 1$ state being lowest (*106, 107*). These differences between Mn^{II}_4 and Cu^{II}_4 were ascribed to differences between diagonal and edge M···M separation, with consequent differences in orbital overlap. The related complex $[Mn^{II}_4(H_2O)_2(P_2W_{15}O_{56})_2]^{16-}$ gave a fit to the same coupling model with $g = 2.0$, $J = -1.2$ cm^{-1}, $J' = -0.2$ cm^{-1}, $J'/J = 0.17$, but required a 40% impurity of mononuclear Mn^{II} to be included (*108*). The overall weak antiferromagnetic exchange results from Mn–O–Mn angles of 90–100°.

A μ-carboxylato-bridged complex $[Mn^{II}_4(\mu\text{-phthalate})_2(bipy)_8]^{4+}$ can be described as rhomboid in shape with edge Mn···Mn distances of 5.16 Å and a short diagonal of 7.337 Å. Interestingly, it showed weak net ferromagnetic coupling, but no analysis was given (*109*).

c. Planar Trigonal Shape in $Mn^{II}Cu^{II}_3$ Species. The design of a Mn^{II} tris-oxamido Cu^{II} complex, $[Mn\{Cu(oxpn)\}_3](ClO_4)_2$, is similar to those discussed in Section III,C,1,e, except that bridging oxamide groups replace oxalates (*7, 110*). The energies and g values of the (S, S') coupled states have been given by Kahn (*7*), where S is the total spin and S' is the spin of the three Cu^{II} atoms. Antiferromagnetic coupling was evident from the μ vs temperature curve, which leveled off below 7 K to a plateau value appropriate to a $S = 1$ ground state. The data were fitted to $J = -13.3$ cm^{-1}, $g_{Mn} = 1.98$, $g_{Cu} = 2.00$.

d. Adamantane-like Structure. The arylthiolato complex $((CH_3)_4N)_2[Mn_4^{II}(SPh)_{10}]$ had a room-temperature moment of 4.61 μ_B per Mn, which, with NMR data, was indicative of antiferromagnetic behavior (*111*).

e. Pair-of-Dimer Complexes. Okawa *et al.* (*111a*) synthesized compounds of type $Mn_4^{II}L(C_6H_5CO_2)_6((CH_3)_2CHOH)_2$ in which the macrocy-

clic ligand, L^{2-}, was formed by a 2 + 2 condensation between 2,6-diformyl-4-methylphenol and a linear tetraamine of type 1,8-diamino-3,6-dialkyl-3,6-diazaoctane (see ligand L^{14} in Fig. 32 for a related macrocycle). The Mn_4 complex contains two pairs of Mn_2^{II} ions bridged by a phenolic oxygen of L^{2-} and benzoate groups. The "intradimer" Mn···Mn distance was 3.487(2) Å, as expected for such a bridging combination whilst the "interdimer" Mn···Mn distances were greater than 11.4 Å. Small J values of -2.8 to -4.4 cm^{-1} were obtained for the intradimer coupling in two examples and no coupling was noted between dimers, as expected.

In summary, tetranuclear Mn(II) complexes generally display weak antiferromagnetic coupling. This is generally also the case in Mn(II) di- and trinuclear clusters (*96, 97, 112*). The strongest coupling to date is provided by the μ-Te^{2-} bridging moiety. The examples showing weak ferromagnetism need further work.

2. Manganese(III)

a. Butterfly Structure, $[Mn^{III}_4O_2]^{8+}$. The synthesis of $[Mn^{III}_4O_2(O_2CCH_3)_7(bipy)_2](ClO_4)\cdot 3H_2O$ and related species by cluster expansion reaction of bipyridine with the trinuclear complex $[Mn^{III}_3O(O_2CCH_3)_6(py)_3](ClO_4)$ allowed Christou and co-workers to develop a fascinating and important series of models for the photosystem II WOC (*98, 113*). The detailed magnetic properties of this complex and of mixed-valence derivatives, as functions of both temperature and field, were studied in collaboration with Hendrickson and Boyd *et al.* (*114*). Aspects of the magnetism, including spin-frustration effects, have been reviewed by Hendrickson (*11, 12*). Only pertinent points of the magnetic analysis and a survey of the series of Mn "butterfly" clusters are given here. From the experimental point of view, it is important to note that the correct measurements were made in order to deduce, not only the ground state, but also the low-lying excited states in a cluster such as this, one which has competing J values of similar size. Subtle effects such as crystallite orientation (so-called "torquing"), which can occur in (anisotropic) Mn^{III} species especially at low T and high H, were also checked for and eliminated. The ground state was confirmed as $S_T = 3$ by magnetization (M) data measurements, made in fields of 1, 3, and 4.8 tesla and at temperatures between 15 and 1.8 K. Calculation of $M/N\beta$ vs H/T curves were made by Brillouin function calculations and by use of the thermodynamic equation for M [Eq. (12)] in the absence, and presence, of zero-field splitting of the $S_T = 3$ state, the latter leading to anisotropy in M. Appropriate powder averaging calculation of M at various temperature intervals, using spin-level energies

obtained from diagonalization of the Heisenberg exchange Hamiltonian, were also discussed (*51*). The best agreement for $[Mn^{III}_4O_2bipy_2(O_2CCH_3)_7](ClO_4) \cdot 3H_2O$ required axial and rhombic ZFS terms, i.e., $S_T = 3$, $g = 1.9$, $D = +1.9\ cm^{-1}$, $E = +0.32\ cm^{-1}$.

The μ/T data, which showed a decrease from 7.96 μ_B (per Mn_4) at 300 K to a broad minimum of 6.3 μ_B (90–20 K), followed by an increase to 6.8 μ_B at 4.2 K, were used to obtain the J values and spin energy levels. The exchange model and Hamiltonian used were the same as those shown for the $Cr^{III}_4O_2$ butterfly cluster in Fig. 15, or the rhomboid cluster in Fig. 9, but with $S_i = 2$ in the present case and with the wing-to-wingtip interaction, J_{24}, assumed zero. The Kambe vector coupling was used as in Eqs. (4) to (6). A spin degeneracy of 625 has 85 individual spin states with S_T ranging from 0 to 8. The energies of the states were given by Eq. (10).

The best-fit values of J_{12} and J_{13} for this and the related anionic cluster, $[Mn^{III}_4O_2(O_2CCH_3)_7(picolinate)_2]^{\ominus}$, (*11, 115*), are given in Table IV. The picolinate complex showed a D of 3.7 cm^{-1} for zero-field splitting of the $S_T = 3$ ground state. Hendrickson (*12*) presented spin-state correlation diagrams for these systems in two formats, one as an E/J_{12} vs J_{13}/J_{12} ratio plot for all the low-lying $\{S_T, S_{13}, S_{24}\}$ states, the other as a J_{12} vs J_{13} parameter space showing the various possible ground states. The occurrence of two states with $S_T = 2$, at only 15 cm^{-1} above the $S_T = 3$ ground state in the bipy complex, is primarily responsible for the observed μ value at 4.2 K being higher than those in the 20–90 K region. Other interesting nuances became apparent for these $[Mn^{III}_4O_2]^{8+}$ butterfly complexes. For instance, spin frustration leads to six unpaired spins in the ground state, even though J_{12} and J_{13} are both antiferromagnetic, the J_{13} (body-body) interaction being

TABLE IV

BEST-FIT PARAMETERS FOR Mn_4O_2 BUTTERFLY CLUSTERS (J VALUES IN cm^{-1})

Cluster	J_{12}	J_{13}	J_{12}/J_{13}	g	Ground, S_T	Ref.
$[Mn^{III}_4O_2(O_2CCH_3)_7(bipy)_2]^+$	−7.8	−23.5	0.33	2.0	3	*114*
$[Mn^{III}_4O_2(O_2CCH_3)_7(pic)_2]^-$	−5.3	−24.6	0.21	1.96	3	*115*
$[Mn^{II}_2Mn^{III}_2O_2(O_2CCH_3)_6(bipy)_2]^a$	−1.97	−3.12	0.63	1.70	2	*114*
$[Mn^{II}_2Mn^{III}_2O_2(O_2CCPh_3)_6 \cdot (OEt_2)_2]^a$	−1.5	−3.8	0.3	1.47	2	*126*
$[Mn^{II}Mn^{III}_3O_2(O_2CC_6H_5)_7(bipy)_2]$	−2.2	−16.6	—	1.85	—	*113*

[a] $Mn_1 = Mn_3 = Mn^{III}$ (body sites); $Mn_2 = Mn_4 = Mn^{II}$.

three times that of J_{12} (body–wingtip). While the spins on Mn_1 and Mn_3 therefore have the greater tendency to pair up, they are not fully coupled (i.e., $S_{13} = 1$), and each wingtip Mn^{III} ion interacts with both Mn_1 and Mn_3. Thus, the spin alignment of the wingtip ions is frustrated. We see later in the $Fe^{III}{}_4O_2$ clusters that J_{12} dominates and the body–body interaction is now frustrated.

b. Fused Open Cubane [$Mn^{III}{}_4O_2(OAr)_4$]. The groups of McKee (*116*) and Chakravorty (*117*) simultaneously reported an interesting fused open cubane $[Mn^{III}{}_4O_2(OAr)_4]$ core in complexes of type $[Mn^{III}{}_4O_2(L^B)_2](Y)_2 \cdot xCH_3CN$, where L^B is the podand ligand shown in Fig. 18. The structures of complexes with $(Y)_2 = MnCl_4{}^{2-}$, $x = 2$, and $Y = PF_6$, $x = 4$, were presented. The Mn···Mn distance across the pyramidally disposed μ_3–O^{2-} ligands was ca. 2.9 Å, a little longer than the "body–body" separation in the butterfly $(Mn_4O_2)^{8+}$ cores. The μ vs temperature data showed rather similar plots, but with differences in absolute magnitude depending on the nature of Y and L. Thus, for the $(Y)_2 = MnCl_4{}^{2-}$ salt, μ (per Mn_4) decreased gradually from 8.4 μ_B at 300 K to 4 μ_B at 4.2 K, indicative of net antiferromagnetism. No analyses of the data were attempted. The coupling model would probably require three J values; the dominant one would be expected to be that associated with the $Mn(\mu_3\text{-}O)_2Mn$ fragment, since μ-oxo-bridged Mn^{III} dimers are known to be weakly antiferromagnetically or ferromagnetically coupled (*114, 118*). These open cubanes are examples where low-temperature magnetization studies would also be useful to define the ground state.

Another similar example of an open cubane Mn^{III} cluster, $[Mn^{II}{}_4(O)_2(L^C)_2(O_2CCH_3)_2]$, was earlier obtained by Mikuriya *et al.* (*119*) by reacting Mn^{III} acetate with the binucleating ligand (L^CH_3), 1,5-bis(salicylideneimine)-3-pentanol. The structure consists of two $Mn^{III}{}_2(O)(L^C)(O_2CCH_3)$ moieties bridged at 90° via the μ-oxo and phenolate oxygen atoms. The moment varied from 8.64 μ_B per Mn_4 at 295 K to 7.12 μ_B at 77 K. This compound also requires further analysis of the magnetism.

c. Tetrahedral [$Mn^{III}{}_4(\mu_4\text{-}O)]^{10+}$ Cluster. Floriani and co-workers, in a "novel" approach to the synthesis of Mn Schiff-base aggregates (*120*), largely by use of sodium reductions, were able to reproducibly obtain the oxidized species $[Mn^{III}{}_2salen_2)_2$ (μ_4-O) $(NaDiglyme)_2]$. The source of O^{2-} was assigned to traces of O_2 in non-degassed ether, the latter added to the diglyme solution of Na reduced Mn^{II} salen. There are no peripheral bridging groups directly joining the four Mn^{III} ions, although Mn_2salen_2 units are formed by C–C bonds at the imine functions, and Na^+ ions link these units via phenolate O atoms. The four $Mn(\mu_4\text{-}O)Mn$

angles were close to the tetrahedral angle, but not equal. The magnetic moment decreased from 9.2 μ_B per Mn_4 at 300 K to 5.6 μ_B at 1.9 K. A three-J analysis of the data was required. It led to the combination of similarly sized antiferromagnetic and ferromagnetic interactions shown in Fig. 20. These parameters led to an $S = 2$ ground state with an excited $S = 3$ state at 6 cm^{-1} and $S = 1$ at 19.2 cm^{-1}, plus many others above 34 cm^{-1}. With the sparse data presented to date, it is not obvious why the J values should have different signs, although it is known, separately, that J can be just positive or just negative in dinuclear $[Mn^{III}_2(\mu_2\text{-O})(\mu\text{-RCO}_2)_2]^{2+}$ complexes (*96, 118*), the latter having MnOMn angles 10° larger than in this $Mn_4(\mu_4\text{-O})$ complex.

d. Pair-of-Dimer Complexes. Attempts to put an alkyl chain across a dinuclear μ-oxo-di-μ-carboxylato dimanganese(III) moiety, by use of "strapped" tripodal pyridylmethylamine ligands of the tptn type, led to formation of tetranuclear species (*121, 122*). As shown later in Fig. 27, for the Fe(III) analogue, the alkane strap has actually formed two $Mn(O)(O_2CCH_3)_2$ Mn groups together rather than just straddling across one such group. The large dimer–dimer separation and lack of any suitable bridging pathway means that the magnetic properties reflect these two noninteracting dinuclear units. Weak ferromagnetic coupling was evident in the moment vs temperature plot, and a best-fit using matrix diagonalization methods gave $J = +11$ cm^{-1}, $g = 1.95$, and $|D| = 7$ cm^{-1}. These values are similar to those found by Wieghardt *et al.* for dinuclear tacn compounds (*96, 118*) and by Nishida *et al.* for a

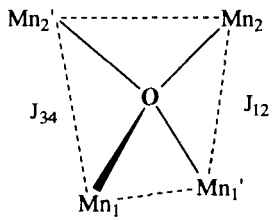

$$J' = J_{Mn_1'Mn_2'} = J_{Mn_1Mn_2} = J_{Mn_1'Mn_1} = J_{Mn_2Mn_2'} = -5.6\ cm^{-1}$$

$$J_{12} = -12.6\ cm^{-1} \quad J_{34} = +22.0\ cm^{-1}$$

(**NB.** The $2J\bar{S}_1.\bar{S}_2$ *vs* $J\bar{S}_1.\bar{S}_2$ convention, and sign, was not defined (*120*))

FIG. 20. Structure and exchange parameters in a tetrahedral $[Mn^{III}_4(\mu_4\text{-O})]^{10+}$ cluster (*120*).

tetranuclear benzimidazole-methylamine ligand system, which had a very similar framework to the tptn complex (*123*).

In recent work, Wieghardt *et al.* (*123a*) have synthesized some very interesting mixed-metal/mixed-ligand complexes such as [{(Me-tacn)-Fe^{III}(μ-O)(μ-succinato)Mn^{III}bipy(H_2O)}$_2$]$^{4+}$. The two dicarboxylate bridging ligands link the strongly-coupled heterodinuclear moieties together. These compounds and their Mn^{III}_4 analogues have been tested for catalase activity towards H_2O_2.

e. "Linear" Tetranuclear. The zigzag chain of four Mn^{III} atoms in $[Mn^{III}_4L^D_2(\mu\text{-}OCH_3OH)_4](ClO_4)_2 \cdot 4CH_3OH$ has {μ-pyrazolate, μ-methoxo} bridges between outer pairs and di-μ-methoxo bridges between the inner pair (*124*). The μ/T behavior is similar to that in Mn^{III} Schiff-base monomers, having ZFS and weak antiferromagnetic coupling (*53*).

3. Mixed-Valency Mn Species

a. Mn_4O_2 Butterfly Complexes. The $[Mn^{III}_2Mn^{II}_2O_2]^{6+}$ core, which occurs in the complex $[Mn_4O_2(O_2CCH_3)_6(bipy)_2] \cdot 2CHCl_3$, was shown by X-ray crystallography to have a planar rhomboidal arrangement of Mn ions in trapped valency states, with the Mn^{III} centers on the "body" positions. The magnetic study and analysis were made in a similar fashion to those described earlier (*11, 12, 114*) for the $Mn^{III}_4O_2$ analogue. μ (per Mn_4) decreased gradually from 8.81 μ_B at 300 K to 4.86 μ_B at 10 K. The best-fit exchange parameters are given in Table IV; these are compatible with six spin-state energy levels lying within 15 cm^{-1} of the ground $S_T = 2$ state. The difference noted in the J_{13} (body–body) value for this mixed-valence complex, compared to the $Mn^{III}_4O_2$ complex, was ascribed to differences in coordination geometry around the high-spin Mn^{III} ions which, in turn, led to attenuation of antiferromagnetic superexchange pathways. Zero-field splitting of the $S_T = 2$ ground state was identified by use of magnetization studies, a D value of -1.93 cm^{-1} indicating that the $M_S = \pm 2$ sublevel was lowest in energy.

A similar complex, but one containing all oxygen-donor carboxylate ligands, $Mn_4O_2(O_2CCPh_3)_6 \cdot (OEt_2)_2$, gave essentially the same J_{12} and J_{13} values, indicating that the peripheral ligands played little part in the exchange mechanism (*125, 126*). The best-fit g value was even smaller than that found in the bipy analogue (Table IV).

b. Trapezoidal $[Mn^{II}Mn^{III}_3(\mu\text{-}O)(\mu\text{-}OH)]^{8+}$ Complexes. Elaboration of the tripodal ligand design, based on the 1,3-diamino-2-hydroxypropane backbone, to include acetate "arms" has enabled Gorun *et al.* (*127, 128*) to obtain a fascinating group of anionic clusters of type $(A)_2[Mn_4(\mu\text{-}O)(\mu\text{-}OH)(O_2CCH_3)_2L^E_2]$, where $(L^E)^{5-}$ = 1,3-diamino-2-hydroxypro-

pane-*N*,*N*,*N*′,*N*′-tetracetate and $(A^{2+})_2$ = Ca, Ba; Ca, Ca; Ba, Ba. These compounds display a catalase activity toward H_2O_2. The central core, shown in Fig. 21, contains a short O···O separation (2.46 Å) within the $(OHO)^{3-}$ bridge and has trapped valencies on the Mn ions, the three Mn^{III} centers displaying axial compression along the *z*-axis due to the Jahn–Teller effect, where *z* is along the Mn-(μ-OHO) direction. Thus, it would be anticipated that little spin-density on the Mn^{III} $d_{x^2-y^2}$ orbitals would overlap with the OHO group, and exchange interactions would predominantly occur via the μ-alkoxo and μ-carboxylato peripheral ligation. There are subtle differences in the way that the alkaline earth cations bridge the Mn ions via bridging to acetate oxygens, in some cases water bridging is also involved.

Since this work is an ongoing collaboration (*128*), only brief comments are given here. Gorun has obtained very detailed susceptibility data in the range 300–1.8 K and magnetization data in the range 2–77 K in fields of 0–5.5 T on the Ba_2Mn_4, Ca_2Mn_4, and $CaBaMn_4$ compounds. The data are generally compatible with the occurrence of overall weak antiferromagnetic coupling, as would be anticipated from previous work on dinuclear μ-alkoxo or μ-carboxylato bridged $Mn^{II}Mn^{III}$ or Mn^{III} Mn^{III} species (*114*). However, there are differences in detail in the μ vs temperature plots of the various salts. For example, μ per Mn_4 decreases gradually from 10 μ_B (Ca_2) and 9.1 μ_B (Ba_2) at 300 K to 3.4 μ_B (Ca_2) and 1.9 μ_B (Ba_2) at 3 K. The uncoupled μ value for $S = \{\frac{5}{2}, 2, 2, 2\}$ is 10.3 μ_B. The corresponding χ plots show small and gradual increases as the temperature is lowered from 300 to 20 K, and then a rapid increase below that. Taken in conjunction with magnetization data, and assuming the absence of magnetic impurities, the ground

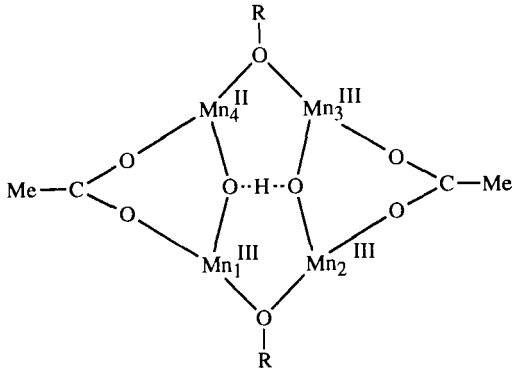

FIG. 21. Structural representation of $[Mn^{II}Mn^{III}_3(O)(OH)(O_2CCH_3)_2L^E_2]^{4-}$.

state in the Ba_2 salt is $S_T = \frac{1}{2}$, whereas that for Ca_2 appears to be higher or to have some admixture of a higher spin. ESR studies at low temperature would be useful to confirm the ground-state spin. Preliminary attempts to fit the susceptibility data have employed a three-J Heisenberg rhomboidal model. Zero-field splitting was not included. The Ba_2 data could be reproduced very well using small negative values of the parameters. However, the relative sizes of the J values probably mean that a more logical model employing four different edge J values, with diagonal interaction values assumed negligible, should be tried. These calculations are in progress. They are not trivial and need irreducible tensor operator theory of the type used in Section III,D,3,e on mixed-valent cubes, by Belinskii. The only other $Mn^{II}Mn^{III}_3$ tetramer system available for comparison, but which has quite different topology, is the butterfly complex, $(Mn_4(O)_2(O_2CPh)_7(bipy)_2]$. It shows a μ value of 8.29 μ_B at 300 K, decreasing to 5.08 μ_B at 5 K. The three parameter fit is shown in Table IV, but the model used has not been located (*113*).

We note that the single-ion spins in the present trapped-valence species are the same as those in $[Fe_4S_4]^+$ cubane clusters, the latter showing delocalization and double-exchange effects, with ground states normally of $S_T = \frac{1}{2}$, or $\frac{3}{2}$; see Section III,E.

c. Linear Tetramer. The groups of Suzuki (*129, 130*) and Armstrong (*131, 132*) have both used the heptadentate tripodal ligand, tphpn, to form pseudolinear arrays of Mn ions with core types $[Mn^{II}(\mu\text{-}RCO_2)(\mu\text{-}OR)Mn^{III}(\mu\text{-}O)Mn^{III}(\mu\text{-}OR)(\mu\text{-}RCO_2)\text{-}Mn^{II}]$ and $[Mn^{II}(\mu\text{-}OR)Mn^{III}(\mu\text{-}O)_2Mn^{IV}(\mu\text{-}OR)Mn^{II}]$. The μ-OR groups represents the alkoxy group in the tphpn backbone. Various anions were employed to isolate the crystals. In the first type, the central $Mn^{III}\cdots Mn^{III}$ separation of 3.55 Å was slightly less than the $Mn^{II}\cdots Mn^{III}$ separation of 3.70 Å, while the Mn^{III}–O–Mn^{III} angle was 180°. μ_{eff} per Mn_4 decreased linearly in the range 300–77 K from 8.7 μ_B to 8.2 μ_B, then reached 6.8 μ_B at 6 K. A vector coupling model shown in Fig. 22 was used (*129*). It effectively treats the system as a trimer, thus reducing the mathematics involved.

The best-fit parameters set was

$$g = 2.0, \qquad J_a = -45\ \text{cm}^{-1}, \qquad J_b = -6\ \text{cm}^{-1}$$

The value of J_b is typical of those found in dinuclear μ-alkoxo μ-carboxylato-bridged $Mn^{II}Mn^{III}$ species (*96, 114*), but J_a is lower than in the few known Mn^{III}–O–Mn^{III} compounds (*133*).

The $Mn^{II}Mn^{III}Mn^{III}Mn^{II}$ complexes were readily oxidized to produce

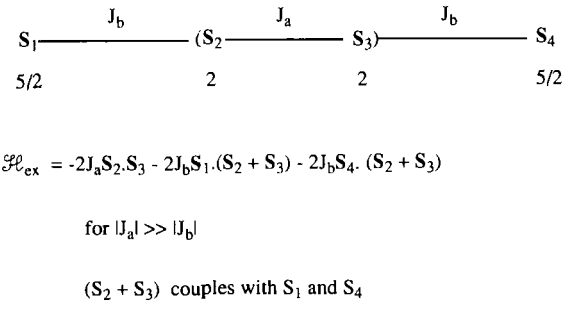

FIG. 22. Spin-coupling model used for a linear tetramer of $\{Mn^{II}Mn^{III}Mn^{III}Mn^{II}\}$ (*129*).

linear core structures containing $[Mn^{II}(\mu\text{-OR})Mn^{III}(\mu\text{-O})_2Mn^{IV}(\mu\text{-OR})\text{-}Mn^{II}]$. A $Mn^{III}\cdots Mn^{IV}$ distance of 2.72 Å and a $Mn^{II}\cdots Mn^{IV}$ distance of 3.87 Å confirmed these oxidation states. The moment of a representative complex, $[Mn_4(O)_2(tphpn)_2(H_2O)_2](ClO_4)_5 \cdot 4H_2O$, stayed constant at 8.2 μ_B between 300 and 77 K, the reduction from the uncoupled value (10.44 μ_B) indicating antiferromagnetic coupling (*130*). No fits of these limited data were presented, but if the compound were to be treated by an effective exchange model of the type used by Solomon *et al.* (*134*) for the $(Mn^{III}(O)_2Mn^{IV})_2$ system, the central $S = \frac{1}{2}$ "dimer" could couple weakly to the terminal Mn^{II} ($S = \frac{5}{2}$) ions to predict μ values of ca. 8.4 μ_B, as observed.

d. Distorted Tetrahedral $[Mn^{II}_2Mn^{III}_2(\mu_4\text{-}O)]^{8+}$ Cluster. In contrast to the planar $[Cu_4L^{13}(\mu_4OH)]^{3+}$ core formed with the $[L^{13}]^{4-}$ tetranucleating ligand (see Section III,H,4), a distorted tetrahedral arrangement was formed in $[Mn^{II}_2Mn^{III}_2(L^{13})(O)(O_2CCH_3)_3(Cl)(CH_3OH)]$ largely as a result of the bonding requirements of Mn^{II} and Mn^{III} (*100, 135*). The μ per Mn_4 value decreased from 10.24 μ_B at 300 K to 9.12 μ_B at 93 K because of weak antiferromagnetic coupling.

e. Cubane and Partial Cubane Mn^{III}, Mn^{IV} Complexes. Hendrickson (*11, 12*) has reviewed magnetic data on three complexes containing the distorted cubane core $[Mn^{IV}Mn^{III}_3(\mu_3\text{–}O)_3(\mu_3\text{–}Cl)]^{6+}$, work done in collaboration with Christou. The core structure was considered as a pyramid of four Mn ions with Mn^{IV} at the apex and the three Mn^{III} in the base, the latter bridged by the μ_3-Cl^- ions. Three μ_3-O^{2-} ions bridged the remaining faces. Peripheral ligands included carboxylates, dibenzoylmethane, imidazole or pyridine, and chlorides. A two-J model reflected this C_3 symmetry and could be solved by vector coupling: one coupling constant, J_1, appropriate to interaction between the three

basal $S = 2$ Mn^{III} centers, and the other, J_2, connecting the apical $S = \frac{3}{2}$ Mn^{IV} ion to the three basal ions. The clusters all behave similarly, showing a gradual increase in μ per Mn_4, with decreasing temperature reaching a maximum of ca. 9.5 μ_B at ca. 60 K, symptomatic of a $S_T = \frac{9}{2}$ ground-state, prior to a rapid decrease in μ as the temperature approaches 4.2 K. Variable field magnetization and variable-temperature ESR measurements confirmed the $S_T = \frac{9}{2}$ ground state. Taking $[Mn_4O_3Cl_4(O_2CCH_3)_3(py)_3]$ as a typical example (*136*), the best-fit parameter set shown below yielded spin-state energy levels such that a $S_T = \frac{7}{2}$ state was 205 cm^{-1} above the $S_T = \frac{9}{2}$ ground state. The rapid decrease in μ at very low temperatures was ascribed to a combination of ZFS of the $\frac{9}{2}$ state ($D = 0.32\ cm^{-1}$) and thermal depopulation of higher-lying Zeeman sublevels, both of which will lead to field-dependent μ vs T curves. The best fit was $g = 1.86$, $J_1(Mn^{III}\cdots Mn^{III}) = +11.3\ cm^{-1}$, $J_2(Mn^{III}\cdots Mn^{IV}) = -23.1\ cm^{-1}$. The stronger antiferromagnetic J_2 interaction dominates and frustrates the basal $Mn^{III}\cdots Mn^{III}$ interactions, so that the three Mn^{III} ions have parallel spins. Substitution of Cl^- by Br^- in the related cubane complex $[Mn_4O_3Cl(O_2CCH_3)_3$(dibenzoylmethane)$_3]$ had no effect on the J values or the ground state, which were similar to those just given (*137*). The arene-carboxylate derivatives, $[Mn_4O_3Cl_4(O_2CAr)_3(py)_3]$, behaved likewise (*138*).

Very recently, a new partial cubane core $[Mn^{IV}Mn^{III}{}_3O_3]^{7+}$ was synthesized (*139*), in the form of $(Mn_4O_3(O_2CPh)_4(dbm)_3]1.5CH_2Cl_2$, by electrolytic oxidation of the butterfly complex $[Mn_4O_2(O_2CPh)_7(dbm)_2]^-$. The crystal structure shows some similarities to the $[Mn_4O_3Cl]^{6+}$ core, but the basal plane of the Mn_4 pyramid does not have equal $Mn^{III}\cdots Mn^{III}$ distances, since a benzoate group bridges these three ions asymmetrically. The shape and magnitude of the μ/T plot is rather similar to that of the $[Mn_4O_3Cl]^{6+}$ systems but the exchange coupling used to fit it utilized three J values, appropriate to the site symmetry (C_s). The best-fit parameters were $g = 1.85$, $J(Mn^{III}\cdots Mn^{IV}) = -28.5\ cm^{-1}$, $J(Mn^{III}\cdots Mn^{III}) = +2.8\ cm^{-1}$, and $J'(Mn^{III}\cdots Mn^{III}) = +2.1\ cm^{-1}$. The corresponding ground state was again $S_T = \frac{9}{2}$. However, spin-correlation plots of the energy of the spin state vs the ratio J'/J $(Mn^{III}\cdots Mn^{IV})$ showed that the ground-state spin could change, e.g., to $\frac{5}{2}$ or $\frac{1}{2}$, if small changes were made to $J'/J(Mn^{III}\cdots Mn^{IV})$. Since J' corresponded to a unique 1,1-bridging mode between two of the Mn^{III} ions in the basal plane by one of the benzoate oxygen atoms, it was felt that substitution of this benzoate by groups such as O^{2-} or OH^- could well, in the future, yield ground states more relevant to the photosystem WOC in oxidation level S_2. The effects on the energy levels of varying the other $J(Mn^{III}\cdots Mn^{III})$ parameters were not reported.

In pursuit of suitable models and theories for the WOC manganese cluster, Noodleman and Hendrickson (*140*) have used LCAO Xα density function calculations, employing the broken symmetry method (see Section III,E,3), to calculate $J(Mn^{III}\cdots Mn^{III})$ and $J(Mn^{III}\cdots Mn^{IV})$ values in the chloro–oxo cubane $[Mn^{IV}Mn^{III}_3O_3Cl_7(O_2CCH_3)_3]^{3-}$. The μ/T behavior of this complex was different in detail from the others described earlier, and good agreement with μ_{obs} was obtained using the Xα calculations, with parameter values of $g = 2.02$, $J(Mn^{III}\cdots Mn^{III}) = +19.3\ cm^{-1}$, $J(Mn^{III}\cdots Mn^{IV}) = -46.6\ cm^{-1}$, and $S_T = \frac{9}{2}$.

These J values are bigger than the others quoted. Ligand spin-polarization effects were felt to be important both in regard to which ground state is stabilized and in regard to the spin-coupling mechanism.

In a very detailed theoretical paper, dealing with $[Mn^{IV}Mn^{III}_3]$ and $[Mn^{IV}_3Mn^{III}]$ clusters, Belinskii (*140a*) has recently addressed the question of which Heisenberg coupling models are most appropriate to the electronic and ESR properties of the S_2 center of photosystem II, in much the same way that he has approached the ferredoxin $[Fe_4S_4]^{z+}$ cluster problems; see Section III,E,3. Generalized solutions of the exchange problem were achieved when using two different Hamiltonians, one having fixed intermediate spins, S_{12}, and mixing of states with different $\mathbf{S}_{34}$ (N.B. $\mathbf{S}_{12} = \mathbf{S}_1 + \mathbf{S}_2$, $\mathbf{S}_{34} = \mathbf{S}_3 + \mathbf{S}_4$, $\mathbf{S} = \mathbf{S}_{12} + \mathbf{S}_{34}$). The other model involved mixing of spin states with different intermediate spins, S_{12}, for fixed S and S_{34}. It was possible to obtain analytical Kambe (*41*) solutions for energies of the biologically important $S = \frac{1}{2}$ states. ITO methods were used for solution of the completely general six-J Hamiltonian (appropriate to the $S = \frac{1}{2}$ ground state) and a large variety of four-Mn topologies were considered. Mixing in of $S_{34} = \frac{1}{2}$ and $\frac{3}{2}$ states was found to be important in clusters having low symmetry.

f. Pair-of-Dimer Mn^{III}, Mn^{IV} Complexes. Two structurally related complexes containing pairs of di(μ-oxo) manganese(III) manganese(IV) dimers have recently been studied in detail by Armstrong, Solomon *et al.* (*134*) and Kusunoki, Suzuki *et al.* (*141*). Both research groups used heptadentate ligands which contained tripodal dipyridylmethylamine end groups attached to a 2-hydroxypropanediamine backbone in the case of the Armstrong group (tphpn), and to the longer 3-hydroxypentanediamine backbone in the case of the Suzuki group (tmdp). These ligands tethered the binuclear $Mn^{III}(O)_2Mn^{IV}$ moieties together, but not quite in the same fashion. The tmdp complex is shown in Fig. 23. The interdimer distances were much longer than the intradimer distance, the latter typically being ca. 2.6 Å. The room temperature μ (per Mn_4) value of the tmdp complex, 3.5 μ_B, was lower than that for the tphpn

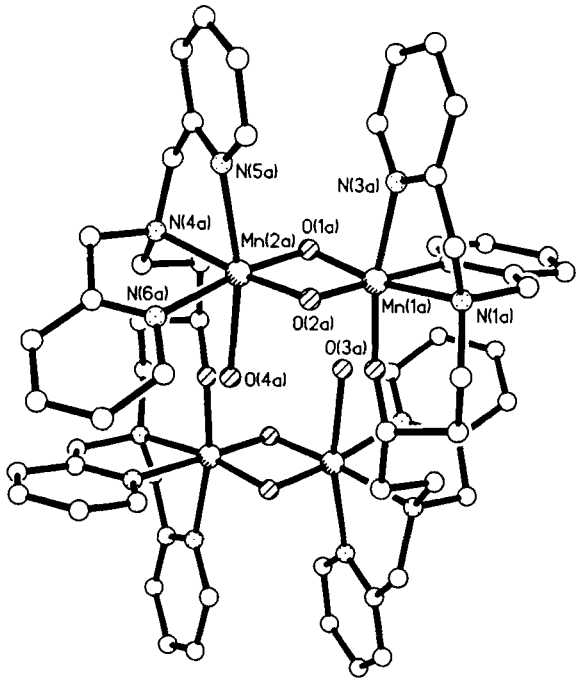

FIG. 23. The structure of one of the crystallographically independent cations in $[\{Mn_2(O)_2(tmdp) \cdot (H_2O)\}_2](CF_3SO_3)_4 \cdot 6H_2O$ (*141*).

complex, 4.05 μ_B, indicative of stronger antiferromagnetic coupling. The μ values decreased gradually with decreasing temperatures in both systems, reaching plateau values of ca. 2.8 μ_B below ca. 100 K, indicative of a spin = 1 ground state. The tphpn complex then showed a small increase to a maximum in μ at ca. 15 K following a rapid decrease from 2.85 to 2.68 μ_B below 10 K. In contrast, the tmdp complex showed a small increase in μ below 14 K.

An isotropic exchange Hamiltonian was employed appropriate to the rectangular disposition of the four Mn atoms, as in Eq. (16) and Fig. 24. ITO calculations were required.

$$\mathcal{H}_{ex} = -2J_1(\mathbf{S}_1 \cdot \mathbf{S}_2 + \mathbf{S}_3 \cdot \mathbf{S}_4) - 2J_2(\mathbf{S}_1 \cdot \mathbf{S}_4 + \mathbf{S}_2 \cdot \mathbf{S}_3) \qquad (16)$$

J_1 corresponds to the short $Mn^{III} \cdots Mn^{IV}$ sides, while J_2 corresponds to the long $Mn^{III} \cdots Mn^{IV}$ sides. The best-fit values of exchange parameters were:

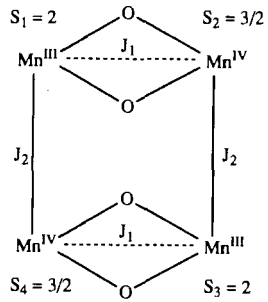

FIG. 24. Spin-coupling model used for pair-of-$Mn^{III}(O)_2Mn^{IV}$ dimers (*134, 141*).

$[(Mn_2O_2)_2(tphpn)_2]^{4+}$ $g = 2.01$ $J_1 = -101.1\ cm^{-1}$ $J_2 = -8.4\ cm^{-1}$

$[(Mn_2O_2)(H_2O)_2(tmdp)_2]^{4+}$ $g = 2.00$ $J_1 = -145.4\ cm^{-1}$ $J_2 = -0.19\ cm^{-1}$

$$\chi(\text{TIP}) = 0.0033\ cm^3\ mole^{-1}$$

The magnitude of J_1, in the tmdp case, is typical of that expected for di(μ-oxo) $Mn^{III}Mn^{IV}$ moieties (*136*), while it is much less in the tphpn case, possibly because of the larger J_2 value, the latter appropriate to the $Mn^{III}(\mu\text{-OR})Mn^{IV}$ bridges. J_2 is very small in the tmdp complex because the dimers are bridged by H-bonded water interactions, as shown in Fig. 23. Spin-state ladders were presented in both studies, although with some disagreements in the values of the energies calculated in terms of J_1 and J_2. Use of the best-fit J values gave separation between the ground $S_T = 1$ and first excited $S_T = 0$ state ($= 8J_2$) of 67 cm^{-1} (tphpn) and 1.52 cm^{-1} (tmdp).

Low-temperature isothermal magnetization data (2–10 K; 0–5.5 T) proved to be very useful in determining splitting of the $S_T = 1$ ground state in the tphpn complex (*134*). In this study, an alternative "effective exchange" formalism was developed between the two strongly antiferromagnetically coupled $Mn^{III}O_2Mn^{IV}$ units, each unit having $S_a = S_b = \frac{1}{2}$, and with a singlet–triplet separation of 2 J'. Use of spatial averaging calculations of χ, in terms of the thermodynamic susceptibility expression of Eq. (12), gave good fits to the magnetization plots and to the μ vs T (2–40 K) data. Anisotropy in J' was invoked to explain ZFS of the $S = 1$ ground state, thus yielding $2J' = +77.7\ cm^{-1}$ (effectively ferromagnetic!), $D' = +1.8\ cm^{-1}$, $E' = -0.15\ cm^{-1}$. An alternative explanation, that the decrease in μ at observed low temperature was due to intermolecular tetramer–tetramer interactions, was thought to be less likely than the ZFS explanation, partly becuase it gave a worse

fit and it did not explain a $g_{eff} \sim 6$ parallel polarization ESR resonance. Magnetization data would also have been useful to obtain in the tmdp case, particularly in view of the deduced spin-state separation of a few wavenumbers. Both groups gave detailed explanations for possible origins of ZFS of the ground state. An interdimer pseudo-dipolar coupling of 0.3 cm^{-1}, originating from mixing of excited-state ZFS split triplet states into the ground state, was proposed in the tphpn case. Kusunoki *et al.* (*141*) disagreed with this proposal and used tensor operator techniques and perturbation theory to suggest that ZFS originated from crystal-field effects on the two Mn^{III} ions which caused mixing of excited spin states into the ground $S = 0$ state, via the J_2 interaction. This research group obtained ZFS parameters for the tmdp complex, of $|D| = 0.07\ cm^{-1}$ and $|E| = 0.023\ cm^{-1}$, by means of simulation of the observed $\Delta M = 1$ and $\Delta M = 2$ ("forbidden") ESR lines, determined at 13 K. The relevance of the electronic structures of these $Mn^{III}O_2Mn^{IV}$-dimer compounds to the biomodeling of the "S_1" oxidation level of the Mn WOC was discussed in detail by Armstrong and Solomon and co-workers (*134*).

4. Manganese(IV)

a. Chain Structure in $[Mn^{IV}_4O_6]^{4+}$. This new type of cationic Mn-oxo cluster, $[Mn^{IV}_4O_6bipy_6](ClO_4)_4 \cdot H_2O$, formed by condensing Mnbipy-$Cl_3 \cdot H_2O$ in water at pH 2, is made up of two di-μ-oxo dimanganese(IV) units linked by a di-μ-oxo bridge (Fig. 25). Girerd *et al.* (*142*) have proposed that it is a reasonable model for the S_3 oxidation level of the WOC in photosystem II, and that its one-electron reduced product is a close model to the $Mn^{III}Mn^{IV}_3$ level S_2. It also bears similarities to

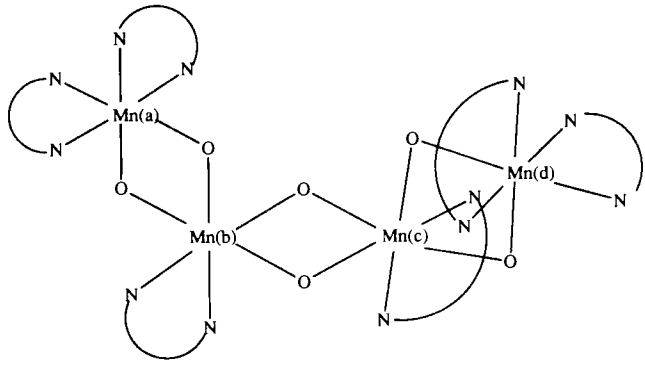

FIG. 25. Structural representation of the "linear" complex $[Mn_4O_6bipy_6]^{4+}$ (*142*).

the chain structural model for the WOC, proposed recently by Klein *et al.* (*143*) and highlighted by Wieghardt (*21*).

$$\mathcal{H}_{ex} = -2J_{ab}\mathbf{S}_a \cdot \mathbf{S}_b - 2J_{bc}\mathbf{S}_b \cdot \mathbf{S}_c - 2J_{cd}\mathbf{S}_c \cdot \mathbf{S}_d \qquad (17)$$

The eigenvalues of the exchange Hamiltonian given in Eq. (17) were calculated by diagonalizing the full spin problem using matrices built with 6*j* coefficients and irreducible tensor operator theory. Terms such as $\mathbf{S}_a \cdot \mathbf{S}_c$ were ignored. Van Vleck's equation was used to calculate μ. The observed values of μ per Mn_4 decrease linearly with temperature from 3.86 μ_B at 294 K to 0.17 μ_B at 12 K, indicative of medium-strength antiferromagnetic coupling and a $S_T = 0$ ground state. The best fit required two J values, one being twice the size of the other: $g = 2.0$; $J_{ab} = J_{cd} = -88$ cm^{-1}; $J_{bc} = -134$ cm^{-1}. The energy levels derived from these parameters showed that a $S_T = 1$ state was 76.1 cm^{-1} above the ground $S_T = 0$ state, and ESR lines from this triplet state were observed at 140 K. Girerd *et al.* (*142*) made spin-coupling calculations on chain and ring adaptations of Klein's WOC model in order to try and define structural requirements compatible with the nature of the ground state. They noted that good magnetization data are needed on the S_2 center of the WOC.

b. Adamantane Structure $[Mn^{IV}_4O_6]^{4+}$. Wieghardt and co-workers (*96, 144*) have shown that the facially coordinating tridentate ligand tacn forms a rich array of Mn compounds, including $[tacn_4Mn^{IV}_4O_6]Br_4 \cdot 5.5H_2O$, in which the four Mn^{IV} ions, within an adamantane skeleton, are tetrahedrally disposed with respect to each other and 3.2 Å apart. The room temperature μ per Mn_4 of 8.54 μ_B increases gradually with decreasing temperature, reaching a maximum of 9.62 μ_B at 84.9 K before decreasing to 9.34 μ_B at 7.5 K. No fitting was attempted, even using a single $J(T_d)$ model, but it was noted that the apparent ferromagnetic coupling did not yield a $S_T = 6$ ground-state value (12.97 μ_B) at the maximum. Armstrong *et al.* (*145*) found similar magnetic behavior for the ClO_4^- salt of $[Mn_4O_6tacn_4]^{4+}$ and obtained a fit using the T_d model $\Sigma_{i>j} - 2J_{ij}\mathbf{S}_i \cdot \mathbf{S}_j$ for $S = \frac{3}{2}$, of $J = +6.9$ cm^{-1}. Inclusion of a second-order term, $j = +3.9$ cm^{-1}, improved the fit. Interestingly, upon protonation, the $[Mn_4O_5(OH)(tacn)_4]^{5+}$ cluster is formed reversibly and has C_{2v} symmetry. This oxo-hydroxo cluster displays antiferromagnetic coupling, having μ (per Mn_4) of 6.62 μ_B at 280 K. Use of a three-J value model yielded a fit with $J_{12} = -22.5$ cm^{-1}, $J_{34} = -1.35$ cm^{-1}, $J_{23}(=J_{24} = J_{13} = J_{14}) = -6.5$ cm^{-1}. It was

proposed that differences noted in the susceptibilities of the S_1 and S_2 WOC states of photosystem II might also involve a related effect, due to bridge protonation rather than to structural differences (*145*).

E. IRON

Polynuclear clusters containing iron have been, and are being, researched actively from a number of bioinorganic perspectives. Synthetic iron–oxo and iron–sulfur clusters are of particular importance in regard to the modelling of nonheme proteins of, respectively, the hemerythrin (and related) types and the ferredoxin types. Hemerythrin is an oxygen-binding example of a growing class of iron–oxo proteins, other members of which display a diverse range of biological activities, but all of which show characteristic antiferromagnetic coupling via μ-oxo (hydroxo) μ-carboxylato bridging interactions, at least in the $Fe^{III}\cdots Fe^{III}$ state (*2, 6, 9, 146–153*). Ferredoxins are now known to possess μ-sulfido bridged cluster cores containing two, three, four, or eight iron atoms, and all display exchange coupling effects (*10, 13, 154–156*). A full understanding of the magnetic and spectral properties of the higher Fe_xS_x aggregates, particularly the mixed-valency species, has faced considerable theoretical challenges in view of effects such as electron delocalization (nontrapped valence states) and double exchange (*10, 13*). An up-to-date brief survey of Fe_4S_4 clusters is given in Section III,E,3. Iron–sulfur clusters, including the unusual P-cluster pairs, have recently been well characterized in the crystal structures of the iron and iron–molybdenum proteins of nitrogenase (*14, 155*).

Oxo/hydroxo bridged iron clusters containing four, six, eight, and much higher (e.g., Fe_{19}) numbers of iron atoms have also been studied in relation to their use in modeling biomineralization phenomena and the iron storage protein ferritin (*149, 157, 158*). These "high nuclearity spin" clusters of iron are also proving to be archetypal building blocks in attempts to make new molecular magnetic materials capable of displaying novel magnetic phenomena (*4, 23–26, 57, 159, 160*). The synthetic chemist's role in preparing and characterizing polyiron cluster species is one which primarily involves new and controlled methods of solubilizing notoriously insoluble iron oxide/ hydroxide phases (rust) (*159, 160*). The properties of tetranuclear iron–oxo (*149*) and iron–sulfur clusters (*10, 13, 154, 161*), in particular, have recently been reviewed. Only new data and salient features of magnetic exchange properties which fit into the present Heisenberg-type coupling survey will be given here.

1. *Iron(II): Cubanes of* Fe_4^{II} *and* Fe_3^{II}/Fe^{III} *with Alkoxo Ligands*

The iron atoms in the $[Fe_4^{II}(OCH_3)_4]^{4+}$ core of $[Fe_4^{II}(OCH_3)_4(CH_3OH)_4(dpm)]$ are weakly ferromagnetically exchange-coupled with a coupling constant $J = +0.94\ cm^{-1}$ and $g = 2.29$ (*61*). This is reflected in the plot of μ vs temperature in which μ (per Fe_4) varies from 11.5 μ_B at 300 K to a maximum of 15.76 μ_B at 5 K, and then decreases slightly. The maximum was less than the $S_T = 8$ value of 16.97 μ_B, and this was thought to be due to zero-field splitting effects. A one-J Heisenberg model assuming T_d symmetry was employed in the fit, but this could not reproduce the data below 30 K. Since the data in this low-temperature region were obtained in a field of only 0.05 T, it is unlikely that the maximum is simply due to thermal depopulation of Zeeman sublevels for $S_T = 8$ (and 7) states, the splitting of which depends on field. Isothermal magnetization data at 1.2 K confirmed that ZFS of the $S_T = 8$ state occurred, and the parameters $D = 3\ cm^{-1}$, $E = 0.22\ cm^{-1}$, $g = 2.2$ were deduced. It should be noted that the preceding treatment assumed no orbital degeneracy of the formally $^5T_{2g}$ iron(II) centers.

In contrast to the ferromagnetism of the Fe^{II} cube, the valence-trapped compound $[Fe^{III}Fe_3^{II}(OCH_3)_4]^{5+}$ showed antiferromagnetic coupling. A two-J Heisenberg Hamiltonian of the form shown in Eq. (18), similar to that employed by Hendrickson *et al.* (*11*, *12*) for Mn cubanes, was employed, where J_1 is the $Fe^{II}\cdots Fe^{II}$ and J_2 is the $Fe^{II}\cdots Fe^{III}$ interaction.

$$\mathcal{H} = -2J_1(\mathbf{S}_1\cdot\mathbf{S}_2 + \mathbf{S}_1\cdot\mathbf{S}_3 + \mathbf{S}_2\cdot\mathbf{S}_3) - 2J_2(\mathbf{S}_A\cdot\mathbf{S}_4)$$

$$\mathbf{S}_A = \mathbf{S}_1 + \mathbf{S}_2 + \mathbf{S}_3; \qquad \mathbf{S}_T = \mathbf{S}_A + \mathbf{S}_4$$

$$E(S_A, S_T) = -J_1[S_A(S_A+1)] - J_2[S_T(S_T+1) - S_A(S_A+1)] \quad (18)$$

The best fit to the data yielded $g_{Fe(II)} = g_{Fe(III)} = 2.18$, $J_1 = -1.3\ cm^{-1}$, $J_2 = -0.81\ cm^{-1}$. These parameters are compatible with a $S_T = \frac{1}{2}$ ground state and $S_T = \frac{3}{2}$ only 0.51 cm^{-1} above it. Five other states are within 10 cm^{-1}. Magnetization data at 1.2 K were not fitted, but would require use of the thermodynamic equation for M on account of Zeeman-level mixing and depopulation effects.

2. *Iron(III): Iron–Oxo Ligand Systems*

As indicated earlier, Lippard reviewed the structural aspects of tetranuclear oxo-iron(III) complexes up to the period of early 1988 (*149*). Magnetochemical details will be summarized here and some emphasis

given to post-1988 work. Mössbauer spectral measurements have also proven to be extremely valuable as a complementary technique used to probe the ground-state and ligand-field effects in these cluster complexes (*6, 147, 148*). Spin-frustration effects in iron clusters have been reviewed by Hendrickson (*11, 12*).

a. Butterfly Structure $[Fe_4^{III}O_2]^{8+}$. Magnetic susceptibility and Mössbauer spectral data reveal a diamagnetic, spin-zero ground state consistent with antiferromagnetic coupling of the $S = \frac{5}{2}$ Fe^{III} centers via the μ-oxo bridges. In a detailed magnetic analysis, Hendrickson and Christou *et al.* (*162*) note that planar and nonplanar (butterfly) $Fe_4(\mu_3\text{-}O)_2$ core structures are now known among the $[Fe_4O_2]^{8+}$ examples. In the nonplanar example, $[Fe_4O_2(O_2CCH_3)_7bipy_2](ClO_4)$, the dissimilar environments around wingtip and body Fe atoms give rise to the observation of two Mössbauer doublets. Taking this complex as a typical example, the moment per Fe_4 decreases gradually from 4.2 μ_B at 277 K to 0.82 μ_B at 5 K as anticipated for a $S_T = 0$ ground-state system. Application of the coupling model for butterfly clusters, already given for Cr^{III} and Mn^{III} analogues, but with $S_i = \frac{5}{2}$, afforded best-fit parameter values given in Table V. It should be noted that the body–body J_{13} value was indeterminate, but probably more positive than -15 cm^{-1}. This is because J_{13} affects only the high-lying spin states which are not populated at 300 K—a situation somewhat akin to the population of the $S_T = 0$ and $S_T = 1$ states only, in Fe_2 μ-oxo iron(III) dimers (*146, 147*). The size of J_{12} was similar to that in trinuclear Fe_3O species (*78*), two of which can be regarded as sharing an edge in the Fe_4O_2 core. Correlation of J_{12} with Fe–O distances, by means of Gorun and Lippard ideas (*163*), proved to be reasonable. J_{12}

TABLE V

BEST-FIT PARAMETERS FOR $[Fe^{III}_4(\mu\text{-}O)_2]^{8+}$ BUTTERFLY CLUSTERS[a]

Cluster	J_{12}	J_{13}	g	χ_{TIP} (cm^3 mol^{-1})	Ref.
$[Fe_4O_2(O_2CCH_3)_7(bipy)_2](ClO_4)$	−45	*b*	2.0	0.0080	*162*
$(Et_4N)[Fe_4O_2(O_2CPh)_7(H_2Bpz_2)_2]$	−42	*b*	2.0	0.0080	*165*
$[Fe_4O_2(O_2CCH_3)_3(salox)_2L_2](ClO_4)$	−47	*b*	2.0	0.0063	*164*

[a] $J_{12} \equiv$ wingtip–body; $J_{13} \equiv$ body–body interactions; values in cm^{-1}. bipy = bipyridine; $[H_2Bpz_2]^-$ = dihydrodipyrazoloborate; $salox^{2-}$ = salicylaldoximate; L = 1,4,7-trimethyl-1,4,7-triazacyclonane.

[b] Indeterminate.

is also essentially independent of the nature of the terminal and other bridging ligands in these compounds, and thus is dominated by the oxo bridging within the Fe_4O_2 core. Hendrickson has pointed out some interesting features of spin frustration in these clusters (*11, 12, 162*). The strong antiferromagnetic wingtip-to-body interaction gives rise to a frustration of the body spins, as shown in Fig. 26.

Energetically, the most stable of the six possible $S_T = 0$ states comes about when S_{13} and S_{24} both have their maximum values of 5. The next higher states $S_T = 1$ (ca. 90 cm^{-1}) and $S_T = 2$ (ca. 280 cm^{-1}) also derive from the coupling of S_{13} and S_{24}. In a subsequent detailed report on the butterfly cluster $[Fe_4O_2(O_2CCH_3)_3(salox)_2L_2](ClO_4)$, where L is the triazacyclononane macrocycle, Chaudhuri and Haase and co-workers (*164*) came to conclusions very similar to those described for the bipy and $[H_2Bpz_2]^-$ compounds, the latter characterized earlier by Lippard and co-workers (*149, 165*).

b. Pair-of-Dimer Complexes. The early 1980s saw a great rebirth in the design and synthesis of hemerythrin model compounds, employing the biologically relevant $\{Fe^{III}(\mu\text{-}O)(\mu\text{-}O_2CR)_2Fe^{III}\}$ cores rather than the earlier studied $Fe^{III}(\mu\text{-}O)Fe^{III}$ species. Toftlund *et al.* (*166*) attempted to perturb the tri-bridged dinuclear core by employing alkane "strapped" di-tripodal ligands of the tptn type (see Fig. 27 and Mn^{III} analogue). This strategy was meant to produce the dinuclear core with the strap joining, but not bonded to, the two Fe centers, in a manner somewhat akin to the effect of a peptide chain. A tetranuclear compound was in fact obtained in which two such straps joined two $Fe(\mu\text{-}O)(\mu\text{-}O_2CCH_3)_2Fe$ moieties. This was largely as a result of the steric effect of the tripodal N atoms being *trans* to the μ-O bridging oxygens (Fig. 27), thus not allowing tptn to bind intramolecularly across a dimer. A number of similar pair-of-dimer compounds were subsequently reported by the groups of Sessler (*167–169*), Nishida (*123*), and Hodgson (*170*). All of these compounds show structural,

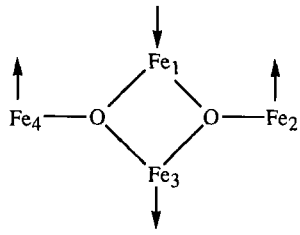

FIG. 26. Spin structure in Fe_4O_2 core (*11, 12*).

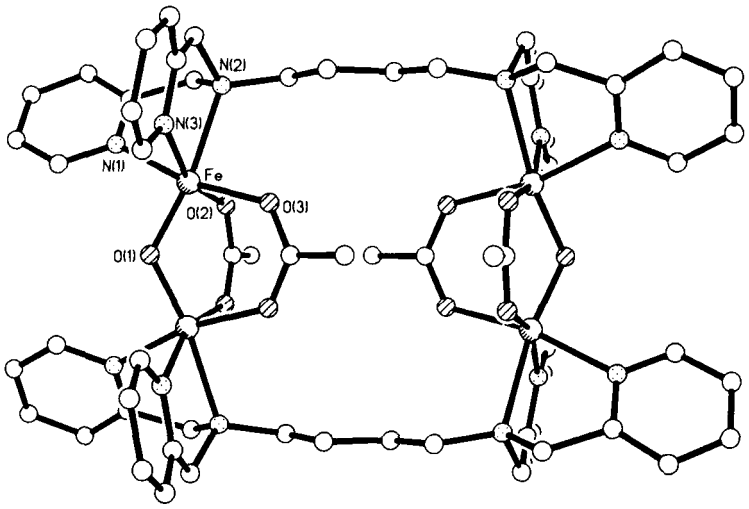

FIG. 27. Structure of $[Fe_2O(OAc)_2tpbn]_2^{2+}$ (*166*).

spectral, and magnetic properties typical of those of dinuclear hemerythrin model compounds (*147–149*). In particular, there is no dimer···dimer exchange coupling, and the compounds behave as two noninteracting antiferromagnetically coupled dimers. The J values are all ca. -120 cm^{-1} and $g \sim 2.0$, while μ (per Fe_4) decreases from ca. 3.2 μ_B to ca. 0.6 μ_B between 300 and 5 K.

Dimer···dimer coupling was evident, however, in a tetranuclear complex which contains oxo, alkoxo, and carbonato bridging groups, viz., $Na_6[Fe_4(O)_2(CO_3)_2L_2^E]$ ca. $2H_2O$, where $(L^E)^{5-}$ = 1,3-diamino-2-hydroxypropane-*N*,*N*,*N*′,*N*′-tetraacetate (Fig. 18) (*171*). The structure is reminiscent of the mixed-valent manganese complexes of this ligand shown in Fig. 21, insofar as it also has two μ-oxo groups some 2.4 Å apart, perhaps hydrogen-bonded to a central proton, the $Fe–O_{\mu\text{-oxo}}$ distances being longer than normal. The *trans*-alkoxo and *trans*-carbonato groups bridge the peripheral position around the rectangular Fe_4 core in a much more direct fashion than was the case in the pair-of-dimers described earlier. μ (per Fe_4) decreases from 4.96 μ_B at 260 K to 0.74 μ_B at 10 K. The complex was viewed as two strongly coupled Fe(μ-O)(μ-CO_3)Fe units, with coupling constant J (= -63.4 cm^{-1}), weakly coupled together by longer Fe(μ-OR)Fe bridges, the latter having coupling constant zJ' (= -11.2 cm^{-1}). A molecular-field approach was employed to fit the data. It incorporated zJ' in a $(T - \theta)$ term of the

denominator of a $S = \frac{5}{2}$ dimer susceptibility equation. A χ(TIP) term of 0.008 cm^3 $mole^{-1}$ was added to this equation. A more desirable approach would have been to attempt matrix-diagonalization/tensor-operator methods for a Heisenberg Hamiltonian appropriate to a rectangle of $S = \frac{5}{2}$ centers in which two different "edge" J and one "diagonal" J interaction occurred. However, this is a formidable problem and would require programs of the type developed by Gatteschi *et al.* (*26*).

The same kind of molecular field approach was subsequently employed by Jameson and Que *et al.* (*172*) in a study of a related, but not identical, tetranuclear complex $[Fe_4(O)_2(O_2CPh)_2L'_2](ClO_4)_2(tos)_2$, where L′ is the ligand first used by McKee *et al.* (*173*) in Cu(II) (and Fe(III)) bioinorganic model studies and contains benzimidazole pendant arms, viz. (L′) = 1,3-diamino-2-hydroxypropane-*N*,*N*,*N*′,*N*′-tetrakis-benzimidazole. This complex was slightly more strongly coupled than the $[Fe_4(O_2)(CO_3)_2L^E_2]^{6-}$ complex, as judged by a μ (per Fe_4) value at 295 K of 3.4 μ_B, the χ vs T curve being similar in shape. The limitation of the molecular field approach, and the need for a full four-spin treatment, was recognized when it was found that zJ' ($= -107$ cm^{-1}) was bigger than J ($= -83$ cm^{-1}), with χ(TIP) = 0.0068 cm^3 mol^{-1} (*172*).

c. Distorted Adamantane Cores. Three examples have been synthesized by hydrolysis of dinuclear precursors. The first, by Que *et al.* (*174*) contains the core $[Fe^{III}_4(\mu_2\text{-}OR)_2(\mu\text{-}OH)_2(\mu_2\text{-}O)_2]^{4+}$, the OR group representing the backbone of an *N*,*N*′-2-hydroxy-5-methyl-1,3-xylylene-bis(N-carboxymethyl)glycine binucleating ligand. The compound showed strong antiferromagnetic coupling between the $S = \frac{5}{2}$ centers, since μ (per Fe_4) was 3.48 μ_B at 295 K, much less than the uncoupled value of 11.83 μ_B. The second, by Wieghardt *et al.* (*175*) contains the $[Fe^{III}_4(\mu_2\text{-}O)_2(\mu_2\text{-}OH)_4]^{4+}$ adamantane core in which a facially coordinating ligand 1,4,7-triazacyclononane caps each Fe octahedron, and I^- acts as anion. χ (per Fe_4) remained at a constant value of 0.006 cm^3mol^{-1} between 300 and 100 K, then decreased a little before increasing because of the effects of monomer impurity. The μ values decreased correspondingly from 3.84 μ_B to 0.70 μ_B (at 2.1 K). It was recognized that a distorted tetrahedron of four high-spin Fe^{III} atoms, with two different types of bridging ligand, would reduce a six-J Heisenberg (T_d) Hamiltonian to a two-J model. One of the constants would be appropriate to coupling across the two μ-oxo bridged edges (i.e., J), and one to coupling across the four μ-hydroxo edges and diagonals (J'). Once more, since $J \gg J'$ for such bridges, the molecular-field approach described earlier was employed, the complex thus being regarded as a dimer-of-dimers. It was found that $g = 2.06$, $J = -106.3$ cm^{-1}, $J' = -15.1$ cm^{-1}, and

%($S = \frac{5}{2}$) monomer = 6.4. The third example, by Sessler *et al.* (175a) was formed from a covalently-linked double-tacn ligand, 1,3-bis(1,4,7-triaza-1-cyclononyl)-2-hydroxypropane. Its $Fe_4^{III}O_6$ core contained oxygen bridges from two oxo, two hydroxo and two alkoxo (ligand) groups. The susceptibility data were fitted very well to a model appropriate to a pair-of-non-interacting μ-oxoiron (III) dimers, and a typical value of J of -93 cm^{-1} was deduced.

d. Other Fe O-donor Tetranuclear Species. An interesting "metallocrown" core, consisting of an [Fe–N–O]$_3$ ring capped by another Fe atom 1.18 Å above, has been obtained by Pecoraro *et al.* (*176*) in the form of $Fe^{III}[Fe^{III}(salicylhydroximate)(CH_3OH)(O_2CCH_3)]_3$. The ring Fe···Fe distances were 4.84 Å, and ring-to-cap Fe···Fe distances were 3.42 Å, the latter involving bridging acetate and bridging O-oximate groups. A combination of χ vs temperature and magnetization measurements, in fields of 0 to 1.5 tesla at 4.2 K, apparently suggested a $S_T = 5$ ground state for this cluster. Application of Heisenberg exchange theory to the pyramidal arrangement of $S = \frac{5}{2}$ centers yielded J_1 (cap-to-ring Fe) = -4.92 cm^{-1}, J_2 (cap-to-ring Fe) = -0.47 cm^{-1}, $g = 2.0$. An intermolecular constant zJ' of -0.16 cm^{-1} was also required to fit the data (the data were not given).

In the absence of crystal structure data, and on the basis of 77–300 K susceptibility data, planar rhomboidal structures were postulated for the following alkoxo–iron (III) species (*177, 178*). Further work is warranted, as was the case for the V^{III} and Cr^{III} analogues described earlier. Mixed alkoxo-β-diketonato species could prove to be more tractable.

$Fe_4Cl_6(OCH_3)_6 \cdot 4CH_3OH$:	$J_A = -9.1$ cm^{-1}	$J_B = -7.7$ cm^{-1}	$J_C = -0.7$ cm^{-1}
$Fe_4Br_6(OCH_3)_6 \cdot 4CH_3OH$:	$J_A = -7.7$ cm^{-1}	$J_B = -3.5$ cm^{-1}	$J_C = 0$ cm^{-1}
$Fe_4(O_2CCH_3)_4 \cdot (OCH_3)_8$:	$J_A = -3.7$ cm^{-1}	$J_B = -3.0$ cm^{-1}	$J_C = -3.0$ cm^{-1}

Cubane or adamantane structures were postulated (*179*) for compounds of stoichiometry $Fe_4X_3(OCH_3)_9$, the fits of magnetic data to a T_d Heisenberg model yielding $J = -10.5$ cm^{-1} (Cl^-) and -9.5 cm^{-1} (Br^-).

3. *Iron–Sulfur Tetranuclear Clusters*

This is an enormous and important topic in bioinorganic chemistry, biophysics, and enzymology, but space allows only a short summary of aspects of magnetism to be given here, one which certainly does not aim to be comprehensive. Volume 38 in this series, published in 1992 in honor of the contribution to ferredoxin biochemistry by H. Beinert, contains a number of authoritative reviews on iron–sulfur proteins,

enzymes, models, structures, electrochemistry, spectra, and theory of spin coupling (*13*). Worthy of mention in the present context is an up-to-date survey by Holm (*180*) on his brilliant synthetic model chemistry with emphasis on subsite-differentiated cubane clusters, Fe_3S_4 cuboidal clusters, and heterometallic MFe_3S_4 cubane clusters [see also a recent related review (*161*)]. In his unique style, Hagen (*181*) has given a very good survey of the ESR spectra of Fe–S proteins, including discussions of exchange coupling, spin ladders, double-exchange effects appropriate to valence delocalization, and integer-spin ESR. Meyer *et al.* (*182*) have summarized the magnetic properties of Fe_4S_4 and Fe_4Se_4 models and proteins with emphasis on ground spin-state variability in $[Fe_4S(e)_4]^+$ clusters, including those in nitrogenase and hydrogenase enzymes.

Noodleman and Case then give a most lucid account of the quantum mechanics and biophysics needed to understand the bonding, electronic structure, spin polarization, and spin coupling in Fe–S clusters (*10*). The mathematics of density-functional theory and broken symmetry methods are given and compared to ab initio methods. Xα-LCAO calculations of energy levels in various spin-coupled configuration of Fe_2S_2, Fe_3S_4, and Fe_4S_4 clusters are presented and related to spin coupling parameters. Particularly important (and challenging!) to "qualitative" magnetochemists such as the present author are discussions on "resonance delocalization" or "double-exchange," which, together with possible contributions from direct exchange, superexchange, and ligand-spin polarization, often adds to the Heisenberg exchange coupling in mixed-valence systems such as $[Fe_3S_4]$ or $[Fe_4S_4]^{1+,2+,3+}$ clusters. In the case of $[Fe_4S_4]$ clusters, calculations were made on models of $[Fe_4S_4(SEt)_4]^{3-,2-,1-}$, using symmetry C_{2v}, after symmetry breaking. We take $[Fe_4S_4]^{2+}$ as an example, assuming it is made up of two Fe^{III}–Fe^{II} pairs (i.e., $Fe^{2.5+}$–$Fe^{2.5+}$), the pairs having spin S_{12} and S_{34}. The energies of the pure spin states obtained by solving the spin Hamiltonian [N.B. The $J\mathbf{S}_1 \cdot \mathbf{S}_2$ convention is used here (*10*)] are given in Eq. (19).

$$E(S) = (J/2)S(S + 1) \pm B(S_{34} + \tfrac{1}{2}) \pm B(S_{12} + \tfrac{1}{2}) \qquad (19)$$

Here, S is the total spin quantum number. The first term is the Heisenberg coupling energy, and the other two terms represent the resonant delocalization (double-exchange) energy of the $Fe^{II}Fe^{III}$ pairs, with parameter B.

Experimental susceptibility and magnetization data were provided by Jordanov *et al.* (*183*) on a 3+ example, $[Fe_4S_4(SR)_4]^-$, where R = 2,4,6,-*i*Pr_3–C_6H_2. The data showed a Curie–Weiss behavior of χ below 15 K, appropriate to an $S_T = \frac{1}{2}$ ground state, with deviations from

linearity above 15 K due to thermal population of $S > \frac{1}{2}$ coupled states, μ (per Fe_4) correspondingly increased from 1.7 μ_B at 5 K to 3.15 μ_B at 300 K, with a slight plateau of ca. 2.0 μ_B near 60 K. Comparison of the fits obtained using a Heisenberg-only model and the Heisenberg plus double-exchange model were made. In the latter, one site of the Fe^{III}–Fe^{III} pair (β) is linked to one site of the Fe^{II}–Fe^{III} pair (α) by the coupling constant J, while the β and α couplings are $J_{12} = J + \Delta J_{12}$ and $J_{34} = J + \Delta J_{34}$, respectively (Fig. 28). ΔJ_{34} was set to zero, and $\Delta J_{12} > 0$ (i.e., antiferromagnetic). In the 3–320 K region, use of a single g value of 2.0 gave the following three-parameter fit of antiferromagnetic coupling constants:

$J = 571\ cm^{-1}$ (i.e., $J = -285\ cm^{-1}$), $B = 598\ cm^{-1}$, $\Delta J_{12} = 144\ cm^{-1}$,

which yield

$B/J = 1.04$, $\Delta J_{12}/J = 0.25$, $J(Fe^{III}\cdots Fe^{III}) = 715\ cm^{-1}$, $J(Fe^{III}\cdots Fe^{II}) = 571\ cm^{-1}$.

These values compared to $J = 397\ cm^{-1}$ and $\Delta J = 0$ for the Heisenberg-only model, which gave a much lower J and was unable to discriminate the Fe···Fe interactions. Extensive use was made of spin-state correlation diagrams of the type referred to in Section II,C and elsewhere in this review when dealing with competing exchange constants. From a plot of E/J vs $\Delta J/J$, it could be readily seen that, for $B/J = 1.04$, the energies of the first excited ($S = \frac{1}{2}$) level were only ca. 11 cm^{-1} from the ground state, with the next level some 160 cm^{-1} away. One

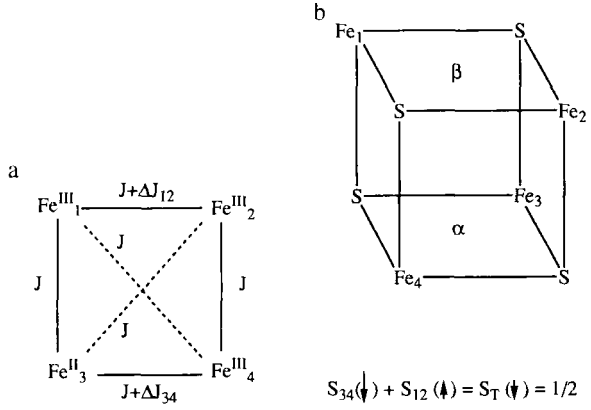

FIG. 28. Two perspectives of the coupling model used in $[Fe_4S_4]^{3+}$ cubanes showing the $Fe^{III}\cdots Fe^{II}$ (α) and $Fe^{III}\cdots Fe^{III}$ (β) pairs. Based on (*196*) and (*199*).

would anticipate that Zeeman mixing/depopulation effects in the magnetization vs temperature data at low temperatures would give interesting effects.

Noodleman (*184, 185*) used his model to interpret ESR g-values and ^{57}Fe Mössbauer hyperfine parameters in Fe–S clusters. In back-to-back papers he presented the Heisenberg-only and Heisenberg plus double-exchange theories of spin-state energies and spectroscopic properties for the $S_T = \frac{1}{2}$ and $S_T = \frac{3}{2}$ states of $[Fe_4S_4]^+$ clusters, present in reduced ferredoxins. Inclusion of double exchange improved the agreement between theory and experiment and the site equivalence in ESR and Mössbauer data. Furthermore, crossing points in the E/J vs $\alpha(= J_2/J_1)$ graphs, for various values of B/J, showed the coexistence of $\frac{1}{2}$ and $\frac{7}{2}$ states in $[Fe_4Se_4]^+$, the precise ordering of which depends on the relative size of $J(Fe^{II}–Fe^{II})$ and $J(Fe^{II}–Fe^{III})$. The values of the J and B constants for Fe_4S_4 cubanes in the 1+, 2+, and 3+ states and the ratio values for J_{red}/J_{ox} and (B/J_{red}) have been collected (*10*). The general trends are $J_{ox} > J_{red}$ and $J(Fe^{II}–Fe^{II}) < J(Fe^{II}Fe^{III}) < J(Fe^{III}–Fe^{III})$. In a very recent example (*186*), this group has provided new analysis of these spectroscopic features in the P^{ox} state of the now structurally characterized P-clusters of nitrogenase, the electronic structure of which, in its various redox states, has caused some intrigue and disagreement over recent years. Each half of the P-cluster was regarded as $[Fe_4S_4]^{1+}$, containing $\{Fe^{III}(Fe^{II})_3\}$, but with different spins, $\frac{1}{2}$ and $\frac{7}{2}$, which give rise to parallel (ferromagnetic) spin coupling, thus producing $S = 4$.

Kahn (*7*) has also discussed the Heisenberg analysis of $[Fe_4S_4]^+$ clusters and has considered the effects of double exchange on the magnetism of mixed-valence species. He has commented on assumptions in the model of Noodleman when applied to Fe–S clusters. In an extensive review which emphasizes the need to use the complementary techniques of ESR, Mössbauer, and magnetic susceptibility, Trautwein and his group discuss double exchange in mixed-valence Fe–S clusters, and also calculate ^{57}Fe hyperfine constants for $[Fe_4S_4]^{1+,2+,3+}$ cubanes (*6*). They also note that in the $[Fe_4S_4]^{1+}$ state, there are examples of proteins and synthetic analogues which show cluster spins S of greater than $\frac{1}{2}$, such as $S = \frac{3}{2}, \frac{5}{2}$, and $\frac{7}{2}$. Indeed, Holm and co-workers (*187, 188*) presented a detailed study of variable-temperature magnetization, ESR g-values, and magnetic Mössbauer spectra for a large range of $[Fe_4S_4(SR)_4]^{3-}$ model complexes and found that, depending on R, the ground spin state could be (i) pure spin $\frac{1}{2}$ or $\frac{3}{2}$, (ii) a physical mixture of these states, or (iii) a spin-admixture of states. Hagen (*181*) subsequently pondered the question of what might be the physical meaning of points (i), (ii),

and (iii), particularly in relation to proteins possessing the cluster $[Fe_4S_4]^+$. Collison and Mabbs had also worked out that the spin states in crystalline $[Fe_4S_4(SR)_4]^{3-}$ models could be $\frac{3}{2}$ or $\frac{5}{2}$ by simulating ESR spectral line shapes (*189*). Gaillard substantiated these spin states for solutions of $[Fe_4S_4]^+$ and $[Fe_4Se_4]^+$ proteins from *C. pasteurianum Fd* by measuring room temperature solution susceptibilities via NMR shift methods (*190*), and also made a comparison with the solution and solid μ_{eff} values found for Holm's model compounds (*187, 188*). Girerd, Münck, Papaefthymiou, and co-workers (*191–194*) have given detailed analyses of Mössbauer hyperfine parameters in Fe_3S_4, MFe_3S_4, and Fe_4S_4 protein clusters in terms of double exchange. They include plots of E/J vs B/J for the low-lying $S = \frac{1}{2}$ and $S = \frac{3}{2}$ states in the $[Fe_4S_4]^{3+}$ core and show that double-exchange leads to a S_{12} value of $\frac{9}{2}$ for any value of B/J (*195*).

Luchinat *et al.* (*196*) have recently applied these ideas on double exchange to paramagnetic NMR shifts and have presented a coupling model for the HIPIP $[Fe_4S_4]^{3+}$ cluster, in much the same way described earlier for the $[Fe_4S_4(SR)_4]^-$ model complex. They have given the energy equation for the spin states appropriate to the experimental study by Bertini *et al.* (*197*). From ^1H NMR shift data, in combination with Mössbauer hyperfine constants for each Fe, it has been possible to identify which cysteine CH_2 protons are bound to the Fe^{III}–Fe^{II} (α) pair in HIPIP and, by noting the relative direction of the Knight shifts, which are attached to the Fe^{III}–Fe^{III} (β) pair. These various physicochemical methods and theories on double exchange have been applied in conjunction with the latest Fourier transform (FT) NMR techniques on the sequence-specific assignments of various HIPIP samples (including temperature dependencies and connectivities between signals). This work has provided a good example of how to identify which Fe is which within the protein framework, and ultimately how to deduce the three-dimensional structure of a paramagnetic HIPIP protein (from *Ectothiorhodospira halophila*) in solution (*198*). In these (*197, 198*) and other recent related papers (*199, 200*), the Florence group of Bertini and Banci and the Bologna group of Luchinat, and their respective coworkers, have combined to produce an impressive series of studies of electronic and NMR structures of HIPIP proteins. Included in these are very clear expositions of double exchange, with all relevant equations (and energy diagrams), for the $[Fe_4S_4]^{3+}$ clusters in $HIPIP_{ox}$ from *Ectothiorhodospira vacuolata*—which actually required a model involving a fast equilibrium between two low-symmetry mixed-valence clusters (*199*)—and earlier (*197*) for HIPIP and $HIPIP_{red}$ in *Chromatium vinosum*. The best-fit J value in the *E. vacuolata* clusters was much

smaller than that found by Noodleman *et al.* for the model complex (*183*) mentioned earlier, while the ΔJ_{12} value was similar. However, ΔJ_{12} was assumed equal to $-\Delta J_{34}$, rather than zero, in the analysis of Bertini *et al.* (*197*).

In an important series of papers, Belinskii has recently summarized the state of knowledge on the electronic structures of Fe_4S_4 clusters, some of which has been outlined here. He has developed the theory of spin coupling in great detail. The papers include the following: Part I. $[Fe_4S_4]^+$ clusters; Theory, exchange levels and g-factors (*201*). Part II. Hyperfine interactions, magnetism, high-spin systems (*202*). Part III. Double-exchange in distorted clusters (*203*). Heisenberg model for HIPIP $[Fe_4S_4]^{3+}$ clusters I. Exchange states, g factors, hyperfine interactions (*204*). II. Double exchange in distorted clusters (*205*). All the facets of exchange theory and ITO theory are in these papers, and energy-level and correlation diagrams, etc., are used with skill. In I (*201*) and II (*202*), the key points to emerge are the effect of the exchange mixing of states with fixed intermediate spins on the energy levels which is brought about by cluster deformations. New analytical solutions for energy and eigenfunctions of the $S = \frac{1}{2}$ ground state are given. The variation of exchange interactions under these structural deformations explains changes in g factors in ferredoxin clusters, including the famous $g = 1.94$ signal. The deformation terms also explain Mössbauer hyperfine variations. Of particular importance to the present review, Belinskii has used his model, including distortion parameters (δ_1 and δ_2), but excluding anisotropic exchange and ZFS effects, to fit the μ/T plots of Holm's (*187, 188*) synthetic clusters $[Fe_4S_4(SR)_4]^{3-}$. Taking just one example of a system with a mixture of spin ground-states:

(n-$Pr_4N)_3[Fe_4S_4(SCH_2Ph)_4]$: $S_{(ground)} = \frac{1}{2}$, 51%, $J_1[Fe^{III}\text{–}Fe^{II}] = -56.7$ cm^{-1}, $\Delta = 11.1$ cm^{-1}, $\delta_1 = 36.7$ cm^{-1}, $\delta_2 = 0$, $S_{(ground)} = \frac{3}{2}$, 49%. $J_1 = -65.3$ cm^{-1}, $\Delta = 30.4$ cm^{-1}, $\delta_1 = 43.7$ cm^{-1}, $\delta_2 = 0$.

Deviation between observed and calculated μ values occurs below 40 K. In Part II, the "distorted" Heisenberg and double-exchange models are joined. A comparison is made with Noodleman's strong double-exchange model (*10, 184, 185*). The deformation parameter, δ_1, was found to act in concert with double exchange. Related kinds of effects are noted in the $[Fe_4S_4]^{3+}$ $HIPIP_{ox}$ papers when the exchange mixing of spin levels is applied (*204, 205*).

F. Cobalt

1. Cobalt(II) Clusters

a. Planar Rhomboidal Shape. The planar rhombus-like moiety $Co^{II}{}_4O_{16}$, found in the heteropoly complex $K_{10}[Co_4O_{14}(H_2O)_2(PW_9O_{27})_2]\cdot$

$22H_2O$, consists of four coplanar $Co^{II}O_6$ distorted octahedra, sharing edges and with Co–O–Co angles of ca. 90°. The μ (per Co_4) value at 300 K of 10.4 μ_B in these formally orbitally degenerate d^7 single ions is greater than the uncoupled value of 7.74 μ_B ($g = 2.0$) on account of spin–orbit coupling effects (*206*). μ remains constant in the range 300–30 K, then increases rapidly as a result of intramolecular ferromagnetic coupling. The data in the range 20–5 K were fitted by use of an anisotropic exchange model containing $J_\parallel$ and $J_\perp$ terms. The best fit was for $J_\parallel = +9.5\ cm^{-1}$, $J_\perp/J_\parallel = 0.32$. The system behaved essentially like an $S = \frac{1}{2}$ doublet, and thus the calculated values were scaled up by $g_\parallel$ and $g_\perp$ values of ca. 7.9 and 2.04, respectively. Actually, two sets of g values were used, since the structure possesses two dissimilar Co^{II} symmetries. Inelastic neutron scattering spectroscopy subsequently provided a more accurate measurement of exchange splitting, the modified $J_\perp/J_\parallel$ value of 0.6 being intermediate between isotropic and anisotropic values (*207*).

b. Cubanes. The crystal structures of O-bridged cubanes $[Co^{II}_4(OCH_3)_4(acac)_4 \cdot (CH_3OH)_4]$ and $[Co^{II}_4Bu^t_2cat)_4]5.5thf$ are known (*208, 209*). Brief mention was made by Smit *et al.* (*102*) of the magnetization data (0 to 5 tesla) on the former complex, which showed saturation at very low applied fields on account of intramolecular ferromagnetic coupling. The complex $[CoX(L)(C_2H_5OH)]_4$, where X = Cl, Br and L is a bidentate {O,N} pyrazolate group, was found to be isostructural with the Ni^{II} chloro analogue, in which the metal ions are octahedral (*210*). A μ value (per Co_4) of 10.2 μ_B and θ of −6.1 K, in the range 80–300 K, were compatible with weak antiferromagnetic coupling. Similar behavior was noted for the structurally characterized complex $[Co_4(OCH_3)_4(2,4,6\ Cl_3C_6H_2O)_4(CH_3OH)_4]$ which had a μ value of 9.44 μ_B at 296 K (*211*).

The best-studied Co^{II} cubanes are fluoro-bridged complexes of type $[Co(F)(N\text{–}R\text{–imidazole})_3]_4(BF_4)_4$, in which the Co centers display six-coordinate $\{N_3F_3Co\}$ geometry (*102*). A detailed study of susceptibilities and high-field magnetization was made, the former showing maxima at ca. 4 K on account of antiferromagnetic coupling. As in the case of the Mn^{II} analogues, the magnetization vs field plots showed "twists" in the curves, probably due to spin-flop occurring for two of the four spins within each tetramer. Since Co^{II} single ions have formally orbitally degenerate states ($^4T_{1g}$) which often yield anisotropic magnetic behavior, Heisenberg and Ising spin Hamiltonian models were both considered. Furthermore, an effective spin of $\frac{1}{2}$ was assumed for each high-spin Co^{II} ion, with g and J employed as variables in the fitting procedure. The following parameter sets gave reasonable fits to the

2–40 K χ vs temperature data. Second-order Zeeman (TIP) effects from excited levels were not included.

Ising model:	$J = -3.5\ \text{cm}^{-1}$	$g = 4.2$
Heisenberg model:	$J = -2.2\ \text{cm}^{-1}$	$g = 3.84$

In contrast, the saturation magnetization field value yielded an estiamte of J of ca. $-9\ \text{cm}^{-1}$, while specific-heat data gave J ca. $-7\ \text{cm}^{-1}$. These latter two values are regarded as more appropriate. It was noted that 90° Co–F–Co pathways gave much smaller (negative) J values than did 180° pathways.

Antiferromagnetic coupling was also evident in the trapped mixed-valency cubane complex $[Co^{II}_2Co^{III}_2(OCH_3)_4(acac)_4(O_2CCH_3)_2]$. The μ values, per Co, decreased from 4.98 μ_B at 298 K to 4.62 μ_B at 77 K (*212*).

c. Linear Tetramer. The violet crystals of $[Co(acac)_2]_4$, obtained by many an undergraduate chemistry student upon dehydration of pink $Co(acac)_2(H_2O)_2$, display an acac-bridged chainlike structure such that each Co^{II} has a CoO_6 environment. Following up on a preliminary report by Martin *et al.* (*31*), Bonner *et al.* (*71*) provided powder susceptibility data in the range 0.35–20 K and 70–295 K, the corresponding μ (per Co_4) values remaining almost constant at ca. 9.6 μ_B in the region 300–100 K and then decreasing very rapidly at low temperatures toward 4.2 μ_B at 0.35 K. Bonner *et al.* (*71*) used a first-order Ising model to fit the data and assumed an effective spin of $\frac{1}{2}$ for Co^{II}, as was subsequently done for the μ-fluorocobalt(II) cubane system, described earlier. The superexchange pathways adopted are shown in Fig. 29 and are appropriate to the structure of the bridging regions. The best fit for the 0.35 to 25 K region was for three antiferromagnetic exchange constants: $J_1 = -3.5\ \text{cm}^{-1}$, $J_2 = -0.7\ \text{cm}^{-1}$, $J_3 = -2.8\ \text{cm}^{-1}$, $g = 5.0$. These parameters underestimated the values of μ at higher temperature, probably because of the neglect of excited energy levels. The fit, and relative sizes of the J values, were discussed in detail. Also, the authors provided one of the early discussions in cluster magnetism to employ such features as (i) the energy ladder for a three-J Ising tetramer model; (ii) energy correlation diagrams, such as E/J_2 vs. J_1/J_2 for a fixed J_3/J_2 ratio, which clearly showed quasi-degeneracy regions of the state energies that had dramatic effects on the temperature dependence of μ at low temperatures. We have seen many such effects elsewhere in this review. (iii) Anisotropy in spin Hamiltonians and in susceptibilities; (iv) adopting a general Heisenberg–Ising model, i.e., use of an anisotropy parameter to calculate energy levels intermediate

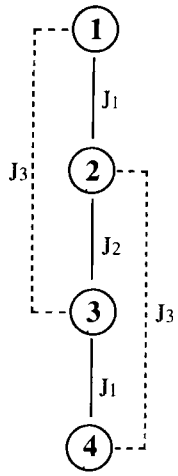

FIG. 29. Spin-coupling model used for Co_4acac_8 (*71*).

between Ising and Heisenberg (isotropic) limits. The authors also predicted the form of the expected magnetization isotherm curve by calculating energies and populations of low-lying Zeeman levels. "Two-step" M vs H curves were thereby calculated; the steps correspond to changes in ground state. Curves of this kind were noted earlier in the Co^{II} cubane work. Further experimental data, including single-crystal data, would therefore still be desirable on $[Co(acac)_2]_4$ and on some of the other tetranuclear Co(II) compounds cited.

d. Tetrahedral $Co^{II}_4(SR)_{11}$ *and Adamantane* $[Co^{II}_4(SR)_{10}]^{2-}$ *Clusters.* Bertini *et al.* (*213*) have developed a model to explain ^1H NMR isotropic shifts in the Co^{II}_7-substituted derivative of rabbit-liver metallothionein-2. The structure of the tetranuclear Co^{II}_4 moiety, found in the α-domain of the protein, consists of four Co^{II}(S–cysteine)$_4$ tetrahedra bridged via the thiolate S atom, except for two opposite cobalt atoms (1 and 4), each of which has two terminal cysteines, compared to only one for $Co_{(2)}$ and $Co_{(3)}$. The expectation value for $\langle S_{iz} \rangle$, used to calculate contact shifts, has the same temperature dependence as magnetic susceptibility (*146*). A T_d Heisenberg model was used with, initially, six different J values, and the 256 × 256 matrix (for $S = \frac{3}{2}$) was blocked and diagonalized numerically. The best agreement with the shift pattern and temperature dependence occurred when J_{14} was set equal to zero and the other five J values were equal to -25 cm^{-1}. This treatment also yielded a J value of -22.5 cm^{-1} for solutions of

the adamantane core in $[Co_4(SEt)_{10}]^{2-}$, which was similar to that obtained from susceptibility data on crystalline $[Co_4(SPh)_{10}]^{2-}$ (*214*).

G. Nickel

1. Nickel(II) Clusters

Some very interesting tetranuclear nickel complexes are known, including thiolato $Ni_4(SR)_8$ species (*215, 216*), in which the coordination geometry around each Ni atom is square-planar and thus the compounds are diamagnetic (*217, 218*). Six or five coordination is required to get paramagnetic Ni(II) (d^8) centers, and hence to get exchange-coupling phenomena. There is one recent example of a zigzag shaped tetranuclear complex, formed with a Robson-type binucleating ligand, in which the two inner Ni(II) atoms are six-coordinate and weakly antiferromagnetically coupled, while the outer two have planar coordination and are thus diamagnetic (*218a*). Tetranuclear Ni(II) clusters were, historically, some of the first examples showing intramolecular ferromagnetic coupling. They followed closely the well-known example of trinuclear Ni_3acac_6 (*31, 37, 219*).

a. Planar Rhomboidal Shape. Coronado's series of M_4O_{16} rhombus-like clusters, formed within the polyoxo anion $[M_4(H_2O)_2(P_2W_{15}O_{56})]^{16-}$, included the ferromagnetically coupled M = Ni^{II} complex (*220*). Use of an isotropic $S = 1$ Heisenberg model of the type shown in Fig. 19 yielded $J = +8.3$ cm^{-1}, $J' = +3.5$ cm^{-1}, $J'/J = 0.42$. A decrease occurred in the μ (per Ni_4) values at very low temperature below a μ_{max} value of 8.95 μ_B at 10 K [cf. $\mu(S = 4) = 8.94$ μ_B]. This was ascribed to intercluster antiferromagnetic coupling ($\theta = -0.65$ K). It would have been useful to check out alternative reasons for this decrease, such as thermal depopulation of Zeeman sublevels from $S_T = 4$ and $S_T = 3$ states, or ZFS effects. To do this, magnetization data at low temperature and use of the thermodynamic expression for χ would be required. Coronado *et al.* (*220*) interpreted the ferromagnetic sign of J in term of 90° Ni–O–Ni angles, which led to appropriate overlaps of Ni and O orbitals.

We see, later, that rhomboidal models have also been used to explain the magnetic data both for distorted cubanes and for square-shaped cores.

b. Cubanes. In 1969, Andrew and Blake (*221*) made one of the first magnetostructural studies on tetranuclear clusters, when they investigated the cubane-shaped complex $[Ni_4(\mu_3\text{-}OCH_3)_4(sal)_4$

$(C_2H_5OH)_4]$, where sal is the bidentate salicylaldehydato chelate. Data were limited to the range 300–77 K, and μ (per Ni) increased from 3.2 μ_B at 302 K to 3.75 μ_B at 90 K. Application of Kambe's vector-coupling model, and an isotropic Heisenberg Hamiltonian under T_d symmetry, led to a closed-form expression for χ. Least-squares fitting of the data to this equation gave $g = 2.17$ and $J = +7$ cm^{-1}, the positive sign of J being rationalized in terms of 90° Ni–O–Ni superexchange pathways of the orthogonal type: $\{Ni(t_{2g})/O(p)/Ni(e_g)\}$ (*31, 37*). Barnes and Hatfield (*222*) extended the temperature range of the susceptibility measurements on this sal complex, and also made magnetization measurements to confirm the $S_T = 4$ ground state. Their best-fit parameters ($g = 2.14$, $J = +7.5$ cm^{-1}) were similar to the earlier values. They noted that the χ values at low temperatures were sensitive to field changes on account of depopulation of Zeeman sublevels from the $S_T = 4$ ground state. This was an example for which the thermodynamic expression for χ should have been used, as it should have in the acac analogue, described later, in which other interactions were proposed. Zero-field splitting effects were not included in either study.

Ginsberg and co-workers (*208*) soon followed with a similar structural and magnetic study on the related cubane complex $\{Ni_4(OCH_3)_4(acac)_4(CH_3OH)_4]$. They gave a clear description of the vector coupling model, including an energy level diagram and calculations of μ vs temperature value for J both positive and negative. A combination of susceptibility (1.6–296 K) and magnetization data (0–1.5 tesla, 1.6–20 K) showed that ferromagnetic coupling again occurred and the $S_T = 4$ ground state was fully populated by 21 K. The best-fit parameters were $g = 2.14$, $J = +7$ cm^{-1}, χ(TIP) per $Ni^{II} = 0.00005$ cgs. Inclusion of a $(T - \theta)$ term in the χ expression yielded $\theta = +0.8$ K, which indicated that intermolecular cluster–cluster interactions were also occurring, weakly and ferromagnetically. This θ term also improved the magnetization vs H/T fitting by use of Brillouin functions, with a molecular field term also being added. Subsequent heat capacity studies on this complex (*223*) suggested, however, that no cluster–cluster interactions were occurring at very low temperature. A detailed and pictorial discussion of the Anderson/Goodenough/Kanamori Ni–O–Ni superexchange pathways, which contributed to the net positive J value, was given by Ginsberg *et al.* (*208*). In a review article, Ginsberg (*37*) also noted that mixed chloro–alkoxo Ni^{II} cubanes of type $Ni_4(\mu_3\text{-}OCH_3)_4(Cl)_4(CH_3OH)_8$, studied by Krüger and Winter (*224*), showed very similar J values to the acac and sal complexes mentioned earlier. This appeared to indicate that "terminal" ligands attached to the Ni atom played little, if any, part in the exchange mechanism. It was proposed that ferromagnetic

coupling persisted in these systems for ranges of Ni–O–Ni angle of $90 \pm 14°$. Indeed, the structure and ferromagnetism of a chloro–alkoxo system $\{Ni_4(L)_4(Cl)_4(C_2H_5OH)_4]$, where L = 1-hydroxymethyl-3,5-dimethylpyrazole (*225*), supported this proposal, the Ni–O–Ni angles all lying between 90° and 100°. However, Gray and Hendrickson and coworkers (*226*) showed that a $[Ni_4(\mu\text{-}OCH_3)_4]^{4+}$ cubane could actually display antiferromagnetic coupling, as evidenced by a maximum in χ occurring at ca. 60 K, with corresponding decreases occurring in the value of the moment, viz, μ (per Ni) = 2.88 μ_B at 286 K and 0.47 μ_B at 4.7 K. A complex $[Ni_4(OCH_3)_4(O_2CCH_3)_2(TMB)_4](BPh_4)_2$, in which TMB is 2,5-dimethyl-2,5-diisocyanohexane, was shown to have acetate groups bridging opposing pairs of Ni atoms, while the TMB group bridged the remaining faces. Three coupling models were used to try and simulate the precise shape and size of χ, especially in the χ_{max} region. These were a one-J Heisenberg T_d model [as in the sal and acac cubes (*208, 221*)], a pair of noninteracting Ni^{II} dimers model, and a three-J rhomboidal model, the last using Dubicki's equation (*29*) and allowing for structural distortions in the cube. The last model was the best and yielded the parameters $g = 2$, $J_{edge} = -9.1$ cm^{-1}, $J_{diag(1)} = +17.7$ cm^{-1}, $J_{diag(2)} = +17.2$ cm^{-1}. These authors presented one of the early examples of the use of a spin-state correlation diagram (of E/J_{edge} vs $J_{diag(1)}/J_{diag(2)}$). The overall antiferromagnetic behavior was attributed to distortions of the cubane core, brought about by the acetate bridge, which led to Ni–O–Ni angles of ca. 93° and ca. 101°, the latter proposed to lead to the negative J_{edge} interaction, the former to the positive interaction. Clearly the Ginsberg conclusion (*208*) of Ni–O–Ni angle vs positive J had to be modified somewhat to allow for distortion and symmetry changes. A similar plot of χ vs temperature and a rhomboidal coupling scheme was later employed on a distorted $[Ni_4(\mu\text{-}OH)_4]^{4+}$ cubane cluster, containing N,S-donor terminal ligands such as $[Ni_4(OH)_4(tzdt)_4(py)_4] \cdot 2py$, where $tzdt^-$ is 1,3-thiazolidine-2-thionate (*227*). This N,S chelating ligand effectively takes the place of TMB in the Gray molecule (*226*), while two pyridines replace each bridging acetate. The best-fit parameters were $g = 2.0$, $J_{edge} = +17.5$ cm^{-1}, $J_{diag(1)=(2)} = -22$ cm^{-1}.

The signs of J are opposite to those given earlier for $[Ni_4(OCH_3)_4(O_2CCH_3)_2(TMB)_4]^{2+}$, but the arguments vis-à-vis the Ni–O–Ni angles are similar.

Boyd and Martin (*229*) summarized magnetostructural correlations in $[Ni_4(\mu_3\text{-}OR)_4]^{4+}$ and $[Ni_4(\mu_3\text{-}OH)_4]^{4+}$ cubanes in a detailed study of susceptibility and magnetization on $[Ni_4(OH)_4(tach)_4](NO_3)_4 \cdot 7H_2O$. The analogous Cr^{III} complex of this cyclohexyl-triamine (tach) ligand,

described in Section III,C,1,b, adopted the $[Cr_4(OH)_6]$ adamantane core. In contrast to the χ or μ data described thus far for the ferromagnetic or antiferromagnetic Ni^{II} cubanes, this compound displayed a temperature dependence of μ_{Ni} very much like that expected for a zero-field split mononuclear Ni^{II} ion, and it thus showed much weaker net coupling. A number of magnetic models were explored, particularly in order to uniquely simulate low-temperature plots of μ_{Ni} vs H/temp, for H values up to 5 tesla. Intercluster and single-ion ZFS effects could be excluded. Once more, use of a three-J rhomboidal model gave excellent agreement with the measured data: $g = 2.2$, $J_{edge} = -0.8\ cm^{-1}$, $J_{diag(1)} = -1.16\ cm^{-1}$, $J_{diag(2)} = +0.95\ cm^{-1}$. Clearly, the coupling is close to a crossover in sign, no doubt because of small structural distortions in the Ni–O–Ni bridges. Bridge angles below 98° lead to small ferromagnetic coupling, while larger ones lead to negative J values.

Heteronuclear cubanes of the type $[Co_2^{II}Ni^{II}_2(OCH_3)_4(L)_4(CH_3OH)_4]$ have recently been prepared, where L = $acac^-$ or sal^- (*230*). The acac complex was isostructural with the Ni_4 and Co_4 parents. It showed a small decrease in μ (per metal) from 4.36 μ_B at 297 K to 4.19 μ_B at 181 K, followed by an increase up to 4.44 μ_B at 103 K. This temperature dependence of μ was attributed to a coexistence of antiferromagnetic and ferromagnetic interactions. The compounds deserve more detailed study.

The μ_3-fluoro bridged cubane cores in molecules such as $[Ni_4(F)_4(5\text{-methylpyrazole})_{12}](BF_4)_4$ show weak antiferromagnetic coupling and a corresponding maximum in χ at 9 K (*231*).

c. Square (Cyclic) Cores. Two examples are known, one showing antiferromagnetic coupling, the other ferromagnetic. In the latter example (*232*), $[Ni_4(\mu\text{-}N_3)(L)_2(LH)_2](ClO_4)_2$, where LH = 1,3-diamino-2-hydroxypropane, the bridging ligands between adjacent octahedral Ni atoms are 1,1-azido and the alkoxo group of LH. The moment increases with decreasing temperature, reaching a maximum of 9.2 μ_B (per Ni_4) at 23 K before decreasing rapidly at lower temperature because of ZFS effects. Population of a $S_T = 4$ state is compatible with the μ_{max} value, and fitting to a rhomboidal exchange model, with diagonal J values assumed zero, gave a J value of $+10.6\ cm^{-1}$. Application of an axial spin Hamiltonian for zero-field splitting of the $S_T = 4$ state yielded $|D| = 6\ cm^{-1}$. A spin polarization mechanism, operating via the μ1,1′-N_3 bridge to two adjacent Ni d_{xy} orbitals, was proposed to explain the ferromagnetic coupling.

The second example (*233, 234*) involved encapsulation of four Ni atoms within a tetranucleating Schiff-base ligand of the Robson type,

LH_4, shown in Fig. 30. A small series of complexes all contained a common $[LNi_4(\mu_4\text{-}OH)(CH_3O\cdots H\cdots OCH_3)]^{2+}$ core (Fig. 31) which had the $\{Ni_4(\mu_4\text{-}OH)\}$ moiety in a rectangular plane at the bottom of the bowl-shaped ligand. The $(CH_3O\cdots H\cdots OCH_3)^-$ group bridged pairs of nickels inside the top of the bowl, and XY μ_2-bridging ligands [$CH_3CO_2^-$ (acetato), $N_3\cdots HOH^-$ (azido), $CH_3O\cdots H\cdots OCH_3^-$ (methoxo)] bonded to the Ni atoms as "legs," outside the bottom of the bowl. Each Ni atom has distorted octahedral geometry. The bowl-like geometry of L^{4-} results from twisting of the aromatic rings and pyramidal coordination of the diamine-derived phenolate O atoms. The three complexes show similar antiferromagnetic χ/T plots with maxima at ca. 85 K, the corresponding μ(per Ni) values decreasing from 2.92 μ_B at 295 K to ca. 0.1 μ_B at 4.2 K. The approach to fitting the data was rather like that adopted by Hendrickson and Gray in their distorted cubane system (*226*). However, in the present case, the pair-of-noninteracting-dimers model gave excellent fits in all cases, with no improvement gained by use of multi-J rhomboidal models. The results show:

Acetato:	$g = 2.17$	$J = -33.3\ cm^{-1}$	χ(TIP) = 0.0004 cgs per Ni
Azido:	$g = 2.17$	$J = -28.5\ cm^{-1}$	χ(TIP) = 0.0004 cgs per Ni
Methoxo:	$g = 2.17$	$J = -30.0\ cm^{-1}$	χ(TIP) = 0.0004 cgs per Ni

The pair-of-dimers model is actually compatible with structural details,

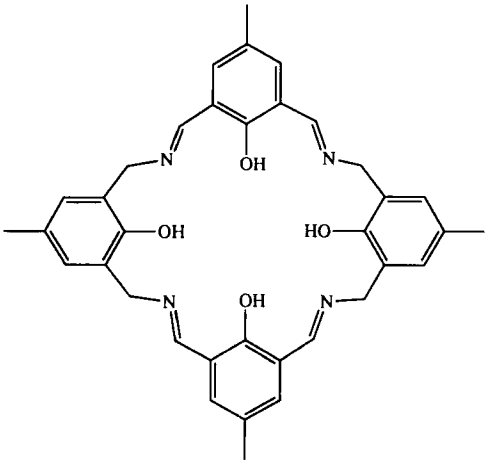

FIG. 30. Tetranucleating ligand, LH_4 (*233, 234*).

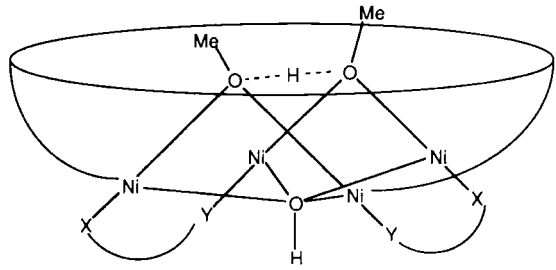

FIG. 31. Structural representation of $[LNi_4(\mu_4\text{-}OH)(CH_3O\text{–}H\text{–}OCH_3)(XY)_2]$, showing bowl-like features (*234*).

despite what might appear, at first glance, to be a square having four equally bridged sides, as was the case in Ribas' μ-azido-μ-alkoxo compound (*232*). In the present case two internally coplanar Ni_2 blocks are hinged together by the pyramidal phenolato O atoms and the central μ_4-OH^-, with no apparent interaction between the blocks. The Ni···Ni distances and Ni–O–Ni angles within the blocks are ca. 3.06 Å and 100°, and between blocks 2.8 Å and 83°. The J values are generally similar to those observed in related planar dinuclear Schiff-base species (*235*), but are more negative than in the cubane species described earlier.

In a follow-up to the preceding analysis, an interested reader asked us to reconsider the possibility of using a square (D_{4h}) model, with all edge J values equal and diagonal J values of zero, rather than the pair-of-noninteracting-dimers model. This query was partly because of the apparently similar bridging interactions (see earlier discussion) and also because the energy separation between S_T states is a function only of S_T, because the S_{13} and S_{24} terms cancel in Eq. (10) under D_{4h} symmetry. Consequently, the energy ladder is $S_T = 0$ (ground), $S_T = 1$ ($2J$), $S_T = 2$ ($6J$), $S_T = 3$ ($12J$) = 4 ($20J$), which compares to $S_T = 0$ (ground), $S_T = 1$ ($2J$), and $S_T = 2$ ($6J$) for a dimer. Indeed, for large $|J|$, only the $S_T = 0$ to 2 sublevels would be populated at 295 K, but, for $|J|$ ca. 30 cm^{-1}, the higher S_T levels would be partly populated. Furthermore, the degeneracies in the denominator of χ would be different between tetramer and dimer. Approaching the query in a different way, rather like that used by Kahn (*236*), we set up a version of Eq. (3) using two parameters, J (intradimer) and J (interdimer), which allowed variations to be made in both, including J (interdimer) = 0—i.e., pair-of-non-interacting dimers. When both J's were allowed to vary for best fit, the azido complex gave J (intradimer) = -27.8 cm^{-1},

J (interdimer) = -1.7 cm^{-1}—essentially the same as before, and not equivalent to a square. It would perhaps be worthwhile to use a rectangular, D_2, model and full matrix diagonalization to attempt finer delineation of the interactions.

d. Other Ni_4 Tetranuclear Clusters. A multichelating ligand containing pyridyl and sulfonated 8-hydroxyquinoline rings, joined by an azo linkage, formed a phenoxo-bridged cyclic structure in the complex $[Ni^{II}_4\,(chelate)_4\,(H_2O)_4] \cdot 20H_2O$. The Ni···Ni distances were ca. 4.0 Å, and Ni–O–Ni angles ca. 141°. χ data in the range 300–80 K clearly showed antiferromagnetic coupling, but no fitting was attempted (*237*). Weak antiferromagnetic coupling also appears to be occurring in an unsymmetrical complex cation of type $[Ni^{II}_4L(\mu_3\text{-}OH)(\mu\text{-}H_2O)_2(ClO_4)]^{2+}$ reported by Nag *et al.* (*237a*). The tetranucleating ligand, LH_4, was formed upon reduction of the {4 + 4} Schiff-base formed by template coordination to Mg^{2+} of 2,6-diformyl-4-methylphenol and 1,2-diaminoethane.

H. Copper(II)

Because of their relative ease of synthesis, and of the design of many new polynucleating ligands for use in bioinorganic model and magnetochemical studies, there are many old and new examples of Cu^{II}_4 clusters. Emphasis will be given here to the more recent advances. It should be noted, as in the Ni^{II} examples, that the Heisenberg theory of coupling for distorted cubes merges into that anticipated for a distorted rhombus. The structures of the chelating ligands used to form tetranuclear Cu(II) species are shown in Fig. 32.

1. Rhomboidal, Parallelogram, Distorted Cubane, and Dimer-of-Dimer Shapes

The tetranuclear M_4O_{16} rhombs which occur in the $\{M_4(H_2O)_2(PW_9O_{34})_2]^{10-}$ (Keggin) and $[M_4(H_2O)_2(P_2W_{15}O_{56})_2]^{16-}$ (Dawson–Wells) polyoxo anions have recently been reviewed by Coronado and Gómez-Garcia (*238*). The M^{II} = Mn, Co, and Ni complexes have already been described in earlier sections, at which point the Cu^{II}–Keggin example was compared to Mn^{II}, particularly in respect to spin frustration resulting in a $S = 1$ ground state for Cu^{II}. The edge J (-3.5 cm^{-1}) was less than the diagonal J' ($J'/J = 3.6$) because Jahn–Teller effects influenced the degree of Cu($d_{x^2-y^2}$) orbital overlap (*206*). Coronado and co-workers (*238*) are presently developing magnetically ordered three-dimensional materials and electrically conducting materials (e.g., with

TTF^+ cations) based on these *d*-block metal-substituted polyoxometallates. The large size of the anions will be the limiting factor in both these pursuits, and new types of structural connectivities will probably need to be developed.

Parallelogram or distorted-cubane shaped complexes formed between Cu^{II} and chelating ligands have been known for many years. Groups such as those of Hatfield (*239*) and of Haase (*240*) have made major contributions. A common way of obtaining a planar parallelogram-like distribution between four Cu atoms is when planar binuclear Cu_2L_2 species (where L is often a meridional tridentate Schiff-base chelate), pair together (i.e., sit on top) in the crystal lattice to form discrete tetranuclear moieties. As we have already seen in Ni^{II} systems, the first recognition of tetramer formation in Cu^{II} compounds often came from efforts to reproduce the size and shape of χ_{max} regions in χ/T susceptibility plots. Dinuclear models tended not to reproduce the shape, and low *g*-values of less than 2.0 were often deduced. Further difficulties arise in strongly coupled systems, in which no maximum is observed in the temperature interval studied, and thus it is not easy to distinguish dimer and tetramer behavior.

Calculations of energy levels and susceptibility equations for tetranuclear clusters of $S = \frac{1}{2}$ centers have been given by a number of authors for a variety of site symmetries. However, use of different numbering schemes often makes comparisons somewhat difficult, and one must also be careful to distinguish vector mathematics from structural/chemical conclusions. Hatfield and co-workers (*241*) and Boyd and Martin (*242*) calculated the eigenvalues for a pair-of-dimers arrangement, shown in Fig. 33, in which opposite parallel sides had equal *J* values, but not equal to each other. This equates to a rhombus when these edge *J*'s are all equal. Sinn (*32*) made general calculations and cautioned against the use of this four-*J* (or three-*J*) model in view of the combinations of similarly sized positive and negative *J* values that emerged from the best fit for a Cu(II) Schiff-base complex (*241*). However, support for such combinations of *J* values has grown over the years, particularly when combined with experimental magnetization data, crystallography, and energy-level correlation diagrams (such as *E* vs J_{diag}/J_{edge}). Jotham and Kettle (*243*) and Merz and Haase (*244*) approached the calculations from a tetrahedral (T_d) disposition of Cu^{II} atoms within a symmetrical Cu_4O_4 cubane core. They then allowed for various distortions to occur, thus making some of the six possible *J* values equal.

Of particular relevance to Haase's extensive series of amino–alkoxo chelated species, of general type $[Cu^{II}(L)(X)]_4$, were the Hamiltonians

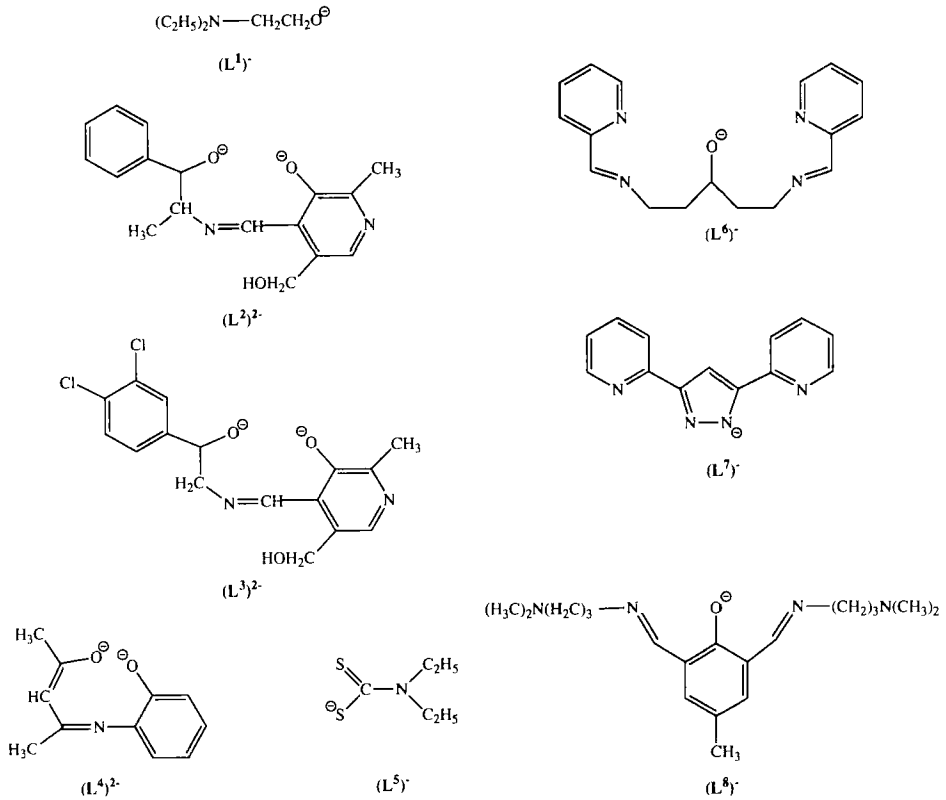

FIG. 32. Ligands used to form tetranuclear Cu(II) clusters.

appropriate to the point groups of S_4 (two J-value, distorted cube, square), C_{2v} (three J-value, rhombus) and C_2 [four J-values; equivalent to Hatfield's planar parallelogram model (*241*)] (*240*); Fig. 34. On occasion, it proved difficult to get a unique fit to one model, but it was possible to make meaningful comparisons of J values between different polymorphs of the same compound, e.g., L = 2-diethylaminoethanolato, X = NCO^- (*240, 244*). Table VI contains the best-fit parameters for a selection of these compounds. The relative sizes and signs of the intradimer (J_{12}) and "interdimer" (J_{13}) interactions were discussed in terms of Cu–O–Cu angles (intradimer) and Cu–O distances (interdimer). The shorter the latter, the more positive was J_{13}. Net ferromagnetism (S_T = 2) was displayed in the X = Cl and Br compounds (*239, 245, 246*), with net antiferromagnetism (S_T = 0) in the X = NCO polymorphs

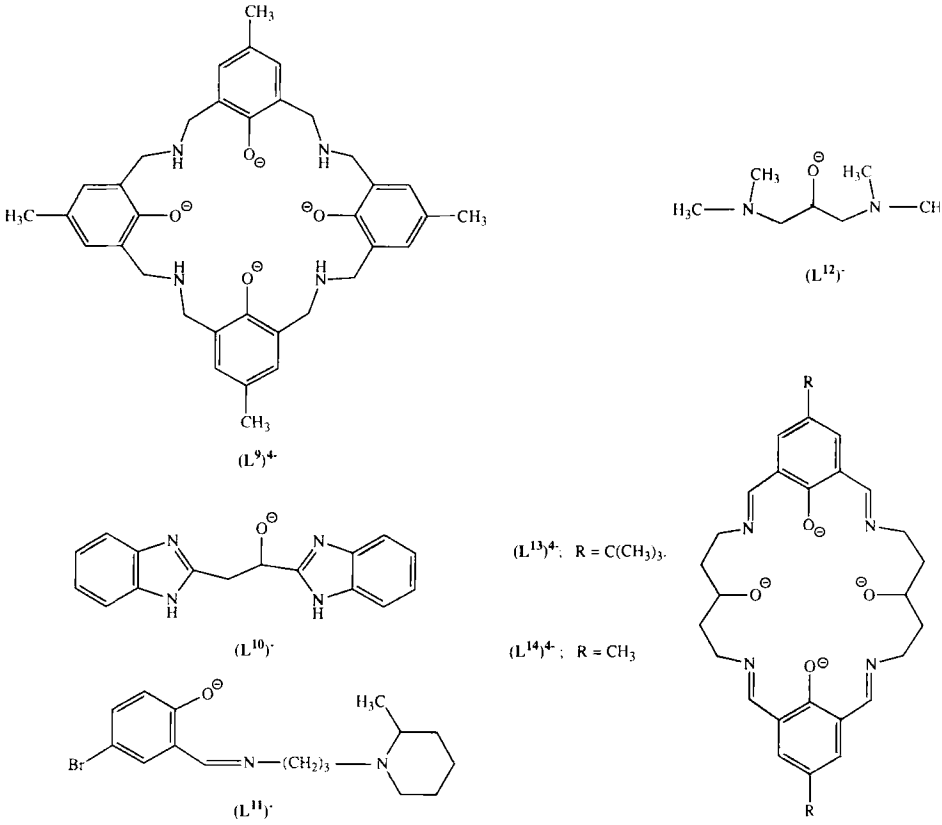

FIG. 32. *Continued.*

(*240, 244*). It is possible to represent these by simple spin-vector diagrams, as in the case of X = NCO, when S_4 symmetry is projected onto a square (Fig. 35). Two distorted cubane complexes formed from tridentate pyridoxal-Schiff-base ligands are also included in Table VI, both showing ferromagnetic ground states (*247, 248*). The structural and magnetic features of these and the $[CuL(X)]_4$ species have been compared (*248*), and their ESR spectral features have been discussed (*249*). In a study of catechol-based tridentate Schiff-base complexes of type $[CuL(NO_3)]_4$, Latour *et al.* (*249a*) found, perhaps surprisingly, that fitting the susceptibility data by use of the S_4 model required only one J value (J_{13}) for the inter-pair coupling, equal to -65 cm^{-1}, with the intra-pair coupling being negligible. The differences in size of these parameters were ascribed to differences in overlap of the Cu($d_{x^2-y^2}$)

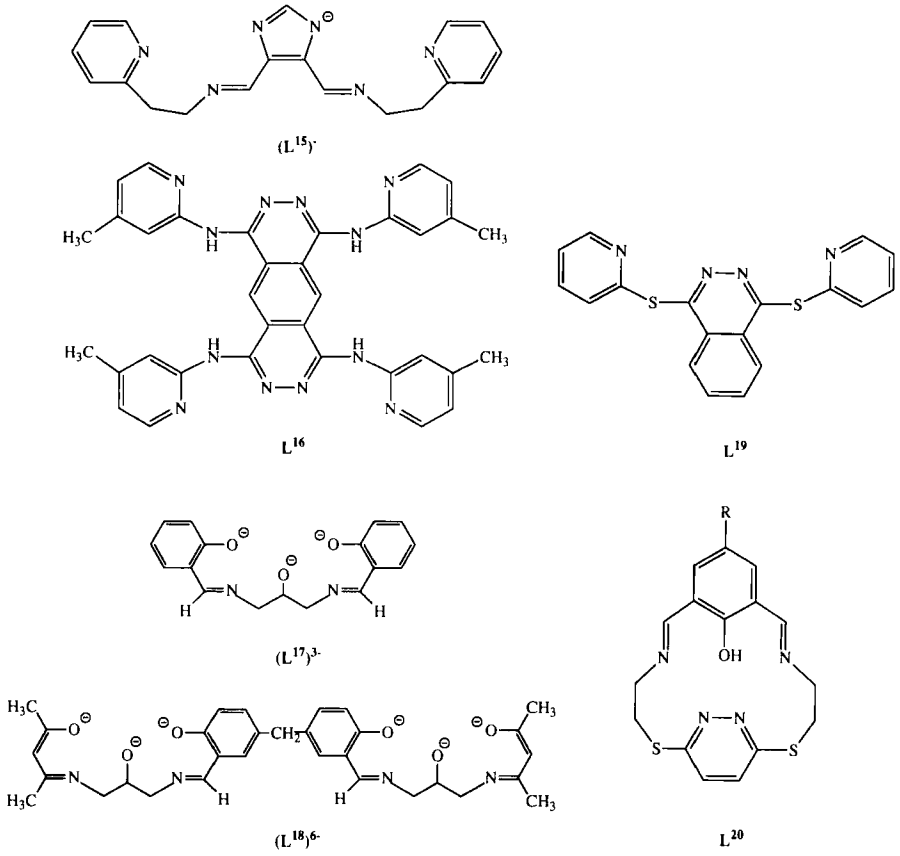

FIG. 32. *Continued.*

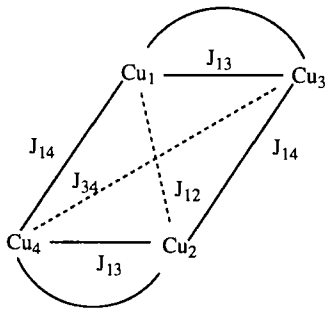

FIG. 33. Spin-coupling model used for planar-parallelogram Cu^{II}_4 cluster (*239*).

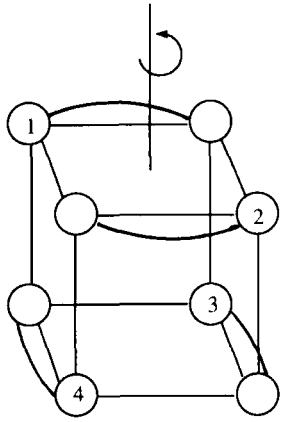

FIG. 34. Distorted Cu^{II}_4 cubane showing different symmetries (*244*).

magnetic orbitals and the bridging phenolate oxygen *p* orbitals relative to axial and equatorial directions about the Cu atoms. The final example in Table VI acts, essentially, as a pair-of-ferromagnetic $[Cu(bipy)(OH)]_2$ dimers, since the dimer–dimer Cu–O(H) distance is very long, 2.6 Å (*250*). Kahn has given the Heisenberg theory for this situation, in terms of two *J* values, starting from the cubane model (*236*).

Some examples of the planar-parallelogram pair-of-dimers are col-

TABLE VI

EXCHANGE PARAMETERS FOR DISTORTED CUBANE Cu(II) COMPLEXES
(*J* VALUES IN cm^{-1})

Complex[a]	Model	*g*	J_{12}	J_{34}	J_{13}	J_{14}	Ref.
$[CuL^1(NCO)]_4$(A)	S_4	2.19	−21.4	—	+12.3	—	*244*
$[CuL^1(NCO)]_4$(B)	S_4	2.19	−58.3	—	+17.4	—	*240*
$[CuL^1(NCO)]_4$(B)	C_{2V}	2.19	−74.9	−42.5	+17.4	—	*240*
$[CuL^1(NCO)]_4$(B)	C_2	2.22	−76.2	−42.2	+20.4	+11.7	*240*
$[CuL^1(Br)]_4 \cdot 4CCl_4$	S_4	2.17	−4.5	—	+40.0	—	*245*
$[CuL^1(Cl)]_4 \cdot 4CCl_4$	S_4	2.08	−5.2	—	+46.9	—	*246*
$[CuL^2]_4 \cdot 8CH_3OH$	S_4	2.12	0	—	+17.1	—	*247*
$[CuL^3]_4 \cdot 9CH_3OH$	S_4	2.08	−9.9	—	+20.5	—	*248*
$[CuL^3]_4 \cdot 9CH_3OH$	C_{2V}	2.06	−14.8	−14.8	+24.9	—	*248*
$[Cu(bipy)(OH)]_4$	S_4	2.07	+7.0	—	+0.16	—	*236, 250*

[a] A = tetragonal form; B = triclinic form.

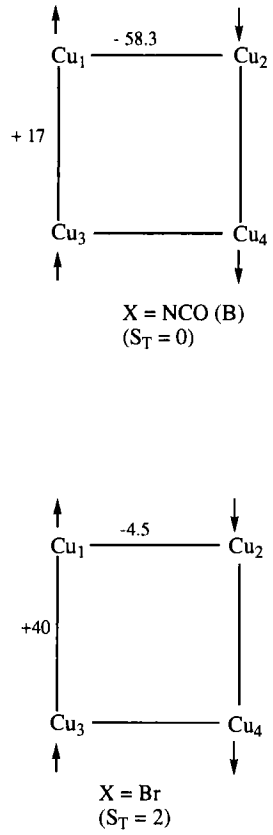

FIG. 35. Representation of the spin structures for $[CuL^1(X)]_4$ structural forms (*240, 244*).

lected in Table VII (*251–258*). In relation to Fig. 34, x is the in-plane intradimer bridge atom between Cu_1 and Cu_3, and y is the out-of-plane interdimer bridge atom(s).

In the case (*252*) of the unsymmetrical Schiff-base systems of type $[Cu_2L^6(OH)]_2$, many of which have been used as models of Type 3 biocopper centers, there is an early example obtained using Robson's ligand (*259*), which contained pyrazolate as an exogenous ligand, but its magnetism was analyzed using a dimer model (*260*). The example $[Cu_4L^9(OCH_3)_2(O_2CCH_3)Cl]$ is an interesting and perhaps surprising one (*255*). Robson's recently synthesized tetranucleating aminophenol ligand (*261*) is flexible enough to allow formation of this kind of core,

TABLE VII

EXCHANGE PARAMETERS FOR PLANAR-PARALLELOGRAM "PAIR-OF-DIMER" Cu(II) COMPLEXES (J VALUES IN cm^{-1})

Complex[a]	Bridge Atom x	y	g	J_{13}	J_{12}	J_{14}	J_{34}	Ref.
$[CuL^4]_4$	O	O	2.33	−140	−48	+134	0	*241, 251*
		S						
$[CuL^5(Cl)]_4$	Cl	Cl	2.02	−52	−28	+11	0	*242*
$[Cu_2L^6(OH)]_2^{2+}$	O	O	2.02	−142	−2	+26	0	*252*
$[CuL^7(H_2O)]_4^{4+}$	N	N	2.34	−181	+1.5	+1.5	0	*253*
	O							
$[Cu_2L^8(N_3)_3](ClO_4)_2$	N	N	2.20	−264	+2	+1	0	*254*
$[Cu_4L^9(OCH_3)_2(O_2CCH_3)Cl]$	O	O	2.09	−60	−93	+74	0	*255*
$[Cu(acac)(OCH_2Ph)]_4$	O	O	2.30	−312	0	0	0	*256*
$[Cu(dbm)(OC_2H_4OCH_3)]_4$	O	O	2.06	−104	0	0	0	*257*
$[Cu(bzac)(OC_2H_4OCH_3)]_4$	O	O	2.01	−120	0	0	0	*257*
$[Cu(Bu^t_2acac)(OC_2H_5)]_4$	O	O	2.06	−130	−27	+27	0	*258*

[a] See Fig. 32 for ligand structures. acac = acetylacetonato; bzac = benzoylacetonato; dbm = dibenzoylmethanato; Bu^t_2acac = 2,2,6,6-tetramethyl-3,5-heptanedionato.

rather than the cyclic planar $Cu_4(\mu_4\text{-OH})$ moiety, described later for McKee's related Schiff-base ligand (*262*). Actually, the Schiff-base analogue of L^9, described earlier for Ni^{II} (*234*), forms Cu_5 and Cu_6, but not Cu_4, clusters (*263*).

All examples of the parallelogram shape to date show net antiferromagnetism. The intradimer coupling is dominant; the halide-bridged system is the most weakly coupled. The out-of-plane "edge" J_{14} interaction is predominantly ferromagnetic, although it is negligible in [Cu(β-diketonato)(OR)]$_4$ examples. These later complexes are useful MOCVD precursors for CuO, needed in high-T_c superconductors, and they adopt a variety of structural types which have recently been classified (*257, 264*) in a somewhat related way to distorted-cubane classification of Haase (*265*). Indeed, a few of them, such as $[Cu(bzac)(OC_2H_4OCH_3)]_4$, adopt the distorted cubane structure of the type shown in Fig. 37 (*257*). We found that it behaved, magnetically, as a pair-of-noninteracting-dimers, with $J = -120.4\ cm^{-1}$, which is in line with the dimer–dimer Cu–O distance of 2.44 Å being much larger than the intradimer distance of 1.95 Å. Other magnetostructural correlations for the $Cu_2(OR)_2$ fragments in such molecules were made (*257*). In contrast, Wang and Thompson *et al.* (*258*), using Hatfield's general D_2-symmetry theory (*239*) to analyze similar data on a distorted-cubane complex, $[Cu(Bu^t_2$

acac)$(OC_2H_5)]_4$, found that the best fit had small interdimer parameters of equal and opposite sign. Reedijk *et al.* have also recently found dimer-of-dimer behavior in a distorted cubane Cu_4O_4 core formed with a tridentate ligand, $[Cu_4(L^8)_4(NO_3)_2(C_2H_5OH)](NO_3)_2 \cdot 3C_2H_5OH \cdot 2H_2O$; J_{13} ca. $-130\ cm^{-1}$ (*266*). One exception to the general finding of negative J_{13} values was in a complex derived from tris buffer (LH_3), $(CuLH_2(Cl)]_4$, which had a stepped structure about the Cu–OR bond within two fused $Cu_2(OR)_2$ rings. Curie-like behavior indicated $J_{13} \approx$ zero (*267*).

2. *Tetrahedral* $[Cu^{II}_4(\mu_4\text{-}O)]^{6+}$ *Cores*

This structural type has had a long and controversial career. Aspects of its magnetism were briefly reviewed by Sinn *et al.* in 1980 (*268*). Complexes of type $(Cu_4OX_6L_4)$, where X = Br, Cl and L = Br, Cl or Lewis base, have four Cu atoms tetrahedrally disposed around the central μ_4-bridging oxygen and six μ-bridging halide atoms over each edge of the tetrahedron. The L group occupies terminal positions around each Cu such that the coordination geometry is trigonal bipyramidal. In this geometry, the d^9 single-ion centers give a *d*-orbital splitting in which an orbitally degenerate $e(xz, yz)$ level lies lowest in energy with $e(x^2-y^2, xy)$ and $a(z^2)$ above. The precise ordering and energy separations are dependent on the ligand field strength around Cu. Sinn *et al.* (*268*) pointed out that the stronger ligand fields produced by L = Br or Cl allowed the μ/temperature behavior to be successfully analyzed by use of Heisenberg T_d theory. In these systems, μ decreased monotonically with decreasing temperature. For L ligands of weak to intermediate strength, the model of Lines *et al.* (*269*) was more appropriate because a broad maximum in μ, at 30–50 K, had to be simulated. In this "orbitally degenerate" model, the theory of which has, in general, long proved to be a formidable exercise [see, for instance, the work of Gerloch (*270*) on Co^{II} benzoate dimers, i.e., ${}^4T_{1g}\cdots{}^4T_{1g}$ pairs], effects such as two-center exchange Hamiltonians and antisymmetric exchange were found to be important. *J* values were defined in terms of the orbitals involved in individual ("local") exchange pathways. Lines *et al.* (*269*) employed the exchange constants J^+ and J^-, where $J^+ = J_1 + J_2$ and $J^- = J_1 - J_2$. The J_1 term involved matrix elements under an $\mathcal{H}_{ex}$ Hamiltonian between (mainly) x^2-y^2 orbitals, while J_2 involved pairs of *xz, yz* orbitals. The special case of $J^+ = J^-$ (i.e., $J_2 = 0$) reduced to the simple Heisenberg theory. The coefficient of the antisymmetric exchange energy term was defined as *D*, where $D = 2\sqrt{2}J^-/3$. Energy correlation diagrams given for the levels of this orbitally degenerate four-spin cluster were of the type *E* vs J^+/D (or D/J^+). Calculated μ vs $kT/|D|$ (or kT/J^+) plots were also given, which, depending on parameter

values, showed the characteristic maxima in μ, as observed experimentally.

Calculations for best fit, using this orbitally degenerate model, employed the parameters D, J^{+}/D, and γ^2, the last being close to 0.5 and originating in the orbital wave function, e.g., $\phi\ (\pm 2) = 2^{-1/2}(1 + \gamma^2)^{-1/2}[d_{x^2-y^2}. \ . \ . \ .]$. Inclusion of spin–orbit mixing between single-ion levels used the parameter ε_1 (usually 0.4), and this led to a scaling factor in g (or μ) of $(1 + \gamma^2 + \varepsilon_1{}^2)$, from $g = 2.0$. Lines *et al.* (*269*), and later Sinn *et al.* (*268*), compared fits on $[Cu_4OX_6(L)_4]$ species, obtained using both a Heisenberg theory model and the degenerate model. Even after allowing for intercluster ($z'J'$) exchange terms in the Heisenberg model, both groups found the degenerate model to be superior, particularly in cases showing maxima in the μ/temp plots. Two examples suffice:

$[Cu_4O(Cl)_6(OPPh_3)_4]$ (*269*): $D = 63\ cm^{-1}$, $J^{+}/D = -0.4$, $\gamma^2 = 0.46$, $\varepsilon_1 = 0.4$; hence, $J_1 \approx 19\ cm^{-1}$, $J_2 \sim -46\ cm^{-1}$.

$[Cu_4O(Cl)_6(dmso)_4]$ (*268*): $D = 61\ cm^{-1}$, $J^{+}/D = +0.14$, $\gamma^2 = 0.65$, $\varepsilon_1 = 0.4$; hence, $J_1 \approx 36\ cm^{-1}$, $J_2 \approx -28\ cm^{-1}$.

The relative signs of J_1 and J_2 were felt to be in reasonable accord with the Cu–Cl–Cu (~90°) and Cu–(μ_4–O)–Cu superexchange pathways. A recently reported example (*271*), $[Cu_4O(Cl)_6(benzimidazole)_4]$, displayed μ values which, like the py complex, were essentially independent of temperature, except for a decrease at very low temperatures. They should provide a good test for Lines theory (*269*) vis-à-vis Heisenberg theory.

Throughout the 1980s, however, a number of groups still remained skeptical about the origin of the maximum in μ values and the great variation in μ vs temperature plots for this structurally similar family of tetranuclear compounds. In addition to the intercluster interactions, single-ion orbital degeneracy, and antisymmetrical exchange effects described earlier, proposals such as nonequivalent J values arising from structural distortions (*272*); fluxional distortions (*273*); four-center Jahn–Teller effects (*274*); and four-center (biquadratic) intramolecular exchange effects (*275*) have all been made at various times.

From the experimental point of view, it was realized that the systems which showed μ_{max} behavior should display ESR lines from the (upper) coupled states, $S_T = 2$ and $S_T = 1$, at appropriate temperatures, perhaps displaying hyperfine splitting and having a characteristic temperature dependence of intensity. Theoretical calculations (*276*) and observed ESR lines from the $S_T = 2$ levels on single crystals of $[Cu_4O(Cl)_6(OPPh_3)_4]$ (*277*) and powders of $[Cu_4O(Cl)_6(quinoline)_4]$ (*278*)

were presented. However, ESR lines from $S_T = 1$ levels have not yet been observed. Perhaps this is a situation where the parallel polarization mode of even-spin line shape detection, developed in recent years by Hendrich *et al.* (*279*), would prove useful, not only in confirming the $S_T = 2$ assignments and zero-field splitting, but in locating $S_T = 1$ lines.

Recently, Blake *et al.* (*280*) have used inelastic neutron scattering methods on $[Cu_4O(Cl)_6(py)_4]$ and $[Cu_4O(Cl)_6(DMSO)_4]$, in a way similar to that used by Güdel *et al.* (*50, 70*) for Cr^{III} clusters, in order to more directly probe the spin energy levels. Two peaks at ca. 0.35 and 0.73 meV (2.8 and 5.9 cm^{-1}) neutron energy loss, with similar intensities, were observed for the py complex at 1.5 K. These were assigned to ground-state splitting arising from a combination of exchange and spin–orbit coupling. In order to simultaneously reproduce the neutron scattering peak energies and the magnetic data of Hatfield *et al.* (*281*), the combined effects of a C_{3v} distortion at very low temperature and spin–orbit coupling on the T_d Heisenberg Hamiltonian were calculated. Further, this required (*269, 282*) an antisymmetric $\Sigma_{ij} \mathbf{d}_{ij} \cdot \mathbf{S}_i \times \mathbf{S}_j$ term to be included in the Hamiltonian. A good fit for the py complex was obtained with the parameter set $g = 2.25$, $J_1 = -19.2\ cm^{-1}$, $J_2 = +33.3\ cm^{-1}$, $d_1 = d_2 = 3.5\ cm^{-1}$ (where $J_1 \equiv J_{12} = J_{23} = J_{31}$ and $J_2 \equiv J_{14} = J_{24} = J_{34}$); $E_s = -J_2[S(S + 1)] + (J_2 - J_1)[S_{123}(S_{123} + 1)]$; $\mathbf{S}_{123} = \mathbf{S}_{12} + \mathbf{S}_3$.

The ^3E level was found to be the ground level, which was split by $\mathbf{L} \cdot \mathbf{S}$ coupling into A_1 and A_2 sublevels of equal energy, with two E sublevels at 3 cm^{-1} and 6 cm^{-1}, as observed.

This lowering of effective cluster symmetry from T_d has recently gained further support. Thus, Reedijk *et al.* (*283*) observed a typical antiferromagnetic χ vs temperature plot, with a maximum at ca. 80 K, for the complex $[Cu_4O(Cl)_6(3\text{-phenyl, }4,5\text{-dimethyl-pyrazole})_4]$. They used a number of Heisenberg models to fit the data, the best being a D_4 (square) distortion yielding $g = 2.11$, $J_1 = -36\ cm^{-1}$, $J_2 = -23\ cm^{-1}$.

Krebs and Haase *et al.* (*284*) have also used a two-J model to interpret typical antiferromagnetic plots, showing decreases in μ with decreasing temperature, for two complexes $[Cu_4O(X)_4(bmmk)_2]$, where $X = Br^-$ or $C_6H_5CO_2^-$, and $bmmk^-$ is a tridentate chelating ligand, 2,6-disubstituted morpholinomethyl-4-methylphenolate. While both complexes possess the familiar $Cu_4(\mu_4\text{-}O)$ core, their structures are significantly distorted from $Cu_4(T_d)$ symmetry by the ligand combinations. In fact, the core was regarded as being made up of two Cu_2O_2 rings sharing the μ_4-O oxygen. A Heisenberg Hamiltonian, similar to that used by Kahn (*236*) for $[Cu(bipy)OH]_4^{4+}$, yielded the following parameters:

$[Cu_4O(O_2CC_6H_5)_4(bmmk)_2]$: $g = 2.01$, $J_{12} = -175$ cm^{-1}, $J_{13} = -18$ cm^{-1} (where J_{12} corresponds to the Cu_2O_2 rings and J_{13} to peripheral bridging).

$Cu_4O(Br)_4(bmmk)_2$: $g = 2.19$, $J_{12} = -296$ cm^{-1}, $J_{13} = -36$ cm^{-1}.

Energy level diagrams showed that J_{13} could not be obtained accurately because the levels affected by it were barely populated, even at 500 K. Only the $S_T = 0$ (ground) and $S_T = 1$ levels were populated.

Some thoughts from the present author for future investigations of $Cu_4(\mu_4\text{-O})$ clusters include the use of variable-field/variable-temperature measurements, at temperatures around and below μ_{max} values for those systems showing such behavior. In combination with the thermodynamic calculations of susceptibilities [Eq. (12)], such data should help sort out the nature and splitting of ground states and the occurrence of multiple J values brought about by structural distortions. Lines *et al.* (*269*) briefly mentioned that field-dependent values of μ were noted only between 4.2 and 1.5 K in $[Cu_4O(X)_6(L)_4]$ clusters. This is in line with the inelastic neutron scattering data (*280*), but it is a feature perhaps worthy of further study. We have, for instance, recently been able to calculate field-dependent μ_{max} behavior observed in a ferromagnetically coupled Cu^{II}_6 hexanuclear cluster in terms of thermal population of Zeeman sublevels derived from a $S_T = 3$ ground state, separated by only a few cm^{-1} from higher-lying $S_T = 2$ and 1 states (*285*). Raman spectroscopic measurements on these $[Cu_4OX_6L_4]$ clusters might reveal spin–orbit splitting effects (so-called electronic Raman bands). Finally, if he has not already done so, it would be worthwhile for Belinskii to revisit (*286*) these clusters using his latest calculational methods, developed for $[Mn^{III}_3Mn^{IV}]$ and $[Fe_4S_4]^{x+}$ species (see Sections III,D and E), in order to quantify the effects of core distortions, spin–orbit coupling and, perhaps, the exchange-induced mixing of states.

3. *Halide- and Carboxylate-Bridged Linear Tetranuclear Clusters*

Apart from the halide-bridged $[Cu_4O(X)_6L_4]$ clusters just described, and an example in Table VII, there are a number of anionic Cu halide clusters of the type much studied by Willett and co-workers (*287*). The complexes $(R_4N)_2[Cu_4X_{10}]$ and $[Cu_4Cl_8terpyridine_2]$, respectively (*288, 289, 291*), contain linear and almost-linear chains of the kind shown in Fig. 36. The two-J Heisenberg theory of susceptibility and eigenvalues were given by Willett *et al.* (*288*). J_{14} coupling was assumed to be zero, and intertetramer interactions likewise. The best-fit parameters are given in Table VIII. It should be noted that while positive values are listed, "inner" J_2 parameters could not be established accurately for the $S_T = 0$ ground state $[Cu_4X_{10}]^{2-}$ compounds. The best-fit parame-

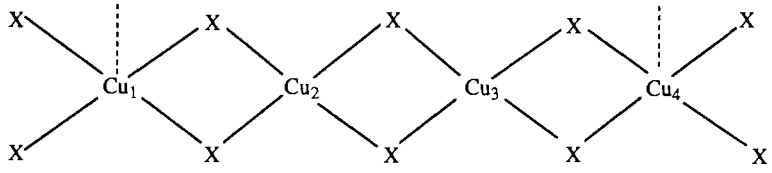

$$\mathcal{H}_{ex} = -2J_1(S_1.S_2 + S_3.S_4) - 2J_2(S_2.S_3)$$

FIG. 36. Structural representation and exchange-coupling scheme for linear cluster $[Cu_4Cl_{10}]^{2-}$ (*288*).

ters for the neutral complex, $[Cu_4Cl_8terpy_2]$, yield a set of zero-field energies with an $S_T = 0$ ground level just 4 cm^{-1} below an $S_T = 1$. Then a gap of 112 cm^{-1} separates an $S_T = 0$, with the remaining levels placed within 150 cm^{-1} of the ground (*289*). The corresponding μ/T plot was, therefore, different from those for the other complexes listed. Nevertheless, it was possible to make magnetostructural correlations, for the outer Cu_2X_2 fragments, between J_1 and features such as Cu–X–Cu angles, bifold angles, and Cu–X distances (*287, 288*). The $[Cu_4Cl_{12}]^{4-}$ example showed net ferromagnetic coupling, but its structural features were markedly different from those of $[Cu_4Cl_{10}]^{2-}$ (*290*).

Two recently synthesized μ-carboxylato analogues, $[Cu_4L^{11}{}_2(O_2CCH_3)_6]$ (*292*) and $[Cu_4L^{12}{}_2(O_2CCH_3)_6(H_2O)_6]_n$ (*293*), have had their magnetism analyzed by the approach of Willett *et al.* (*288*). The latter

TABLE VIII

BEST-FIT PARAMETERS FOR HALIDE-BRIDGED "LINEAR" TETRANUCLEAR Cu(II) SPECIES

Complex[a]	g	J_1 (cm^{-1})	J_2 (cm^{-1})	Cu–Cl–Cu outer (°)	r(Cu–μ–X) (Å)	Ref.
$(4MAP)_2[Cu_4Cl_{10}]$	2.16	−43	+25	94.5	2.276	*288*
$((CH_3)_4N)_2[Cu_4Cl_{10}]$	2.09	−42	+18	94.6	2.294	*288*
$[Cu_4Cl_8terpy_2]$	2.05 (g_1) 2.31 (g_2)	−9	−48	—	—	*289*
$((C_2H_5)_4N)_4[Cu_4Cl_{12}]$	—	+7[b]	+7[b]	95.5 88.3	2.402	*290*
$((CH_3)_3NH)_2[Cu_4Br_{10}]$	—	−130	—	94.8	2.445	*291*

[a] 4 MAP = 4-methyl-2-aminopyridinium; terpy = 2,2′:6′,2″-terpyridine.
[b] Not accurately evaluated.

complex provided a precursor chemical for $YBa_2Cu_3O_{7-x}$ superconducting materials. The L^{11} complex showed a gradual decrease in μ (per Cu_4) from 3.21 μ_B at 290 K to 2.53 μ_B at 80 K, then a plateau until 10 K, below which μ rapidly decreased toward zero. In contrast to the assumption made by Willett *et al.* (*288*) of zero $Cu_1 \cdots Cu_3$ and $Cu_1 \cdots Cu_4$ interactions (Fig. 36), Piovesana *et al.* (*292*) included all such terms in their calculations of χ and of the six S_T energy levels. Exploration of a number of possible fits and spin frustration situations led to a grouping of states at energy $-2J_2$ of ca. -320 cm^{-1} (for $g = 2.1$) and two low-lying states, an $S_T = 0$ ground-state, with an $S_T = 1$ some 3.5 cm^{-1} above it. This situation and the corresponding μ/T plot are similar to those found for $[Cu_4Cl_8terpy_2]$, described earlier, which was analyzed by a two-J approximation. It was concluded that the 3.5 cm^{-1} separation was determined primarily by a $-2J_4(\mathbf{S}_1 \cdot \mathbf{S}_4)$ interaction—that is, a coupling from end-to-end, a fourth-neighbor interaction. The best fit for the L^{11} complex was $g = 2.1$, J_1 = ill-defined, $J_2 \simeq -160$ cm^{-1}, J_3 = ill-defined, $J_4 = -1.75$ cm^{-1}. The structure of this complex consists of a $\{Cu_2\ acetate_4\}$-like central portion [$r(Cu_2 \cdots Cu_3) = 2.63$ Å], with axial positions bridged, asymmetrically, by acetate groups to terminal CuL^{11} fragments [$r(Cu_1 \cdots Cu_2) = 4.62$ Å]. A continuous, albeit unsymmetrical, $Cu_1 \cdots acetate \cdots Cu_4$ superexchange pathway therefore exists, and consideration of orbital overlap of the type $Cu_1(z^2) \cdots Cu_2(x^2-y^2)$ predicts a very weak J_4 value, as deduced. Since the equally small $\Delta[(S_T = 1) - (S_T = 0)]$ separation in the $[Cu_4Cl_8terpy_2]$ systems was calculated with J_4 equal to zero, this fourth-neighbor interaction postulate perhaps remains tentative. However, we (*294*), and others (*219*) have observed third-neighbor interactions in linear trinuclear systems, across distances of ca. 7.2 Å, even when continuously delocalized ligand pathways were not available.

Two two-J fit obtained by Wang *et al.* (*293*) for the L^{12} complex was $g = 2.23$, $J_1 = -85.6$ cm^{-1}, $J_2 = +13.1$ cm^{-1}. In this zigzag structure, the Cu_1 and Cu_2 atoms were doubly bridged by μ-alkoxo (from L^{12}) and μ-1,2-acetato groups, with $r(Cu_1 \cdots Cu_2) = 3.49$ Å, while Cu_2 and Cu_3 were doubly bridged by μ-1,1-acetato groups, with $r(Cu_2 \cdots Cu_3) = 3.54$ Å. Another interesting complex prepared by Latour *et al.* (*249a*) used a binucleating Schiff-base derived from 2-aminoethylpyridine and 2,3-dihydroxybenzaldehyde. Within each binuclear fragment one Cu is coordinated within the catecholate $(O)_2$ chelating site while the other is in the tridentate (N_2O) site, the bridging groups being the phenolate oxygen and two exogenous μ-1,2-acetates. The binuclear fragments are bridged centrosymmetrically by the 3-phenolato oxygen atoms such that this *inter*–$Cu \cdots Cu$ distance (i.e., $Cu_2 \cdots Cu_3$ in Fig. 36) is shorter

than the *intra*–Cu···Cu distance $Cu_1 \cdots Cu_2$. The μ vs temperature plot for this complex levelled off to a plateau value below 100 K appropriate to the presence of two non-interacting $S = \frac{1}{2}$ centers i.e., Cu_1 and Cu_4. Above 100 K, an increase in μ originated from antiferromagnetic *inter*-dimer coupling, with J_2 being -130 cm^{-1}. The lack of *intra*dimer coupling was ascribed to a folding between the Cu_1 and Cu_2 basal planes. The magnetic data are generally similar to those noted in Section III,B for a vanadyl Schiff-base complex (*62*). Other related zigzag structures include $[Cu_4Cl_{12}]^{4-}$ and $[Cu_4Cl_8terpy_2]$.

4. Planar Cyclic Cu_4 Cores

The design of tetranucleating chelating ligands and of their tetranuclear complexes has advanced rapidly in recent years, particularly through the work of McKee *et al.* (*99, 100, 262*) and Robson *et al.* (*233, 234, 263*), who have made 4 + 4 Schiff-base macrocycles by linking 2,6-diformyl(4-alkyl)phenol or 2,6-diacetylpyridine groups with diamino-alcohol or diamino-phenol spacers, either directly or by alkaline-earth template condensations. More recently, Robson *et al.* (*261*) have made the fully reduced tetraamino-tetraphenolic macrocycles and their metal complexes. The extra flexibility in this more saturated framework made the Cu^{II}_4 species noncoplanar. The magnetism of the parallelogram-like cluster has been discussed in Section III,H,1. These and related tetranuclear compounds are important in bioinorganic modeling, multi-electron transfer, catalytic, and new extended-materials studies, as well as in magnetochemical investigations.

The planar $Cu^{II}_4(\mu_4\text{-OH})$ core in $[Cu^{II}_4L^{13}(OH)](NO_3)_3 \cdot 3H_2O$ showed antiferromagnetic coupling, with μ(per Cu_4) decreasing from 2.51 μ_B at 300 K to 0.74 μ_B at 6 K (*262*). Slightly stronger coupling was observed for the related "dimeric" octacopper(II) complex, $[Cu^{II}_4L^{14}(\mu_5\text{-}O)(ClO_4)]_2(ClO_4)_4$. No detailed analyses are yet available, but they may turn out to be similar to that recently given by Chaudhuri *et al.* (*295*), for $[tacn_4Cu_4(imidazolate)_4]^{4+}$. In that complex, μ (per Cu_4) decreased monotonically from 3.39 μ_B at 295 K to 0.33 μ_B at 2 K, while the χ/T plot showed a maximum at ca. 75 K. A one-J D_{4h} Heisenberg analysis was used, which is reasonable in the light of no central bridging atom and an assumption of negligible third-neighbor coupling. A best fit g of 2.16 was similar to the ESR value, and J was -35 cm^{-1}. The energy levels for such an $S = \frac{1}{2}$ system are well isolated, with separations dependent only on S_T. The levels are $S_T = 0$ (ground), $S_T = 1$ (at $E = 2J$), $S_T = 1,1$, and 0 ($E = 4J$), and $S_T = 2$ ($E = 6J$). The Zeeman sublevels are all thermally populated at room temperature.

Pioneering work on a cyclic imidazolate-bridged tetramer was

done by Kolks and Lippard (*296*). The complex $[Cu_2L^{15}(im)]_2(NO_3)_4 \cdot 4H_2O$ displayed a rectangular cyclic structure with no diagonal bridging groups. Fitting of the χ data to the Jotham and Kettle two-J model calculations (*243*) yielded $g = 2.13$, $J_1 = -87.6$ cm^{-1}, $J_2 = -35$ cm^{-1}. Comparison with dinuclear Cu_2L^{15} data showed that J_1 corresponded to the {CuL^{15}Cu} = bridged edge, while J_2 corresponded to the {Cu(im)Cu} edge, its value being the same as in the tacn analogue (*295*). Detailed arguments on superexchange pathways involving Cu(im)Cu bridges were given (*296*), which were relevant to Cu(im)Zn pathways in the enzyme superoxide dismutase. Very recently, Nonoyama *et al.* (*297*) have made square tetranuclear compounds containing binucleating imidazole-4,5-dicarboxyamide ligands and found J values of ca. -60 cm^{-1}.

Thompson *et al.* (*298*) have recently made an interesting series of planar-rectangular copper(II) clusters by use of tetranucleating tetrapyridylbenzodipyridazine ligands. In essence, a central aromatic ring bridges between two {μ-hydroxo, μ-diazino} copper(II) dimers such that the tetranuclear array is coplanar, with an interdimer distance some four times longer than the intradimer distance (ca. 3.2 Å). All the compounds showed strong antiferromagnetic coupling, with a decrease in the small observed χ values occurring between 300 and 100 K, much as in related dinuclear species, followed by a low-temperature increase in χ due to monomer impurity. An isotropic Heisenberg model based on rectangular, D_2, symmetry was employed, again using the energy levels deduced by Jotham and Kettle (*243*) via matrix diagonalization techniques. The short-edge J_1 term was dominant, and the long-edge and diagonal terms were assumed equal on account of similar bridging pathways. Taking one typical structurally characterized example, $[Cu_4(L^{16})(\mu_2\text{-}OH)_2(H_2O)_8](CF_3SO_3)_6$, the best-fit parameters were (*298*) $g = 2.04$, J_1(short-edge) $= -167$ cm^{-1}, J_2(long edge) $= -60$ cm^{-1}. Even though the least-square fittings were not very sensitive to small changes in the J values, it was significant that cross-ring coupling can occur across some eight bonds, presumably via a π-delocalization mechanism.

Wang *et al.* (*299*) extended their linear tetranuclear $Cu_4L^{12}{}_2$ species to encompass a series of cyclic planar complexes of type $[Cu^{II}{}_4L_2{}^{12}(\mu\text{-}O_2CCH_3)_4](PF_6)_2$, in which opposing pairs of copper are bridged by {μ-alkoxo(L^{12}), μ-acetato} and μ-acetato groups, the corresponding Cu···Cu separations being 3.43 Å and 3.30 Å. While the magnetic properties were not reported for this complex, they were for the mixed-metal compound of formula $[Cu^{II}{}_4L^{12}{}_2(\mu\text{-}O_2CCH_3)_2(\mu\text{-}OH)_2](Hg(O_2CCH_3)Cl_2)_2(HgCl_2)$, which formed a polymeric structure involving

linking of $[Cu_4L^{12}{}_2]$ units by diamagnetic $Hg^{II}{}_3$ chains. The χ/T plot for this compound was, somewhat worryingly, dependent on field (H = 0.05 to 0.7 tesla) at all temperatures. Nevertheless, the lowest-field plot showed strong antiferromagnetic features with a broad maximum in χ at ca. 350 K. It was analyzed by a three-J rectangular model and gave g = 2.19, J_1(short-edge) = -186 cm^{-1}, J(diag) = $+39.7$ cm^{-1}, J(long-edge) = -4.4 cm^{-1}. The dominant short-edge interaction was assumed equivalent to Cu(μ-OH)(μ-O_2CCH_3)Cu rather than Cu(μ-OR)Cu pathways, while the ferromagnetic interaction was thought to originate from out-of-plane dimer···dimer-like interactions of the type discussed in Section III,H,1.

5. Pair-of-Dimer $(Cu_2)_2$ Structures

In contrast to the coplanar $(Cu_2)_2$ moiety existing in Thompson's bis-diazine system, described earlier (*298*), a number of noncoplanar/noninteracting $(Cu_2)_2$ assemblies have recently been synthesized. In our own work, we have adopted two synthetic strategies. The first has involved linking together two binuclear $[L^{17}Cu^{II}{}_2]^+$ fragments at the exogenous positions by dipyrazolato bridging groups. The structure of one such example, $[(Cu_2L^{17})_2(mdpz)]$, is given in Fig. 37 and shows a large twisting around the central C(20)–C(42) bond of ~68°, generated by the steric interactions of methyl groups on the 4,4′-di-3,5-dimethylpyrazolate rings (*300*). The r(Cu···Cu) distances in the LCu_2 "end-groups" are much like those in dinuclear analogues (*252*), 3.37 Å, while the cross-dipyrazole Cu···Cu separations are ca. 10 Å. Interestingly, as often is the case in Cu(II) salicylideneimines (*301*), intermolecular Cu···Cu separations of ca. 3.7 Å occur between neighboring $[Cu_2L^{17}(mdpz)]_2$ molecules in the crystal lattice brought about by Cu–O (phenolate) bridging interactions. This intermolecular aggregation affected the magnetic behavior, which, while dominated by the strong intramolecular coupling in the binuclear end groups (J = -190 cm^{-1}, g = 2.05), required a "dimer···dimer" exchange parameter of ca. -20 cm^{-1} to improve the fit. There was, of course, no cross-pyrazole intramolecular coupling. Homotetranuclear $[Ni_2L^{17}(mdpz)]_2$ and heterotetranuclear $[(NiCuL^{17})_2mdpz]$ compounds have also been made, the former being diamagnetic (*218*). The second synthetic approach was to make pseudolinear pair-of-dimers structures by joining the endogenous Schiff-base backbone using a disalicylaldehydo-methane spacer. Thus, compounds of formula $[Cu^{II}{}_4L^{18}(\mu\text{-pyrazolate})_2]$ have been made and show antiferromagnetic coupling (*300*). Lintvedt *et al.* (*301a*) used a related approach to obtain an hexaketonato complex in which a 1,3-benzene spacer was employed to link together two [Cu_2 triketonato$_2$]

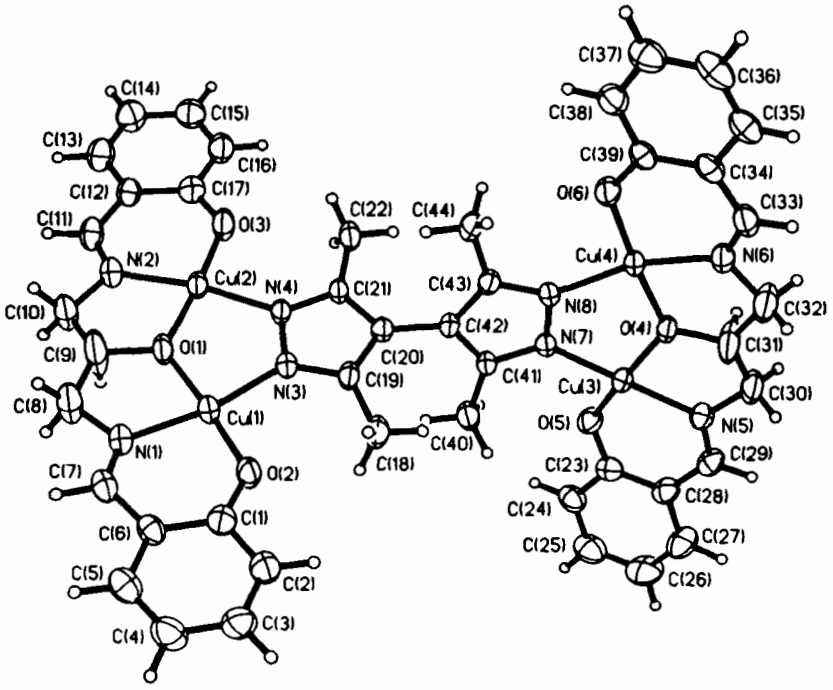

FIG. 37. Structure of $[(Cu_2L^{17})_2\ (mdpz)]$ (*300*).

moieties, the Cu···Cu distance in the latter being much shorter (3.02 Å) than the cross-spacer distance of 6.9 Å. The antiferromagnetic coupling is extremely strong in this overall planar complex such that it was found to be diamagnetic even at room temperature. Other pseudo-linear pair-of-dimer designs, including heterotetranuclear species, have recently been reviewed (*40a*).

Thompson *et al.* (*302*) have also made a number of "pair-of-noninteracting-dimers" structures. In $[Cu_2L^{19}(\mu_3\text{-}OH)(NO_3)_3(H_2O)]_2$, the four Cu atoms are linked by both diazine and pyramidal μ_3-OH bridges, thus forming a central $Cu_2(\mu_3\text{-}OH)_2$ ring with Cu···Cu separations similar to those in the Cu_2L^{19} moieties. A one-J dimer model was adequate to fit the data, yielding $g \approx 2.04$, $J = -156\ cm^{-1}$—values similar to those found in authentic dimers of this ligand. Somewhat similar dimer-of-dimer complexes were made involving μ_3-methoxo bridges (*303*) in very strongly coupled complexes of type $[Cu_4(L^{20})_2(\mu_3\text{-}OCH_3)_2(\mu_2\text{-}Cl)_2Cl_2]$. The featureless and tiny χ values in the χ/T plot led to a best-fit parameter set of $g = 2.04$ and $J = -411\ cm^{-1}$, for the intradimer interactions, with an interdimer θ value [in $(T\text{-}\theta)$] of +4 K, indicative

of weak ferromagnetic coupling via the 90° Cu–O–Cu and Cu–Cl–Cu pathways. Structures of this parallelogram type have also been discussed in Section III,H,1 by use of the coupling model shown in Fig. 33.

These polynucleating macrocyclic ligands sometimes have a mind of their own and do not form the desired tetranuclear species. Thus, under certain conditions, ligands of type $L^{13}H_4$ or $L^{14}H_4$, which contain short-chain alcohol backbones, do not deprotonate at the secondary alcohol moiety. They form polymeric species with Cu(II) halides or azides, probably because of the small macrocyclic ring size (*304*). Somewhat similar effects were alluded to earlier in regard to the tetraphenolic Schiff-base macrocycles (*263*), and we have had related experiences with open-chain analogues (*305*).

6. *Trigonal-Shaped Heterotetranuclear Species*

Oxamido bridging ligands of the type much used by Kahn (*7, 35*) and Nonoyama (*297*) have been assembled around lanthanide(III) ions in complexes of type $(Cu^{II}\ \text{oxamide})_3Ln(ClO_4)_3$ (*306*). The structural type has been discussed in Section III,C,e and in Fig. 14. A Gd^{III} example showed weak ferromagnetic coupling with $J_{GdCu} = +2.7\ cm^{-1}$ and a ground spin state $S = 5$. Structural data are required on these compounds since a second $(Cu^{II}\ \text{oxamide})_3Gd^{III}$ complex was found to display antiferromagnetic behavior (*306*).

IV. Conclusions

This survey has shown the tremendous amount of growth that has occurred over the last 25 years or so in our understanding of exchange-coupled clusters, the tetranuclear class providing the present focus. It is an area which has brought together the skills and imagination of the synthetic chemist and the mathematical abilities and instrumental expertise of the theoretician and physicist. The subdisciplines of biophysics and magnetic materials have received a clear benefit, which will increase, from the understanding gained of mixed-valent Mn and Fe–S clusters, and of mixed-metal clusters, the latter often showing spin-frustration phenomena and high-spin ground states.

In traversing the first-row *d*-block, we have seen the following:

(i) Ti and V clusters remain relatively unexplored, probably because of difficulties in synthesis and stability.

(ii) Cr^{III} tetramers have had their magnetochemical features well

established and show good scope, through their kinetic stability, for the production of new mixed-metal and high-spin clusters.

(iii) Tetranuclear Mn cluster chemistry has grown tremendously in the last 10 years and has revealed a fascinating array of topologies and valency combinations. It has been spurred on by attempts to model the WOC center of photosystem II and, interestingly, has often involved the use of relatively simple chelating ligands in the synthesis of low–molecular-weight models. Fitting the susceptibility and magnetization data, particularly for those of the mixed-valent clusters, has required a detailed understanding of Heisenberg exchange theory, tensor operators, and matrix diagonalization techniques. A full understanding of the peculiar magnetic and ESR features of the *S*2 oxidation level of the WOC will soon emerge from this concentrated research effort.

(iv) There have been two broad areas of growth in tetranuclear Fe systems, one in Fe–oxo clusters and one in Fe–S clusters. The magnetic features of small Fe–oxo clusters are presently being used to provide a basis for trying to understand the much more complicated behavior (e.g., metamagnetism) of the very large clusters and extended lattices which occur in Fe biominerals and in iron oxide/hydroxide (nanoscale) magnetic materials. The variable ground-state properties observed via magnetic and Mössbauer measurements on synthetic Fe–S tetranuclear complexes have recently been rationalized by means of Heisenberg and double-exchange theory, combined with subtle nuances such as cluster distortions and the exchange-induced mixing of spin states. The same interpretation applies to the many ferredoxin and HIPIP protein samples, although in some cases, an equilibrium between distorted clusters has been involved.

(v) Co_4 and Ni_4 systems were largely investigated in the 1970s. The use of tetranucleating organic ligands and polyoxometallate hosts is now leading to some interesting new topologies and behavior. Anisotropic exchange in Co^{II} clusters is not well understood and provides a challenge for the future in both theory and experiment, e.g., on single crystals.

(vi) Cu^{II}_4 cluster chemistry continues to flourish, particularly in the areas of new ligand designs and biocopper model studies. While the magnetism is by and large well understood, it remains to be seen if this large array of compounds will provide new and useful applications in reactivity (e.g., redox and small molecule binding), catalysis, etc.

The pioneers of cluster magnetochemistry, whose work in the period 1960–1970 has been cited, can be well pleased with the subsequent growth in, and wide scope of, their subject.

ACKNOWLEDGMENTS

The author gives special thanks to Kevin Berry for his great contributions to theoretical aspects of this work. The help provided by the following colleagues is gratefully acknowledged: Dr. Boujemaa Moubaraki, Dr. Gary Fallon, Adrian van den Bergen, Scott Courtney, Margaret Hodgkinson, and Liza Verdan. Drs. Richard Robson, Antony Blake, Paul Krüger, and Sergiu Gorun are thanked for kindly providing unpublished data. Professor Tony Wedd and colleagues at the University of Melbourne are thanked for hosting the author on a study leave. The financial support for the author's research work that is reported herein is provided by an Australian Research Council Large Grant and an Australian Research Council Post-doctoral Fellowship (to Dr. Moubaraki).

REFERENCES

1. "Magnetostructural Correlations in Exchange Coupled System", NATO ASI Series C; Willett, R. D.; Gatteschi, D.; Kahn, O., Eds.; D. Reidel: Dordrecht, 1985; Vol. 140.
2. "Metal Clusters in Proteins", ACS Symposium Series; Que, L. Jr., Ed.; American Chemical Society: Washington, D.C., 1988; Vol. 372.
3. See a series of articles: Physics and Chemistry of Metal Clusters in Biology, *New J. Chem.;* Girerd, J. J., Ed.; **1991,** *15,* 407.
4. "Magnetic Molecular Materials", NATO ASI Series; Gatteschi, D.; Kahn, O.; Miller, J. S.; Palacio, F., Eds.; Kluwer Academic: Dordrecht, 1991; Vol. 198.
5. Day, E. P.; Sendova, M. S. In "Research Frontiers in Magnetochemistry", O'Connor, C. J., Ed.; World Scientific: Singapore, 1993; 395–415.
6. Trautwein, A. X.; Bill, E.; Bominaar, E. L.; Winkler, H. *Struct. Bonding* **1991,** *78,* 1.
7. Kahn, O. "Molecular Magnetism"; V.C.H.: New York, 1993.
8. O'Connor, C. J. Ed. "Research Frontiers in Magnetochemistry"; World Scientific: Singapore, 1993.
9. Que, L. Jr.; True, A. E. *Progr. Inorg. Chem.* **1990,** *38,* 97.
10. Noodleman, L.; Case, D. A. In "Advan. Inorganic Chem.", Cammack, R.; Sykes, A. G., Eds.; 1992; Academic Press: San Diego, Vol. 38, 424.
11. McCusker, J. K.; Schmitt, E. A.; Hendrickson, D. N. In "Magnetic Molecular Materials", NATO ASI Series E; Gatteschi, D.; Kahn, O.; Miller, J. S.; Palacio, F., Eds.; 1991; Vol. 198, 297–319.
12. Hendrickson, D. N. In "Research Frontiers in Magnetochemistry", O'Connor, C. J., Ed.; World Scientific: Singapore, 1993; 87–108.
13. See a series of articles in "Advan. Inorganic Chem.", Cammack, R.; Sykes, A. G., Eds.; 1992; Academic Press: San Diego, Vol. 38.
14. Rees, D. C.; Chan, M. K.; Kim, J. In "Advan. Inorganic Chem.," Sykes, A. G., Ed.; Academic Press: San Diego, 1993; Vol. 40, 89.
15. Messerschmidt, A. In "Advan. Inorg. Chem.," Sykes, A. G., Ed.; Academic Press: San Diego, 1993; Vol. 40, 121.
16. Solomon, E. I.; Baldwin, M. J.; Lowery, M. D. *Chem. Rev.* **1992,** *92,* 521.
17. Babcock, G. T.; Wikström, M. *Nature (London)* **1992,** *356,* 301.
18. Malmstrom, B. G. *Chem. Rev.* **1990,** *90,* 1247; *Acc. Chem. Res.* **1993,** *26,* 332.
19. Brunori, M.; Antonini, G.; Giuffre, A.; Malatesta, F.; Nicoletti, F.; Sarti, P.; Wilson, M. T. *FEBS Lett.* **1994,** *350,* 164.

20. A series of articles on cytochrome C oxidase that appeared in *J. Bioenerg. Biomembr.* **1993,** *25,* 69–188.
21. Wieghardt, K., *Angew. Chem., Intl. Edn. Engl.* **1994,** *33,* 725.
22. Andreasson, L.-E.; Vänngard, T. In "Encyclopedia of Inorganic Chemistry", King, R. B., Ed.; Wiley: Chichester, 1994; Vol. 4, 2101–2111.
23. Gatteschi, D.; Caneschi, A.; Pardi, L.; Sessoli, R. *Science* **1994,** *265,* 1054.
24. Gatteschi, D. *Adv. Mater.* **1994,** *6,* 635.
25. Delfs, C. D.; Gatteschi, D.; Pardi, L. *Comments Inorg. Chem.* **1993,** *15,* 27.
26. Gatteschi, D.; Pardi, L. In "Research Frontiers in Magnetochemistry", O'Connor, C. J., Ed.; World Scientific: Singapore, 1993; 67–86.
27. Sessoli, R.; Tsai, H.-L.; Schake, A. R.; Wang, S., Vincent, J. B.; Folting, K.; Gatteschi, D.; Christou, G.; Hendrickson, D. N. *J. Am. Chem. Soc.* **1993,** *115,* 1804.
28. Dubicki, L., Ph.D. thesis, University of Melbourne, 1968.
29. Dubicki, L.; Kakos, G.; Winter, G. *Austral. J. Chem.* **1968,** *21,* 1461.
30. Gruber, S. J.; Harris, C. M.; Sinn, E. *J. Inorg. Nucl. Chem.* **1968,** *30,* 1805.
31. Martin, R. L., In "New Pathways in Inorganic Chemistry", Ebsworth, E. A. V.; Maddock, A. G.; Sharpe, A. G., Eds.; Cambridge University Press: Cambridge, 1978, Chap. 9.
32. Sinn, E. *Coord. Chem. Rev.* **1970,** *5,* 313.
33. Griffiths, J. S. *Struct. Bonding* **1972,** *10,* 87.
34. O'Connor, C. J. *Progr. Inorg. Chem.* **1982,** *29,* 203.
35. Kahn, O. *Struct. Bonding* **1987,** *68,* 89.
36. Hotzelmann, R.; Wieghardt, K.; Flörke, U.; Haupt, H.-J.; Weatherburn, D. C.; Bonvoisin, J.; Blondin, G.; Girerd, J.-J. *J. Am. Chem. Soc.* **1992,** *114,* 1681.
37. Ginsberg, A. *Inorg. Chim. Acta Rev.* **1971,** *5,* 45.
38. Drillon, M.; Darriet, J. *Struct. Bonding* **1992,** *79,* 55.
39. Mabbs, F. E.; Machin, D. J. "Magnetism and Transition Metal Complexes"; Chapman and Hall: London, 1973.
40. Carlin, R. L. "Magnetochemistry"; Springer–Verlag: Berlin, 1986.
40a. Guerriero, P.; Tamburini, S.; Vigato, P. A. *Coord. Chem. Rev.* **1995,** *139,* 17.
41. Kambe, K. *J. Phys. Soc. Jpn.* **1950,** *5,* 48.
42. Andersen, P.; Damhus, T.; Pedersen, E.; Petersen, A. *Acta. Chem. Scand.* **1984,** *A38,* 359.
43. Berry, K. J.; Clark, P. E.; Murray, K. A.; Raston, C. L.; White, A. H. *Inorg. Chem.* **1983,** *22,* 3928.
44. Gatteschi, D., Pardi, L. *Gazz. Chim. Ital.* **1993,** *113,* 231.
45. Silver, B. L. "Irreducible Tensor Methods, An Introduction for Chemists"; Academic Press: New York, 1976.
46. Rotenborg, M.; Bivins, R.; Metropolis, N.; Wooten, J. K., Jr. "The 3-j and 6-j Symbols" M.I.T. Press: Cambridge, 1959.
47. Wigner, E. P. "Group Theory and Its Application to the Quantum Mechanics of Atomic Spectra"; Academic Press: New York, 1959.
48. Fano, U.; Racah, G. "Irreducible Tensorial Sets" Academic Press: New York, 1959.
49. Gerloch, M. "Magnetism and Ligand-Field Analysis"; Cambridge University Press: Cambridge, 1983; Chap. 8.
50. Güdel, H. U.; Hauser, U.; Furrer, A. *Inorg. Chem.* **1979,** *18,* 2730.
51. Vermaas, A.; Groenveld, W. L. *Chem. Phys. Lett.* **1974,** *27, 583.*
52. Van Vleck, J. H. "The Theory of Electric and Magnetic Susceptibilities", Oxford University Press: London, 1932.
53. Kennedy, B. J.; Murray, K. S. *Inorg. Chem.* **1985,** *24,* 1552.

54. Chaudhuri, P.; Birkelbach, F.; Winter, M.; Staemmler, V.; Fleischauer, P.; Haase, W.; Flörke, U.; Haupt, H-J. *J. Chem. Soc., Dalton Trans.* 1994, 2313.
55. Stumpf, H. O.; Ouhab, L.; Pei, Y.; Bergerat, P.; Kahn, O. *J. Am. Chem. Soc.* **1994,** *116,* 3866.
56. Kahn, O.; Pei, Y.; Journaux, Y. In "Inorganic Materials", Bruce, D. W.; O'Hare, D., Eds.; Wiley: Chichester, 1992; 60–115.
57. Day, P. *Science* **1993,** *261,* 431.
58. Ibers, J. A. *Nature (London)* **1963,** *197,* 686.
59. Wieghardt, K.; Ventur, D.; Tsai, Y. H.; Krüger, C. *Inorg. Chim. Acta* **1985,** *99,* L25.
60. Kakos, G. A.; Winter, G. *Austral. J. Chem.* **1970,** *23,* 15.
61. Taft, K. L.; Caneschi, A.; Pence, L. E.; Delfs, C. D.; Papaefthymiou, G. C.; Lippard, S. J. *J. Am. Chem. Soc.* **1993,** *115,* 11753.
62. Hughes, D. L.; Kleinkes, U.; Leigh, G. J.; Maiwald, M.; Sanders, J. R.; Sudbrake, C. *J. Chem. Soc., Dalton Trans.* **1994,** 2457.
63. Wentworth, R. A. D.; Saillant, R. *Inorg. Chem.* **1967,** *6,* 1436.
64. Flood, M. T.; Barraclough, C. G.; Gray, H. B. *Inorg. Chem.* **1969,** *8,* 1855.
65. Barraclough, C. G.; Gray, H. B.; Dubicki, L. *Inorg. Chem.* **1968,** *7,* 844.
66. Flood, M. T.; Marsh, R. E.; Gray, H. B. *J. Am. Chem. Soc.* **1969,** *91,* 193.
67. See reference to work of Jasiewicsz, B.; Rudolf, M. F.; Jezowska-Trebiatowska, B. *Pr. Nauk. Inst. Chem., Nieorg. Met., Pierwiastkow Rzadkich. Politech. Wroclaw* **1973,** *16,* 155 In König, E.; König, G. Landolt-Börnstein Tables New Series, Group II, "Magnetic Properties of Coordination and Organometallic Compounds. Subvolume A"; Springer–Verlag: Berlin, 1984; Vol. 12, Suppl. 4.
68. Güdel, H. U.; Hauser, U. *J. Solid State Chem.* **1980,** *35,* 230.
69. Güdel, H. U. *Comments Inorg. Chem.* **1984,** *3,* 189.
70. Furrer, A.; Güdel, H. U.; Hauser, U. *J. Appl. Phys.* **1979,** *50,* 2043.
71. Bonner, J. C.; Kobayashi, H.; Tsujikawa, I.; Nakamura, Y.; Friedberg, S. A. *J. Chem. Phys.* **1975,** *63,* 19.
72. Bossek, U.; Wieghardt, K.; Nuber, B.; Weiss, J. *Angew Chem., Intl. Edn.* **1990,** *29,* 1055.
73. Hodgson, D. J. In "Magnetostructural Correlations in Exchange-Coupled Systems", NATO ASI Series C; Willett, R. D.; Gatteschi, D.; Kahn, O., Eds.; Reidel: Dordrecht, 1985; Vol. 140, 497–522.
74. (a) Springborg, J. In "Adv. Inorg. Chem.", Sykes, A. G., Ed.; Academic Press: San Diego, 1988; Vol. 32, 55. (b) Andersen, P. *Coord. Chem. Rev.* **1989,** *94,* 47.
75. Glerup, J.; Hodgson, D. J.; Pedersen, E. *Acta Chem. Scand.* **1983,** *A37,* 161.
76. Glerup, J.; Weihe, H.; Goodson, P. A.; Hodgson, D. J. *Inorg. Chim. Acta* **1993,** *212,* 281.
77. Hodgson, D. J. *Progr. Inorg. Chem.* **1975,** *19,* 173.
78. Cannon, R. D.; White, R. P. *Progr. Inorg. Chem.* **1988,** *36,* 195.
79. Blake, A. B.; Yavari, A.; Hatfield, W. E.; Sethulekshi, C. N. *J. Chem. Soc., Dalton Trans.* **1985,** 2509.
80. Akhter, L.; Clegg, W.; Collison, D.; Garner, C. D. *Inorg. Chem.* **1985,** *24,* 1725.
81. Damhus, T.; Pedersen, E. *Inorg. Chem.* **1984,** *23,* 695.
82. Hauser, U.; Güdel, H. U. *Theor. Chim. Acta* **1983,** *62,* 319.
83. Güdel, H. U.; Hauser, U. *Inorg. Chem.* **1980,** *19,* 1325.
84. Hodgson, D. J.; Michelsen, K.; Pedersen, E.; Towle, D. K. *Inorg. Chem.* **1991,** *30,* 815.
85. Hodgson, D. J.; Michelsen, K.; Pedersen, E. *J. Chem. Soc., Chem. Commun.* **1988,** 1558.
86. Pei, Y.; Journaux, Y.; Kahn, O. *Inorg. Chem.* **1989,** *28,* 100.

87. Mitsumi, M.; Okawa, H.; Sakiyama, H.; Ohba, M.; Matsumoto, N.; Kurisaki, T.; Wakita, H. *J. Chem. Soc., Dalton Trans.* **1993,** 2991.
88. Tamaki, H.; Zhong, Z. J.; Matsumoto, N.; Kida, S.; Koikawa, M.; Achiwa, N.; Hashimoto, Y.; Okawa, H. *J. Am. Chem. Soc.* **1992,** *114,* 6974.
89. Decurtins, S.; Schmalle, H. W.; Oswald, H. R.; Linden, A.; Ensling, J.; Gütlich, P.; Hauser, A. *Inorg. Chim. Acta* **1994,** *216,* 65.
90. Decurtins, S.; Schmalle, H. W.; Schneuwly, P.; Ensling, J.; Gütlich, P. *J. Am. Chem. Soc.* **1994,** *116,* 9521.
91. Mathoniere, C.; Carling, S. G.; Yaisheng, D.; Day, P. *J. Chem. Soc., Chem. Commun.* **1994,** 1551.
92. Bino, A.; Johnston, D. C.; Goshorn, D. P.; Halbert, T. R.; Stiefel, E. I. *Science* **1988,** *241,* 1479.
93. Bino, A.; Chayat, R.; Pedersen, E.; Schneider, A. *Inorg. Chem.* **1991,** *30,* 856.
94. Ellis, T.; Glass, M.; Harton, H.; Folting, K.; Huffmann, J. C.; Vincent, J. B. *Inorg. Chem.* **1994,** *33,* 5522.
95. Chaudhuri, P.; Winter, M.; Fleischauer, P.; Haase, W.; Flörke, U.; Haupt, H-J. *J. Chem. Soc., Chem. Commun.* **1993,** 566.
96. Wieghardt, K. *Angew. Chem., Intl. Edn.* **1989,** *28,* 1153.
97. Brudvig, G. W.; Crabtree, R. H. *Progr. Inorg. Chem.* **1988,** *37,* 99.
98. Christou, G. *Acc. Chem. Res.* **1989,** *22,* 328.
99. McKee, V. In "Adv. Inorg. Chem.", Sykes, A. G., Ed.; Academic Press: San Diego, 1993; Vol. 40, 323.
100. Brooker, S.; McKee, V.; Shepard, W. B.; Pannell, L. K. *J. Chem. Soc., Dalton Trans.* **1987,** 2555.
101. Aussoleil, J.; Cassoux, P.; de Loth, P.; Tuchagues, J.-P. *Inorg. Chem.* **1989,** *28,* 3051.
102. Smit, J. J.; Nap, G. M.; de Jongh, L. J.; van Ooijen, J. A. C.; Reedijk, J. *Physica* **1979,** *97B,* 365.
103. Ten Hoedt, R. W. M.; Reedijk, J. *Inorg. Chim. Acta* **1981,** *51,* 23.
104. Stephan, H.-O.; Chen, C.; Henkel, G.; Griesar, K.; Haase, W. *J. Chem. Soc., Chem. Commun.* **1993,** 886.
105. Gómez-Garcia, C. J.; Coronado, E.; Gómez-Romero, P.; Casan-Pastor, N. *Inorg. Chem.* **1993,** *32,* 3378.
106. Gómez-Garcia, C. J.; Casan-Pastor, N.; Coronado, E.; Baker, L. C. W.; Pourroy, G. *J. Appl. Phys.* **1990,** *67,* 5995.
107. Gómez-Garcia, C. J.; Coronado, E.; Borrás-Almenar, J. J. *Inorg. Chem.* **1992,** *31,* 1667.
108. Gómez-Garcia, C. J.; Borrás-Almenar, J. J.; Coronado, E.; Ouhab, J. *Inorg. Chem.* **1994,** *33,* 4016.
109. Jiang, Z.-H.; Ma, S.-L.; Liao, D.-Z.; Yan, S.-P.; Wang, G.-L.; Yao, X.-K.; Wang, R.-J. *J. Chem. Soc., Chem. Commun.* **1993,** 745.
110. Lloret, F.; Journaux, J.; Julve, M. *Inorg. Chem.* **1990,** *29,* 3967.
111. Costa, T.; Dorfman, J. R.; Hagen, K. S.; Holm, R. H. *Inorg. Chem.* **1983,** *22,* 4091.
111a. Sakiyama, H.; Tokuyama, K-I.; Matsumara, Y.; Okawa, H. *J. Chem. Soc., Dalton Trans.* **1993,** 2329.
112. Menage, S.; Vitols, S. E.; Bergerat, P.; Codjovi, E.; Kahn, O.; Girerd, J.-J.; Guillot, M.; Solans, X.; Calvet, T. *Inorg. Chem.* **1991,** *30,* 2666.
113. Vincent, J. B.; Christou, G. In "Adv. Inorg. Chem.", Sykes, A. G., Ed.; Academic Press: San Diego 1989, Vol. 33, 197.
114. Vincent, J. B.; Christmas, C.; Chang, H.-R.; Li, U.; Boyd, P. D. W.; Huffmann, J. C.; Hendrickson, D. N.; Christou, G. *J. Am. Chem. Soc.* **1989,** *111,* 2086.

115. Libby, E.; McCusker, J. K.; Schmitt, E. A.; Folting, U.; Huffmann, J. C.; Hendrickson, D. N.; Christou, G. *Inorg. Chem.* **1991,** *30,* 3486.
116. Gedye, C.; Harding, C.; McKee, V.; Nelson, J.; Patterson, J. *J. Chem. Soc., Chem. Commun.* **1992,** 392.
117. Chandra, S. K.; Chakraborty, P.; Chakravorty, A. *J. Chem. Soc., Dalton Trans.* **1993,** 865.
118. Weighardt, K.; Bossek, U.; Ventur, D.; Weiss, J. *J. Chem. Soc., Chem. Commun.* **1985,** 347.
119. Mikuriya, M.; Yamato, Y.; Tokii, T. *Chem. Lett.* **1991,** 1429.
120. Gallo, E.; Solari, E.; de Angelis, S.; Floriani, C.; Re, N.; Chiesi-Villa, N.; Rizzoli, C. *J. Am. Chem. Soc.* **1993,** *115,* 9850.
121. Toftlund, H.; Markiewicz, A., Murray, K. S. *Acta Chem. Scand.* **1990,** *44,* 443.
122. Chan, M. K.; Armstrong, W. H. *Abstracts of the 1989 International Chemical Congress of Pacific Basin Societies, Honolulu, HI, 1989,* Part 1, INOR 310, **1989**
123. Nishida, Y.; Nasu, M.; Tokii, T. *Z. Naturforsch, B: Chem. Sci.* **1990,** *45B,* 567.
123a. Wieghardt, K.; Othmann, R.; Saher, M. "Metal Ions in Biological Systems"; Abstracts of EUROBIC II Conference, Florence, Italy, August 1994, p. 335.
124. Shindo, K.; Mori, Y.; Motoda, K.; Sakiyama, H.; Matsumoto, N.; Okawa, H. *Inorg. Chem.* **1992,** *31,* 4987.
125. Kulawiec, R. J.; Crabtree, R. H.; Brudvig, G. W.; Schultz, G. K. *Inorg. Chem.* **1988,** *27,* 1309.
126. Thorp, H. H.; Sarneski, J. E.; Kulawiec, R. J.; Brudvig, G. W.; Crabtree, R. H.; Papaefthymiou, G. C. *Inorg. Chem.* **1991,** *30,* 1153.
127. Stibrany, R. T.; Gorun, S. M. *Angew Chem., Intl. Edn. Engl.* **1990,** *29,* 1156.
128. Gorun, S.; Berry, K. J.; Murray, K. S., unpublished work.
129. Suzuki, M.; Sugisawa, T.; Senda, H.; Oshio, H.; Uehara, A. *Chem. Lett.* **1989,** 1091.
130. Suzuki, M.; Senda, H.; Suenaga, M.; Sugisawa, T.; Uehara, A. *Chem. Lett.* **1990,** 923.
131. Chan, M. K.; Armstrong, W. H. *J. Am. Chem. Soc.* **1989,** *111,* 9121.
132. Chan, M. K.; Armstrong, W. H. *J. Am. Chem. Soc.* **1990,** *112,* 4985.
133. Kipke, C. A.; Scott, M. J.; Gohder, J. W.; Armstrong, W. H. *Inorg. Chem.* **1990,** *29,* 2193.
134. Kirk, M. L.; Chan, M. K.; Armstrong, W. H.; Solomon, E. I. *J. Am. Chem. Soc.* **1992,** *114,* 10432.
135. McKee, V.; Tandon, S. K. *J. Chem. Soc., Chem. Commun.* **1988,** 1334.
136. Hendrickson, D. N.; Christou, G.; Schmitt, E. A.; Libby, E.; Bashkin, J. S.; Wang, S.; Tsai, H.-L.; Vincent, J. B.; Boyd, P. D. W.; Huffmann, J. C.; Folting, K.; Li, Q.; Streib, W. E. *J. Am. Chem. Soc.* **1992,** *114,* 2455.
137. Wang, S.; Tsai, H.-L.; Streib, W. E.; Christou, G.; Hendrickson, D. N. *J. Chem. Soc., Chem. Commun.* **1992,** 1427.
138. Wemple, M. W.; Tsai, H.-L.; Folting, K.; Hendrickson, D. N.; Christou, G. *Inorg. Chem.* **1993,** *32,* 2025.
139. Wang, S.; Tsai, H.-L.; Hagen, K. S.; Hendrickson, D. N.; Christou, G. *J. Am. Chem. Soc.* **1994,** *116,* 8376.
140. Schmitt, E.-A.; Noodleman, L.; Baerends, E. J.; Hendrickson, D. N. *J. Am. Chem. Soc.* **1992,** *114,* 6109.
140a. Belinskii, M. I. *Chem. Phys.* **1994,** *179,* 1.
141. Kawasaki, H.; Kusunoki, M.; Hayashi, Y.; Suzuki, M.; Munezawa, K.; Suenaga, M.; Senda, H.; Uehara, A. *Bull. Chem. Soc. Japan* **1994,** *67,* 1310.
142. Philouze, C.; Blondin, G.; Girerd, J.-J.; Guilhem, J.; Pascard, C.; Lexa, D. *J. Am. Chem. Soc.* **1994,** *116,* 8557.

143. Yachandra, V. K.; de Rose, V. J.; Latimer, M. J.; Mukerji, I.; Sauer, K.; Klein, M. P. *Science* **1993,** *260,* 675.

144. Wieghardt, K.; Bossek, U.; Nuber, B.; Weiss, J.; Bonvoisin, J.; Corbella, M.; Vitols, S. E.; Girerd, J.-J. *J. Am. Chem. Soc.* **1988,** *110,* 7398.

145. Hagen, K. S.; Westmoreland, T. D.; Scott, M. J.; Armstrong, W. H. *J. Am. Chem. Soc.* **1989,** *111,* 1907.

146. Murray, K. S. *Coord. Chem. Rev.* **1974,** *12,* 1.

147. Kurtz, D. M. Jr. *Chem. Rev.* **1990,** *90,* 585.

148. (a) Kurtz, D. M. Jr. In "Encyclopedia of Inorganic Chemistry", King, R. B., Ed.; Wiley: Chichester, 1994; 1847–1859. (b) Lynch, W. E.; Kurtz, D. M. Jr. *ibid* Vol. 4, 1726–1735.

149. Lippard, S. J. *Angew Chem., Intl. Edn. Engl.* **1988,** *27,* 344.

150. Lippard, S. J.; Berg, J. M. "Principles of Bioinorganic Chemistry"; University Science Books: Mill Valley, 1994; Chap. 11.

151. Vincent, J. B.; Olivier-Lilley, G. L.; Averill, B. A. *Chem. Rev.* **1990,** *90,* 1447.

152. Wilkins, R. G. *Chem. Soc. Reviews* ***1992,*** 171.

153. Doi, K.; Anatanaitis, B. C.; Aisen, P. *Struct. Bonding* **1988,** *70,* 1.

154. Nakamura, A.; Ueyama, A. "Encyclopedia of Inorganic Chemistry", King, R. B., Ed.; Wiley: Chichester, 1994; Vol. 4, 1883–1896.

155. Stiefel, E. I.; George, N. G. In "Bioinorganic Chemistry" (Bertini, I.; Gray, H. B.; Lippard, S. J.; Valentine, J. S., Eds.; University Science Books: Mill Valley, 1994; Chap. 7.

156. Johnson, M. K. In "Encyclopedia of Inorganic Chemistry", King, R. B., Ed.; John Wiley: Chichester, 1994; Vol. 4, 1896–1915.

157. Hagen, K. S. *Angew. Chem., Intl. Edn. Engl.* **1992,** *31,* 1010.

158. "Biomineralization; Chemical and Biochemical Perspectives" (Mann, S.; Webb, J.; Williams, R. J. P., Eds.; VCH: Weinheim, 1989; Chaps. 9 and 10.

159. Micklitz, W.; McKee, V.; Rardin, R. L.; Pence, L. E.; Papaefthymiou, G. C.; Bott, S. G.; Lippard, S. J. *J. Am. Chem. Soc.* **1994,** *116,* 8061, and references therein.

160. Heath, S. L.; Powell, A. K. *Angew. Chem., Intl. Edn. Engl.* **1992,** *31,* 191.

161. Holm, R. H.; Ciurli, S.; Weigel, J. A. *Progr. Inorg. Chem.* **1990,** *38,* 1.

162. McCusker, J. K.; Vincent, J. B.; Schmitt, E. A.; Mino, M. L.; Shin, K.; Coggin, DeA. K.; Hagen, P. M.; Huffmann, J. C.; Christou, G.; Hendrickson, D. N. *J. Am. Chem. Soc.* **1991,** *113,* 3012.

163. Gorun, S. M.; Lippard, S. J. *Inorg. Chem.* **1991,** *30,* 1625.

164. Chaudhuri, P.; Winter, M.; Fleischauer, P.; Haase, W.; Flörke, U.; Haupt, H-J. *Inorg. Chim. Acta* **1993,** *212,* 244.

165. Armstrong, W. H.; Roth, M. E.; Lippard, S. J. *J. Am. Chem. Soc.* **1987,** *109,* 6318.

166. Toftlund, H.; Murray, K. S.; Zwack, P. R.; Taylor, L. F.; Anderson, O. P. *J. Chem. Soc., Chem. Commun.* **1986,** 191.

167. Sessler, J. L.; Silbert, J. W.; Lynch, V.; Markert, J. T.; Wooten, C. L. *Inorg. Chem.* **1993,** *32,* 621.

168. Sessler, J. L.; Hugdahl, J. D.; Lynch, V.; Davis, B. *Inorg. Chem.* **1991,** *30,* 334.

169. Sessler, J. L.; Silbert, J. W.; Lynch, V. *Inorg. Chem.* **1990,** *29,* 4143.

170. Arulsamy, N.; Glerup, J.; Hodgson, D. J. *Inorg. Chem.* **1994,** *33,* 3043.

171. Jameson, D. L.; Xie, C. L.; Hendrickson, D. N.; Potenza, J. A.; Schugar, H. J. *J. Am. Chem. Soc.* **1987,** *109,* 740.

172. Chen, Q.; Lynch, J. B.; Gomez-Romero, P.; Ben-Hussain, A.; Jameson, G. B.; O'Connor, C. J.; Que, L. Jr. *Inorg. Chem.* **1988,** *27,* 2673.

173. McKee, V.; Zvagulis, M.; Reed, C. A. *Inorg. Chem.* **1985,** *24,* 2914.

174. Murch, B. P.; Bradley, F. C.; Boyle, P. D.; Papaefthymiou, V.; Que, L. Jr. *J. Am. Chem. Soc.* **1987,** *109,* 7993.
175. Drüeke, S.; Wieghardt, K.; Nuber, B.; Weiss, J.; Bominaar, E. L.; Sawayn, A.; Winkler, H.; Trautwein, A. X. *Inorg. Chem.* **1989,** *28,* 4477.
175a. Sessler, J. L.; Silbert, J. W.; Burrell, A. K.; Lynch, V.; Markert, J. T.; Wooten, C. L. *Inorg. Chem.* **1993,** *32,* 4277.
176. Lah, M. S.; Kirk, M. L.; Hatfield, W. E.; Pecoraro, V. L. *J. Chem. Soc., Chem. Commun.* **1989,** 1606.
177. Kakos, G. A.; Winter, G. *Austral. J. Chem.* **1969,** *22,* 97.
178. Catterick, J.; Thornton, P.; Fitzsimmons, B. W. *J. Chem. Soc., Dalton Trans.* **1977,** 1420.
179. Kokot, E.; Mockler, G. M.; Sefton, G. L. *Austral. J. Chem.* **1973,** *26,* 2105.
180. Holm, R. H. In "Adv. Inorg. Chem.", Sykes, A. G., Ed.; Academic Press: San Diego, 1992; 38, 1.
181. Hagen, W. R. In "Adv. Inorg. Chem.", Sykes, A. G., Ed.; Academic Press: San Diego, 1992; 38, 73.
182. Meyer, J.; Moulis, J-M.; Gaillard, J.; Lutz, M. In "Adv. Inorg. Chem.", Sykes, A. G., Ed.; 1992, 38, 73.
183. Jordanov, J.; Roth, E. K. H.; Fries, P. H.; Noodleman, L. *Inorg. Chem.* **1990,** *29,* 4228.
184. Noodleman, L. *Inorg. Chem.* **1991,** *30,* 246.
185. Noodleman, L. *Inorg. Chem.* **1991,** *30,* 256.
186. Mouesca, J.-M.; Noodleman, L.; Case, D. A. *Inorg. Chem.* **1994,** *33,* 4819.
187. Carney, M. J.; Papaefthymiou, G. C.; Spartalian, K.; Frankel, R. B.; Holm, R. H. *J. Am. Chem. Soc.* **1988,** *110,* 6084.
188. Laskowski, E. J.; Frankel, R. B.; Gillum, W. O.; Papaefthymiou, G. C.; Renard, J.; Ibers, J. E.; Holm, R. H. *J. Am. Chem. Soc.* **1978,** *100,* 5322.
189. Collison, D.; Mabbs, F. E. *J. Chem. Soc., Dalton Trans.* **1982,** 1573.
190. Gaillard, J.; Moulis, J. M.; Meyer, J. *Inorg. Chem.* **1987,** *26,* 320.
191. Münck, E.; Papaefthymiou, V.; Surerus, V. V.; Girerd, J. J. "Metal Clusters in Proteins", ACS Symposium Series; Que, L. Jr., Ed.; American Chemical Society: Washington, D.C., 1988; Vol. 372, 302–325.
192. Blondin, G.; Borshch, S. A.; Girerd, J. J. *Comments Inorg. Chem.* **1992,** *12,* 315.
193. Blondin, G.; Girerd, J. J. *Chem. Rev.* **1990,** *90,* 1359.
194. Bominaar, E. L.; Borshch, S. A.; Girerd, J. J. *J. Am. Chem. Soc.* **1994,** *116,* 5362; 7957.
195. Girerd, J. J.; Papaefthymiou, V.; Surerus, K. K., Münck, E. *Pure Appl. Chem.* **1989,** *61,* 805.
196. Luchinat, C.; Ciurli, S.; Capozzi, F. "Perspectives in Coordination Chemistry", Williams, A. F.; Floriani, C.; Merbach, A. E., Eds.; VCH: Weinheim, NY, 1992; pp. 245–269.
197. Bertini, I.; Briganti, F.; Luchinat, C.; Scozzafava, A.; Sola, M. *J. Am. Chem. Soc.* **1991,** *113,* 1237.
198. Banci, L.; Bertini, I.; Eltis, L. D.; Felli, I. C.; Kastrau, D. H. W.; Luchinat, C.; Piccioli, M.; Pierattelli, R.; Smith, M. *Eur. J. Biochem.* **1994,** *225,* 715.
199. Banci, L.; Bertini, I.; Ciurli, S.; Ferretti, S.; Luchinat, C.; Piccioli, M. *Biochemistry* **1993,** *32,* 9387.
200. Bertini, I.; Ciurli, S.; Luchinat, C. *Angew. Chem., Intl. Edn. Engl.* 1994, in press.
201. Belinskii, M. I. *Chem. Phys.* **1993,** *172,* 189.
202. Belinskii, M. I. *Chem. Phys.* **1993,** *172,* 212.
203. Belinskii, M. I. *Chem. Phys.* **1993,** *173,* 27.
204. Belinskii, M. I. *Chem. Phys.* **1993,** *176,* 15.

205. Belinskii, M. I. *Chem. Phys.* **1993,** *176,* 37.
206. Casan-Pastor, N.; Bas-Serra, J.; Coronado, E.; Pourroy, G.; Baker, L. C. W. *J. Am. Chem. Soc.* **1992,** *114,* 10380.
207. Gomez-García, C. J.; Coronado, E.; Aebarsold, M.; Güdel, H. U. *Physica B (Amsterdam)* **1992,** *B238,* 181.
208. Bertrand, J. A.; Ginsberg, A. P.; Kaplan, R. I.; Kirkwood, C. E.; Martin, R. L.; Sherwood, R. C. *Inorg. Chem.* **1971,** *10,* 240.
209. Olmstead, M. M.; Power, P. P.; Siegel, G. *Inorg. Chem.* **1988,** *27,* 580.
210. Paap, F.; Bouwman, E.; Driesseu, W. L.; de Graaf, R. A. G.; Reedijk, J. *J. Chem. Soc., Dalton Trans.* **1985,** 737.
211. Simonov, Yu-A.; Matuzenko, G. S.; Botoshanskii, M. M.; Yampolskaya, M. A.; Gerbeleu, N. V.; Malinoskii, T. I. *Russ. J. Inorg. Chem.* **1982,** *27,* 231.
212. Bertrand, J. A.; Hightower, T. C. *Inorg. Chem.* **1973,** *12,* 206.
213. Bertini, I.; Luchinat, C.; Messori, L.; Vasak, M. *J. Am. Chem. Soc.* **1989,** *111,* 7300.
214. Dance, I. G. *J. Am. Chem. Soc.* **1979,** *101,* 6264.
215. Krüger, T.; Krebs, B.; Henkel, G. *Angew. Chem., Intl. Edn. Engl.* **1989,** *28,* 61.
216. Krüger, T.; Krebs, B.; Henkel, G. *Angew. Chem., Intl. Edn. Engl.* **1992,** *31,* 54.
217. Gaete, W.; Ros, J.; Solans, X.; Font-Alba, M.; Brianso, J. L. *Inorg. Chem.* **1984,** *23,* 39.
218. Krüger, P. E.; Fallon, G. D.; Moubaraki, B.; Murray, K. S. *J. Chem. Soc., Chem. Commun.* **1992,** 1726.
218a. Mikuriya, M.; Nakadera, K.; Kotera, T. *Chem. Lett. (Japan)* **1993,** 637.
219. Ginsberg, A. P.; Martin, R. L.; Sherwood, R. C. *Inorg. Chem.* **1968,** *7,* 932.
220. Gómez-Garcia, C. J.; Coronado, E.; Ouhab, L. *Angew Chem., Int. Edn. Engl.* **1992,** *31,* 649; and Ref. (*108*).
221. Andrew, J. E.; Blake, A. B. *J. Chem. Soc. A.* **1969,** 1456.
222. Barnes, J. E.; Hatfield, W. E. *Inorg. Chem.* **1971,** *10,* 2355.
223. Sorai, M.; Yoshikawa, M.; Arai, N.; Suga, H.; Seki, S. *J. Phys. Chem. Solids* **1978,** *39,* 413.
224. Krüger, A. G.; Winter, G. *Austral. J. Chem.* **1970,** *23,* 1.
225. Paap, F.; Bouwman, E.; Driessen, W. L.; de Graaff, R. A. G.; Reedijk, J. *J. Chem. Soc., Dalton Trans.* **1985,** 737.
226. Gladfelter, W. L.; Lynch, M. W.; Schaeffer, W. P.; Hendrickson, D. N.; Gray, H. B. *Inorg. Chem.* **1981,** *20,* 2390.
227. Ballester, L.; Coronado, E.; Gutiérrez, A.; Monge, A.; Perpiñán, M. F.; Pinilla, E.; Rico, T. *Inorg. Chem.* **1992,** *31,* 2053.
228. Deleted in proof.
229. Boyd, P. D. W.; Martin, R. L.; Schwarzenbach, G. *Austral. J. Chem.* **1988,** *41,* 1449.
230. Yampolskaya, M. A.; Matuzenko, G. S.; Gerbeleu, N. V. *Russ. J. Inorg. Chem.* **1989,** *34,* 681.
231. Te Hoedt, R. W. M.; Reedijk, J. *Inorg. Chim. Acta* **1981,** *51,* 23.
232. Ribas, J.; Monfort, M.; Costa, P.; Solans, X. *Inorg. Chem.* **1993,** *32,* 695.
233. Bell, M.; Edwards, A. J.; Hoskins, B. F.; Kachab, E. H. *J. Am. Chem. Soc.* **1989,** *111, 3603.*
234. Edwards, A. J.; Hoskins, B. F.; Kachab, E. H.; Markiewicz, A.; Murray, K. S.; Robson, R. *Inorg. Chem.* **1992,** *31,* 3585.
235. Spiro, C. L.; Lambert, S. L.; Smith, T. J.; Duesler, E. N.; Gagne, R.; Hendrickson, D. N. *Inorg. Chem.* **1981,** *20,* 1229.
236. Kahn, O. "Molecular Magnetism"; VCH: New York, 1993; 237.
237. Huang, H.; Kai, F.; Asai, Y.; Hirohata, M.; Nakamura, M. *Chem. Lett.* **1991,** 65.
237a. Nanda, K. K.; Venkatsubramanian, K.; Majumdar, D.; Nag, K. *Inorg. Chem.* **1994,** *33,* 1581.

238. Coronado, E.; Gómez-Garcia, C. J. In "Polyoxometalates: From Platonic Solids to Anti-Retroviral Activity"; Pope, M. T.; Müller, A., Eds.; Kluwer Academic: Dordrecht, 1994; 233–243.
239. Hall, J. W.; Estes, W. E.; Estes, E. D.; Scaringe, R. P.; Hatfield, W. E. *Inorg. Chem.* **1977,** *16,* 1572.
240. Schwabe, L.; Haase, W. *J. Chem. Soc., Dalton Trans.* **1985,** 1909.
241. Hatfield, W. E.; Inman, G. W. Jr. *Inorg. Chem.* **1969,** *8,* 1376.
242. Boyd, P. D. W.; Martin, R. L. *J. Chem. Soc., Dalton Trans.* **1977,** 105.
243. Jotham, R. W.; Kettle, S. F. A. *Inorg. Chim. Acta* **1970,** *4,* 145.
244. Merz, L.; Haase, W. *J. Chem. Soc., Dalton Trans.* **1978,** 1594.
245. Mergehenn, R.; Merz, L.; Haase, W. *J. Chem. Soc., Dalton Trans.* **1980,** 1703.
246. Merz, L.; Haase, W.; Keller, G. *Ber. Buns. Phys. Chem.* **1976,** *80,* 305.
247. Laurent, J.-P.; Bonnet, F.; Nepveu, F.; Astheimer, H.; Walz, L. *J. Chem. Soc., Dalton Trans.* **1982,** 2433.
248. Astheimer, H.; Nepveu, F.; Walz, L.; Haase, W. *J. Chem. Soc., Dalton Trans.* **1985,** 315.
249. Nepveu, F. *Inorg. Chim. Acta* **1987,** *134,* 43.
249a. Gojon, E.; Latour, J.-M.; Greaves, S. J.; Povey, D. C.; Ramdas, V.; Smith, G. W. *J. Chem. Soc., Dalton Trans.* **1990,** 2043.
250. Sletten, J.; Sorensen, A.; Julve, M.; Journaux, Y. *Inorg. Chem.* **1990,** *29,* 5054.
251. Hanson, M. V.; Simpson, G. D.; Marsh, W. E.; Carlisle, G. O. *J. Inorg. Nucl. Chem.* **1980,** *42,* 139.
252. Mazurek, W.; Berry, K. J.; Murray, K. S.; O'Connor, M. J.; Snow, M. R.; Wedd, A. G. *Inorg. Chem.* **1982,** *21,* 3071.
253. Pons, J.; Lopez, X.; Casabo, J.; Teixidor, F.; Caubet, A.; Rius, J.; Miravittles, C. *Inorg. Chim. Acta* **1992,** *195,* 61.
254. Loroesch, J.; Paulus, H.; Haase, W. *Inorg. Chim. Acta* **1985,** *106,* 101.
255. Grannas, M.; Hoskins, B. F.; Moubaraki, B.; Murray, K. S.; Robson, R., to be submitted.
256. Andrew, J. E.; Blake, A. B. *J. Chem. Soc., Dalton Trans.* **1976,** 477.
257. Fallon, G. D.; Moubaraki, B.; Murray, K. S.; van den Bergen, A. M.; West, B. O. *Polyhedron* **1993,** *12,* 1989.
258. Wang, S.; Chuan, J.; Hall, J. R.; Thompson, L. K. *Polyhedron,* **1994,** *13,* 1039.
259. Hoskins, B. F.; Robson, R.; Vince, D. *J. Chem. Soc., Chem. Commun.* **1973,** 392.
260. Robson, R. *Austral. J. Chem.* **1970,** *23,* 2217.
261. Grannas, M. J.; Hoskins, B. F.; Robson, R. *J. Chem. Soc., Chem. Commun.* **1990,** 1644.
262. McKee, V.; Tandon, S. S. *J. Chem. Soc., Dalton Trans.* **1991,** 221.
263. Hoskins, B. F.; Robson, R.; Smith, P. *J. Chem. Soc., Chem. Commun.* **1990,** 488.
264. Poncelet, O.; Hubert-Pfalzgraf, L. G.; Daran, J. C. *Inorg. Chem.* **1990,** *29,* 2883.
265. Mergehenn, R.; Haase, W. *Acta Crystallogr. Sect B. Struct. Crystallogr. Cryst. Chem. 1977,* **33,** 1877.
266. van Albada, G. A.; Reedijk, J.; Hämäleinen, R.; Turpeinen, U.; Spek, A. L. *Inorg. Chim. Acta* **1989,** *163,* 213.
267. Masi, D.; Mealli, C.; Sabat, M.; Sabatini, A.; Vacca, A.; Zanabini, F. *Helv. Chim. Acta* **1984,** *67,* 1818.
268. Wong, H.; tom Dieck, H.; O'Connor, C. J.; Sinn, E. *J. Chem. Soc., Dalton Trans.* **1980,** 786.
269. Lines, M. E.; Ginsberg, A. P.; Martin, R. L.; Sherwood, R. C. *J. Chem. Phys.* **1972,** *57,* 1.

270. Gerloch, M. *Progr. Inorg. Chem.* **1979,** *26,* 1.
271. Tosik, A.; Buzowska-Strzyzewska, M.; Mrozinski, J. *J. Coord. Chem.* **1991,** *24,* 113.
272. Jones, D. H.; Sams, J. R.; Thompson, R. C. *Inorg. Chem.* **1983,** *22,* 1399.
273. Jones, D. H.; Sams, J. R.; Thompson, R. C. *J. Chem. Phys.* **1983,** *79,* 3877.
274. Polinger, V. Z.; Chibotaru, L. F.; Bersuker, I. B. *Mol. Phys.* **1984,** *52,* 1271.
275. Kamase, K.; Osaki, K.; Uryu, N. *Phys. Lett.* **1979,** *A73,* 241.
276. (a) Buluggiu, E. *J. Chem. Phys.* **1986,** *84,* 1243. (b) Rubins, R. S.; Black, T. D.; Barak, J. *J. Chem. Phys.* **1986,** *85,* 3770.
277. Black, T. D.; Rubins, R. S.; De, D. K.; Dickinson, R. C.; Baker, W. A. Jr. *J. Chem. Phys.* **1984,** *80,* 4620.
278. Dickinson, R. C.; Helm, F. T.; Baker, W. A. Jr.; Black, T. D.; Watson, W. H. Jr. *Inorg. Chem.* **1977,** *16,* 1530.
279. Juarez-Garcia, C.; Hendrich, M. P.; Holman, T. R.; Que, L. Jr.; Münck, E. *J. Am. Chem. Soc.* **1991,** *113,* 518.
280. Blake, A. B.; Cannon, R. D.; Jayasooria, U. A.; Saad, A.; White, R. P.; Summerfield, D., to be submitted.
281. Drake, R. F.; Crawford, V. H.; Hatfield, W. E. *J. Chem. Phys.* **1974,** *60,* 4525.
282. Moriya, T. "Magnetism", Rado, G. T.; Suhl, H., Eds.; Academic Press: New York. 1963; Vol. 1, 85.
283. Keij, F. S.; Haasnoot, J. P.; Oosterling, A. J.; Reedijk, J.; O'Connor, C. J.; Zhang, J. H.; Spek, A. L. *Inorg. Chim. Acta* **1991,** *181,* 185.
284. Teipel, S.; Griesar, K.; Haase, W.; Krebs, B. *Inorg. Chem.* **1994,** *33,* 456.
285. Krüger, P. E.; Fallon, G. D.; Moubaraki, B.; Murray, K. S. *Inorg. Chem.* **1995,** *34,* in press.
286. Simonov, Yu. A.; Yampolskaya, M. A.; Belinskii, M. I.; Dvorkin, A. A. Chemical Abstracts 1985, *103,* 226343; *Struktur. Issled. Neorgan. i Organ. Soedin,* Kishinev 1985, 40 (Russ).
287. Willett, R. D. "Magneto-Structural Correlations in Exchange Coupled Systems", Willett, R. D.; Gatteschi, D.; Kahn, O., Eds.; Reidel: Dordrecht, 1985; 389–420.
288. Halvorson, K. E.; Grigereit, T.; Willett, R. D. *Inorg. Chem.* **1987,** *26,* 1716.
289. Folgado, J.-V.; Gómez-Romero, P.; Sapina, F.; Bettran-Porter, D. *J. Chem. Soc., Dalton Trans.* **1990,** 2325.
290. Willett, R. D.; Geiser, U. *Inorg. Chem.* **1986,** *25,* 4558.
291. Geiser, U.; Willett, R. D.; Lindbeck, M.; Emerson, K. *J. Am. Chem. Soc.* **1986,** *108,* 1173.
292. Chiari, B.; Piovesana, O.; Tarantelli, T.; Zanazzi, P. F. *Inorg. Chem.* **1993,** *32,* 4834.
293. Wang, S.; Smith, K. D. L.; Phang, Z.; Wagner, M. J. *J. Chem. Soc., Chem. Commun.* **1992,** 1594.
294. Berry, K. J.; Moubaraki, B.; Murray, K. S.; Nichols, P. J.; Schulz, L. D.; West, B. O. *Inorg. Chem.* **1995,** *34.*
295. Chaudhuri, P.; Karpenstein, I.; Winter, M.; Lengen, M.; Butzlaff, C.; Bill, E.; Trautwein, A. X.; Flörke, U.; Haupt, H.-J. *Inorg. Chem.* **1993,** *32,* 88.
296. Kolks, G.; Lippard, S. J.; Waszczack, J. V.; Lilienthal, H. R. *J. Am. Chem. Soc.* **1982,** *104,* 717.
297. Nonoyama, K.; Mori, W.; Nonoyama, M. *Polyhedron* **1994,** *13,* 891.
298. Tandon, S. S.; Mandal, S. K.; Thompson, L. K.; Hynes, R. C. *Inorg. Chem.* **1992,** *31,* 2215.
299. Wang, S.; Trepanier, S. J.; Zheng, J.-C.; Pang, Z.; Wagner, M. J. *Inorg. Chem.* **1992,** *31,* 2118.
300. Krüger, P. E.; Fallon, G. D.; Moubaraki, B.; Murray, K. S., unpublished work.

301. Hobday, M. D.; Smith, T. D. *Coord. Chem. Rev.* **1972,** *9,* 311.
301a. Lintvedt, R. L.; Zehetmair, J. K. *Inorg. Chem.* **1990,** *29,* 2204.
302. Chen, L.; Thompson, L. K.; Bridson, J. N. *Inorg. Chem.* **1993,** *32,* 2938.
303. Tandon, S. S.; Thompson, L. K.; Bridson, J. N.; Bubenik, M. *Inorg. Chem.* **1993,** *32,* 4621.
304. Tandon, S. S.; Thompson, L. K.; Bridson, J. N.; McKee, V.; Downard, A. J. *Inorg. Chem.* **1992,** *31,* 4635.
305. Bertoncello, K.; Fallon, G. D.; Murray, K. S. *Polyhedron* **1990,** *23,* 2867.
306. Li, Y-T.; Jiang, Z-H.; Liao, D-Z.; Yan, S-P.; Ma, S-L; Li, M-Y.; Wang, G-L. *Polyhedron* **1993,** *12,* 2781.

ADVANCES IN INORGANIC CHEMISTRY, VOL. 43

DIIRON–OXYGEN PROTEINS

K. KRISTOFFER ANDERSSON* and ASTRID GRÄSLUND†

*Dept. of Biochemistry, University of Oslo, P.O. Box 1041, Blindern, N-0316 Oslo, Norway; and † Dept. of Biophysics, Stockholm University, Arrhenius Laboratories, S-106 91 Stockholm, Sweden

I. Introduction and Relevance

This review will describe an emerging class of proteins that we would like to call the diiron–oxygen proteins, which are part of a general class of iron–oxygen proteins. We will specifically deal with proteins

Copyright © 1995 by Academic Press, Inc.
All rights of reproduction in any form reserved.

with a dinuclear μ-oxo or μ-hydroxo bridged core. Several proteins with this type of metal site have been described. For the future we predict that tri- and tetranuclear iron–oxygen proteins may also be found, since this type of metal site can be obtained in inorganic model compounds. The review will cover some of the developments from 1990 to 1994 for dinuclear iron–oxygen proteins, with an emphasis on ribonucleotide reductase and methane monooxygenase. For previous reviews and other general articles see (*1–10*). Inorganic model compounds will not be discussed here, and the reader is referred to (*11–14*).

The presentation in 1993 of the structure of the hydroxylase component of methane monooxygenase (MMOH) by Rosenzweig *et al.* (*15*) is the third published three-dimensional structure of a diiron–oxygen protein (Fig. 1). The previous two are from hemerythrin (Hr) (*16, 17*) and protein R2 of *E. coli* ribonucleotide reductase (RNR-R2) (*18, 19*). Some other dinuclear iron proteins with known μ-oxo or μ-hydroxo bridges are purple acid phosphatases (PAP) [(e.g., uteroferrin (Uf)] (*20, 21*), ferritins (in early stages of nucleation) (*22*), rubrerythrin (Rr) (*23–26*), nigerythrin (*26*), and soluble stearoyl–acyl carrier protein Δ^9 desaturase (Δ-ACP) (*27, 28*).

The overall structure of MMOH reveals an extensive similarity to the *E. coli* R2 protein of ribonucleotide reductase. Surprisingly both the α- and β-subunits of MMOH possess folds very similar to those of the RNR-R2 subunit, despite the absence of any significant sequence homology. The coordination of these two diiron cores (and the bacterioferritin cluster) is also similar, perhaps revealing a distant evolutionary relation between these proteins. More proteins are expected to have a similar dinuclear iron cluster, based on protein sequence homology with RNR or MMOH. These include a phenol hydroxylase, a toluene hydroxylase, and perhaps also rubrerythrin and stearoyl–acyl carrier protein Δ^9 desaturase [see discussion in (*15, 27–29*)]. Their sequences are very divergent, and the presumed iron ligands are the only conserved amino acids among these proteins, as was first suggested by Kurtz and Prickril (*29*). The diiron clusters of MMOH, Hr, RNR-R2, bacterioferritin, and possibly others are all bound by a so-called four-helix bundle in the protein structure. However, this may not be a general feature for all iron–oxygen proteins.

The metal clusters are not the only similarity in the diiron–oxygen protein group. Another common denominator is that all can react with dioxygen, albeit in different states of oxidation. RNR-R2 (*30*) and MMOH (*31*) proteins have in common that both cleave an oxygen–oxygen bond, with the iron cluster as an active participant. Hemerythrin is different from these others with five histidines (*1–7*) in the cluster

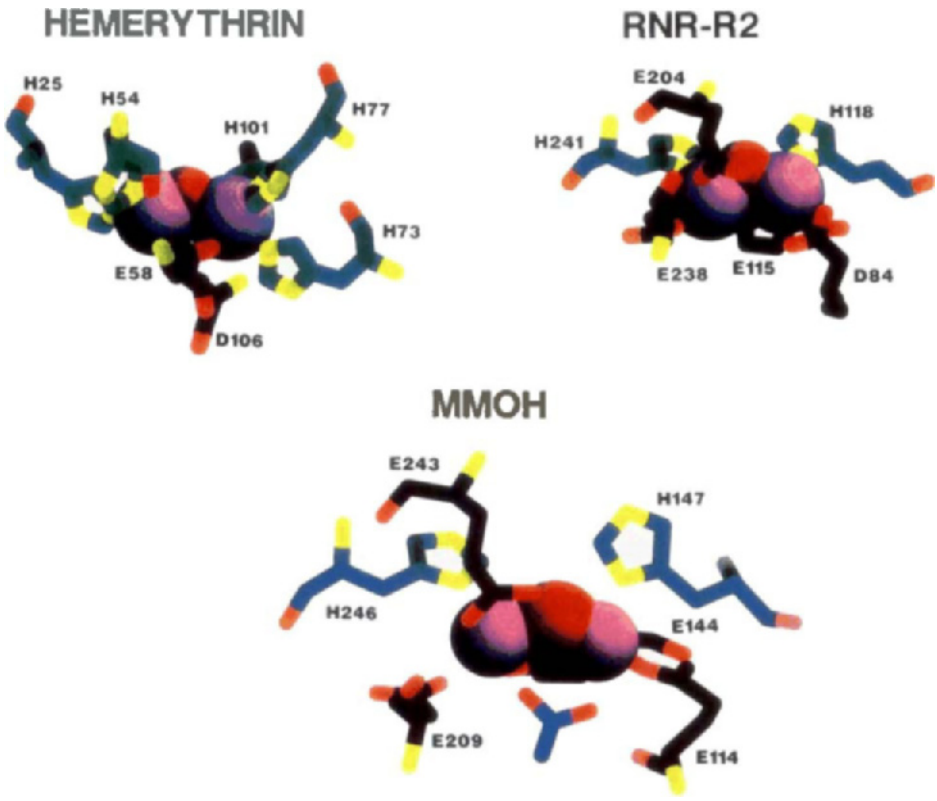

FIG. 1. Diferric iron clusters form hemerythrin, ribonucleotide reductase R2 subunit, and methane monooxygenase hydroxylase. The figure was made with the RasMol 2.0 program, and the protein coordinates as PDB files were obtained from Brookhaven Protein Data Bank. Only the amino acids (histidines, green; carboxylates, black; oxygen, red; nitrogen, yellow; acetate, blue; iron, violet) coordinated to the iron cluster are shown, coordinated waters are not indicated. The first subunit containing the cluster is shown. Diferric Hr is from sipunculid worm (*Themiste dyscritra*). The RNR-R2 is from *E. coli*. The MMOH is from *Methylococcus capsulatus* (Bath).

R1
substrate binding site

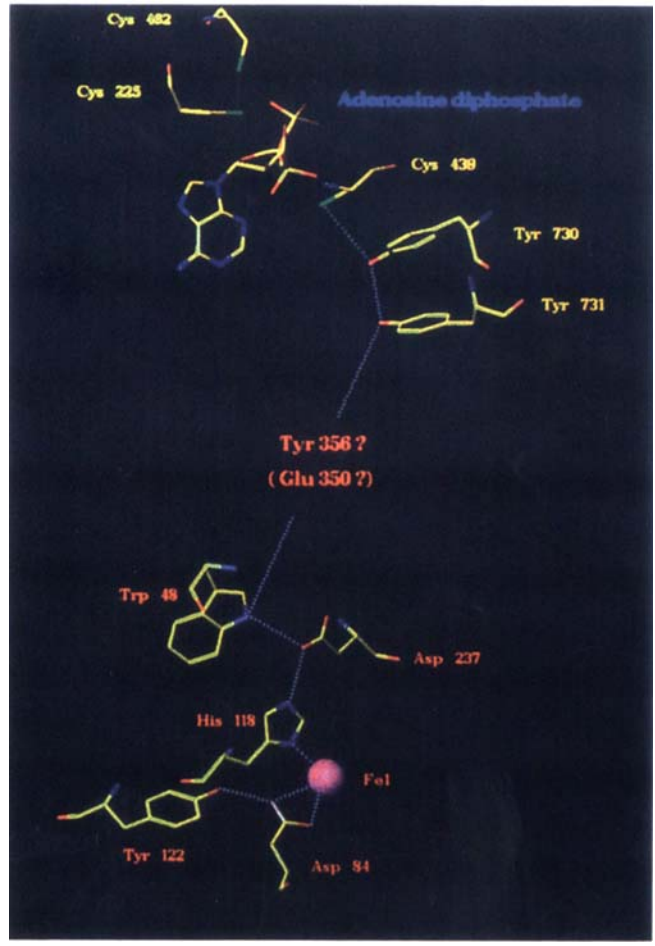

R2
iron/radical site

FIG. 4. Suggested long-range electron transfer pathway from the substrate binding site in protein R1 to the tyrosyl radical in protein R2 in *E. coli* ribonucleotide reductase. The figure is adapted from (*73*) with permission from B-M. Sjöberg.

and higher redox potentials (Table I), which might help to explain why it only binds oxygen reversibly (*1–7*) and does not cleave the oxygen–oxygen bond as the others do. The stearoyl–acyl carrier protein Δ^9 desaturase also uses oxygen in its desaturation. The purple acid phosphatases can react rapidly with hydrogen peroxide (*20*). In contrast to all others in the group, the mammalian PAP cannot form a stable diferrous form, but in the red kidney bean (plant) PAP, a diferrous form has been reported (*36*). Perhaps mammalian PAP only needs to donate one electron to an oxygen-derived species, while the others must be able to give two electrons (if one considers oxyhemerythrin as hydrogen peroxide coordinated to diferric hemerythrin).

The diiron–oxo protein group has very high biological, medical, and biotechnological importance, as exemplified by the following:

1. Ribonucleotide reductase (*19, 37–41*) catalyzes a highly regulated essential reaction for all living cells, the reduction of all four ribonucleotides to their corresponding deoxyribonucleotides. The iron-containing class I RNR is found in some bacteria and eukaryotic cells, and it is

TABLE I

MIDPOINT POTENTIALS FOR SELECTED DIIRON–OXYGEN PROTEINS[a]

	E_{m1} (mV)	E_{m2} (mV)	pH	Ref.
Hr[b] (met → semi → deoxy)	+110	+350	8.2	*32*
Uf[c]	+242		7.0	*32*
Uf	+181		7.9	*32*
MMOH[d]	+76	+21	7.0	*33*
MMOH + MMOB[e]	−52	−115	7.0	*33*
Rubrerythrin	+339	+246	7.0	*26*
Nigerythrin	+300	+209	7.0	*26*
RNR-R2,[f] *E. coli* (direct two-electron reduction)	−115		7.0	*34*
RNR-R2, mouse, in 20% glycerol (estimated from partial chemical reduction experiment)	$+150 > E_{m1} > 10$	$10 > E_{m2} > -150$	7.5	*35*

[a] E_{m1} and E_{m2} designate the potentials for the first and second electron additions to the fully oxidized state.

[b] Hemerythrin.

[c] Uteroferrin.

[d] Methane monooxygenase hydroxylase.

[e] Methane monooxygenase B component.

[f] Ribonucleotide reductase.

also coded for by certain bacteriophages and eukaryotic viruses. It is composed of a one-to-one complex of two homodimeric components designated proteins R1 and R2. The medical importance concerns mainly the development of new types of drugs against pathogenic organisms and certain forms of tumors.

2. Methane monooxygenase (*9, 15, 31, 42*) from methanotrophic bacteria carries out one of the most difficult monooxygenations known, the conversion of the inert methane to methanol at ambient temperature and pressure. The industrial three-step production of methanol from methane is not direct. It needs H_2 and CO, as well as high temperatures (up to 900°C) and high pressure (up to 100 bar). Thus, a possible enzymatic mechanism with MMO has great industrial interest. Perhaps the soluble iron-containing form of MMO could also be involved in converting natural gas into biomass by obligate methanotrophic bacteria. There are some factories that have produced 1000 tons of biomass/month from natural gas. Methanotrophic bacteria also have an important ecological role. These bacteria are situated in aerobic sediments or in the metalimnion layer (a nearly semi-anaerobic layer) of landfills, rice fields, lakes, or oceans, where they utilize the flux of methane from the lower anaerobic sediments. Apart from their biological and environmental importance (*31*), MMOs have attracted attention because of their unique ability to oxidize a broad range of hydrocarbons in addition to methane (*31, 42*). These properties have led to several applications for methanotrophic bacteria, including bioremediation of land contaminated by oil spills and the oxidative removal of trichloroethylene from drinking water. Several patents have been obtained using the bacteria or purified components.

3. The purple acid phosphatases (*3, 4, 20, 43, 44*) can be found in various organs in mammals, where they might be implied in different diseases. The proteins show high tartrate-resistant acid phosphatase activities, but other roles have also been suggested (*3, 4, 20, 43, 44*). For instance, uteroferrin is found in the uterine fluid during midpregnancy and is believed to be involved in iron transport to the fetus. When found in macrophages, osteoclast, Gaucher cells, and spleen, the PAPs are located in lysosomes. Some researchers believe that it might be important for generation of reactive oxygen species, in analogy with the function of myeloperoxidase. The PAPs are believed to be implied in Gaucher's disease, hairy cell leukemia, and giant-cell tumor of bone (osteoclastoma) (*43, 44*). A somewhat related purple acid phosphatase is also found in plants, but it contains a zinc–iron center, which, however can be reconstituted into an iron–oxygen cluster with the enzymatic activity still present.

4. The soluble stearoyl–acyl carrier protein Δ^9 desaturase from higher plants such as castor, cucumber, spinach, turnip, rape, and avocado catalyzes an important step in plant lipid desaturation (*27, 28, 45*). The reaction is important for regulation of membrane fluidity and is also an important factor in nutrition.

5. Hemerythrin and myohemerythrin have roles as oxygen carriers in marine invertebrates, a function similar to that of the heme proteins hemoglobin and myoglobin in mammals and the copper–protein hemocyanin in mollusks and arthropods (*1–7, 13*).

6. The role of the iron–oxygen cluster in ferritin is not clear, but it is suggested that it plays a role in the first step (nucleation) of the multiiron aggregate in ferritin. Ferritin has an important role as a transport and storage protein for iron in many organisms (*1, 22*).

7. The biological functions for rubrerythrin and nigerythrin are not known at present (*23–26*), but they might be important in reactions involving peroxides or oxygen. They are found in anaerobic bacteria, so non–oxygen-related reactions could also very well be their function, as is possibly the case for the PAPs.

It is clear that the iron–oxygen proteins constitute a large group of proteins with manifold diverse functions. This group of proteins has more diverse roles and different structures than, for instance, the class of noncomplex iron sulfur proteins, which "only" in most cases transport electrons (except aconitase and iron hydrogenase, which are enzymes). We will describe some general features and then the different diiron-oxygen proteins by themselves, and draw some general conclusions and perspectives at the end of the review.

II. General Features of the Diiron–Oxygen Proteins

Figures 1 and 2 show the structures of the diferric iron cores with ligands including the μ-oxo or μ-hydroxo bridge of Hr, RNR-R2, and MMOH. These three clusters might be considered as patterns for three major groups of diiron–oxygen clusters. A similar core is also known for some ferritins (see discussion in Section IX). Generally, in the proteins the iron ligands consist of a (sometimes substituted) bridging μ-oxo atom, at least one bridging carboxylate, histidines, carboxylate(s), and sometimes perhaps an oxygen from asparagine (Sträter, Krebs, and Witzel, personal communication). A bacterioferritin structure with an iron–oxygen cluster is solved (*22*), as well as a plant purple acid phosphatase structure, but the latter is not yet published

E. coli Ribonucleotide reductase R2

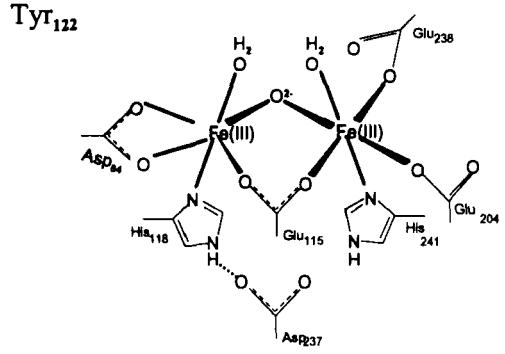

Methylococcus capsulatus (Bath) MMOH

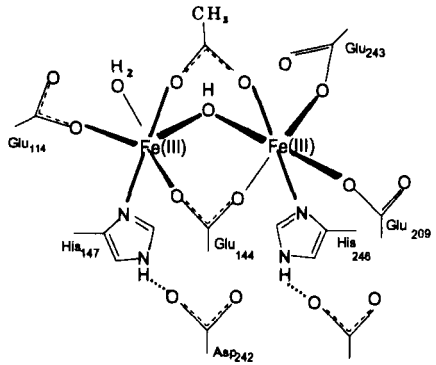

FIG. 2. Diferric iron clusters from ribonucleotide reductase R2 subunit and methane monooxygenase hydroxylase. The drawings are based on (*18, 19*) for RNR-R2 and (*15*) for MMOH.

(Sträter, Krebs, and Witzel, personal communication). The bacterioferritin cluster is very similar to the MMOH cluster. In the near future the structures of the stearoyl–acyl carrier protein Δ^9 desaturase (*46*), and rubrerythrin will be solved.

The main characteristics of the diferric iron–oxygen clusters in these proteins can be discussed in terms of the following:

1. The number of histidines coordinated to the cluster (five for Hr and two for MMOH, RNR-R2, and bacterioferritin).

2. The numbers of bridging carboxylates: two (Hr), one plus a nearly bridging carboxylate (MMOH), or one (RNR-R2). In RNR-R2 the Glu115 is bidentately coordinated to both irons (Fig. 2). In some cases an oxygen from a carboxylate may serve as a bridge between the irons.
3. The presence of an oxo bridge (Hr, RNR, Rr, Δ-ACP) or a hydroxo bridge (MMOH and probably PAP) between the two irons.
4. The presence of a tyrosine ligand (PAP).
5. The absence or presence of a tyrosine 5–6 Å from the iron cluster, but not coordinated, which may form a free radical under special reaction conditions (RNR-R2 and ferritin) (*13*).

Furthermore, the iron-coordinated amino acids differ in their participation in hydrogen bonds, exemplified by the histidines in Fig. 2. There is also a question of the presence or absence of bidentate iron-coordinated carboxylates (nonbridging), e.g., Asp84 in RNR-R2 (Fig. 2).

In general, these binuclear iron clusters can exist in at least three oxidation states: diferric or resting [Fe(III)Fe(III)], half-reduced or mixed-valent [Fe(II)Fe(III)], fully reduced or diferrous [Fe(II)Fe(II)], and possibly also in ferryl-containing states [Fe(IV)Fe(IV) and Fe(III) Fe(IV)]. The change of the oxidation state of the irons can lead to changes in or loss of the bridging oxygen [e.g., the oxo bridge is converted into a hydroxo bridge in mixed-valent Hr (*47, 48*) and possibly in RNR-R2 from mouse and HSV1 (*35*)]. Reorganization of amino acids coordinated to dinuclear iron centers has been observed upon change of the redox states [for instance, carboxylate shifts (*10, 15*)].

The differences in ligandation of the two irons in the proteins are reflected in the differences in the redox potential of the proteins (Table I) as well as magnetic coupling between the two irons (Table II). There is no clear correlation between the redox potentials and the nature of the iron ligands, except that a tyrosine ligand seems to prevent formation of the stable diferrous state (mammalian PAP, but not kidney bean PAP). Very subtle changes of the clusters might make drastic changes in redox behavior of the clusters. For example, mouse and herpes simplex virus type 1 (HSV1) RNR-R2 can exist in stable mixed-valent forms under mild reduction conditions, while the homologue *E. coli* RNR-R2 cannot stabilize a similar mixed-valent form. Also, there is a change in redox potential of MMOH upon interaction with MMOB (and MMOR) (Table I). For the observed magnetic couplings between the irons, it seems clear that the nature and interactions of the bridging atom(s) determine the strength of this coupling, and only minor effects are created by other iron ligands (Table II).

The best criteria to establish the presence of an iron–oxygen cluster are observations along the following lines:

TABLE II

SELECTED VALUES FOR MAGNETIC COUPLING BETWEEN THE DIMERIC IRON IONS IN IRON–OXYGEN PROTEINS

Protein	State of iron center	Coupling constant $J(cm^{-1})$ ($\mathcal{H} = -2JS_1 * S_2$)	Ref.
Hr[a]	Fe(III)–Fe(III)	−134	*1–4, 11–14*
Oxy Hr		−77	*1–4, 11–14*
RNR—R2[b]			
—*E. coli*		−92	*49*
—mouse H_2O		−77	*49*
—mouse D_2O		−70	*49*
—HSV1[c]		−66	*49*
—*S. typhimurium*		−69	*49*
MMOH[d]		−7.5	*50*
PAP[e]		−10 to −20	*51*
Hr	Fe(III)Fe(II)	−8	*52*
MMOH		−30	*53*
MMOH + MMOB[f]		−5	*53*
PAP		−11	*54*
RNR—R2			
—mouse		−7.5	*35*
—HSV1		−6.5	*35*
Deoxy Hr	Fe(II)Fe(II)	$-12 \leq J \leq -38$	*1–4, 11–14*
Deoxy Hr + N_3^-		+2	*55, 56*
MMOH		+0.3	*56*
MMOH + MMOB		+0.4	*56*
RNR-R2, mouse + N_3^-		+0.3	*57*

[a] Hemerythrin.
[b] Ribonucleotide reductase.
[c] Herpes simplex virus type 1.
[d] Methane monooxygenase hydroxylase.
[e] Purple acid phosphatase.
[f] Methane monooxygenase B component.

1. The μ-oxo-bridged proteins have typical strong ($\varepsilon > 5000\ M^{-1}\ cm^{-1}$) light absorption bands in the 300–450 nm region and sometimes even at higher wavelengths (especially the azide complexes), which are missing or very weak in μ-hydroxo-bridged proteins or model compounds. This makes it possible to observe an ^{18}O induced shift in the resonance Raman spectrum of the symmetric (-10 to $-20\ cm^{-1}$) and sometimes antisymmetric (-20 to $-40\ cm^{-1}$) Fe–O–Fe vibration modes of the oxygen-to-iron charge transfer transition (Table III). Thus far, no Fe–O–Fe Raman modes have been reported for μ-hydroxo bridges

TABLE III

RESONANCE RAMAN PARAMETERS FOR IRON–OXYGEN PROTEINS

Diiron–oxo protein	ν_s(Fe–O–Fe)[a] (cm^{-1})			ν_{as}(Fe–O–Fe)[a] (cm^{-1})		
	ν	$\Delta^{18}O$	ΔD	ν	$\Delta^{18}O$	ΔD
Hr[b] (oxy)	486	−14	+4	753	−37	n.d.[c]
Hr ($metN_3$)	507	−14	0	768	−35	n.d.
PAP[d]	n.o.[e]					
Δ-ACP[f]	519	−18	0	747	−34	+3
Rr[g]	514	−18	+2	n.o.		
RNR-R2[h] (met)	493	−13	+3	756	−25	n.d.
MMOH[i]	n.o.					

All the data in this table were obtained by the Loehr group (*28*) except for rubrerythrin which was obtained by Kurtz (*25*).

[a] Vibrational frequencies in cm^{-1} in $H_2{}^{16}O$. Isotopic shifts in cm^{-1} are for $H_2{}^{18}O$–$H_2{}^{16}O$ ($\Delta^{18}O$) or D_2O–$H_2{}^{16}O$ (ΔD).

[b] Hemerythrin.

[c] Not determined.

[d] Purple acid phosphatase.

[e] Not observed.

[f] Stearoyl acyl carrier protein Δ^9-desaturase.

[g] Rubrerythrin.

[h] Ribonucleotide reductase from *E. coli*.

[i] Methane monooxygenase hydroxylase.

in proteins. For in-depth analyses of the optical, Raman, CD, and MCD properties of diferric clusters, see (*1, 5, 7, 12, 13, 58, 59*).

2. Relatively short iron–iron and iron–oxygen distances are obtained by EXAFS (*14, 21*) or other X-ray–dependent techniques. The iron–oxygen clusters with an oxygen bridge have shorter distances (i.e., Fe–O 1.7–1.8 Å and Fe–Fe 2.9–3.2 Å for the diferric state) than those with hydroxo or alkoxo bridges (i.e., Fe–O 1.9–2.1 Å and Fe–Fe 3.2–3.6 Å). Comparing a single nonsubstituted oxo bridge and a single substituted bridge (hydroxo, water, alkoxo), one generally finds weaker magnetic coupling between the irons for the latter (e.g., $-J$ = 90–150 cm^{-1} and 5–17 cm^{-1} for the diferric state, respectively; Table II). An additional hydrogen bond to a μ-oxo bridge might lower the magnetic interaction [e.g., oxyHr (*1, 7, 12, 58*) and perhaps also for mouse, HSV1, and *S. typhimurium* diferric RNR-R2 proteins (*49*)]. A good general method to distinguish bridges is described by Gorun and Lippard (*14*), who show that the Fe–O distance is the determining factor for the magnetic coupling. It is, however, possible that their relation is not

valid in the presence of two (hydr)oxo bridges. In the diferric state, it is only possible to observe EPR signals of hydroxo-bridged proteins with parallel-mode EPR of excited states (best in the temperature range 20–60 K) (*50*) (see point 5 later). For oxo-bridged proteins, these excited states are populated only at much higher temperature, and the resonances are then probably too broad to be observed.

3. Mixed-valent [Fe(II)Fe(III)] antiferromagnetically coupled (i.e., with an $S = \frac{1}{2}$ ground state) EPR spectra should show all three g-values below 2.0 for diiron–oxygen proteins. This distinguishes them from, e.g., iron–sulfur proteins, which have at least one g-value above 2.0. However, some complexes, such as that of Uf with phosphate, have g-values above 2.0 (*3*). Under certain conditions (e.g., X-radiation at 77 K, leading to low-temperature reduction, followed by annealing at 165 K) (*60, 61*), the mixed-valent state may have a weakly coupled ferromagnetic ground state with typical $S = \frac{9}{2}$ EPR signals (see Section IV and Fig. 7). Deuterium exchange observed by ENDOR or ESEEM methods (*47, 48*) is a definitive way to establish the presence of a μ-hydroxo bridge. Another method to establish the nature of the bridge is to estimate the strength of the antiferromagnetic coupling by the temperature dependence of the EPR microwave power saturation (*53*). This method gives a good indication of the presence of a μ-hydroxo bridge if the estimated $-J < 35\ \text{cm}^{-1}$.

4. The Mössbauer spectra of the diferric, diferrous, and also, in the cases where they are found, the diferryl states, should show quadrupole doublet(s), demonstrating the presence of non-Kramers doublets of spin-interacting clusters (*1–4 ,6, 13, 50, 62–64*). The diferric, mixed-valent, diferrous, and diferryl Mössbauer spectra are distinct for diiron–oxygen proteins. Not only are the isomer shifts and ΔE_q different from those of iron–sulfur clusters, but also the magnetic exchange couplings are weaker. Furthermore, the iron–oxygen cluster does not show the typical cysteine- or sulfur-induced changes in the hyperfine coupling constant. Thus far, no iron–oxygen cluster has been found with cysteine ligands, but there is no reason to exclude that in the future one or more cysteines may also be found in iron–oxygen proteins (and such a protein should then have different light absorption, MCD, and Raman spectra). Information on the ligands in the various redox states of the diiron cluster in iron–oxygen proteins has also been obtained from NMR studies of the paramagnetically shifted ligand proton resonances (*3, 4, 20, 41*).

5. The diferrous state can have an integer spin EPR signal with a g-value in the range 18 to 12. Such signals are in general best observed

in parallel mode EPR at very low temperature when they arise from a ground state. The resonance condition for such a signal is:

$$(h\nu)^2 = \Delta^2 + (g_{\text{eff}}\beta B\cos\theta)^2,$$

where h is Planck's constant, ν is the microwave frequency, Δ is the zero-field splitting of the spin doublet which gives rise to the resonance, g_{eff} is the g-factor, β is the Bohr magneton, B is the magnetic field, and θ is the angle between the principal axis and the static field B (*65a,b*). This kind of integer spin signal in an iron–oxygen protein was first observed in the ferromagnetically coupled diferrous Hr-azide (*66*). Later it was also observed in MMOH, and its origin was analyzed by Hendrich as an $S = 4$ state (*65a,b, 67*) and in RNR-R2 in presence of azide (*68*). It was recently reported that it is also possible to use these signals for ESEEM and ENDOR measurements (*69, 70*). [Warning: It seems that when Δ is small enough that the signal may be observed by X-band EPR, mononuclear iron centers such as ferrous EDTA (*65a*) with an $S = 2$ state can show similar signals in the $g = 16$ region. Also, in X-band EPR a relatively weak signal which integrates to 5% of the clusters might in reality represent 100% of the clusters if Δ is larger than 0.3 cm^{-1} (X-band EPR) (*57*).]

III. Hemerythrin

Hemerythrin is the oxygen carrier and storage protein of certain marine invertebrates and is a functional counterpart to the hemoglobin and myoglobin found in higher organisms. It exists either as oligomeric or monomeric forms. Each subunit has a molecular weight around 14 kD and has a μ-oxo-bridged dinuclear iron center. Hr has two distinct functional forms in nature: either the reduced deoxy form with a hydroxy-bridged diferrous iron center, or the oxygen-bound form, which is an oxy-bridged diferric form with oxygen bound as a peroxide. The crystal structures of various forms of Hr have been reported [(*4*) and references cited therein)].

The spectroscopic properties of the iron center of Hr have been elucidated in considerable detail. These properties have often been used for comparison with properties of new proteins to probe the likelihood of having found a new member of the diiron-oxygen class of proteins. Some of the spectroscopic properties of Hr are included in Tables I–III.

A mixed-valent state of the iron center of Hr was found by one

electron reduction of the oxidized state or oxidation of the reduced state. Although these states were found to give somewhat different EPR spectra, they were both characterized as antiferromagnetically coupled $S = \frac{1}{2}$ states. Both have hydroxy bridges (*47, 48*). The hydroxy bridge and deoxy form of the protein is interesting in that it has one five-coordinated and one six-coordinated ferrous ion, with a hydroxy bridge and relatively weak antiferromagnetic coupling between them. Addition of anions occurs readily to the five-coordinate form, which leads to a transformation into a weakly ferromagnetically coupled state, as shown by EPR and MCD measurements (*71, 66*). It was suggested that the azide-bound form of deoxyHr has an additional proton in its bridging ligand, making it an aquo bridge (*66*). Recently, metal substitutions (Co and Mn) into the apo form of Hr have been reported. The results showed that the presence of a metal site generally increases the stability of the tertiary structure of the protein (*72*).

IV. Ribonucleotide Reductase

A. Overall Structure

Ribonucleotide reductases (RNR) from different origins have been shown to contain different metal ions and require different cofactors. This has led to a systematic definition of three major classes at present, I–III (*40*). All RNRs seem to use a radical mechanism at some stage of their catalytic process. The class I enzymes, which contain iron and a stable tyrosyl free radical in the active state, are found in certain bacteria, e.g., *E. coli*, and also in eukaryotes. Certain bacteriophages and eukaryotic viruses also carry genes for their own RNR of this class.

The best-characterized class I RNR is that of *E. coli*. Excellent reviews have recently been written on this enzyme (*37–39, 73*). The enzyme consists of the nonidentical proteins R1 and R2, each of which is a homodimer. The holoenzyme therefore has an $\alpha_2\beta_2$ structure. The crystal structures of the *E. coli* R1 and R2 proteins have recently been reported (*18, 19, 74*). Protein R1 has 2×761 residues and contains the substrate binding sites, as well as the binding sites for the allosteric effectors. The exact localization of the specific binding sites for the effectors and the substrate, as well as the area of subunit interaction in the active enzyme, has so far only been modeled into the R1 structure. Protein R2 has 2×375 residues and contains the sites for the iron center as well as the tyrosyl radical. The crystal structure is obtained for the met form, i.e., without tyrosyl free radical. There is one site for

the dinuclear iron center and one for the potential tyrosyl radical in each polypeptide chain of protein R2 (*75a*).

B. Structure of the Iron Center

The iron center of protein R2, which is one of the focal points of this review, is an antiferromagnetically coupled pair of high-spin ferric ions in the active state. Figure 3 shows the known redox states of the iron/tyrosyl radical site in the protein. The crystal structure of the met form, i.e., the diferric form without radical, around the iron site (Figs.

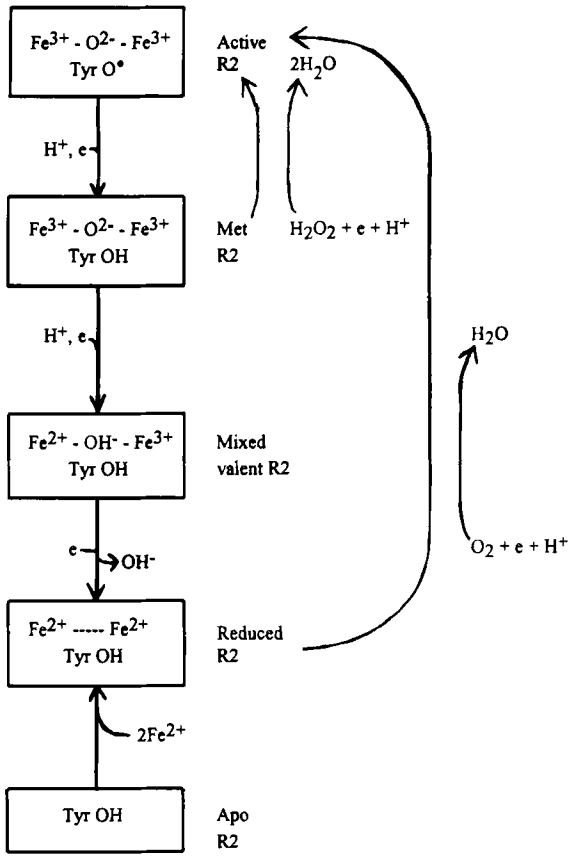

FIG. 3. Scheme of various redox states of ribonucleotide reductase protein R2, as well as known reactions to move between the states. Tyr O• represents the tyrosyl radical; Tyr OH is the normal tyrosyl residue (Y122 in *E. coli* ribonucleotide reductase).

1 and 2) shows that the ligands are mainly carboxylic acids, with one histidine liganding each iron ion. The tyrosyl residue [Y122 in *E. coli* (*75b*)] which harbors the free radical is located in the vicinity of the iron site, but is not close enough to be a ligand. The distance between the tyrosyl hydroxyl group and the closest iron is 5.2 Å. One intriguing question regarding RNR concerns the role of the tyrosyl radical in the enzymatic mechanism and the requirement for a very specific and long-range (appr. 35 Å) electron transfer if and when the tyrosyl radical takes part in each enzymatic cycle. Figure 4 shows a hypothetical scheme depicting the proposed route of the electron based on the crystal structures and model building of the whole complex (*73, 74*). The suggested role of the stable free radical in protein R2 is to create a transient free radical at one of the active-site cysteines in R1, which is suggested to be the direct source of radical chemistry in the reduction of the substrate (*76*). The iron center has a proposed role in the formation of the free radical, but it is also suggested as one of the participants in the electron transfer route, presumably operating during catalysis.

C. Formation of the Iron Center and Tyrosyl Radical

The formation of the iron site in apoprotein R2 from RNR occurs concomitantly with the formation of the free radical on the neighboring tyrosyl residue (Y122 in *E. coli*). In RNR the reaction requires apoprotein R2, ferrous iron, and molecular oxygen (*77–79*) and in the absence of external reductants may be summarized as

$$3Fe(II) + P\text{-tyr-OH} + O_2 + H^+ \rightarrow Fe^{III}O^{2-}\text{-}Fe^{III}\text{-P-tyr-}O^{\cdot} + H_2O + Fe(III) \quad (1)$$

where P designates the iron binding site of the R2 protein and tyr-OH the neighboring tyrosyl residue which harbors the free radical. It is a complex reaction with several intermediates, which to some extent have been characterized; see later discussion (*80–83*). Formally, the reaction is similar to the terminal oxidase reaction in the cell respiratory cycle, in that molecular oxygen is reduced to water in a four-electron reduction.

One of the reducing equivalents is supplied by the tyrosyl residue in forming the radical; two equivalents are provided by the ferrous ions when they become ferric in the diiron center, and the fourth equivalent can be provided by a third ferrous ion (*78, 82, 84*). Resonance

Raman experiments have shown that one of the oxygen atoms of the molecular oxygen forms the μ-oxo bridge between the iron ions (*30*).

The reaction has also been studied in a point mutant, R2 Y122F, where the native radical-generating tyrosyl residue is replaced with phenylalanine (*80, 86a,b*). In that case the reaction with ferrous iron and oxygen is generally slower. The early intermediates in the reaction appear to be similar to the wild-type ones, but at later times, after the formation of the apparently normal oxygen-bridged diiron site is complete, a number of secondary paramagnetic species are observable on a time scale of minutes or more. Some of these transients are free radicals associated with tryptophan residues (*85, 86a,b*). An interesting observation on the mouse RNR system with the R2 mutant Y177F, corresponding to Y122 in *E. coli* R2, suggested that transient radicals of this type could give a low but specific activity of the enzyme (*87*).

In a series of elegant studies, Stubbe and co-workers have elucidated the kinetics and characterized some of the transient species in the radical regeneration reaction in protein R2. Early intermediates, formed before the formation of the iron center and the tyrosyl radical is complete (i.e., before 0.5 s), include an iron-linked free radical (species X) and a suggested free radical on a tryptophan residue, W48 (*80–83*).

Figure 5 shows a suggested scheme of events, essentially based on the previous proposals (*80–83*), but we have here explicitly suggested that the iron-linked free radical is OH· derived from the molecular

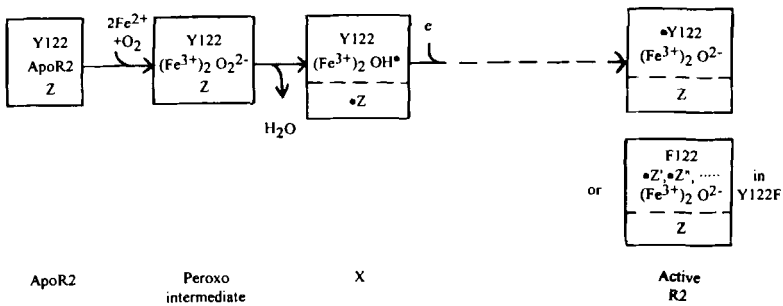

FIG. 5. Schematic representation of events during the reconstitution with ferrous iron and oxygen of the diferric/tyrosyl radical site in RNR-R2. The X intermediate (*80, 82, 83*) is proposed to arise from the added dioxygen, formally as a hydroxyl radical bound to the diferric site. Y122 is the tyrosyl residue to become the stable radical (*E. coli* numbering). Z is a tryptophan and/or tyrosine residue (probably the conserved W48 and/or Y356 along the suggested electron transfer pathway) that temporarily harbors a free radical formed by loss of an electron. Y122F is the R2 point mutant, where the stable Y122 radical cannot be formed.

oxygen as one stage in the formation of the oxo bridge [cf. (*78*)]. Note that the scheme should be equally appropriate for wild-type protein and for the Y122F mutant, until the very last stage when the Y122 radical is formed in the wild-type protein. In the Y122F mutant, approximately concomitantly with X on the 0.3 s time scale, EPR studies showed the appearance of an early transient free radical which is not metal-linked and could be on W48. There was also a probably different early radical on Y356 observed by transient light absorption (*86b*). This is the reason for not suggesting a definite identity of $Z^{\cdot}$ which might involve more than one residue.

The model in Fig. 5 includes the following events: Oxygen binds to the two protein-bound Fe(II) to become a peroxide. Water is split off in a reaction which abstracts a third electron from a suitable source Z and creates X, which is a diferric hydroxyl radical species. Species Z is an oxidizable amino acid such as W48 and/or Y 356, which becomes a free radical $Z^{\cdot}$. It should be noticed that W48 as well as Y356 are part of the proposed electron transfer chain which links the active site in protein R1 with the iron site in protein R2 (Fig. 4). Species X will oxidize Y122 to form the stable tyrosyl radical. The reduced X will be the oxo-bridged diferric site. Depending on the supply of external reductants, Z may be more or less long-lived. Thus, X is the formal oxidant creating the Y122 radical in the suggested scheme in Fig. 5. Alternatively, Z might be considered as the immediate oxidizing agent for Y122, as suggested in (*80–83*). Circumstantial evidence showing the necessity for $Z^{\cdot}$ involvement is that formation of the functional tyrosyl radical (on Y177, mouse numbering) in mouse R2 is critically dependent on the nature and ease of oxidation of W103, corresponding to W48 in the *E. coli* protein. In the reconstitution reaction of the point mutant W103F, the amount of Y177 radical is less than 5% of the normal yield, whereas in W103Y it is close to normal (*88*). It seems that if $Z^{\cdot}$ cannot be transiently formed and stabilized, then Y122 cannot be oxidized.

Although the electron balance is relatively well understood in the foregoing ferrous iron/oxygen reaction, the involvement of protons is not. Formally, one proton is lost from Y122 when it forms a free radical, since ENDOR studies have shown that the radical is a neutral phenoxy-type radical (*89*). Two protons are needed to form one molecule of water. The oxygen bridge is not protonated in the μ-oxo diferric state. Thus, the radical-generating reaction should require participation of at least one protein-bound or exogeneous proton in order to be balanced.

The question of proton transfer can also be raised in the context of the enzymatic cycle. If Y122 alternates between the radical and nonradical state at each enzymatic cycle, which seems likely, the ques-

tion arises whether this requires transfer not only of an electron, but also of a proton. There is some evidence from the crystal structure of the met form of *E. coli* R2 that the OH group of Y122 is hydrogen-bonded to one of the carboxylate oxygens of Asp 84, which is a bidentate ligand to Fe1 (*18, 19*). In anticipation of a crystal structure of the active form of R2, one might speculate that the tyrosyl hydroxyl hydrogen is transferred to Asp84 when Y122 becomes a free radical, which could result in making Asp 84 a monodentate ligand in the active form of R2. As will be discussed in more detail in Section IV,G, there is spectroscopic evidence of different ligand geometry and differences in hydrogen bonding between the various redox forms of the iron/radical site.

D. Spectroscopy of the Diferric Iron Center

Certain spectroscopic properties of the oxidized iron center were characterized at an early stage (*77*) and compared with those of hemerythrin, which was at that time the best-characterized protein with a diferric μ-oxo-bridged iron center. A prominent light absorption in the 300–400 nm region, with partly resolved bands around 320 and 360 nm (ε around 10,000 M^{-1} cm^{-1}) and two weak bands (ε around 1000 M^{-1} cm^{-1}) at 500 and 600 nm were found to be common characteristics. This light absorption is due to charge-transfer interactions between iron and its ligands, particularly the μ-oxo bridge. In the active form of protein R2, the tyrosyl radical contributes to the light absorption with a sharp band at about 410 nm (ε = 6600 M^{-1} cm^{-1}) and a broader feature around 390 nm (ε = 2000 M^{-1} cm^{-1}) in the *E. coli* protein (*77*). In mouse R2 the sharp band is at about 415 nm (*79*).

Raman bands assigned to symmetric and antisymmetric modes of (Fe–O–Fe) have been reported at 493 cm^{-1} and 756 cm^{-1}, respectively, for both active and met forms of protein R2 (Table III).

In contrast to the tyrosyl free radical, the diferric iron center in active and met R2 is EPR-silent, since its ground state is antiferromagnetic. However, most preparations of R2 display low-temperature EPR signals at g = 4.3, because of rhombic Fe(III) in small and varying amounts. This so-called nonspecific iron EPR signal can be suppressed by careful purification of the protein. It is reasonable that when the protein has undergone the radical generation reaction with exogenous ferrous iron and no external reductants, one-third of the added iron should end up as Fe(III) outside the dinuclear site. This Fe(III) may be more or less completely removed by the subsequent purification.

E. Spectroscopy of the Tyrosyl Radical

The tyrosyl radical is characterized by an EPR spectrum as well as by the characteristic light absorption band around 410 nm. EPR spectra of tyrosyl radicals observed in several R2 proteins from different species display some minor variations, most of which are due to different geometries of the locked tyrosyl ring relative to the protein backbone and the two β protons (*90–92*). Typical EPR spectra at 9 GHz and low temperature of protein R2 tyrosyl radicals found in *E. coli*, mouse, and HSV1 proteins are shown in Figs. 6a–c. The EPR spectra of the tyrosyl radicals of RNR-R2 are generally difficult to saturate by microwave power, because of exchange interactions with the iron center (*49*). The figure also includes an EPR spectrum of a radical found in the R2F protein of an inactive RNR in the bacterium *Salmonella typhimurium* (Fig. 6d). This EPR spectrum has a remarkable similarity to that of the photosystem II (PSII) tyrosyl radical (*49*). A careful analysis of the spectral parameters of this type of R2 EPR spectrum (*S. typhimurium*) as compared with those of the *E. coli* R2 EPR spectrum revealed that a major difference exists mostly in the spin density distribution in the two radicals (*93*). In the *E. coli* case, a comparatively larger spin density resides at the C1 carbon. Previous comparisons between the RNR tyrosyl radicals and that observed in PSII have pointed out that the

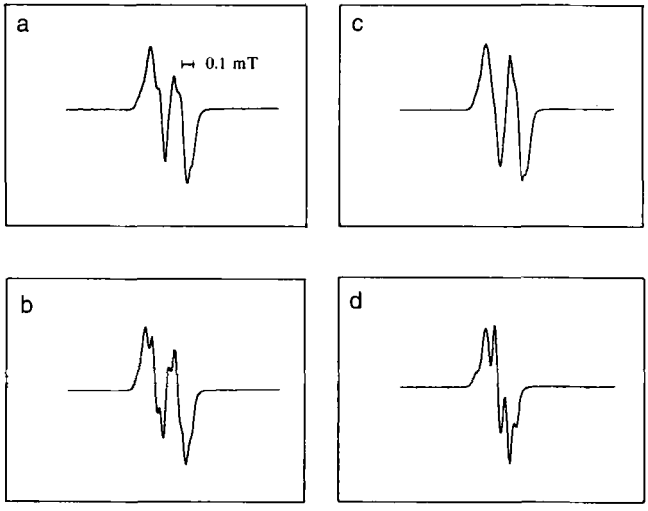

FIG. 6. EPR spectra recorded around 20 K of tyrosyl radicals in RNR-R2 from different species: (a) *E. coli*, (b) recombinant mouse, (c) recombinant herpes simplex type 1, (d) *Salmonella typhimurium* R2F protein. Adapted from (*49*).

overall difference in spin-density distribution should be related to the presence of electric charges around the radical and possibly the presence or absence of a hydrogen bond to the phenol oxygen (*92*). ENDOR studies have suggested the absence of a hydrogen bond in the radical of *E. coli* R2 and the presence of a hydrogen bond in the radical of PSII (*89, 92*). The observation of a new RNR radical with a spin-density distribution like that of the PSII radical may be relevant for a better understanding of these matters.

High frequency (140 GHz) EPR spectra have yielded precise estimations of the *g*-value anisotropy of the *E. coli* R2 tyrosyl radical (*94*). Similar studies at 245 GHz have been performed on the *S. typhimurium* R2F radical (*93*).

Temperature-dependent saturation recovery experiments by pulsed EPR have been performed on the RNR radicals, to assess the interactions between the radical and the iron center in the R2 proteins from different species (*95, 49*). The J couplings of the diferric sites evaluated from these and other studies are shown in Table III. The interaction with iron explains why the EPR signal of the tyrosyl radical of mouse RNR-R2 is nearly impossible to saturate with microwave power at 77 K.

F. Redox Properties of the Iron Center

Figure 3 shows a scheme of the various redox states of the iron/radical center of protein R2 of ribonucleotide reductase characterized up to now. Three electrons are needed for full reduction of the site in active R2 (*96*). As previously mentioned, O_2 and an extra electron are needed for regeneration of active R2 from the fully reduced state. A shortcut radical generation pathway can yield the active form from the met form of *E. coli* R2 by reaction with hydrogen peroxide, possibly via a combination of reduction and oxidation (*97a,b*). From analogy with, e.g., hemerythrin, the mixed-valent state of *E. coli* R2 was postulated to exist, but for a long time could not be generated. It required particular conditions, such as treatment with diimide or hydrazine (*98, 99*), or ionizing irradiation in the frozen state leading to low-temperature reduction (*60, 61*), to stabilize a mixed valent state in the *E. coli* protein. In contrast, in mouse or HSV1 protein R2, mild chemical reduction gave rise to a mixed-valent state which was stable at room temperature (*35*). The ability to form a stable mixed-valent state may be related to the suggested additional hydrogen bond to the oxo bridge in the diferric mouse and HSV1 proteins, which is absent in *E. coli* R2 (*49*). Table III shows the redox potentials that have been estimated for the R2 proteins.

G. Mixed-Valent Form of the Iron Center

In mouse and HSV1 R2, the mixed-valent state is an antiferromagnetically coupled $S = \frac{1}{2}$ state. In *E. coli* protein R2, radiolytic reduction in frozen solution at 77 K gives a primary antiferromagnetically coupled $S = \frac{1}{2}$ state, which transforms into an $S = \frac{9}{2}$ state after annealing at about 165 K and becomes EPR-invisible after annealing at about 230 K (*61*). The mixed-valent state produced by radiolytic reduction at 77 K should retain the ligand geometry characteristic of the diferric state while kept at the low temperature, and structural relaxation occurs as the temperature is raised. Figure 7 shows EPR spectra of mixed-valent states of mouse, HSV1, and *E. coli* R2 proteins produced in different ways, displaying the $S = \frac{1}{2}$ signals below $g = 2$ (0.35–0.45 T in the figure) for all three proteins, and in addition the $S = \frac{9}{2}$ signal

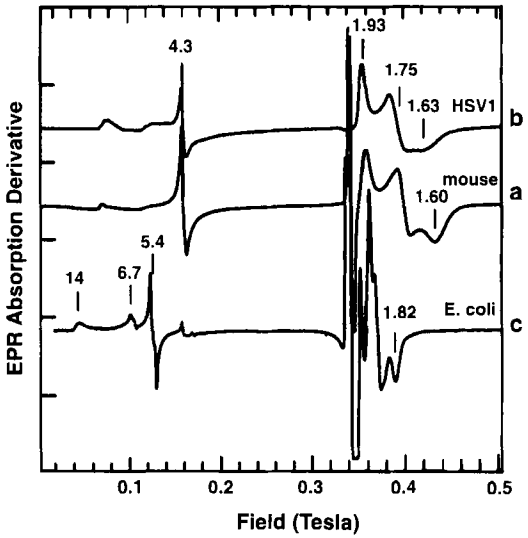

FIG. 7. EPR spectra of mixed-valent states of the diiron site in RNR-R2: (a) 1.0 mM mouse R2 and (b) 0.6 mM herpes simplex virus type 1 R2 after 60 min treatment with 10 mM hydrazine showing the $S = \frac{1}{2}$ signal in the $g > 2$ region. The $g = 4.3$ signal arises from rhombic Fe(III), probably unspecifically bound. (c) Low-temperature reduced (*61*) met R2 from *E. coli*, 1.3 mM in 50% glycerol, 50 mM tris-HCl, 0.1 M KCl. The sample was γ-irradiated at 77 K with 5.4 Mrad, giving the $S = \frac{1}{2}$ signal at $g > 2$, and photobleached for 2 hours at 77 K, which partially transformed the signal to a $S = \frac{9}{2}$ signal in the $g = 14$–5 region. The spectra were recorded at 3.6 K (a,b) or 7 K (c), with 16 mW microwave power, at 9.62 GHz and 10 G modulation amplitude. Obtained from S. Kuprin and R. Davydov, as a personal communication.

for the *E. coli* protein (0.02–0.14 T) and the small amount of the rhombic Fe(III) signal at $g = 4.3$ (0.156 T) for the mouse and HSV1 proteins. In the experiment shown in Fig. 7, the partial transformation to the ferromagnetically coupled $S = \frac{9}{2}$ state was achieved by photobleaching (S. Kuprin and R. Davydov, personal communication).

An interesting observation is that the radical neighboring form and the met form of the iron center of *E. coli* protein R2 gave slightly different EPR spectra after radiolytic reduction at 77 K, indicating a different ligand geometry in the diferric states in the two cases (*100*). At present the EPR differences cannot be directly interpreted in terms of structural differences.

The antiferromagnetic coupling constant J ($\mathcal{H} = -2JS_1 * S_2$) of the $S = \frac{1}{2}$ states can be evaluated from the EPR parameters and was found to be quite low (appr. -10 cm^{-1}) for the $S = \frac{1}{2}$ mixed-valent states observed in the R2 proteins (Table II). The results are consistent with a protonation of the oxo bridge to a hydroxo bridge between the iron ions in this state (*35, 61*).

H. Diferrous Form of the Iron Center

The fully reduced iron center in *E. coli* R2 is structurally characterized from analogy with a Mn-containing R2 protein (*101*). There was no evidence of any bridging ligand in the structure, also in agreement with preliminary data on the diferrous form of R2 (Pär Nordlund, personal communication).

Mössbauer, MCD, and EPR spectroscopy have been used to study the diferrous form of the iron center. EPR spectra of the fully reduced *E. coli* R2 protein have been reported (*68*). Parallel-mode EPR experiments showed a signal originating from a ferromagnetically coupled high-spin diferrous cluster, i.e., with $S = 4$. Azide was shown to bind to the iron cluster, and high concentrations of azide caused a shift as well as an increase in intensity of the EPR signal (*68*).

Figure 8 shows EPR spectra observed in the perpendicular and parallel mode for the fully reduced state obtained by chemical reduction of the mouse R2 protein in a solution containing 20% glycerol. Prominent signals are observed in the low–magnetic-field region. Because parallel-mode EPR will particularly detect systems with integer spins, a signal at $g = 17$ suggests the origin to be an integer spin system. A broader signal is also observed in the normal perpendicular EPR mode from this state, as shown in the figure. Magnetic susceptibility measurements are under way to examine the fully reduced state in the absence and presence of azide (*57*).

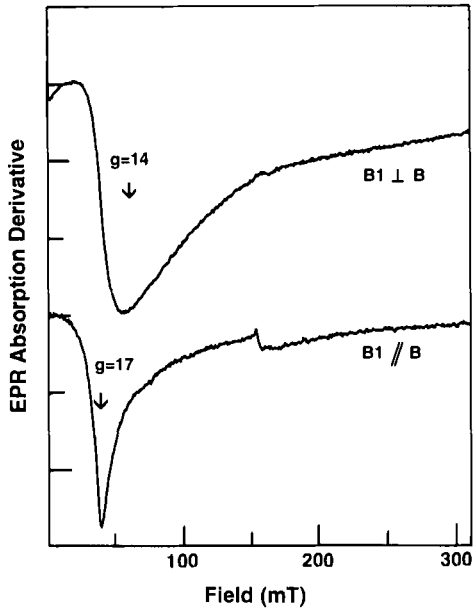

FIG. 8. EPR spectra at 4 K of fully reduced diiron site in RNR-R2 from mouse. The reduction was made at room temperature in 20% glycerol, 0.1 M tris-HCl, pH 7.5, using dithionite as reductant and methyl viologen as a mediator. The spectra were recorded in the normal perpendicular mode with 9.62 GHz microwave frequence (upper trace) and in the parallel mode with 9.32 GHz microwave frequency [*cf.* (*68*)] (lower trace). The microwave power was 16 mW.

The effects of point mutations in certain residues surrounding the iron site in *E. coli* R2 have been studied. In the mutant F208Y R2, protein the ferrous iron/oxygen reconstitution reaction leads to a ferric iron–dihydroxyphenylalanine (dopa) site, with a highly characteristic light absorption giving a blue-green color to the protein. In the reconstituted F208Y R2, the dopa is a bidentate ligand to one of the irons in the iron center (*30, 102, 103*). In a study on the R2 mutant S211A, it was found that the conserved S211 is essential for reduction of the iron site. The mutated protein could not be reduced, either by chemical or by enzymatic methods (*104*).

I. INHIBITORS TO IRON-CONTAINING RIBONUCLEOTIDE REDUCTASE

Because ribonucleotide reductase activity is necessary for DNA replication, inhibition of the enzyme means that cell division cannot take

place. Understanding the molecular mechanisms of its interactions with inhibitors and substrates and how its two components interact in an active enzyme can lead to the development of cytostatic drugs with a completely new target compared to those currently used.

Today we can envisage at least five important and potentially useful types of inhibitors that could inhibit ribonucleotide reductase in different ways:

1. Reduction of the free radical in the R2 protein,
2. Chelation of the iron,
3. Reactions of suicidal substrate analogues,
4. Inhibitory oligopeptides or peptidomimetics,
5. Modification of the redox-active sulfhydryl groups of protein R1.

Specific inhibitors of ribonucleotide reductase such as hydroxyurea (type 1 in the list) and azidocytidine (type 3) have already been used in cancer therapy. Hydroxyurea sensitivity is so strongly a characteristic of the class I RNR enzymes that it is commonly used as a diagnostic for this class (*105*). The functional tyrosyl radical is effectively reduced by hydroxyurea (*106–108*). In mouse and HSV1 enzymes, the iron center is also reduced and labilized in this process (*109*), whereas in *E. coli* protein R2, the iron center remains intact. This is a reason why hydroxyurea can be considered as a reversible inhibitor for the mouse and HSV1 enzymes, since regeneration of the active form will spontaneously take place in a medium containing reductant and oxygen. A new class of substances with a mechanism probably similar to that of hydroxyurea but with considerably higher efficiency is the *p*-alkoxyphenols (*110*).

Iron chelators (type 2) are of medical interest as agents that can block cell proliferation. To what extent this is due to interference with RNR is not well understood. However, recent experiments on the isolated proteins show that an agent such as desferrioxamine can destroy the radical and chelates iron from the active form of the HSV1 protein (*111*), whereas it has no direct effect on the tyrosyl radical of mouse R2 (*112*). However, it seems that the iron in the dinuclear sites *without* neighboring tyrosyl radical is accessible to desferrioxamine complexation in mouse as well as HSV1 R2, again suggesting a structural difference between iron sites with and without a neighboring radical.

Peptide inhibitors or peptidomimetics (type 4) may represent a totally new type of drug with species-specific cytostatic activity (*113*). For HSV1 ribonucleotide reductase, it was first shown that a short peptide (nine amino acid residues) with the same sequence as the C-terminal end in protein R2 inhibits the enzyme activity, probably by competitive

binding to protein R1 (*114, 115*). Similar observations have been made for other species of RNR, each with a nonconserved C-terminal sequence of its own (*116–118*). The likely explanation for these observations is that the C terminal end peptide of protein R2 is mainly responsible for binding to protein R1 (*119a,b*). An example of a sulfhydryl reacting agent is caracemide, which has been shown to be an irreversible inhibitor affecting protein R1 (*120*).

V. Methane Monooxygenase

In later years the advance in knowledge of the soluble iron–oxygen containing methane monooxygenase system (MMO) from methanotrophic bacteria (bacteria which utilize methane as their only source of carbon and energy) has been remarkable, regarding both the reaction mechanism and the structure (*9, 10, 15, 31, 121, 122a,b*). The methanotrophic bacteria have two different systems that carry out methane oxidation (*31, 123*): a soluble MMO (*124*) and a less-studied, probably copper-containing and unstable membrane-bound particulate methane monooxygenase (*125, 126*). Mainly two soluble MMOs have been studied in detail. The first one is from *Methylosinus trichosporium* OB3b (*31, 127*) and has two iron–oxygen clusters per dimer and the high specific activity of 1700 nmol propenoxide formed per milligram protein and per minute. The second one, with normally one iron cluster per dimer and much lower activity, is from *Methylococcus capsulatus* (Bath) (*9, 42, 121, 122, 124*). The latter MMO is described in detail in other recent reviews (*9, 10, 121, 122a,b*). In the present review we will mainly focus on the *M. trichosporium* OB3b [see also another recent review (*31*)].

The methanotrophic bacteria have one known pathway for aerobic methane oxidation to CO_2 (*31, 42, 123*). MMO catalyzes the first energetically difficult step in the formation of methanol from methane. The second step is catalyzed by methanol dehydrogenase (with a PQQ cofactor) and results in formation of formaldehyde, which is then converted by formaldehyde dehydrogenase (with no known cofactor) to formate. Finally, carbon dioxide is produced by formate dehydrogenase (with five different iron–sulfur clusters, a Mo–pterin cofactor, and an unusual flavin) (*31, 42, 123*). MMOs have a unique ability to oxidize a broad range (*31, 42, 128, 129*) of hydrocarbons in addition to methane. One other system with a similar broad substrate utilization is the monoheme cytochrome P_{450} family, but in this case different isozymes show different specific activities (*31*). For soluble MMO, one single

enzyme carries out oxidation of more than 100 different substrates (*31, 42, 128, 129*). The soluble iron–containing MMO system consists of three proteins: the hydroxylase (MMOH) component with two iron-oxygen clusters (Fig. 1) [$(\alpha\beta\gamma)_2$-subunit structure and M_r of 245 kDa], the reductase component (MMOR) with a $(FeS)_2$ cluster and flavin (single subunit and M_r of 38 kDa) and the small B (MMOB) component with no known cofactors (single subunit and M_r of 16 kDa) (*31*). The amino-acid sequences of all three components are known (*130, 131*). MMO catalyzes the first and rate-limiting step in the carbon fixation in obligate methanotrophic bacteria by reaction (2a):

$$CH_4 + NADH + H^+ + O_2 \rightarrow CH_3OH + NAD^+ + H_2O, \qquad (2a)$$

$$CH_4 + H_2O_2 \rightarrow CH_3OH + H_2O. \qquad (2b)$$

The MMOR transfers electrons from NADH to the oxygen activation site on the iron–oxygen clusters on MMOH. The role of the MMOB is very complex and not yet clarified (*31*). The electrons from NADH can be replaced by chemical reduction of the two iron–oxygen clusters of MMOH (by, e.g., dithionite) in so-called single-turnover reactions by the MMOH alone (128). MMOH alone can also use the H_2O_2 reaction (2b) as a replacement for both electrons and oxygen (*132*) in a so-called peroxide shunt reaction. Both these results clearly demonstrate that the active site is on the MMOH, and that methanol formation does not involve the other two components.

A. Spectroscopy of the MMOH Cluster

1. Light Absorption and Resonance Raman of MMOH

The resting highly purified and active MMOH is colorless, but in concentrations over 50 mg/mL a slight yellow color is observed (*127*). It is mostly derived from the protein absorption band, with no clear light absorption features above 300 nm. Impure hydroxylase can have distinct bands around 410–420 nm and 550 and/or 650 nm. The lack of near-UV and visible-light absorption bands is consistent with the presence of a μ-hydroxo bridge between the irons. Addition of different phenols to diferric MMOH turns the color into red for phenol (*133*) or orange for *p*-CN–phenol (*134*). Corresponding intense (700–1500 $M^{-1}cm^{-1}$/cluster) light absorption spectra, typical for the presence of phenolate-to-Fe(III) charge transfer transitions (ligand-to-metal

charge transfer, LMCT), can be observed (Fig. 9). It was demonstrated with resonance Raman (*133*) spectra of ^{13}C, D, or ^{18}O isotope-labeled phenol complexes that two enhanced bands at 602 cm^{-1} and 628 cm^{-1} shifted as a pair in all labeled phenols, showing that they were derived mainly from Fe–O bending and ring-derived modes involving the exogenous phenolate-generated LMCT band. No bands could be assigned to the symmetric or antisymmetric Fe–O–Fe vibration modes (Table III). A similar absence of these modes has been reported for PAP. PAP (*3, 4*) has a single mode at around 580 cm^{-1} similar to the two phenol modes in MMOH. These two MMOH modes at 602 cm^{-1} and 628 cm^{-1} probably reflect two binding orientations of phenols accessible to the two irons in MMOH, consistent with the observation that exogenous acetate or bicarbonate can form an iron-bridge (Figs. 1 and 2), as shown in the X-ray structure of MMOH (*15*). At this time no other resonance Raman results of MMOH have been published, but work is in progress dealing with the strongly colored reaction intermediates (see later discussion).

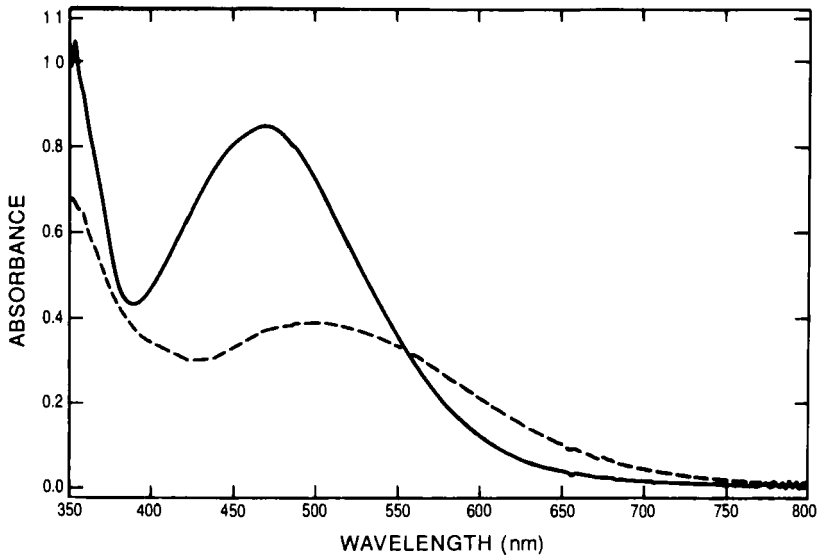

FIG. 9. Light absorption spectra of OB3b MMOH in presence of phenol or *p*-CN–phenol at pH 7.2. Difference optical spectra at 4°C and 0.1 M MOPS pH 7.2 of 25 mM phenol (———) or *p*-CN–phenol (—) + 71 mg of MMOH/mL minus 71 mg of MMOH/mL. Samples were incubated for at least 15 min prior to the recording of the spectra (*133, 134*).

2. *Magnetic and X-Ray Related Spectroscopies of Diferric, Mixed-Valent, and Diferrous States*

The first evidence for the presence of an iron–oxygen cluster in MMOH came from the typical mixed-valent EPR signal, with all g-values below 2.0, by Dalton's group (*135*). This observation was strengthened by the observation of a diferric spin-coupled pair in Mössbauer spectra (*136*). The resting mixed-valent EPR signal (g = 1.94, 1.86, and 1.76) shows large variations depending on the presence of the MMOB (g = 1.87, 1.77, and 1.62) (*53*) and can also be changed by addition of a number of small organic molecules such as methanol and dimethylsulfoxide (g = 1.94, 1.87, and 1.80) (*137*). The effect of MMOB on MMOH (*33, 53*) is remarkable in that even the magnetic coupling between the irons is drastically decreased (Table II), as well as the two redox potentials (Table I). Addition of MMOR to form a ternary MMOH/MMOB/MMOR complex increases the two potentials again (*33*). Deuterium ENDOR experiments show that dimethylsulfoxide binds close to the cluster (*137*), and in its presence, the mixed-valent EPR spectrum has the narrowest line width. This was a prerequisite for obtaining and simulating the Mössbauer spectra of this species, as well as for obtaining the ^{57}Fe-ENDOR spectrum (*50*). The ^{14}N-ENDOR spectrum of this species indicates subtle and unprecedented changes of the histidine coordinated to the ferrous ion (Fig. 10), while perturbation of the histidine coordinated to the ferric ion Fe(III) could not be observed at X-band (*137*). This ENDOR study by Hendrich *et al.* was the first solid proof for the presence of histidines coordinated to both irons, and in addition gave theoretical tools for understanding the mixed-valent signals. The observations were confirmed and extended by recent studies with pulsed ENDOR (*138*). The first ENDOR study showed partial exchange of protons in MMOH after eight hours of incubation in D_2O (*137*). One of the protons had strong enough hyperfine coupling (13 MHz at g_3) to suggest that it could arise from a hydroxo bridge. This was later independently confirmed, after a 24-hour incubation of MMOH in D_2O, by pulsed ENDOR and ESEEM experiments, where the whole set of proton hyperfine couplings (e.g., a very strong 23 MHz coupling was observed at g_1) were also obtained by using mixed-valent Hr as a model compound (*47, 48*). Mössbauer (*50*) spectra of the diferric, mixed-valent, and diferrous state have distinguishable parameters for each of the irons (see Fig. 11 for some Mössbauer parameters of these states), while the intermediates during turnover show one single iron species (see later discussion).

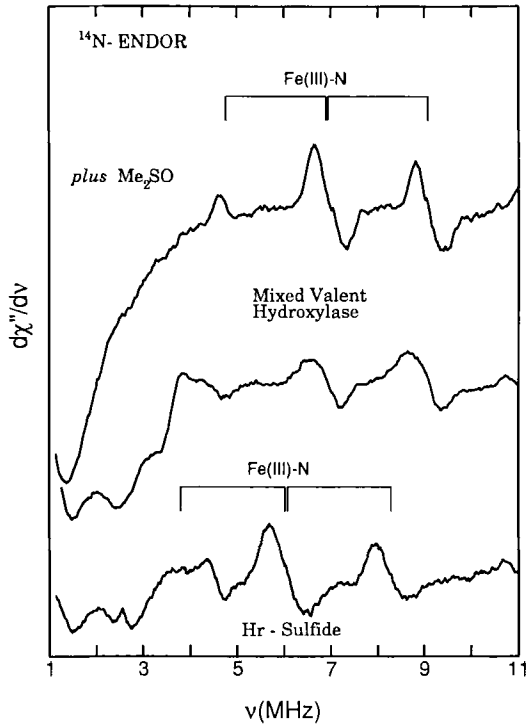

FIG. 10. ^{14}N-ENDOR spectra at 10 K of mixed-valent MMOH (resting and dimethylsulfoxide complex) and Hr (sulfide complex). Resting MMOH in 0.1 M MOPS pH 7.0, cw ENDOR spectra obtained at $g_1 = 1.94$. Dimethylsulfoxide (0.3 M) complexed MMOH at 0.1 M MOPS pH 6.5, cw ENDOR spectra obtained at $g_1 = 1.94$. Hr sulfide complex at pH 8, cw ENDOR spectra obtained at $g_1 = 1.88$. The bars labeled Fe(III)-N mark the resonances for nitrogen coordinated to Fe(III). The resonances at low frequency observed in absence of dimethylsulfoxide are from the nitrogen coordinated to Fe(II). Adapted from (*137*).

The best evidence for the presence of a hydroxo bridge in the diferric MMOH, obtained before the three-dimensional structure was available, came from EXAFS data, which showed an Fe–Fe distance of 3.42 Å and an Fe–O distance of 2.04 Å (*139*), and from the temperature dependence of the weak integer spin EPR signal at $g = 8$, which demonstrated a weak antiferromagnetic coupling $J = -7.5$ cm^{-1} (*50*). This signal was assigned to an excited state ($S = 2$ manifold, as it is detectable only above 20 K and obviously is not a ground state) (Table II) of the iron cluster. The diferrous MMOH has a strong $g = 16$ EPR signal at liquid-helium temperatures, both in perpendicular-mode and parallel-

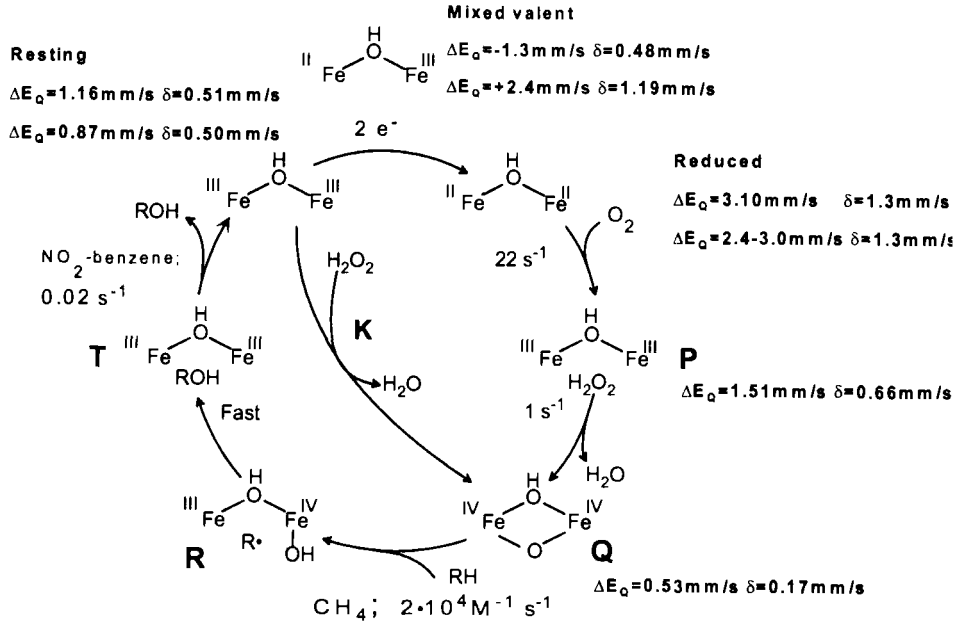

FIG. 11. Suggested catalytic cycle for active MMOH (J. D. Lipscomb version). The cycle, compiled from (*31, 48, 50, 53, 56, 63, 64, 127–129, 132, 136, 147–150*), represents different compounds that have been characterized and some hypothetical compounds (**K**, **R**). The rate constants are from single-turnover experiments at 4°C (*147*).

mode EPR (*67*). Simulation of the spectrum and integration of this signal show that it represents 80% of the diferrous clusters (*67*). This weakly ferromagnetically coupled signal has been studied in detail by EPR (*67*) as well as with MCD methods (*56*). The MCD analysis was helped by a detailed comparison with Hr, and it gave rise to a satisfactory model of the cluster of MMOH, which corresponds well with the subsequently reported 3D structure (*15*). It seems that diferrous MMOH probably has a water bridge, and pulsed ENDOR and ESEEM data on the Bath enzyme indicate that the histidine ligands are still present (*69*).

B. X-RAY STRUCTURE OF MMOH

The structure of the MMOH iron cluster (*15, 122*) is shown in Figs. 1 and 2. It has one histidine ligand to each iron, one carboxylate ligand to each iron, one carboxylate bridge, one nearly bridging carboxylate,

one hydroxo bridge, and one iron-coordinated water or hydroxide. The cluster is at the end of a hydrophobic pocket, which is needed for binding of substrate (*15*). What is unique for MMOH and not at all expected was the presence of a bidentate coordinated bridging acetate to the iron cluster. Interestingly, the suggested acetate might be a formate or a bicarbonate (*15*). Formate is the last product before carbon dioxide (bicarbonate) in the metabolic pathway catalyzed by MMO. Thus, the formation of such a complex might have relevance to the regulation of the pathway, suggesting that such a complex might be a feedback-inhibited form of the MMOH, in analogy with the catecholamines coordinated to Fe(III) in bovine or rat tyrosine hydroxylase (*140, 141*). This inhibition can be specifically reversed by phosphorylation of Ser40 of both the latter enzymes (*141, 142*).

C. Reaction Mechanism and Intermediates of Soluble MMOH

The present model (*31*) of the catalytic cycle of MMO is shown in Fig. 11. The time constants are from single-turnover experiments with the OB3b hydroxylase, which starts with the oxygenation of the diferrous state (as only two electrons are supplied in these experiments, the hydroxylase can only do one turnover). The Mössbauer data (*50, 63*) are from the OB3b enzyme, except for compound P, which is from the Bath enzyme obtained by Lippard *et al.* (*64*). This catalytic cycle was first suggested in analogy with the cycle of the monooxygenase cytochrome P_{450} (*143–146*). Several differences, however, exist in comparison with the cyt P_{450} cycle, which explains some earlier erroneous suggestions for the cycle of MMO. For instance, in cyt P_{450}, the O_2 binding occurs after one electron reduction, while in MMOH, O_2 reacts with the two-electron reduced protein (the mixed-valent MMOH is relatively stable in the presence of air). Furthermore, substrate binding occurs at different steps in the cycles, and the modulation via protein–protein interactions seems to be different and more complex for MMO. The excellent single-turnover studies with the MMOH (*127*), the discovery of the peroxide shunt (*132*), transient kinetic studies (*63, 147*), and analysis of different combinations of MMOH with other components (*33, 53, 129*) developed by Lipscomb *et al.* have given a clear model for the monooxygenation reaction, as shown in Fig. 11. This can now serve even as a model for cyt P_{450}, since more reactive intermediates have been better characterized for MMO.

The resting enzyme is in the diferric state, but it can be reduced to the mixed-valent state (*127, 135*). By enzymatic means with the MMOR, a very small fraction of the total iron will be in this state. Non-enzy-

matic methods of reduction, i.e., by redox poising in the presence of redox dyes, can yield up to 80% of the iron clusters in the mixed-valent state (*33*). The mixed-valent state lacks biological significance, as it does not react with oxygen and normally is not observed or is present in very low yields in the presence of the MMOR and NADH. The enzymatically relevant reduced state of MMOH is obtained by a two-electron reduction of the resting state to the diferrous state (*127*). This state reacts rapidly with oxygen (*127*) and then forms an intermediate called compound **P** (*147*) [sometimes called compound L or peroxy compound (*64*)]. Compound **P** has not yet been stabilized for the OB3b enzyme, but it was correctly predicted from analysis of single-turnover data, which showed that the rate (22 s^{-1}) of the decay of the diferrous form (e.g., the $g = 16$ EPR signal) in the presence of oxygen could not account for the 22 times slower rate of formation of the next intermediate, **Q** (*147*). Thus, complex **P** must be postulated. Compound **P** might be blue, as observed for other peroxide complexes (*122b*). Compound **P** could correspond formally to oxyhemerythrin with a peroxide coordinated to a diferric cluster. The isomer shift, 0.66 mm/s, of compound **P** is clearly not typical of the ferrous state, but it is somewhat large to be only from a diferric state (*64*). Therefore, it might also contain a small ferrous component. Interestingly, it has Mössbauer parameters indicating a single symmetric iron environment. This is clearly different from oxyHr, which has two different iron environments, demonstrating that in oxyHr only one of the irons binds the peroxide. Thus, it is likely that the peroxide is coordinated to both irons in a symmetrical fashion in compound **P** [see discussion by Lippard in (*122b*) and (*10, 31*) for several resonance forms of the compounds]. It is possible to predict in the peroxide shunt an equivalent compound **K** to compound **P**. A compound **K** is probably formed (but it has not yet been observed) when the diferric enzyme is reacted with hydrogen peroxide to form compound **Q**. The peroxide shunt is the alternative pathway for turnover (*133*). It is analogous to such a shunt in cyt P_{450}, and it was one strong indication of a similar reaction mechanism and similar hydroxylating species for the two enzymes (*129, 133*).

After compound **P** (or **K**), the heterolytic cleavage of the oxygen–oxygen bond occurs and the two electrons leave together with the formed water. This results in another symmetric oxygen–iron compound, **Q**, which is probably an iron-bound oxene (*31, 63, 147*). The compound **Q** has two fewer electrons than the diferric state. Since a perferryl state is not expected to occur as a stable form in a biological compound, **Q** needs two iron ions. Besides, a mononuclear iron without a second redox partner would probably lead to formation of toxic amino acid

radicals. In this electron-deficient compound **Q**, the oxygen presumably has most of the available valence electrons, which leaves the two iron ions in a ferryl state. A low-spin diferric state can not be completely excluded, as the isomer shift (0.17 mm/s) of this complex could possibly also be consistent with a low-spin diferric conformation (*63*). An analogous high-valent compound to compound **Q** is postulated as the second oxygen compound for cyt P_{450} (see next section).

Compound **Q** is strongly colored (*147*), and it has absorption maxima at 320 nm (ε = 7300 $M^{-1}cm^{-1}$) and 430 nm (ε = 7300 $M^{-1}cm^{-1}$). The color of compound **Q** is probably the result of an oxygen-to-iron charge transfer transition, but this needs to be verified by resonance Raman. The strong color made it possible to follow the kinetics of formation and decomposition of compound **Q** by optical stopped flow (*147*). The presence of MMOB and absence of substrate were required for stabilization of the intermediate **Q** in high yield. Without MMOB, the yield of compound **Q** is low, and in the presence of both MMOB and a substrate, rapid breakdown of the intermediate occurs because of rapid continuing turnover.

The substrate binding occurs after the formation of compound **Q**. Interestingly, this is a second-order reaction (*147*), depending on the concentrations of substrate and compound **Q**. It can be followed by the disappearance of the colored compound **Q**. Then the scheme contains a postulated compound called **R**, one electron more reduced, which should correspond to a hydroxyl coordinated to a ferric–ferryl cluster. A resonance structure would be a hydroxyl radical coordinated to a diferric cluster. Compound **R** is believed to be obtained after hydrogen (proton + electron) abstraction from the substrate, resulting in a substrate radical close to the cluster. The formation of such a very short-lived substrate radical in the active site of MMOH has been demonstrated by elegant carrier-free tritium NMR experiments using chiral ethene as substrate for MMOH turnover with the reductase and MMOB (*148*) or with the peroxide shunt (*149*). Both methods yield little more than one-third racemization of the product of the turnover. A non-inversion of the product could indicate a so-called concerted reaction mechanism, and full racemization of the enantiomeric substrates could indicate participation of long-lived radicals (outside of the active site). The intramolecular deuterium isotope effect was determined to be 4.2 at room temperature, suggesting a C–H bond breaking during the reaction (*148*). The substrate radical mechanism in MMO is supported by studies of deuterated substrates (*150*) showing a similar product distribution (e.g., epimerization) previously used to demonstrate this type of radical mechanism for cyt P_{450} (*144–146*). Furthermore, a ki-

netic isotope effect on K_m (*150*) was observed, as expected from the fact methane binds to compound **Q**. Also, the observed substituent migration (an example of a so-called NIH-shift) of halogenated ethylenes (*128*) is analogous to cyt P_{450}. The product distribution studies in the presence of MMOB clearly demonstrate that a hydroxyl radical, i.e., Fenton chemistry, does not occur (*129*). [With the Bath enzyme, conflicting reports have been presented (*9, 10, 151.*)]

In the next step of the reaction cycle, the enzyme–product compound (**T**) is formed by radical recombination of the iron-bound hydroxyl radical and the substrate radical. Finally, the product is released in the rate-limiting step (*31*) of the reaction. This step is also dependent on MMOB, and the cycle is complete. It is possible that compounds **P**, **K**, **Q**, and **R** all have an additional oxygen-derived bridge in addition to the hydroxo bridge. Thus, compounds **P** and **K** would have one μ-peroxo and one μ-hydroxo bridge, and compounds **Q** and **R** could have one μ-hydroxo and one μ-oxo bridge each [cf. (*122b, 10, 31*)].

D. Generalization Ideas for Monooxygenases Derived from the Reaction Mechanism of MMO

In the two cases [cytochrome P_{450} (*143–146*) and MMO (*31*)] in which the metal-dependent monooxygenase mechanism is known in some molecular detail, the postulated hydroxylating species occurs after heterolytic cleavage of the two-electron reduced oxygen (supplied as 2 electrons + $\mathbf{O}_2$ or $\mathbf{H_2O_2}$) bound to a metal $\mathbf{M^n}$. This generates a metal-based oxene with two reducing equivalents less than the starting $\mathbf{M^n}$ (the two added electrons leave with the water), according to

$$\mathbf{C^m M^n} + \mathbf{O}_2 + 2\,e^- + 2H^+ \rightarrow \mathbf{C^m M^n O_2 H_2} \rightarrow [\mathbf{M^{n+1}OC^{m+1}}] + \mathbf{H_2O}.$$

Here, $\mathbf{M^n}$ designates a metal [Fe(III)] and $\mathbf{C^m}$ designates a second center. It is not clear if Cu(II) could be $\mathbf{M^n}$, as Cu(III) or Cu(IV) has not been firmly demonstrated in enzymes, but recently Klinman *et al.* (*152*) suggested somewhat similar ideas for dopamine hydroxylase.

The oxygen-binding step to the metal can occur after one electron reduction (cytochrome P_{450}) $\mathbf{M^{n-1}}$, or after two electron reduction (MMO) $\mathbf{M^{n-2}}$ or $\mathbf{C^{m-1}\,M^{n-1}}$, while the peroxide shunt does not pass through any state further reduced than $\mathbf{M^n}$. The hydroxylating metal–oxene $[\mathbf{M^{n+1}OC^{m+1}}]$ corresponding to compound **Q** in Fig. 11

has several particular characteristics (see Fig. 12 for some suggested species). The suggested tetrahydro-pteridine species occurs after heterolytic cleavage of a peroxide–pterin–Fe(III) complex. The Fe(III) state seems to be part of the catalytic cycle of tyrosine and phenylalanine monooxygenases (*140–142*):

1. The hydroxylating species is relatively unstable (except for MMO and a related species in peroxidases; see later discussion).
2. It is nonspecific and can oxidize several substrates (otherwise difficult to oxidize), e.g., alkanes, alkane groups, or nonsubstituted phenyls.
3. It shows NIH shifts [migration of deuterons, alkyl groups or halides, during turnover (*128, 153*)].
4. It has a significant deuterium isotope effect in its hydroxylation reaction (intramolecular or kinetic effect on the hydrogen abstraction step) by a factor of more than 3 when hydroxylating alkane groups. [Hydroxylation of aromatic substrates might not show any large isotope effects, as observed for pterin-dependent hydroxylases and MMO. They probably hydroxylate these substrates through an arene-oxide mechanism (*153*), as indicated by the NIH shifts, or at least not via a rate-limiting hydrogen abstraction step.]

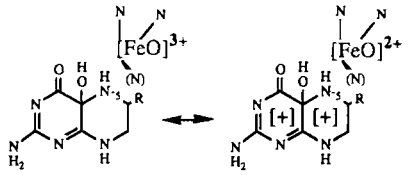

Pterin monooxygenases

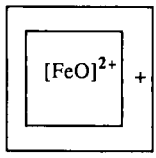

Cytochrome P450

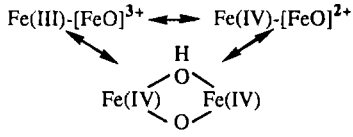

Methane monooxygenase

FIG. 12. Hypothetical high-valent hydroxylating species for different monooxygenases. For the pterin monooxygenases, the "N" represents histidine residues coordinated to the catalytically active Fe in tyrosine, phenylalanine, and tryptophan hydroxylases (*140, 141*). The two squares for cytochrome P_{450} represent the porphyrin ring, and the "+" represents a π-radical delocalized over this ring.

All of these characteristics must be present in the hydroxylating metal-oxene [$\mathbf{M^{n+1}OC^{m+1}}$] system. An interesting idea is that the oxene O might be bridging the centers, in the cases with ring porphyrin radicals and MMOH. Other systems can perform similar, less difficult oxidation reactions, and some heme peroxidases can also attain these [$\mathbf{M^{n+1}OC^{m+1}}$] states (31, 143–146). It is not likely that the high-oxidation $\mathbf{M^{n+2}O}$ state, i.e., two electrons less than Fe(III), Fe(V), exists by itself in proteins even if it possibly could exist in nonbiological inorganic compounds. In general, this **M**-based high oxidation state, in hydroxylases or peroxidases, must be stabilized by another center $\mathbf{C^m}$ that can give one electron to the bound oxene. The oxene might also be bound between two centers **M** and **C**, as suggested for compound **Q** in Fig. 11, but it seems not to occur in most cases. The second center can be a metal (Fe for MMO), amino acid (Trp for cytochrome *c* peroxidase, perhaps a Tyr for dopamine hydroxylase), or an organic aromatic structure (porphyrin group for cytochrome P_{450} and horseradish peroxidase, the oxidation of which results in a porphyrin-located π^+ radical, or the pterin ring for the pterin-dependent hydroxylases). It is highly unlikely that the one electron-rich state $\mathbf{M^{n+1}O}$ obtained by homolytic cleavage of the oxygen–oxygen bond in a $\mathbf{M^n}$–peroxy complex or heterolytic cleavage in a $\mathbf{M^n}$–superoxide complex [e.g., Fe(II) + $\mathbf{O_2}$] has strong enough oxidizing power to perform the described hydroxylations. The same is true for the $\mathbf{M^n}$–peroxy complex without oxygen cleavage. These latter complexes might be able to hydroxylate in less difficult oxidation reactions such as alkene epoxidations and some desaturation reactions, as observed for cytochrome P_{450} (*145, 146*). It might be noted that there is a striking formal similarity between the reaction stage with species X of RNR-R2 (Fig. 5) and that with compound **Q** of MMOH (Fig. 11). However, no ferryl species has been detected for the reconstitution reaction of RNR-R2 (Fig. 5).

E. Component Interactions of MMOH

One interesting complex relationship in the catalytic cycle of MMO concerns the interactions among the three different protein components. Both direct and indirect observations of the interaction have given some clues to this puzzle. Several techniques have been employed to study the interactions: chemical cross-linking (*53*); changes in EPR signals (*53, 129*); product distribution studies (*129*); steady-state and transient kinetic studies (*129, 147*); and redox and affinity measurements (*33*). It is clearly demonstrated that the MMOB and MMOH interact in most of the redox states of MMOH (probably not state R),

and that the affinity between the components changes depending on the redox state of MMOH (*33*). The affinity of the MMOB to the diferric MMOH (K_d in the nanomolar range) is very high, while this is not the case for the moderate interaction with the diferrous MMOH (K_d two orders of magnitudes higher). The studies of the interactions between the different components have been greatly helped by the fact that it is possible to make turnover experiments with MMOH alone, by using the peroxide shunt or single-turnover experiments. The specific effects of MMOB or/and MMOR on MMOH reactions could be monitored by subsequent titration with the other components. In this way, three different enzyme-dependent systems could be used to carry out the reaction with the same substrate (*129*).

It seems from product distribution studies that even after dissociation of the MMOB from the diferrous MMOH, the active site in MMOH remembers that it had just been in complex with MMOB. This is presumably because MMOB induces a metastable (on the time scale of catalysis) conformation of the MMOH (*129*). The effect is observed as a hysteresis effect upon titration with MMOB to the diferrous MMOH (see Fig. 13 for a model), where a ratio 0.1 of MMOB/(MMOH active site) could induce a complete metastable conformation of MMOH. This could be observed by a drastic change in product distribution, and no further change in product distribution was observed in the presence of higher ratios of MMOB/MMOH. The model was corroborated by the low ratio of MMOB/MMOH needed to induce the MMOB-dependent changes of the diferrous MMOH EPR signal (*129*). The affinity between MMOB and MMOH depends on the redox state of MMOH. This explains

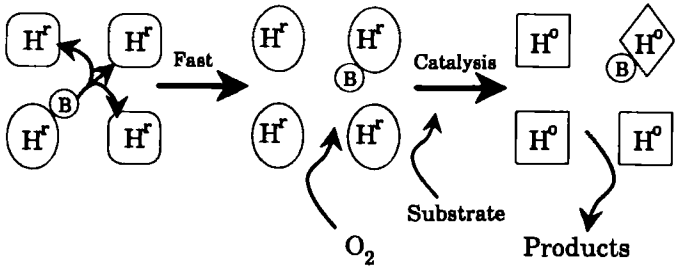

FIG. 13. Hypothetical scheme to explain semistable conformation of diferrous MMOH after interaction with MMOB. MMOB (B) can rapidly change the diferrous MMOH (H^r) conformation. H^r keeps this changed conformation for some time after its contact with MMOB, so that MMOB at a particular time needs to bind to only a small proportion of MMOH during the rapid catalysis. When MMOH is in the diferric (H^o) state, it can form a one-to-one complex with MMOB. Adapted from (*129*).

why no hysteresis effect is observed with the diferric MMOH, as the complex is very stable in that case. The structural basis for the induced changes in the iron cluster of MMOH upon binding of MMOB is not well understood and represents a very interesting and challenging problem. Perhaps MMOB binding regulates a carboxylate shift in the MMOH iron cluster. Probably it is also related to perturbations in the histidine–iron coordination which could be observed upon binding of dimethylsulfoxide (see Fig. 10). It is clear that the MMOB has several different roles in catalysis. Some of these are (a) to regulate the redox states of MMOH; (b) to make certain that the substrate is available and in its proper site; (c) to regulate the product release; and (d) to regulate the interaction between the MMOH and MMOR. For a more detailed discussion of the component interactions and reaction mechanisms, see (*31*).

VI. Purple Acid Phosphatase

Some major advances during recent years in the PAP field concern the following:

1. Structure and electrochemical studies of the cluster ligandation and interaction with small molecules in mammalian PAPs by NMR, EXAFS, and microcoulometric titrations.
2. Studies of the plant PAP with Mössbauer spectroscopy and X-ray crystallography (*154*), and determination of the sequence of the protein and its accompanying oligosaccharides.
3. Clarification of the reaction mechanism for hydrolysis of phosphate esters and studies with Zn–Fe enzymes.
4. Genetic studies with the cloning and expression of two mammalian enzymes in a Baculovirus system which show that the single subunit forms of PAP are similar to Uf.

The biological function of PAP is still not yet clear, but a phosphatase role seems likely. Some groups suggest a function in reactions with various forms of oxygen (*36*, *155a*). Interestingly, the secreted mammalian bone PAP in osteoclasts might have a defined role, as it is probably involved in dephosphorylation of osteopontin and bone sialoprotein (*156*), which is related to the motility of the osteoclast on the bone surface. It is possible that the PAPs might be multifunctional enzymes.

The mammalian PAPs are single-subunit 35–40 kDa glycoproteins. Earlier, many preparations of PAP were of proteolyzed forms which had a phosphatase activity twice that of the single-subunit Uf. Now,

available single-subunit forms (*155a, 157, 158*) have activity similar to that of Uf, and after proteolysis they increase by a factor of two in activity. The PAPs are also called type 5 tartrate-resistant acid phosphatase, TRAP (*3, 4, 43, 44*). For a detailed description of basic properties, PAP's location in lysosomes and various secreted forms, kinetics, and interaction with various anions, the reader is referred to (*3, 4, 20, 21, 32, 54, 43, 44, 155b,c, 159, 160*).

The basic and distinguishing property of the PAPs in the diiron–oxygen group of proteins is that they all have a purple (diferric, enzymatically inactive form) and a pink (mixed-valent, phosphatase-active form) color associated with strong tyrosinate-to-Fe(III) LMCT bands (*3, 4, 13,20*). This is exemplified in Fig. 14, showing the first light absorption spectra from the osteoclast enzyme in the resting and active forms (*158*). This strong band normally has ε at its maximum around 4000 $M^{-1}cm^{-1}$, but higher and lower values have been reported (*3, 4, 20*). The color and phosphatase activity remain if the ferrous iron in the mammalian enzymes is substituted with, for instance, Zn (*3, 4, 20, 159*). Similarly, the plant Zn–Fe(III) cluster can be replaced by a diiron–iron cluster without loss of activity (*36*). Thus, the phosphatase activity seems to need both Fe(III) and Fe(II) or Zn(II). One of the metals in

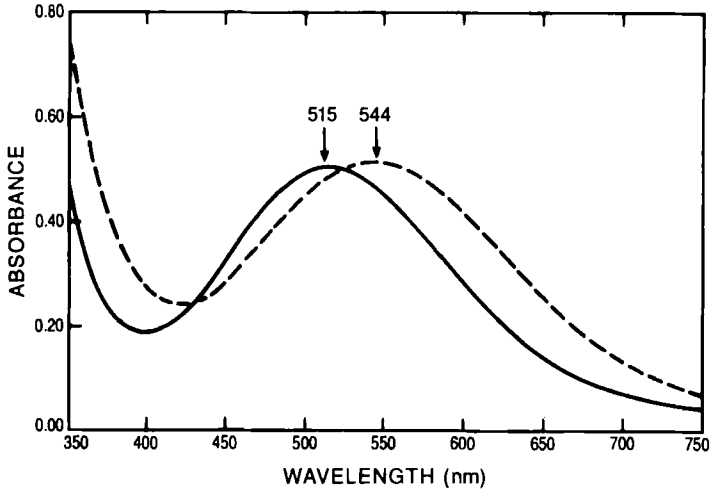

FIG. 14. Light absorption spectra of oxidized and reduced PAP from rat osteoclast. The spectrum of resting (– – – –) PAP (about 6 mg/mL at pH 5.5) is from rat osteoclast expressed by a Baculovirus system. Spectrum of the active form is after two hours' room-temperature incubation with 1 mM ascorbate and 0.1 mM iron (———). Adapted from (*158*).

the cluster can bind OH^- (*160*), and this strong nucleophilic hydroxide can then, via a S_n2 mechanism, hydrolyze the phosphate bond. This mechanism agrees with studies with chiral S_p-2′, 3′-methoxymethylidene-ATP$\gamma^{18}O\gamma^{17}O\gamma S$, which was hydrolyzed by bovine spleen PAP and analyzed by ^{31}P NMR (*161*). The reaction showed an inversion at the phosphorus and demonstrated the direct transfer of a phospho group to water. Other mechanisms have also been suggested (*155b,c, 162*).

Advanced structural results were obtained by Que, Averill, and others in NMR studies observing paramagnetically shifted proton resonances. The studies included NOE and NOESY spectroscopy of mammalian PAPs, sometimes substituted with other metals such as Co (*163, 164*). They have suggested that the iron ions are coordinated by one tyrosine [at the Fe(III)], as well as carboxylates and histidines (both δ and ε nitrogens can coordinate the iron). The electrochemical (*32*) and EXAFS (*21*) data (e.g., Fe–O distance of 1.95 Å) demonstrated the presence of a hydroxy bridge between the two ferric irons, and the anion complexes suggested that the carboxylate bridge between the irons could be monodentate, in contrast to the bidentate carboxybridges observed in Hr, RNR-R2, and MMOH (Figs. 1 and 2). These cluster studies of the mammalian PAP might show differences with the red kidney bean PAP. Therefore, a generalization from the bean PAP to the mammalian PAP might not be valid. One obvious difference, for instance, is that the bean PAP can stabilize the diferrous form, whereas the mammalian PAP diferrous cluster can be obtained after 30 min dithionite treatment, but this cluster falls apart (*155b*). The bean PAP is a dimer of 432 amino acids (50, 236 Da) (*165*). It shows no obvious sequence homology with mammalian PAP, but it may be related to other plant PAPs (*165*). Several studies show that both mammalian and bean PAP are quite complex glycoproteins.

The sequences of several mammalian PAPs show large homology and are produced by equivalent genes (*4, 166, 167*). Two groups have expressed the human (*155a*) and rat (*158*) PAP enzymes in a Baculovirus system. The human form has a specific activity that is lower by a factor of two. Both groups have a native single-subunit enzyme, which has also recently been purified from bovine spleen (*157*). All three single-subunit PAPs are very similar to the Uf, but differ from two subunit forms in activity and the light absorption spectra. The native mammalian single-subunit PAP has a purple form with an absorption maximum around 545 nm, as observed for Uf (155a, 157, 158). A similar maximum can be observed in the phosphate-complexed two-subunit forms (resting two-subunit forms have maxima around 566 nm). The native single subunit reduced form seems to be similar to Uf, with a

light absorption maximum around 515–518 nm (*157, 158*). The reported 531 nm maximum for the human PAP seems to have a large uncertainty because of the low amount of protein examined (*155a*). The first low-temperature EPR spectrum of a mixed-valent Baculovirus-expressed PAP has typical g-values at 1.96, 1.74, and 1.60 (*158*), suggesting that the dinuclear iron site is not complexed with phosphate [cf. results on Uf–phosphate complexes (*3*)]. These native cloned and expressed PAPs make it possible to study site-directed mutants of PAPs.

VII. Rubrerythrin and Nigerythrin

Rubrerythrin (Rr) and nigerythrin can both be found in the anaerobic sulfate-reducing bacterium *Desulfovibrio vulgaris* (*23–26*). Rr is also found in *Desulfovibrio desulfuricans* ATCC 27774 (*24*). The functional roles of the proteins are unknown. Both proteins are homodimers and are predicted to have in each subunit one diiron–oxygen cluster and one rubredoxinlike mononuclear iron–sulfur center (*24, 26, 29*). The iron quantification is difficult in most iron–oxygen proteins. For instance, RNR-R2 and MMOH both were believed for a long time to contain only one iron cluster per dimer. For Rr and nigerythrin, the ratio of iron per dimer varies between 4 and 8 (*23–26, 62*). They differ in subunit size, 22 kDa and 27 kDa for Rr and nigerythrin, respectively. The redox potentials are similar and quite high for a diiron–oxygen protein (Table I). It seems that in the mixed-valent form, nigerythrin has a lower antiferromagnetic coupling than Rr. The g-values for the mixed-valent states are very similar (g = 1.96, 1.74, and 1.54–53) (*26*). Resonance Raman experiments (*25*) show that the light absorption spectra of Rr can be explained as a combination of a slightly distorted rubredoxin center and a diiron–oxygen cluster, with an oxo bridge. When the function of the proteins does become known, interesting mechanistic studies could be made. It has been suggested that Rr has a pyrophosphatase activity (*168*).

VIII. Soluble Stearoyl–Acyl Carrier Protein Δ^9 Desaturase

Δ-ACPs in higher plants are homodimeric soluble proteins of about 70 kDa. They catalyze the first and most important desaturation of stearoyl–acyl carrier protein, resulting in an oleoyl–acyl carrier protein, which is a major precursor in fatty acid biosynthesis in plants. Δ-ACP is involved in controlling the ratio of saturated to unsaturated

fatty acids. Δ-ACP uses O_2, ferredoxin, ferredoxin reductase, and NADPH for the desaturation (*45*), and its diferrous cluster is oxidized by O_2 (*27*). Δ-ACP from castor (*Ricinus communis*) expressed in *E. coli* is shown by optical, Mössbauer, and resonance Raman spectroscopy to contain an oxo-bridged diiron–oxygen cluster (*27, 28*), which can bind azide. The cluster has an oxygen bridge, and it exchanges the oxygen rapidly with water, as observed for RNR-R2 (*28*). From extended comparisons of amino acid sequences and similarities in reactions with oxygen, it was suggested that the cluster and reactions of Δ-ACP are very similar to RNR-R2 and MMOH (Fig. 2) with two bridging bidentate carboxylates (*28*). Based on similar arguments, membrane-bound fatty acid desaturases from several different sources, together with alkane hydroxylase and xylene monooxygenase, are suggested to constitute a class of membrane-bound iron–oxygen proteins with several histidine ligands. The importance of these histidine ligands has also been demonstrated by site-directed mutagenesis experiments (*169*).

IX. Ferritin

Ferritins are iron storage proteins in animals, plants, and bacteria. Ferritins have protein shells and store iron as a ferric–oxo–hydroxo-phosphate complex in the center (*170–173*). As many as 4500 iron atoms can be held in storage in the core of the ferritin particle. This is a useful way of keeping iron available for its biological roles in the organism, despite the low solubility of ferric iron and the easy oxidation of ferrous iron in an oxygen-containing environment and at physiological pH.

Iron uptake into ferritin occurs via oxidation of Fe(II) and formation of μ-oxo-bridged dimers of Fe(III). The stoichiometry of the reaction seems to be dependent on the stage of iron loading in the molecule. In horse spleen ferritin, two Fe(II) are oxidized per O_2. Peroxide is produced during the initial stages of iron uptake, and then approaches 4 Fe(II) per O_2 as more iron is loaded (*174–175*). An interesting observation is that a transient intermediate with light absorption in the 550 nm range is formed during initial Fe(II) oxidation (*176, 177*). It was interpreted as an Fe(III)–tyrosine charge-transfer band. Considering the transient light absorption that appears in the same wavelength region during formation of the iron center [i.e., oxidation of Fe(II)] in protein R2 of RNR (*80*), it is tempting to speculate that both species could be of similar origin. In the case of protein R2, a free radical,

possibly on tryptophan, has been suggested to be responsible for the light absorption (*83, 86b*).

The three-dimensional structure of the human H ferritin has been solved (*178*) and shows that the putative μ-oxo-bridged ferric dimer is located in the middle of and along the length of a four-helix bundle, similar to the situation in *E. coli* RNR protein R2. In a bacterial ferritin, three iron sites per subunit have been found in an X-ray crystallographic study (*22*). Two of the iron ions make up the diferric site. The third ferric site remains an enigma as to its functional role, if any. Also here, it is interesting to compare protein R2 in RNR, where a third ferrous iron has been shown to participate in formation of the iron/free radical site (*78, 84, 82*).

X. Conclusions and Perspectives

Study of the diiron–oxygen protein group is a rapidly expanding field, with several new three-dimensional structures expected to emerge within the next few years. The functional diversity of the group is large, as demonstrated in this review. As exemplified by Rr and nigerythrin, other metal centers can also be present in iron–oxygen proteins. Iron–oxygen clusters will probably also be reported as part of complex structures such as the Mo–Fe protein in the nitrogenase (*179, 180a,b*). In general, we find that several new di- or trinuclear metal (*8*) or metal–organic molecule centers (*181*) have recently been discovered and reported:

1. The 24-heme containing hydroxylamine oxidoreductase recently has been reported to contain a diheme cluster in the active site (*182*). This new cluster might contain a μ-oxo or a μ-hydroxo bridge, but it is more likely that a histidine is the bridging ligand.
2. A Fe–Ni cluster seems to be present in nickel–iron hydrogenase (*183*).
3. A Wo–pterin cofactor is found in aldehyde ferredoxin oxidoreductase (*184*).

From considerations of these new clusters, as well as other, better-known ones such as those found in cytochrome oxidase (*185*) and di- and trinuclear copper clusters (*186*), one can almost get the impression that some lonely metals do not want to be single and need a (redox) partner. This partner could in some cases be an iron ion, and they are linked by a μ-oxo or μ-hydroxo bridge! More seriously, as discussed in, e.g., (*10, 185*), the bimetallic enzyme sites are ideally suited to react

with molecular oxygen in an efficient and controlled manner. The diiron–oxygen proteins have the controlled reaction with molecular oxygen as a common feature, either as a direct part of their function, or as a prerequisite to form a functional redox-active site in the protein.

Note Added in Proof

After this review was finished, a three-dimensional structure of plant PAP with a Fe–Zn cluster was published; Sträter, N.; Klabunde, T.; Tucker, P.; Witzel, H.; Krebs, B. *Science* **1995** *268*, 1489. The iron ligands in this PAP can also be sequence aligned to the mammalian PAPs (Klabunde, T.; Sträter, N.; Krebs, B.; Witzel, H. *FEBS Lett.* **1995,** *367*, 56–60). It should be noted that the PAP structure shows that the iron cluster is located in β-sheets and not in a four-helix bundle, and that an aspargine is coordinated to the cluster. The three-dimensional structure of the mouse RNR-R2 protein has been solved, and is quite similar to *E. coli* R2 (Hans Eklund, personal communication). The three-dimensional structure of the soluble stearoyl-acyl carrier protein Δ^9 desaturase has been solved (Ylva Lindqvist, personal communication). The structure is similar to those of the iron containing subunits of RNR and MMO. Also the structure of rubrerythrin is solved (Pär Nordlund, personal communication) and shows the diiron cluster in a four-helix bundle. New crystallographic data on the Bath methane monooxygenase at −160°C show the presence of a hydroxo and water bridges in the diferric form. The iron distance is shortened from 3.4 Å (4°C) to 3.1 Å (−160°C). The bridging acetate is no more coordinated to the cluster. The diferrous form is shown to have a water bridge (Rosenzweig, A.; Nordlund, P.; Takahara, P.; Frederick, C.; Lippard, S. *Chemistry & Biology* **1995,** *2*, 409).

Acknowledgments

We thank J. D. Lipscomb and B.-M. Sjöberg for help with figures; N. Sträter, B. Krebs and H. Witzel for sharing information prior to publication; and M. Sahlin, B.-M. Sjöberg, and A. Ehrenberg for valuable comments on the manuscript. This work was supported by grants from the Bank of Sweden Tercentenary Foundation, the Swedish Natural Science Research Council, and the Magn. Bergvall Foundation.

References

1. Sanders-Loehr, J. In "Iron Carriers and Iron Proteins"; Loehr, T. M., Ed., Physical Bioinorganic Chemistry Series, VCH Publishers: New York, 1989; pp. 373–466.
2. Sanders-Loehr, J.; Loehr, T. M. *Adv. Inorg. Biochem.* **1979,** 235–252.
3. Que, L., Jr.; True, A. E. *Progr. in Inorg. Chem.* **1990,** *38*, 97–200.
4. Vincent, J. B.; Olivier-Lilley, G. L.; Averill, B. A. *Chem. Rev.* **1990,** *90*, 1447–1467.
5. Cormick, J. M.; Reem, R. C.; Foroughi, J.; Bollinger, G. M.; Jensen, G. M.; Stephens, P. J.; Stubbe, J.; Solomon, E. I. *New J. Chem.* **1991,** *15*, 439–444.

6. Wilkins, R. G. *Chemical Soc. Reviews*, **1992,** *21,* 171–178.
7. Solomon, E. I.; Zhang, Y. *Acc. Chem. Res.* **1992,** *25,* 343–352.
8. Karlin, K. D. *Science* **1993,** *261,* 701–708.
9. Wilkins, P. C.; Dalton, H. *Biochem. Soc. Transactions* **1994,** *22,* 700–704.
10. Feig, A. L.; Lippard, S. J. *Chem. Rev.* **1994,** *94,* 759–805.
11. Lippard, S. J. *Angew. Chem., Int. Ed. Eng.* **1988,** *27,* 344–361.
12. Sanders-Loehr, J.; Wheeler, W. D.; Shiemke, A. K.; Averill, B. A.; Loehr, T. M. *J. Am. Chem. Soc.* **1989,** *111,* 8084–8093.
13. Kurtz, D. M., Jr. *Chem. Rev.* **1990,** *90,* 585–606.
14. Gorun, S. M.; Lippard, S. J. *Inorg. Chem.* **1991,** *30,* 1625–1630.
15. Rosenzweig, A. C.; Frederick, C. A.; Lippard, S. J.; Nordlund, P. *Nature* **1993,** *366,* 537–543.
16. Scheriff, S.; Hendrickson, W. A.; Smith, J. L. *J. Mol. Biol.* **1987,** *197,* 273–296.
17. Holms, M. A.; Stenkamp, R. E. *J. Mol. Biol.* **1991,** *220,* 723–737.
18. Nordlund, P.; Sjöberg, B.-M.; Eklund, H. *Nature* **1990,** *345,* 593–598.
19. Nordlund, P.; Eklund, H. *J. Mol. Biol.* **1993,** *232,* 123–164.
20. Doi, K.; Antanaitis, B. C.; Aisen, P. *Structure Bonding.* **1988,** *70,* 1–26.
21. True, A. E.; Scarrow, R. C.; Randall, C. R.; Holz, R. C.; Que, L., Jr. *J. Am. Chem. Soc.* **1993,** *115,* 4246–4255.
22. Hempstead, P. D.; Hudson, A. J.; Artymiuk, P. J.; Andrews, S. C.; Banfield, M. J.; Guest, J. R.; Harrison, P. M. *FEBS Lett.* **1994,** *350,* 258–262.
23. LeGall, J.; Prickril, B. C.; Moura, I.; Xavier, A. V.; Moura, J. J. G.; Huynch, B.-H. *Biochemistry* **1988,** *27,* 1636–1642
24. Moura, I.; Tavares, P.; Ravi, N. *Meth. Enzymol.* **1994,** *243,* 216–240.
25. Dave, B. C.; Czernuszewics, R. S.; Prickril, B. C.; Kurtz, D. M. *Biochemistry* **1994,** *33,* 3572–3576.
26. Pierik, A. J.; Wolbert, R. B. G.; Portier, G. L.; Verhagen, M. F. J. M.; Hagen, W. R. *Eur. J. Biochem.* **1993,** *212,* 237–245.
27. Fox, B. G.; Shanklin, J.; Somerville, C.; Münck, E. *Proc. Natl. Acad. Sci. USA* **1993,** *90,* 2486–2490.
28. Fox, B. G.; Shanklin, J.; Ai, J.; Loehr, T. M.; Sanders-Loehr, J. *Biochemistry* **1994,** *33,* 12776–12786.
29. Kurtz, D. M., Jr.; Prickril, B. C. *Biochem. Biophys. Res. Commun.* **1991,** *181,* 337–341.
30. Ling, J.; Sahlin, M.; Sjöberg, B.-M.; Loehr, T.; Sanders-Loehr, J. *J. Biol. Chem.* **1994,** *269,* 5595–5601.
31. Lipscomb, J. D. *Annu. Rev. Microbiology* **1994,** *48,* 371–399.
32. Wang, D. L.; Holz, R. C.; David, S. S.; Que, L., Jr.; Stankovich, M. T. *Biochemistry* **1991,** *30,* 8187–8194.
33. Paulsen, K. E.; Liu, Y.; Fox, B. G.; Lipscomb, J. D.; Münck, E.; Stankovich, M. T. *Biochemistry* **1994,** *33,* 713–722.
34. Silva, K. E.; Stankovich, M. T.; Que, L., Jr. *J. Inorg. Biochem.* **1993,** *51,* 306.
35. Atta, M.; Andersson, K. K.; Ingemarson, R.; Thelander, L.; Gräslund, A. *J. Am. Chem. Soc.* **1994,** *116,* 6429–6430.
36. Suerbaum, H.; Körner, M.; Witzel, H.; Althaus, E.; Mosel, B.-D.; Müller-Warmuth, W. *Eur. J. Biochem.* **1993,** *214,* 313–321.
37. Eriksson, S.; Sjöberg, B.-M. In "Allosteric Enzymes", Hervé, G., Ed.; CRC Press Inc.: Boca Raton, FL, 1989; pp. 189–215.
38. Stubbe, J. *Adv. Enzymol.* **1990,** *63,* 349–419.
39. Fontecave, M.; Nordlund, P.; Eklund, H.; Reichard, P. *Adv. Enzymol.* **1992,** *65,* 147–183.

40. Reichard, P. *Science* **1993,** *260,* 1773–1777.
41. Thelander, L.; Gräslund, A. In "Metal Ions in Biology", Sigel, H.; Sigel, A., Eds.; Marcel Dekker: New York, 1994; Vol. 30, 109–129.
42. Dalton, H. *Adv. in Appl. Micro.* **1980,** *26,* 71–87.
43. Vincent, J. B.; Averill, B. A. *FASEB J.* **1990,** *4,* 3009–3014.
44. Andersson, G.; Ek-Rylander, B.; Minkin, C. In "Biology and Physiology of the Osteoclast", Rifkin, B. R.; Gay, C. V., Eds.; CRC Press: Boca Raton, FL, 1992; pp. 55–80.
45. Shanklin, J.; Somerville, C. *Proc. Natl. Acad. Sci. USA* **1991,** *88,* 2510–2514.
46. Schneider, G.; Lindqvist, Y.; Shanklin, J.; Somerville, C. *J. Mol. Biol.* **1992,** *225,* 561–564.
47. DeRose, V. J.; Liu, K. E.; Kurtz, D. M.; Hoffman, B. M.; Lippard, S. J. *J. Am. Chem. Soc.* **1993,** *115,* 6440–6441.
48. Thomann, H.; Brenardo, M.; McCormick, J. M.; Pulver, S.; Andersson, K. K.; Lipscomb, J. D.; Solomon, E. I. *J. Am. Chem. Soc.* **1993,** *115,* 8881–8882.
49. Galli, C.; Atta, M.; Andersson, K. K.; Gräslund, A.; Brudvig, G. W. *J. Am. Chem. Soc.* **1995,** *117,* 740–746.
50. Fox, B. G.; Hendrich, M. P.; Surerus, K. K.; Andersson, K. K.; Froland, W. A.; Lipscomb, J. D.; Münck, E. *J. Am. Chem. Soc.* **1993,** *115,* 3688–3701.
51. Gering, S.; Fleischnauer, P.; Haase, W.; Dietrich, M.; Witzel, H. *Biol. Chem. Hoppe-Seyler* **1990,** *371,* 786–787.
52. McCormick, J. M.; Reem, R. C.; Solomon, E. I. *J. Am. Chem. Soc.* **1991,** *113,* 9066–9079.
53. Fox, B. G.; Liu, Y.; Dege, J. E.; Lipscomb, J. D. *J. Biol. Chem.* **1991,** *266,* 540–550.
54. Avrill, B. A.; Davis, J. C.; Burman, S.; Zirino, T.; Sanders-Loehr, J.; Loehr, T. M.; Sage, J. T.; Debrunner, P. G. *J. Am. Chem. Soc.* **1987,** *109,* 3760–3767.
55. Hendrich, M. P.; Pearce, L. L.; Que, L., Jr.; Chasteen, N. D.; Day, E. P. *J. Am. Chem. Soc.* **1991,** *113,* 3039–3044.
56. Pulver, S.; Froland, W. A.; Fox, B. G.; Lipscomb, J. D.; Solomon, E. I. *J. Am. Chem. Soc.* **1993,** *115,* 12409–12422.
57. Andersson, K. K.; Atta, M.; Debeacker, N.; Latour, J.-M.; Thelander, L.; Gräslund, A. *J. Inorg. Biochem.* **1995,** in press.
58. Reem, R. C.; McCormick, J. M.; Richardson, D. E.; Devlin, F. J.; Stephens, P. J.; Musselman, R. L.; Solomon, E. I. *J. Am. Chem. Soc.* **1989,** *111,* 4688–4704.
59. Brown, C. A.; Remar, G. J.; Musselman, R. L.; Solomon, E. I. *Inorg. Chem.* **1995,** *34,* 688–717.
60. Hendrich, M. P.; Elgren, T. E.; Que, L. Jr. *Biochem. Biophys. Res. Commun.* **1991,** *176,* 705–710.
61. Davydov, R.; Kuprin, S.; Gräslund, A.; Ehrenberg, A. *J. Am. Chem. Soc.* **1994,** *116,* 11120.
62. Ravi, N.; Prickril, B. C., Kurtz, D. M. Jr.; Huynh, B. H. *Biochemistry* **1993,** *32,* 8487–8491.
63. Lee, S.-K.; Fox, B. G.; Froland, W. A.; Lipscomb, L. D.; Münck, E. *J. Am. Chem. Soc.* **1993,** *115,* 6450–6451.
64. Liu, K. E.; Wang, D., Huynh, B. H.; Edmondson, D. E.; Salifoglou, A.; Lippard, S. J. *J. Am. Chem. Soc.* **1994,** *116,* 7465–7466.
65a. Hendrich, M. P.; Debrunner, P. G. *Biophys. J.* **1989,** *56,* 489–506.
65b. Hendrich, M. P.; Day, E. P.; Wang, C. P.; Synder, B. S.; Holm, R. H.; Münck, E. *Inorg. Chem.* **1994,** *33,* 2848–2856.
66. Reem, R. C.; Solomon, E. I. *J. Am. Chem. Soc.* **1987,** *109,* 1216–1226.
67. Hendrich, M. P.; Münck, E.; Fox, B. G.; Lipscomb, J. D. *J. Am. Chem. Soc.* **1990,** *112,* 5861–5865.

68. Elgren, T. E.; Hendrich, M. P.; Que, L. Jr. *J. Am. Chem. Soc.* **1993,** *115,* 9291–9292.
69. Hoffman, B. M.; Sturgeon, B. E.; Doan, P. E.; DeRose, V. J.; Liu, K. E.; Lippard, S. J. *J. Am. Chem. Soc.* **1994,** *116,* 6023–6024.
70. Hoffman, B. M. *J. Phys. Chem.* **1994,** *98,* 11657–11665.
71. Reem, R. C.; Solomon, E. I. *J. Am. Chem. Soc.* **1984,** *106,* 8323.
72. Zhang, J.-H.; Kurtz, D. M., Jr. *Proc. Natl. Acad. Sci. USA* **1992,** *89,* 7065.
73. Sjöberg, B.-M. *Structure* **1994,** *2,* 793.
74. Uhlin, U.; Eklund, H. *Nature* **1994,** *370,* 533.
75a. Lynch, J. B.; Juarez-Garcia, C.; Münck, E.; Que, L., Jr. *J. Biol. Chem.* **1989,** *264,* 8091.
75b. Larsson, Å.; Sjöberg, B.-M. *EMBO J.* **1986,** *5,* 2037.
76. Mao, S. S.; Holler, T. P.; Yu, G. X.; Bollinger, J. M.; Booker, S.; Johnston, M. I.; Stubbe, J. *Biochemistry* **1992,** *31,* 9733.
77. Petersson, L.; Gräslund, A.; Ehrenberg, A.; Sjöberg, B.-M.; Reichard, P. *J. Biol. Chem.* **1980,** *255,* 6706.
78. Ochiai, E.-I.; Mann, G.; Gräslund, A.; Thelander, L. *J. Biol. Chem.* **1990,** *265,* 15758.
79. Mann, G.; Gräslund, A.; Ochiai, E.-I.; Ingemarsson, R.; Thelander, L. *Biochemistry* **1991,** *30,* 1939.
80. Bollinger, J. M.; Edmondson, D. E.; Huynh, B. H.; Filley, J., Jr.; Norton, J. R.; Stubbe, J. *Science* **1991,** *253,* 292.
81. Ravi, N.; Bollinger, J. M.; Huynh, B. H.; Edmondson, D. E.; Stubbe, J. *J. Am. Chem. Soc.* **1994,** *116,* 8007.
82. Bollinger, J. M., Tong, W. H.; Ravi, N.; Huynh, B. H.; Edmondson, D. E.; Stubbe, J. *J. Am. Chem. Soc.* **1994,** *116,* 8015.
83. Bollinger, J. M., Tong, W. H.; Ravi, N.; Huynh, B. H.; Edmondson, D. E.; Stubbe, J. *J. Am. Chem. Soc.* **1994,** *116,* 8024.
84. Elgren, T. E.; Lynch, J. B.; Juarez-Garcia, C.; Münck, E.; Sjöberg, B.-M.; Que, L., Jr. *J. Biol. Chem.* **1991,** *266,* 19265.
85. Bollinger, J. M., Jr.; Ravi, N.; Tong, W. H.; Edmondson, D. E.; Huynh, B. H.; Stubbe, J. *J. Inorg. Biochem.* **1993,** *51,* 6.
86a. Sahlin, M.; Lassmann, G.; Pötsch, S.; Sjöberg, B.-M.; Gräslund, A. *J. Biol. Chem.* **1994,** *269,* 11699.
86b. Sahlin, M.; Lassmann, G.; Pötsch, S.; Sjöberg, B.-M.; Gräslund, A. *J. Biol. Chem.* **1995,** *270,* 12361.
87. Henriksen, M. A.; Cooperman, B. S.; Sahlem, J. S.; Li, L. S.; Rubin, H. *J. Am. Chem. Soc.* **1994,** *116,* 9773.
88. Rova, U.; Goodtzova, K.; Ingemarson, R.; Behravan, G.; Gräslund, A.; Thelander, L. *Biochemistry* **1995,** *34,* 4267.
89. Bender, C. J.; Sahlin, M.; Babcock, G. T.; Barry, B. A.; Chandrashekar, T. K.; Salowe, S. P.; Stubbe, J.; Lindström, B.; Petersson, L.; Ehrenberg, A.; Sjöberg, B.-M. *J. Am. Chem. Soc.* **1989,** *111,* 8076.
90. Sahlin, M.; Gräslund, A.; Ehrenberg, A.; Sjöberg, B.-M. *J. Biol. Chem.* **1982,** *257,* 366.
91. Gräslund, A.; Sahlin, M.; Sjöberg, B.-M. *Environ. Health Perspect.* **1985,** *64,* 139.
92. Hoganson, C. W.; Babcock, G. T. *Biochemistry* **1992,** *31,* 11874.
93. Allard, P.; Barra, A. L.; Andersson, K. K.; Schmidt, P.; Atta, M.; Gräslund, A. *J. Inorg. Biochem.* **1995,** in press.
94. Gerfen, G. J.; Bellew, B. F.; Un, S.; Bollinger, J. M., Jr.; Stubbe, J.; Griffin, R. G.; Singel, D. J. *J. Am. Chem. Soc.* **1993,** *115,* 6420.

95. Hirsh, D. J.; Beck, W. F.; Lynch, J. B.; Que, L., Jr.; Brudvig, G. W. *J. Am. Chem. Soc.* **1992,** *114,* 7475.
96. Sahlin, M.; Gräslund, A.; Petersson, L.; Ehrenberg, A.; Sjöberg, B.-M. *Biochemistry* **1989,** *28,* 2618.
97a. Sahlin, M.; Sjöberg, B.-M.; Backes, G.; Loehr, T.; Sanders-Loehr, J. *Biochem. Biophys. Res. Commun.* **1990,** *1647,* 813.
97b. Fontecave, M.; Gerez, C.; Atta, M.; Jeunet, A. *Biochem. Biophys. Res. Comm.* **1990,** *168,* 659–664.
98. Gerez, C.; Gaillard, J.; Latour, J.-M.; Fontecave, M. *Angew. Chem. Int. Ed. Engl.* **1991,** *30,* 1135.
99. Gerez, C.; Fontecave, M. *Biochemistry* **1992,** *31,* 780.
100. Davydov, R.; Sahlin, M.; Kuprin, S.; Gräslund, A.; Ehrenberg, A., unpublished results.
101. Atta, M.; Nordlund, P.; Åberg, A.; Eklund, H.; Fontecave, M. *J. Biol. Chem.* **1992,** *26,* 20682.
102. Ormö, M.; de Maré, F.; Regnström, K.; Åberg, A.; Sahlin, M.; Ling, J.; Loehr, T. M.; Sanders-Loehr, J.; Sjöberg, B.-M. *J. Biol. Chem.* **1992,** *267,* 8711.
103. Regnström, K.; Åberg, A.; Ormö, M.; Sahlin, M.; Sjöberg, B.-M. *J. Biol. Chem.* **1994,** *269,* 6355.
104. Åberg, A.; Ormö, M.; Nordlund, P.; Sjöberg, B.-M. *Biochemistry* **1993,** *32,* 9845.
105. Lammers, M.; Follmann, H. *Structure Bonding* **1983,** *54,* 27.
106. Lassmann, G.; Thelander, L.; Gräslund, A. *Biochem. Biophys. Res. Commun.* **1992,** *188,* 879.
107. Lam, K.-Y.; Fortier, D. G.; Thomson, J. B.; Sykes, A. G. *J. Chem. Soc., Chem. Commun.* **1990,** 658.
108. Swarts, J. C.; Aquino, M. A. S.; Han, J.-Y.; Lam, K.-Y.; Sykes, A. G. *Biochim. Biophys. Acta* **1995,** *247,* 215.
109. Nyholm, S.; Johansson, A.; Thelander, L.; Gräslund, A. *Biochemistry* **1993,** *32,* 11569.
110. Pötsch, S.; Drechsler, H.; Liermann, B.; Gräslund, A.; Lassmann, G. *Molec. Pharmacol.* **1994,** *45,* 792.
111. Nyholm, S.; Ingemarson, R.; Thelander, L.; Gräslund, A., unpublished results.
112. Nyholm, S.; Mann, G. J.; Johansson, A. G.; Bergeron, R. J.; Gräslund, A.; Thelander, L. *J. Biol. Chem.* **1993,** *268,* 26200.
113. Liuzzi, M.; Déziel, R.; Moss, N.; Beaulieu, P.; Bonneau, A.-M.; Bosquet, C.; Chafouleas, J. G.; Garneau, M.; Jaramillo, J.; Krogsrud, R. L.; Lagacé, L.; McCollum, R. S.; Nawoot, S.; Guindon, Y. *Nature* **1994,** *372,* 695.
114. Dutia, B. M.; Frame, M. C.; Subak-Sharpe, J. H.; Clark, W. N.; Marsden, H. S. *Nature* **1986,** *321,* 439.
115. Cohen, E. A.; Gaudreau, P.; Brazeau, P.; Langelier, Y. *Nature* **1986,** *321,* 441.
116. Yang, F.-D.; Spanevello, R. A.; Celiker, I.; Hirschmann, R.; Rubin, H.; Cooperman, B. S. *FEBS Lett.* **1990,** *272,* 61.
117. Cosentino, G.; Lavallée, P.; Rakhit, S.; Plante, R.; Gaudette, Y.; Lawetz, C.; Whitehead, P. W.; Duceppe, J.-S.; Lépine-Frenette, C.; Dansereau, N.; Guilbault, C.; Langelier, Y.; Gaudreau, P.; Thelander, L.; Guindon, Y. *Biochem. Cell. Biol.* **1991,** *69,* 79.
118. Climent, I.; Sjöberg, B.-M.; Huang, C. Y. *Biochemistry* **1991,** *30,* 5164.
119a. Filatov, D.; Ingemarson, R.; Gräslund, A.; Thelander, L. *J. Biol. Chem.* **1992,** *267,* 15816.
119b. Lycksell, P.-O.; Ingemarson, R.; Davis, R.; Gräslund, A.; Thelander, L. *Biochemistry* **1994,** *33,* 2838.

120. Kjøller-Larsen, I.; Cornett, C.; Karlsson, M.; Sahlin, M.; Sjöberg, B.-M. *J. Biol. Chem.* **1992,** *267,* 12627–12631.
121. Pilkington, S. J.; Dalton, H. *Methods Enzymol.* **1990,** *188,* 181–190.
122a. Rosenzweig, A. C.; Lippard, S. J. *Acc. Chem. Res.* **1994,** *27,* 229–236.
122b. Liu, K. E.; Lippard, S. J. *Adv. Inorg. Chem.* **1995,** *42,* 263.
123. Anthony, C. "The Biochemistry of the Methylotrophs"; Academic Press: London, 1982.
124. Colby, J.; Stirling, D. I.; Dalton, H. *Biochem. J.* **1977,** *165,* 395–402.
125. Smith, D. D. S.; Dalton, H. *Eur. J. Biochem.* **1989,** *182,* 667–671.
126. Nguyen, H.-H. T.; Shiemke, A. K.; Jacobs, S. J.; Hales, B. J.; Lidstrom, M. E.; Chan, S. I. *J. Biol. Chem.* **1994,** *269,* 14995–15005.
127. Fox, B. G.; Froland, W. A.; Dege, J.; Lipscomb, J. D. *J. Biol. Chem.* **1989,** *264,* 10023–10033.
128. Fox, B. G., Borneman, J. G., Wackett, L. P.; Lipscomb, J. D. *Biochemistry* **1990,** *29,* 6419–6427.
129. Froland, W. A.; Andersson, K. K.; Lee, S.-K.; Liu, Y.; Lipscomb, J. D. *J. Biol. Chem.* **1992,** *267,* 17588–17597.
130. Stainthorpe, A. C.; Lees, V.; Salmond, G. P. C.; Dalton, H.; Murrell, J. C. *Gene* **1990,** *91,* 27–34.
131. Cardy, D. L. N.; Laidler, V.; Salmond, G. P. C.; Murrell, J. C. *Molec. Microbiol.* **1991,** *5,* 335–342.
132. Andersson, K. K.; Froland, W. A.; Lee, S.-K.; Lipscomb, J. D. *New J. Chem.* **1991,** *15,* 411–415.
133. Andersson, K. K.; Elgren, T. E.; Que, L., Jr.; Lipscomb, J. D. *J. Am. Chem. Soc.* **1992,** *114,* 8711–8713.
134. Andersson, K. K.; Elgren, T. E.; Fox, B. G.; Hendrich, M. P.; Froland, W. A.; Münck, E.; Que, L., Jr.; Lipscomb, J. D. *J. Inorg. Biochem.* **1993,** *51,* 299.
135. Woodland, M. P.; Patil, D. S.; Cammack, R.; Dalton, H. *Biochem. Biophys. Acta* **1986,** *873,* 237–242.
136. Fox, B. G.; Surerus, K. K.; Münck, E.; Lipscomb, J. D. *J. Biol. Chem.* **1988,** *263,* 10553–10556.
137. Hendrich, M. P.; Fox, B. G.; Andersson, K. K.; Debrunner, P. G.; Lipscomb, J. D. *J. Biol. Chem.* **1992,** *267,* 261–269.
138. Bender, C. J.; Rosenzweig, A. C.; Lippard, S. J.; Peisach, J. *J. Biol. Chem.* 1994, *269,* 15993–15998.
139. DeWitt, J. G.; Bensten, J. G.; Rosenzweig, A. C.; Hedman, B.; Green, J.; Pilkington, S.; Papaefthymiou, G. C.; Dalton, H.; Hodgson, K. O.; Lippard, S. J. *J. Am. Chem. Soc.* **1991,** *113,* 9219–9235.
140. Andersson, K. K.; Cox, D. D.; Que, L., Jr.; Flatmark, T.; Haavik, J. *J. Biol. Chem.* **1988,** *263,* 18621–18626.
141. Andersson, K. K.; Vassort, C.; Brennan, B.; Que, L., Jr.; Haavik, J.; Flatmark, T.; Gros, F.; Thibault, J. *Biochem. J.* **1992,** *284,* 687–695.
142. Andersson, K. K.; Haavik, J.; Martinez, A.; Flatmark T.; Petersson L. *FEBS Lett.* **1989,** *258,* 9–12.
143. White, R. E.; Coon, M. J. *Annu. Rev. Biochem.* **1980,** *49,* 315–356.
144. Murray, T. J.; Groves, J. T. In "Cytochrome P-450 Structure, Mechanism, and Biochemistry"; Ortiz de Montellano, P. R., Ed.; Plenum Press: New York, 1986; pp. 1–28.
145. Ortiz de Montellano, P. R. In "Cytochrome P-450 Structure, Mechanism, and Biochemistry"; Ortiz de Montellano, P. R., Ed.; Plenum Press: New York, 1986; pp. 217–271.

146. Guengerich, F. P. *Crit. Rev. Biochem. Mol. Biol.* **1990,** *25,* 97–153.
147. Lee, S.-K.; Nesheim, J. C.; Lipscomb, J. D. *J. Biol. Chem.* **1993,** *268,* 21569–21577.
148. Priestley, N. D.; Floss, H. G.; Froland, W. A.; Lipscomb, J. D.; Williams, P. G.; Morimoto, H. *J. Am. Chem. Soc.* **1992,** *114,* 7561–7562.
149. Floss, H. G.; Lee, S. *Acc. Chem. Res.* **1993,** *26,* 116–122.
150. Rataj, M. J., Kauth, J. E.; Donnelly, M. I. *J. Biol. Chem.* **1991,** *266,* 18684–18690.
151. Deighton, N.; Podmore, I. D.; Symons, M. C. R.; Wilkins, P. C.; Dalton, H. *J. Chem. Soc., Chem. Commun.* **1991,** 1086–1088.
152. Tian, G.; Berry, J. A.; Klinman, J. P. *Biochemistry* **1994,** *33,* 226–234.
153. Dix, T. A.; Benkovic, S. J. *Acc. Chem. Res.* **1988,** *21,* 101–107.
154. Sträter, N.; Fröhlich, R.; Schiemann, A.; Krebs, B.; Körner, M.; Suerbaum, H.; Witzel, H. *J. Mol. Biol.* **1992,** *224,* 511–513.
155a. Hayman, A. R.; Cox, T. M. *J. Biol. Chem.* **1994,** *269,* 1294–1300.
155b. Aquino, M. A. S.; Lim, J.-S.; Sykes, A. G. *J. Chem. Soc., Dalton Trans.* **1994,** 429–436.
155c. Aquino, M. A. S.; Sykes, A. G. *J. Chem. Soc., Dalton Trans.* **1994,** 683–687.
156. Ek-Rylander, B.; Flores, M.; Wendel, M.; Heinegård, D.; Andersson, G. *J. Biol. Chem.* **1994,** *269,* 14853–14856.
157. Orlando, J. L.; Zirino, T.; Quirk, B. J.; Averill, B. A. *Biochemistry* **1993,** *32,* 8120–8129.
158. Ek-Rylander, B.; Berkhem, T.; Husman, B.; Öhman, L.; Andersson, K. K.; Andersson, G., unpublished results.
159. David, S. H.; Que, L., Jr. *J. Am. Chem. Soc.* **1990,** *112,* 6455–6463.
160. Dietrich, M.; Münstermann, D.; Suerbaum, H.; Witzel, H. *Eur. J. Biochem.* **1991,** *199,* 105–118.
161. Mueller, E. G.; Crowder, M. W.; Averill, B. A.; Knowles, J. R. *J. Am. Chem. Soc.* **1993,** *115,* 2974–2975.
162. Vincent, J. B.; Crowder, M. W.; Averill, B. A. *TIBS* **1992,** *17,* 105–110.
163. Holz, R. C.; Que, L., Jr.; Ming, L.-J. *J. Am. Chem. Soc.* **1992,** *114,* 4434–4436.
164. Wang, Z.; Ming, L.-J.; Que, L., Jr.; Vincent, J. B.; Crowder, M. W.; Averill, B. A. *Biochemistry* **1992,** *31,* 5263–5268.
165. Stahl, B.; Klabunde, T.; Witzel, H.; Krebs, B.; Steup, M.; Karas, M.; Hillenkamp, F. *Eur. J. Biochem.* **1994,** *220,* 321–330.
166. Ek-Rylander, B.; Bill, P.; Norgård, M.; Nilsson, S.; Andersson, G. *J. Biol. Chem.* **1991,** *266,* 24684–24689.
167. Ling, P.; Roberts, M. *J. Biol. Chem.* **1993,** *268,* 6896–6902.
168. Van Beeumen, J. J.; Van Driessche, G.; Liu, M.-Y.; LeGall, J. *J. Biol. Chem.* **1991,** *266,* 20645.
169. Shanklin, J.; Whittle, E.; Fox, B. G. *Biochemistry* **1994,** *33,* 12787–12794.
170. Harrison, P. M.; Artymiuk, P. J.; Ford, G. C.; Lawson, D. M.; Smith, J. M. A.; Treffry, A.; White, J. L. In "Biomineralization: Chemical and Biochemical Perspective"; Mann, S.; Webb, J.; Williams, R. J. P., Eds.; VCH Verlagsgesellschaft: Weinheim, 1989; pp. 257–294.
171. Theil, E. C. *Annu. Rev. Biochem.* **1987,** *56,* 289.
172. Andrews, S. C.; Arosio, P.; Bottke, W.; Briat, J.-F.; von Darl, M.; Harrison, P. M.; Laulhère, J.-P.; Levi, S.; Lobreaux, S.; Yewdall, S. J. *J. Inorg. Biochem.* **1992,** *47,* 161.
173. Harrison, P. M.; Bauminger, E. R.; Hechel, D.; Hodson, N. W.; Nowik, I.; Treffry, A.; Yewdall, S. J. In "Progress in Iron Research"; Hershko, C. et al., Eds., Plenum Press: New York, 1994; pp. 1–12.
174. Treffry, A.; Sowerby, J. M.; Harrison, P. M. *FEBS Lett.* **1978,** *95,* 221.

175. Xu, B.; Chasteen, N. D. *J. Biol. Chem.* **1991,** *266,* 19965.
176. Waldo, G. S.; Ling, J.; Sanders-Loehr, J.; Theil, E. C. *Science* **1993,** 796.
177. Bauminger, E. R.; Harrison, P. M.; Hechel, D.; Hodson, N. W.; Nowik, I.; Treffry, A.; Yewdall, S. J. *Biochem. J.* **1993,** *296,* 709.
178. Lawson, D. M.; Artymiuk, P. J.; Yewdall, S. J.; Smith, J. M. A.; Livingstone, J. C.; Treffry, A.; Luzzago, A.; Levi, S.; Arosio, P.; Cesareni, G.; Thomas, C. D.; Shaw, W. V.; Harrison, P. M. *Nature* **1991,** *349,* 541.
179. Kim, J.; Rees, D. C. *Nature* **1992,** *360,* 553–560.
180a. Kim, J.; Rees, D. C. *Science* **1992,** *257,* 1677–1682.
180b. Rees, D. C.; Chan, M. K.; Kim, J. *Adv. Inorg. Chem.* **1993,** *40,* 89.
181. Pedersen, J. Z.; Finazzi-Agro, A. *FEBS Lett.* **1993,** *325,* 53–58.
182. Hendrich, M. P.; Logan, M.; Andersson, K. K.; Arciero, D. M.; Lipscomb, J. D.; Hooper, A. B. *J. Am. Chem. Soc.* **1994,** *116,* 11961–11968.
183. Volbeda, A.; Charon, M.-H.; Piras, C.; Hatchikian, E. C.; Frey, M.; Fontecilla-Camps, J. C. *Nature* **1995,** *373,* 580–587.
184. Chan, M. C.; Mukund, S.; Kletzin, A.; Adams, M. W. W.; Rees, D. C. *Science* **1995,** *267,* 1463–1469.
185. Babcock, G. T.; Wikström, M. *Nature* **1992,** *356,* 301–309.
186. Kitajima, N.; Moro-oka, Y. *Chem. Rev.* **1994,** *94,* 737–757.

ADVANCES IN INORGANIC CHEMISTRY, VOL. 43

CARBON DIOXIDE FIXATION CATALYZED BY METAL COMPLEXES

KOJI TANAKA

Institute for Molecular Science, Myodaiji, Okazaki 444, Japan

I. Introduction

There has been a growing interest in the utilization of CO_2 as a potential C1 source for chemicals and fuels to cope with the predictable oil shortage in the near future. Insertion reactions of CO_2 into M–H, M–O, M–N, and M–C bonds are well documented, where these reactions are explained in terms of the electrophilicity of CO_2 (*1, 2*). Catalytic syntheses of lactones (*3–9*) and pyrones (*10–16*) are also established by incorporation of CO_2 into dienes and alkynes activated on low-valent metal complexes. Carbon dioxide shows only an electrophilicity under usual reaction conditions, but it exhibits a nucleophilicity upon coordination to low-valent metals because of the intramolecular charge transfer from metals to CO_2. Metal–CO_2 formation may be the key species in electro- and photochemical CO_2 reductions. Since the first characterization of [Ni(PCy_3)$_2$(η^2(C,O)-CO_2)] (*17*), a variety of metal

Copyright © 1995 by Academic Press, Inc.
All rights of reproduction in any form reserved.

complexes with η^1-(*18–25*), η^2-(*17, 26–30*), μ_2-(*31*), and μ_3-CO_2 modes (*32–34*) have been prepared. The η^1(C)–CO_2 mode is composed of the electron transfer from the filled metal d_{z^2} orbital to the CO_2 π^* orbital, and the η^2(C,O)–CO_2 mode involves a filled CO_2 π to metal σd bonding and a filled metal πd to the empty CO_2 π^* back bonding. The increase in the electron density of the CO_2 moiety in metal–η^1(C)–CO_2 complexes leads to reversible protonation of oxygen, forming metal–COOH and –CO complexes (*35, 40*), but such conversion from metal–η^2(C,O)–CO_2 complexes has not been demonstrated. Metal complexes with the η^1(C)–CO_2 mode are, therefore, generally accepted as active species for CO generation in electro- and photochemical CO_2 reductions. Furthermore, multielectron reduction of CO_2 accompanied by carbon–carbon bond formation is advancing by taking advantage of the smooth conversion from metal–η^1(C)–CO_2 to metal–CO complexes (*41*).

Carbon dioxide easily forms a 1 : 1 adduct with various organic bases, in which the CO_2 structure possibly reflects the electron donor ability of the bases. The linear OCO is essentially maintained in the ammonium adduct, $(NH_3)(CO_2)$ (*42*), while the OCO angle of the imidazolidone–CO_2 adduct $[OOC–\overline{NC(O)NHCH_2CH_2}]^-$ is calculated to be 132° (*43*). Indeed, the OCO angle in the latter is quite close to those of Co^- (*18*) and Rh–η^1(C)–CO_2 complexes (*19*), suggesting that CO_2 bonded on strong bases is also activated as it is on Co(I) and Rh(I). Although CO_2 reduction using metal complexes is generally considered to take place on metal centers, the reactivity of CO_2 activated on non-transition metals is of interest in relation to biological CO_2 fixation. This article reviews electro- and photochemical CO_2 reductions by metal complexes, and model reactions of biological CO_2 fixation.

II. Metal–η^1(C)–CO_2 Complexes

Most CO_2 metal complexes are prepared by an electrophilic attack of CO_2 on either an unsaturated 16-electron or an 18-electron metal atom with a good leaving group. The first η^1(C)–CO_2 metal complex is prepared by the reaction of CO_2 with $[Co^I(salen)M^+]$ (M = Li, Na, K, and Cs) in which M^+ strongly interacts with the oxygen of CO_2 (*18*):

$$[Co^{II}salen] + M \rightarrow [Co^I(salen)M^+], \quad (1)$$

$$[Co^I(salen)M^+] + CO_2 \rightleftharpoons [Co^I(salen)M^+(CO_2)]. \quad (2)$$

Alkali metals used to reduce the Co(II) are essential as M^+ ions to give CO_2 binding to Co(I). A large number of Co–η^1(C)–CO_2 complexes have been prepared by this method. The kinetics and equilibrium of CO_2 binding to a series of tetraazamacrocycle Co(I) complexes,

$$\text{Co(I)} + CO_2 \rightleftharpoons \text{Co}{-}CO_2, \tag{3}$$

have been well studied by means of gas-uptake (*18, 20*), pulse-radiolysis (*44*), spectroscopic (*38, 45*), and electrochemical methods (*46–50*). The binding constants of the Co(I) complexes for CO_2 have a general tendency to increase with the negative potential shift of the reduction potential of the Co(I)/Co(II) couple. The complexes with reduction potentials more positive than -1.2 V lose practically the ability to bind CO_2 at room temperature (Table I). Thus, the charge transfer from Co(I) to CO_2 is the crucial factor for the stabilization of the Co–CO_2 bonds. Except for the Co(I) complexes, there is little thermodynamic information on the affinity of metal complexes for CO_2 because of the limited number of well-characterized η^1(C)–CO_2 complexes. Neutral Rh(I)- and Ir(I)–η^1(C)–CO_2 complexes are prepared by the reaction of $[Ir^I(dmpe)_2Cl]$ and $[Rh^I(diars)_2Cl]$ with CO_2 and lose CO_2 under evacuation (*19, 21*). The frameworks of the Co and Rh–η^1(C)–CO_2 adducts are depicted in Fig. 1. The OCO angle (135° and 132°) and the C–O bond distances (av. 1.23 Å) of those complexes are close to those of CO_2^- (135.2° and 1.24 Å) obtained by ab initio MO calculations (*51*). Both $[Co(Pr\text{-}salen)K(CO_2)]$ and $[RhCl(diars)_2(CO_2)]$, therefore, are approximated by M(II)-CO_2^- rather than M(I)-CO_2.

III. Equilibrium of CO_2 and CO on Metals

An alternative preparation method for metal η^1(C)–CO_2 complexes is the deprotonation of hydroxycarbonyl complexes (*25*). A general route for the preparation of hydroxycarbonyl complexes is a nucleophilic attack of OH^- or H_2O on cationic metal carbonyl species (*52*):

$$[\text{M-CO}]^{n+} + OH^- \rightarrow [\text{M-C(O)OH}]^+. \tag{4}$$

The first stable hydroxycarbonyl complex $[IrCl_2L_2(CO)(C(O)OH)]$ (L = PMe_2Ph and $AsMe_2Ph$) was obtained by hydrolysis of $[IrCl_2L_2(CO)(C(O)OMe)]$ (*53*). A specific reaction is CO insertion into the metal–

TABLE I

BINDING CONSTANTS OF $[CoL]^+$ WITH CO_2

Ligand	$E_{1/2}$ (V vs SCE)	K (m^{-1})
Me_2[14]1,3-diene	−0.89	<0.5
Me_8[14]4,11-diene	−1.28	4.0
rac-Me_6[14]4,11-diene	−1.34	1.2×10^4
Me_2[14]4,11-diene	−1.51	5×10^5

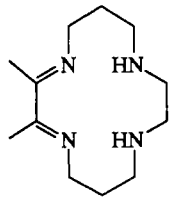

Me_2[14]1,3-diene

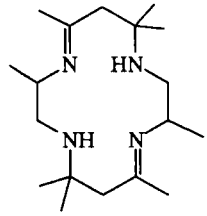

Me_8[14]4,11-diene

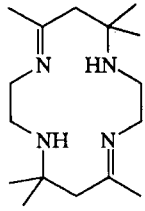

Me_6[14]4,11-diene

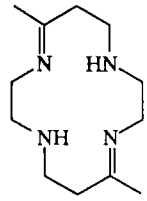

Me_2[14]4,11-diene

hydroxy bond of $[Pt(C_6H_5(PEt_3)_2(OH)]$, affording $[Pt(C_6H_5)(PEt_3)_2(C(O)OH)]$ (*36*):

$$[Pt(C_6H_5)(PEt_3)_2(OH)] + CO \rightarrow [Pt(C_6H_5)(PEt_3)_2(C(O)OH)]. \quad (5)$$

Thermally labile $[FeCp(CO)_2(C(O)OH)]$ is subject to decarboxylation, while $[FeCp(CO)(PPh_3)(CO_2)K]$ is isolated by treatment of $[FeCp(CO)(PPh_3)(C(O)OH)]$ with excess of KOH (*24, 54*). The wide range of pK_a values for hydroxycarbonyl complexes (Table II) may reflect the degree of electron transfer from the metal to CO_2.

The pK_a value of $[Ru(bpy)_2(CO)(C(O)OH)]^+$ is 9.6 at 20°C (*55*). The

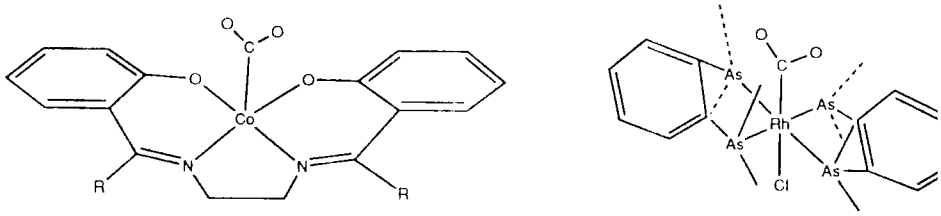

M-C 1.99(3) Å
C-O ave. 1.23(3) Å
O-C-O angle 135(3)°

M-C 2.05(2) Å
C-O 1.20(2), 1.25(2) Å
O-C-O angle 132°

FIG. 1. Structural frameworks of Co- and Rh-η^1 CO_2 complexes.

interconversion among $[Ru(bpy)_2(CO)_2]^{2+}$, $[Ru(bpy)_2(CO)(C(O)OH)]^+$, and $[Ru(bpy)_2(CO)(CO_2)]$ in H_2O,

$$[Ru(bpy)_2(CO)_2]^{2+} \rightleftharpoons [Ru(bpy)_2(CO)(C(O)OH)]^+ \rightleftharpoons [Ru(bpy)_2(CO)(CO_2)], \quad (6)$$

is very rapid, and these three species exist in equilibrium mixtures in weakly alkaline solutions (Fig. 2). Dissociation of the terminal proton from $[Ru(bpy)_2(CO)(C(O)OH)]^+$ gives rise to an increase with the electron density of the resulting $\eta^1(C)$–CO_2 moiety. As a result, $[Ru(bpy)_2(CO)(CO_2)]$ reacts smoothly with CH_3I to give $[Ru(bpy)_2(CO)(C(O)OCH_3)]^+$ (*25*), which is also obtained in the reaction of $[Ru(bpy)_2(CO_2)]^{2+}$ with CH_3O^- in an almost quantitative yield (*35*):

$$[Ru(bpy)_2(CO)(CO_2)] + CH_3I \rightarrow [Ru(bpy)_2(CO)(C(O)OCH_3)]^+ + I^-, \quad (7)$$

TABLE II

pK_a VALUES FOR HYDROXYCARBONYL METAL COMPLEXES

Complex	pK_a	Ref.
$[ReCp(NO)(CO)(C(O)OH)]$	11	*39, 56*
$[Ru(bpy)_2(CO)(C(O)OH)]^+$	9.6	*55*
$[Pt(C_6H_5)(PEt_3)(C(O)OH)]$	14	*36*
$[CoL(C(O)OH)]^{2+}$	3.1	*38*
$[Co(en)_2(H_2O)(C(O)OH)]^{2+}$	2.5	*37*

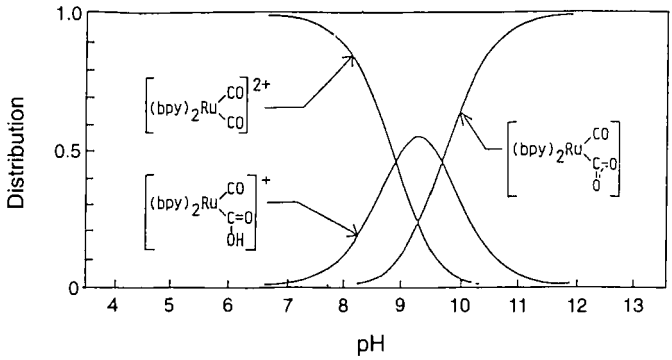

FIG. 2. Distribution of $[Ru(bpy)_2(CO)_2]^{2+}$, $[Ru(bpy)_2(CO)(C(O)OH)]^+$, and $[Ru(bpy)_2(CO)(CO_2)]$ with pH in H_2O at 25°C.

$$[Ru(bpy)_2(CO)_2]^{2+} + CH_3O^- \rightarrow [Ru(bpy)_2(CO)(C(O)OCH_3)]^+. \quad (8)$$

The frameworks of the CO, $C(O)OCH_3$, and CO_2 moieties of $[Ru(bpy)_2(CO)_2](PF_6)_2$, $[Ru(bpy)_2(CO)(C(O)OCH_3)]B(C_6H_5)_4 \cdot CH_3CN$, and $[Ru(bpy)_2(CO)(CO_2)] \cdot 3H_2O$ as determined by X-ray diffraction studies (*25*) are depicted in Fig. 3. The Ru–C bond distances of $[Ru(bpy)_2(CO)(C(O)OCH_3)]^+$ and $[Ru(bpy)_2(CO)(CO_2)]$ are longer than that of $[Ru(bpy)_2(CO)_2]^{2+}$, and the former two are close to the Rh–CO_2 bond distance (2.05 Å). The average of the two C–O bond distances (formally double and single bonds) of $[Ru(bpy)_2(CO)(C(O)OCH_3)]^+$ (1.27 Å) is consistent with that of the CO_2 moiety of $[Ru(bpy)_2(CO)(CO_2)]$, suggesting that the bond order of the two C–O bonds of the latter is approximately 1.5. The short Ru–C bond distance of $[Ru(bpy)_2(CO)(C(O)OCH_3)]^+$ (2.04 Å) as compared with that of $[Ru(bpy)_2(CO)(CO_2)]$ (2.06 Å) indicates the multiple bond character of the Ru–CO_2 bond is not greater than that of Ru–$C(O)OCH_3$. Furthermore, the OCO angle of

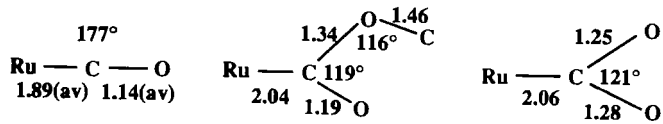

FIG. 3. Structural features, including bond lengths (Å), for the Ru–CO, Ru–$C(O)OCH_3$, and Ru–CO_2 moieties in $[Ru(bpy)_2(CO)_2](PF_6)_2$, $[Ru(bpy)_2(CO)(C(O)OCH_3)]PF_6$, and $[Ru(bpy)_2(CO)(CO_2)] \cdot 3H_2O$.

the CO_2 adduct (121°) is much smaller than those of $[RhCl(diars)_2(CO_2)]$ (132°) and $[Co(Pr\text{-}salen)K(CO_2)]$ (135°). The Ru–CO_2 bond may, therefore, be formulated as Ru^{II}–CO_2^{2-}. The accumulation of the negative charge on the CO_2 moiety is possibly related to the relatively high pKa value of $[Ru(bpy)_2(CO)(C(O)OH)]^+$ (Table II). A hydroxycarbonyl complex, $[Pt(C_6H_5)(PEt_3)_2(C(O)OH)]$ (p$K_a \approx 14$) exists as a hydrogen-bonded dimer structure in the solid state (*36*). The OCO angle of 117.7° may also result from the strong basicity of the CO_2 moiety.

A. Decarboxylation of M–COOH and M–CO_2

Loss of CO_2 from hydroxycarbonyl and CO_2 adducts would be expected to produce metal-hydride and coordinatively unsaturated low-valent

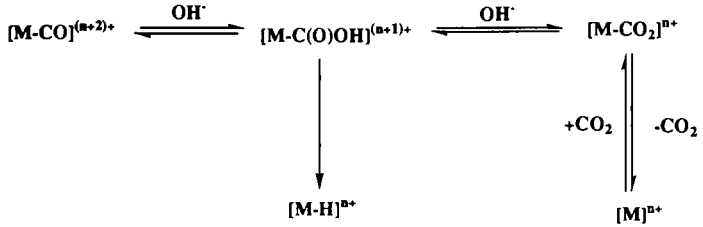

SCHEME 1. Decarboxylation from hydroxycarbonyl– and CO_2–metal complexes.

metal complexes (Scheme 1). At present, a general tendency for the rates of decarboxylation from hydroxycarbonyl- and CO_2- metal complexes is not provided; $[Ru(bpy)_2(CO)(C(O)OH)]^+$ (*35*) and $[FeCp(PPh_3)(CO)(C(O)OH)]$ (*36*) lose CO_2 (β-elimination) faster than the deprotonated forms (CO_2 adduct), but the reverse is true in the case of the $[ReCp(NO)(CO)(C(O)OH)]$ (*56*) and $[IrCl_2(PMe_2Ph)_2(CO)(C(O)OH)]$ (*53*) complexes. For example, an aqueous solution of $[Ru(bpy)_2(CO)_2]^{2+}$ at pH 11, where only $[Ru(bpy)_2(CO)(CO_2)]$ exists in H_2O, does not undergo a serious change at 100°C for 3 h, while the same solution at pH 9.5 (the maximum concentration of $[Ru(bpy)_2(CO)(C(O)OH)]^+$ evolves an almost stoichiometric amount of CO_2 using the same procedure. The unusual thermal stability of $[Ru(bpy)_2(CO)(CO_2)]$ may result from thermodynamically unfavorable formation of the pentacoordinate Ru(0) complex $[Ru(bpy)_2(CO)]$.

Decarboxylation from hydroxycarbonyl and carbon dioxide complexes is the key step for water gas shift reactions (WGSR),

$$CO + H_2O \rightarrow CO_2 + H_2, \tag{9}$$

as the reverse reaction of the CO_2 reduction, and various metal complexes have proven to be active in the WGSR (*57*). In the WGSR under aqueous alkaline conditions, CO readily reacts with OH^- to form $HCOO^-$ quantitatively at elevated temperatures, which functions as a buffer to some extent, adjusting the pH value of the initial solution to around 8.5 (*58*). Formato complexes, therefore, are likely to be generated by the reaction of formate with metal complexes used for the catalyst precursors in the reaction media. Furthermore, hydroxycarbonyl complexes, if the p*K*a value is larger than the pH of the solution, are also expected to be formed by a reaction of OH^- or H_2O with metal carbonyl species. Thermal decarboxylation of formato- and hydroxycarbonyl–metal complexes leads to formation of metal-hydride species as the precursors to H_2 evolution. The WGSRs of $[Fe(CO)_5]$ and $[Ru_3(CO)_{12}]$ have been shown to proceed via the decarboxylation of the hydroxycarbonyl species, and the $[M(CO)_6]$ complexes (M = Cr, Mo, W) preferentially catalyze the WGSRs through the decomposition of formato complexes. The rate of decarboxylation of $[Ru(bpy)_2(CO)(C(O)OH)]^+$ is about 150 times faster than that of $[Ru(bpy)_2(CO)(O_2CH)]^+$ under the same conditions. So, the WGSR by $[Ru(bpy)_2(CO)_2]^{2+}$ in weakly alkaline solutions proceeds via the hydroxycarbonyl complex, and a number of species involved in the catalytic cycle of the WGSR by $[Ru(bpy)_2(CO)_2]^{2+}$ have been isolated (Scheme 2) (*35*).

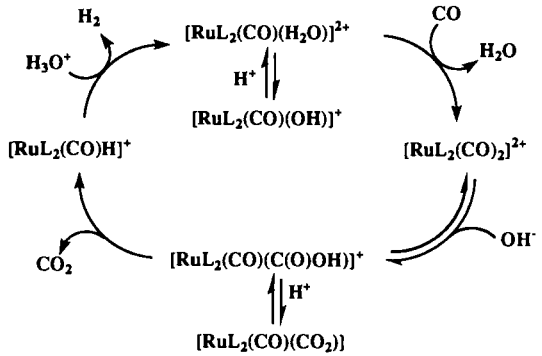

SCHEME 2. Water gas shift reaction (WGSR) catalyzed by $[Ru(bpy)_2(CO)_2]^{2+}$.

A nucleophilic attack of OH^- (or H_2O) on metal carbonyl complexes is thermodynamically unfavorable in acidic and neutral conditions. In fact, almost pure $[Ru(bpy)_2(CO)_2]^{2+}$ is obtained in high yield from weakly acidic aqueous solutions of $[Ru(bpy)_2Cl_2]$ under CO pressure at 100°C without catalyzing the WGSR. On the other hand, the susceptibility of metal–carbonyl complexes to a nucleophilic attack of H_2O (or

OH^-), is enhanced by protonation of the central metals in acidic conditions. The WGSR catalyzed by $[Rh(bpy)_2(CO)]^+$ (*59*) has been shown to proceed via the formation of the hydroxycarbonyl complex assisted by protonation of Rh (Scheme 3).

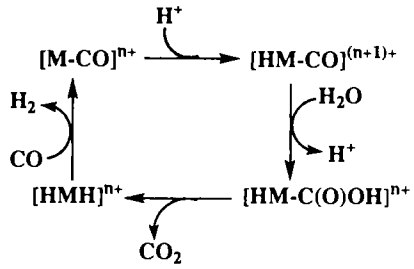

SCHEME 3. Proposed mechanism for the water gas shift reaction in acidic conditions.

IV. Electro- and Photochemical Reduction of CO_2

There are numerous reports on electro- and photochemical reductions of CO_2 catalyzed by metal complexes. Formato and hydroxycarbonyl metal complexes are again considered as key intermediates. Most CO_2 reductions by metal complexes are accompanied by H_2 evolution resulting from a competitive electrophilic attack of H^+ and CO_2 on the metal center. Insertion of CO_2 into metal-hydride bonds generally produces formato complexes (normal insertion) rather than hydroxycarbonyl metal complexes (abnormal insertion). The generation of dihydrogen and formate in electro- and photochemical reductions of CO_2 is most likely explained by the participation of metal-hydride species in the catalytic cycles. The addition of CO_2 to metals followed by the acid–base equilibrium affording metal carbonyl complexes (Scheme 1) is accepted as the general route for the production of CO as a result of the reduction of CO_2, although the possibility of isomerization from formato to hydroxycarbonyl complexes is not excluded. Furthermore, hydroxycarbonyl species are possible precursors to the formation of formate if the redox reactions give rise to protonation of the hydroxycarbonyl carbon, either by intramolecular migration of the terminal proton or by intermolecular reaction (Fig. 4), prior to dissociation of OH^-. This is more likely to occur in organic solvents than in aqueous conditions.

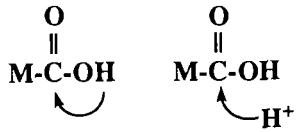

FIG. 4. Intra- and intermolecular protonation of the hydroxycarbonyl carbon.

A. ELECTROCHEMICAL CO_2 REDUCTION

Although $[Ru(bpy)_2(CO)(CO_2)]$ does not participate in the WGSR catalytic cycle of $[Ru(bpy)_2(CO)_2]^{2+}$ (Scheme 2), it appears to be the active species in the electro- and photochemical reduction of CO_2. Experiments on the controlled potential electrolysis of $[Ru(bpy)_2(CO)_2]^{2+}$ at -1.20 V (vs SCE) in DMF/H_2O(1 : 9 v/v, pH 6.0) under a CO_2 atmosphere have been reported to give CO and H_2 in a 1.2 : 1.3 mole ratio, while the same electrolysis conducted at pH 9.5 gave H_2, CO, and $HCOO^-$ in a mole ratio of 1.1 : 1.2 : 1.5 (*60*). Furthermore, the electrochemical reduction of CO_2 in the presence of $[Ru(bpy)_2(CO)_2]^{2+}$ in dry CH_3CN with the addition of Me_3NHCl produces $HCOO^-$ as the dominant product, with a current efficiency of 85% (*61*). The variations in the main product depend on the proton concentration and relate to the equilibration of $[Ru(bpy)_2(CO)_2]^{2+}$, $[Ru(bpy)_2(CO)(C(O)OH)]^+$, and $[Ru(bpy)_2(CO)(CO_2)]^0$. In agreement with this, electrochemical reduction of $[Ru(bpy)_2(CO)_2]^{2+}$ at pH 9.5 gives formate in high yield. Based on these observations, the electrochemical reduction of CO_2 in the

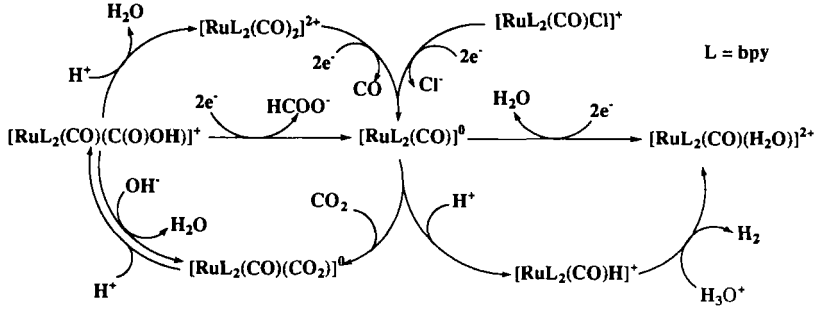

SCHEME 4. Proposed mechanism for two-electron reduction of CO_2 catalyzed by $[Ru(bpy)_2(CO)_2]^{2+}$.

presence of $[Ru(bpy)_2(CO)_2]^{2+}$ is explained by Scheme 4. Two-electron reduction of the 18-electron complex, $[Ru(bpy)_2(CO)_2]^{2+}$, causes CO dissociation with generation of $[Ru(bpy)_2(CO)]^0$, which is then subject to

competitive electrophilic attack by CO_2 and H^+ to produce $[Ru(bpy)_2(CO)(CO_2)]$ and $[Ru(bpy)_2(CO)H]^+$. Both $[Ru(bpy)_2(CO)_2]^{2+}$ and $[Ru(bpy)_2(CO)(C(O)OH)]^+$ formed from the protonation of $[Ru(bpy)_2(CO)(CO_2)]$ function as the precursors to CO and $HCOO^-$. Dihydrogen evolution is ascribed to the reaction of protons with $[Ru(bpy)_2(CO)H]^+$ under electrolysis conditions. Carbon dioxide–assisted quantitative protonation of $[Ru(bpy)_2(CO)(CO_2)]^0$ in CH_3OH,

$$[Ru(bpy)_2(CO)(CO_2)] + CH_3OH + CO_2 \rightarrow [Ru(bpy)_2(CO)(C(O)OH)]^+ + CH_3OCO_2^-, \quad (10)$$

supports the generation of $[Ru(bpy)_2(CO)(C(O)OH)]^+$ ($pKa = 9.5$) in organic solvents (*25*).

Meyer *et al.*, on the other hand, report CO_2 insertion into $[Ru(bpy)_2(CO)H]^0$ forming $[Ru(bpy)_2(CO)(OC(O)H)]^0$,

$$[Ru(bpy)_2(CO)H]^0 + CO_2 \rightarrow [Ru(bpy)_2(CO)(OC(O)H)]^0, \quad (11)$$

as the precursor to the release of formate under electrolysis conditions (*62*):

$$[Ru(bpy)_2(CO)(OC(O)H)]^0 + e^- \rightarrow HCOO^- + [Ru(bpy)_2(CO)(solvent)]. \quad (12)$$

An interesting observation is that of Ziessel *et al.*, who found a dark-blue film adhering to the working electrode (C or Pt) during the controlled potential electrolysis of $[Ru(bpy)_2(CO)_2]^{2+}$ at -1.65 V in CH_3CN–5% H_2O (*63*). The Ru polymer which they proposed, composed of $[Ru(bpy)(CO)_2]_n$ units having Ru–Ru bonds, shows quite high activity for CO generation in the electrochemical CO_2 reduction in H_2O, and the transformation from CO_2 to CO is explained by the hydroxycarbonyl intermediate (Scheme 5). At present, three different pathways have been proposed in the reduction of CO_2 by $[Ru(bpy)_2(CO)X]^{n+}$ (X = Cl, H, CO, and CH_3CN; $n = 1, 2$) (*60, 62, 63*).

Among examples of the electrochemical reduction of CO_2 by metal complexes having macrocyclic ligands, the case of $[Ni(cyclam)]^{2+}$ adsorbed on an Hg electrode of especial interest from the viewpoint of high current efficiency and CO generation (almost 100% current efficiency) in H_2O under relatively low overpotential conditions (*64*). The selectivity of CO/H_2 formation in the CO_2 reduction is largely dependent on the substituents of the Ni macrocycle complexes. Recently,

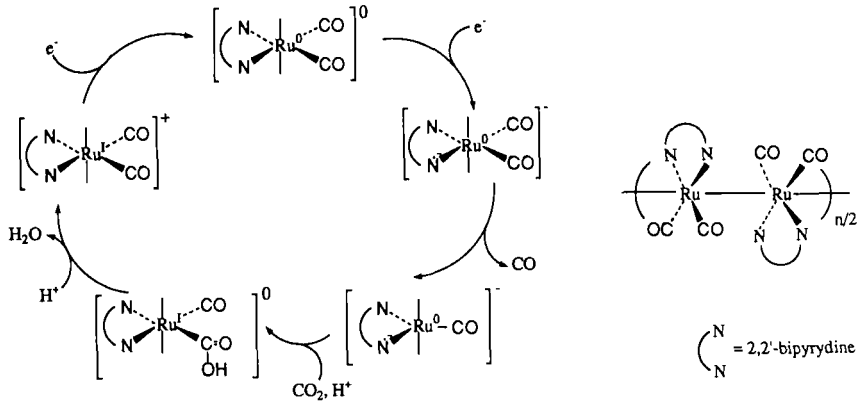

SCHEME 5. Proposed structure of a Ru polymer and two-electron reduction of CO_2 by the Ru polymer modified electrode.

RRSS-NiHTIM^{2+} and NiDMC^{2+} have been shown to be better catalysts than [Ni(cyclam)]$^{2+}$ (*65*).

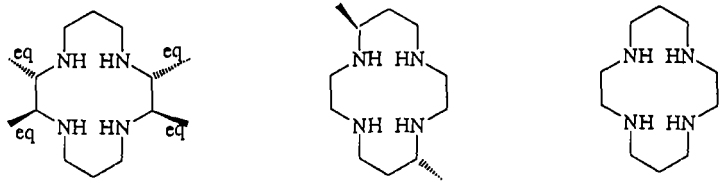

RRSS-HTIM DMC cyclam

However, little is known as to why selective generation of CO takes place in the electrochemical reduction by these Ni macrocycle species adsorbed on the surface of an Hg electrode in H_2O. Sakaki *et al.* carried out SCF ab initio calculations for $[NiF(NH_3)_4]^+$ as the model of [Ni(cyclam)]$^+$ adsorbed on Hg (Fig. 5), and a Ni^I–η^1–CO_2 adduct with an OCO angle of 135.3° is suggested as the active species during CO_2 reduction (*66, 67*). The increase in electron density of an O-atom of the terminal CO_2 from $-0.33e$ (free CO_2) to $-0.58e$ upon coordination to Ni^I supports the proposed mechanism for the catalytic cycle involving an hydroxycarbonyl intermediate.

1. Reduction of CO_2 under Aprotic Conditions

Thermally labile $[W(CO)_5(\eta^1\text{–}CO_2)]^{2-}$ undergoes an oxide-abstraction reaction by CO_2 to produce $[W(CO)_6]$ (*68*) at room temperature:

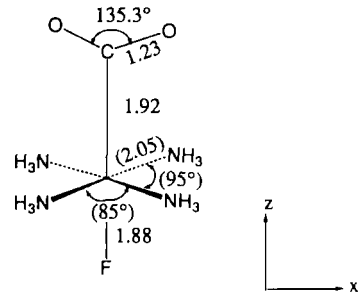

FIG. 5. Molecular structure including bond lengths (Å) of $Ni^{I}F(NH_3)_4(\eta^1\text{–}CO_2)$ as determined by SCF ab initio MO calculations.

$$[W(CO)_5(CO_2)]^{2-} + CO_2 \rightarrow [W(CO)_6] + CO_3^{2-}. \quad (13)$$

A number of examples in which CO and CO_3^{2-} formation occurs (reductive disproportionation reaction of CO_2) are reported in the electrochemical reduction of CO_2 in organic solvents. In connection with this, the reaction of $[Ir(C_8H_{14})Cl(PMe_3)_3]$ with CO_2 affords a product $[IrCl(C_2O_4)(PMe_3)_3]$ (*69*), in which two CO_2 molecules are condensed in a unique fashion (Fig. 6). The adduct might be as the suitable model for the disporprotionation reaction of CO_2. Alternatively, the η^1–CO_2 moiety with a high electron density would undergo direct oxide abstraction by CO_2 dissolved in solutions without changing the coordination numbers of the complex. A Co macrocycle complex, [Co(Me$_6$[14]4,11-diene)]$^+$, reversibly binds CO_2 with the binding constant $1.2 \times 10^4\ M^{-1}$ in CH_3CN at 298 K. The disappearance of $[CoL(CO_2)]^+$ follows second-order kinetics ($-d[CoL(CO_2)^+]/dt = k[CoL(CO_2)^+]^2$; $k = 1.0 \times 10^{-3}\ M^{-1}\ s^{-1}$) with generation of CO and HCO_3^-. The reaction may involve a binuclear intermediate, since a dimeric bridged OCO moiety can be isolated from the reaction mixture (*45*).

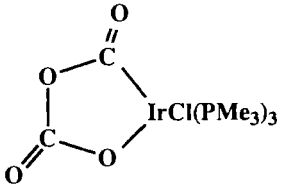

FIG. 6. X-ray structure of the product $IrCl(C_2O_4)(PMe_3)_3]$.

2. Oxalic Acid Formation

Oxalate is produced in the uncatalyzed electrochemical reduction of CO_2 at electrode surfaces in dry conditions:

$$2CO_2 + 2e^- \rightarrow C_2O_4^{2-}. \quad (14)$$

In the case in which reduction of CO_2 is catalyzed by metal complexes in anhydrous conditions, a reductive disproportionate reaction of CO_2 takes place preferentially, and oxalate formation does not appear to be favorable in homogeneous systems. Becker *et al.* have reported that silver and palladium octaethylporphyrin complexes catalyze the oxalate formation in the electrochemical reduction of CO_2 in CH_2Cl_2, but the selectivity and the yields are not clear (*70*). Recently, selective oxalate formation has been achieved in the electrochemical CO_2 reduction by $[(RhCp^*)_3(\mu_3\text{-}S)_2]^{2+}$ at -1.50 V (vs SCE) in CH_3CN. Two strong bands (1680 and 1605 cm^{-1} assignable to $\nu(CO_2)$ appear in the IR spectra during CO_2 reduction in CD_3CN, and the oxidation of the solution regenerates $[(RhCp^*)_3(\mu_3\text{–}S)_2]^{2+}$. A coupling reaction of two CO_2 molecules bonded on either two Rh or sulfur and Rh of $[(RhCp^*)_3(\mu_3\text{-}S)_2]^0$ is proposed for the active species giving rise to oxalate formation (*71*).

B. Photochemical CO_2 Reduction

In photochemical reduction of CO_2 by metal complexes, $[Ru(bpy)_3]^{2+}$ is widely used as a photosensitizer. The luminescent state of $[Ru(bpy)_3]^{2+*}$ is reductively quenched by various sacrificial electron donors to produce $[Ru(bpy)_3]^+$. Metal complexes used as catalyst in the photochemical reduction of CO_2 using $[Ru(bpy)_3]^{2+}$ are prerequisites which are reduced at potentials more positive than that of the $[Ru(bpy)_3]^{+/2+}$ redox couple (-1.33 V vs SCE) (*72*). Irradiation with visible light of an aqueous solution containing $[Co^{II}(Me_4(14)\text{-}4,11\text{-}dieneN_4)]^{2+}$, $[Ru(bpy)_3]^{2+}$, and ascorbic acid at pH 4.0 produces CO and H_2 with a mole ratio of 0.27 : 1 (*73*). Similarly, photochemical reduction of CO_2 is catalyzed by the $[Ru(bpy)_3]^{2+}/[Ni(cyclam)]^{2+}$ system at pH 5.0 and also gives H_2 and CO. However, the quantum efficiency of the latter is quite low (0.06% at $\lambda = 400$ nm), and the catalytic activity for the CO_2 reduction decreases to 25% after 4 h irradiation (*64, 74, 75*). This contrasts with the high activity for the electrochemical reduction of CO_2 by $[Ni(cyclam)]^{2+}$ adsorbed on Hg.

Kimura *et al.* have prepared bifunctional complexes $[Ru(bpy)_2(bpy\text{-}cyclam\text{-}Ni)]^{4+}$ and $[Ru(phen)_2(phen\text{-}cyclam\text{-}Ni)]^{4+}$, in which the reac-

tion site and photosensitizer are covalently bonded (*76, 77*). The catalytic activity of $[Ru(bpy)_2(bpy\text{-}cyclam\text{-}Ni)]^{4+}$ for the photochemical

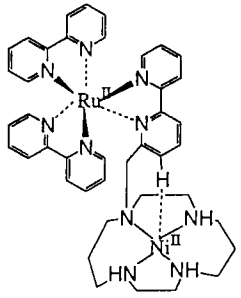

$[Ru(bpy)_2(bpy\text{-}cyclam\text{-}Ni)]^{4+}$

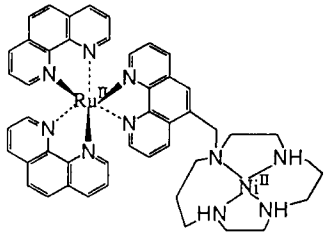

$[Ru(phen)_2(phen\text{-}cyclam\text{-}Ni)]^{4+}$

reduction of CO_2 is not so high, and the $Ru(bpy)_3$ unit dissociates under irradiation because of the steric congestion of the two sites. On the other hand, $[Ru(phen)_2(phen\text{-}cyclam\text{-}Ni)]^{4+}$ shows a high stability compared with the reference system composed of $[Ru(phen)_3]^{2+}$ and $[Ni(cyclam)]^{2+}$ under irradiation with visible light. Irradiation of $[Ru(phen)_2(phen\text{-}cyclam\text{-}Ni)]^{4+}$ in CO_2-saturated ascorbate buffer solution (pH 4.0) at 25°C for 4 h produces almost identical amounts of CO and H_2 as the reference system. Thereafter, $[Ru(phen)_2(phen\text{-}cyclam\text{-}Ni)]^{4+}$ retains its activity for CO generation and 44 h after irradiation has generated about 3 molar equivalent of CO as compared with the reference system.

Irradiation by visible light of a catalytic system composed of $[Ru(bpy)_3]^{2+}/[Ru(bpy)_2(CO)_2]^{2+}$ in DMF/TEOA (4 : 1 v/v) (TEOA: triethanolamine) selectively produced HCOOH with the quantum yield (ϕ) of 14% under CO_2 atmosphere. On the other hand, both CO and HCOOH are produced with ϕ = 14.8 and 2.7%, respectively, in the photoirradiation of the same system in H_2O/DMF (3 : 7 v/v) solutions containing BNAH (1-benzyl-1,4-dihydronicotinamide) (0.1 M) as a sacrificial electron donor. The change in the main product from HCOOH to CO depending on the proton concentrations in DMF/TEOA and DMF/H_2O appears to uphold the validity of the mechanism of Scheme 4 in the photochemical reduction of CO_2 by $[Ru(bpy)_2(CO)_2]^{2+}$. Irradiation of $[Ru(pby)_3]^{2+}$ in DMF/TEOA also produces HCOOH due to the partial decomposition of the complex under conditions leading to the photochemical reduction of CO_2 (*78–80*). Furthermore, the catalytic system composed of $[Ru(bpy)_3]^{2+}/[Ru(bpy)_2(CO)H]^+$ has almost the same activity for the photochemical reduction of CO_2 as the $[Ru(bpy)_3]^{2+}/[Ru(bpy)_2(CO)_2]^{2+}$ system (*81*). Both $[Ru(bpy)_2(CO)(C(O)OH)]^+$ (Scheme 4) and $[Ru(bpy)_2(CO)(OC(O)H)]^+$ formed by CO_2 insertion into

$[Ru(bpy)_2(CO)H]^0$ [Eqs. (11) and (12)] may operate for photochemical formate generation.

The most notable catalyst in the photochemical reduction of CO_2 is $[ReCl(bpy)(CO)_3]$ and its derivatives because of their bifunctional ability as phosensitizer and catalyst in the photoreduction of CO_2 to CO (*82*). In the case of the anionic complex $[ReX(CO)_3(bpy)]^-$, an active precursor is formed upon irradiation of $[ReX(CO)_3(bpy)]$ in the presence of electron donors such as TEOA, TEA, and BNAH (*83*). The 19-electron intermediate is thought to dissociate CO, followed by another electron transfer along with the addition of CO_2 to the resulting pentacoordinate species to give $[ReX(bpy)(CO)_2(CO_2)]^-$ (*84*). However, CO_2 addition to other pentacoordinated species formed by either Cl^- dissociation or dechelation of the bpy ligand is not completely excluded. Recently, a quite high quantum yield of CO (ϕ = 23–30% at 365 nm) was achieved in the photochemical reduction of CO_2 by $[Re(CO)_2(bpy)(P(OEt)_3)]^+$ in TEOA/DMF (*84*).

V. Multi-electron Reduction of CO_2

Discovery of the formation of highly reduced species such as CH_4, CH_2CH_2, C_2H_5OH, and C_3H_7OH in the electrochemical reduction CO_2 of a Cu electrode in H_2O (*85*) has given an impetus to the multi-electron reduction of CO_2 on solid electrodes. On the other hand, most reduction products in CO_2 reduction catalyzed by metal complexes are either CO and/or HCOOH. Calculated reduction potentials E^0 (vs SCE) for the multi-electron reduction of CO_2 at pH 7.0 are as follows (*86*):

$$CO_2 + 2H^+ + 2e^- \rightarrow HCOOH, \qquad E^0 = -0.85\ V,$$

$$CO_2 + 2H^+ + 2e^- \rightarrow CO + H_2O, \qquad E^0 = -0.76\ V,$$

$$CO_2 + 4H^+ + 4e^- \rightarrow HCHO + H_2O, \qquad E^0 = -0.72\ V,$$

$$CO_2 + 6H^+ + 6e^- \rightarrow CH_3OH + H_2O, \qquad E^0 = -0.62\ V,$$

$$CO_2 + 8H^+ + 8e^- \rightarrow CH_4 + 2H_2O, \qquad E^0 = -0.48\ V.$$

The positive potential shift of the E^0 values with increasing number of electrons indicates that multi-electron reduction of CO_2 is energetically favored compared with two-electron reduction of CO_2. Assuming that transformation of CO_2 to CO proceeds via metal-carbonyl species, the strategy for the multi-electron reduction of CO_2 by metal complexes is

to reduce the carbonyl ligand prior to the metal–carbon bond cleavage. Some of metal carbonyl complexes are reduced to formyl and hydroxymethyl and methyl derivatives successively, depending on conditions, by hydride donors such as $NaBH_4$ and metal-hydrides (*87–89*):

$$M\text{-}CO \rightarrow M\text{–}CHO \rightarrow M\text{–}CH_2OH \rightarrow M\text{–}CH_3. \quad (15)$$

Treatment of $[Ru(bpy)_2(CO)_2]^{2+}$ and $[Ru(bpy)(trpy)(CO)]^{2+}$ (trpy = 2,2′:6′,2″-terpyridine) with 4 moles of $NaBH_4$ in CH_3CN/H_2O at −20°C produces CH_3OH in yields of 10 and 100%, respectively, and $[Ru(bpy)_2(CO)(CHO)]^+$ and $[Ru(bpy)_2(CO)(CH_2OH)]^+$ are isolated as the intermediates. The electrochemical reduction of CO_2 by $[Ru(bpy)_2(CO)_2]^{2+}$ at −1.40 V vs SCE in C_2H_5OH/H_2O (8:2 v/v) at −20°C produces only CO and HCOOH, while reduction of CO_2 by $[Ru(bpy)(trpy)(CO)](PF_6)_2$ under the same conditions gives not only CO and $HCOO^-$, but also HC(O)H, CH_3OH, H(O)CCOOH, and $HOCH_2COOH$:

$$n CO_2 \xrightarrow[-1.50\ V\ in\ EtOH/H_2O]{[Ru(bpy)(trpy)(CO)]^{2+}} HCOOH + CO + HCHO + CH_3OH + HOOCCHO + HOOCCH_2OH. \quad (16)$$

The difference in $[Ru(bpy)(trpy)(CO)]^{2+}$ and $[Ru(bpy)_2(CO)_2]^{2+}$ toward the multi-electron reduction of CO_2 is ascribed to the stability of $[Ru(bpy)(trpy)(CO)]^0$ at that temperature, while $[Ru(bpy)_2(CO)_2]^0$ decomposes even at −40°C. The reaction of $[Ru(bpy)(trpy)(CO)]^0$ with H_2O at −30°C produces the formyl complex, presumably through a hydroxycarbyne intermediate formed by protonation of the carbonyl oxygen:

$$[L_1L_2Ru\text{–}CO]^0 \xrightarrow{H^+} [L_1L_2Ru\text{–}COH]^+ \rightarrow [L_1L_2Ru\text{–}CHO]^+, \quad (17)$$

L_1 = bpy, L_2 = trpy.

The proposed catalytic cycle of the multi-electron reduction of CO_2 by $[Ru(bpy)(trpy)(CO)]^{2+}$ is represented in Scheme 6. The reaction path affording CO and HCOOH is same as that by $[Ru(bpy)_2(CO)_2]^{2+}$ (Scheme 4). Thermally labile $[Ru(bpy)(trpy)(CHO)]^+$ produced in Eq. (17) is further reduced to $[Ru(bpy)(trpy)(CH_2OH)]^+$, which serves as precursor to HCHO and CH_3OH. Carboxylation of those intermediates under the electrolysis conditions would produce HOOCCHO and $HOOCCH_2OH$, respectively (*41*).

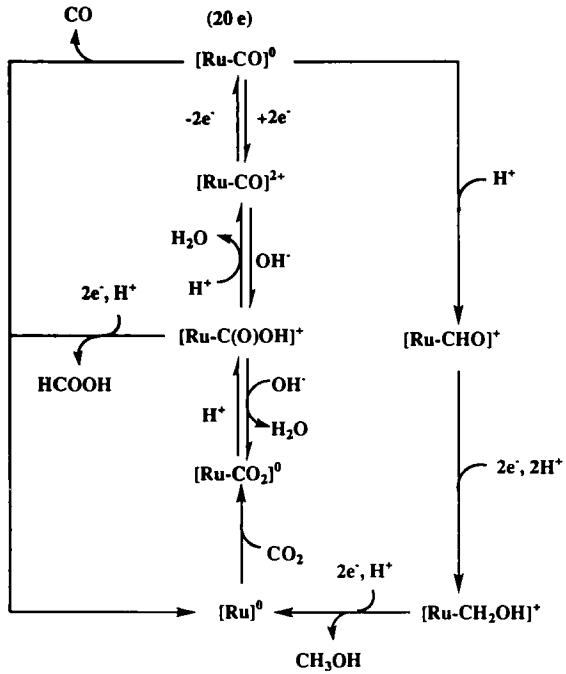

SCHEME 6. Proposed mechanism for multi-electron reduction of CO_2 catalyzed by $[Ru(bpy)(trpy)(CO)]^{2+}$.

VI. Reaction Modeling of Biological CO_2 Fixation

Most CO_2 assimilation takes place at α- and β-carbons of carbonyl groups of organic molecules to give α-hydroxy-, α-keto, and β-keto acids (*90, 91*). There has been no report of α-hydroxyketo acid formation by artificial CO_2 fixation with the intention to mimic CO_2 assimilation in green plants, in which two moles of 3-phosphoglycerate (PGA) are produced by CO_2 fixation to ribulose-1,5-bisphosphate(RuDP):

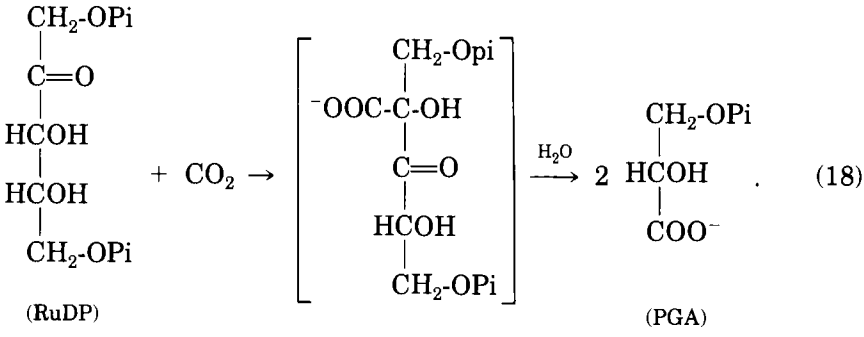

(18)

Pi = phosphate

In the reductive carboxylic acid cycle of photosynthetic bacteria (*92–94*), which plays a role in the conversion of CO_2 to precursors of fatty acids, amino acids, and porphyrins, four molecules of CO_2 are fixed in one turn; two of them are fixed to α-carbons of carbonyl groups of acetylcoenzyme A and succinyl-coenzyme A to generate pyruvate and α-keto glutarate, respectively:

$$RC(O)SCoA + CO_2 + 2e^- \rightarrow RC(O)COO^- + CoAS^- \qquad (19)$$

(R = CH_3, CH_2CH_2; CoA = coenzyme A).

The other two CO_2 are introduced to β-carbons of the carbonyl groups of α-keto glutarate and pyruvate to produce isocitrate and oxalacetate, respectively:

$$RCH_2C(O)COOH + CO_2 \rightarrow RCH(COOH)C(O)COOH \qquad (20)$$

(R = CH_2COOH, CH_3).

These two cases will be considered.

A. α-Keto Acid Formation

Tabushi *et al.* found that the reaction of $C_6H_5CH_2C(O)SC_8H_{17}$ with CO_2 in the presence of $[Fe(S_2C_2Ph_2)_2]_2^{2-}$ and $Na_2S_2O_4$ produces a small amount of $C_6H_5CH_2C(O)COO^-$ in H_2O (*95*):

$$C_6H_5CH_2C(O)SC_8H_{17} + CO_2 + 2e^- \xrightarrow{-C_8H_{17}S^-} C_6H_5CH_2C(O)COO^-. \qquad (21)$$

This is the first α-keto acid formation by nonenzymatic CO_2 fixation to thioesters as a model of RC(O)SCoA. The mechanism of the reactions [Eqs. (19) and (20)] is of interest from the viewpoint of the introduction of CO_2 to the positively polarized carbonyl carbon of a thioester.

Photochemically generated reduced ferredoxins can function as electron donors in CO_2 assimilation [Eq. (19)]. In aqueous micellar solutions, the reduction potentials for the $[Fe_4S_4(SC_6H_4C_8H_{17})_4]^{2-/3-}$ and $[Mo_2Fe_6S_8(SEt)_3(SC_6H_4C_8H_{17})_6]^{3-/5-}$ couples are shifted by -60 mV/pH and -30 mV/pH because of reversible protonation of the reduced forms (*96, 97*). Protonation of $[Fe_4X_4(YC_6H_4C_4H_9)_4]^{3-}$ (X, Y = S, Se) is demonstrated to take place on core sulfur and selenium from the pH-dependent reduction potentials of the clusters in aqueous micellar solutions (*96*), and the pK_a values of protonated $[Fe_4S_4(SC_6H_4C_nH_{2n+1})_4]^{3-}$ and $[Mo_2Fe_6S_8(SEt)_3(SC_6H_4C_nH_{2n+1})_6]^{5-}$ (n = 4–12) are determined to be $\approx$9.0 and $\approx$11, respectively (*97*). The difference in basicity of the cluster

compounds shows an interesting reactivity to CO_2; $[Mo_2Fe_6S_8(SEt)_9]^{5-}$ reversibly reacts with CO_2 to form an adduct in dry CH_3CN, while $[Fe_4S_4(SEt)_4]^{3-}$ has no interaction with CO_2 in the same solvent. Furthermore, $[Mo_2Fe_6S_8(SEt)_9]^{3-}$ catalyzes CO_2 fixation to RC(O)SEt (R = CH_3, C_2H_5, and C_6H_5) to produce $RC(O)COO^-$ with current efficiencies of 27 (CH_3), 49 (C_2H_5), and 13% (C_6H_5) under controlled potential electrolysis at −1.50 V vs SCE in CH_3CN (*98*):

$$RC(O)SEt + CO_2 + 2e^- \rightarrow RC(O)COO^- + EtS^-, \quad (22)$$

$$R = CH_3, C_2H_5, \text{and } C_6H_5.$$

Thioesters as a model of RC(O)SCoA [Eq. (19)] have a special meaning in α-keto acid formation [Eq. (22)], since strong acylating agents such as acetyl chloride, acetic anhydride, acetyl sulfide, and acetylimidazole readily decompose $[Mo_2Fe_6S_8(SEt)_9]^{3-}$ during electrolysis. Although the reaction is essentially same as the CO_2 fixation by pyruvate synthase [Eq. (18)], $RC(O)COO^-$ formation practically stops after 6 mol of EtS^- are liberated from RC(O)SEt in the reaction. Free EtS^- does not block CO_2 adduct formation with $[Mo_2Fe_6S_8(SEt)_9]^{5-}$, but strongly interferes with α-keto acid formation. An electrophilic attack by CO_2 on the core sulfur of $[Mo_2Fe_6S_8(SEt)_9]^{5-}$ and the subsequent substitution of EtS^- ligated on Fe by RC(O)SEt is proposed as the active species for the reaction (Scheme 7). The carbon–carbon bond formation is explained by the intramolecular addition of reductively activated CO_2 on sulfur to the carbonyl carbon of RC(O)SEt ligated on Fe.

B. β-Keto Acid Formation

Although $[Fe_4S_4(SR)_4]^{3-}$ does not show any interaction with CO_2, presumably because of the low basicity of the core sulfur ($pK_a \approx 9$), controlled potential electrolysis of CO_2-saturated DMF solutions containing $[Fe_4S_4(SR)_4]^{2-}$ (R = Et, CH_2Ph), Bu_4N^+, and $PhC(O)CH_3$ at −2.0 V vs SCE produces formic acid in DMF (*99*) and $C_6H_5C(O)CH_2COO^-$ in CH_3CN (*100*):

$$(C_4H_9)_4N^+ + CO_2 + 2e^- \rightarrow HCOO^- + CH_2{=}CHC_2H_5 + (C_4H_9)_3N, \quad (23)$$

$$C_6H_5C(O)CH_3 + 2CO_2 + 2e^- \rightarrow C_6H_5C(O)CH_2COO^- + HCOO^-. \quad (24)$$

The role of $[Fe_4S_4(SR)_4]^{2-}$ in these reactions remains unclear, however, because of the extremely labile nature of $[Fe_4S_4(SR)_4]^{4-}$, which would

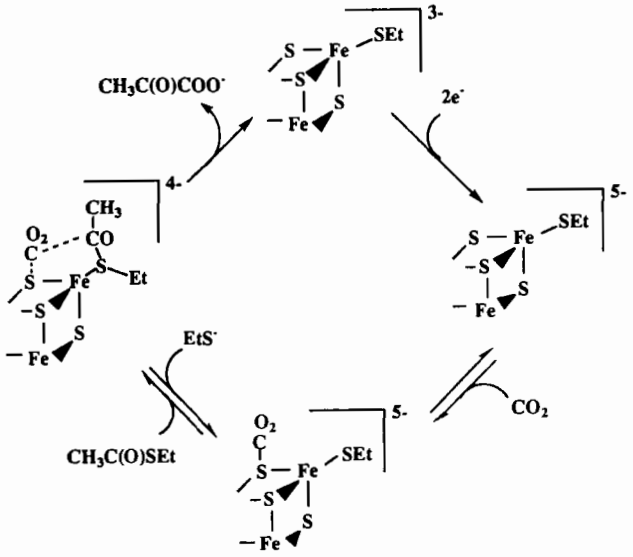

SCHEME 7. Proposed catalitic cycle for α-keto acid formation.

be produced under the electrolysis conditions. On the other hand, $[Fe_4S_4(SPh)_4]^{3-}$ can function as active catalyst for carboxylation of ketones in the presence of nitrite, where the latter reversibly binds to Fe of $[Fe_4S_4(SPh)_4]^{3-}$, forming the nitro adduct:

$$[Fe_4S_4(SPh)_4]^{3-} + NO_2^- \rightleftharpoons [Fe_4S_4(SPh)_3(NO_2)]^{3-} + SPh^-. \quad (25)$$

The controlled-potential electrolysis of $[Fe_4S_4(SPh)_4]^{2-}$ in CH_3CN in the presence of $PhC(O)CH_3$ and NO_2^- at −1.25 V vs SCE produces $PhC(O)CH_2COO^-$, N_2, and N_2O with current efficiencies of 78, 70, and 6.6%, respectively (*100*):

$$2NO_2^- + 8RCOCH_3 + 8CO_2 + 6e^- \rightarrow N_2 + 8RCOCH_2COO^- + 4H_2O. \quad (26)$$

The reaction proceeds continuously until one of the substrates is consumed. The reduction of NO_2^- to N_2 by $[Fe_4S_4(SPh)_4]^{3-}$ has been shown to proceed via NO^-, $N_2O_2^{2-}$, and N_2O:

$$2NO_2^- \xrightarrow[-2H_2O]{4H^+,4e^-} 2NO^- \rightleftharpoons N_2O_2^{2-} \xrightarrow[-H_2O]{2H^+} N_2O \xrightarrow[-H_2O]{2H^+,2e^-} N_2. \quad (27)$$

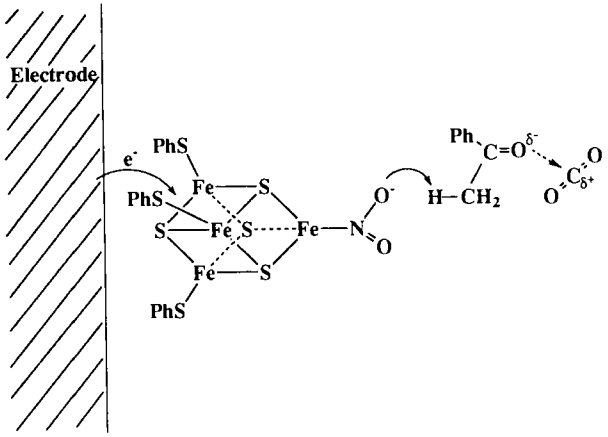

FIG. 7. Proposed species of the rate-determining step in CO_2 fixation coupled with NO_2^- reduction.

The eight protons which are required for the NO_2^- reduction are provided by eight molecules of $PhC(O)CH_3$, and the reaction of the resulting $PhC(O)CH_2^-$ with CO_2 generates eight molecules of $PhC(O)CH_2COO^-$. The rate of the reaction in Eq. (27) is first-order in concentration of $[Fe_4S_4(SPh)_4]^{3-}$, CO_2, NO_2^-, and $PhC(O)CH_3$. Carbon dioxide–assisted reduction of NO_2^- on the Fe_4S_4 cluster is proposed as the rate-determining step for the reaction of Eq. (25) (Fig. 7). The carboxylation coupled with nitrite reduction is applicable to organic molecules with acidic hydrogens of pK_a less than around 20.

Inoue *et al.* have developed photochemical carboxylation of ketones by the virtue of photo-enhanced nucleophilic reactivities of aluminum porphyrin complexes. Treatment of $[(TPP)AlNEt_2]$ with aromatic ketones produces the corresponding porphinatoaluminum enolate products,

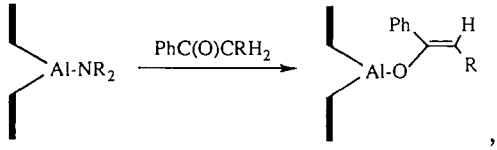

(28)

which react smoothly with CO_2 in the presence of *N*-methylimidazole to afford the corresponding β-ketocarboxylato complex on photo-irradiation with visible light (*101*):

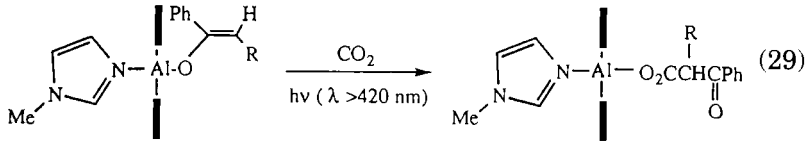

(29)

Although the carboxylation of the enol adduct of the aromatic ketones [Eqs. (28) and (29)] is a stoichiometric reaction, these reactions are related to biological CO_2 fixation, where the phosphoenolpyruvate product from pyruvate is carboxylated into oxaloacetate:

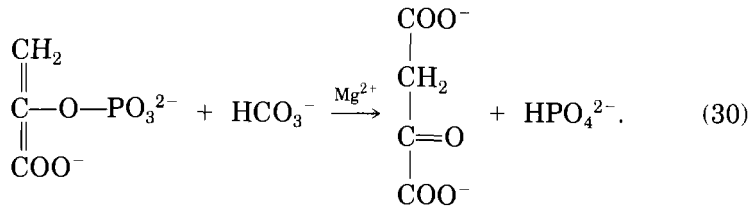

(30)

The keto–enol conversion on aluminum porphyrin is applied to catalytic CO_2 fixation forming malonate species (*102*). Photo-irradiation of benzene solutions containing methacrylic esters or methacrylonitrile, (TPP)AlEt, and diethylzinc under CO_2 catalytically produces the malonate species. The catalytic cycle of Scheme 8 is composed of three elementary reactions: generation of aluminum enolate by 1,4-addition

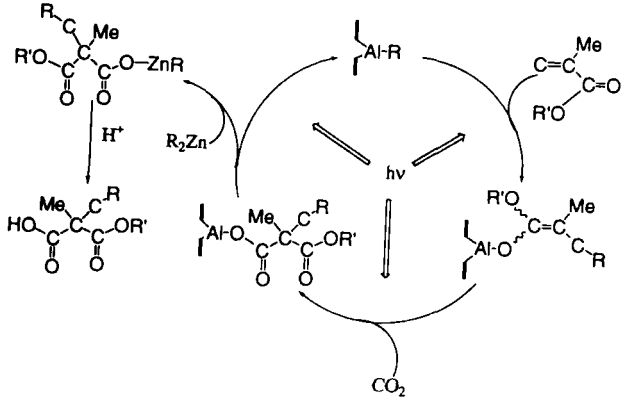

SCHEME 8. Photocatalytic conversion from methacrylic esters to malonate species.

of the Al–Et bond to methacrylate; aluminum malonate formation by an electrophilic attack of CO_2 on the enolate species; and regeneration of the Al–Et bond, liberating zinc malonate. The striking feature of the catalytic cycle is that all the elementary steps are accelerated by photo-irradiation.

List of Abbreviations

BNAH	1-benzyl-1,4-dihydronicotinamide
bpy	2,2′-bipyridine
dmpe	1,2-bis(dimethylphosphino)ethane
CoA	coenzyme A
Cy	cyclohexyl
Cp	cyclopentadienyl
DMF	*N*,*N*-dimethylformamide
DMC	*C-meso*-5,12-dimethyl-1,4,8,11-tetraazacyclotetradecane
Me_2[14]1,3-diene	2,3-dimethyl-1,4,8,11-tetraazacyclotetradecane-1,3-diene
Me_2[14]4,11-diene	5,12-dimethyl-1,4,8,11-tetraazacyclotetradecane-4,11-diene
salen	*N*,*N*′-disalicylideneethylenediamine
en	ethylenediamine
Me_6[14]4,11-diene	5,7,7,12,14,14-hexamethyl-1,4,8,11-tetraazacyclotetradecane-4,11-diene
Me_8[14]4,11-diene	3,5,7,7,10,12,14,14-octamethyl-1,4,8,11-tetraazacyclotetradecane-4,11-diene
Cp*	pentamethylcyclopentadienyl
phen	1,10-phenanthroline
diars	*o*-phenylenebis(dimethylarsine)
SCE	standard calomel electrode
trpy	2,2′:6′,2″-terpyridine
cyclam	1,4,8,11-tetraazacyclotetradecane
HTIM	2,3,9,10-tetramethyl-1,4,8,11-tetraazacyclotetradecane
TPP	5,10,15,20-tetraphenylporphyrinato
TEOA	triethanolamine
TEA	triethylamine

References

1. Darensbourg, D.; Kudaroski, R. A. *Adv. Organomet. Chem.* **1987,** *22,* 129.
2. Behr, A. *Angew. Chem., Int. Ed. Engl.* **1988,** *27,* 661.
3. Inoue, Y.; Sasaki, Y.; Hashimoto, H. *Bull. Chem. Soc. Jpn.* **1978,** *51,* 2375.
4. Musco, A.; Perego, C.; Tartari, V. *Inorg. Chim. Acta.* **1978,** *28,* L147.
5. Braunstein, P.; Matt, D.; Nobel, D. *J. Am. Chem. Soc.* **1988,** *110,* 3207.
6. Inoue, Y.; Hibi, T.; Satake, M.; Hashimoto, H. *J. Chem. Soc., Chem. Commun.* **1979,** 982.
7. Binerg, P.; Weintz, H-J. *Chem. Ber.* **1984,** *117,* 654.
8. Döhring, A.; Jolly, P. W. *Tetrahedron Lett.* **1980,** *21,* 3021.

9. Aresta, M.; Quaranta, E.; Ciccarese, A. C_1 *Mol. Chem.* **1985,** *1,* 293.
10. Inoue, Y.; Itoh, Y.; Hashimoto, H. *Chem. Lett.* **1977,** 855.
11. Inoue, Y.; Itoh, Y.; Hashimoto, H. *Chem. Lett.* **1978,** 633.
12. Inoue, Y.; Itoh, Y.; Kazama, H.; Hashimoto, H. *Bull. Chem. Soc. Jpn.* **1980,** *53,* 3329.
13. Walther, D.; Schönberg, H.; Dinjus, E.; Sieler, J. *J. Organomet. Chem.* **1987,** *334,* 377.
14. Tsuda, T.; Morikawa, S.; Sumiya, R.; Saegusa, T. *J. Org. Chem.* **1988,** *53,* 3140.
15. Tsuda, T.; Morikawa, S.; Saegusa, T. *J. Chem. Soc., Chem. Commun.* **1989,** 9.
16. Hoberg, H. *Carbon Dioxide as a Source of Carbon,* NATO ASI Series C, **1987,** *206,* 275.
17. Aresta, M.; Nobile, C. F.; Aibano, V. G.; Forni, E.; Manassero, M. *J. Chem. Soc., Chem. Commun.,* **1975,** 636.
18. Fachinetti, G.; Floriani, C.; Zanazzi, P. F. *J. Am. Chem. Soc.* **1978,** *100,* 7405.
19. Calabrese, J. C.; Herskovitz, T.; Kinney, J. B. *J. Am. Chem. Soc.* **1983,** *105,* 5914.
20. Gambarotta, S.; Arena, F.; Floriani, C.; Zanazzi, P. F. *J. Am. Chem. Soc.* **1982,** *104,* 5082.
21. Herskoviz, T. *Inorg. Synth.* **1982,** *21,* 99.
22. Lee, G. R.; Maher, J. M.; Cooper, N. J. *J. Am. Chem. Soc.* **1987,** *109,* 2956.
23. Fujita, E.; Creutz, C.; Sutin, N.; Brunschwig, B. S. *Inorg. Chem* **1993,** *32,* 2657.
24. Giuseppetti, M. E.; Cutler, A. R. *Organometallics* **1987,** *6,* 970.
25. Tanaka, H.; Tzeng, B.-C.; Nagao, H.; Peng, S.-M.; Tanaka, K. *Inorg. Chem.* **1993,** *32,* 1508.
26. Alvarez, R.; Carmona, E.; Marin, J. M.; Poveda, M. L.; Gutierrez-Puebla, E.; Monge, A. *J. Am. Chem. Soc.* **1986,** *108,* 2286.
27. Bristow, G. S.; Hitchcock, P. B.; Lappert, M. F. *J. Chem. Soc., Chem. Commun.* **1981,** 1145.
28. Jegat, C.; Mascetti, J. *New J. Chem.* **1991,** *15,* 17.
29. Jegat, C.; Fouasier, M.; Mascetti, J. *Inorg. Chem.* **1991,** *30,* 1521.
30. Jegat, C.; Fouasier, M.; Tranquille, M.; Mascetti, J. *Inorg. Chem.* **1991,** *30,* 1529.
31. John, G. R.; Johnson, B. F. G.; Lewis, J.; Wong, K. C. *J. Organomet. Chem.* **1979,** *169,* C23.
32. Eady, C. R.; Guy, J. J.; Johnson, B. F. G.; Lewis, J.; Malatesta, M. C.; Sheldrick, G. M. *J. Chem. Soc., Chem. Commun.* **1976,** 602.
33. Beck, W.; Raab, K.; Nagel, U.; Steimann, M. *Angew. Chem., Int. Ed. Engl.* **1982,** *115,* 2271.
34. Lundquist, E. G.; Huffman, J. C.; Folting, K.; Mann, B. E.l Caulton, K. G. *Inorg. Chem.* **1990,** *29,* 128.
35. Ishida, H; Tanaka, K.; Morimoto, M.; Tanaka, T. *Organometallics* **1986,** *5,* 724.
36. Bennett, M. A.; Robertson, G. B.; Rokicki, A.; Wickramasinghe, W. *J. Am. Chem. Soc.* **1988,** *110,* 7098.
37. Katz, N.; Szalda, D. J.; Chou, M. H.; Creutz, C.; Sutin, N. *J. Am. Chem. Soc.* **1988,** *110,* 6591.
38. Creutz, C.; Schwarz, H. A.; Wishart, J. F.; Fujita, E.; Sutin, N. *J. Am. Chem. Soc.* **1989,** *111,* 1153.
39. Sweet, J. R.; Graham, W. A. G. *Organometallics* **1982,** *1,* 982.
40. Bercaw, J. E.; Goh, L.-Y.; Halpern, J. *J. Am. Chem. Soc.* **1972,** *94,* 6534.
41. Nagao, H.; Mizukawa, T.; Tanaka, K. *Inorg. Chem.* **1994,** *33,* 3415.
42. Sakaki, S.; Aizawa, T.; Koga, N.; Morokuma, K.; Ohkubo, K. *Inorg. Chem.* **1989,** *28,* 103.
43. Sakaki, S., personal communication.

44. Goldstein, S.; Czapski, G.; Cohen, H.; Meyerstein, D. *J. Am. Chem. Soc.* **1988,** *110,* 3903.
45. Fujita, E.; Szalda, D. J.; Creutz, C.; Sutin, N. *J. Am. Chem. Soc.* **1988,** *110,* 4870.
46. Gangi, D. A.; Durand, R. R. *J. Chem. Soc., Chem. Commun.* **1986,** 697.
47. Schmidt, M. H.; Miskelly, G. M.; Lewis, N. S. *J. Am. Chem. Soc.* **1990,** *112,* 3420.
48. Bard, A. J.; Faulkner, L. R. "Electrochemical Methods and Applications"; Wiley: New York, 1980.
49. Nicholson, R. S.; Shain, I. *Anal. Chem.* **1964,** *36,* 706.
50. O'Dea, J. J.; Osteryoung, J.; Osteryoung, R. A. *Anal. Chem.* **1981,** *53,* 695.
51. Pacansky, J.; Wahlgren, V.; Bagus, P. S. *J. Chem. Phys.* **1975,** *62,* 2740.
52. Grice, N.; Kao, S. C.; Pettit, R. *J. Am. Chem. Soc.* **1979,** *101,* 1627.
53. Bowman, K.; Deeming, A. J.; Proud, G. P. *J. Chem. Soc., Dalton Trans.* **1985,** 857.
54. Forschner, T.; Menard, K.; Cutler, A. *J. Chem. Soc., Chem. Commun.* **1984,** 121.
55. Tanaka, K.; Morimoto, M.; Tanaka, K. *Chem. Lett.* **1983,** 901.
56. Casey, C. P.; Andrews, M. A.; Rinz, J. E. *J. Am. Chem. Soc.* **1979,** *101,* 741.
57. Ford, P. C. In "Electrochemical and Electrocatalytic Reactions of Carbon Dioxide"; Sullivan, B. P.; Krist, K.; Guard, H. E., Eds.; Elsevier: Amsterdam/New York, 1993; pp. 68–93.
58. King, A. D., Jr.; King, R. B.; Yang, D. B. *J. Am. Chem. Soc.* **1980,** *102,* 1028.
59. Mahajan, P.; Creutz, C.; Sutin, N. *Inorg. Chem.* **1985,** *24,* 2063.
60. Ishida, H.; Tanaka, K.; Tanaka, T. *Organometallics* **1987,** *6,* 181.
61. Ishida, H.; Tanaka, K.; Tanaka, T. *J. Chem. Soc., Chem. Commun.* **1987,** 131.
62. Pugh, J. R.; Bruce, M. R. M.; Sullivan, B. P.; Meyer, T. J. *Inorg. Chem.* **1991,** *30,* 86.
63. Chardon-Noblat, S.; Collomb-Dunand-Sauthier, M.-N.; Deronzier, A.; Ziessel, R.; Zsoldos, D. *Inorg. Chem.* **1994,** *33,* 4410.
64. Beley, M.; Collin, J.-P.; Ruppert, R.; Sauvage, J.-P. *J. Am. Chem. Soc.* **1986,** *106,* 7461.
65. Fujita, E.; Haff, J.; Sanzenbacher, R.; Elias, H. *Inorg. Chem.* **1994,** *33,* 4627.
66. Sakaki, S. *J. Am. Chem. Soc.* **1990,** *112,* 7813.
67. Sakaki, S. *J. Am. Chem. Soc.* **1992,** *114,* 2055.
68. Maher, J. M.; Lee, G. R.; Cooper, N. J. *J. Am. Chem. Soc.* **1982,** *104,* 6797.
69. Herskovitz, T.; Guggenberger, L. J. *J. Am. Chem. Soc.* **1976,** *98,* 1615.
70. Becker, J. Y.; Vainas, B.; Eger, R.; Kaufman, L. *J. Chem. Soc., Chem. Commun.* **1985,** 1471.
71. Kushi, Y.; Nagao, H.; Nishioka, T.; Isobe, K.; Tanaka, K. *Chem. Lett.* **1994,** 2175.
72. Kalyanasundaram, K. *Coord. Chem. Rev.* **1982,** *46,* 159.
73. Tinnemans, A. H. A.; Koster, T. P. M.; Thewissen, D. H. M. W.; Mackor, A. *Recl. Trav. Chim. Pays-Bas.* **1984,** *103,* 288.
74. Beley, M.; Collin, J.-P.; Ruppert, R.; Sauvage, J.-P. *J. Chem. Soc., Chem. Commun.* **1984,** 1315.
75. Collin, J.-P.; Jouaiti, A.; Sauvage, J.-P. *Inorg. Chem.* **1988,** *27,* 1990.
76. Kimura, E.; Wada, S.; Shionoya, M.; Takahashi, T.; Iitaka, Y. *J. Chem. Soc., Chem. Commun.* **1990,** 397.
77. Kimura, E.; Xianhe, B.; Shionoya, M.; Wada, S.; Maruyama, S. *Inorg. Chem.* **1992,** *31,* 4542.
78. Ishida, H.; Tanaka, K.; Tanaka, T. *Chem. Lett.* **1987,** 1035.
79. Ishida, H.; Tanaka, K.; Tanaka, T. *Chem. Lett.* **1988,** 339.
80. Ishida, H.; Terada, T.; Tanaka, K.; Tanaka, T. *Inorg. Chem.* **1990,** *29,* 905.
81. Lehn, J. M.; Ziessel, R. *J. Organomet. Chem.* **1990,** *382,* 157.
82. Kutal, C.; Corbin. A. J.; Ferraudi, G. *Organometallics* **1987,** *6,* 553.

84. Ishitani, O.; George, M. W.; Ibusuki, T.; Johnson, F. P. A.; Koike, K.; Nozaki, K.; Pac, C.; Turner, J. J.; Westwell, J. R. *Inorg. Chem.* **1994,** *33,* 4712.
85. Hori, Y.; Murata, A.; Takahashi, R.; Suzuki, S. *J. Chem. Soc., Chem. Commun.* **1988,** 17.
86. Ziessel, R. *Nouv. J. Chim.* **1983,** *7,* 613.
87. Treichel, P. M.; Schubhin, R. L. *Inorg. Chem.* **1967,** *6,* 1328.
88. Lapinte, C.; Astruc, D. *J. Chem. Soc., Chem. Commun.* **1983,** 430.
89. Lapinte, C.; Catheline, D.; Astruc, D. *Organometallics* **1988,** *7,* 1683.
90. Inoue, S.; Yamazaki, N., Ed.; "The Organic and Bioorganic Chemistry of Carbon Dioxide"; Halstead Press: New York, 1982.
91. Friedli, H.; Lotscher, H.; Siegenthaler, U.; Stauffer, B. *Nature (London),* **1986,** *324,* 237.
92. Edwards, G.; Walker, D. "C3, C4: Mechanisms, and Cellular and Environmental Redulation of Photosynthesis"; Blackwell Sci.: Oxford, 1983.
93. Taiz, L.; Zeiger, E. "Plant Physiology"; Benjamin–Cummings: Redwood City, California, 1991.
94. Lawlor, D. W. "Photosynthesis: Molecular, Physiological and Environmental Processes", 2nd ed.; Harlow Essex, 1993.
95. Nakajima, T.; Yabushita, Y.; Tabushi, I. *Nature (London),* **1975,** *256,* 60.
96. Tanaka, K.; Tanaka, T.; Kawafune, I. *Inorg. Chem.* **1984,** *23,* 516.
97. Tanaka, K.; Moriya, M.; Tanaka, T. *Inorg. Chem.* **1986,** *25,* 835.
98. Komeda, N.; Hagao, H.; Matusi, T.; Adachi, G.; Tanaka, K. *J. Am. Chem. Soc.* **1992,** *114,* 3625.
99. Tezuka, M.; Yajima, T.; Tsutuya, A.; Matsumoto, Y.; Uchida, Y.; Hidai, M. *J. Am Chem. Soc.* **1982,** *104,* 6835.
100. Tanaka, K.; Wakita, R.; Tanaka, T. *J. Am. Chem. Soc.* **1989,** *11,* 2428.
101. Hirai, Y.; Aida, T.; Inoue, S. *J. Am. Chem. Soc.* **1989,** *111,* 3062.
102. Komatsu, M.; Aida, T.; Inoue, S. *J. Am. Chem. Soc.* **1991,** *113,* 8492.

INDEX

R

S

CONTENTS OF PREVIOUS VOLUMES

VOLUME 36

VOLUME 37

VOLUME 38

VOLUME 42